Tectonic evolution of the Southern Ocean between Antarctica, South America and Africa over the past 84Ma

Thesis submitted for the degree of Doctor of Philosophy, Michaelmas 1997

by

Adrian P. Nankivell

Department of Earth Sciences

and

Worcester College

University of Oxford

1997



RADCLIFFE SCIENCE LIBRARY OXFORD
DEPOSITED
18 JUN 1998
THESIS

Supervisors: Dr. B. Parsons and Dr. R.A. Livermore (British Antarctic Survey)

"Out of life's school of war: What does not destroy me, makes me stronger."

Nietsche, Twilight of the Idols (1888)

Adrian P. Nankivell
Worcester College

Doctor of Philosophy
Michaelmas 1997

Tectonic evolution of the Southern Ocean between Antarctica, South America and Africa over the past 84Ma

Abstract

An improved method has been developed for carrying out 2-plate reconstructions, in which fracture zone locations are fitted to synthetic flowlines and magnetic anomaly picks are rotated and fitted to great circles representing other, not necessarily conjugate, anomaly isochrons. This enables the determination of finite rotation poles for regions with sparse data coverage, or where much of one or both plates has been subducted. Misfits and partial derivatives are calculated for each type of data, and combined in a single iterative inversion, allowing the direct calculation of confidence intervals. This method is then extended to a 3-plate reconstruction, taking closure into consideration.

The South American - African - Antarctic plate system is then studied. Fracture zone locations are identified from a gravity map constructed from GEOSAT altimeter data, and magnetic anomalies are identified from ship profiles. Two-plate reconstructions are carried out for each plate pair, giving good fits to the observed data, and then all three datasets are combined in a 3-plate reconstruction. Comparison of the results reveals a discontinuity in spreading in the Weddell Sea, believed to be related to pseudo-asymmetric spreading caused by ridge re-organisation in the Paleocene and early Eocene. A revised 3-plate inversion, taking this discontinuity into account, produces an internally consistent set of poles, indicating a closed 3-plate system since anomaly 34 (83Ma), with no evidence for a Malvinas Plate extending into the Weddell Sea in the Late Cretaceous. Disruption to the system from anomaly 32 (71Ma) until anomaly 24 (52Ma), appears to be related to the collision of Africa with Eurasia.

A study of the past motion, configuration and stability of the Bouvet Triple junction suggests that for the majority of the past 50Ma it has been in a RFF configuration, in theory considerably less stable than RRR, the other possible configuration.

Extended Abstract

In this thesis, improved methods for carrying out 2 and 3-plate reconstructions to determine finite rotation poles have been developed. Previous iterative inversion methods that incorporate both magnetic anomaly isochrons and fracture zone azimuths, such as that of Shaw & Cande (1990), have relied on fitting to conjugate magnetic isochrons. In regions where some or all of one plate has been subducted, then conjugate isochrons do not always exist, and so conjugate fitting is not possible. A 2-plate reconstruction method has been developed that fits magnetic anomaly picks to their conjugate isochrons wherever possible, or to non-conjugate isochrons where this is necessitated through poor data coverage or lack of a corresponding region on the opposing plate. Fracture zone location picks are fitted to synthetic flowlines generated from a reference seed point determined at some point along the fracture zone, and in addition, transform fault locations are fitted to small circles of the current pole of motion.

For each type of data, a misfit is defined which gives a measure of how well the current set of poles fits the data. Partial derivatives are calculated which determine the change in misfit with respect to changes in each of the inversion pole parameters. The misfits and partial derivatives for the three datasets are then incorporated into a single least squares inversion which minimises the sum of squared misfits. After several iterations, a satisfactory, stable solution is obtained. Confidence intervals for the finite rotation poles can be obtained directly from the partial derivatives, and data importances are extracted in a similar fashion.

This method is then extended in order to carry out reconstructions for a closed 3-plate circuit. In order to take the interdependence of the 3 sets of finite rotation poles into account, only the parameter sets for two of the plate pairs are used as parameters for the inversion. The datasets for these two plate pairs are then treated in the same way as for a 2-plate reconstruction. For the third plate pair, the partial derivatives must be determined not with respect to the 3rd set of poles parameters, but with respect to the parameters of the two other (independent) plate pairs.

These methods are applied to the South America - Africa - Antarctica (SAM-AFR-ANT) 3-plate system in the Southern Ocean. The methods were designed with this plate system in mind because of the difficulties in resolving the South American-Antarctic spreading history. Although all of the Antarctic flank is present, most of the South American Plate created at

the South American-Antarctic Ridge has since been subducted by a trench system which is currently located at the South Sandwich Trench. The Antarctic seafloor lying in the Weddell Sea, representing the oldest seafloor created by South American-Antarctic spreading, has no opposing flank, the corresponding South American plate having been completely subducted beneath the South Sandwich Trench and its predecessors. Conventional reconstruction methods are thus unable to use data from this region to resolve South American-Antarctic plate motions. To date, the sole plate reconstruction for this region (Barker & Lawver, 1988) only used SAM-ANT data from seafloor created at the present-day South American-Antarctic Ridge to obtain finite rotation poles only back as far as anomaly 21 (46Ma).

A high resolution free-air gravity map of the Southern Ocean was constructed from GEOSAT altimeter GM profiles, using a deflection of the vertical FFT processing method. In order to determine a correct procedure for identifying fracture zone locations from this gravity map, modelling of the gravity signal over a fracture zone was carried out, taking into account both the thermal and crustal structure. The study showed that the location of the fracture zone could be picked from the short-wavelength gravity low that appears over the fracture zone trough. Fracture zones, flowlines and transform faults were then identified from the map and locations along these features were picked through a combination of an automated picking procedure and use of a purpose-built interactive graphics package.

Some of the magnetic anomaly locations were obtained from databases of picks from various sources, but much was picked directly from along-track cruise files. Another purpose-built interactive picking program was used, in which the along-track total field magnetics could be displayed alongside synthetic profiles and the reversal boundaries picked through comparison of the observed anomalies with a model.

Once datasets had been compiled for all three plates, 2-plate reconstructions were carried out for each plate pair, and in each case, the solution poles successfully modelled the plate motions as described by the observed data. The results were also compared with previous reconstructions for each plate boundary. The three datasets were then combined, and a 3-plate reconstruction carried out for the South America - Africa - Antarctica plate circuit. From the results of this inversion, as a consequence of the need for closure within the plate circuit (assuming rigid plates), differences were discovered between the South America-Antarctica rotation poles from the 2 and 3-plate reconstructions. These discrepancies were determined to originate from the fracture zone

and magnetic anomaly data in the Weddell Sea, where the spreading rates and azimuths predicted by the 2 sets of poles differed significantly between anomaly 32 (71Ma) and anomaly 20 (43Ma). During this period, there appeared to be considerably less extension in the region than that predicted by the 3-plate reconstruction, and this was associated with a disturbance to the flowlines which had previously been interpreted as a region of significant changes in spreading direction (Livermore & Woollett, 1993). On consideration of the evidence available, it appeared that this discontinuity was related to ridge re-orientation during a period of change in plate motions in the region. This resulted in a form of pseudo-asymmetric spreading causing less accretion of seafloor onto the Antarctic Plate in the Weddell Sea than would be predicted, during the period from around anomaly 30 (65Ma) until anomaly 21(46Ma).

The South American-Antarctic dataset was adjusted to take this discontinuity into account, and a revised 3-plate reconstruction was carried out. The set of solution poles obtained from this were found to satisfactorily fit the datasets on all three plates, improving the fits to the observed data relative to the 2-plate reconstructions for the South American-Antarctic Ridge and Southwest Indian Ridge, which had both suffered through a lack of quality data. From the internal consistency of this successful inversion, it was possible to conclude that the South American, African, and Antarctic plates represented a closed three plate system, with the spreading history successfully defined without any evidence for the existence of any (micro)plates, such as the postulated Malvinas Plate (LaBrecque & Hayes, 1979) in the Agulhas Basin.

During the period from anomaly 32 (71Ma) until shortly after anomaly 24 (52Ma), disturbances to the 3-plate system were seen on all three plate boundaries, in the form of significant changes in spreading rate and direction, ridge re-orientation, and ridge jumps. The internal consistency of the 3-plate inversion suggests that these changes were not caused by events within the SAM-AFR-ANT circuit, and it is proposed that there has been an external influence on the 3-plate system that led to these effects. The exact nature of this could not be specified, but it appears to be related to the collision of Africa with tectonic plates around the Mediterranean, which is seen in the cessation of motion between Africa and Europe between 68 and 51Ma (Dewey *et al.*, 1989).

The gravity field over the Southern Ocean was then reconstructed for two different ages, c24 (52 Ma) and c34 (84 Ma). This provided some additional insights into seafloor spreading in the region which were not readily apparent from the kinematic results obtained earlier in the

study. This was primarily information about the timing of ridge jumps and changes in patterns of seafloor spreading along all three ridges, which could be inferred from the study of the seafloor fabric as represented by the gravity field in the reconstructions.

A study was made of the evolution of the Bouvet Triple Junction using the results of the revised 3-plate inversion. From the sets of finite rotation poles obtained, a series of instantaneous stage poles were determined for several intervals in the past, and the variation of the velocity triangle around the triple junction was examined. The configuration of the Bouvet Triple Junction is known to have varied between ridge-ridge-ridge (RRR), which is in theory always stable, and ridge-fault-fault (RFF), theoretically only stable when the velocity triangle around the triple junction is isoceles. Through the modelling of the triple junction motion and stability as determined from the velocity triangles, theoretical traces of the triple junction were obtained. By comparing these traces to the actual trace interpreted from a gravity map, it was found that the RFF configuration appeared to be stable even when the velocity triangle was between 5° and 10° away from isoceles. Consequently, it was determined that the triple junction has spent the majority of the past 50Ma in the RFF configuration, proving more predominant than the theoretically more stable RRR mode.

Acknowledgements

Firstly, I would like to thank Barry Parsons and Roy Livermore for coming up with such an interesting, multi-disciplinary project, and for providing me with guidance and support throughout. I am grateful to Steve Cande for supplying me with magnetic anomaly data for the South Atlantic, and to Roy for providing South American - Antarctic data. The routines used to process the satellite altimeter data were originally written by Andrew Goodwillie, and many of the reconstruction routines are based on programs written initially by Peter Shaw and adapted by Richard Woollett. The GMT system developed by Paul Wessel and Walter Smith has proved invaluable in much of the data processing and production of figures. My four years in front of a computer screen would no doubt have been far more painful had it not been for the help of Steve Usher at Oxford and all of the NCS staff at the British Antarctic Survey. My thanks must also go out to all of the postgrads, past and present, of the Earth Sciences Department in Oxford, and those working in the Geoscience Division at BAS who have assisted me over the years. The scientists and crew involved in the JR09 cruise in Jan/Feb '95 all contributed to a most welcome diversion from Oxford, with the RRS James Clark Ross proving to be a very pleasant introduction to life on the ocean wave.

On a more personal level, this thesis has to be dedicated to my parents without whom it simply wouldn't exist, and who I'm sure will be glad to have finally witnessed my transition from sponger to taxpayer. Thanks too for Ness, for her big sisterly support, and my apologies to Daniel for neglecting him in the first 6 months of his life.

I have immensely enjoyed all the sport I have played in Oxford, in particular my exploits with the University Korfball Club, and many people have made the transition from team-mates to close friends, Claire, Karen, Dom and Geoff in particular. I have also made many good friends at Worcester College, within the Department and at BAS, and I thank them all for keeping me amused, at work and at play. The T4 crew have managed to provide me with endless lunchtime distractions, as well as a neverending supply of hot water. Cheers, but remember boys, 5-3-2 is best.

Finally, my thanks to Pierre Smirnoff for sustaining me through good and bad times.

Contents

Abstract i

Extended abstract ii

Acknowledgements vi

Table of Contents vii

1 Introduction **1**

1.1 Background of plate tectonics 1

1.2 Tectonic setting of the Southern Ocean 7

1.2.1 Gondwana breakup 9

1.2.2 South America - Africa spreading history 11

1.2.3 Africa - Antarctica spreading history 16

1.2.4 South America - Antarctica spreading history 20

1.2.5 Evolution of the Scotia Sea 22

1.3 Outline of thesis 24

2 Fracture zone locations **27**

2.1 Introduction 27

2.2 Construction of satellite gravity map 33

2.2.1 Satellite altimetry 33

2.2.2 Theory 34

2.2.3 Processing 38

2.3 Modelling of a fracture zone 43
2.3.1 Modelling gravity from a 1-d topographic profile 45
2.3.2 Modelling gravity for an age step in the seafloor 49
2.3.3 Method and results of modelling 51
2.4 Picking procedure for fracture zones 63
2.5 Summary of data 69
2.5.1 South America - Africa seafloor spreading 69
2.5.2 Africa - Antarctica seafloor spreading 71
2.5.3 South America - Antarctica seafloor spreading 73

3 Magnetic anomaly isochrons **76**

3.1 Introduction 76
3.2 Block models 78
3.3 Data compilation and picking procedure 82
3.3.1 Synchronisation of isochron picks 87
3.4 Example anomaly profiles and summary of data 88
3.4.1 South America - Africa seafloor spreading 88
3.4.2 Antarctica - Africa seafloor spreading 95
3.4.3 South America - Antarctica seafloor spreading 109

4 An inversion method for 2 and 3-plate reconstructions **114**

4.1 Basics of spherical geometry and rotations on a sphere 114
4.1.1 Notation 114
4.1.2 Coordinate systems 115
4.1.3 Circles on a sphere 116
4.1.4 Vector products 117
4.1.5 Rotations on a sphere 118

4.1.6 Exponential parametrisation 120
4.1.7 Instantaneous, finite and stage poles 121
4.2 Overview of inversion methods 123
4.3 Method for a 2-plate reconstruction 131
4.3.1 Inversion theory 131
4.3.2 Magnetic anomaly isochrons 134
4.3.3 Fracture zone locations 140
4.3.4 Transform fault locations 143
4.4 Data weighting and selection 145
4.4.1 Magnetics data 145
4.4.2 Fracture zone data 147
4.4.3 Transform fault data 148
4.4.4 Outliers and data selection 148
4.5 Statistical analysis 150
4.5.1 Distribution of errors 150
4.5.2 Confidence intervals 152
4.5.3 Data importances 155
4.6 Extension to a 3-plate problem 157
4.6.1 General consequences 157
4.6.2 Partial derivatives 158
4.6.3 Statistical analysis 159

5 A new set of finite rotation poles for the SAM-AFR-ANT 3-plate system 162

5.1 Inversion procedure 162
5.1.1 Preparation of fracture zone data 162
5.1.2 Preparation of magnetic data 164

5.1.3 **xsortdata** 164

5.1.4 Preprocessing of magnetic data 167

5.1.5 Iterative inversions 167

5.2 South America - Africa 2-plate reconstruction 169

5.3 Antarctica - Africa 2-plate reconstruction 177

5.4 South America - Antarctica 2-plate reconstruction 185

5.5 A SAM-AFR-ANT 3-plate reconstruction 192

6 Implications for seafloor spreading in the Southern Ocean 206

6.1 Evidence for a discontinuity in seafloor spreading in the Weddell Sea 206

6.2 A revised 3-plate reconstruction for the SAM-AFR-ANT system 214

6.3 Implications for South America - Antarctica seafloor spreading 225

6.4 Seafloor spreading history of the SAM-AFR-ANT 3-plate system 228

6.5 Gravity field reconstructions 236

6.5.1 c24 (52 Ma) reconstruction 237

6.5.2 c34 (84 Ma) reconstruction 241

6.6 Conclusions 247

7 Evolution of the Bouvet Triple Junction 250

7.1 Stability and motion of a triple junction 250

7.2 Modelling the configuration and motion of the Bouvet Triple Junction 252

7.3 Models for the evolution of the Bouvet Triple Junction 257

8 Evaluation of inversion methods and future work 263

8.1 Success of the 2 and 3-plate inversion methods 263

8.2 Future applications of the inversion method 265

8.3 Extensions to the inversion method 266

8.4 Development of an interactive reconstruction program. 267

A Partial Derivatives for Rotations **269**

A.1 Partial derivatives of matrix and vector products 269

A.2 Partial derivatives for a 2-plate inversion 270

A.2.1 Derivatives of a pole as a vector 270

A.2.2 Derivatives of a rotation matrix 271

A.2.3 Partial derivatives of a rotation pole from its matrix 273

A.2.4 Partial derivatives of a stage pole 274

A.3 Partial derivatives for a 3-plate inversion 277

A.3.1 Partial derivatives of a rotation matrix 277

A.3.2 Partial derivatives of a rotation pole from its matrix 277

A.3.3 Partial derivatives of a stage pole 278

B Summaries of computer programs for data processing and analysis **281**

B.1 Reconstruction programs 281

B.2 Reconstruction subroutines 283

B.2.1 Main subroutines 283

B.2.2 Geometric operations and partial derivative subroutines 286

B.3 Programs for data manipulation and display 288

B.4 UNIX/AWK scripts 291

References **292**

Chapter 1

Introduction

1.1 Background of plate tectonics

Some of the same observations that led to the development of the theory of plate tectonics had initially been made many centuries ago, Francis Bacon amongst others noting the similarity of fit between the opposing continents of the Atlantic. However, it was not until the start of the 20th century that the revolution in geological thinking began. Explanations of the similarities of flora and fauna across the oceans had previously been attempted in the form of hypothetical ancient continents sinking to form the oceans, or long-since disappeared land bridges. These theories are of course now easily rejected, and were so at the time from some quarters of scientific thinking. Wegener (1924) took the notion of matching the continents of South America and Africa a step further, and suggested that the two continents had once been part of a single land mass, Gondwanaland, which had since broken apart. This hypothesis of 'continental drift' was substantiated by a large amount of geological and climatic evidence, and supported by striking similarities in the flora and fauna across the continental divide. However, though the majority of scientific society dismissed this idea, some, such as Du Toit (1937), collated more evidence which concurred with Wegener's proposals. The stumbling block for the supporters of continental drift was providing a mechanism for this drift, explaining how these continents were supposed to have been driven through the ocean floor that separated them.

Further evidence for continental drift emerged in the late 50's and early 60's when palaeomagnetic studies such as that by Runcorn (1959) revealed that the pole of the earth's magnetic field appeared to have wandered in the past from its present position, marking out a path across the globe. However, the wandering poles determined for different continents followed differing paths and unless each continent was affected by a different magnetic pole, then the continents must have moved relative to each other.

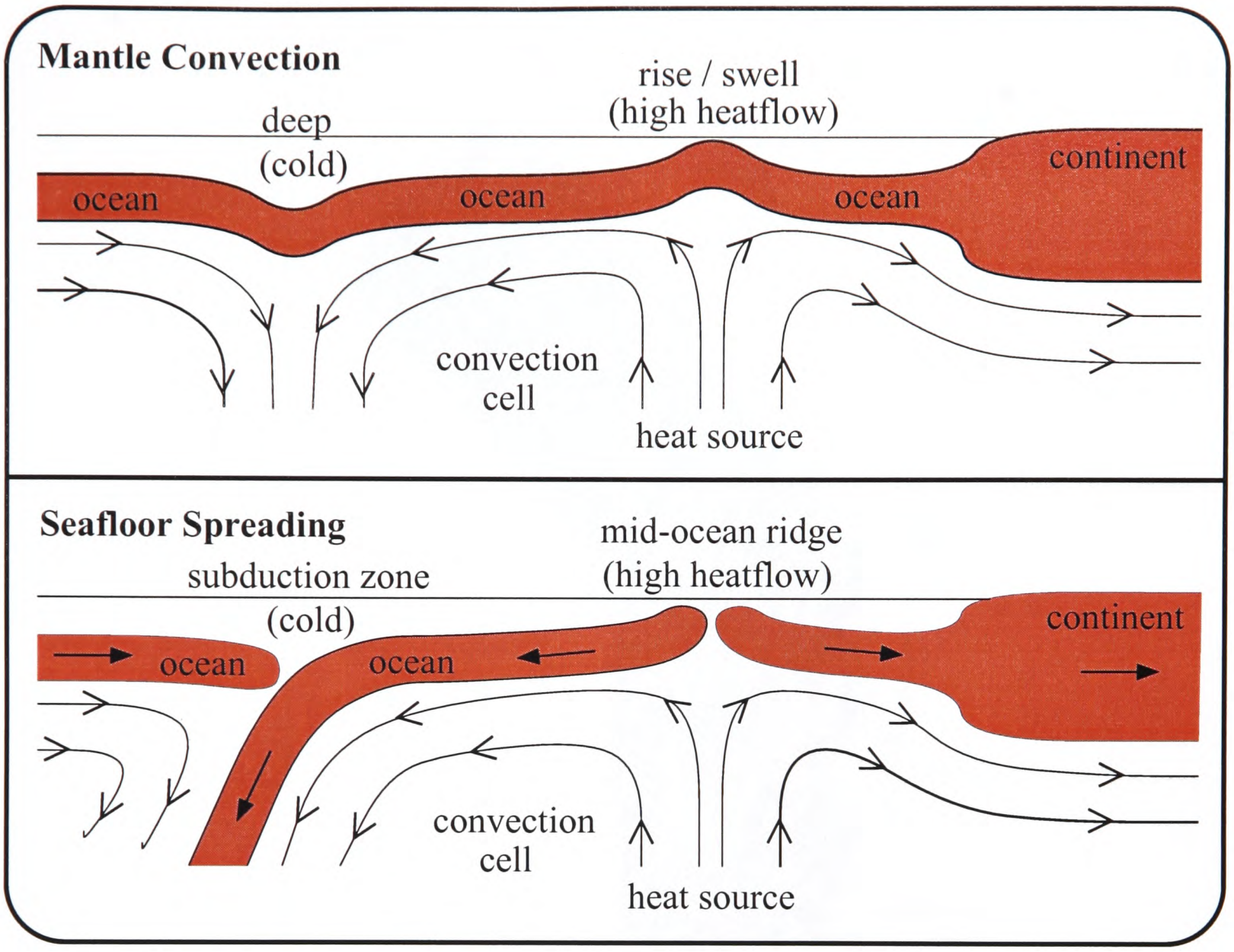

Figure 1.1: A Cartoon showing the difference between the two theories of mantle convection and seafloor spreading.

In the early part of the century, Arthur Holmes proposed the existence of convection cells under the earth's crust, causing flow in the mantle (Holmes, 1926, 1944), in order to account for fracturing and deformation of the earth's crust. It was this basic premise that Dietz (1961) and Hess (1962) independently developed to form the hypothesis of seafloor spreading as a mechanism to drive continental drift. Both took the idea of convection cells and realised they could account for the existence of high heat flow and topographic rises at the mid-ocean ridges (Figure 1.1). Each suggested further that these convection cells would provide the driving force for continental drift, and proposed that new seafloor was created at mid-ocean ridges and carried away by the motion of the underlying mantle. Thus continents need not plough through oceanic rock in order to satisfy the notions of continental drift. Instead, on fracturing initially, they would drift away from the central spreading ridge, with new seafloor created between them. The hypothesis of Hess (1962) also proposed the destruction and subsequent recycling of old oceanic crust at the

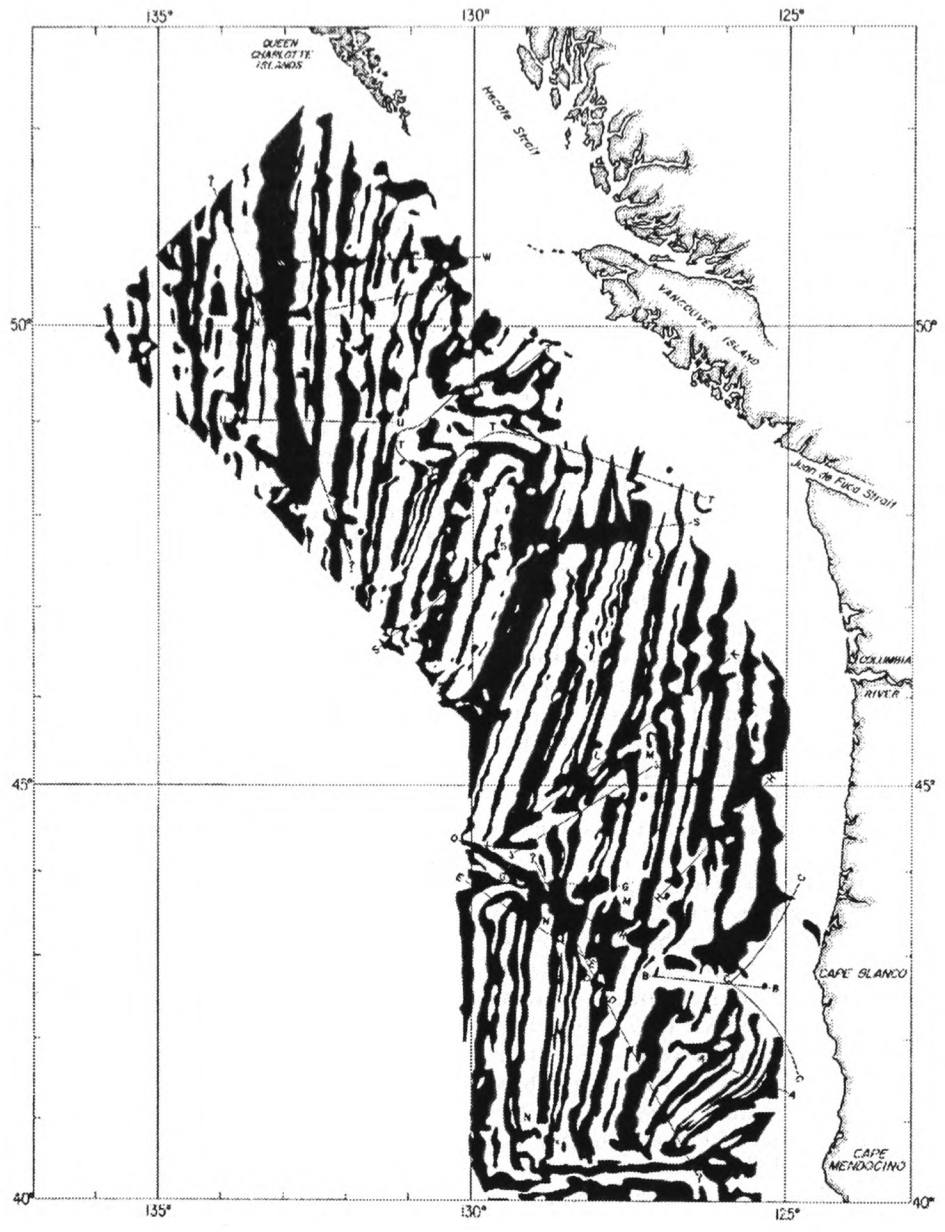

Figure 1.2: The magnetic anomaly survey carried out off the western coast of North America, revealing linear 'stripes' of alternating positive and negative anomalies (From Raff & Mason (1961)).

---

oceanic trenches, where the crust sinks below that of the neighbouring continent or ocean basin.

It was around the same time that more evidence in favour of continental drift appeared from analysis of the magnetic fields at mid-ocean ridges. A magnetic survey (Raff & Mason, 1961) of the Juan de Fuca Ridge, off the Pacific coast of North America had revealed a series of linear positive and negative magnetic anomalies, resembling a set of stripes, as can be seen in Figure 1.2. Prompted by the seafloor spreading hypothesis of Hess (1962), Vine & Matthews (1963) (and Morley (1986), though unrecognised and unpublished at the time) interpreted these as the record of a series of geomagnetic dipole reversals (Cox & Doell, 1962; Cox *et al.*, 1963) which had been 'fossilised' in the new seafloor being created at a mid-ocean ridge, before being transported away by seafloor spreading. Magnetic minerals in the newly formed seafloor should record the orientation of the earth's magnetic field at the time it was formed, in the form of

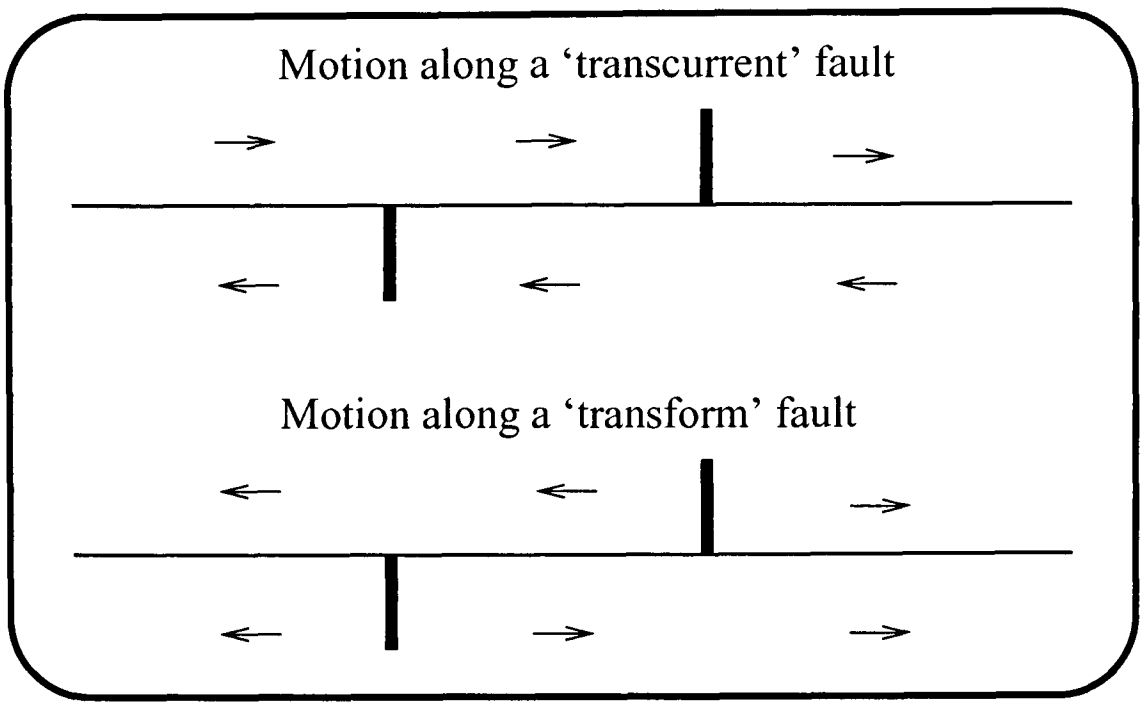

Figure 1.3: A diagram showing the difference between the motions along transcurrent and transform faults.

remanent magnetisation. Given that the assumption that the Earth's geomagnetic field reverses its polarity at regular intervals (less than 0.5Ma on average), then the magnetic fields recorded by the rocks should alternate on moving away from a mid-ocean ridge. This result was subsequently confirmed in further work by Vine (1966) for several widespread mid-ocean ridge systems.

The existence of mid-ocean ridges and trenches was known, and could now be explained by seafloor spreading, but the final piece of the puzzle was put in place by Wilson (1965) when he determined the true nature of transform faults. These large 'transcurrent' faults, as they were then known, were seen to extend across large tracts of seafloor (Menard, 1955), offsetting features such as the East Pacific Rise by hundreds of kilometres, but were seen to terminate on reaching the continental shelf, with no corresponding offset visible within the continent. When considered as strike-slip faults, there should be displacement along the length of the fault and such abrupt ends to the faults would not be expected without interaction with other tectonic features. Wilson (1965) proposed that the motion along these faults was in the opposite direction to that previously assumed (Figure 1.3), such that the faults were only active when linking tectonic features such as ridges and trenches, which would account for the properties of the faults as previously determined. When offsetting two spreading sections of a mid-ocean ridge, the transforms would no longer be moving the two segments apart, but would be considered as an original feature of the ridge geometry, and would subsequently give rise to inactive fault traces, the fracture zones, away from the ridge, as shown in Figure 1.4. Studies by Sykes (1967) on fault plane solutions for

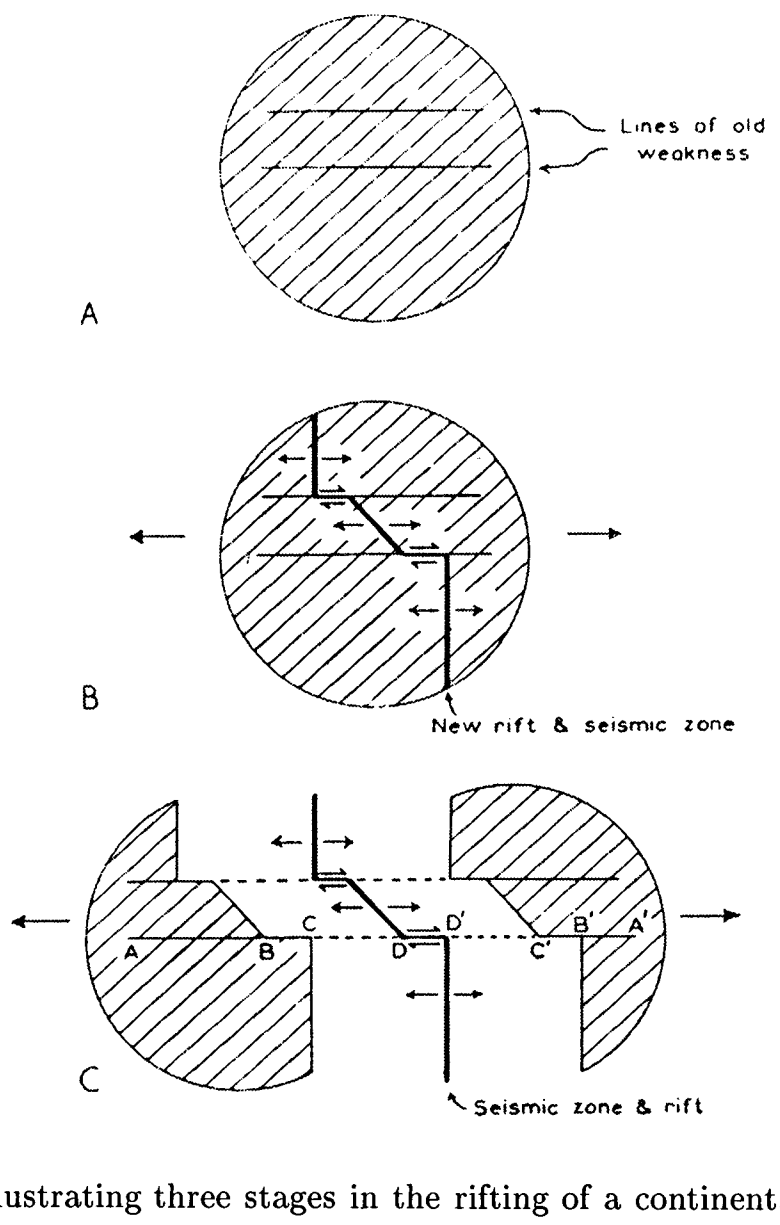

Figure 1.4: A diagram illustrating three stages in the rifting of a continent, and the role of transform faults (such as D-D') in offsetting spreading segments of a mid ocean ridge, leading to the creation of the inactive fracture zones crossing the seafloor (C-D, D'-C'). From Wilson (1965).

---

earthquakes along the active sections of transform faults subsequently confirmed these theories, which constituted compelling evidence for the acceptance of plate tectonic theory. Thus the globe could be divided into several large rigid plates, with large-scale crustal deformation confined to the continuous belts of ridges, trenches and transforms bounding the plates. This division of the earth into new tectonic units in continuous motion relative to one another was corroborated by others (McKenzie & Parker, 1967; Le Pichon, 1968; Morgan, 1968) with seismological studies (Isacks *et al.*, 1968; Barazangi & Dorman, 1969) further confirming the theories and showing that the majority of earthquakes worldwide were limited to the seismically active boundaries marking the outlines of the plates (Figure 1.5).

Oceanic and continental crust were no longer considered as separate units, the rigid plates comprising of the crust underlain by a substantial region of upper mantle that moved as a single unit, the lithosphere, riding above the ductile mantle known as the asthenosphere (Figure 1.6),

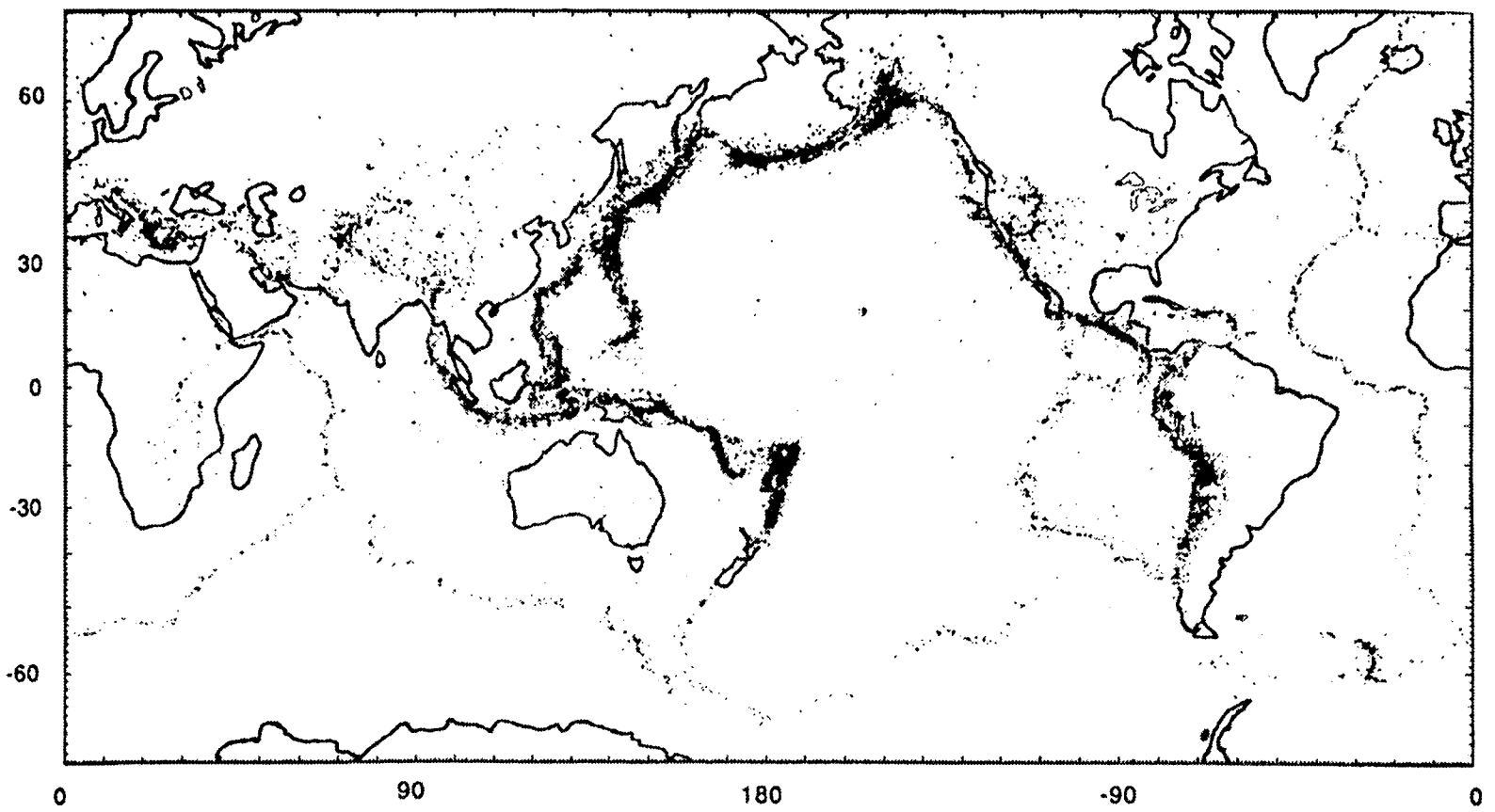

Figure 1.5: A map of global seismicity ('61-'67), which reveals the majority of earthquakes occurring along plate boundaries (From Barazangi & Dorman (1969)).

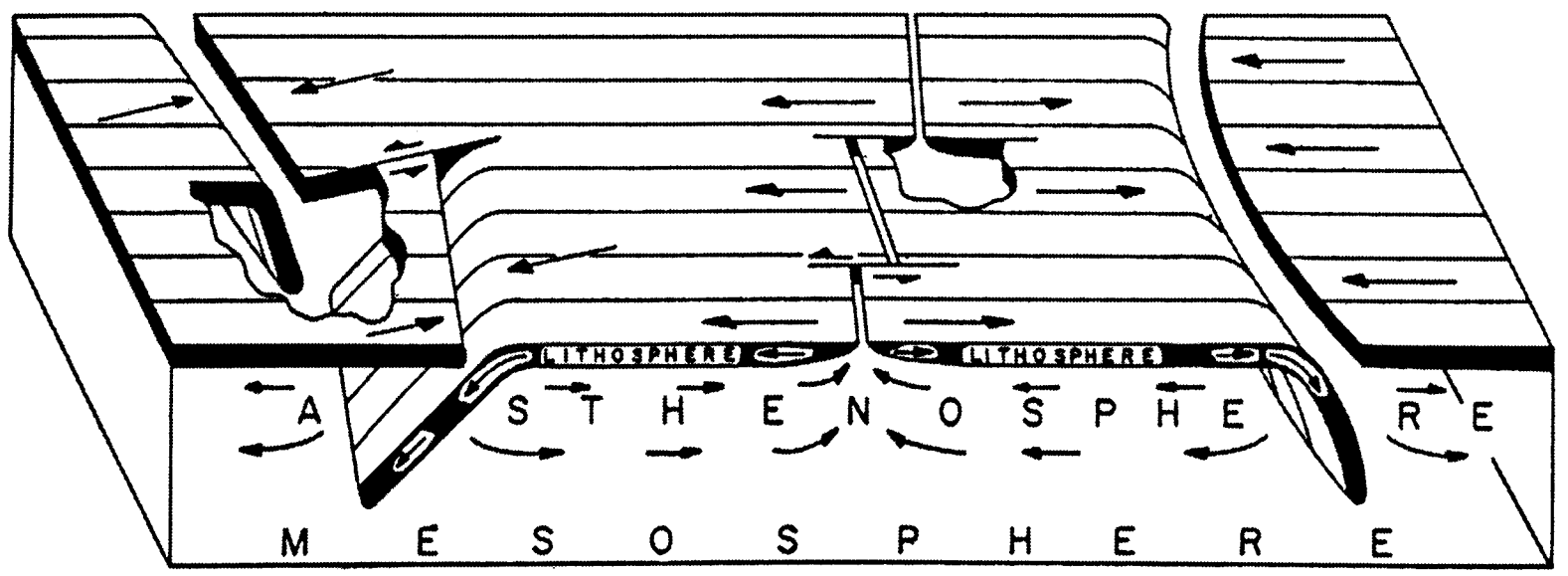

Figure 1.6: A cartoon showing the plate tectonic model as slabs of lithosphere supported on the asthenosphere (From Isacks *et al.* (1968)).

with large-scale crustal deformation thus limited to the boundaries of these plates. Some of these plates consisted solely of oceanic lithosphere (Pacific plate) whilst others consisted of part oceanic lithosphere, part continental lithosphere (African plate). And so the framework of plate tectonic theory was complete: at some time in the distant past, the surface of the Earth consisted of a supercontinent, Pangea, surrounded by a giant ocean, Panthalassa, which subsequently broke apart into several major tectonic plates along with several smaller units. These plates, and others created subsequently, have since undergone a complicated sequence of motions and collisions to arrive at the present-day global plate tectonic geometry.

Euler's theorem states that the relative movement of two rigid objects on a sphere can be described by a single rotation about an axis defined by a pole on the surface of the sphere (covered in more detail in Chapter 4). This representation can be extended to define a finite rotation pole which reconstructs the relative position of two plates at some time in the past (though it is not an true Euler pole as such, since a finite rotation pole does not necessarily describe the actual motion between the plates). Bullard *et al.* (1965) used such a finite rotation to provide a fit between the South American and African continents, the accuracy of the fit, though slightly overlapping in places, proving the inherent rigidity of the tectonic plates. Plate reconstructions determining a series of finite rotations between two plates for a sequence of times in the past, such as the study of the Indian Ocean by McKenzie & Sclater (1971), served to complete the acceptance of plate tectonic theory by successfully tracing the motion of continents over a substantial period of time.

1.2 Tectonic setting of the Southern Ocean

The area of study of this thesis is detailed in the tectonic map in Figure 1.7. The region is dominated by the three major plates: the South American (SAM) plate; the African (AFR) plate; and the Antarctic (ANT) plate. The boundaries between the plates are all extensional, consisting of sections of mid-ocean ridge spreading centres offset by transform faults, with all three plates meeting at the Bouvet Triple Junction (0°E, 55°S). The other plates involved with the system are those in the region of the Scotia Sea, which is tectonically quite complex, consisting of several smaller plates: the Scotia (SCO); Sandwich (SAN); Drake (PHX); and South Shetland (SSH) plates. The plate boundaries bordering the Scotia Sea to the N and S are poorly-defined diffuse transform boundaries, the aptly named North Scotia Ridge to the north (SCO/SAN-

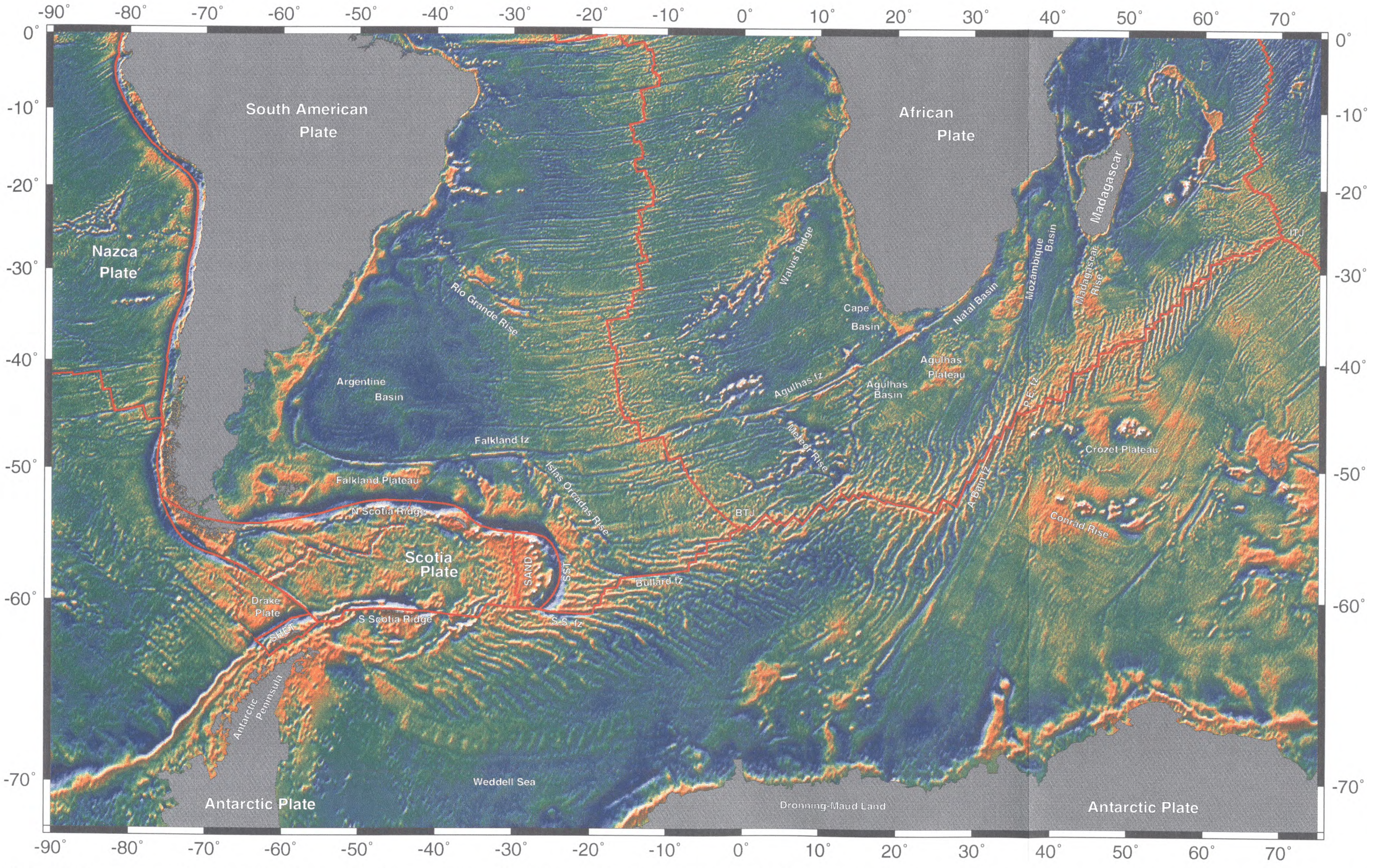

Figure 1.7: A map showing the major tectonic features of the Southern Ocean. Abbreviations: SAND - Sandwich Plate; SHET - Shetland Plate; BTJ - Bouvet Triple Junction; ITJ - Indian Ocean Triple Junction; SST - South Sandwich Trench; S.S. fz - South Sandwich fracture zone; P.E. fz - Prince Edward fracture zone.(Background gravity field processed by Smith & Sandwell (1995))

SAM boundary) and the South Scotia Ridge to the south (SCO/SAN-ANT boundary), with the South Sandwich Trench to the east. This subduction zone is presently only subducting South American seafloor, but is thought to have been in a more SW-NE orientation in the past(Barker & Griffiths, 1971; Barker & Hill, 1981), with the geometry changing though interaction with the South American-Antarctic Ridge.

The Bouvet Triple Junction has been the subject of much research, primarily based on studies of the stability of such features (Sclater *et al.*, 1976; Apotria & Gray, 1985, 1988; Kleinrock & Morgan, 1988). Since the Eocene, the triple junction has alternated between a ridge-ridge-ridge (RRR) and a ridge-fault-fault (RFF) configuration, with the latter appearing to be the more prevalent. This is contrary to the theories of geometrical stability of triple junctions (McKenzie & Morgan, 1969; Kleinrock & Morgan, 1988), which suggest that the RFF configuration is only stable when the plate velocities form an isoceles vector triangle (*i.e.* when the velocities along the two transform boundaries are equal). This has not always been the case for the SAM-AFR-ANT system, such that the Bouvet Triple Junction has proved more stable in the RFF configuration than would be predicted. Apotria & Gray (1985, 1988) sought to explain this by proposing that once the absolute motion of the triple junction takes it away from a position where it would have an isoceles vector triangle, it switches to a RRR configuration, which in turn causes the triple junction to migrate back to a position where RFF proves more stable, and so it reverts to this geometry until it becomes unstable again, and the cycle repeats itself. The triple junction was thought to have been in the more dominant RFF configuration for approximately the last 3-4Ma (Sclater *et al.*, 1976), but a more recent study (Ligi *et al.*, 1997) has suggested that it is currently undergoing a period of change with the actual triple junction, most recently in a RRR configuration, currently imprecisely defined. Ligi *et al.* (1997) have located overlapping spreading segments of the Southern Mid-Atlantic Ridge (SMAR) to the west, with a spreading section of the Southwest Indian Ridge (SWIR), the Speiss ridge, propagating northwards towards the SMAR, where it will eventually form a new triple junction, with a RRR configuration.

1.2.1 Gondwana breakup

Before going into more detail about the past spreading history between specific pairs of plates, it is useful to look at the overall breakup of Gondwanaland. Figure 1.8 shows a series of reconstructions from Lawver *et al.* (1992) which details the separation of the major fragments of Gondwanaland at

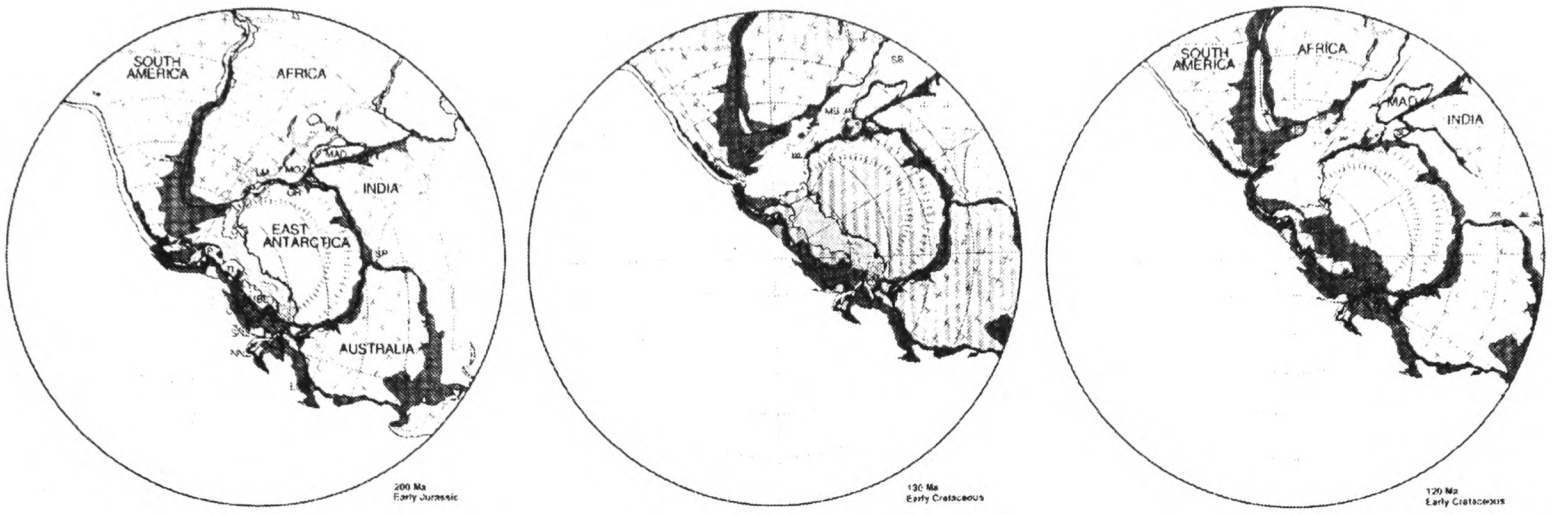

(a) 200Ma (b) 130Ma (c) 120Ma

(d) 100Ma (e) 80Ma

Figure 1.8: A series of reconstructions showing the breakup of Gondwanaland around Antarctica (From Lawver *et al.* (1992))

---

several finite times in the past. Breakup began with the separation of East Gondwana, consisting of Antarctica, Australia, India and Madagascar, from West Gondwana, comprising of South America and Africa, in the Jurassic. The oldest anomalies generated from this separation, M22 (≈150Ma), are located to the north of the SWIR in the Mozambique Basin (Simpson *et al.*, 1979), and to the south in the vicinity of Dronning-Maud Land (Bergh, 1977), though initial rifting and separation is believed to have begun earlier.

South America and Africa, both fragments of West Gondwana, are estimated to have begun separating in the Mesozoic, prior to M12 (135 Ma), dated from anomalies found in the vicinity of the Falkland Plateau and Argentine Basin on the South American plate, and in the Natal and Cape Basins off the coast of South Africa (Larson & Ladd, 1973; Rabinowitz, 1976; du Plessis,

1977; Rabinowitz & LaBrecque, 1979; Martin *et al.*, 1982). At around the same time, India and Madagascar broke away from the rest of East Gondwana, as a single unit, though by 120Ma, motion between Africa and these two plates had virtually ceased, and Madagascar is thought to have reached its final position relative to Africa by around 105Ma. The gradual separation of Antarctica and Australia appears to have begun at around 100Ma (Mutter *et al.*, 1985), with the more rapid separation of India from Africa/Madagascar also commencing soon afterwards.

By the late Cretaceous (≈80Ma), the patterns of spreading seen in the present day had all been established, with the major tectonic units all separating from each other: South America; West Antarctica (East and West are now fused as a single plate); Africa; India; and Australia.

1.2.2 South America - Africa spreading history

With the fit of South America and Africa providing the primary stimulus for the development of plate tectonics, this boundary has the been the subject of much research.

The original continental rift was very similar to the current outlines of the continents as they exist today, as is to be expected, with the exception of the Falkland Plateau to the south. A large spur of continental crust, this was originally tucked around the western cape of South Africa, in the Natal Basin, when rifting began (Martin *et al.*, 1982). There are two major aseismic ridges located in the South Atlantic, which oppose each other at around 30°S, the Walvis ridge to the east, and the Rio Grande Rise to the west. These features are volcanic in origin, the traces of a hotspot which is presently located in the region of Tristan da Cunha (O'Connor & Duncan, 1990). The ridge axis was initially located above the hotspot, which lead to the symmetrical formation of the hotspot traces either side of the ridge, but later, the spreading axis moved west, away from the the hotspot, so that formation of the Rio Grande Rise ceased, while intraplate hotspot volcanism continued along the Walvis Ridge.

The Mid-Atlantic Ridge, the extensional boundary between the two plates, has retained the same basic geometry throughout the spreading history of the South Atlantic. This is best shown by rotating the epicentres of earthquakes along the current ridge axis (McKenzie & Sclater, 1971; Sclater & McKenzie, 1973; Rabinowitz & LaBrecque, 1979) by the same poles used for reconstructions, the symmetry or otherwise of the continental boundaries about the rotated ridge position showing the areas where any ridge jumps may have occurred. Figure 1.9 shows

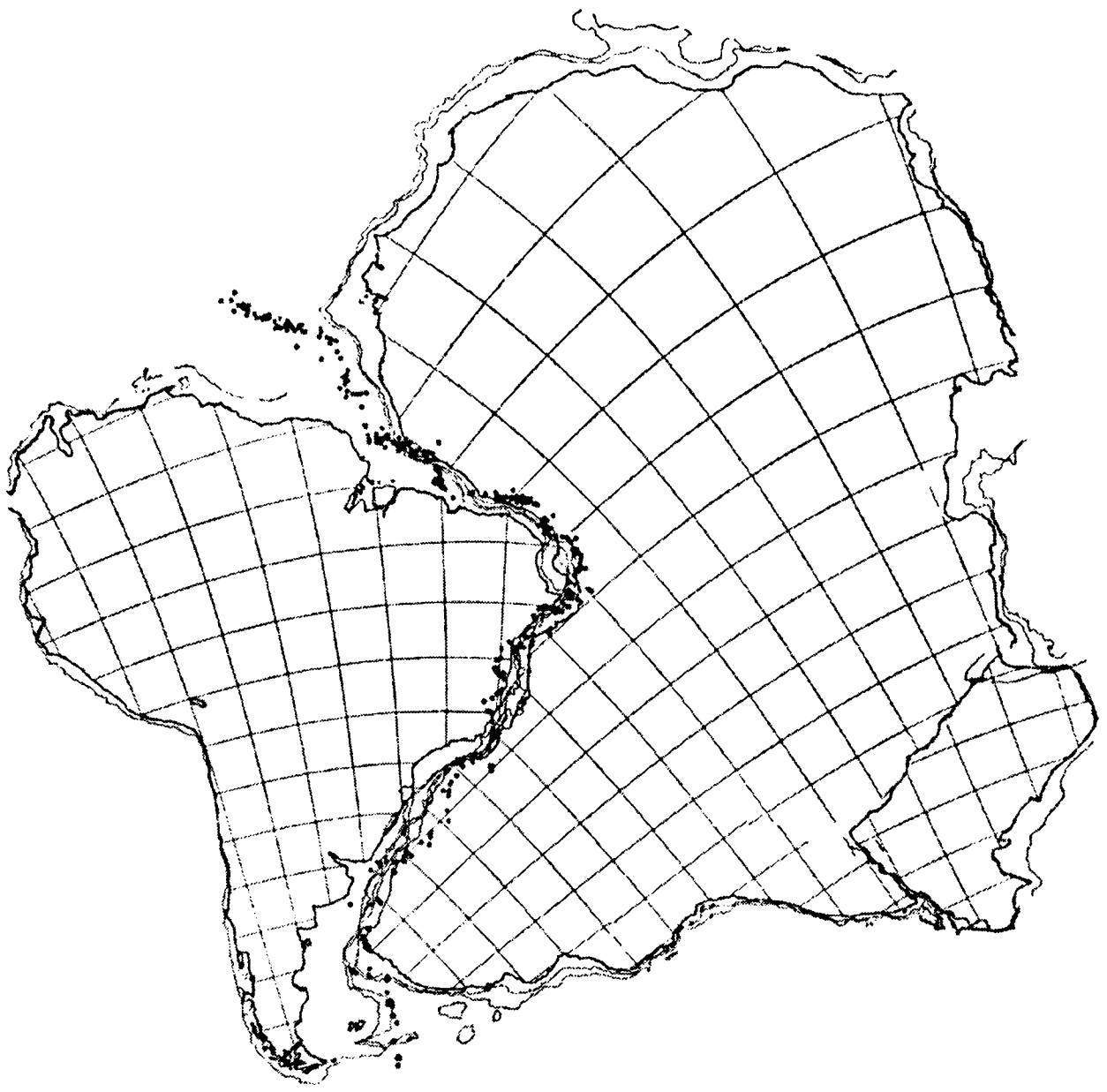

Figure 1.9: A diagram showing the fit of South America and Africa by Bullard *et al.* (1965) along with the rotated epicentres of earthquakes along the current ridge axis (After McKenzie & Sclater (1971)).

---

the fit of the continents in the South Atlantic obtained by Bullard *et al.* (1965), combined with the rotated locations of earthquakes from the current ridge axis. The match is very good in the South Atlantic, with the exception of the regions around the Rio Grande Rise - Walvis ridge system, and the Falkland Plateau. Such offsets can be explained by ridge jumps, or by highly asymmetric spreading, the latter being unlikely to have caused offsets of over 1000km, which are observed in the neighbourhood of the Falkland Plateau.

Francheteau & Le Pichon (1972) and Rabinowitz & LaBrecque (1979) used this evidence to propose ridge jumps in the vicinity of the Rio Grande Rise - Walvis ridge. There is evidence of a former ridge jump south of the Rio Grande Rise (Cande *et al.*, 1988), where magnetic anomalies indicate the presence of a minor spreading centre from around anomaly 34 (84Ma) to anomaly 32 (72Ma). To the north, no direct evidence can be found from studying magnetic anomaly profiles

because the ridge jumps occurred prior to anomaly 34, during the Cretaceous quiet period, when no magnetic reversals occurred.

South of the Falkland-Agulhas fracture zone, there have been several well-documented ridge jumps in the past, (Scrutton, 1973; du Plessis, 1977; LaBrecque & Hayes, 1979; Barker, 1979). The original offset of the Falklands-Agulhas fracture zone was around 1300 km (Martin *et al.*, 1982), the full extent of the Falkland Plateau, but through subsequent ridge jumps, this has been reduced to around 240km (Barker, 1979). The most prominent of the former ridge systems is located in the Agulhas basin, at around 15°E, where a fossil spreading centre is clearly visible on gravity maps, as can be seen in Figure 1.7.

This was identified as a fossil spreading centre by du Plessis (1977), Barker (1979) and LaBrecque & Hayes (1979), though these studies were based on topographic and magnetic profiles, without access to high-resolution gravity maps on which this fossil ridge appears as a clear feature on the seafloor. From the identification of the symmetrical patterns of anomalies around this fossil ridge (Barker, 1979), it has been determined that it was active from the late Cretaceous (anomaly 34) to the early Eocene (around anomaly 25), since when the ridge has moved to its present location. Whether this was achieved through a single jump has not been firmly ascertained (Barker, 1979; LaBrecque & Hayes, 1979), but the topographic features, the Meteor Rise and the Islas Orcadas Rise, are thought to have formed as a consequence of the ridge jump(s).

The jump from that spreading centre to the current ridge axis does not account for the whole of the reduction in offset along the Falklands-Agulhas fracture zone, but the locations of other abandoned ridges are not so apparent as that of the system in the Agulhas Basin and unlikely to be determined because again, any earlier jumps would have occurred during the Cretaceous quiet zone. The best guide are the regions of anomalous topography in the area. Scrutton (1973) suggested the Agulhas Plateau as the location of a fossil spreading centre, and both Barker (1979) and LaBrecque & Hayes (1979) came to the same conclusion, dating the time of the jump at around 98Ma. LaBrecque & Hayes (1979) also suggested that the region may have been the site of a triple junction in the Cretaceous, hypothesising the brief existence of a Malvinas plate in the Agulhas Basin for the period c34-c31, in order to account for discrepancies in the strike of isochrons to the west of the fossil ridge in the Agulhas Basin. The extent of this plate as shown in Figure 1.10, if it existed, is the subject of debate (Shipboard Scientific Party, 1988; LaBrecque *et al.*, 1979; Livermore & Woollett, 1993), with Livermore & Woollett (1993) suggesting it was

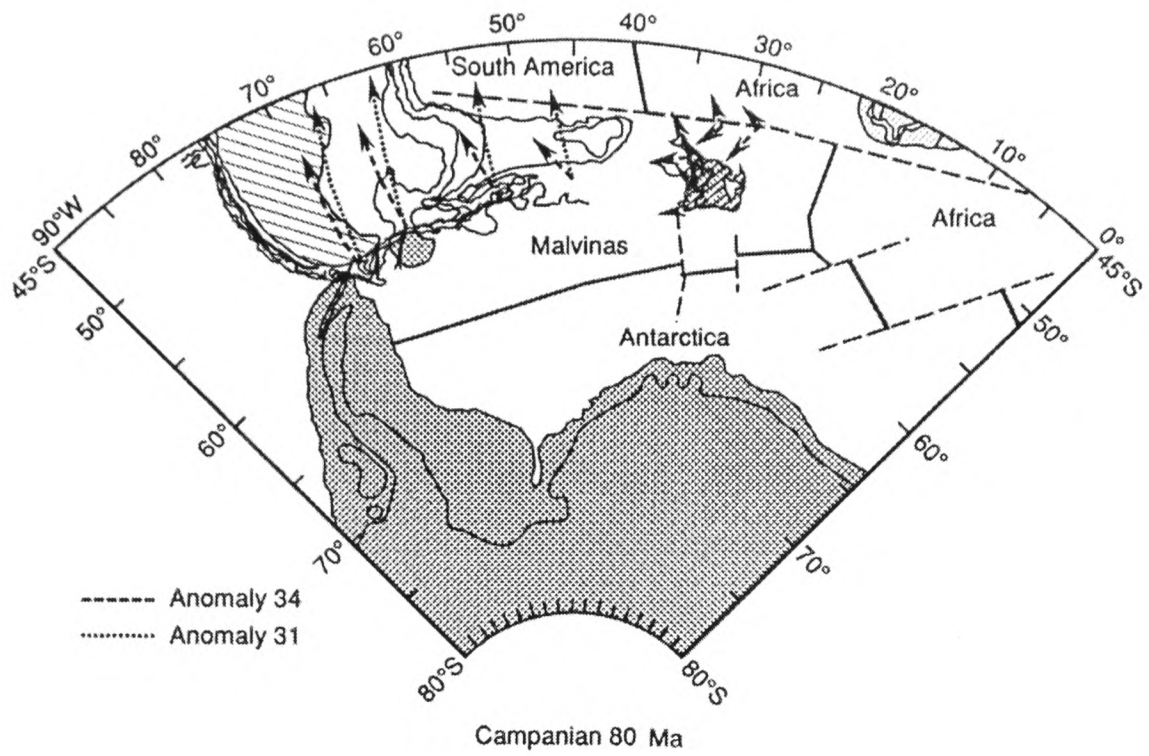

Figure 1.10: A diagram showing the proposed location of the Malvinas Plate between anomaly 34 (≈84Ma) and anomaly 31 (≈68Ma). (After Shipboard Scientific Party (1988)).

unlikely to have extended beyond the Agulhas Basin.

After the initial fit for the South Atlantic by Bullard *et al.* (1965), work on the South Atlantic concentrated on the nature of the early rifting (Francheteau & Le Pichon, 1972; Scrutton, 1973) and the determination of the early opening poles. Morgan (1968) and Le Pichon (1968) used the strike of Atlantic fracture zones to determine a single pole to describe the opening of the Atlantic to the present day, whilst Le Pichon & Hayes (1971) used the strikes of fracture zones at the continental margins to determine poles for early opening. With the identification of Mesozoic anomalies in the basins off Argentina and South Africa (Larson & Ladd, 1973; Rabinowitz, 1976), estimates for the timing of the initial rifting were improved, and greater knowledge of the original rifting structure was obtained (Rabinowitz & LaBrecque, 1979; Martin *et al.*, 1982).

Little work was done initially on the nature of the spreading history, though Dickson *et al.* (1968) used the locations of magnetic anomalies back to c31 to determine the symmetric spreading pattern about the Mid-Atlantic Ridge. The first proper series of finite rotation poles detailing the kinematic history of the South Atlantic were determined by Ladd (1974) from analysis of magnetic anomaly isochrons, and though Sibuet & Mascle (1978) obtained poles for Atlantic opening from fracture zone trends in the Equatorial Atlantic, the poles of Ladd (1974) were not improved upon until much later. Shaw (1987) used altimeter data to map large numbers of South Atlantic fracture zones and flowlines, and from these obtained a sequence of finite rotation poles

at regular intervals of time, back to anomaly 32. Cande *et al.* (1988) compiled a large database of anomaly isochrons and utilised this to determine a substantial series of poles back to anomaly 34, and then Shaw & Cande (1990) combined the use of fracture zone and isochron datasets to determine a well defined smoothly varying sequence of poles.

The direction of spreading has not undergone any drastic changes as can be seen by the continuity of the fracture zones in the region, and Gibert *et al.* (1989) took this concept a step further by determining a single rotation pole that satisfactorily fitted fracture zone trends south of the equator back to 35Ma. Shaw & Cande (1990) generally agreed with this result, finding that the first major change in trend of the flowlines occurred at around anomaly 13 (≈35Ma). A more significant change was observed at around anomaly 30, which coincides with changes in the plate motion at neighbouring plate boundaries, and is also the period when the large ridge jumps were occurring at the Falkland-Agulhas fracture zone, presumably to accommodate this change in spreading direction.

Considerable work has also been done on improving the inital fit of the continents beyond that obtained by Bullard *et al.* (1965). Though the quality of the fit was compelling evidence for the theory of plate tectonics, it is not possible to obtain a fit which satisfactorily matches the continental outlines in the South and equatorial Central Atlantic simultaneously. Research by Fairhead (1988); Fairhead & Binks (1991); Binks & Fairhead (1992) concentrated on rifting in Western and Central Africa, principally in the region of the Benue Trough. Deformation in this region is sufficient to account for the differential opening between the Central and South Atlantic Oceans from opening until ≈80Ma, when these processes appear to have been curtailed by a compressional event within Africa. During this time, stress between the two oceans appears to have been alleviated at the southern boundary, along 're-activated' equatorial fracture zones, but stress release since then has been limited to the northern margin (Central-Northern Atlantic).

Research by Nürnberg & Müller (1991) incorporated the subdivision of South America and Africa into several smaller plates until around the Late Cretaceous (anomaly 34, 85Ma), and used evidence of intra-continental rifting and deformation to determine a better closure fit for the South and Central Atlantic than had been previously obtained. Thus through these various reconstructions, the kinematic history of South American - African spreading is extremely well defined, from opening until the present day.

Cande *et al.* (1988) determined that the spreading rate was at a maximum at around anomaly

34, when it was around twice the current rate, but there was a slow period of spreading after anomaly 30 (67Ma) before the rate increased again at anomaly 20 (45Ma), since when it has remained relatively stable. Both global plate models (Minster *et al.*, 1974; DeMets *et al.*, 1990) and fine scale reconstructions along the ridge axis (Weiland *et al.*, 1995) are able to determine highly accurate estimates of the current spreading poles, and the current spreading rate has been determined to be around 32 mm/yr at 30°S (Weiland *et al.*, 1995).

1.2.3 Africa - Antarctica spreading history

The Southwest Indian Ridge is just one of three major mid-ocean ridges in the Indian Ocean, the others being the Central Indian Ridge separating the African and Indian plates, and the Southeast Indian Ridge separating the the Indian/Australian and Antarctic plates. All three spreading centres meet at the Indian Ocean Triple Junction which is currently in a stable RRR configuration, and has been a feature of the AFR-IND-ANT system for at least 10Ma, and possibly as far back as 40Ma (Tapscott *et al.*, 1980).

This study is concerned purely with the motion of Africa and Antarctica since the late Cretaceous, and so for this purpose, Africa and Madagascar will be considered as parts of the same rigid plate.

Much of the spreading ridge towards the eastern end of the SWIR has been created relatively recently by the rapid eastward movement of the Indian Ocean Triple junction (Tapscott *et al.*, 1980; Sclater *et al.*, 1981), and the trace of the triple junction is clearly visible on bathymetric and gravity maps (Figure 1.7). The spatial location of the plate boundary relative to the two continents appears to have been basically unchanged throughout the history of opening, though changes in spreading direction in the Eocene led to alterations to the small-scale geometry, and number, of spreading segments along the ridge, in particular in the vicinity of the long offset transforms of the A.Bain fracture zone. As reflected in the complex topography in the vicinity (Figure 1.7), the fracture zone appears to have fragmented in response to the initial change in spreading direction. However, as Patriat *et al.* (1985) noted, the accreting boundary seems to have retained a memory of its previous geometry, with the ridge returning to a geometry close to its original, long-term, configuration with the current direction of plate motion close to that for the initial separation. The oldest section of the ridge is in the region of the Prince Edward and A.Bain fracture zones, with the sections of ridge west of around 20°E and east of 50°E having

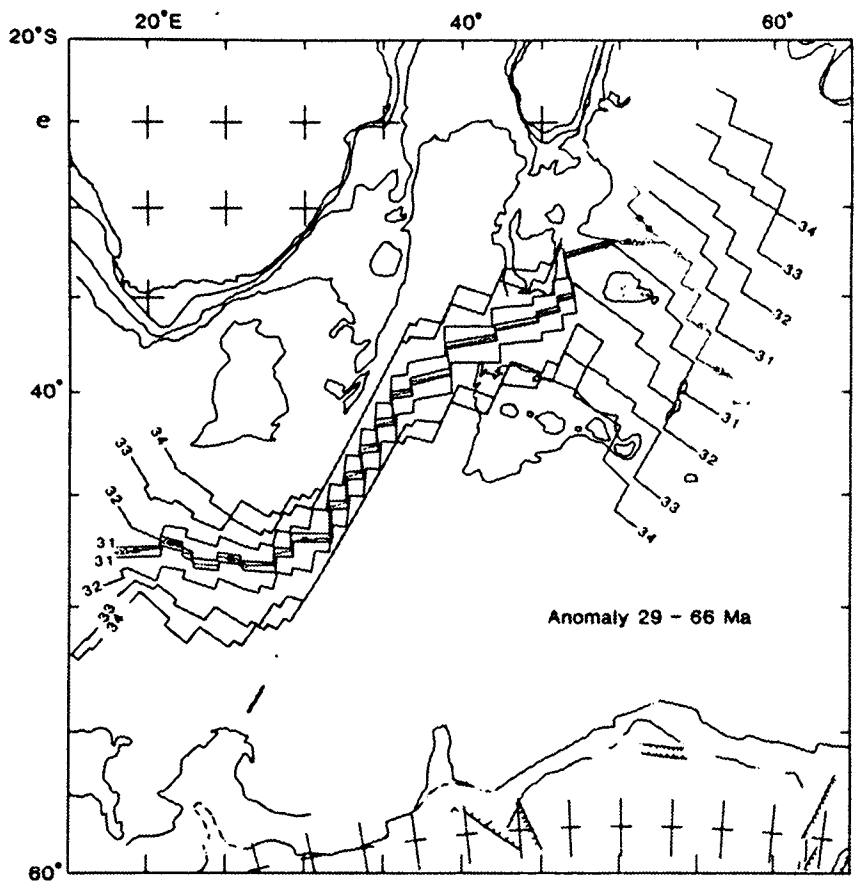

Figure 1.11: The anomaly 29 reconstruction of Africa and Antarctica by Royer *et al.* (1988), showing the substantial change in ridge geometry prompted by changes in spreading direction during the Eocene.

been generated since the initial opening by the motions of the respective triple junctions.

The kinematic history of Antarctic - African plate motion has been the subject of much study (McKenzie & Sclater, 1971; Bergh & Norton, 1976; Norton & Sclater, 1979; Sclater *et al.*, 1981; Fisher & Sclater, 1983; Patriat *et al.*, 1985; Royer *et al.*, 1988), much of it the result of collaboration of working groups at several institutions in different countries (principally USA, France and South Africa), currently working under the nom de plume 'Alliance Exotique'. As such, the spreading history is relatively well known, though some of the precise interpretations have changed over the years. Bergh & Norton (1976) concentrated on spreading in the region around the Prince Edward fracture zone, and although suggesting a change of spreading direction in the Cretaceous, at around anomaly 33, considered there to be no great changes in direction since. In response to discrepancies in the series of anomalies observed, Bergh & Norton (1976) proposed the existence of ridge axis jumps, or periods during which no spreading took place, though any attempts to justify these theories suffered through the lack of data in the region.

Norton & Sclater (1979) used summation through the Indian Ocean plate circuit for the periods where the study by Bergh & Norton (1976) had suffered through lack of data to determine a more convincing history of continuous relative motion between the African and Antarctic plates,

as part of their reconstructions for the whole of the Indian Ocean. Their poles of motion for AFR-ANT spreading showed gradual changes throughout the opening, but with more noticeable changes in spreading direction during the Eocene (from around 40-60Ma), which also coincided with a substantial decrease in spreading rate.

Fisher & Sclater (1983) considered the motion of the two plates to have been continuous since the Cretaceous, with very little change in spreading rates or direction for Africa-Antarctica motion since anomaly 34. The first identifications of late Cretaceous anomalies (C32,33,34) south of the SWIR allowed Patriat *et al.* (1985) to infer a slight change in spreading direction at around that time. From the location of a newly discovered fracture zone south of the ridge in the region of the Prince Edward fracture zone, they also found evidence for a change of spreading direction between the c32 to c24 period, disproving the stable pole hypothesis of Fisher & Sclater (1983) who had been misled by assuming that the offset in the late Cretaceous anomalies in the Mozambique Basin was caused by the Prince Edward fracture zone.

This change of spreading direction in the Eocene was confirmed by the work of Royer *et al.* (1988), who also predicted substantial reorganisation along the plate boundary in order to accommodate for this change in spreading direction, as is shown in their anomaly 29 reconstruction shown in Figure 1.11. Though the location of the accreting boundary did not necessarily change, they found evidence for the subdivision of long offset transforms, particularly in the region of the A.Bain fracture zone, such that they metamorphosed into a series of stepped spreading segments and short transforms aligned with the (altered) direction of plate motion at that time. Figure 1.12 shows different types of ridge geometry that may result from a change in spreading direction. Of these, the subdivision of the transform into a staircase pattern of short ridge and transform sections Figure 1.12(d) represents the most likely scenario as it involves the least disruption to the system.

However, after the spreading direction returned to the more prevalent NNE-SSW orientation, the transforms returned to the earlier geometry. Royer *et al.* (1988) considered the origin of this change of spreading direction to be linked to the other changes in plate motion in the region: ridge jumps in the Cape Basin for SAM-AFR spreading; the northward motion of India commencing at around c31 time; and an overall slowing down of spreading in all of the neighbouring extensional basins. The Southwest Indian Ridge is the slowest of the three mid-ocean ridges studied in this thesis, with current spreading rates of 14-16mm/yr (DeMets *et al.*, 1990).

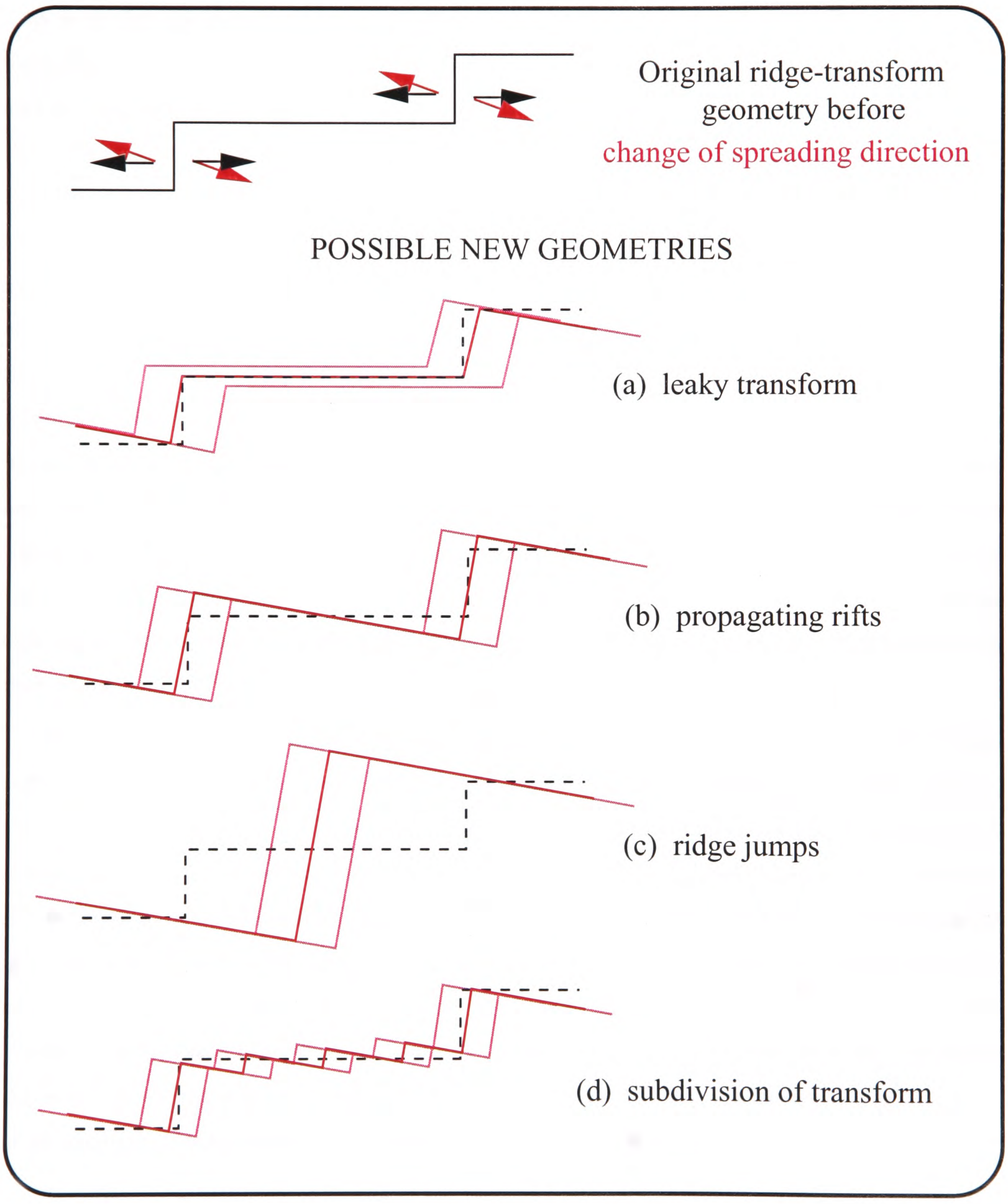

Figure 1.12: A diagram showing the different types of ridge-transform geometry for a long-offset transform that can result from a change in spreading direction.

1.2.4 South America - Antarctica spreading history

This is by far the least-studied and least-understood of the three boundaries. When the first mapping of tectonic plates was being carried out, the nature of the boundary was entirely unknown and any representations were both tentative and speculative. The best clues to the location of the current ridge system were from earthquake epicentre location maps (Barazangi & Dorman, 1969), but with the Scotia Sea plates complicating matters, the spreading history was poorly known. The first significant study of the area was by Forsyth (1975) who used earthquake source mechanisms to infer the geometry of the plate boundary west of the South Sandwich trench, and also determined a current pole of relative motion for the South American and Antarctic plates. Studies of the Bouvet Triple Junction such as that by Sclater *et al.* (1976) also incorporated information from the SAM-ANT boundary, in order to determine instantaneous poles, but only used magnetic and topographic data from the vicinity of the triple junction, which did not shed any light on the overall development of South American - Antarctic spreading. Magnetic and topographic data from a cruise by the US research ship RV. *Melville*, which traversed much of the ridge, was used by Lawver & Dick (1983) to determine the current geometry of spreading centres and transforms for most of the ridge, and to determine estimates for the instantaneous pole of rotation and spreading rate.

Barker & Jahn (1980) studied cruise data from tracks in the Weddell Sea and whilst finding sufficient ambiguity in the magnetic anomalies recorded, they considered the likely origin of the anomalies to be SAM-ANT spreading. This was also the conclusion reached by LaBrecque & Barker (1981), who were attempting to resolve the history of the Weddell Sea, in order to facilitate reconstructions of Gondwanaland which avoided the overlap between the Antarctic Peninsula and the Falklands Plateau, which had been an unwelcome feature of Gondwana reconstructions such as those by Smith & Hallam (1970); Norton & Sclater (1979). Their conclusions were that the Weddell Sea appeared to have been created by the southern section of a spreading ridge (probably the South-American Antarctic Ridge), which had since been subducted by the Sandwich trench, or an ancestor of this trench in the region of the South Scotia Ridge.

The first substantial study of the area was carried out by Barker & Lawver (1988) who combined fracture zone information and magnetic anomaly isochrons from the SAM-ANT and AFR-ANT boundaries, as well as utilising a set of poles for South Atlantic spreading (Cande *et al.*, 1988) in order to constrain South American - Antarctic motion since the Eocene (anomaly

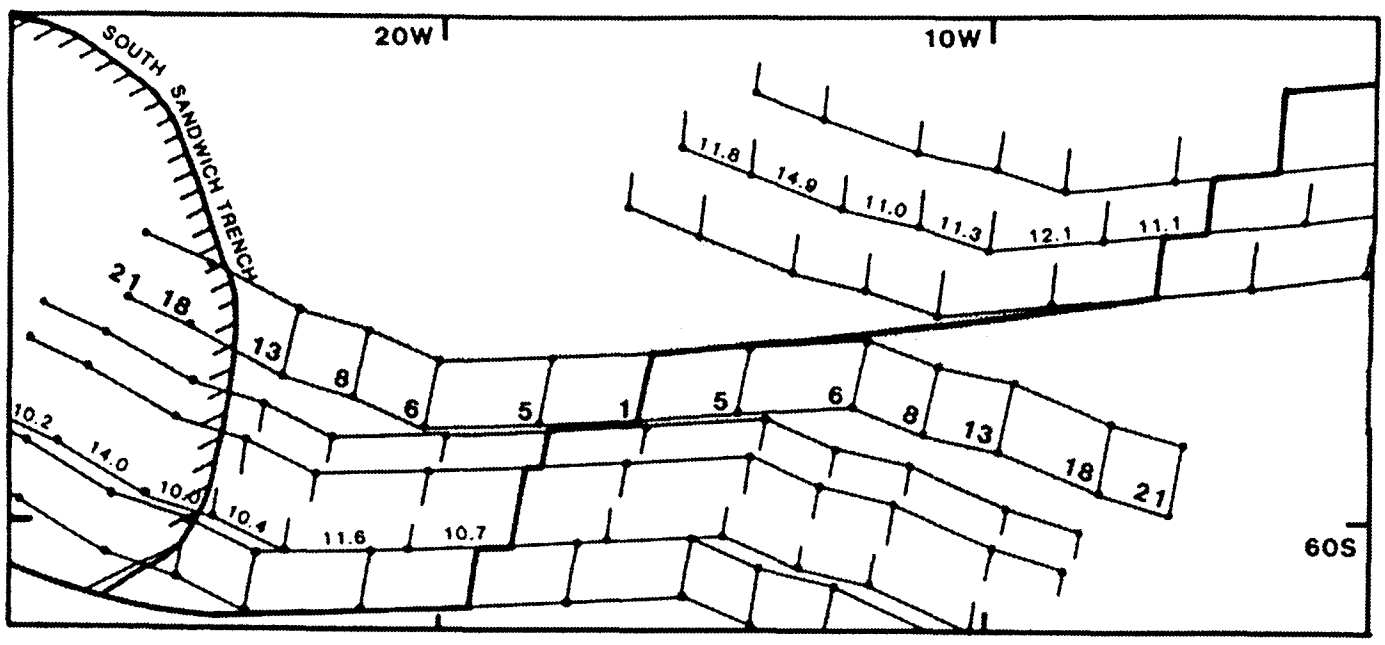

Figure 1.13: Synthetic flowlines for South American - Antarctic motion determined by Barker & Lawver (1988).

21, $\approx$ 50Ma). The most significant result of the study was the determination of a change of spreading direction at around anomaly 6 time ($\approx$ 20Ma), as can be seen in Figure 1.13. From similar considerations to those of Royer *et al.* (1988), they suggested that this change in direction had involved reorganisation of the ridge geometry, initiating the formation of the two long-offset fracture zones along the ridge, the Bullard and South Sandwich fracture zones. Prior to anomaly 6, the strike of these transforms would be incompatible with the direction of plate motion, and while it is considered possible for short ridge segments and transforms to re-orientate themselves in order to adjust for changes in spreading direction, this cannot be considered to be true for large offset transforms.

The probable changes in geometry of the ridge are related to those shown in Figure 1.12, but in reverse (suggesting different manners in which a long-offset transform can be created through a change in spreading direction, as opposed to predicting the response of a long-offset transform to such a change). For the ridge to have existed in the geometry now present would have required highly oblique spreading along leaky transforms, as shown in Figure 1.12(a). Re-orientation of the long-offset transforms in the new spreading direction (Figure 1.12(b)) would have resulted in large stress forces being generated along these transforms, and would be unlikely to have happened as a single step. It is more likely that prior to the change in spreading direction, the plate boundary in these regions would have consisted of several smaller offset transforms, which then merged to form the long transforms (Figure 1.12(d)). This is discussed in more detail in Chapter 6. The study of Barker & Lawver (1988) was restricted to reconstructing seafloor spreading from the

existing ridge back to c21, and was unable to provide any information about the origin of the Weddell Sea, knowledge of which is essential for correctly reconstructing the south-western region of Gondwanaland.

Release of high resolution GEOSAT satellite altimeter data extending into the Weddell Sea enabled Livermore & Woollett (1993) to determine flowlines for plate motions in the region, and interpretation of magnetic anomalies in the region provided sufficient data to obtain estimates for stage poles of motion through visual fittings of models and observed data. Significant changes in spreading direction and a decrease in spreading rate, similar to that recorded on the other plate boundaries in the region were observed between anomalies c21 and c31. In addition, comparison of plate motions that would be predicted from a existence of a Malvinas plate in the late Cretaceous with those actually observed provided evidence that a Malvinas plate was unlikely to have extended further west than the Meteor Rise, and was not responsible for the creation of seafloor in the Weddell Sea. Livermore & Woollett (1993) concluded that the Weddell Sea had been created from SAM-ANT spreading and that further work based on studying the three plate SAM-AFR-ANT system would reveal important information about the relative motion of East and West Gondwana, and studies of closure around the system would solve the Malvinas dilemma.

The South American and Antarctic plates are currently diverging at a rate of approximately 19mm/yr in a direction which is slightly north of East (DeMets *et al.*, 1990).

1.2.5 Evolution of the Scotia Sea

Between the South American and Antarctic plates lies the Scotia Sea, a tectonically complex region which has evolved since the opening of the Drake Passage (the gap between the tips of South America and the Antarctic Peninsula). At present, the region consists of just two plates, the larger Scotia plate, and the Sandwich plate at the eastern boundary, created through back-arc spreading behind the South Sandwich Trench. Figure 1.14 shows the major features of the Scotia Sea, many of which can be correlated with gravity signatures seen in Figure 1.7.

The main opening of the Drake Passage appears to have occurred at around 25Ma, following an earlier 'chaotic' spreading/opening episode (Barker & Burrell, 1977). Rifting leading to the creation of the Scotia Sea initially began at a spreading centre at the western end, at which

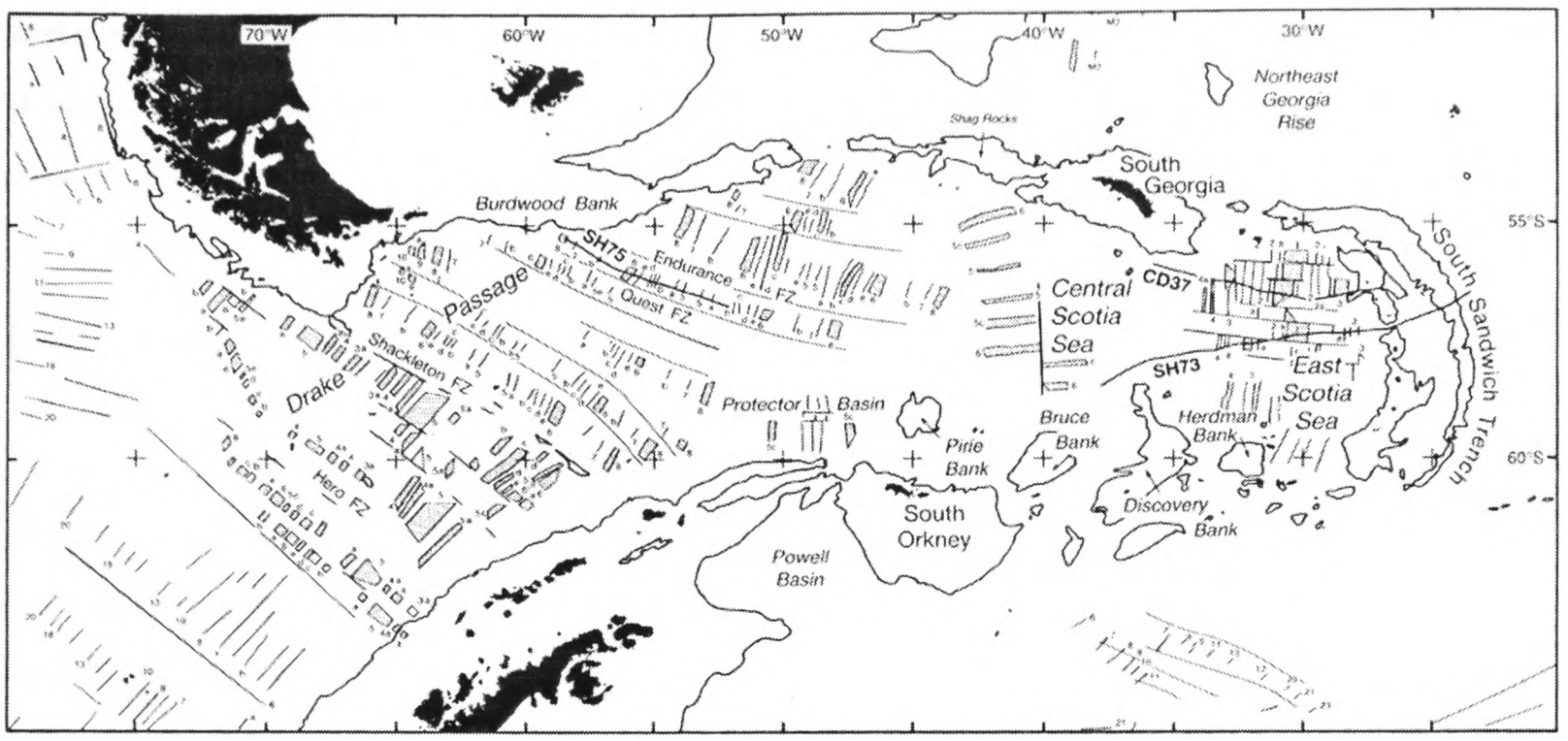

Figure 1.14: Tectonic map of the Scotia Sea (from Livermore *et al.* (1994)). GEBCO 2000 and 6000 m contours are marked, along with identified magnetic anomaly sequences.

spreading continued until around 7Ma (Livermore *et al.*, 1994). This fossil ridge system can clearly be seen on gravity maps (Figure 1.7) running from around 60°W to 40°W, striking approximately SW-NE. Interpretation of magnetic anomalies in the region suggests an initial spreading rate of around 56mm/yr decreasing to around 22mm/yr prior to cessation of spreading (Livermore *et al.*, 1994).

In the central Scotia Sea, there appears a further set of magnetic lineations aligned E-W, tentatively identified by Barker & Hill (1981) as being generated by N-S spreading from around c6 (20Ma) to c4 (7Ma). Hill & Barker (1980) also suggested an alternative interpretation of these anomalies, for spreading between approximately c17 (33Ma) and c7 (24Ma), meaning that some of this crust would pre-date the opening of the Drake Passage. It is important to note that there is no visible gravity minima marking any fossil spreading centres in this region, despite the fact that the mid-ocean ridge to the west was also active at this time, and has given rise to a continous high-amplitude gravity low over the relic median valley. The nature of spreading is not at all clear, with Livermore *et al.* (1994) suggesting that diffuse, disorganised spreading may have occurred.

The only remaining active spreading centre is located in the East Scotia Sea, just to the west of the South Sandwich Trench and is marked by a gravity low (relative to the significant regional high seen in the area), though lower in magnitude in comparison to the fossil ridge in the

western Scotia Sea. Back-arc spreading at this mid-ocean ridge system is believed to have begun at around 7Ma (Barker & Hill, 1981) and is presently spreading at a fast rate of ≈70mm/yr in an E-W direction.

1.3 Outline of thesis

The primary aim of this thesis was to develop inversion methods for plate reconstructions, in particular a method for a 3-plate reconstruction, that would provide a means by which the kinematic history of the Southern Ocean could be determined with an accuracy and confidence that could not have been achieved through existing methods.

The main problem which had to be overcome is that a large proportion of the western flank of the ocean floor created by South American - Antarctic spreading has since been subducted by the trench presently on the eastern border of the Scotia Sea. Established methods for reconstructions, such as those by Hellinger (1981) and Shaw & Cande (1990), are unable to derive series of finite rotation poles for a 2-plate systems such as this, due to the lack of conjugate pairs of magnetic anomalies on opposing flanks. A reconstruction method has been developed, an extension to that of Shaw & Cande (1990), which combines the use of magnetic isochron and fracture zone data in a single inversion, but which allows the fitting of magnetic isochrons to non-conjugate anomalies, such that it can be applied to areas where only one flank of the ridge exists. This enables a full set of finite reconstruction poles for SAM-ANT spreading to be determined, back to anomaly 34, using data from the Antarctic plate in the Weddell Sea which would previously been necessarily excluded from a SAM-ANT inversion.

This inversion method was then developed further in order to carry out 3-plate reconstructions for the SAM-AFR-ANT 3-plate system that would incorporate both fracture zone locations and magnetic anomaly isochrons from all three plate boundaries into a single dataset, in order to determine a set of poles that described the relative motions of the three plates over a substantial period of time, whilst taking plate closure into consideration. The only previous method to carry out genuine 3-plate reconstructions was developed by Tapscott (1979), and was an extension to the two-plate fitting method of Hellinger (1981). This method is based on the fitting of magnetic anomaly picks to conjugate isochrons, and for the same reasons as given above, could not be applied usefully to the SAM-AFR-ANT system. It was used in some form by Barker &

Lawver (1988) to determine rotation poles back to anomaly 21, but only incorporating data from the region bordering the South American-Antarctic Ridge itself and involved the 'generation' of conjugate isochrons where none existed, through interpolation from existing isochrons.

By combining data from all three plate boundaries it was hoped to produce a method that would automatically compensate for the lack of data, of a particular type or for a certain period of spreading, on one plate boundary by relying more on the data from the other two boundaries, in order to produce a continuous, well-defined set of poles for each spreading regime. Determining the relative motions of all three plate simultaneously should also provide information about the correlation and propagation of changes in plate motion within the system. In addition, by comparing poles determined from 2-plate reconstructions for each plate pair with the internally consistent sets obtained from the 3-plate reconstruction, questions about closure of plate circuits and internal deformation of tectonic plates can be answered. Another aspect of the reconstruction is the production of instantaneous poles of motion for the three plates, which can be compared with those from global plate models such as (DeMets *et al.*, 1990), and the determination of a velocity triangle for the three plates which can be used to predict the stability and configuration of the triple junction linking the three plate boundaries. Through application of the whole series of finite rotation poles for the three plate system, it is also possible to estimate velocity triangles for various intervals in the past, which can be used to study the evolution of the triple junction over a substantial period of time.

The first two main chapters are concerned with the compilation of the datasets for the reconstructions. The determination of fracture zone locations firstly involved the construction of gravity maps from radar altimeter data, and then the modelling of the gravity signal over fracture zones. The identification of magnetic anomalies required the production of synthetic anomaly profiles from reversal timescales, for comparison with along-track magnetics anomalies recorded by geophysical cruises, in order to aid the picking process. The final compilation of the magnetic anomaly isochron data involved the organisation, sorting, and arrangement of a substantial dataset.

Chapter 4 begins by briefly covering the spherical geometry involved in the determination of finite rotations, and then goes on to summarise the major work carried out on plate reconstructions since the advent of plate tectonic theory in the 60's, and the development of plate reconstruction inversions. The inversion methods for 2 and 3-plate reconstructions are then de-

scribed in detail, including the weighting schemes involved, the methods of error analysis to be applied to the residuals of the datasets, and the determination of confidence intervals of the final solution poles.

The results of the 2 and 3-plate inversions for the SAM-AFR-ANT system are given in Chapter 5. The solution poles are given, and displayed along with their confidence intervals, and poles produced by previous inversion for comparison. The fit of the datasets to the solution poles are displayed graphically, along with figures showing the data importances and the distributions of the residuals.

Chapter 6 starts by discussing some of the problems brought to light by the 3-plate inversion. A revised 3-plate reconstruction is then presented which takes into account a spreading discontinuity revealed in the Weddell Sea. The implications of the results obtained from the improved inversion are then considered, and the nature, and cause, of changes in plate motion within the SAM-AFR-ANT 3-plate system are discussed.

A detailed study of the evolution of the Bouvet Triple Junction is carried out in Chapter 7, looking at the configurations, motion and stability of the Bouvet Triple Junction over the past 45Ma. Finally, the effectiveness of the inversion methode are discussed in Chapter 8, along with some possibilities of future extensions to, and applications of, these techniques.

Chapter 2

Fracture zone locations

2.1 Introduction

Fracture zones are formed as the traces of transform faults and discontinuities at a mid-ocean ridge. Fracture zones were first discovered as linear topographic features on the seafloor by Menard (1955) but thought to be the results of stress-induced plastic deformation of the seafloor. The precise role of transform faults as origins of fracture zones, and their relevance to plate tectonics was first noted by Wilson (1965). Along a mid-ocean ridge, transform faults occur between two offset spreading centres, with a strike which is theoretically in a direction parallel to the current plate motion. Along this type of plate boundary, the two plates are moving sub-parallel to each other and the strike of the transform, as shown in Figure 2.1. The faults are defined as either sinistral or dextral, from the sense of the offset and the relative motion of the two plates to each other.

Transform faults are active plate boundaries between the two spreading centres. Beyond these limits, a record of the transform fault remains as a scar across the seafloor, but there is no longer any large-scale motion across this discontinuity as the two sides are part of the same rigid plate, although of different ages, and it can no longer be considered an active fault. These intra-plate tectonic features are known as fracture zones and have distinct characteristics derived from their origins as transform faults.

The magnitude of the age offset is dependent on the length of the transform fault, and the spreading rates at the ridge. The length of transform faults vary from a few kilometres up to hundreds of kilometres, and in addition, fracture-zone-like traces can also be found from small-scale ridge segmentation, when no ridge offset is apparant (Schouten & White, 1980), or the offset is of non-transform type. Because the motion along a transform fault is typically parallel

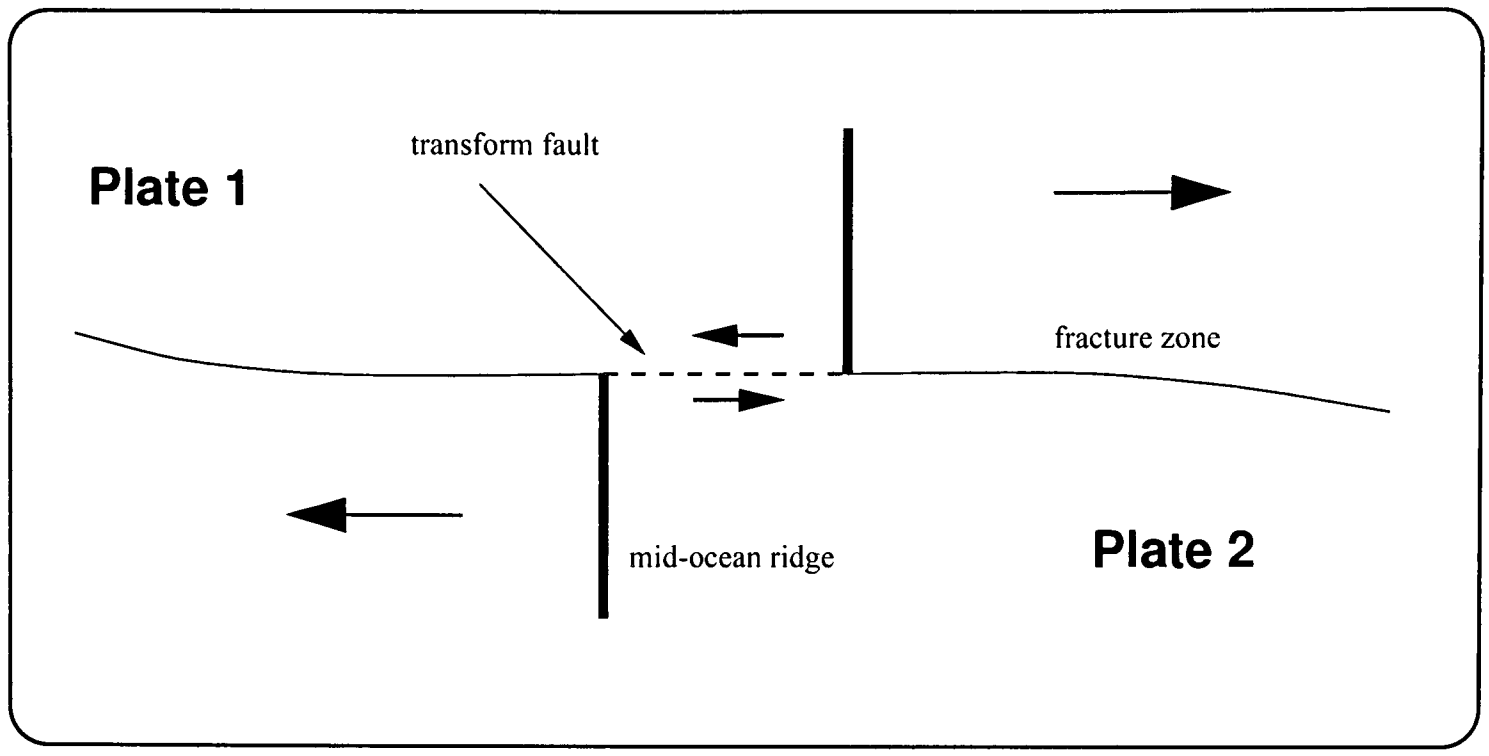

Figure 2.1: Cartoon showing a transform fault on a mid-ocean ridge.

to the current spreading direction, the trace of the transform fault, the fracture zone, represents a flowline for the motion between the two plates and as such, records the past direction of spreading between the two plates. Any given section of a fracture zone theoretically represents a small circle locus for the relevant stage pole, given constant spreading motion for that period. The size of the offset of the fracture zone has some effect on the validity of these assumptions however, since large offset fracture zones, such as the Falklands-Agulhas fracture zone on the Mid-Atlantic Ridge, (Barker, 1979), can be affected by any intra-plate deformation or large changes in spreading direction. The best indicators of past plate motion are the medium offset fracture zones, with offsets of around the order of 100km.

Because the two sides are of different ages, plate cooling theory, *e.g.* Parsons & Sclater (1977), suggests that there should be a topographic step across a fracture zone because of the differential thermal subsidence. The valley of the transform fault remains also a feature of this fossil boundary, but the general appearance of fracture zones does differ between plate boundaries. For example, the fracture zones in the Pacific have typically large topographic steps across them with often a large scarp slope marking the boundary between the two sides (Figure 2.2), whereas in the South Atlantic the major feature of the fracture zones is a distinctive bathymetric trough, and there is usually no obvious step feature across the fracture zone (Figures 2.3, 2.4), though this is possibly often obscured by the relatively 'rough' topography in the area.

Various studies have been carried out on the formation and structure of transform faults and

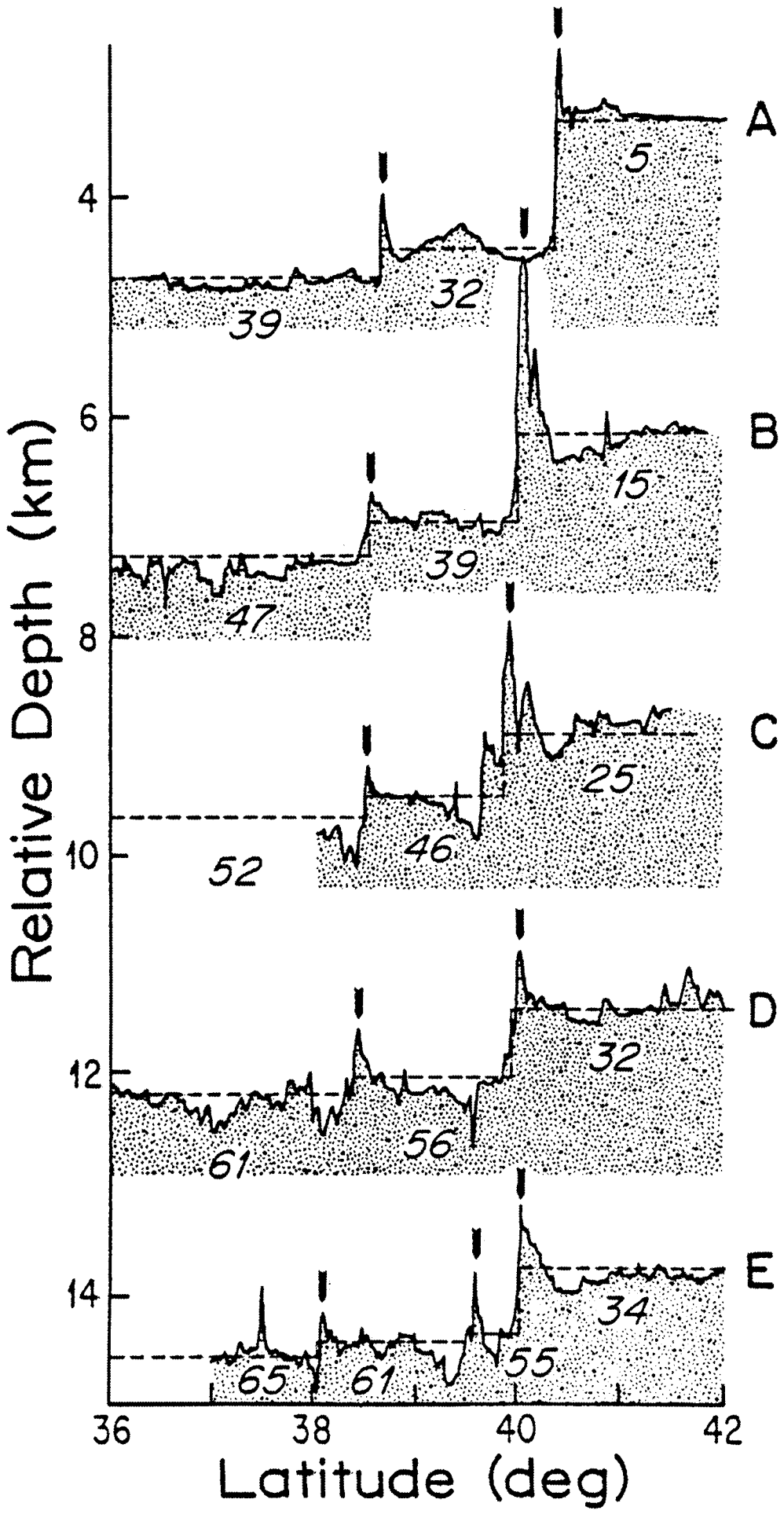

Figure 2.2: A series of bathymetric profiles across a set of Pacific fracture zones, showing clearly the steep scarp slopes and bathymetric steps marking the location of the fracture zones. The numbers indicate the approximate age of seafloor in Ma. From Sandwell & Schubert (1982).

fracture zones. Both Collette (1974) and Turcotte (1974) considered the possibility of fractures zones being created not as traces of a transform fault, but rather as features of thermal contraction of the plates parallel to the ridge. However, it was later proved that this effect would not account for the amount of extension typically found across a fracture zone (Francheteau *et al.*, 1976). Subsequent work has concentrated on the crustal structure across fracture zones, and it was discovered that in the vicinity of a fracture zone the crust is often found to be thinner than that of the surrounding plate, as can be seen in Figure 2.3, or of anomalous density, leading to relatively low seismic velocities, (Detrick & Purdy, 1980; Detrick *et al.*, 1982; White *et al.*, 1984; Abrams *et al.*, 1988).

Fox & Gallo (1984) concentrated on the modelling of ridge-transform intersections (RTIs) and concluded the thin crust in the vicinity of a fracture zone could be caused by disrupted accretionary process at the RTI, due to restricted magma supply at the end of a ridge segment, and also the effect of a relatively cold slab abutting onto a spreading centre. Detrick *et al.* (1982), in their study of the Kane fracture zone, found crust which was not particularly thin, as found by Detrick & Purdy (1980), but did find low crustal velocities and attributed this to the crust in the vicinity of the fracture zone being intensely fractured and disrupted due to the shearing along the transform. Most of the studies had concentrated on large offset fracture zones, but White *et al.* (1984) looked at some small-offset fracture zones in addition and still found anomalous crust, suggesting that since the adjoining slab would not be too 'cold' due to the small offset, the anomalous crustal structure was due to fracturing, rather than thermal effects. However, they also agreed that for the larger offset fracture zones, the thin crust was probably caused by changes in accretion patterns at the RTI.

As mentioned previously, the dominant feature of South Atlantic fracture zones is the bathymetric trough along the axis, formed initially in the region of the active transform fault. The major feature of the formation of the transform valley appears to be the shallowness of the crust in the vicinity. Various models have been put forward for the geological structure within the region of the fracture zone valley (Francheteau *et al.*, 1976; Fox *et al.*, 1976) but the extensive fracturing within the active zone of a transform fault make it difficult for the structure to be fully understood (Figure 2.4). An additional feature is the deposition of sediments into the fracture zone valley after formation, which is not shown in the models of Figure 2.4, but with time, there will be a degree of sediment infill. The average amount of sediment depth in ocean basins is

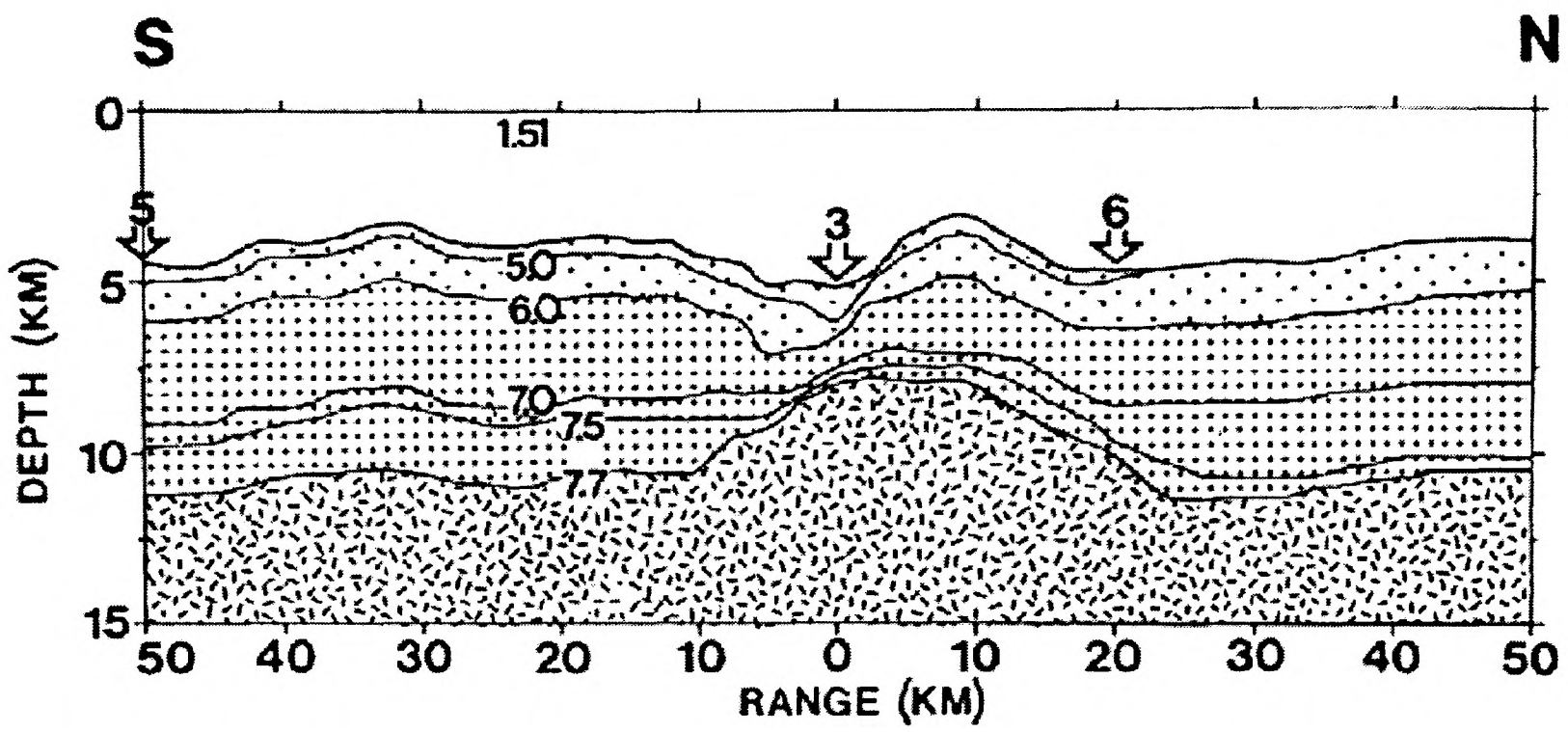

Figure 2.3: A cross-section across an Atlantic fracture zone, showing the thinning of the crust (Kane fracture zone, from Abrams *et al.* (1988)).

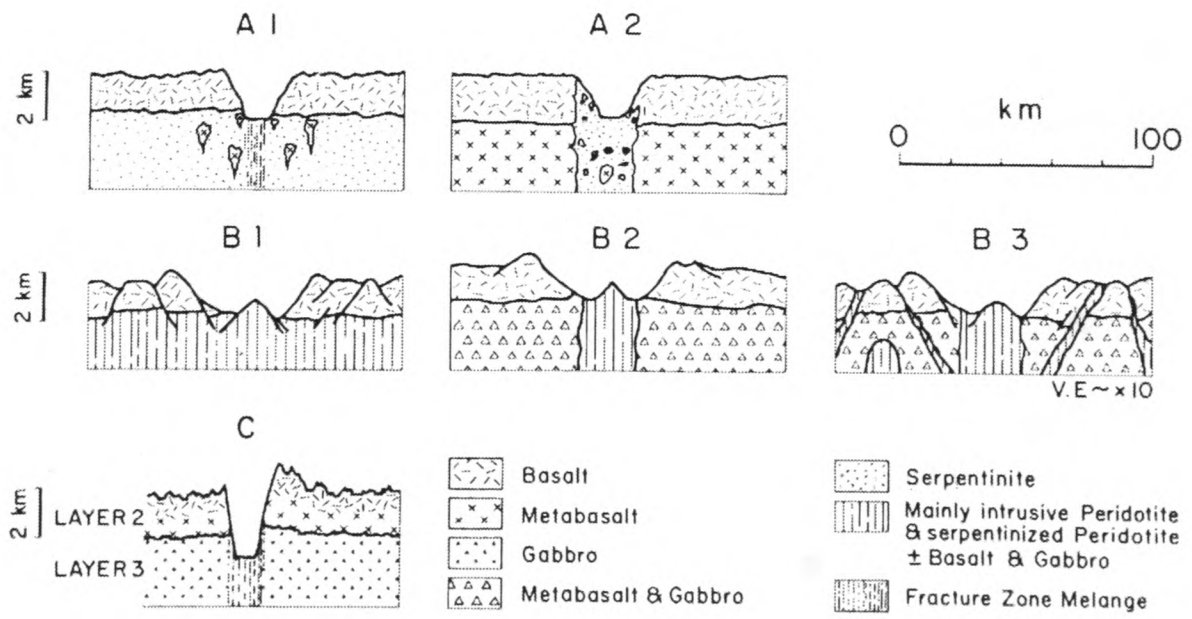

Figure 2.4: Six simplified cross-sections illustrating different notions of surface and sub-surface geology of an oceanic fracture zone. After Francheteau *et al.* (1976).

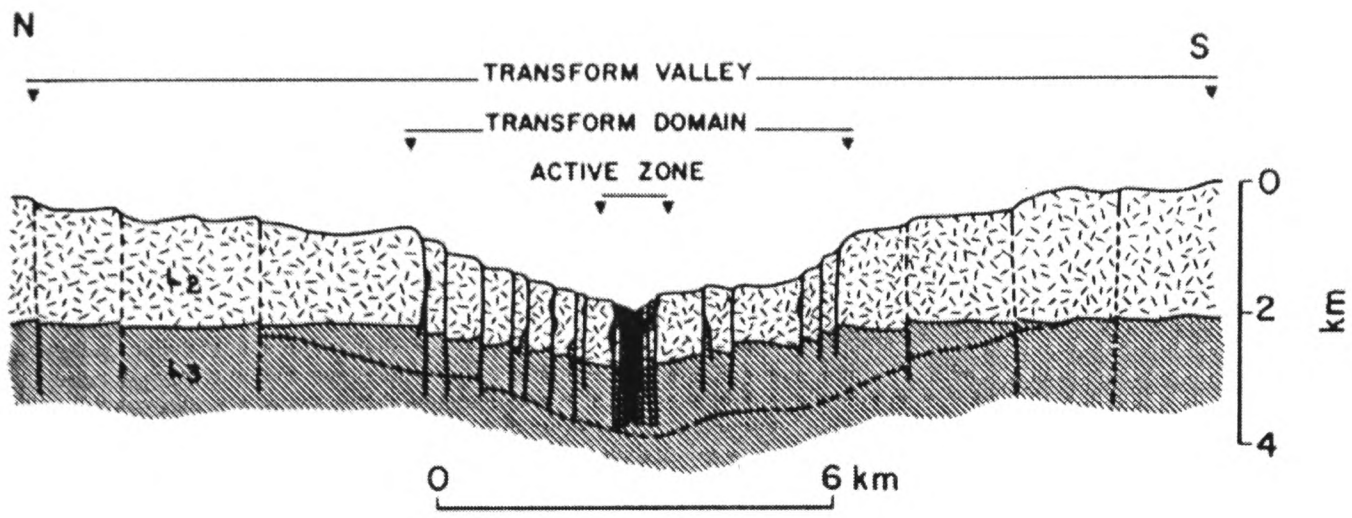

Figure 2.5: A cross-section across a fracture zone, showing the distribution of fractures and the location of the active faulting region (while an active transform fault) located in the centre of the valley. The dotted line marks the lower boundary of layer 2 had it been of constant thickness. From Francheteau *et al.* (1976).

---

around 0.5-1km, with an approximate deposition rate of around 0.02km/Ma (Gee, pers. comm.), but is is hard to estimate the additional amount that would build up within a fracture zone valley after being swept in by ocean currents.

When trying to determine the location of a fracture zone on a perpendicular profile, the aim is in effect to determine the trace of the active fault line of the transform. Le Pichon *et al.* (1973) determined that for a fracture zone in the North Atlantic, the axis of the trough followed a small circle to within 3km over a large distance while for the same section, the scarp slopes flanking the fracture zone deviated from the small circle by as much as 10km. Sonar studies (Searle, 1981; Tamsett & Searle, 1990) are able to trace the active fault along transforms, and although it does not always necessarily run along the deepest part of the valley, it is always contained within the central part of the transform valley. In the schematic cross-section of Francheteau *et al.* (1976) shown in Figure 2.5, the active region of the transform is centred within the fracture zone valley, and in this study, the centre of the valley will be considered to represent the the best estimate for the boundary between the two sides of the fracture zone. Typically, a free-air gravity profile across a fracture zone will show a distinct short-wavelength minimum over the fracture zone valley, which leads to fracture zones appearing as clearly visible linear features on high-resolution gravity maps.

In order to map fracture zones for use in an inversion, a series of 'picks' needs to be made: locations of the fracture zone determined from profiles crossing the fracture zone. In this study, fracture zones are located from gravity profiles crossing fracture zones, sampled from a gravity

map generated from satellite altimeter data. A decision had to be made as to exactly how this picking should be carried out, to construct a method for determining the centre of the fracture zone valley from the profiles. Shaw (1987) and Shaw & Cande (1990) picked the centre of the geoid low across South Atlantic fracture zones, fitting a Gaussian trough to satellite tracks crossing the fracture zones. This was done on the understanding that while the geoid trough might not coincide exactly with the bathymetric trough, this would be a systematic error that would not affect the actual flowline that was being mapped. Barker & Lawver (1988) mapped flowlines from lineations on gravity maps, and Nürnberg & Müller (1991), whilst realising that the bathymetric trough is the most prominent feature of South Atlantic fracture zones, picked the maximum/minimum geoid slopes from satellite tracks. This would in theory be picking the geoid step as opposed to the fracture zone trough, but they too accepted that they were mapping tectonic flowlines as opposed to the actual fracture zones.

To come to a decision as to how to pick the centre of the fracture zone from a gravity map or perpendicular gravity profile, some modelling of fracture zones was carried out, this is detailed in Section 2.3.

2.2 Construction of satellite gravity map

2.2.1 Satellite altimetry

In order to determine the location and traces of fracture zones, a high resolution satellite gravity field was constructed, using satellite altimeter data from the GEOSAT Geodetic Mission (GM). Satellite altimeters work by transmitting pulses of microwave radiation directed at the Earth's surface, and using the return time and knowledge of the satellite's orbit to determine the height of the sea surface (relative to a reference level) at the point on the earth below. This mean sea surface height measurement can be used as an approximation of the geoid height.

In the case of Geosat GM, such measurements were made approximately every tenth of a second, and the data used were binned and averaged in one-per-second groups. Before general release, the satellite dataset is preprocessed to remove data spikes, data flagged as over land or over sea ice, or where the standard deviation of the data within a 'bin' was unreasonably large. Corrections are also carried out to take into account both tides, and tropospheric and ionospheric effects, details of which can be found in Cheney *et al.* (1987, 1991). However, the

largest source of error in the GEOSAT data is from the tracking of the satellite orbit height, which must be known in order to convert two-way travel times into mean-sea-surface height measurements. Systematic variation in the orbit height of the satellite as it precesses around the earth can lead to differences in the altimeter readings from two different passes intersecting at a crossover point. The method used for processing the satellite data detailed below helps to minimise the effect of these crossover errors, by using along-track gradients which eliminates the effect of such long-wavelength (along-track) effects.

The 'footprint' of each pulse, due to dispersion of the beam as it travels to the Earth's surface, is of the order of 5km (varying from 2-9km depending on sea state) and with the ground speed of the altimeter being approximately 6800m/s, the 1-second binned data correspond to values with an along-track spacing of around 7km. The cross-track spacing (and distance between crossover points) is around 3-5km at the equator. Thus, in general, features with a wavelength of less than around 15 km are unlikely to be resolved by the satellite data.

2.2.2 Theory

The gravity dataset is provided in its raw form as mean sea surface heights, from which are obtained along-track gradients, which may be regarded as along-track geoid gradients. The first step is to obtain the the northern and eastern components of the deflection of the vertical (d.o.v.) from the separate ascending and descending satellite tracks.

Considering the values of the geoid gradient (N') along-track at a crossover point, as displayed in Figure 2.6, the geoid gradients of the ascending (N'_a) and descending (N'_d) tracks can be split into components in the x (eastern) and y (northern) directions as follows

$$N'_a = -\cos\alpha_a \frac{\partial N}{\partial x} + \sin\alpha_a \frac{\partial N}{\partial y} \tag{2.1a}$$

$$N'_d = -\cos\alpha_d \frac{\partial N}{\partial x} - \sin\alpha_d \frac{\partial N}{\partial y} \tag{2.1b}$$

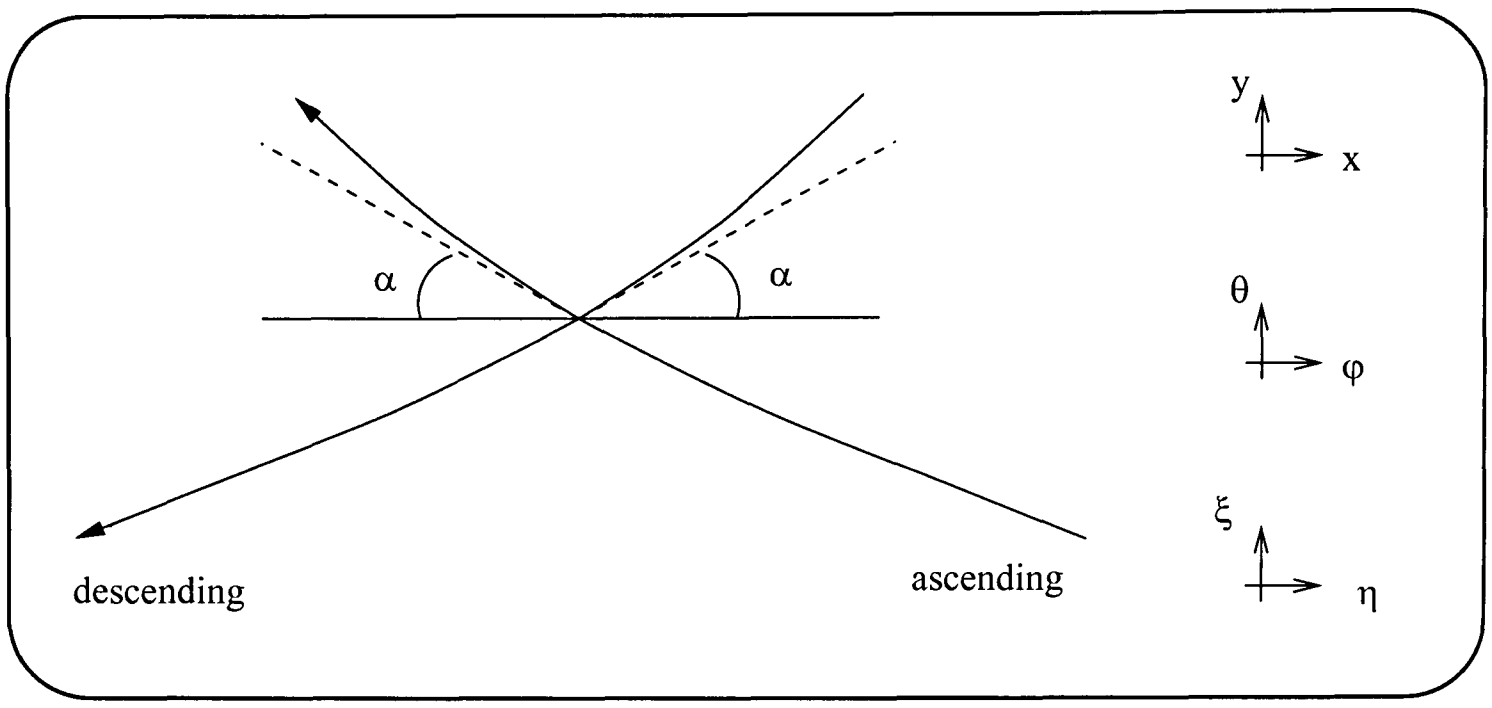

Figure 2.6: Diagram showing the intersection of ascending and descending GEOSAT tracks intersecting at a crossover point, with azimuth angle from horizontal α, showing the orientation of the axes for x and y, longitude (ϕ) and latitude (θ), and eastern (η) and northern (ξ) deflections of the vertical.

---

where the azimuth α of tracks crossing at a point (longitude ϕ and latitude θ) is given by

$$\alpha = \tan^{-1}\left(\frac{\dot{\theta}}{\dot{\phi}\,\cos\theta}\right) \tag{2.2}$$

where $\dot{\phi}$ and $\dot{\theta}$ are the longitudinal and latitudinal ground track velocities respectively.

Sandwell (1984) shows that at crossover points, the following relationships are accurate to better than 0.1%

$$\dot{\theta}_a = -\dot{\theta}_d \qquad \dot{\phi}_a = \dot{\phi}_d$$

and so at a crossover point, it can said to be true that

$$\alpha_a = \alpha_d = \alpha$$

The eastern (η) and northern (ξ) components of the deflection of the vertical (d.o.v.) are defined as the negative slope of the geoid in the $x(\phi)$ and $y(\theta)$ directions respectively.

$$\eta = -\frac{\partial N}{\partial x} \tag{2.3a}$$

$$\xi = -\frac{\partial N}{\partial y} \tag{2.3b}$$

these are substituted into (2.1), and subsequent manipulation gives

$$\eta = \frac{N'_a + N'_d}{2\cos\alpha} \tag{2.4a}$$

$$\xi = \frac{N'_a - N'_d}{2\sin\alpha} \tag{2.4b}$$

If the along track gradient is binned into grid cells of a standard rectangular grid, with interpolation to fill empty grid cells, Sandwell (1984) shows that grid cells are analogous to crossover points, so that at collocated grid cells for ascending and descending geoid slopes, the northern and eastern components of the deflection of the vertical are given by the above equations. However, the azimuth angle α is required, and although many grid cells will contain a crossover point, where the azimuth will be known, some grid cells will not, and so a method needs to be found to determine the azimuth angle for a hypothetical crossover point at a given location. The azimuth angle in terms of the satellite ground velocity was defined previously in (2.2). I shall not go into the derivation of α, which involves satellite geodesy theory, since it is only the end result which is of interest, but the steps of determining the ground velocities can be found in Sandwell (1992) such that the azimuth angle is given by

$$\alpha = \tan^{-1}\left(\frac{\frac{\omega_s}{(1-f)^2}\frac{\cos\theta}{\cos^2\theta_c}\sqrt{1-\frac{\cos^2 I}{\cos^2\theta_c}}}{\omega_s\frac{\cos I}{\cos^2\theta_c}-(\omega_e-\omega_n)}\right) \tag{2.5}$$

where I is the inclination of the satellite orbit, ω_s and ω_n are the orbit and precession frequencies of the satellite, ω_e the rotation frequency of the earth and θ_c is the geocentric latitude, correcting for the flattening of the earth (f), where

$$\theta_c = \tan^{-1}((1-f^2)\tan\theta) \tag{2.6}$$

The final stage is converting deflections of the vertical into gravity. The gravitational potential at a height z above the reference level $z = 0$ is given as $V(\mathbf{x}, z)$. The geoid height is related to this by Brun's formula, to a first approximation,

$$N(\mathbf{x}) = \frac{1}{g_0} V(\mathbf{x}, 0) \tag{2.7}$$

where g_0 is the average acceleration due to gravity

The gravity anomaly is given as

$$\Delta g(\mathbf{x}) = -\frac{\partial V(\mathbf{x}, 0)}{\partial z} \tag{2.8}$$

The eastern (η) and northern (ξ) components of the deflection of the vertical (d.o.v.) are defined as the slope of the geoid in the x and y directions respectively,

$$\eta = -\frac{\partial N}{\partial x} \approx -\frac{1}{g_0}\frac{\partial V}{\partial x} \tag{2.9a}$$

$$\xi = -\frac{\partial N}{\partial y} \approx -\frac{1}{g_0}\frac{\partial V}{\partial y} \tag{2.9b}$$

Taking further derivatives of (2.8) and (2.9) and substituting into Laplace's equation

$$\frac{\partial^2 V}{\partial x^2} + \frac{\partial^2 V}{\partial y^2} + \frac{\partial^2 V}{\partial z^2} = 0 \tag{2.10}$$

leads to

$$-g_0\frac{\partial \eta}{\partial x} - g_0\frac{\partial \xi}{\partial y} - \frac{\partial \Delta g}{\partial z} = 0 \tag{2.11}$$

which can be rearranged to give

$$\frac{\partial \Delta g}{\partial z} = -g_0\left(\frac{\partial \eta}{\partial x} + \frac{\partial \xi}{\partial y}\right) \tag{2.12}$$

The Fourier transform ($\mathcal{F}$) of a function is given as

$$F(\mathbf{k}) = \mathcal{F}(f(\mathbf{x})) = \int_{-\infty}^{\infty}\int_{-\infty}^{\infty} f(\mathbf{x}) e^{-i2\pi \mathbf{k}.\mathbf{x}}\, d^2\mathbf{x} \tag{2.13}$$

where $\mathbf{x}$ is the coordinate (x, y) and $\mathbf{k}$ is the wavenumber vector (k_x, k_y). The Fourier transforms

of the derivatives of the function are given by

$$\mathcal{F}\left(\frac{\partial f(\mathbf{x})}{\partial x}\right) = -i2\pi k_x F(\mathbf{k}) \tag{2.14a}$$

$$\mathcal{F}\left(\frac{\partial f(\mathbf{x})}{\partial y}\right) = -i2\pi k_y F(\mathbf{k}) \tag{2.14b}$$

So by Fourier transforming (2.12) we obtain

$$\frac{\partial \Delta g(\mathbf{k}, z)}{\partial z} = -i2\pi g_0 \left[k_x \eta(\mathbf{k}) + k_y \xi(\mathbf{k})\right] \tag{2.15}$$

Solving Laplace's equation in the wavenumber domain leads to the upward continuation formula, which relates the gravity anomaly at a height z to the gravity anomaly at the surface of the earth ($z = 0$)

$$\Delta g(\mathbf{k}, z) = \Delta g(\mathbf{k}, 0) e^{-2\pi|\mathbf{k}|z} \tag{2.16}$$

where $|\mathbf{k}| = \sqrt{k_x^2 + k_y^2}$. Differentiating this with respect to z and setting z=0 as required, then equating with (2.15) we obtain

$$\Delta g(\mathbf{k}, 0) = i g_0 \left[\frac{k_x}{|\mathbf{k}|}\eta(\mathbf{k}) + \frac{k_y}{|\mathbf{k}|}\xi(\mathbf{k})\right] \tag{2.17}$$

This formula relates the gravity anomaly at the earth's surface to the Fourier transforms of the two components of the deflection of the vertical.

2.2.3 Processing

The processing stages, outlined below, are displayed in Figure 2.7. The satellite dataset used was from the Geosat Geodetic Mission (GM), and included the data up to 30°S, which was released in 1992. Some time after the completion of the map, the construction of which is detailed in this section, further Geosat GM data were declassified, but the map was not extended to include this data.

The first step was to bin the raw data in the form of along-track gradients, separately for

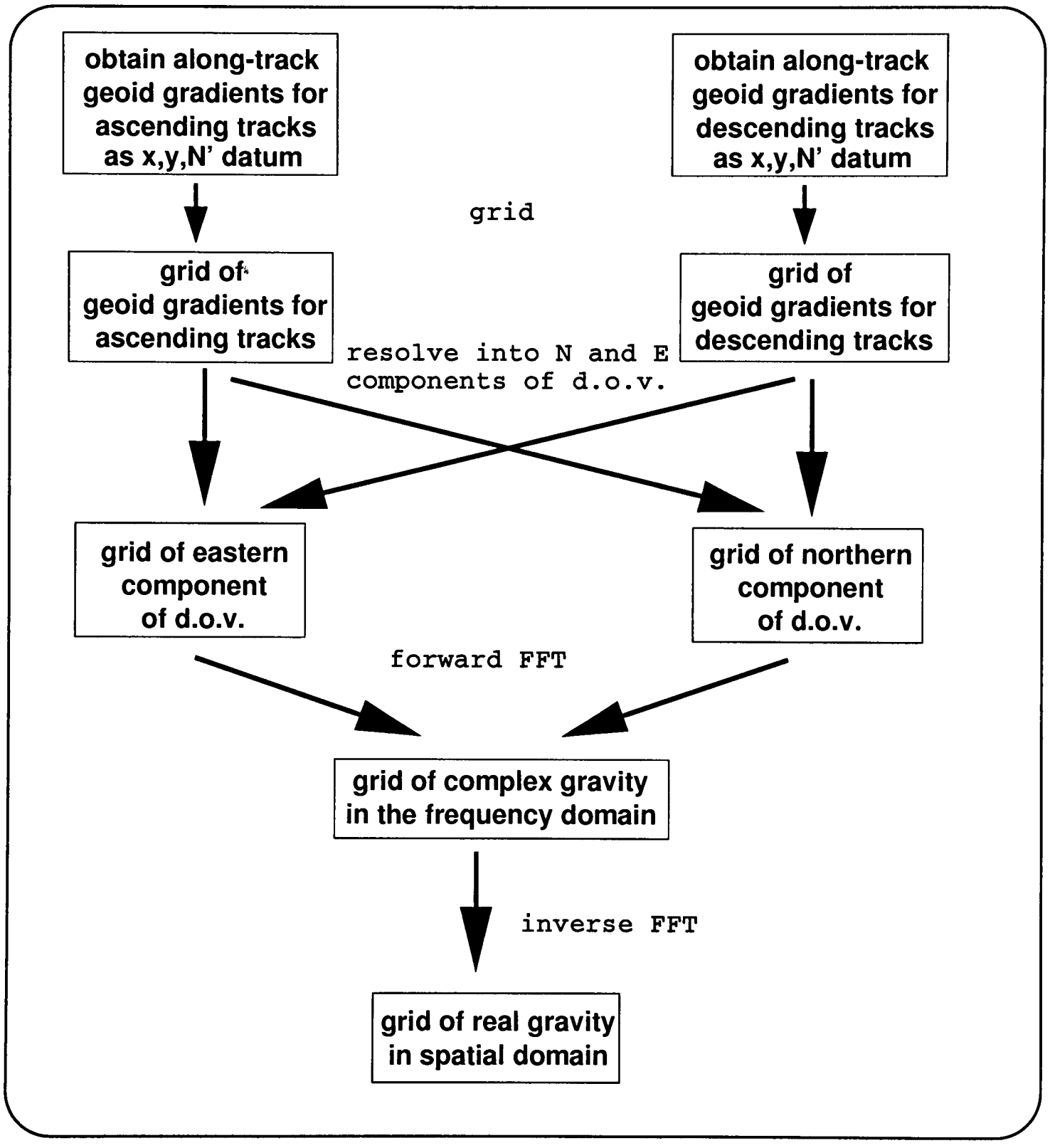

Figure 2.7: Processing stages for creating satellite gravity maps (after Goodwillie (1993)).

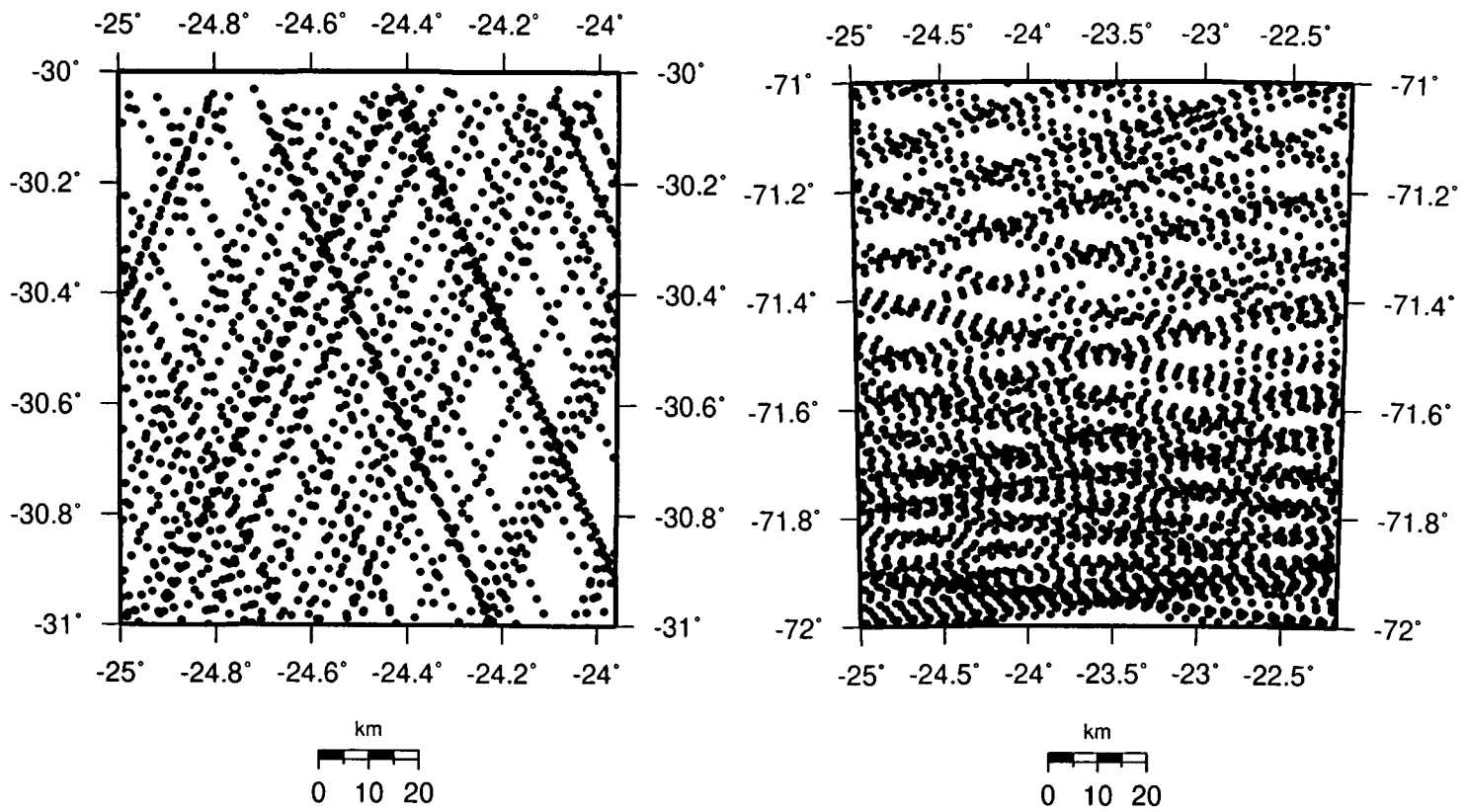

(a) At northern limit of Geosat GM data.

(b) At southern limit of Geosat GM data.

Figure 2.8: Two 100km square regions within the study area showing the distribution of Geosat GM altimeter data points.

ascending and descending tracks, into a grid with cells of a suitable size. For my processing I chose to use cells of .116 degrees longitude by .036 degrees latitude, which led to a grid size of 3.5km x 3.5km at 72°S, the southernmost limit of the GM data, increasing to ≈11km x 3.5km at 30°S, at the northern edge of the study area. The increase in dimension and area of the grid cells was an undesirable but unavoidable consequence of using a latitude-longitude grid. This grid spacing kept the dataset within manageable proportions, though the completed map, from 90°W to 60°E, and from 72°S to 30°S still consisted of over 1.5 million grid cells. To limit introducing artifacts that would arise from using a grid spacing smaller than the maximum resolution, and to remove high-frequency noise, a 7km wide Gaussian filter was used to smooth the extracted along-track gradients. In addition, during the gridding process, a reference geoid field derived from the gravitational model GEM-T1 (Marsh, 1988) was removed, to degree and order 36 (corresponding to a wavelength of the order of 1100km), so that the flat earth approximations used in the determination of (2.17) are valid. This reference field was not replaced at the end of the processing, as the wavelength of the fracture zone features being studied were of the order of 10-100km, and so wavelengths of over 1000km were not required.

Figure 2.8 show the density of the satellite tracks for 100km squares at the northern and

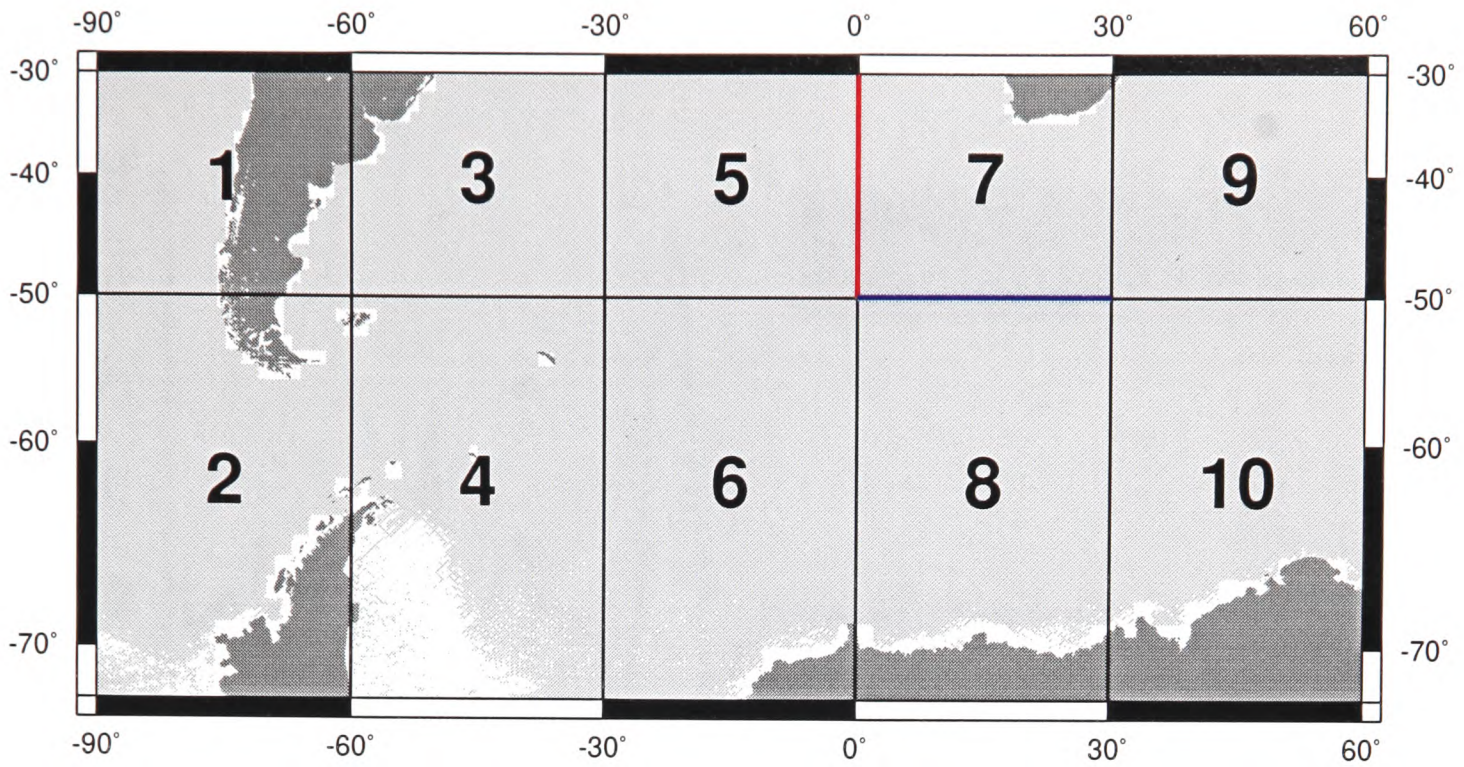

Figure 2.9: Map showing the 10 constituent grids from which the final grid was constructed. Gravity profiles sampled along the highlighted boundaries (5-7, red and 7-8, blue) are given in Figure 2.10. The extent of the satellite data coverage is shown in light grey.

---

southern extremes of the region. These give a measure of the data density, track azimuth, and average cross-track distance and crossover spacing at each location. The data for ascending and descending tracks were gridded separately at this stage, using the GMT routine *blockmean.* Interpolation was then carried out to fill any empty grid-nodes, for which the GMT routine *surface* was used, which incorporates a minimum curvature algorithm. The two gridded datasets for ascending and descending tracks were then processed to create separate gridded files of eastern and northern deflections of the vertical, according to (2.4). These grids were then tapered before Fourier transforming, and then combined according to (2.17). The inverse transform was then applied to the resulting grid to obtain the free-air gravity anomaly.

Rather than process one large grid, which would involve a large amount of computation, the area was split into 10 smaller tiles, as shown in Figure 2.9. These were then processed individually using the same grid spacing (0.116° x 0.036°), trimmed and joined together to form one large grid. By virtue of using large overlaps between the tiles of the order of the long-wavelength filter (1100km) during the processing, there were no visible joins in the final mosaic. When profiles along the final boundary between two adjacent tiles were sampled from both of these tiles before cropping, the RMS error between the two profiles was negligible (an RMS error of less than 1 mgal). Figure 2.10 shows two sets of gravity profiles sampled along the two tile boundaries marked on Figure 2.9, which displays the correlation between the neighbouring tiles. In addition,

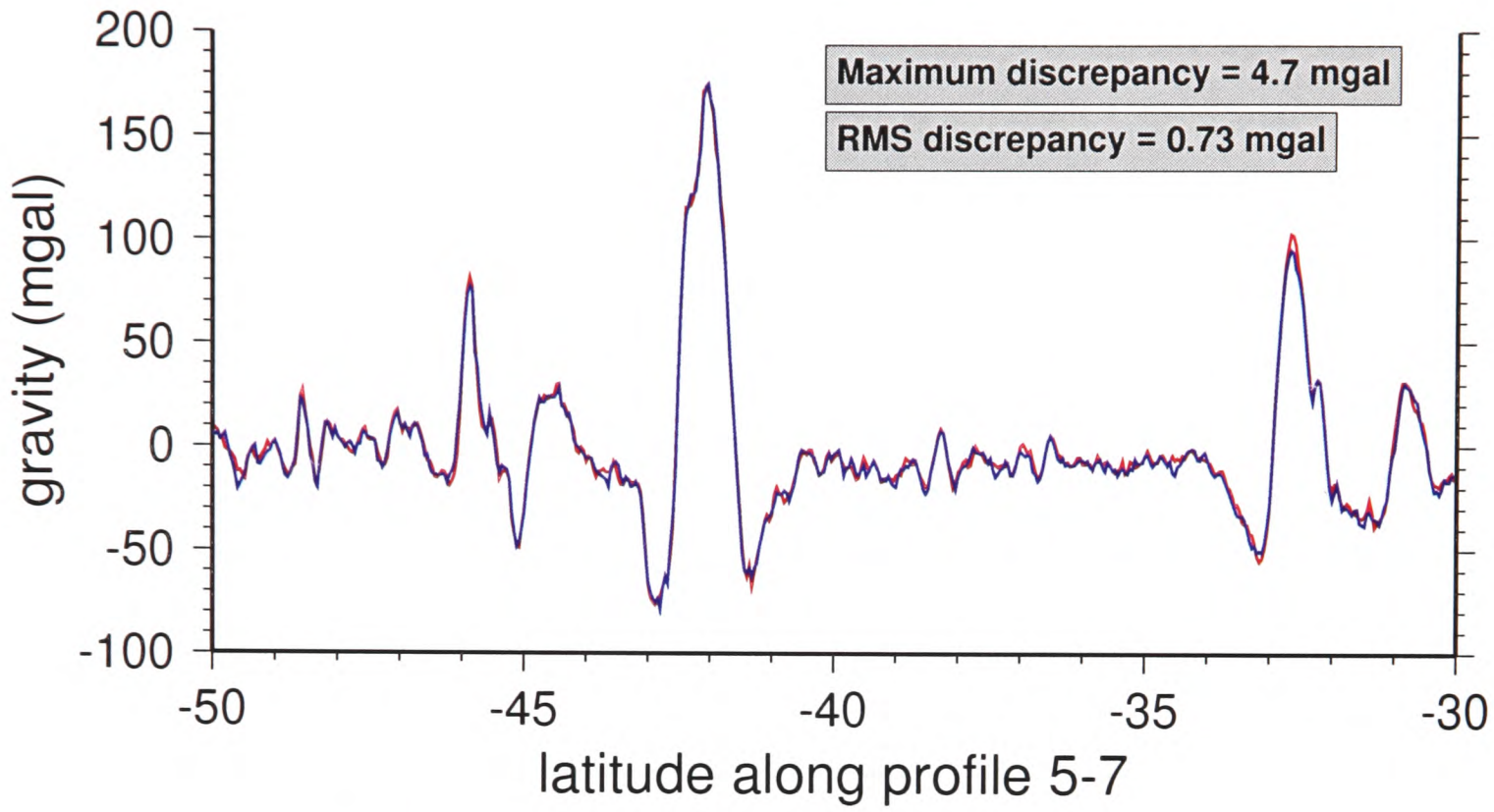

(a) Gravity profiles sampled from tiles 5(red) and 7(blue) along the join between the two tiles.

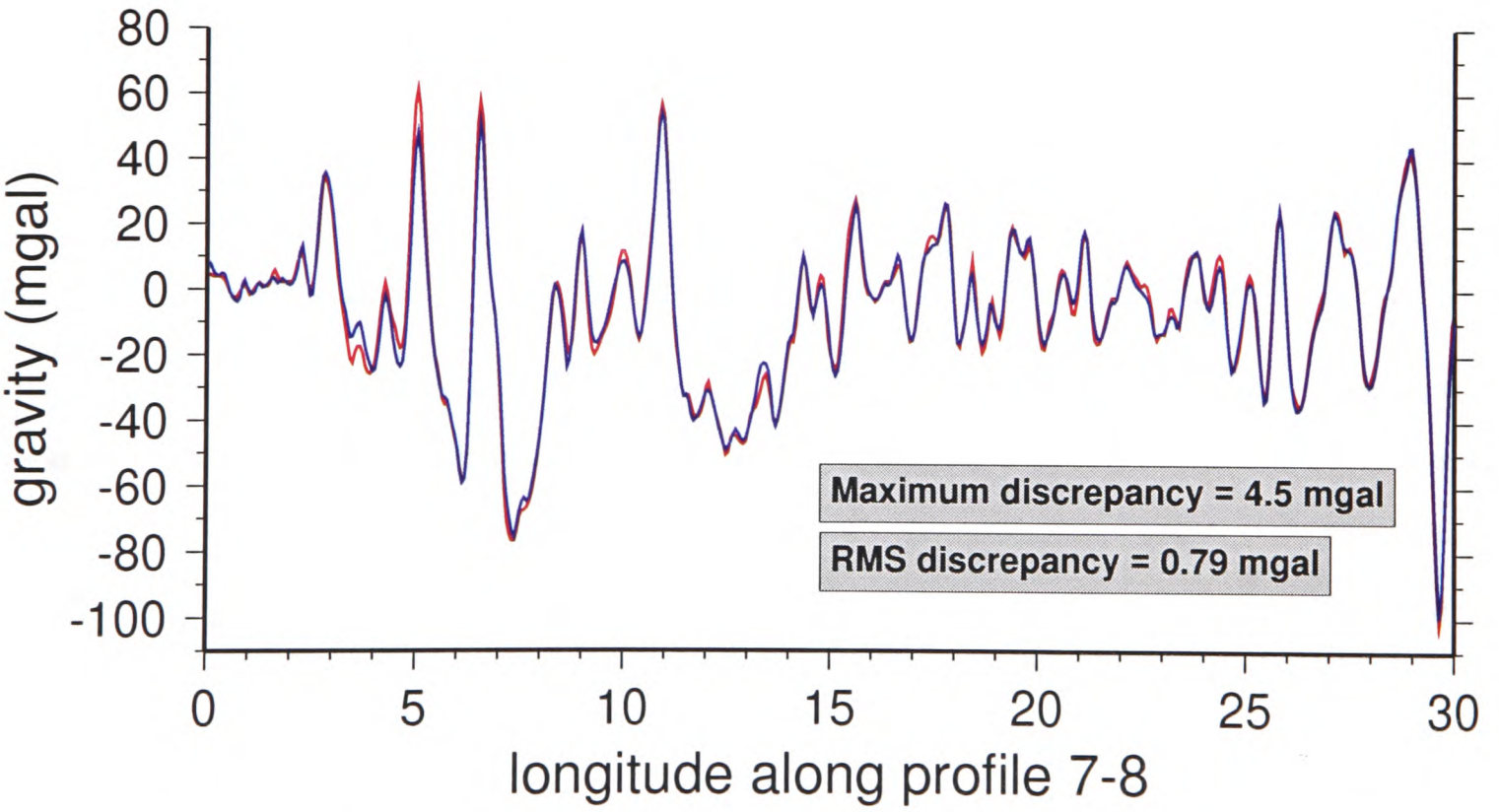

(b) Gravity profiles sampled from tiles 7(red) and 8(blue) along the join between the two tiles.

Figure 2.10: Gravity profiles sampled along boundaries between smaller processing tiles before combining to form the final gravity grid.

subsequent comparison was made to the later gravity map of Smith & Sandwell (1995) (which also included ERS-1 and Geosat ERM altimeter data) along the profiles shown in Figure 2.10 and the RMS misfit was calculated to be 1.13 mgal along line 5-7, and 1.8 mgal along line 7-8. However, the gravity image of Smith & Sandwell (1995) also included wavelengths greater than 1100km, which were excluded from this gravity map, and so the true correspondence was likely to be significantly better.

An image of the final gravity map is shown in Figure 2.11. This was used for all of the images and sampled gravity profiles in this thesis, unless otherwise stated.

2.3 Modelling of a fracture zone

Gravity anomalies result from lateral variations in density, related to the deficiency or excess of mass beneath the area of the observation. Thus variation in topographic relief across a length of seafloor, coupled with the associated isostatic mass compensation at the base of the crust gives rise to a gravity anomaly, which can easily be modelled. A degree of isostatic compensation is assumed though features with wavelengths of the order of $\approx$100km are not considered to be isostatically compensated, as this is effectively ensured by taking plate flexure into account. The fracture zone trough would be expected to give rise to a negative gravity anomaly on a profile crossing a fracture zone, with the gravity anomaly minimum coinciding with the bathymetric minimum along the profile.

The effects of sediment infill are not considered, as the additional rate of sedimentation within a fracture zone valley relative to the flanking seafloor is not known. Although the overall gravity signature of a fracture zone is seen to decrease far from the mid-ocean ridge, it is assumed that sediment would be draped evenly across the central fracture zone valley and so would only have an effect of the amplitude, and not location, of the minimum of the free-air anomaly associated with the fracture zone topography.

If the gravity signal due to the topographic variation across a fracture zone was the only factor contributing to the local free-air anomaly, then picking the exact location of the bathymetric minimum of the fracture zone from a series of perpendicular gravity profiles would be a simple task. However, as rock moves away from the spreading centre at which it was created, it cools, at a rate that is easily modelled (Parsons & Sclater, 1977). As a fracture zone is a boundary

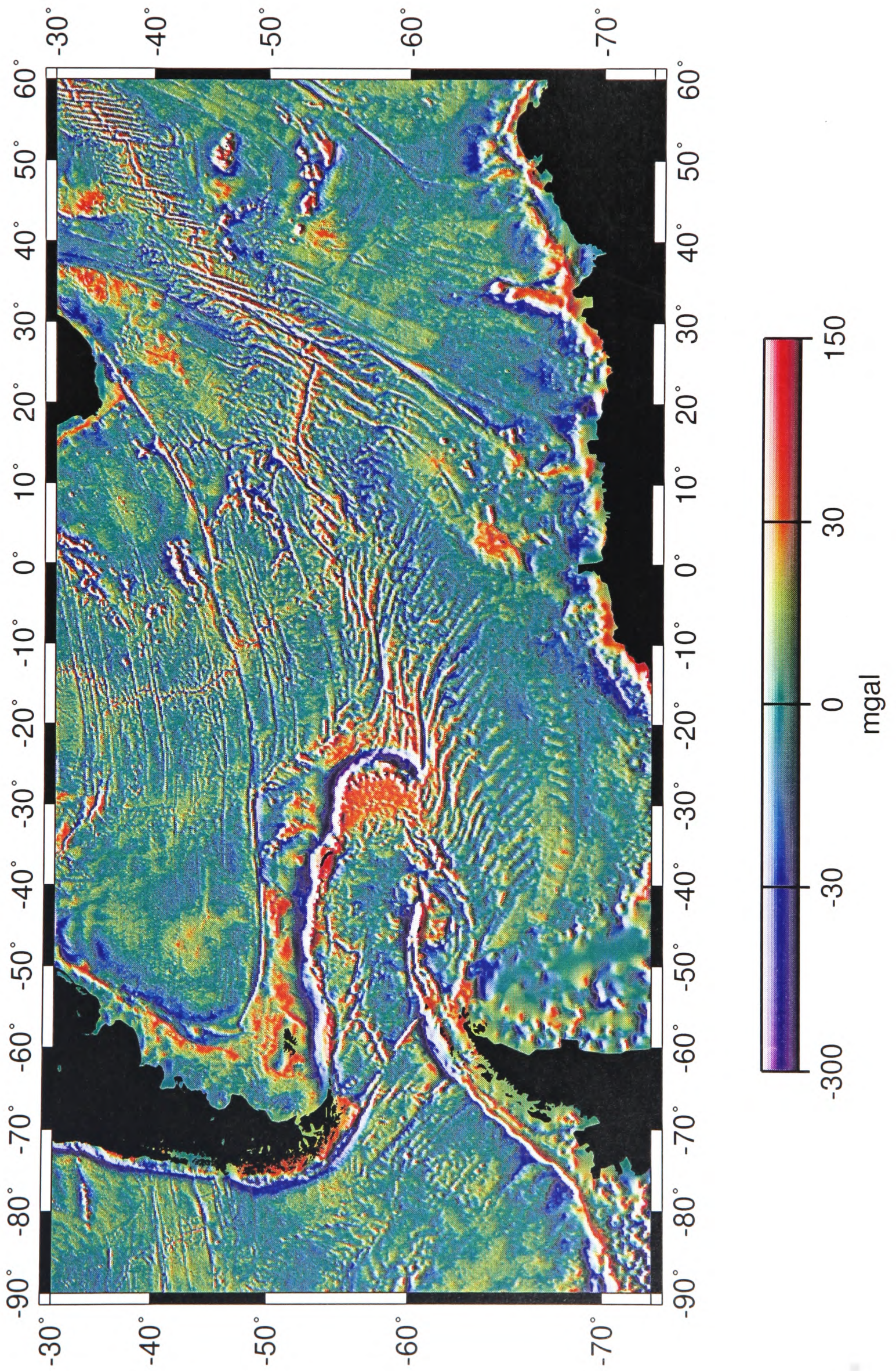

Figure 2.11: Final version of gravity map processed from Geosat GM data.

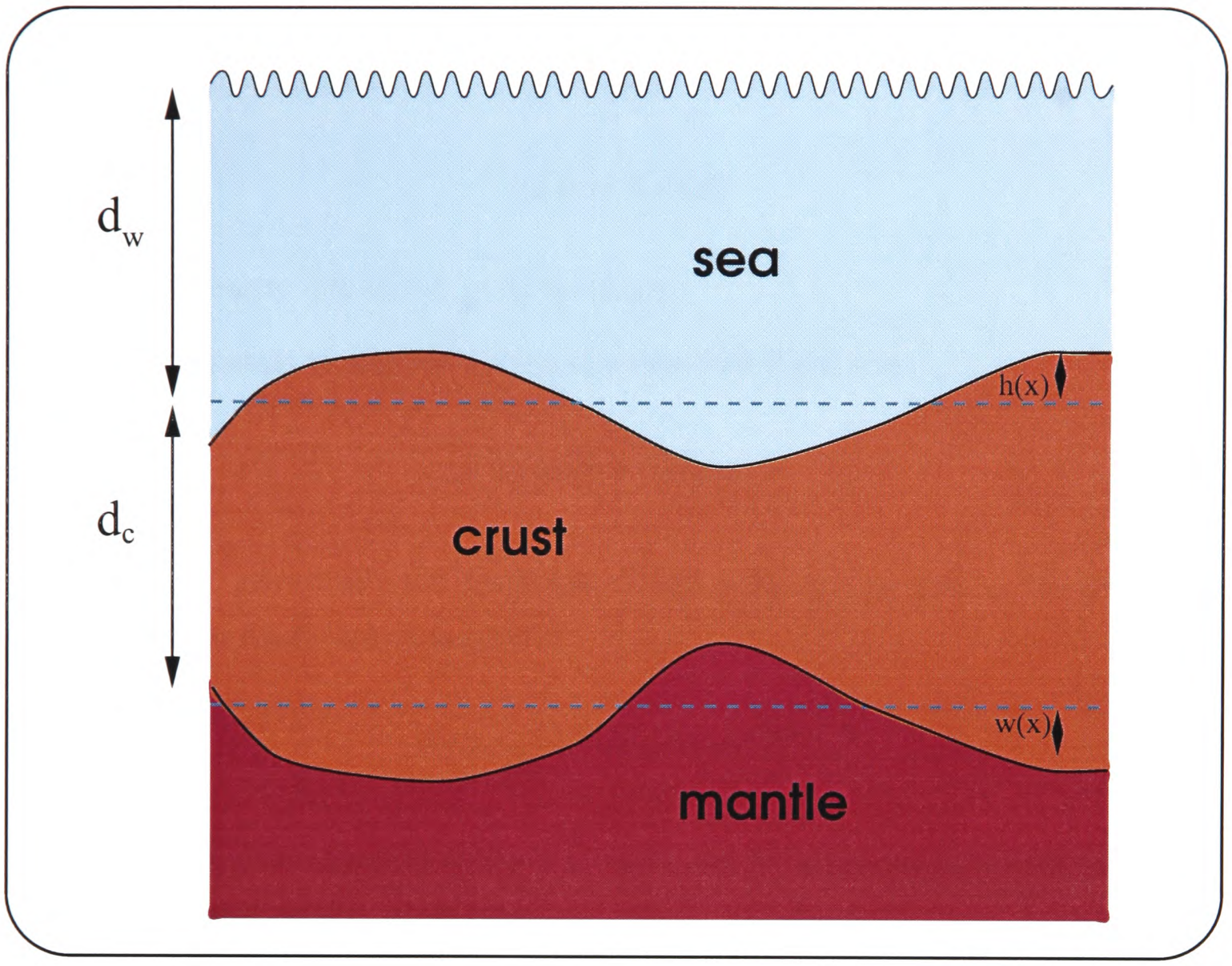

Figure 2.12: Cartoon showing the isostatic compensation mechanism for topographic relief on the seafloor (not to scale).

between rocks of two different ages, then it is also a boundary between rocks with a different thermal structure, and hence different densities, which will also give rise to a gravity anomaly. So, to determine a realistic model of a fracture zone, both these effects need to be taken into consideration.

2.3.1 Modelling gravity from a 1-d topographic profile

Given a 1-d topographic profile we wish to determine the gravity profile $g(x)$ associated with this. Figure 2.12 shows graphically the model used. The seafloor, at an average depth d_w has a continuous topographic variation, $h(x)$, which is isostatically compensated at the compensation depth d_c, by a deviation in the level of the mantle-crust boundary $w(x)$. As stated previously, effects of sediment deposition is not considered.

To consider the gravity signal caused by this mass distribution, each boundary is considered as an infinitesimally thin shell with a mass variation σ_s along the boundary, such that

$$\sigma_s(x) = \Delta\rho h(x) \tag{2.18}$$

where $\Delta\rho$ is the density differential at the boundary.

The gravity anomaly at any point along this thin shell is given by

$$\Delta g(x) = 2\pi G\sigma_s(x) \tag{2.19}$$

and from this, and utilising the upward continuation formula for gravity, the gravity signal at a height z above the boundary is given by

$$\Delta g(x,z) = 2\pi G\Delta\rho h(x)e^{-2\pi kz} \tag{2.20}$$

and so combining the signals from the crust-water and the crust-mantle boundary, the gravity anomaly at the water surface, is given by

$$\Delta g(x) = 2\pi G\left((\rho_c - \rho_w)h(x)e^{-2\pi kd_w} + (\rho_m - \rho_c)w(x)e^{-2\pi k(d_w+d_c)}\right) \tag{2.21}$$

This can only be solved in the frequency domain and after taking Fourier transforms, this becomes

$$\Delta G(k) = 2\pi Ge^{-2\pi kd_w}\left((\rho_c - \rho_w)H(k) + (\rho_m - \rho_c)W(k)e^{-2\pi kd_c}\right) \tag{2.22}$$

where $\Delta G(k)$, $H(k)$ and $W(k)$ are the 1-d Fourier transforms of $\Delta g(x)$, $h(x)$ and $w(x)$ respectively.

All that remains is to determine $W(k)$. For the model to be isostatically compensated, the forces (pressures) at depth $d_w + d_c$ must be equal at every point along the profile. By simple

mass balance this gives

$$d_w\rho_w g_0 + d_c\rho_c g_0 = [d_w - h(x)]\,\rho_w g_0 + [d_c + h(x) + w(x)]\,\rho_c g_0 - w(x)\rho_m g_0 \tag{2.23}$$

Rearranging this equation we obtain

$$w(x) = -\left(\frac{\rho_c - \rho_w}{\rho_m - \rho_c}\right) h(x) \tag{2.24}$$

To solve this, we take the Fourier transform, and apply the definition of the transform of a derivative, (2.14), to obtain

$$W(k) = \left(\frac{\rho_c - \rho_w}{\rho_m - \rho_c}\right) H(k) \tag{2.25}$$

Substituting for $W(k)$ into (2.22) gives

$$\Delta G(k) = 2\pi G(\rho_c - \rho_w) H(k) e^{-2\pi k d_w} \left(1 - e^{-2\pi k d_c}\right) \tag{2.26}$$

If we wish to include flexural effects, then a term $-D\frac{d^4w}{dx^4}$ must be added to the right of (2.23), where D is the flexural rigidity of the plate, defined as

$$D = \frac{E t_e^3}{12(1-\sigma^2)} \tag{2.27}$$

where E is Young's modulus and σ Poisson's ratio, and t_e is the elastic thickness of the plate. For a plate of age τ, the elastic thickness is given as

$$t_e = 2\sqrt{\kappa\tau}\,\mathrm{erf}^{-1}\left(\frac{T_l}{T_m}\right) \tag{2.28}$$

where κ is the thermal diffusivity, T_m the mantle temperature and T_l the stress relaxation temperature (the isotherm that defines the base of the mechanical plate, Wessel & Haxby (1990)).

(2.26) then becomes

$$\Delta G(k) = 2\pi G(\rho_c - \rho_w) H(k) e^{-2\pi k d_w} \left(1 - \left[1 + \left(\frac{k^4 D}{g_0(\rho_m - \rho_c)}\right)\right]^{-1} e^{-2\pi k d_c}\right) \tag{2.29}$$

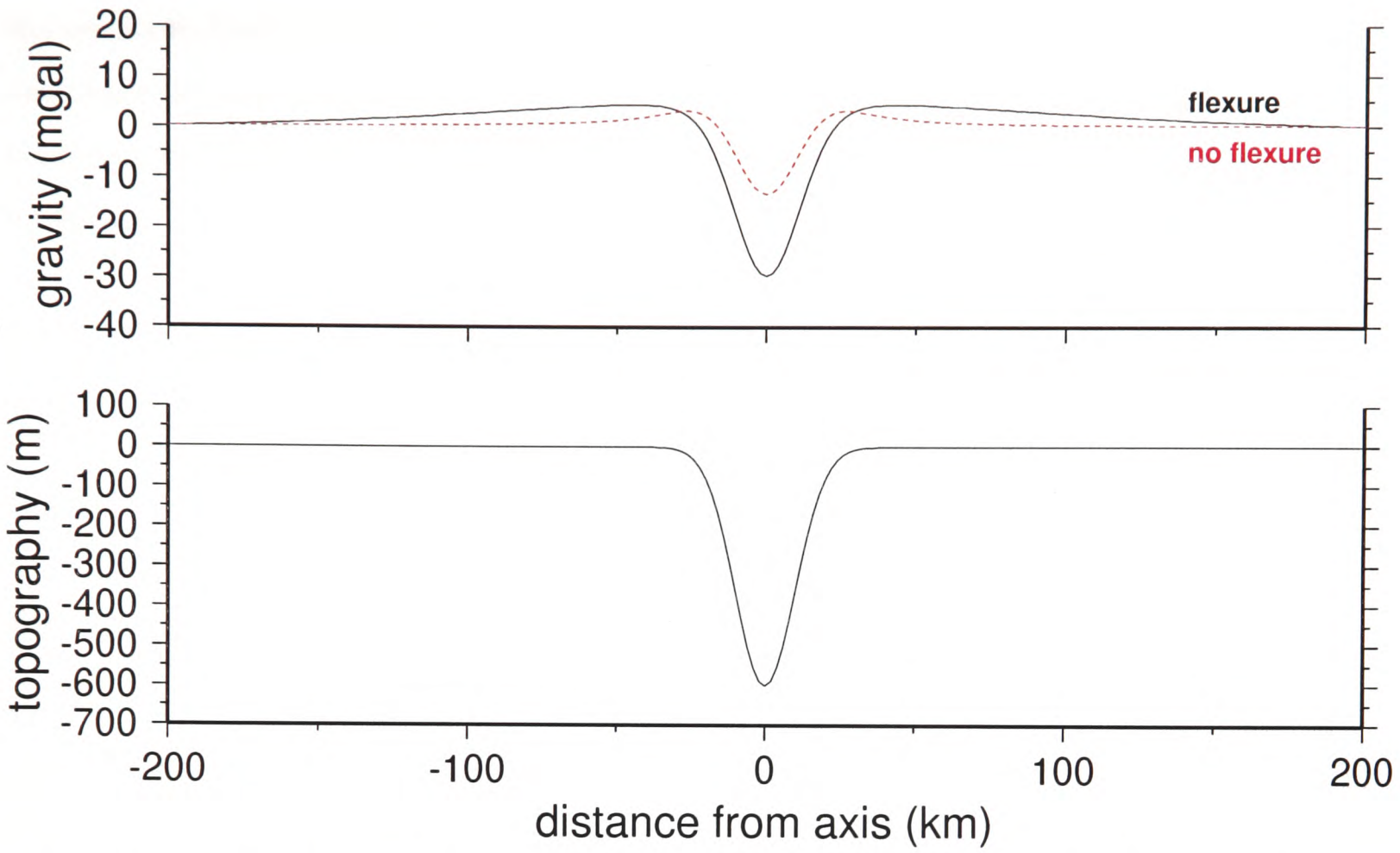

Figure 2.13: Modelling the gravity for a simple model of a fracture zone trough, with a lithospheric age of 20Ma, giving a t_e of 18.5km.

To obtain the theoretical gravity signal produced by a known 1-d topographic profile, the Fourier transform of the profile is found, then the operation(s) above carried out in the wavenumber domain, then the inverse transform applied to recover the gravity signal.

The topographic profile itself can either be a theoretical model, or real topography from a ship track crossing. For a real topographic profile, the average seafloor depth must first be removed, as a simple trend in the data, before any Fourier transforms are calculated. Removing a trend rather than a constant depth will lead to the loss of a long-wavelength component of the gravity, but the effects we are interested in are short-wavelength, and so this is inconsequential. A gravity profile derived from a simple topographic model for a fracture zone, a basic Gaussian minimum, is given in Figure 2.13.

This shows how the gravity reflects the shape of the topography, with the minima coinciding exactly. The rises either side of the minima reflect the effect of the flexural term. The validity of modelling for a plate with constant elastic thickness and density across the fracture zone can be questioned. However, with the crustal structure close to the axis of a fracture zone unable to be modelled with any great confidence (Figure 2.4), it provides a useful basic model and, as

the results in Section 2.3.3 show, it is remarkably effective. The values for the elastic thickness, and hence flexural rigidity of the plate were determined for the average age of the fracture zone, according to (2.27) and (2.28). Table 2.1 gives the values for various constants used in the modelling.

2.3.2 Modelling gravity for an age step in the seafloor

It is known that the geoid height above a region of seafloor decreases with the age of the seafloor, and much work has been done on the calculation and modelling of the geoid step across a fracture zone (Driscoll, 1987; Driscoll & Parsons, 1988; Freedman & Parsons, 1990; Sandwell, 1981, 1984; Wessel & Haxby, 1989).

The model used here is the plate-cooling model, where the seafloor created at a mid-ocean ridge is taken to have a finite plate thickness, and the base of this plate is held at a constant temperature by a heat reservoir. This model accurately predicts the change in seafloor depth with age, which results from the thermal contraction of the plates during cooling.

The temperature $T(\tau, z)$ at depth z below the seafloor of age τ is given by

$$T(\tau, z) = T_m \left[\frac{z}{a} + \frac{2}{\pi} \sum_{n=1}^{\infty} \frac{1}{n} \exp\left(\frac{-n^2 \pi^2 \kappa \tau}{a^2} \right) \sin\left(\frac{n\pi z}{a} \right) \right] \tag{2.30}$$

where T_m is the mantle temperature, κ is the thermal diffusivity and a is the plate thickness.

The isostatic geoid anomaly over a section with temperature structure $T(\tau, z)$, relative to zero age lithosphere, is given by

$$\Delta N(t) = \frac{-2\pi G \rho_m}{g} \int_0^a z\alpha \left(T_m - T(\tau, z) \right) dz \tag{2.31}$$

A profile representing the geoid step across a fracture zone with young age τ and offset $\Delta\tau$ at $x = 0$ was determined by Driscoll & Parsons (1988), utilising the above relationships and taking

into account horizontal conduction across the fracture zone, to be

$$N(x) = \frac{1}{2}\left[1 + \mathrm{erf}\left(\frac{x}{2\sqrt{\kappa\tau}}\right)\right]\theta(\tau) + \frac{1}{2}\left[1 - \mathrm{erf}\left(\frac{x}{2\sqrt{\kappa\tau}}\right)\right]\theta(\tau + \Delta\tau)$$

$$\text{with} \quad \theta(\tau) = \frac{4G\rho_m\alpha T_m a^2}{\pi g}\sum_{n=1}^{\infty}\frac{(-1)^{n+1}}{n^2}\exp\left(\frac{-n^2\pi^2\kappa\tau}{a^2}\right) \tag{2.32}$$

where ρ_m is the mantle density and α is the volume coefficient of thermal expansion. The function $\theta(\tau)$ represents the value for the geoid distant from the fracture zone.

It is a simple step to convert a 1-d geoid profile into a gravity profile in the frequency domain, using the following relationship

$$\Delta g = g_0 k N(k) \tag{2.33}$$

So the expected gravity anomaly profile perpendicular to a fracture zone, due to the age step across it, can easily be modelled if the ages of the seafloor either side of the fracture zone are known, and assuming the thermal gradient along the fracture zone is not too high. The amplitude of the theoretical profile across a fracture zone of defined age and offset is affected only by one value, the thermal plate thickness, a. This is the depth below the crustal surface at which the temperature is kept constantly at the mantle temperature, for this cooling model. All of the other parameters used in the modelling calculations are reasonably well-defined for oceanic plates, and the values used are given in table 2.1.

An example of the gravity signal resulting from the geoid/age step across a fracture zone is shown in Figure 2.14 for a theoretical fracture zone with young age 20Ma and offset 5Ma. The main feature of interest is that the gravity low on the profile is offset from the central axis of the fracture zone, on the older side of the fracture zone. The amplitude of the anomaly, however, is low, especially when compared to the magnitude of the anomaly produced by topographic effects. Figure 2.15 shows a series of profiles at increasing distance from the spreading centre (i.e. average age increasing) it can be seen that the amplitude of this thermal signal decreases as the rocks both sides of the fracture zone become older.

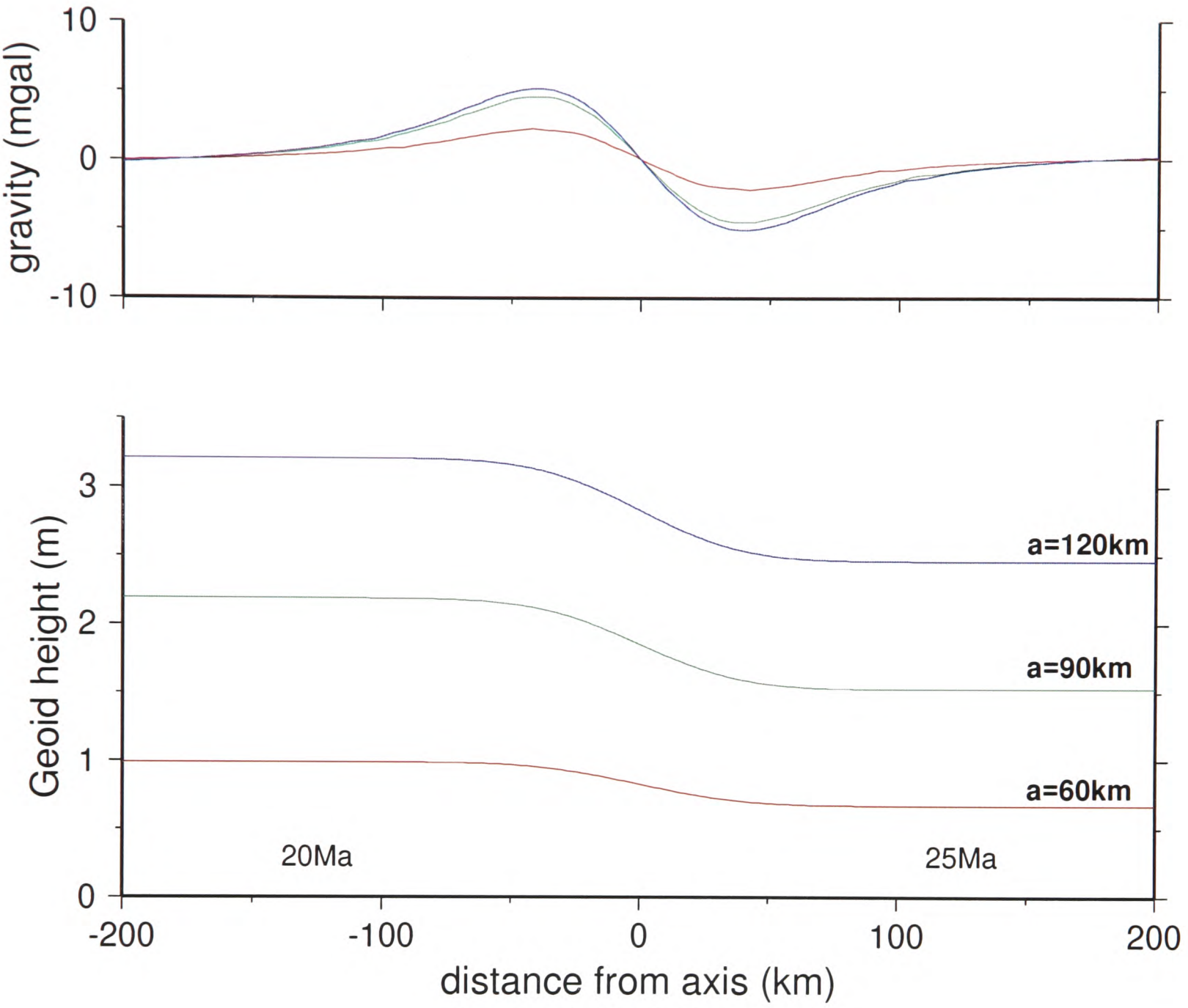

Figure 2.14: Modelling the gravity resulting from the geoid-age step across a fracture zone with young side 20Ma, and offset 5Ma, for three different values of thermal plate thickness(a). The geoid heights have been dc-shifted slightly to enable easy comparison.

2.3.3 Method and results of modelling

So, to create a complete model, the gravity signals from a topographic model and the thermal (density variation) model for a fracture zone need to be combined. The approximate ages of the neighbouring seafloor on both sides are required to produce the thermal model, and a perpendicular topographic profile needs to be supplied.

The aim of the modelling is to determine a picking procedure for the fracture zone. The best measure of the location of a fracture zone in this study is considered to be the centre of the axial valley of the fracture zone, as opposed to the scarp face of the topographic step. However, from the simple models of the thermal and topographic components of the gravity signal shown

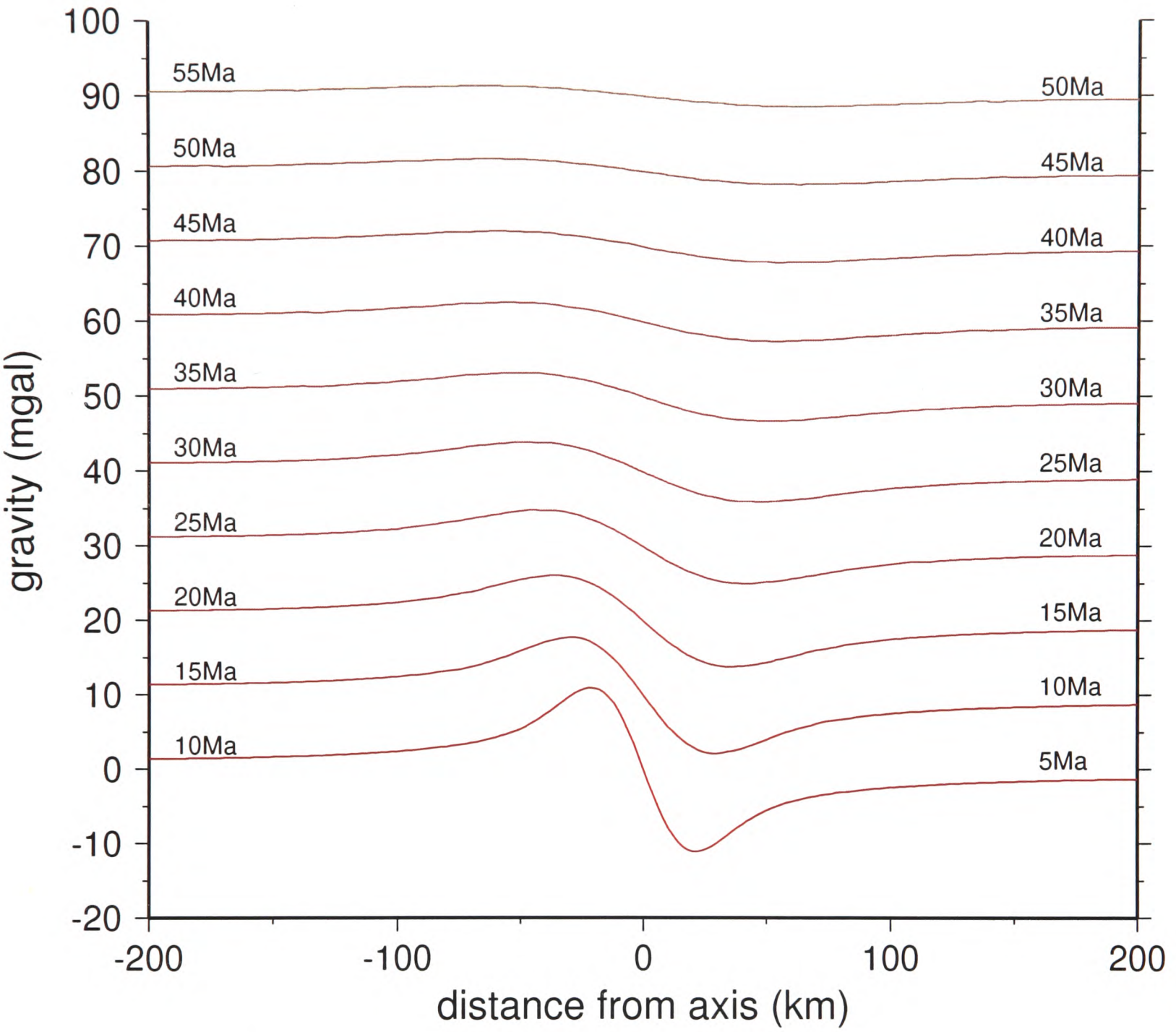

Figure 2.15: A sequence of modelled gravity profiles for the thermal structure across a fracture zone, at increasing distance from the axis (assuming constant spreading rate). Each gravity profile has been cumulatively dc-shifted by 10mgal.

---

previously it can be seen that while the fracture zone trough will provide a gravity minimum centred over the axis of the fracture zone, the thermal offset gives rise to a 'single wave' gravity signal with a minimum offset to the side of the older seafloor. The purpose of the exercise is to determine whether the thermal contribution will shift the observed gravity minimum to one side of the axis of the fracture zone, leading to inaccurate picks for a fracture zone if they have been made by consistently picking the observable minimum on gravity profiles crossing the fracture zone. Thus it needs to be determined where the fracture zone should be picked on a perpendicular gravity profile, and as the thermal signal decreases with average age of the seafloor, whether this decision would vary depending on the age and offset of the fracture zone.

Figure 2.16 shows the locations of the fracture zones that were used for the modelling detailed here, with the work concentrated on South Atlantic fracture zones created along the Mid-Atlantic Ridge. This was because the fracture zones in general have a greater separation and the surrounding topography is smoother than along the other ridges in the study. To create the best possible model, the gravity signal due to crustal thickness variations was calculated using an actual bathymetric profile from ship data. The gravity anomaly along-track was also sampled from the satellite gravity maps, to be used as a comparison to the more accurate gravity anomalies recorded by the ship. Ship tracks crossing fracture zones were selected fulfilling the following criteria: (i) both bathymetric and gravity data were being recorded; (ii) the track crosses the fracture zone at an angle as close to perpendicular as possible; (iii) the fracture was as far separated from another fracture zone as possible to avoid any contamination of the signal; (iv) the ship track was not in the vicinity of a hotspot or seamount.

The location of the first fracture zone, Christmas fracture zone, that I concentrated on is shown in 2.17, along with the ship tracks used in the modelling. The approximate age of the seafloor where the ship tracks cross, required for the modelling were determined from synthetic flowlines created from the poles determined for the South Atlantic by Shaw & Cande (1990). As stated before, the along-track topography was used to calculate the gravity signal due to crustal thickness variations, but before this was done, the topographic profile was projected onto a line

Parameter	Definition	Value
ρ_w	Density of seawater	1025 kg/m^3
ρ_c	Density of crust	2800 kg/m^3
ρ_m	Density of mantle	3300 kg/m^3
d_w	Mean water depth	3000 m
d_c	Depth of compensation (average crustal thickness)	8000 m
T_m	Mantle temperature	1365 °C
T_l	Stress relaxation isotherm*	600 °C
κ	Thermal diffusivity*	8.0x10^{-7} m^2/s
α	Volume coefficient of thermal expansion*	3x10^{-5} K
E	Young' modulus*	1.0x10^{11}Pa
σ	Poisson's ratio*	0.25
G	Gravitational constant	6.67x10^{-11} Nm^2/kg^2
g_0	Average gravitational acceleration	9.81 m/s^2

Table 2.1: Values of parameters used in modelling the gravity anomalies. * Taken from Wessel & Haxby (1990)

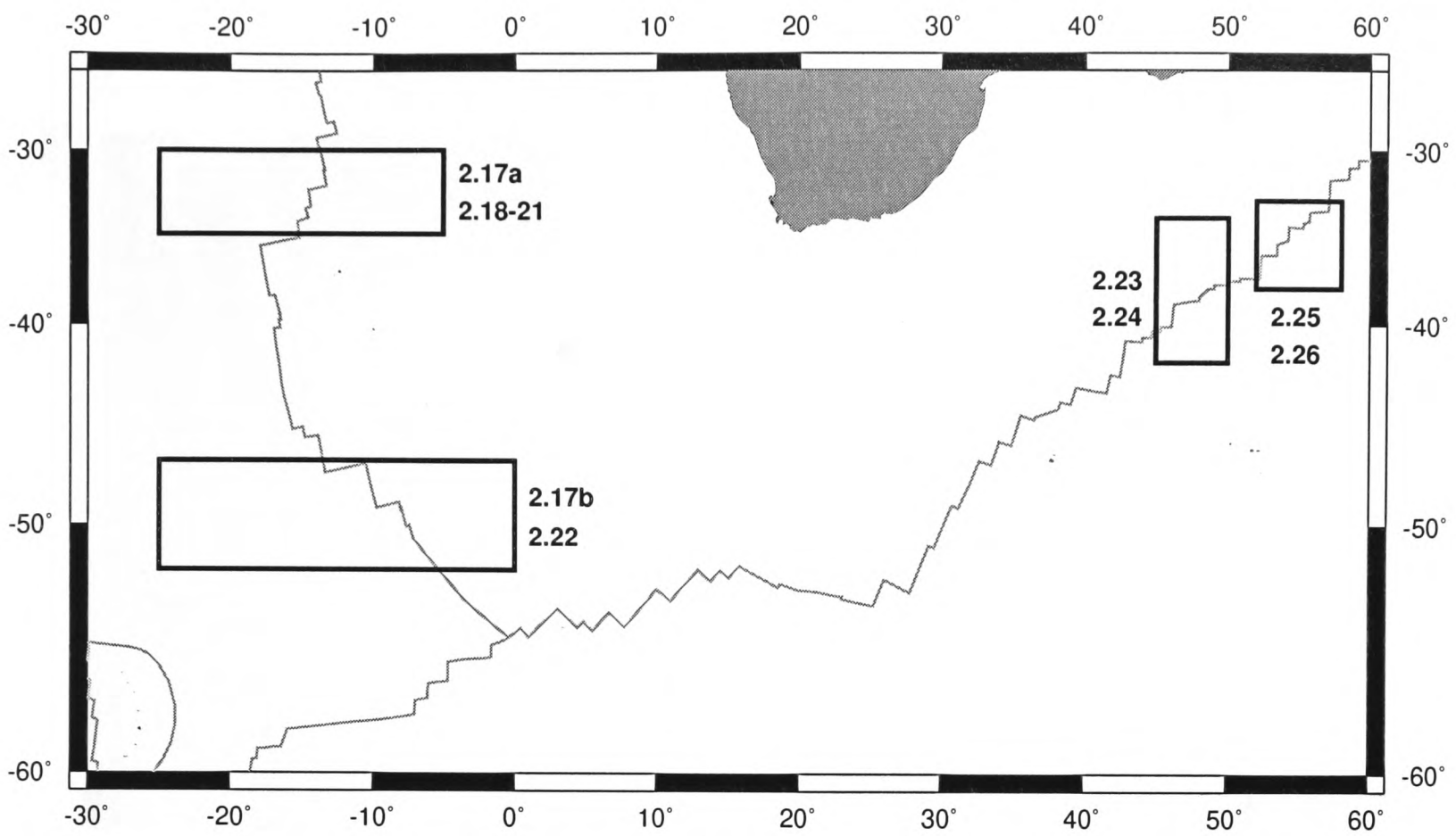

Figure 2.16: Map showing the locations of the principal fracture zones used in the gravity modelling. The numbers of the corresponding figures are shown for each area.

perpendicular to the fracture zone. The ages of the seafloor either side of the fracture zone were used to find the expected signal from the thermal structure across the fracture zone for a variety of thermal plate thicknesses, varying from 50km to 100km.

The results of the modelling are shown in Figure 2.18. The first thing to notice is that the ship and satellite gravity profiles are a very good match, which is to be expected. Looking at the profiles created by the model, and comparing them with the component of the model determined from the seafloor topography, it can be seen that the latter dominates the gravity signal. The thermal signal is apparent only as a slight amplitude offset either side of the fracture zone axis and doesn't appear to affect the location of the central gravity low of the profile. All the major features of the model, the peaks and troughs, come from the topographic component of the model, and closely match the position and amplitude of the true features as appearing on the gravity profiles. Taking the ship gravity as the most accurate of the two profiles, then neither of the plate thicknesses provide an exact match for the model, but the only difference between the effects of the two thermal components is in the amplitudes of the closest maxima and minima flanking the fracture zone axis. It would be hard to choose the most likely plate thickness mainly because the thermal component affects the features of the total model so little.

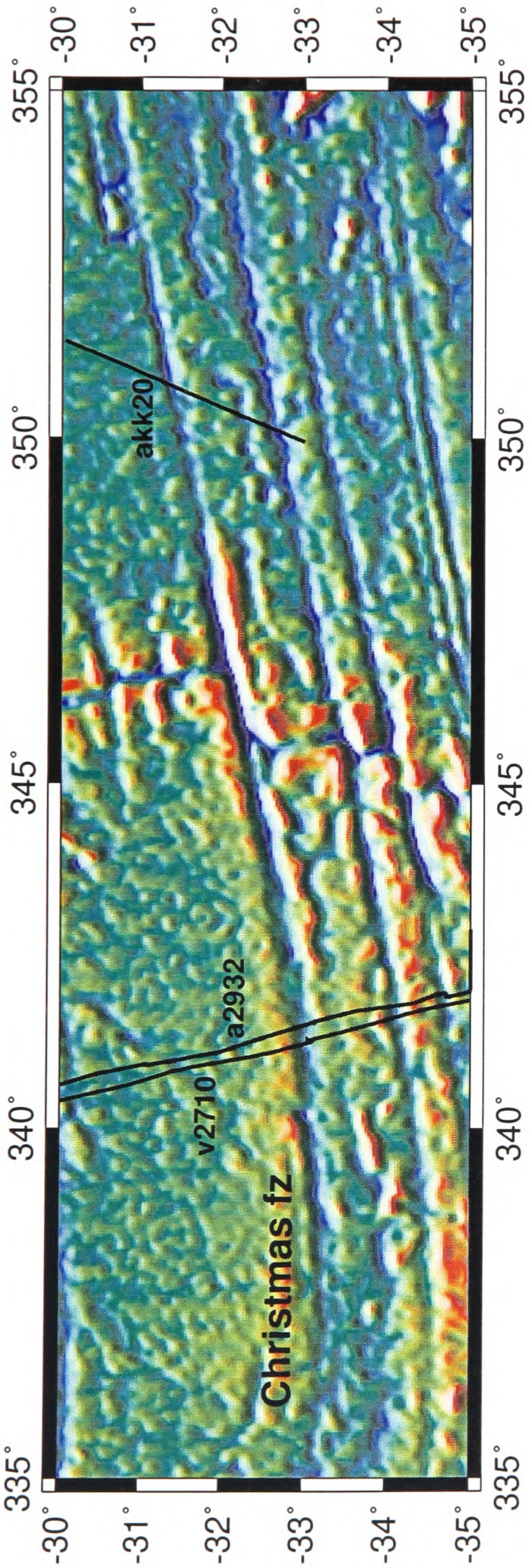

(a) Christmas Fracture zone.

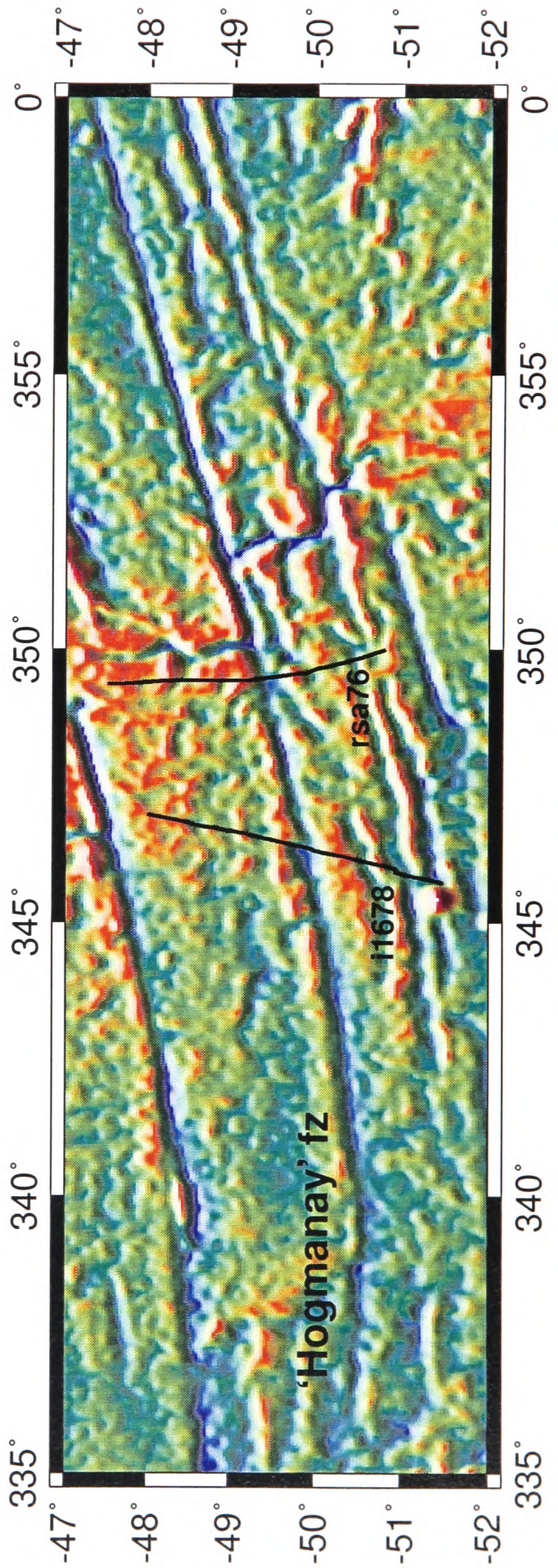

(b) 'Hogmanay' Fracture zone.

Figure 2.17: The location of the two fracture zones and ship crossings in the South Atlantic used for modelling gravity signals over fracture zones.

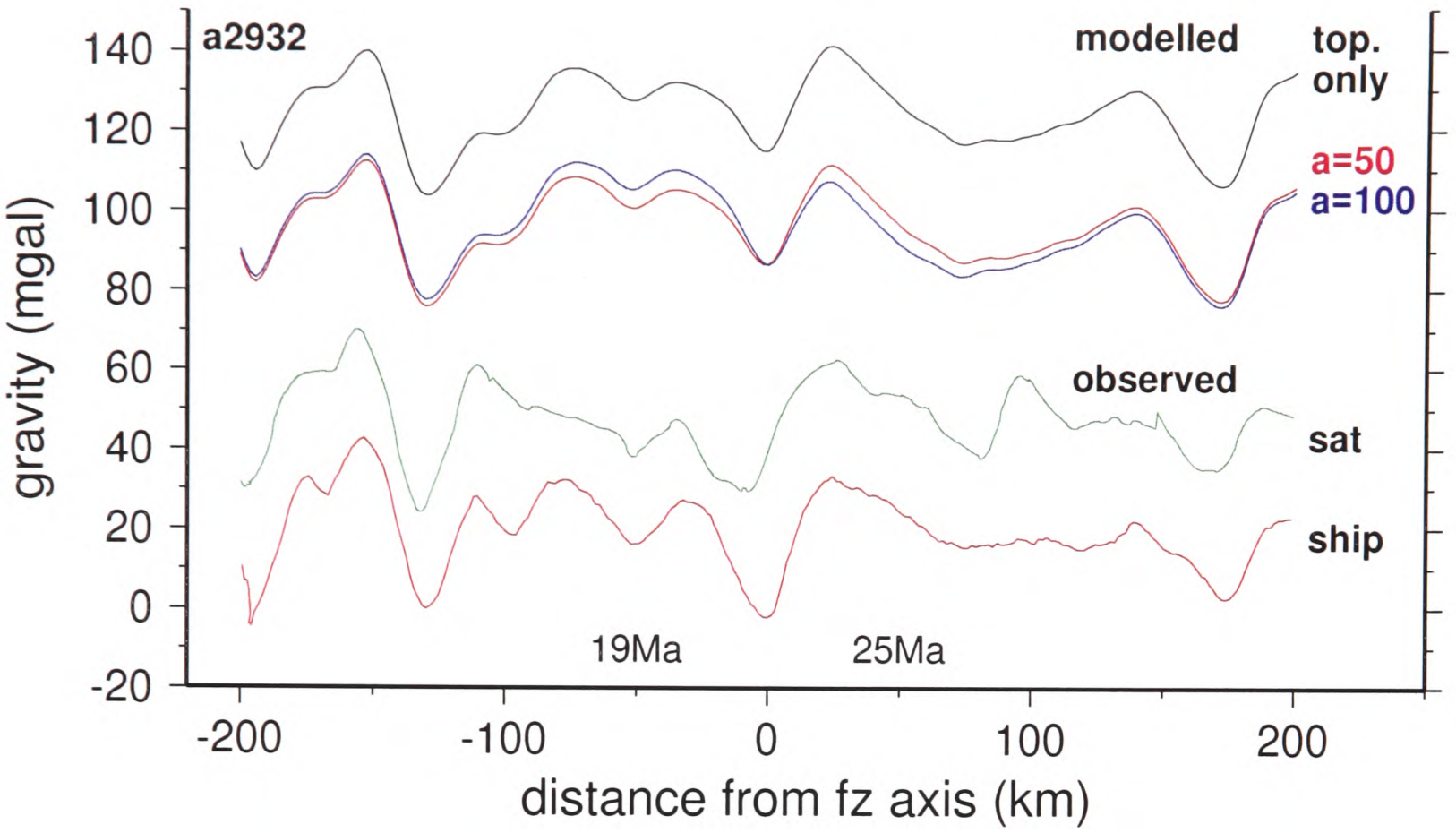

Figure 2.18: Gravity profiles across Christmas fracture zone in the South Atlantic, for two crossings on the western flank (marked on Figure 2.17(a)). In each case, the free-air gravity recorded by the ship is shown in red, and the sampled satellite gravity (from Figure 2.11) in green. Two profiles are displayed for the total modelled (expected) gravity anomaly, where the thermal component was determined for thermal plate thicknesses, a, of 50 and 100km, in red and blue respectively. In addition, the component of the model determined from the observed topography alone (no thermal component) is shown in black. The gravity profiles have been dc-shifted relative to each other (except for the two total models) for easier comparison.

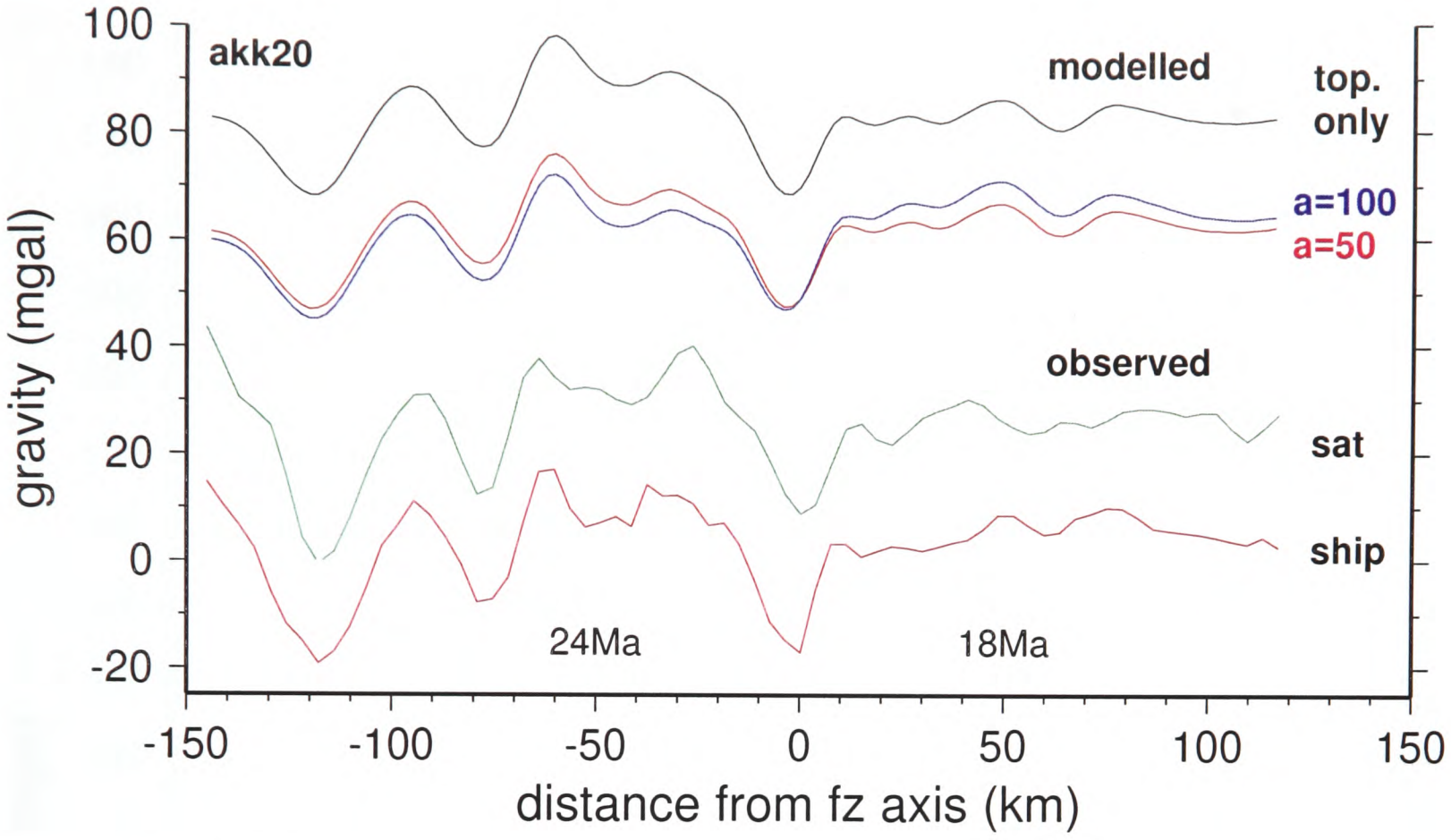

Figure 2.19: Gravity profiles across Christmas fracture zone in the South Atlantic, for a crossing on the eastern flank (marked on Figure 2.17(a)). The free-air gravity recorded by the ship is shown in red, and the sampled satellite gravity (from Figure 2.11) in green. Two profiles are displayed for the total modelled (expected) gravity anomaly, where the thermal component was determined for thermal plate thicknesses, a, of 50 and 100km, in red and blue respectively. In addition, the component of the model determined from the observed topography alone (no thermal component) is shown in black. The gravity profiles have been dc-shifted relative to each other (except for the two total models) for easier comparison.

Looking at the gravity profiles on the eastern branch of the fracture zone, in Figure 2.19, again, the component of the gravity model calculated from the observed topography reflects the main features of the true gravity. The thermal component alters the amplitude of the profile off-axis, but has negligible effect on the central gravity minimum.

So from this, it appears that when picking the centre of the fracture zone, the central gravity low will correspond to the axial topographic minimum, and there is no worry about the minimum being offset. To confirm this suspicion I created a series of modelled profiles across the fracture zone for a range of distances away from the spreading ridge. Due to the lack of ship tracks in the area, a theoretical topography profile had to be used, a simple Gaussian minimum, identical to that shown in Figure 2.13. A topographic step across the fracture zone was not used in the model, for the same reasons as detailed previously. However, the width and depth of the modelled profile was based on the topographic profiles from the few ship tracks crossing the fracture zone. The series of stacked theoretical profiles are shown in 2.20.

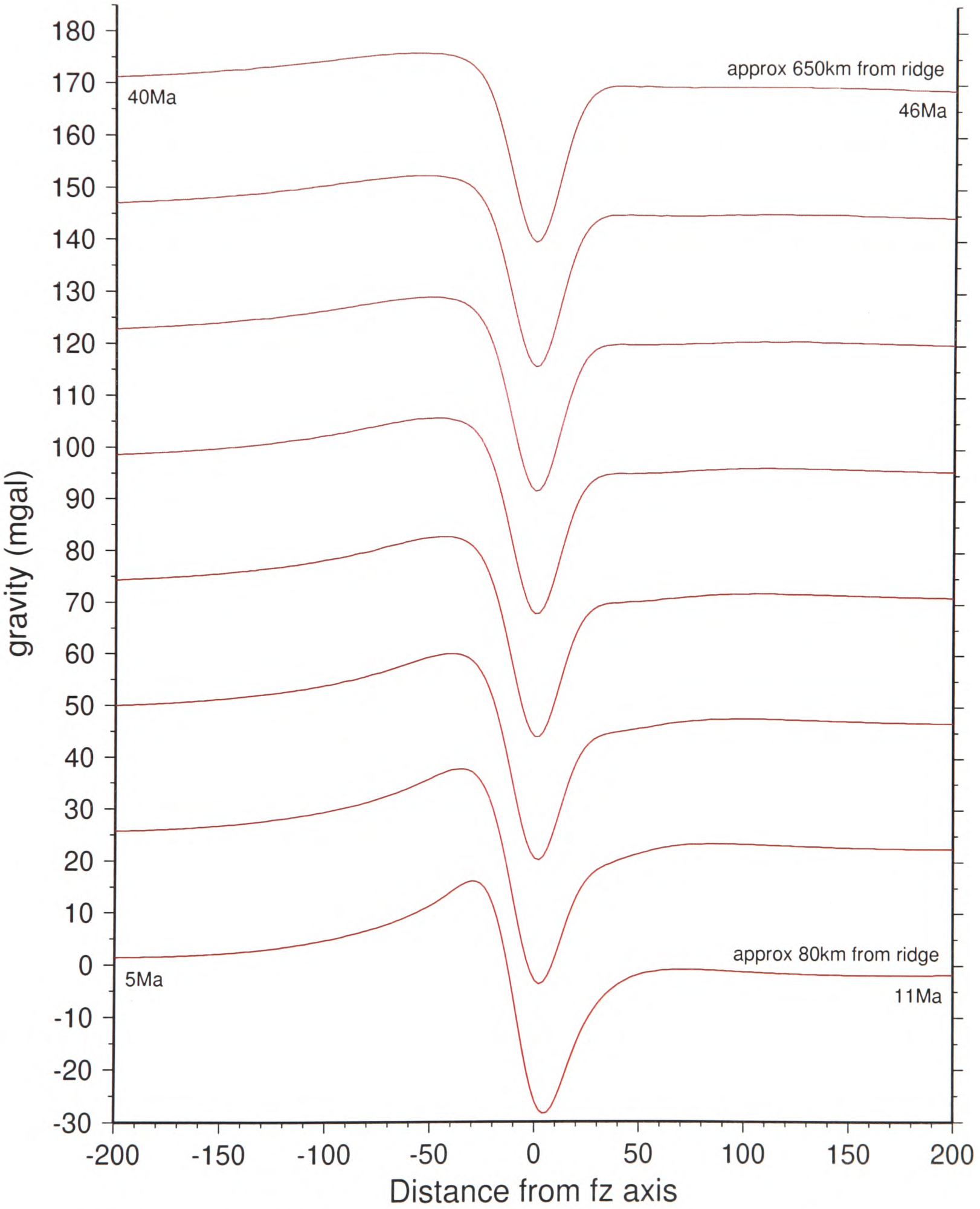

Figure 2.20: A series of stacked theoretical gravity profiles for the western branch of Christmas fracture zone, for increasing distance (and hence age) from the spreading centre. Each model/profile incorporates the expected gravity signal from the theoretical fz valley shown in Figure 2.13, and an age-varying component determined from the theoretical thermal variation across the fracture zone (similar to Figure 2.15). Each gravity profile has been cumulatively dc-shifted by 25mgal.

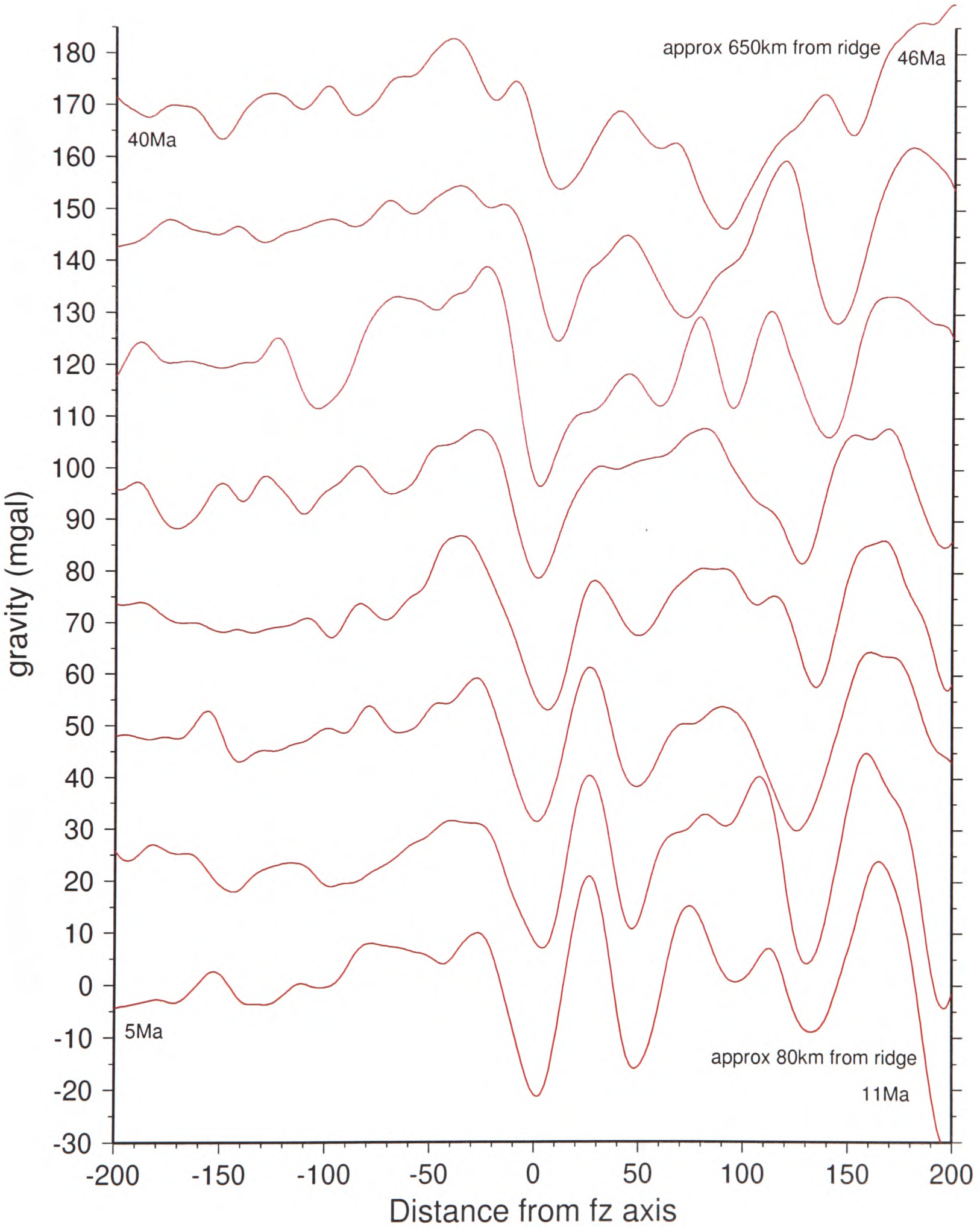

Figure 2.21: A series of stacked sampled gravity profiles across the western branch of Christmas fracture zone, for increasing distance (and hence age) from the spreading centre. Each gravity profile has been cumulatively dc-shifted by 25mgal.

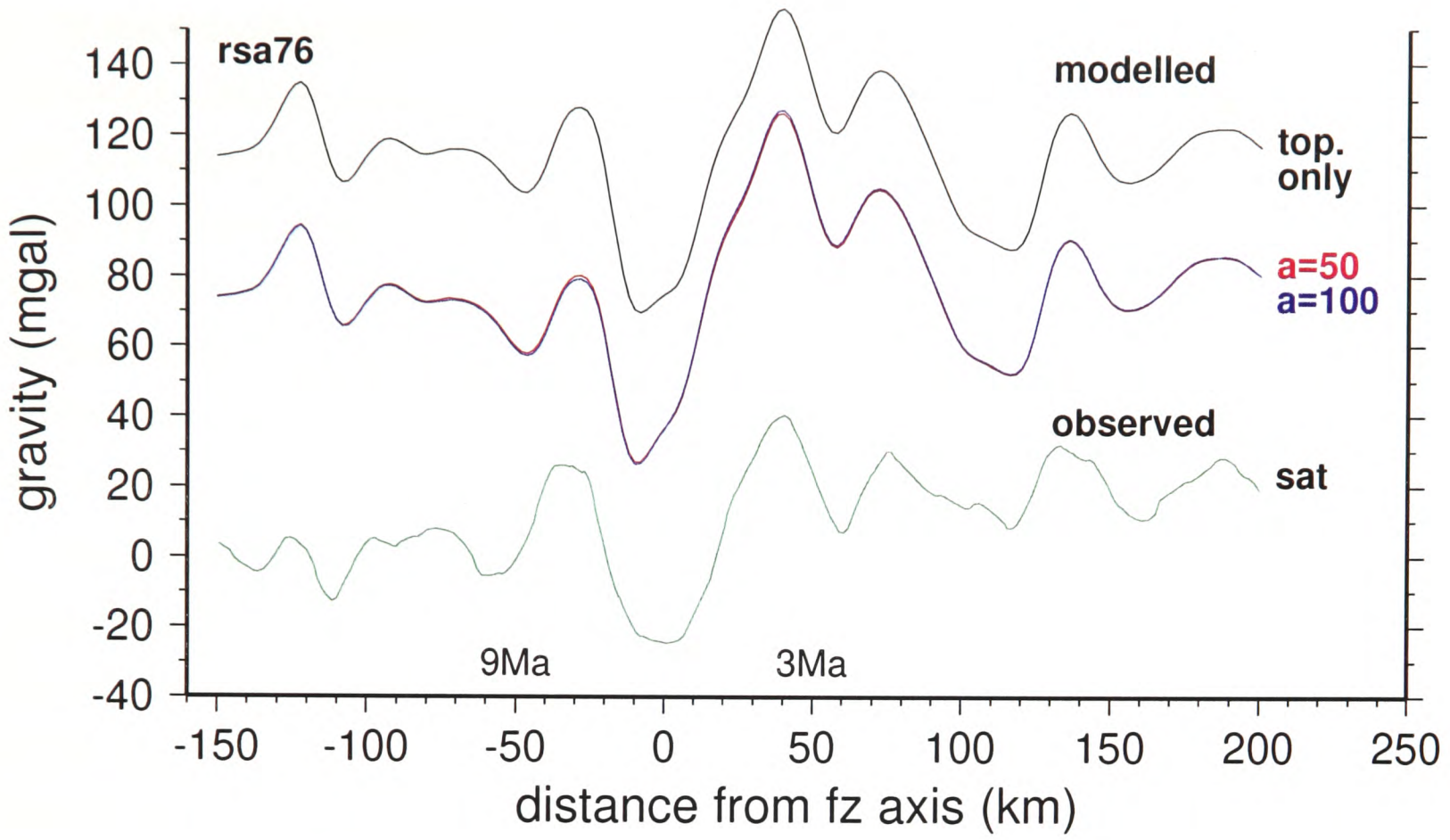

Figure 2.22: Gravity profiles across 'Hogmanay' fracture zone in the South Atlantic, for the two crossings marked on Figure 2.17(b). In each case, the free-air gravity recorded by the ship (not available for rsa76) is shown in red, and the sampled satellite gravity (from Figure 2.11) in green. Two profiles are displayed for the total modelled (expected) gravity anomaly, where the thermal component was determined for thermal plate thicknesses, a, of 50 and 100km, in red and blue respectively. In addition, the component of the model determined from the observed topography alone (no thermal component) is shown in black. The gravity profiles have been dc-shifted relative to each other (except for the two total models) for easier comparison.

In these modelled profiles, the crustal thickness contribution to the model again dominates, the central minimum appearing clearly throughout the series. The thermal contribution can be seen as a bulge to the right of the central minimum and a corresponding decrease in the signal on the left. As expected, the thermal signal is strongest closest to the spreading axis, decreasing in amplitude away from the ridge. Closest to the ridge though, there is actually a slight offset to the minimum, as would be expected, but it is less than two kilometres, which is a smaller distance than the grid spacing of the satellite gravity maps anyway, so is likely to be within error and not affect the picking process.

For comparison with this, Figure 2.21 shows a series of gravity profiles across the same fracture zone, sampled from the gravity map. The signals are quite 'noisy' with all the relief in the area, but the central low over the fracture zone can be followed through all the profiles. The amplitude of the gravity signal around the trough appears to be greater nearer the spreading ridge, but there is no particular bulge on the left-hand side, as predicted by the modelling. So it appears that either the thermal signal is not present, or it is not significant enough to be noticed in the overall gravity signal across the fracture zone.

To confirm this result, I repeated these modelling procedures for further fracture zones in the South Atlantic which had different age offsets and distances from the ridge axis, but the results were virtually identical. The location of the other fracture zone I concentrated on, 'Hogmanay' fracture zone, is given in 2.17. Figure 2.22 shows two profiles taken across 'Hogmanay' fracture zone, which lead to the same conclusions as before. The rsa76 crossing did not record gravity, but the satellite gravity appeared to match well, and it was a useful profile, being an almost perpendicular crossing of the fracture zone, close to the ridge-transform intersection. For both crossings, the modelled gravity is always dominated by the topographic component, with the gravity signal due to the thermal structure of the fracture zone not really having any major contribution to the overall model or visible on either the ship or satellite gravity profiles.

The study would not be complete however, without some further investigations. Along the SWIR, particularly towards the eastern end, the fracture zones are very closely spaced, and the thermal signals of neighbouring fracture zones are likely to interact. Initially, profiles across a relatively isolated fracture zone, Indomed fracture zone, were studied, the location of which is shown in Figure 2.23, and the gravity profiles displayed in Figure 2.24. The profiles lead to the same conclusions as before, on the MAR, with the features of the crustal signal dominating.

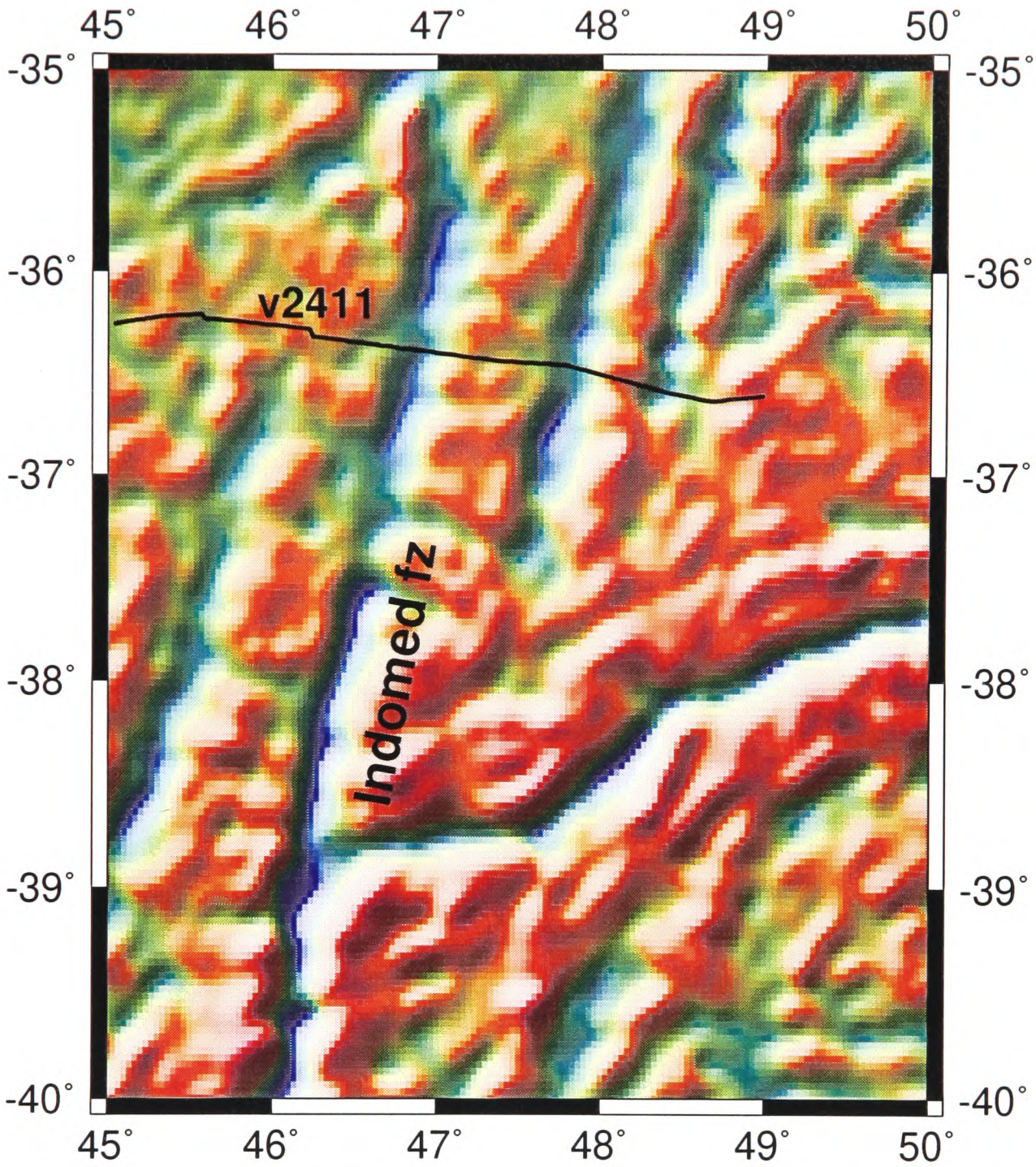

Figure 2.23: The location of Indomed fracture zone on the Southwest Indian Ridge, and the ship crossing used for modelling.

Next, a profile across a closely spaced set of fracture zones was studied, shown in Figure 2.25. To model the thermal signal for this, a model for the geoid across a set of 4 fracture zones was used, based on the model determined by using a simple extension to (2.32). The gravity profiles are shown in Figure 2.26. The modelled gravity profiles very closely follow the real gravity, with the thermal signal not noticeably offsetting the minima. There is a fifth fracture zone located at approximately 125km, but the offset is negligible and it would not have affected the model greatly.

The conclusions I was able to draw from this modelling work was that the gravity signal across a fracture zone was dominated by the component resulting from the topographic variation across

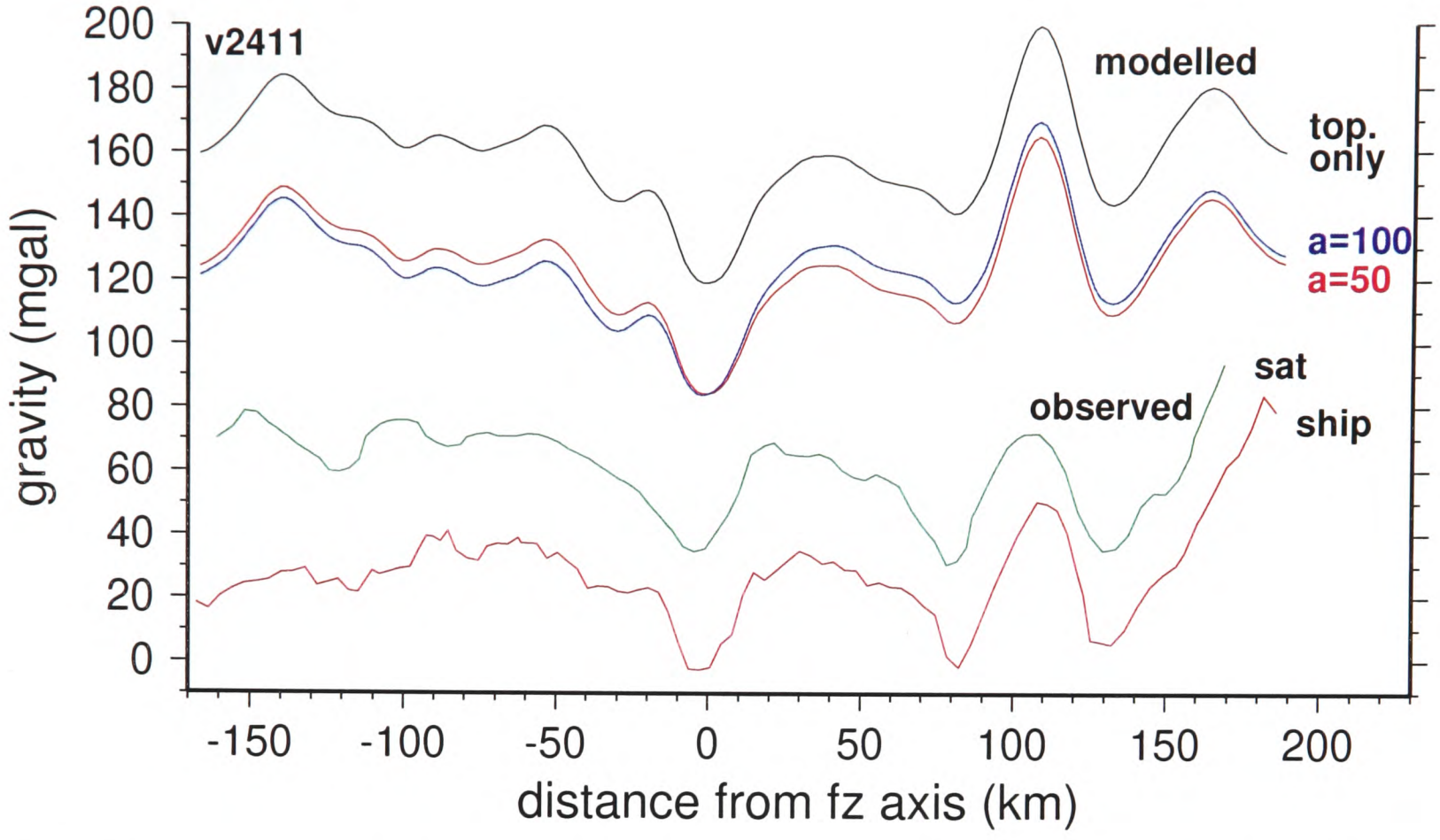

Figure 2.24: Gravity profiles across Indomed fracture zone on the Southwest Indian Ridge, for the crossing marked on Figure 2.23. The free-air gravity recorded by the ship is shown in red, and the sampled satellite gravity (from Figure 2.11) in green. Two profiles are displayed for the total modelled (expected) gravity anomaly, where the thermal component was determined for thermal plate thicknesses, a, of 50 and 100km, in red and blue respectively. In addition, the component of the model determined from the observed topography alone (no thermal component) is shown in black. The gravity profiles have been dc-shifted relative to each other (except for the two total models) for easier comparison.

---

a fracture zone. Furthermore, this meant that when wishing to make my picks for the centre of the fracture zone, I could take the centre of the gravity low to be the centre of the bathymetric trough, regardless of the ages of the surrounding rocks.

2.4 Picking procedure for fracture zones

In order to speed up and simplify the fracture zone picking process, an automated picking procedure was implemented. A routine **makeprofs**, was written, which took a few approximate picks in the rough area of the fracture zone as seeds, then created a whole series of perpendicular profiles crossing the fracture zone, with the profile separation, length and sample spacing set by the user. The gravity values were then automatically sampled from a given gravity map, using GMT. These profiles were then processed to select the gravity minimum along the profile most likely to be marking the centre of a fracture zone.

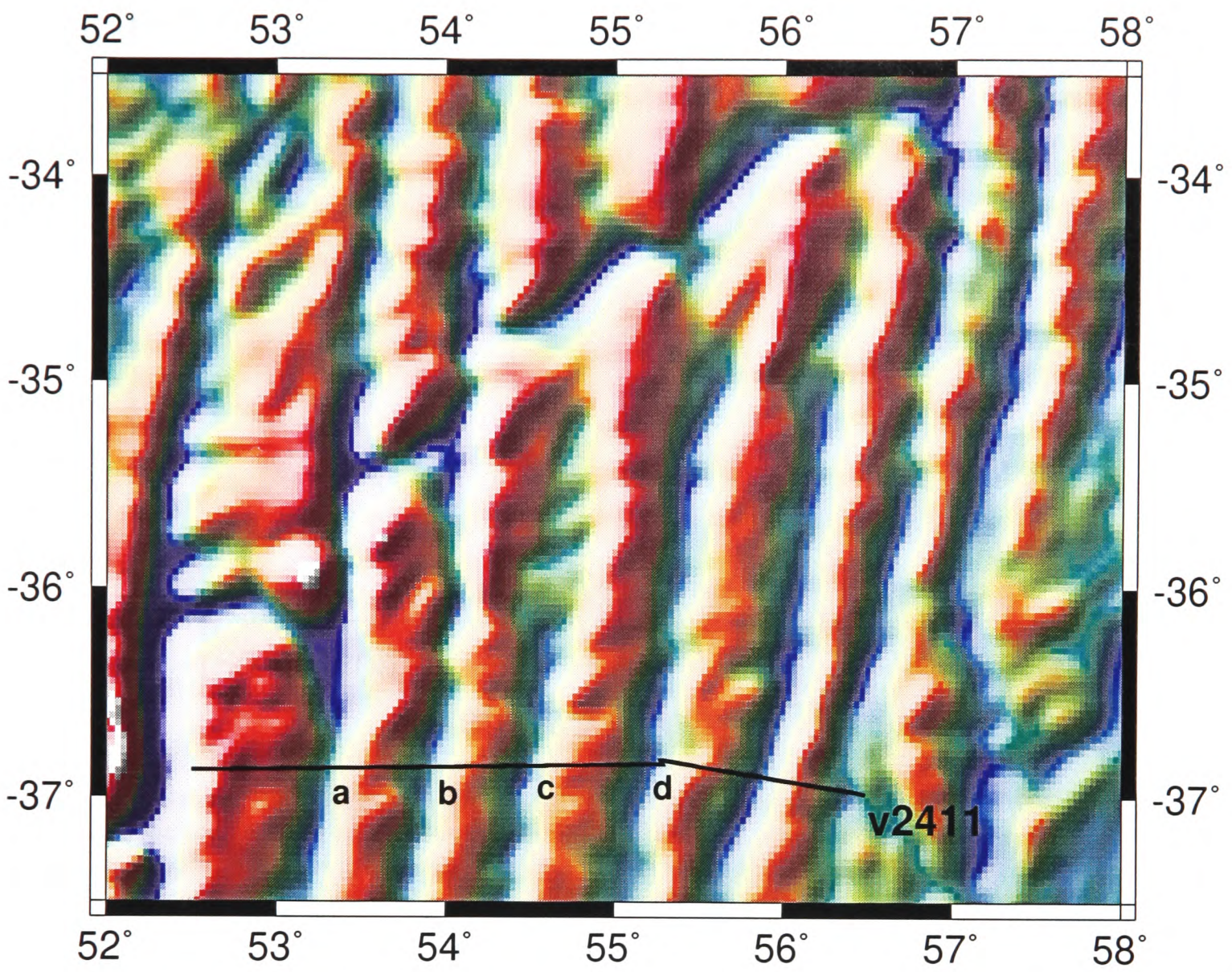

Figure 2.25: The location of the multiple fracture zone group on the Southwest Indian Ridge and the ship crossing used for modelling the gravity signal over a closely-spaced group of fracture zones.

This automatic picking method used the following criteria:

(a) find all local minima which have a depth of 75% of the overall difference between the minimum and maximum values of gravity along the profile, whilst ignoring any data spikes;

(b) if only one minimum is found, this is chosen;

(c) if more than one minimum exists, the two most dominant minima are considered, and if they are similar in proportion, an average is taken (In practice, this average is not used, but is helpful as an indication of the two most likely minima).

This worked well for most fracture zones, but has to be done manually for certain profiles, generally where there is a lot of relief flanking the fracture zone, and also where there is another fracture zone close by. In the latter case, a fracture zone is correctly picked, but not the one we were hoping the routine would find. To make the process of checking and altering any inconsistent picks, an interactive picking program was written for X-windows, **xfzpick**. A series of profiles

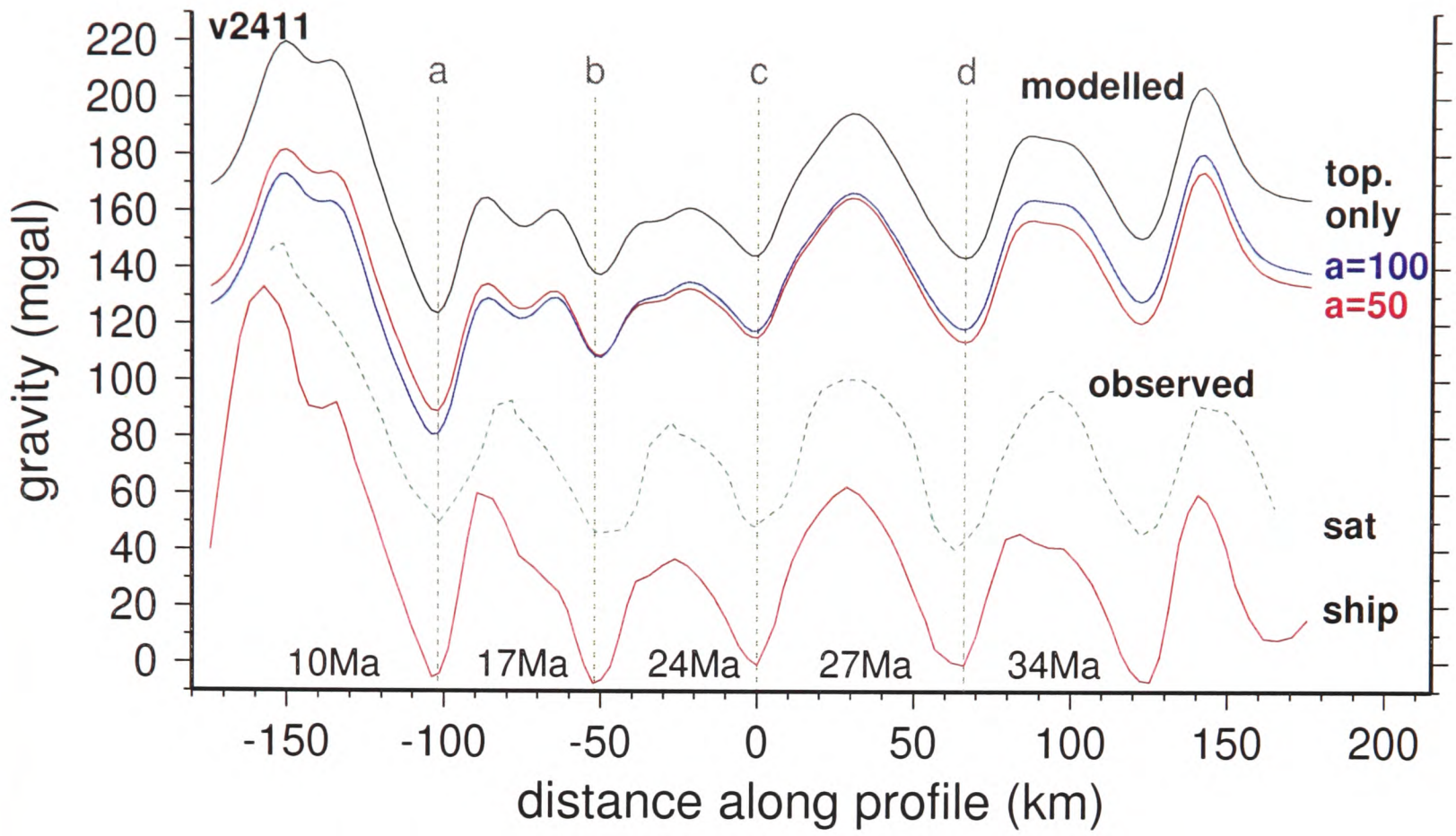

Figure 2.26: Gravity profiles across the multiple fracture zones series "a" to "d" along the Southwest Indian Ridge, for the crossing marked on Figure 2.25. The free-air gravity recorded by the ship is shown in red, and the sampled satellite gravity (from Figure 2.11) in green. Two profiles are displayed for the total modelled (expected) gravity anomaly, where the thermal component was determined for thermal plate thicknesses, a, of 50 and 100km, in red and blue respectively. In addition, the component of the model determined from the observed topography alone (no thermal component) is shown in black. The gravity profiles have been dc-shifted relative to each other (except for the two total models) for easier comparison.

---

along a fracture zone could be loaded up, and a certain number of consecutive profiles viewed at any one time. Picks could be made or altered on screen using simple mouse operations, and also saved to file. A basic map also displayed the current set of picks which showed continuity for the picks along the fracture zone. This made the picking of fracture zones a very quick and painless process.

A screen-shot of this program in use is given in Figure 2.27, and the procedure for making picks of fracture zone locations is shown in Figure 2.28.

The main area where the automatic fracture zone picking broke down was in the area of the 'double' fracture zones, with the automatic routine choosing the deeper trough sometimes in preference to the central fracture zone. However, this problem could be solved by restricting the picking routine to a narrower profile that didn't extend as far as the second fracture zone, or limiting the chosen point to the central 60-70% of the profile. Where there were two very similar shaped and sized minima close to one another, the routine would choose a point midway between

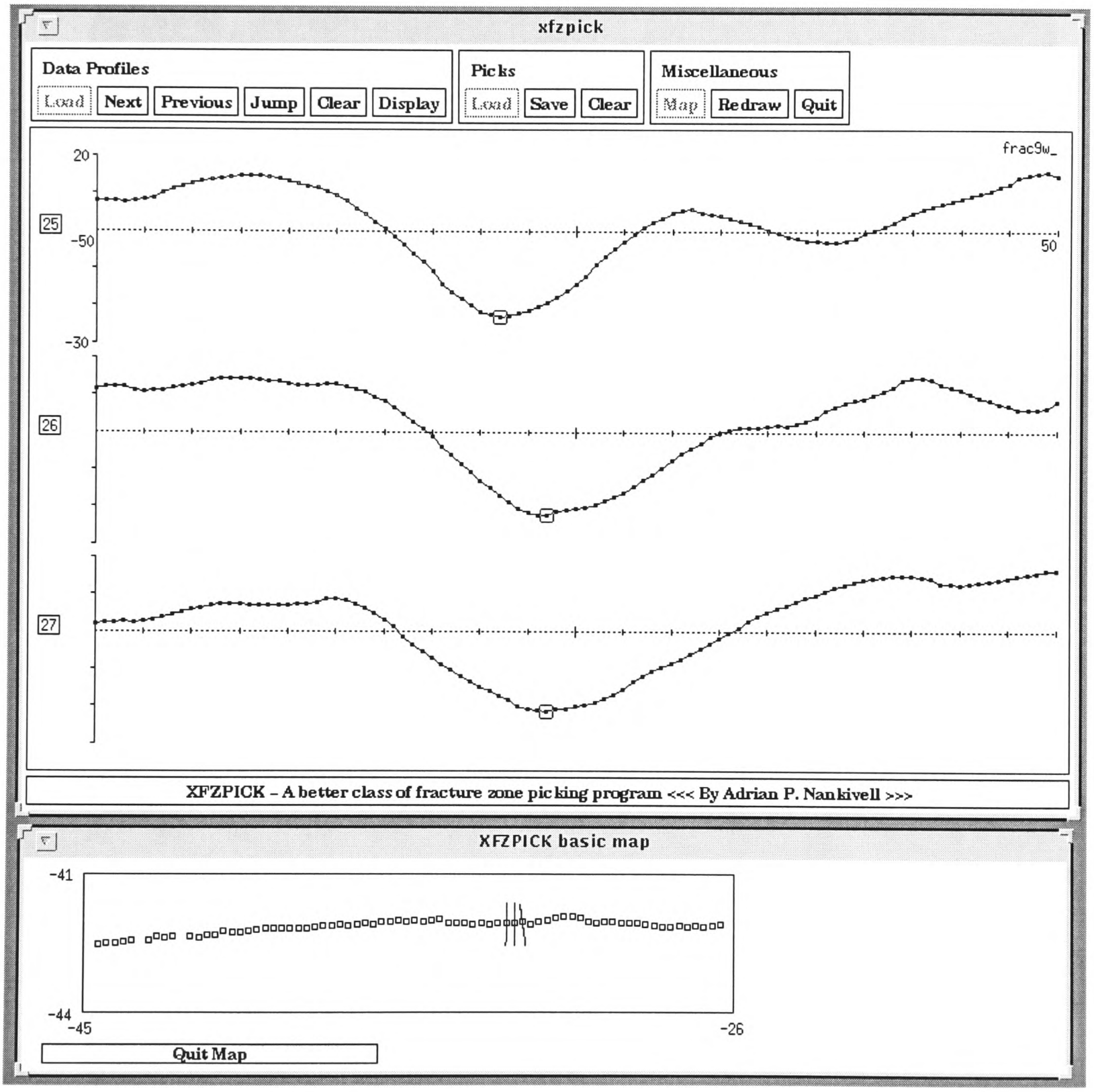

Figure 2.27: The X-Windows fracture zone picking program **xfzpick**.

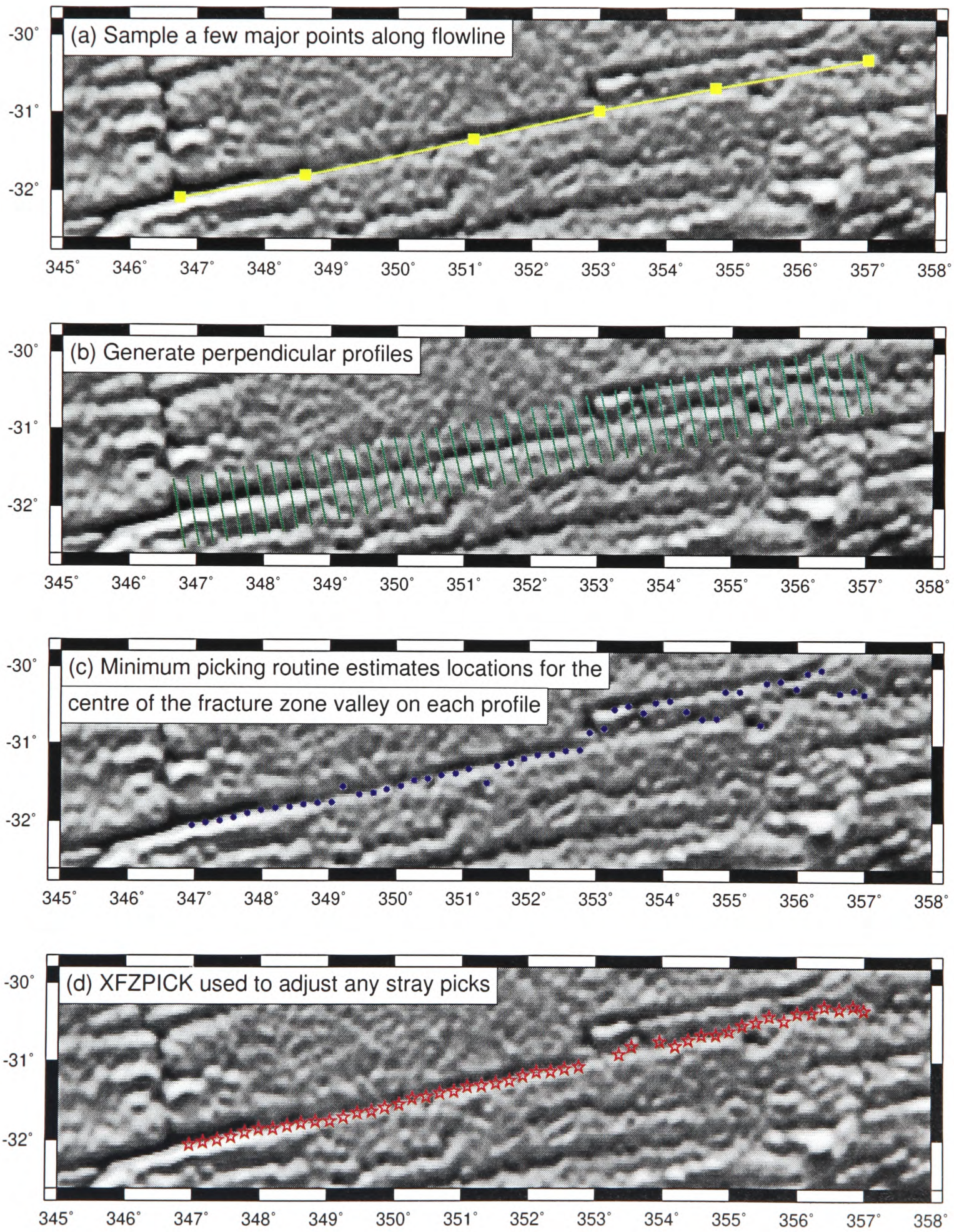

Figure 2.28: The steps in making the fracture zone location picks, using the western branch of Christmas fracture zone as an example.

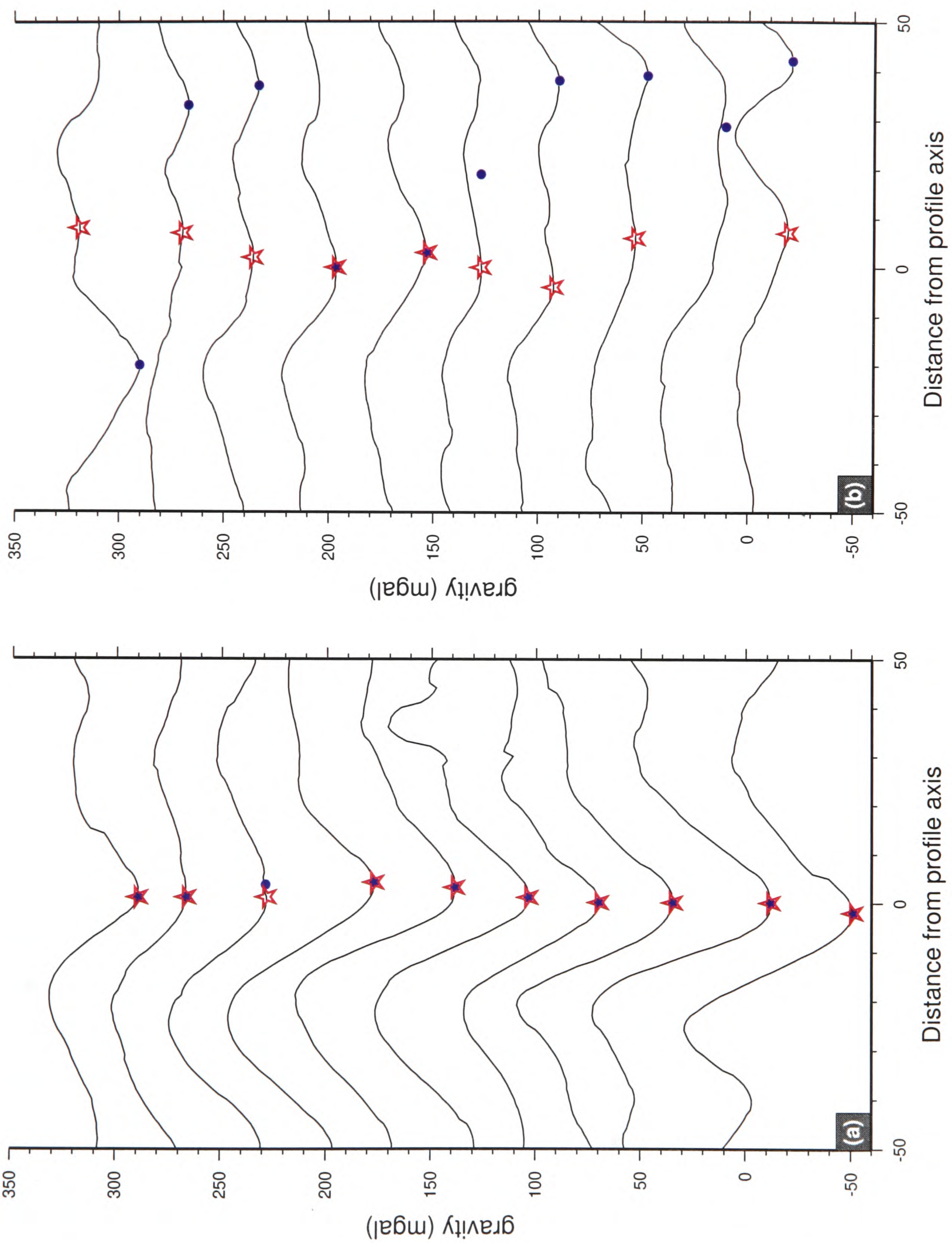

Figure 2.29: A series of sampled gravity profiles along a the western branch of Christmas fracture zone, showing the picks made by the automatic picking procedure, denoted by blue circles, and red stars marking where the actual picks were chosen. (a) shows profiles 1-10, where there the automatic picking routine has little problem, but (b) shows profiles 33-42, where the presence of another fracture zone to the north confuses the routine.

the two, suggesting that it couldn't choose between them. However, with the interactive picking program, shifting any offset picks was a very routine operation.

Figure 2.29 shows two series of gravity profiles across a fracture zone (Western branch of Christmas fracture zone, used earlier in the modelling process), with a blue circles marking where the picking routine chose the centre of the fracture zone to be, and a red star marking where a fz pick was made for the final inversion. The first series of profiles are close to the ridge-transform intersection, where the signal is strong, and there are no other flanking fracture zones, and so the correct locations are automatically chosen every time. In the second series, another small fracture zone is located to the north, and the automatic picking routine has problems choosing between the two relatively shallow troughs.

2.5 Summary of data

Throughout, the gravity profiles were sampled from the gravity map shown in Figure 2.11, with the exception of the picks from the Mid-Atlantic Ridge north of 30°S, which were sampled from the gravity field of Smith & Sandwell (1995).

2.5.1 South America - Africa seafloor spreading

The full set of picks made from the South Atlantic spreading from the Mid-Atlantic ridge is given in Figure 2.30. The majority of the fracture zones are substantial in length, representing clear flowlines across the plates. Not all of these picks were necessarily used in the inversions, some of the fracture zones being discarded for various reasons, which are given later. The subset of fracture zone data used as input for the inversions can be seen in Figure 5.4 in Chapter 5.

The main fracture zone for which inclusion into the dataset is debatable is the Falkland-Agulhas fracture zone (centred at approximately 12 °W, 47 °S). It is a long-offset fracture zone, around 250km which represents an age offset of approximately 15 Ma at current spreading rates. Because this is so large, it is possible that the fracture zone is unlikely to reflect more minor changes in spreading direction. This is because the forces generating the motion between the plates may not be sufficient to overcome the inter-plate stresses that would be generated across the transform fault. If the transform did adjust to accommodate the change in spreading direction, the process might take a significant time, and so the fracture zone trace produced by the transform

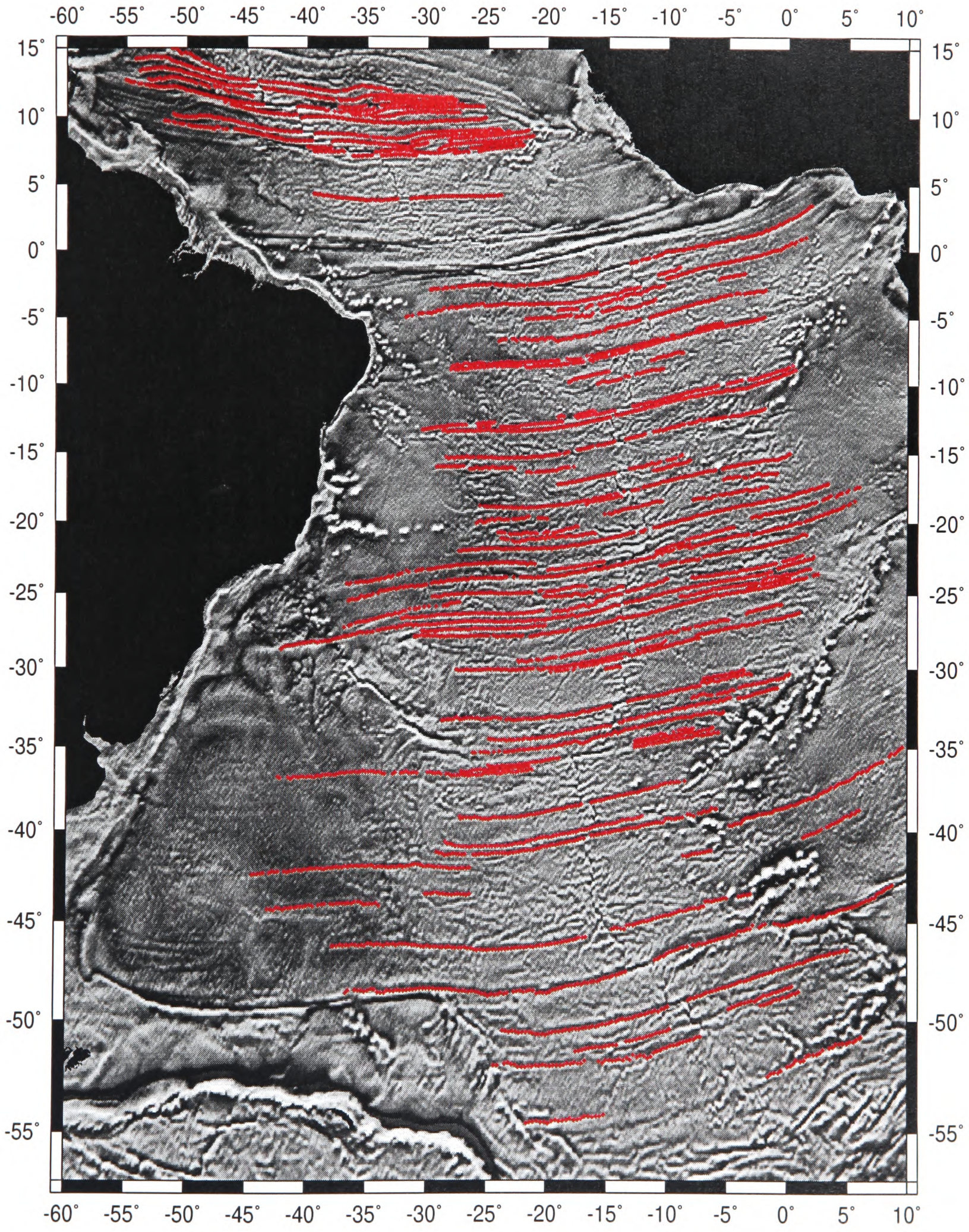

Figure 2.30: The complete set of fracture zone picks made in the South Atlantic. (Gravity field produced by Smith & Sandwell (1995)).

may in fact represent a time-delayed response and not a true flowline as expected.

Several fracture zones to the north of the equator are included, close to the boundary between South America-Africa (SAM-AFR) and North America-Africa (NAM-AFR) spreading. Their inclusion was very important because they lie close to the poles of motion and so reflect any changes in the poles of motion to a greater extent than fracture zones to the south. Cande *et al.* (1988) showed that the fracture zones south of (and including) Marathon Fracture Zone, the northernmost fracture zone included in this study, matched synthetic flowlines for South Atlantic (SAM-AFR) spreading, but not those for Central Atlantic (NAM-AFR) spreading, and so their inclusion is justified.

2.5.2 Africa - Antarctica seafloor spreading

The fracture zone picks made from the Southwest Indian Ridge are given in Figure 2.31.

There are relatively few fracture zones towards the western end of the ridge, close to the Bouvet Triple Junction, and those that do exist are quite short. There is then a section of ridge, from around 15 °E to 25 °E where there are no transform faults, and subsequently, no fracture zones.

The central section of ridge, from 25 °E to 40 °E is the only section from which fracture zones can be traced for any length. To the south, these long traces are more numerous and are spread further east and westwards than those to the north, though in both cases much of the spreading is beyond the range of the inversions in this study. The tectonic features around the Prince Edward fracture zone, centred at around 30 °E, 50 °S, are very complex. Away from the ridge, several small fracture zones appear to have been generated by a change in spreading direction, and then blend back close together again, forming a kind of herring-bone pattern. Relatively hard to map because of the close spacing, and complex topography, they are also unlikely to be of much use in an inversion, because of the short era of spreading that they represent, while more accurate information can be obtained from the longer, more continuous fracture zones in the area.

At the eastern end, from around 50°E to 60°E, where the ridge trends NE towards the Indian Ocean Triple Junction, there are a whole series of short-offset fracture zones, all following very similar flowlines, and it is likely that these will give a very good constraint on the more recent spreading directions.

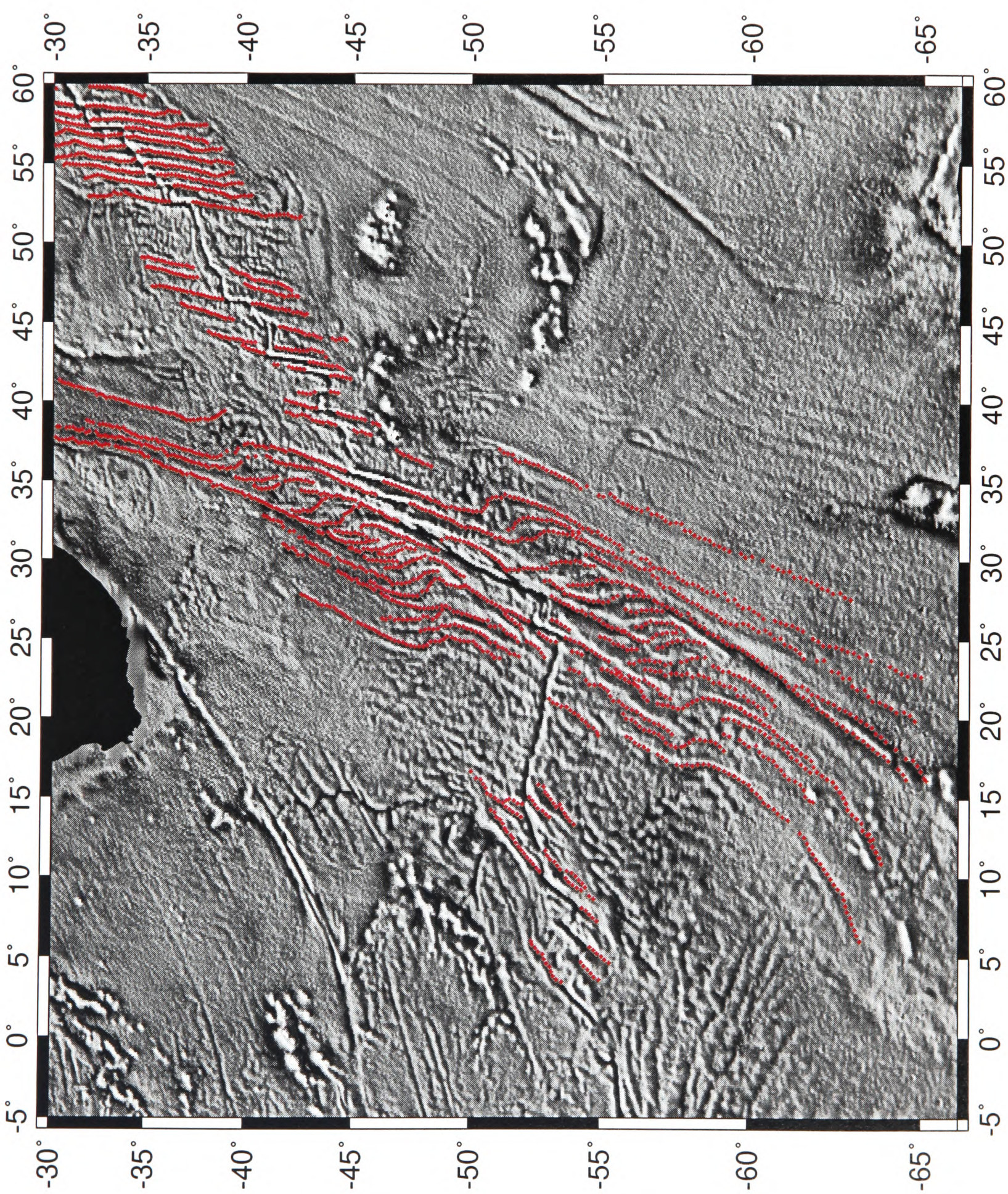

Figure 2.31: The complete set of fracture zone picks for the Southwest Indian Ridge.

2.5.3 South America - Antarctica seafloor spreading

The full set of picks made from fracture zones created by South American - Antarctic spreading are given in Figure 2.32, comprising of picks in the region of the South American-Antarctic Ridge, and in the Weddell Sea.

As discussed previously, there is only a short length of actual mid-ocean ridge at the northern end of the boundary between the two plates. The majority of fracture zones generated from this section of ridge are also limited in length, the ones to the west have mostly been subducted into the bordering trench, and the fracture zones to the west are not simple to trace, with much evidence of ridge segmentation occurring in the complex basement morphology apparent from the gravity maps. Further south, the fracture zones become more distinct with substantial ridges bordering each fracture zone trough. They extend far into the Weddell Sea, and several changes in spreading direction can be seen.

At the change in spreading direction in the Weddell Sea marked by the dotted blue line, the features of the fracture zones deteriorate and are quite hard to trace through this region - there is even the possibility of some of the fracture zones dying out during this period, and regenerating after the changes in spreading direction. However, enough of the fracture zones are sufficiently distinct to be able to confidently trace the motion at this time, making it then possible to join up the two sides of a couple of the less distinct fracture zones across this discontinuity.

Further south in the Weddell Sea, just after the fracture zone traces visibly fade at around 67°S, there is a distinct major change in spreading direction reflected in the 'herring-bone' pattern, just before all the features terminate at a visible boundary marked by a gravity low, some distance from the continental shelf. This change occurred earlier than C34 and so is not covered in the studies of plate motion in this thesis, but Livermore & Hunter (1996) determined that it occurred during the Cretaceous magnetic quiet zone, at around 90Ma.

In the north of the Weddell Sea, the seafloor morphology becomes very complex due to the interaction of the South American and Antarctic plates with the Sandwich trench and Scotia Sea plates. It is believed (Barker *et al.*, 1984) that the South American plate has been steadily subducted by the Sandwich trench, but when the active South American - Antarctic ridge crest has reached the subduction zone, both spreading and subduction have ceased and that the boundary has become strike-slip in nature. It is likely that some small-scale rotation has occurred in the

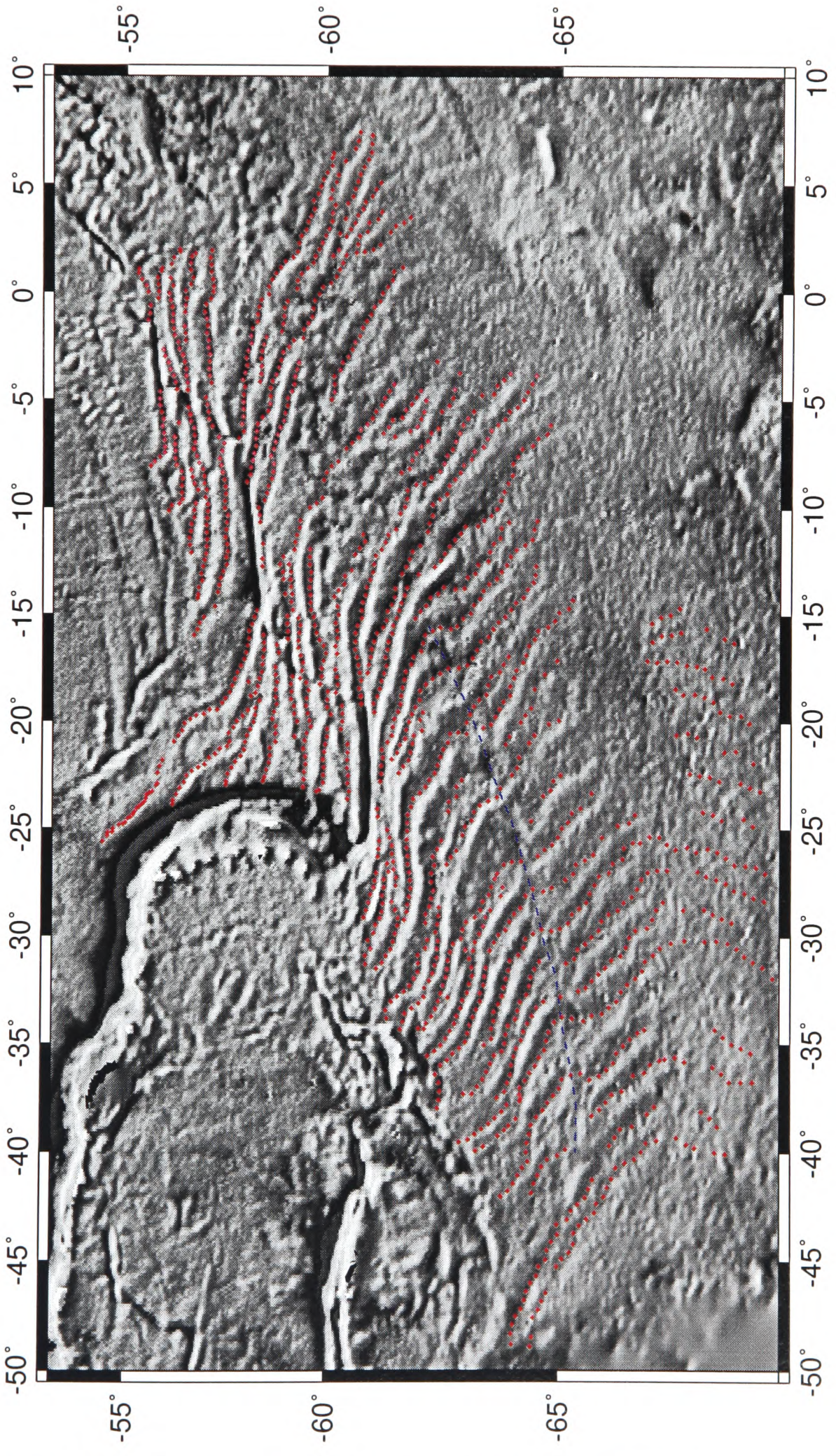

Figure 2.32: The complete set of fracture zone picks for SAM-ANT spreading.

northern Weddell Sea as a result of shearing forces generated during subduction (Menard, 1978), and so there is some doubt as to whether the northernmost ends of the Weddell Sea fracture zones represent a true picture of the SAM-ANT flowlines at that period.

Chapter 3

Magnetic anomaly isochrons

3.1 Introduction

The Earth's magnetic field can be modelled to a good approximation as a simple dipole field, with an axis slightly tilted, at approximately 10° to the rotational axis of the earth. It is this axial offset which must be taken into account whilst using a compass, through the application of magnetic variations. The magnetic 'north' pole does in fact drift in position, precessing around the rotational axis of the earth in what is termed the secular variation, such that with time, the average position of the magnetic north pole does in fact coincide well with the true geographic north pole. The geomagnetic 'north' pole is actually a true magnetic south pole, but is labelled as such because the north end of a compass needle will point towards it (even though it is strictly a south magnetic pole). The local magnetic field at any point on the globe can be predicted by a spherical harmonic model, such as the IGRF-80 model (Peddie, 1982). The actual processes leading to the existence of the earths magnetic field, are not completely understood, though it is generally believed that motion in the molten core leads to some kind of dynamo effect (Elsasser, 1956a,b; Carrigan & Gubbins, 1979).

From studies of lava flows early in the twentieth century (Matuyama, 1929) it was discovered that igneous rocks of certain ages had magnetic properties that could only be explained by a reversely orientated magnetic field. This was reinforced by the study of cores taken from the ocean floor, where it was discovered that the magnetic orientation of minerals in the core varied with depth in the core (Cox & Doell, 1962). The only plausible explanation that emerged for these results was that the Earth's magnetic field alternated between two states: the 'north' pole of the dipole field being located at the geographic north pole; and a reversed orientation where the magnetic 'north' pole was in fact at the geographic south pole.

Timescales for a series of reversals between these two states were determined initially through Potassium-Argon dating (Cox *et al.*, 1963; McDougall & Tarling, 1963; Cox *et al.*, 1964) back to 4Ma, and then to the Late Cretaceous (≈80Ma) from marine magnetic profiles (Heirtzler *et al.*, 1968).

New seafloor is created at a mid-ocean ridge by magma rising through dykes and extruding onto the seafloor in an 'emplacement zone' in the axial region of a mid-ocean ridge. When the magma cools, the magnetic minerals within record the orientation of the local magnetic field, which in turn indicates the current orientation of the earths dipole field. The mechanism by which this occurs is that the iron-based magnetic minerals such as magnetite (Fe_3O_4) and haematite (Fe_2O_3), spontaneously align themselves with the local field as the rock cools below the Curie temperature for those minerals, (typically around 580°C for Fe_3O_4, 680°C for Fe_2O_3). This recorded magnetisation, called the thermo-remanent magnetisation (TRM) becomes effectively permanent when the rocks cool further to below a 'blocking temperature', such that this stored orientation of the minerals cannot be changed without reheating the rock.

In addition to this, the minerals can acquire a lower level of magnetisation at lower temperatures from the current local field. This induced magnetisation may be different from the TRM in that the magnetic field of the earth may change, or the rock may have moved to a different position on the earth. However, the magnitude of the TRM is large when compared to the induced magnetisation (The ratio of remanent to induced magnetisation is denoted by the Könisberger Ratio Q). Thus for the lifetime of the rock, the local magnetic field at the time of its formation remains, and if the latitude of its place of creation (paleolatitude), and initial orientation are known, then the orientation of the global dipole field can be estimated.

The implications and relevance of the magnetic reversals recorded in newly formed seafloor were described in Chapter 1. The common analogy used is of both sides of a mid-ocean ridge being considered as lengths of magnetic tape, with a tape head at the mid-ocean ridge recording the current orientation of the dipole field on both sides of the ridge simultaneously. The first extensive reversal timescale, published by Heirtzler *et al.* (1968), was determined by studying magnetic profiles crossing mid-ocean ridges and ocean basins which showed a record of the series of reversals. With the assumption of a constant spreading rate, and using the radiometric dates obtained for the younger reversals seen on land as a starting point, estimates for the timings of the geomagnetic field reversals were obtained back to almost 80Ma. This method of using series

of magnetic profiles recorded across ocean basins to determine the pattern and timing of reversals has been used as the basis for most subsequent timescales.

The source of the marine magnetic anomalies was initially considered to be the whole of the oceanic crust. However, after studying the magnetic properties of rocks from the seafloor (Fox & Opdyke, 1973), it was determined that the main source of the magnetisation was likely to be only from what is known as layer 2A of the crust; the sheet flows and pillow lavas extruded from the dykes along the mid-ocean ridge, being those rocks which cooled the fastest as they came into contact with the sea-water, along with the uppermost part of the dykes. This layer of rocks is usually taken to be around between 500m and 1km thick, which, given the magnitude of the magnetic susceptibility of the pillow lavas, was sufficient to account for the magnetic fields recorded. Layer 2B, the dyke structures feeding the layer 2A basalt flows are also weakly magnetised but, cooling at a slower rate, don't have as high a stable magnetisation as the layer 2A rocks. Layer 3, rocks in the lower crust, where much of the minerals have crystallised out in the magma chamber, have much lower magnetisations and contribute very little to the overall magnetic field, though some models of the magnetic source in the crust do include this second layer (Cande & Kent, 1976).

3.2 Block models

To assist in the identification of magnetic anomalies on the seafloor recorded by ship-based (or airborne) magnetometers, synthetic magnetic anomalies need to be created.

These are constructed by considering the magnetic field as being generated by a series of positively or reversely magnetised blocks, of a given thickness and infinite width, which are generated at an mid-ocean ridge. These blocks are situated at a given depth below the seafloor, determined by considering the depth at a mid-ocean ridge to be fixed (2.5km), and calculating the depth away from the mid-ocean ridge according the depth-age relationship (Parsons & Sclater, 1977) for the ocean floor. If the seafloor spreading rate is equal for both sides of the ridge, then the pattern of normally and reversed blocks is symmetrical across the ridge. However, the resultant model depends on many factors, primarily the latitude of the blocks at time of formation and time of observation, the strike of the ridge and the spreading rate of the ridge. As shown in Figure 3.1 the magnetic field in a block can be split into three components: a component along

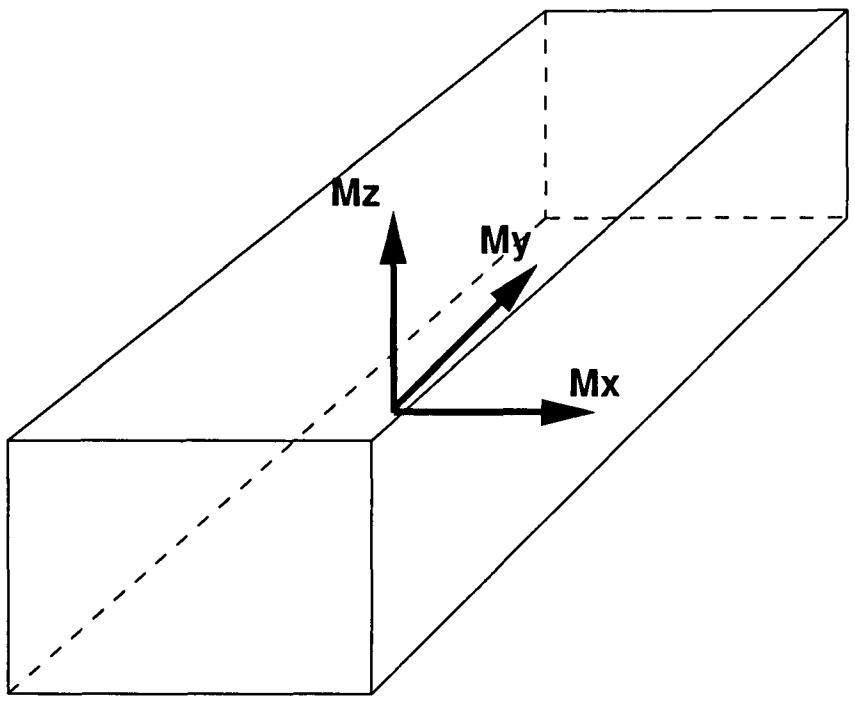

Figure 3.1: Diagram showing the three components of the magnetisation of a block.

the block; a horizontal component perpendicular to the block; and a vertical component.

The component of the magnetic field along the magnetised block does not contribute to the magnetic field outside the block, because the field lines are contained entirely within the block. Thus the only components contributing to the external field are the horizontal component perpendicular to the block, and the vertical component. The resultant anomaly is calculated by determining the perpendicular and vertical components of the magnetisation of the block, adding them to the local reference field, and determining the resultant field. The magnitude of the resultant is found, and the difference found between this and the magnitude of the local reference field, and the value obtained is the magnetic anomaly. For east-west spreading, the perpendicular component is zero, and so the field is dependent on only the vertical component, which is in turn dependent on the inclination of the dipole field at that point on the globe. Because there is no horizontal component contributing to the external field, the pattern of anomalies observed on both sides of the ridge are in theory perfectly symmetrical. At high latitudes, the angle of inclination of the local reference field is large, whereas at the (magnetic) equator, the lines of field run parallel to the surface of the earth. Thus for east-west spreading at the magnetic equator, the blocks are parallel to the local reference field, such that the magnetic field has zero inclination and is contained entirely within the block, and as such does not give rise to a magnetic anomaly at the sea surface. The magnitude of the anomaly 'wiggle' sequence produced is dependent on the latitude of formation and observation, because of the angle of inclination of the local reference field. This is shown graphically in Figure 3.2 and described below.

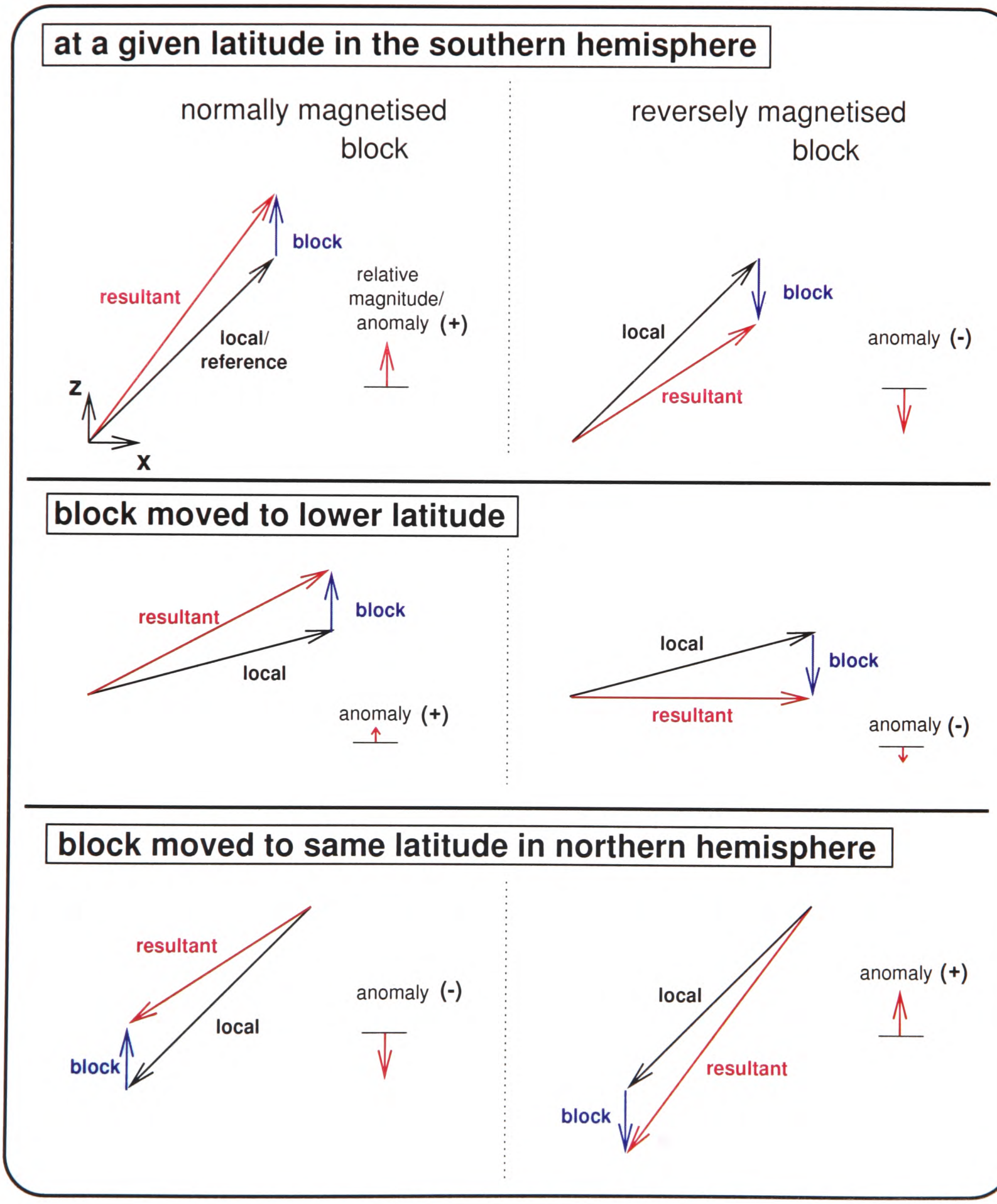

Figure 3.2: Diagram showing the effect of the field within a magnetised block on the local field, and the resultant magnetic anomaly, for east-west spreading.

A normally magnetised block created by east-west spreading in one hemisphere will give rise to a positive anomaly in the same hemisphere, the magnitude increasing towards the pole, and decreasing towards the equator. At the magnetic equator, the block would give rise to a approximately zero anomaly, and if the block was subsequently moved into the opposite hemisphere, then it would give rise to a negative anomaly. The opposite applies to a reversely magnetised block.

The symmetry of an idealised dipole field means that the angle of inclination at a given magnetic latitude in the northern magnetic hemisphere is equal and opposite to that at the corresponding magnetic latitude in the southern magnetic hemisphere. Thus a normally magnetised block created by east-west spreading at a given magnetic latitude would give rise to the same magnitude of anomaly as a similar normally magnetised block created at the same magnetic latitude in the opposing magnetic hemisphere. Because of the symmetry of the dipole field, an anomaly sequence created by east-west spreading at a ridge striking at an angle α east of north will be identical to that created by east-west spreading at a ridge striking α west of north. This is because for a given block, the vertical components will be identical, the only difference will be in the opposing signs of the perpendicular component, which will be of equal magnitude, so that the magnitudes of the resultant anomalies are identical.

If the direction of spreading is not east-west, then there is a perpendicular component of the magnetisation within the block, and this has an effect on the symmetry and magnitude of the anomaly patterns. Figure 3.3 shows how a magnetic anomaly profile crossing a semi-infinite block caused by north-south spreading reveals a skewed anomaly in comparison to a similar profile across a block generated by east-west spreading. This effect is less noticeable at high magnetic latitudes because of the high angles of inclination, which means that the magnetisation of the block is dominated by the vertical component. The variation of magnetic anomalies, created at mid-ocean ridges, with latitude and strike of the ridge is covered in detail by the analysis of marine magnetic anomalies by McKenzie & Sclater (1971), and also more fundamentally by Schouten (1971). Basic synthetic profiles can easily be created for seafloor created at a given location, provided the approximate strike of the ridge and spreading rate is known, through reasonably straightforward modelling procedures, using line integral or Fourier techniques. Figure 3.4 shows a generated synthetic profile and some of the parameters used to generate it.

The spreading rate at time of formation has an effect on the small-scale definition of the

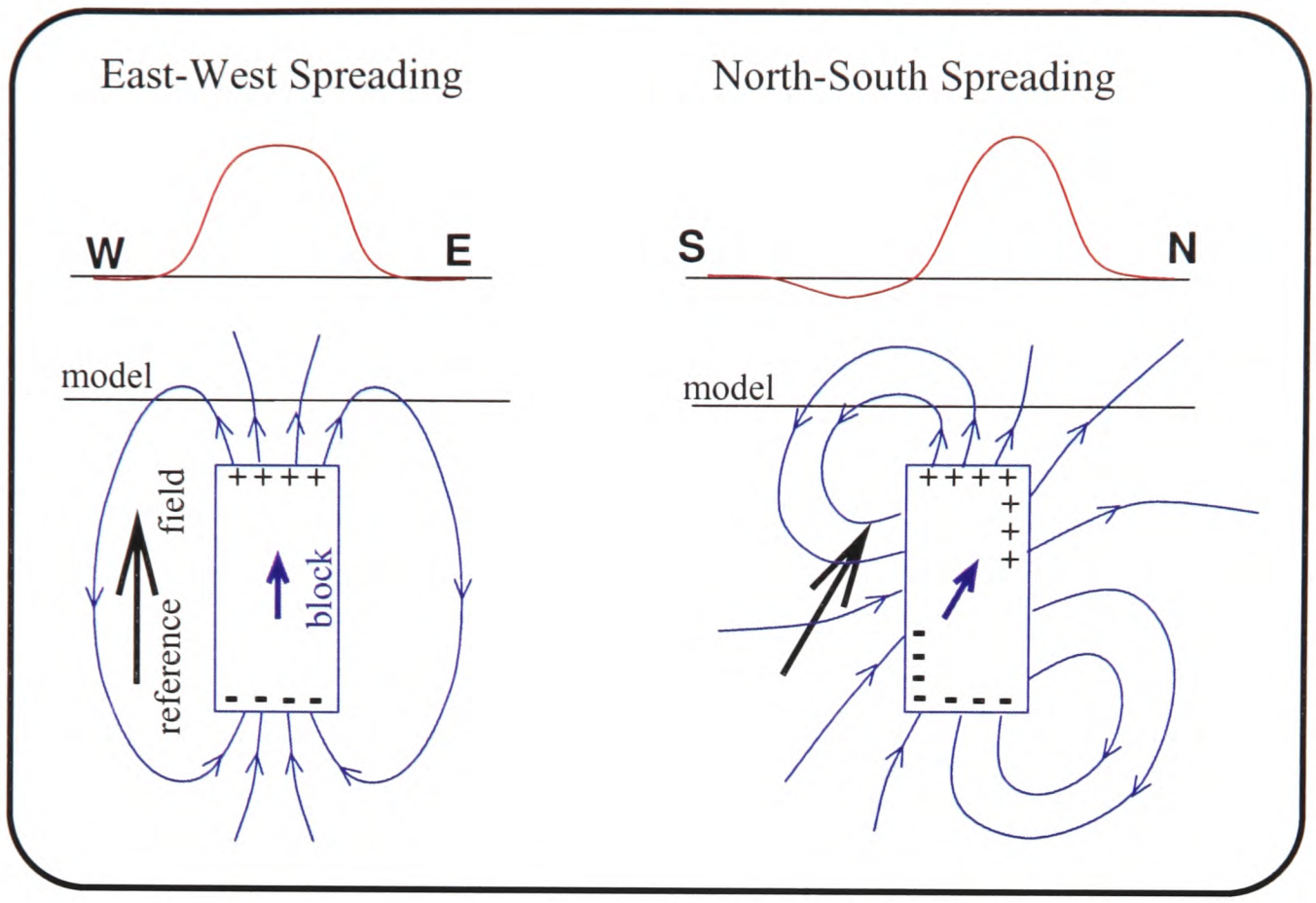

Figure 3.3: Diagram showing how a normally magnetised block created by N-S spreading gives rise to a skewed anomaly in comparison to the symmetric anomaly generated by E-W spreading (Southern hemisphere).

resulting anomalies. Anomalies formed at a fast-spreading ridge are not only more widely spaced because of the speed of formation, but in addition, many more fine scale variations and minor reversals are visible. With slow-spreading ridges, only major reversals are visible, and the features are far more smooth.

Figure 3.5 shows synthetic profiles for an imaginary ridge spreading E-W at 60°S at rates of 20 mm/yr and 40 mm/yr full-rate. The profiles are plotted against age along profile, rather than distance along profile, in order to clearly show the difference in definition of the reversals. The figure clearly shows the greater definition of the same features for the faster spreading profile.

3.3 Data compilation and picking procedure

The particular group of anomaly reversals chosen for use in the inversions were all for the young end of the corresponding reversal, except in the case of c33r, which represented the end of the normal polarity interval, and the beginning of the reversed polarity interval, of anomaly 33. The reversals used, and the corresponding ages are given in Table 3.1. Some of the magnetic

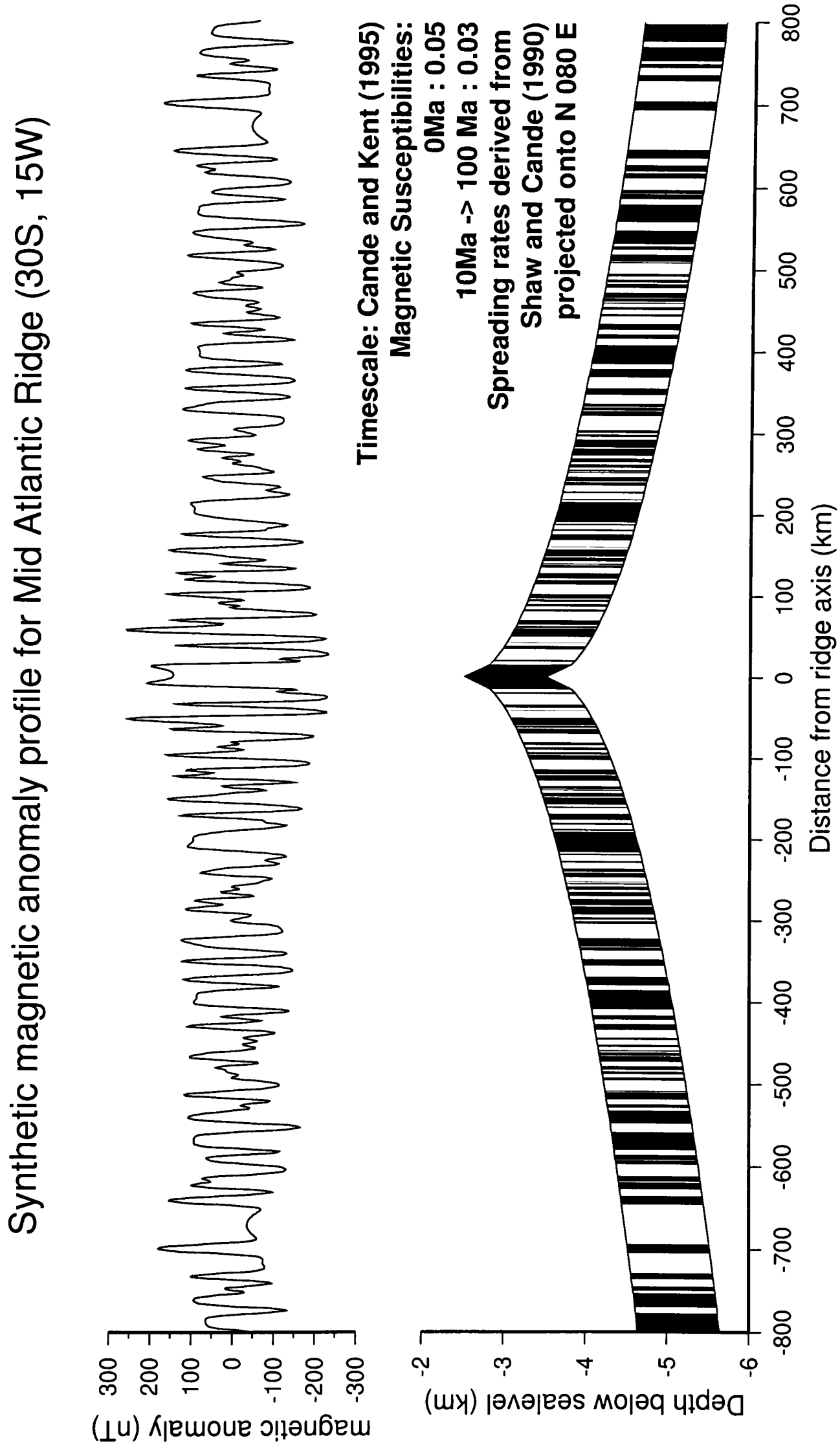

Figure 3.4: Diagram showing a synthetic magnetic anomaly profile, giving the model for the magnetised layer in the crust of the seafloor which gives rise to the anomalies, with blocks with normal magnetisation displayed in black, and reversely magnetised blocks in white.

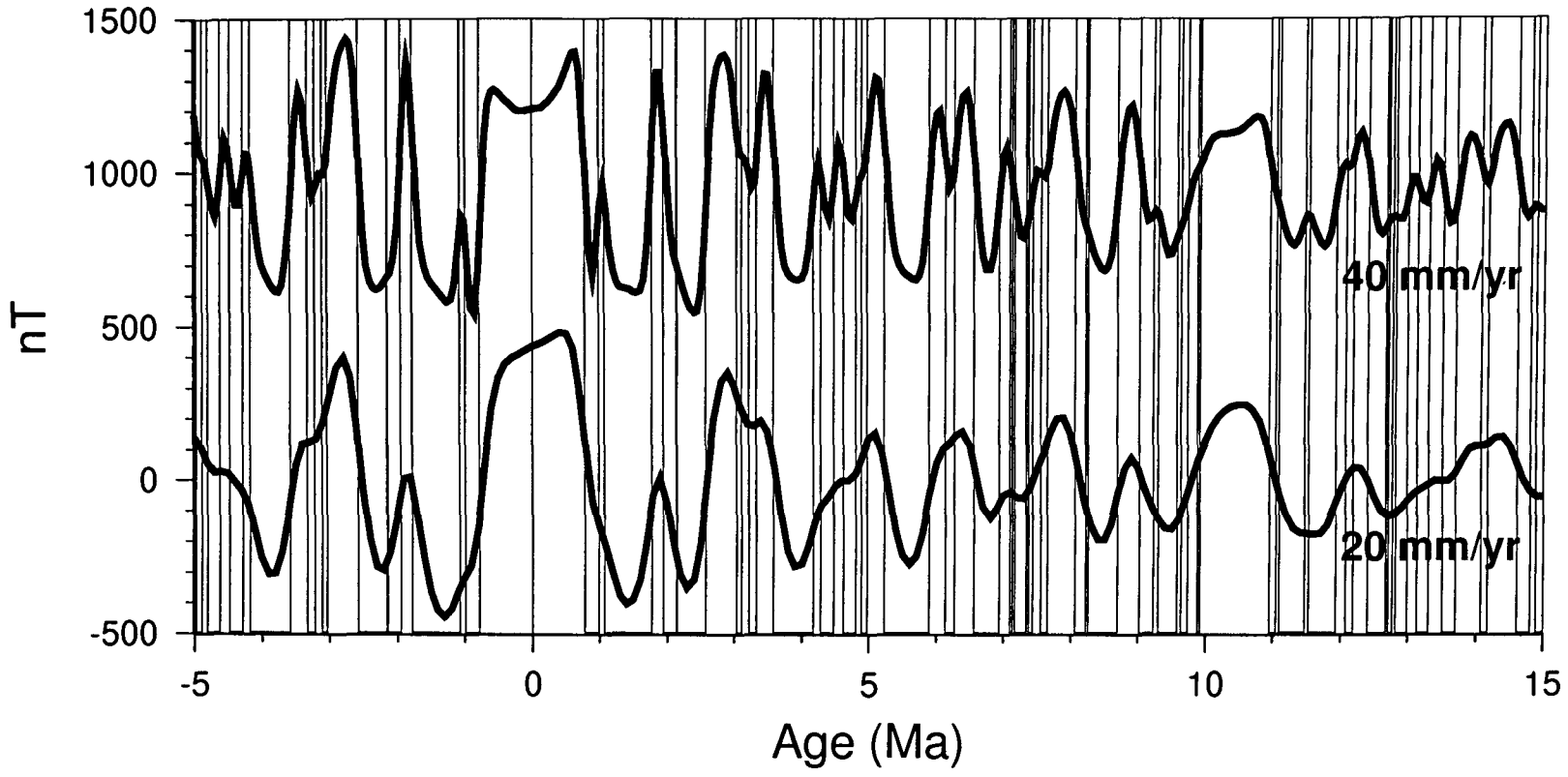

Figure 3.5: Diagram showing the difference in definition between two synthetic magnetic anomaly profiles for two different spreading rates (for east-west spreading), generated from the same timescale.

picks used in the inversions were obtained from databases of magnetic picks, but many were picked directly from marine magnetic cruise records. In particular, the majority of picks for the African-Antarctic spreading were made in this way (see below).

The first step in the picking procedure is to obtain the underway marine cruise data from which the magnetic anomaly picks are to be made. For each ocean basin, a search was made for cruises on which the total field magnetic anomaly was recorded along-track, from the British Antarctic Survey database, the database at the University of Oxford, and the latest NGDC GEODAS releases. Each cruise was then examined to see if it contained magnetics data in the regions required, and discarded if the cruise only passed through regions of ocean floor not created at the ridge in question, if the data were of poor quality, or if the cruise only passed through the desired areas at such an angle to the flowlines to render it of little use. All the ship tracks of the chosen cruises for a given area were then plotted on a large-scale map, along with the along-track magnetic wiggles projected onto a direction approximately parallel to the local spreading direction. The locations of fracture zones in the area were also included so that it could be seen where a ship track crossed a fracture zone, which would cause a break in the anomaly pattern. These wiggle plots were then studied to determine possible correlations of wiggles in areas where several ship tracks appeared close together, and to identify by eye as many anomalies as possible. To speed the physical picking process, another interactive program for X-Windows

Chron	Cande & Kent (1995)	Age (Ma)
c2A	2An.1	2.58
c5	5n.1	9.74
c6	6	19.05
c8	8n.1	25.82
c13	13	33.06
c18	18n.1	38.43
c20	20	42.54
c21	21	46.26
c24	24n.1	52.36
c30	30	65.58
c32	32n.1	71.07
c33	33	73.62
c33r	33 (R)	79.08
c34	34	83.00

Table 3.1: The main geomagnetic reversals picked from anomaly profiles, and the corresponding ages determined by Cande & Kent (1995).

was written, **xmagpick**. This program (based on a structure of a picking program written for a Tektronix terminal (Wilson, 1993)), reads in an entire cruise file in GMT, MGD77 or ASCII x,y,m format and displays on screen the along-track anomaly, the topography (if available) and the heading. A relevant synthetic profile can also be loaded and a chosen section displayed on screen alongside the recorded magnetics for comparison. This synthetic profile is projected onto the current heading of the ship to compensate for when the ship is not travelling parallel to the flowlines. Picks can be made with the mouse and labelled on screen with the appropriate chron identifier. A separate window displays a map of the ship track, highlighting the section currently on screen and, optionally, any picks made for the cruise, the digitised ridge and any flowlines/fracture zones in the region. A screenshot of this program in use is given in Figure 3.6.

A variety of synthetic profiles were created for each area, for a range of different spreading rates and directions, but based around instantaneous and reconstruction poles determined in previous studies. These synthetic profiles were created by the Fortran program **magsynth**, obtained from the British Antarctic Survey, modified slightly so that the output was in a suitable format for use in **xmagpick**.

Picks made from the program were stored into ASCII files in a particular format recognised by **xmagpick**, which allowed the picks to be loaded up and displayed at a later date for checking

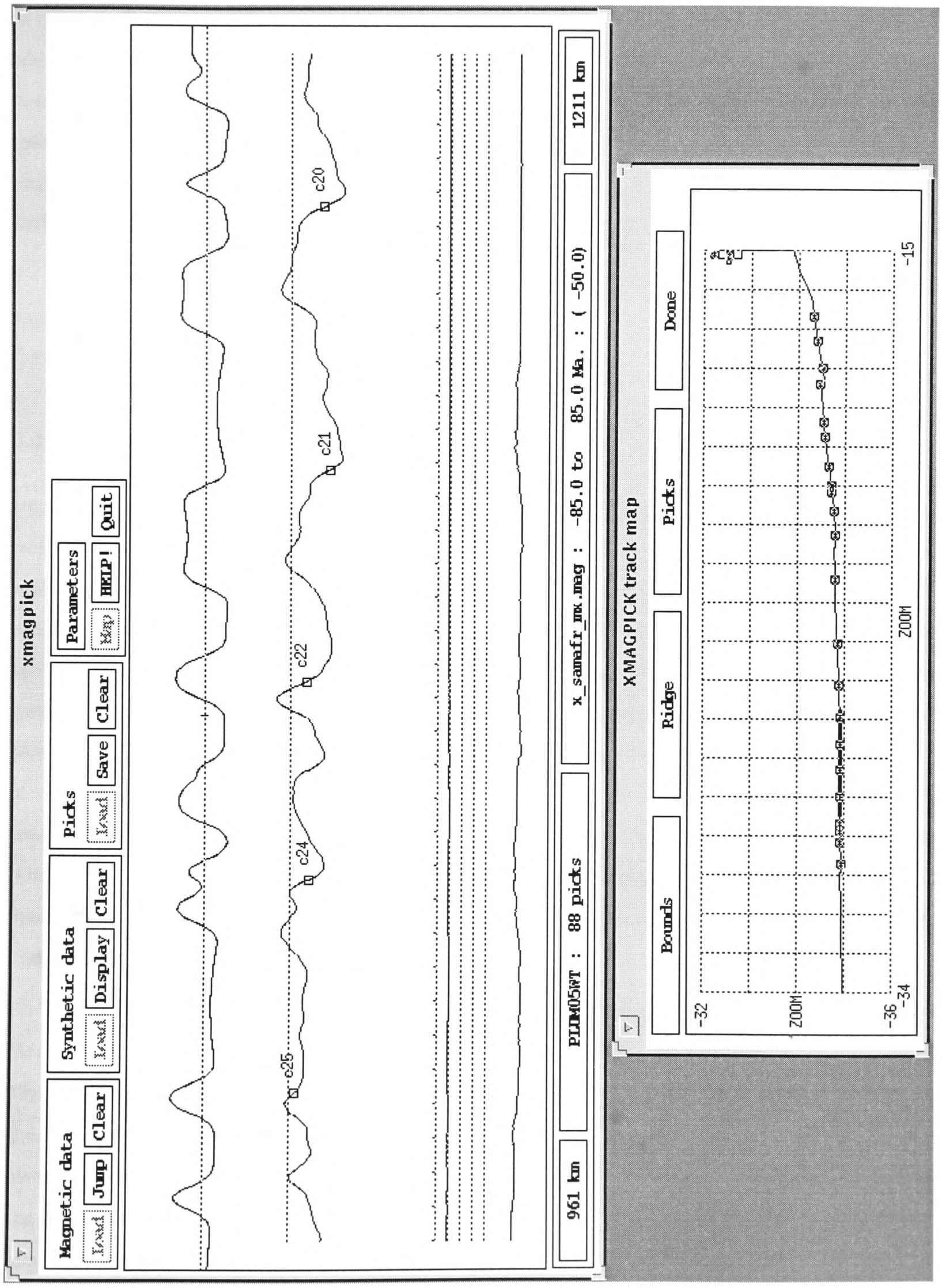

Figure 3.6: The X-Windows magnetic anomaly picking program **xmagpick**.

or reference, and also be used directly with standard plotting programs such as GMT's *psxy*. In addition, the program **mpicks2screen** was written which displays all the anomalies from one or more pick files as a PostScript file, with different symbols according to the anomaly identifier, and **split_magpicks** which converts the picks into the requisite format for use in the reconstruction routines. After initial picks were made for each cruise, the large-scale wiggle plots were redrawn with the identified anomalies overlaid so that any mismatches could be examined.

The final form of the raw dataset for each plate pair was a single file containing all the magnetic anomaly reversal identifications identified from seafloor created by spreading between the pair of plates in question.

3.3.1 Synchronisation of isochron picks

During the picking procedure described above, along-track marine magnetic anomalies were directly compared to synthetic profiles in order to identify the relevant anomalies. In accordance with standard picking procedures, the boundaries of the reversals were picked, generally at the young end of the normal epoch of the chrons, with the exception of 33r. For the SAM-AFR and SAM-ANT plate boundaries, this was straightforward due to the fact that the majority of spreading was approximately east-west, and so the reversal boundaries could be picked from the zero crossing or inflection points on the profiles. However, for the AFR-ANT boundary, most of the spreading has been in a north-south orientation, and so the anomalies are skewed such that the inflection points of the magnetic wiggles no longer coincide with the actual reversal boundaries. This means that in order to make a pick which is consistent in timing with the picks made for the other plate boundaries, it was necessary to choose to make the picks at the peaks and troughs of the anomalies.

This is shown in Figure 3.7, which shows a set of 3 synthetic profiles, one across each of the three ridges, displayed so that the anomalies are projected onto the same timescale on the x-axis. The minor differences between the shapes of the SAM-ANT and SAM-AFR profiles are due to the lower spreading rate of the SAM-ANT ridge smoothing out the smaller reversals, as was discussed for Figure 3.5. The reversal boundaries for the c5(y), c6(y) and c8(y) chrons as well as the central c1 anomaly are marked by red lines running down across the profiles. It can be clearly seen that for the SAM-AFR and the SAM-ANT profiles, picking the 'young' end of the reversals is simply a job of picking the inflection points, or the zero-crossing points, of the appropriate

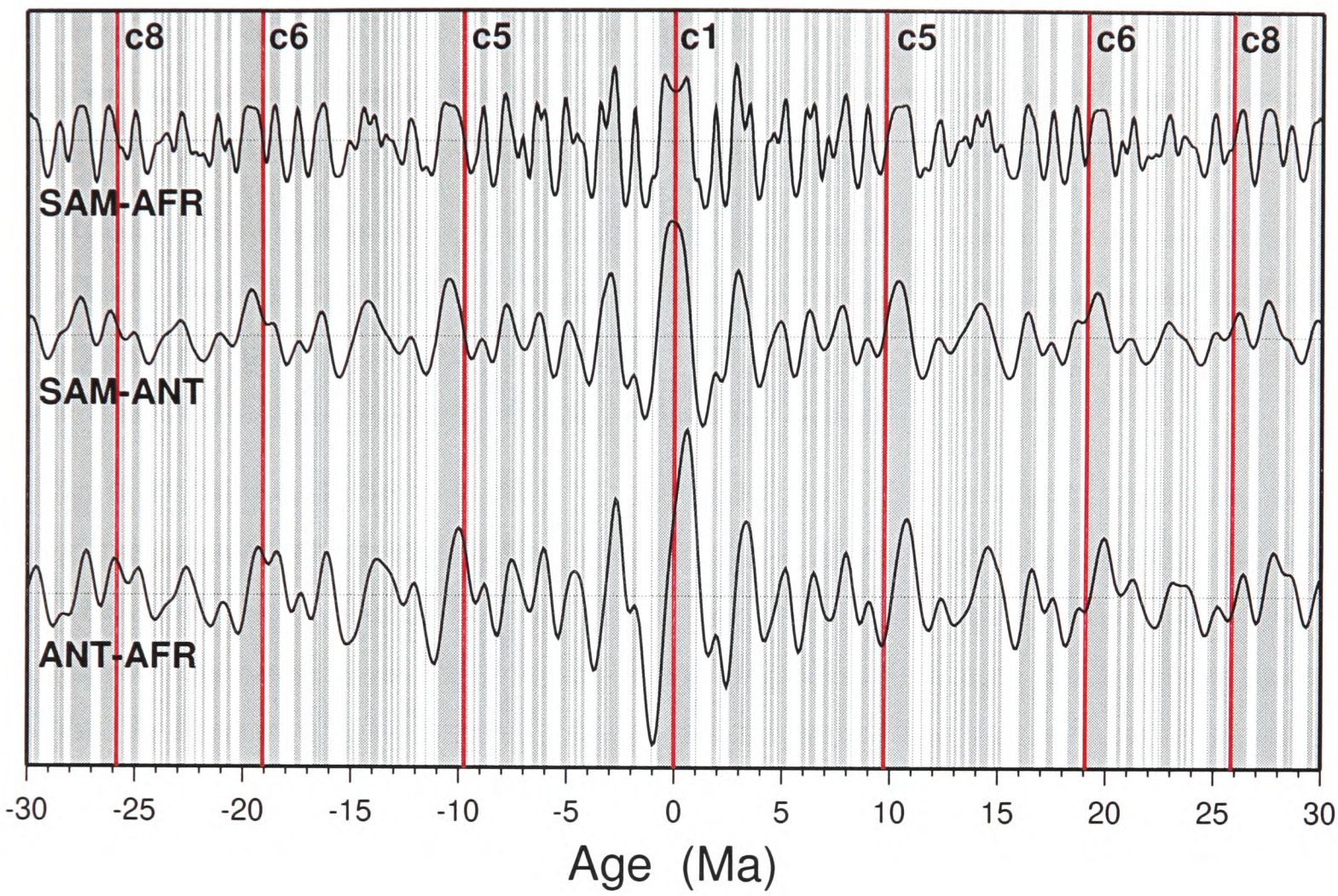

Figure 3.7: A diagram showing how care must be taken when picking reversal boundaries on magnetic profiles, since in regions where the field is highly skewed (AFR-ANT spreading), the boundaries coincide with the peaks and troughs of the magnetic anomalies, instead of the zero crossing/inflection points.

---

anomaly. However, for the ANT-AFR profile, the anomalies are skewed such that the reversal boundaries are marked by either a peak or a trough of the skewed magnetic anomalies generated by the block model. If the inflection points had been picked instead of the maxima/minima on the ANT-AFR magnetic profiles, this would have lead to the introduction of a systematic error in the region of 5km.

3.4 Example anomaly profiles and summary of data

3.4.1 South America - Africa seafloor spreading

The majority of the data used for this plate pair was the dataset compiled by Cande *et al.* (1988), used in the subsequent study by Shaw & Cande (1990), and others since. It is regarded as the most comprehensive collection of data for the region, and accepted as a reliable set of anomaly identifications. However, there have since been more cruises in the area, and there some cruises

that were unavailable to Cande at the time, and so picks I have made from these cruises are shown in the following figures. Figure 3.8 shows the tracks of the additional ship cruises from which magnetic anomaly data were interpreted for this study.

Estimates of spreading rates from which to create synthetic models were determined from the poles of Shaw & Cande (1990). Figures 3.9 to 3.12 show the ship tracks projected along the approximate direction of spreading (N80°E) and compared to a generated synthetic profile. Identifications of selected magnetic anomaly chrons are shown.

The picks were made independently of those made by Cande, without comparison during the picking process, but when plotted on a map alongside those from the previous study, Figure 3.13, the correlation is very good. This is only to be expected however, given the quality of the magnetic anomalies generally produced at the Mid-Atlantic Ridge. The inversion method, described in Chapter 4, allows the use of picks for the central Brunhes anomaly (c1y), and so picks were made for this anomaly for all the cruises available for the South Atlantic, though in fact these were not actually used in the final inversion.

Figure 3.14 shows the collection of magnetic anomaly picks made for the South Atlantic. Not all of these picks are used in the inversion, by virtue of the pre-processing of picks required for the inversion, and described in Section 4.3.2 of Chapter 4. This applies equally to the set of picks for each ridge boundary.

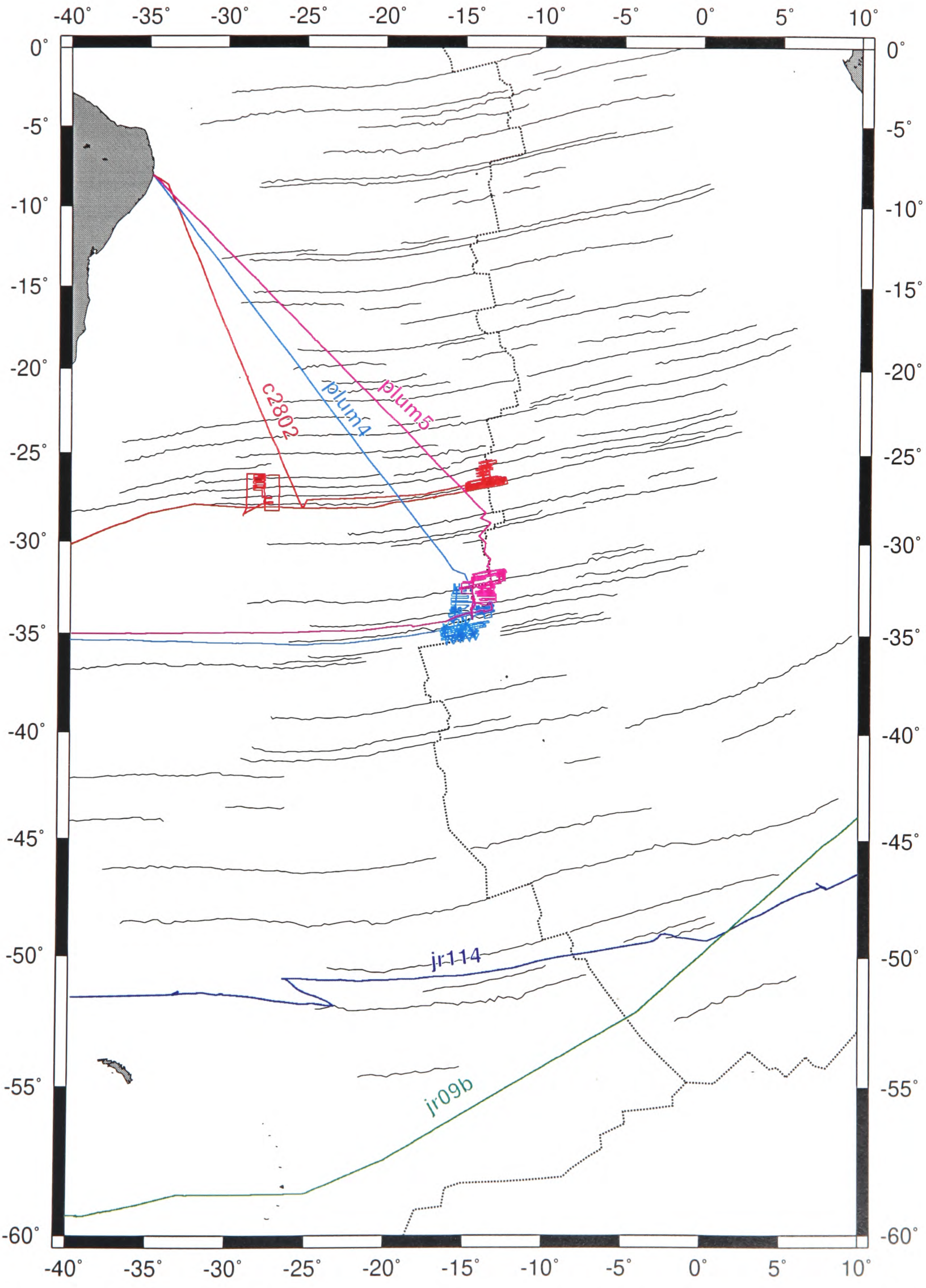

Figure 3.8: A track plot showing the cruises from which magnetic anomaly data were obtained for SAM-AFR spreading, in addition to those isochrons identified by Cande *et al.* (1988).

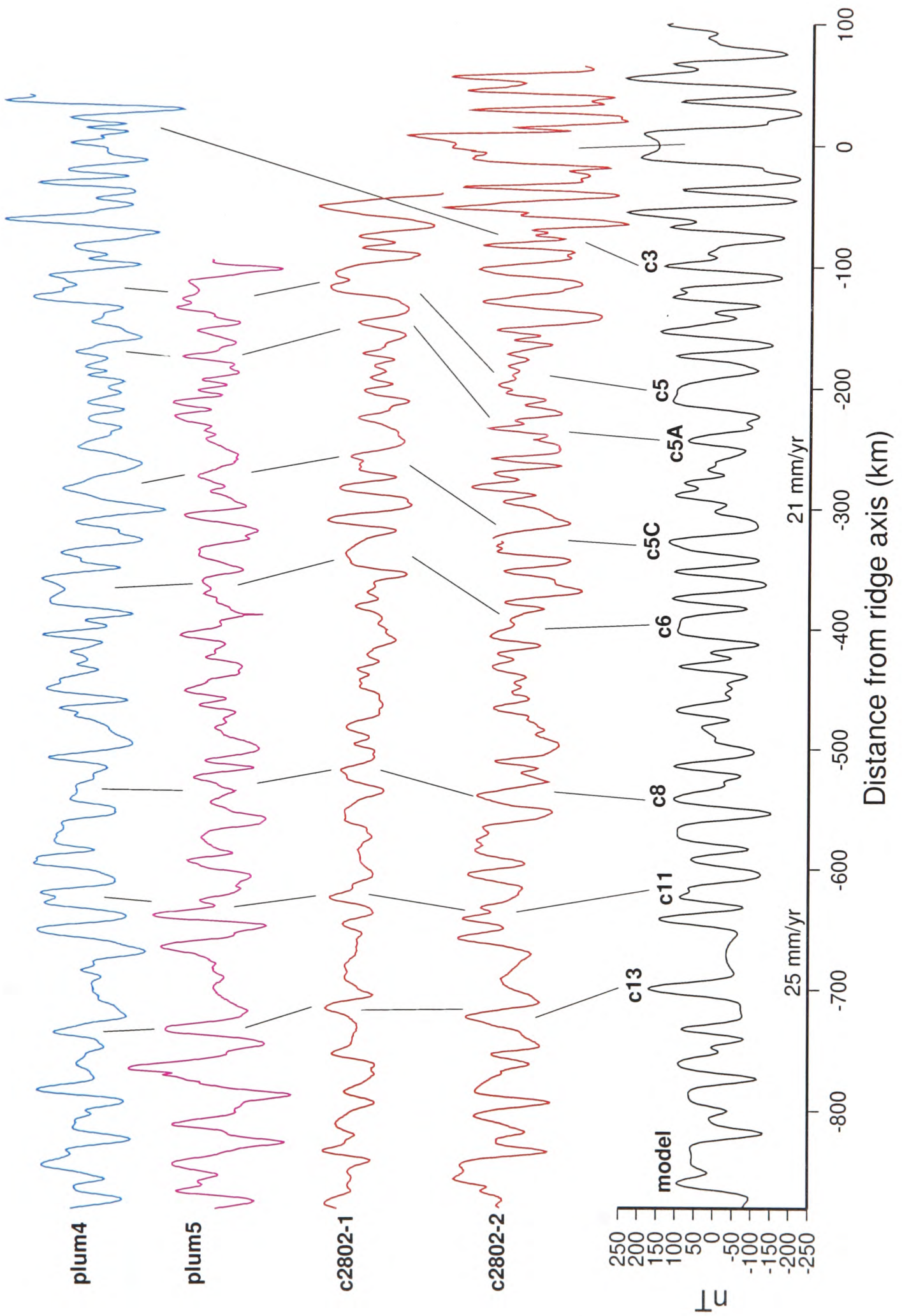

Figure 3.9: Ship track magnetic anomaly profiles from the Mid-Atlantic Ridge projected onto N80°E, and compared to a synthetic magnetic anomaly profile, with selected anomaly chrons labelled and identified in the profiles. Approximate spreading rates are indicated below the synthetic anomaly model.

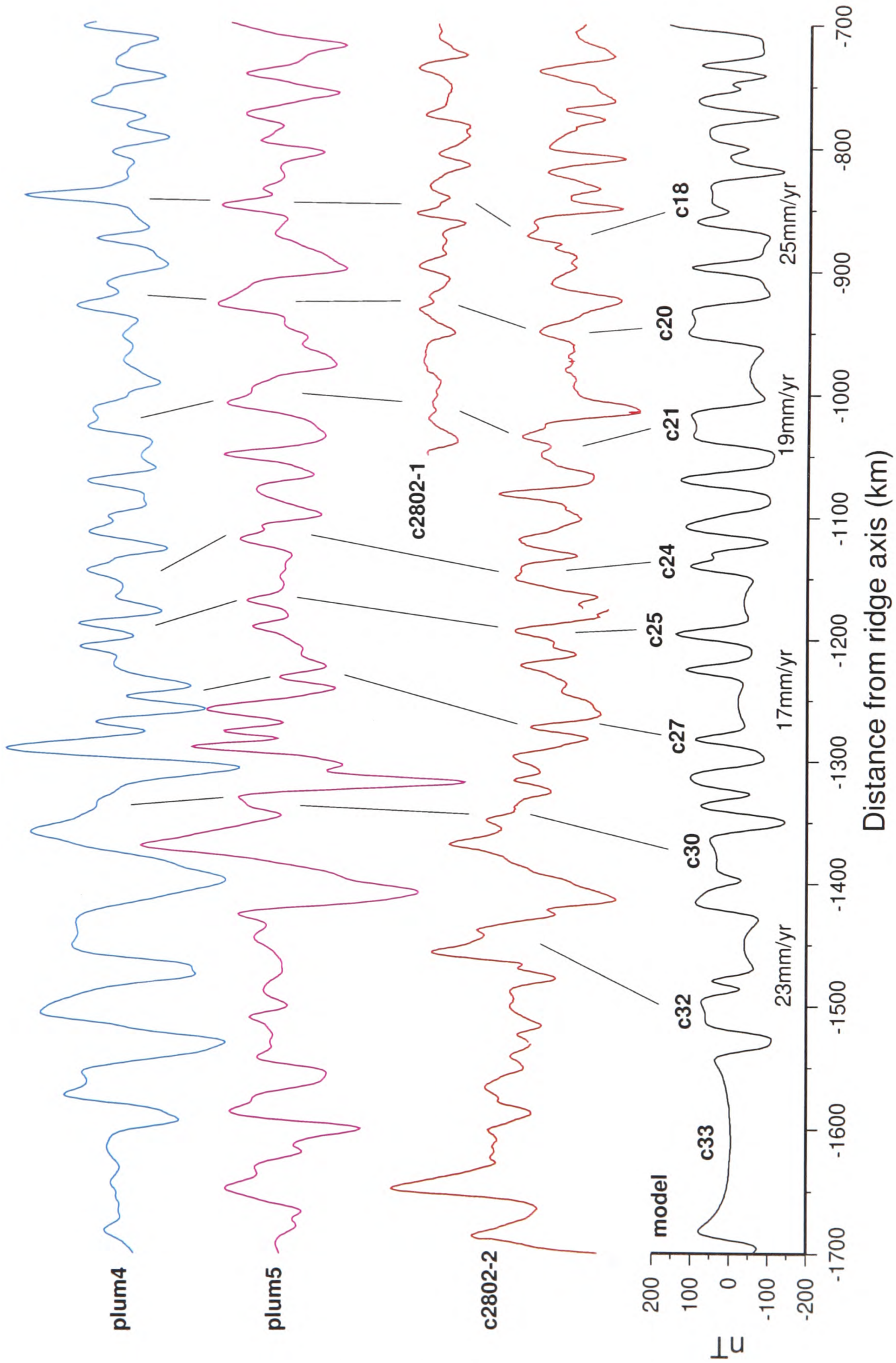

Figure 3.10: Ship track magnetic anomaly profiles from the Mid-Atlantic Ridge projected onto N80°E, and compared to a synthetic magnetic anomaly profile, with selected anomaly chrons labelled and identified in the profiles. Approximate spreading rates are indicated below the synthetic anomaly model.

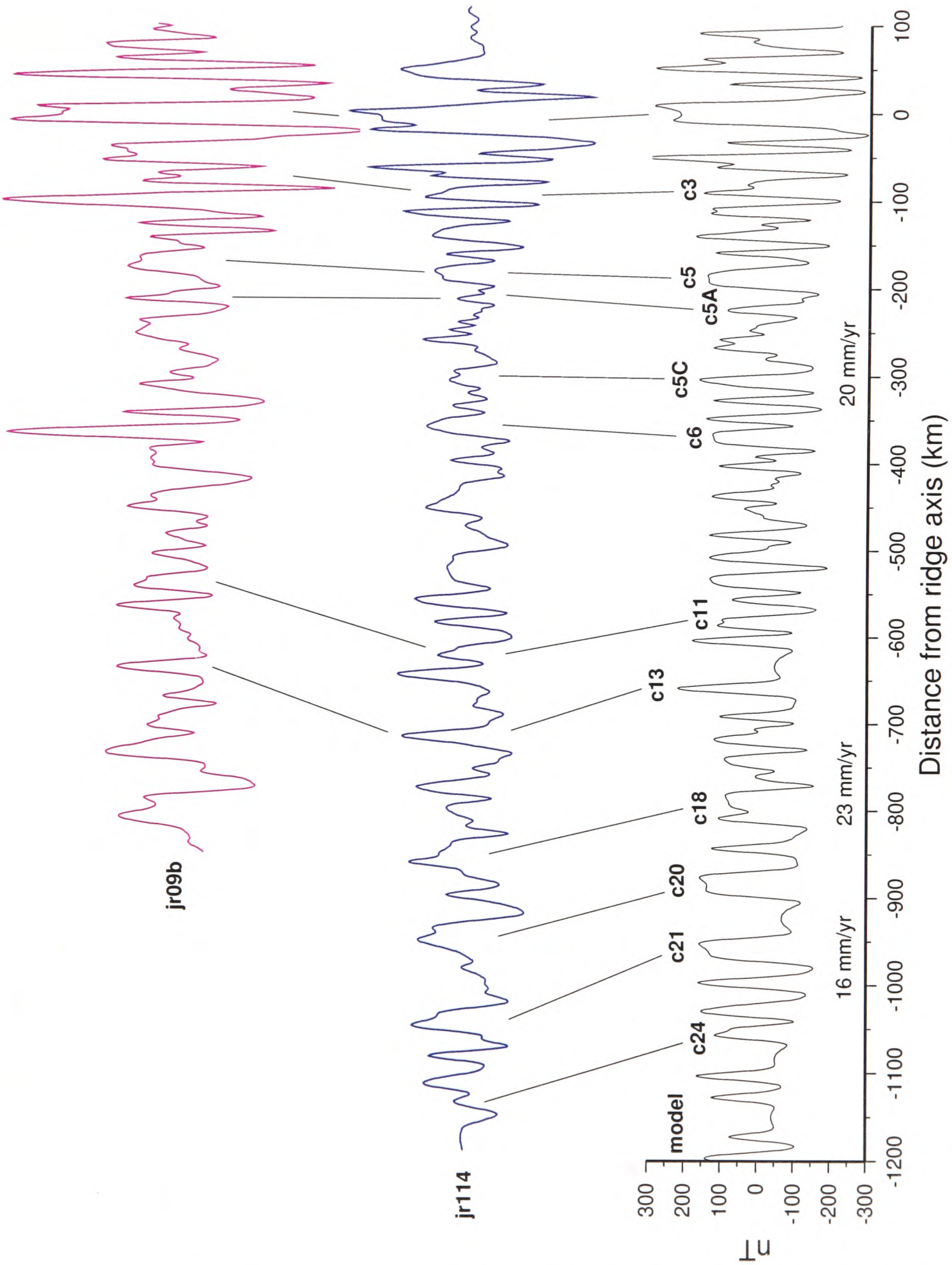

Figure 3.11: Ship track magnetic anomaly profiles from the Mid-Atlantic Ridge projected onto N70°E, and compared to a synthetic magnetic anomaly profile, with selected anomaly chrons labelled and identified in the profiles. Approximate spreading rates are indicated below the synthetic anomaly model.

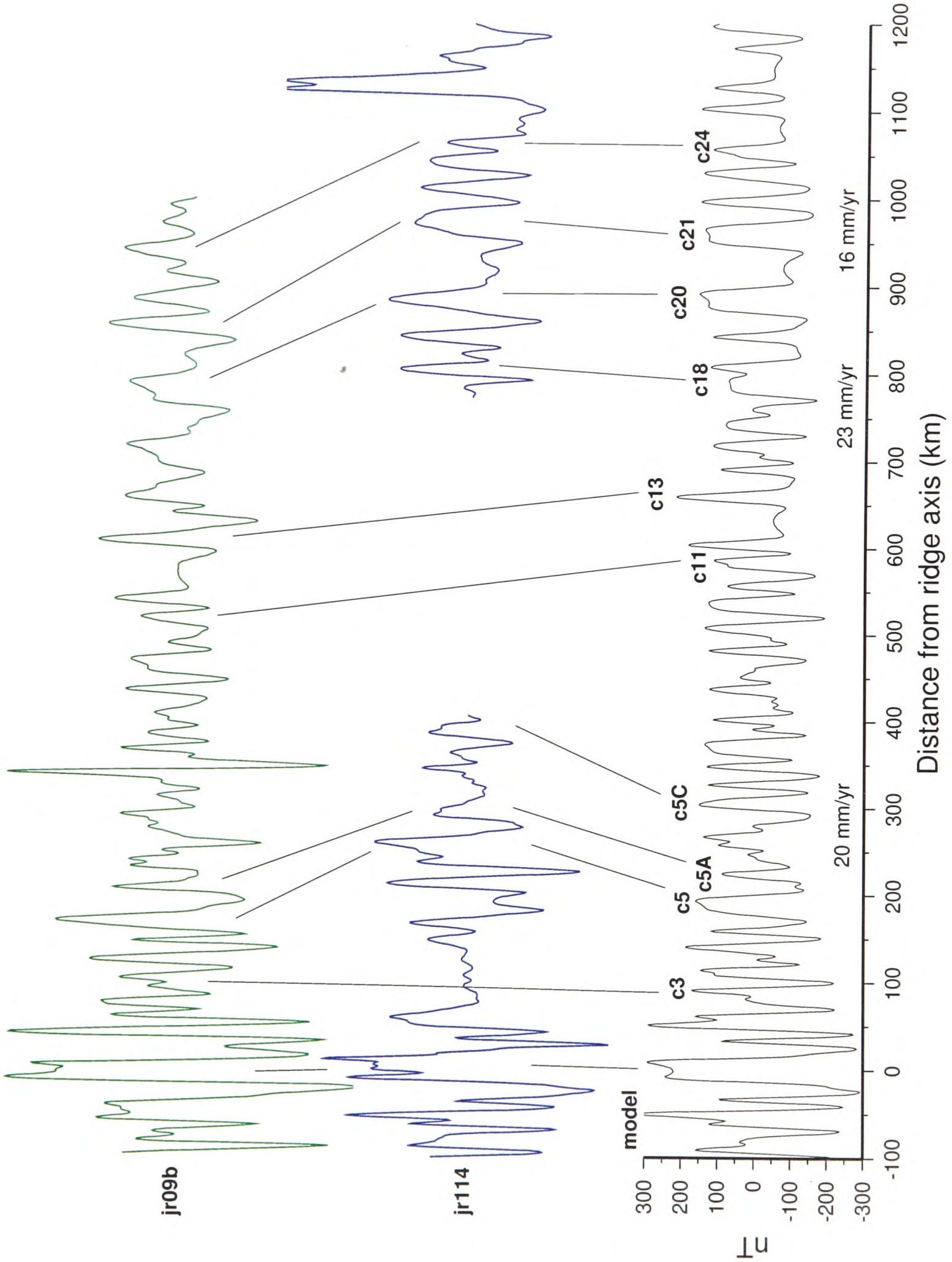

Figure 3.12: Ship track magnetic anomaly profiles from the Mid-Atlantic Ridge projected onto N70°E, and compared to a synthetic magnetic anomaly profile, with selected anomaly chrons labelled and identified in the profiles. Approximate spreading rates are indicated below the synthetic anomaly model.

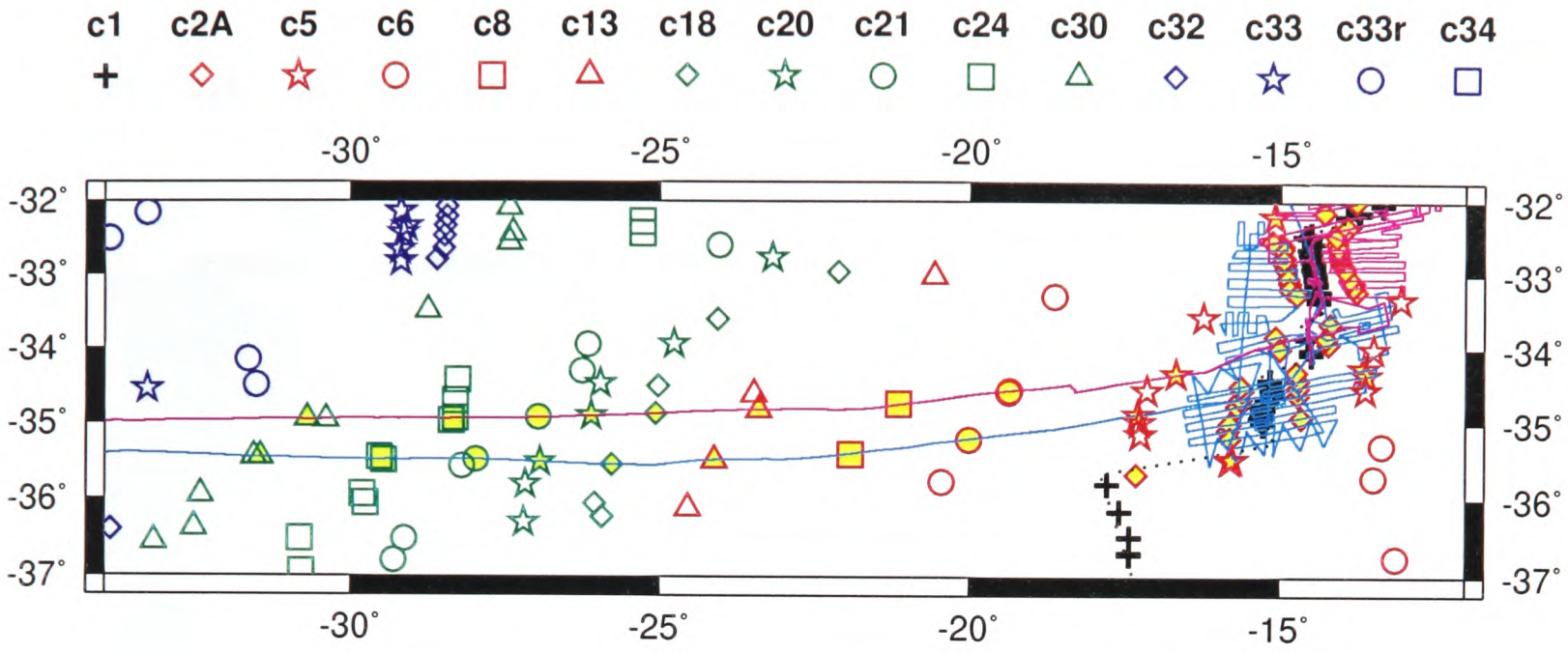

Figure 3.13: A small map showing the close correlation of isochrons identified from ship tracks processed by the author (symbols with yellow fill), and those isochrons identified by Cande *et al.* (1988) (no fill), in one region of the South Atlantic.

3.4.2 Antarctica - Africa seafloor spreading

The ship tracks from which magnetic isochron locations were determined are displayed in Figure 3.15. Identification of anomalies in this region is complicated by the low spreading rates, leading to poorer definition of reversals (Figure 3.5), high skewness of the anomalies, and rough topography, especially in the vicinity of the A.Bain Fracture Zone system (≈30°E). The process of identification of anomalies was aided by previous interpretations of cruise profiles in the area (Fisher & Sclater, 1983; Royer *et al.*, 1988) and from the comprehensive set of anomaly identifications of the IODCP/Alliance Exotique working group (Sclater *et al.*, 1996).

The synthetic profiles used for identifying the magnetic anomalies were created from rates and azimuths based on several different sets of theoretical finite rotation poles determined for Antarctic - African spreading (Royer *et al.*, 1988; Barker & Lawver, 1988; Fisher & Sclater, 1983).

The general locations of the four series of example magnetic anomaly profiles displayed in the following figures, were shown by the boxes outlined in white in Figure 3.15. The first two sets of profiles are from the NE end of the Southwest Indian Ridge, in the region of the Atlantis II Fracture Zone, and Figure 3.16 shows the series of ship tracks from which the profiles were obtained. Figure 3.17 shows a series of profiles which are sub-parallel to the actual fracture zone, and the gradual deterioration of the magnetic anomalies in the fracture zone valley can be clearly seen. However, the anomalies do not disappear abruptly, and anomalies on the Antarctic plate

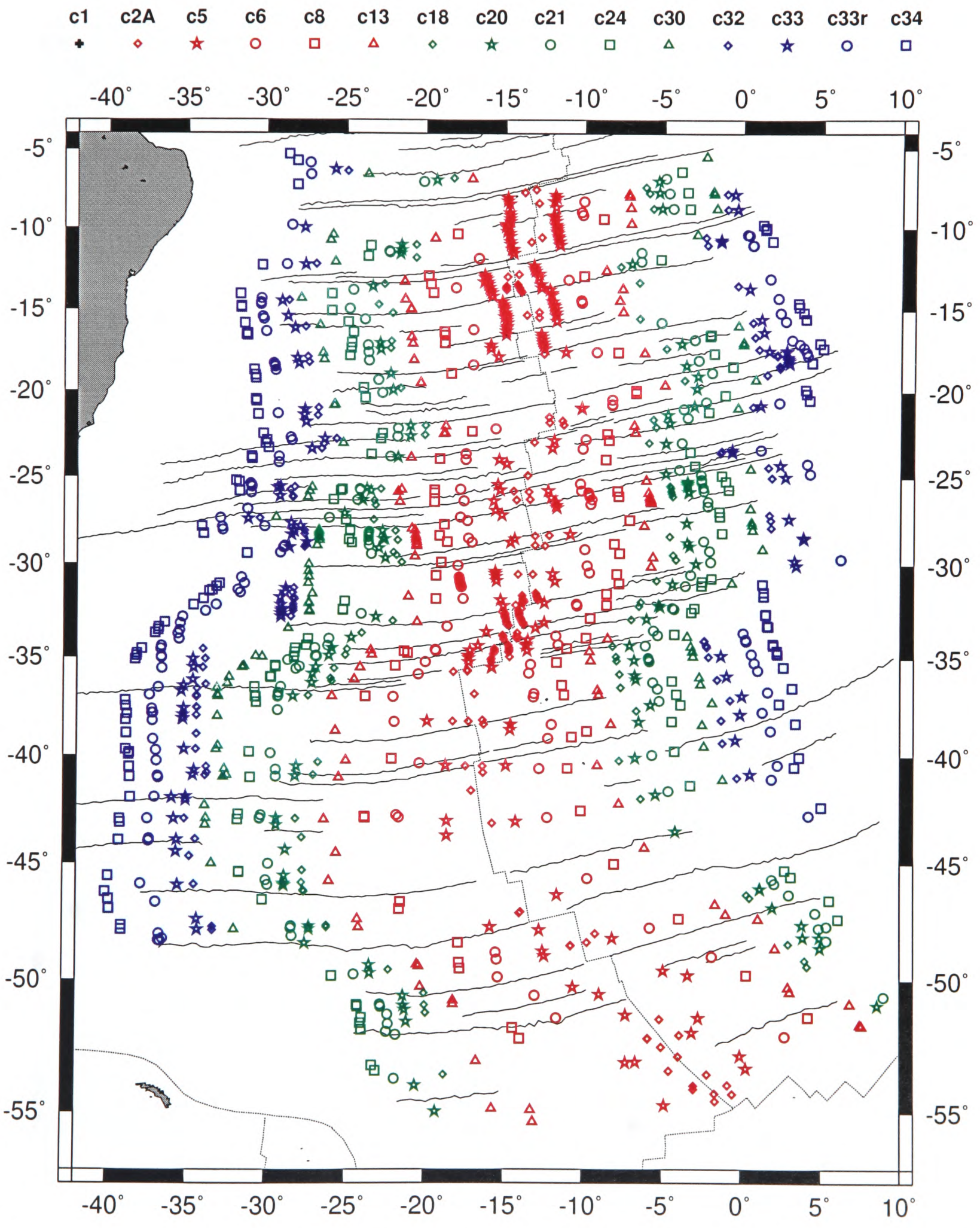

Figure 3.14: A map showing the complete set of magnetic anomaly identifications made for South American - African spreading.

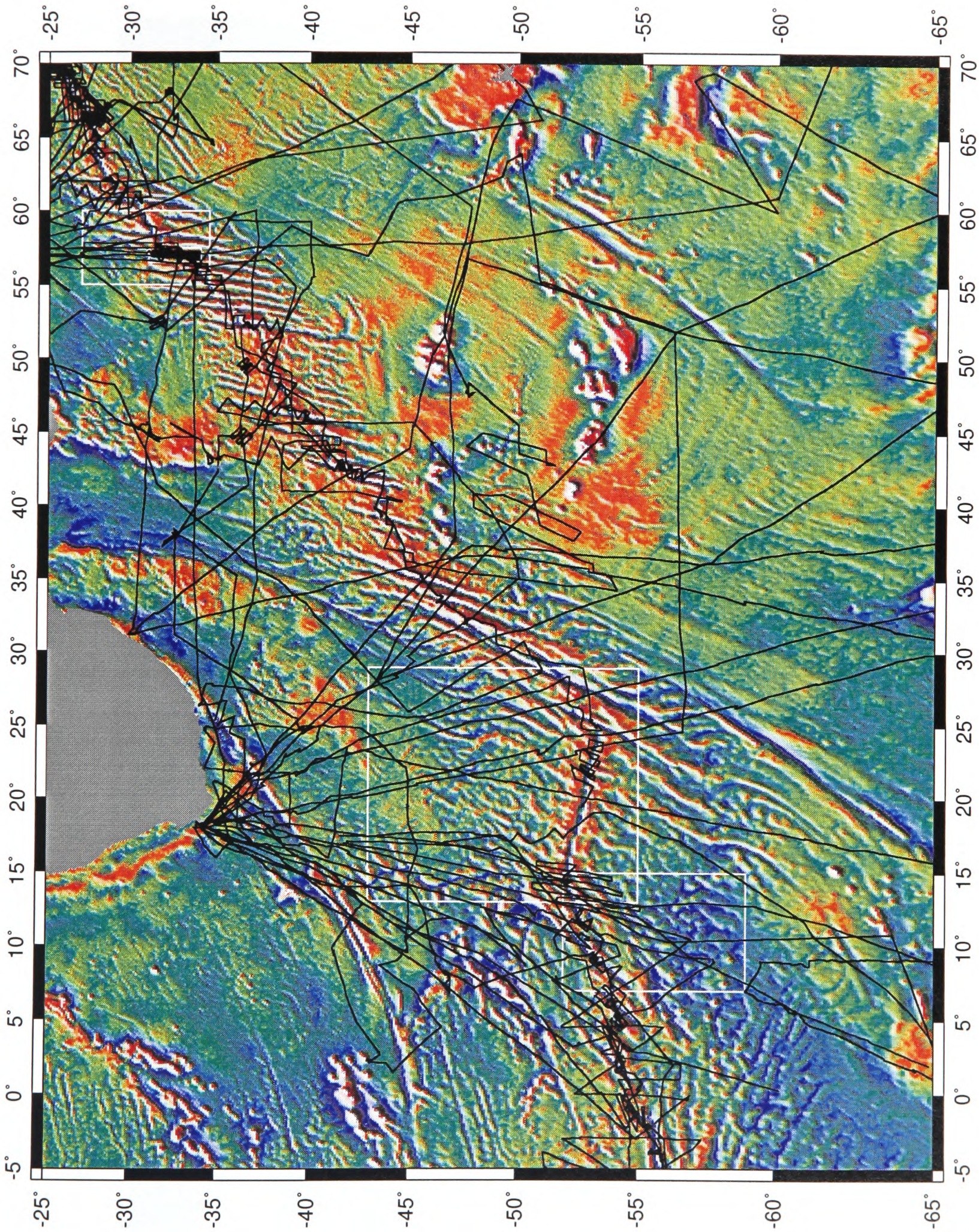

Figure 3.15: A chart showing the ship tracks from which magnetic anomalies created from Antarctic - African spreading were identified. The boxed areas outlined in white refer to regions from which selected profiles and corresponding anomaly identifications are displayed in Figures 3.16 to 3.22. (The gravity anomaly basemap is derived from the gravity image created by Smith & Sandwell (1995)).

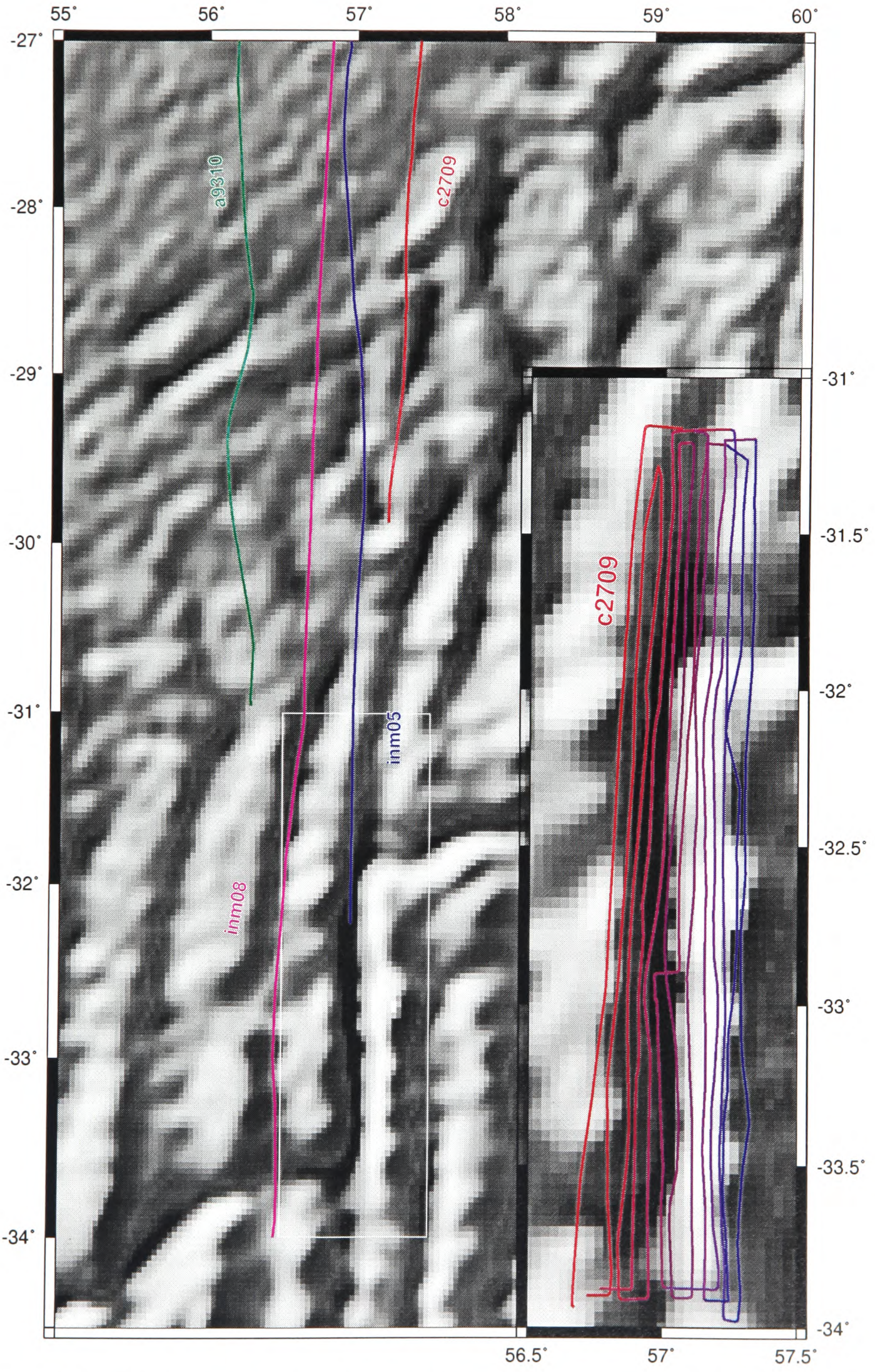

Figure 3.16: Maps showing the ship tracks from which the profiles displayed in Figures 3.17 (inset), and 3.18, were obtained.

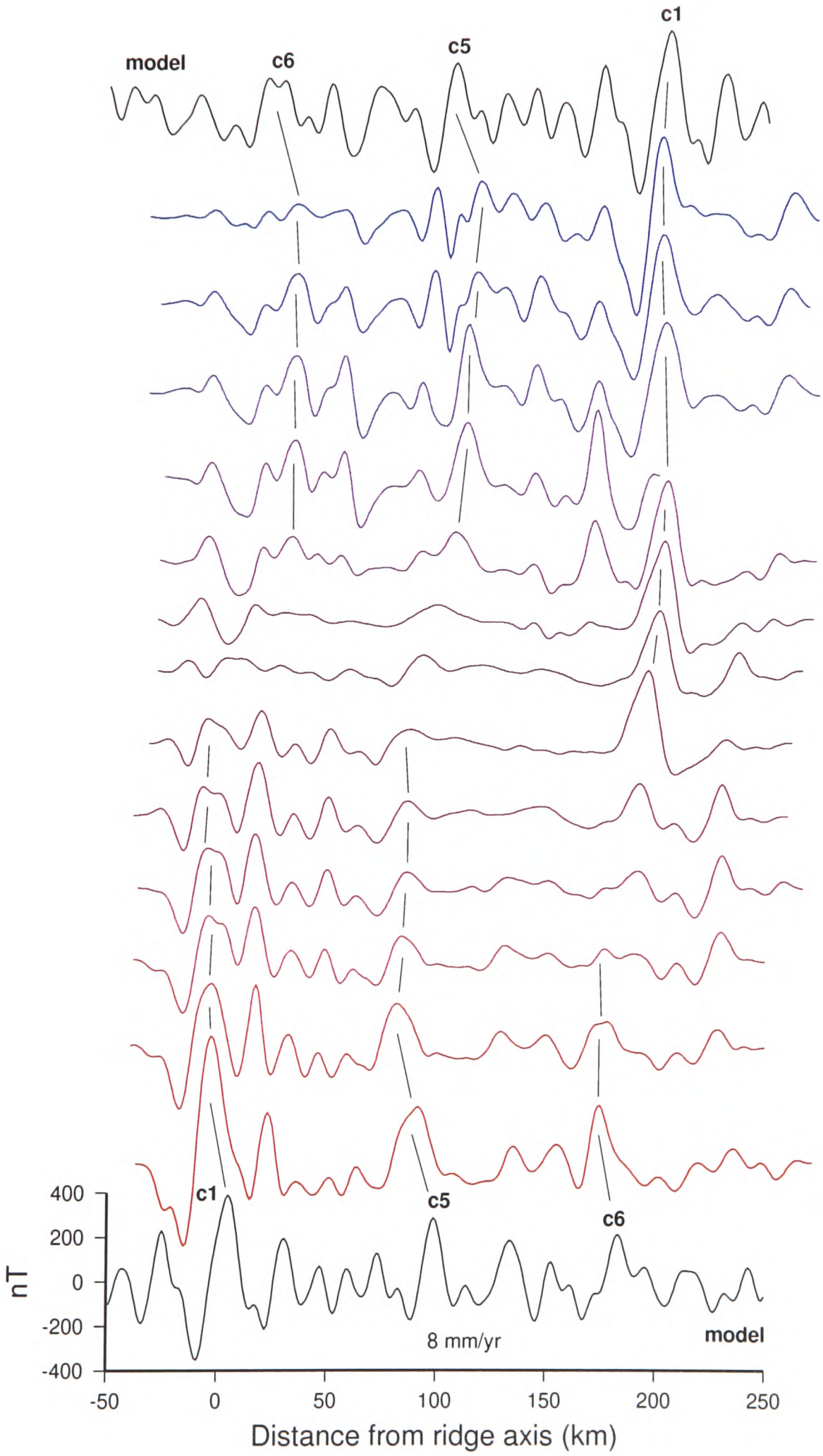

Figure 3.17: A series of along-track magnetic profiles from the cruise c2709 in the region of the Atlantis II fracture zone on the Southwest Indian Ridge, projected onto N 10°E, with a synthetic profile shown for comparison and selected anomalies identified on the profiles.

can be seen to slowly merge into anomalies on the African plate and visa versa, which of course complicates the job of picking clear anomalies in the region of a fracture zone.

Figure 3.18 shows a series of profiles on the African plate in the region of the Atlantis II fracture zone. Picking clear anomalies in this region was not an easy task as there are several fracture zones running through the area, and the seafloor morphology in the vicinity is quite complex. This illustrates the difficulties encountered identifying anomalies along the Southwest Indian Ridge, particularly to the east. Even in areas where there is a relatively high density of ship tracks, the complex topography often means that there is little chance of correlating anomalies between two relatively close ship tracks.

Anomaly identification was more straightforward in the areas either side of the ridge from 15°E to 25°E, since there were no significant fracture zones offsetting the anomalies and the topography was of a smaller scale than that found further towards the Indian Ocean Triple Junction. Figure 3.19 is a map showing a set of tracks in this region, on the African plate, and the along track anomaly profiles are given in Figure 3.20, projected onto N20°E, along with a synthetic profile, with selected anomaly reversals labelled. The profiles are much clearer and the anomalies more easily identified than those in the previous figure, as would be expected, but despite the lack of any major fracture zones in this region, the disturbed topography in the region suggests a history of small-scale segmentation along the ridge, and so, small offsets in the anomaly patterns can be expected in this region. Identifications of anomalies from tracks on the opposing Antarctic flank in the same region (Figure 3.21) are given in Figure 3.22. Identifications of younger anomalies on these profiles is complicated by the fracture zone and other complex topography towards the northern end of this area, running SW-NE, visible on the gravity basemap.

Additional anomalies in the region were identified from maps of along-track magnetic wiggles published in papers by Royer *et al.* (1988), and Fisher & Sclater (1983), and the picks digitised from large scale plots of the figures. This was necessary because the cruises were not stored in any of the available databases. Figure 3.23 shows the collection of magnetic anomaly picks, digitised from these maps, which were used in the inversions.

Figure 3.24 shows the collection of magnetic anomaly picks made for Antarctica - Africa spreading.

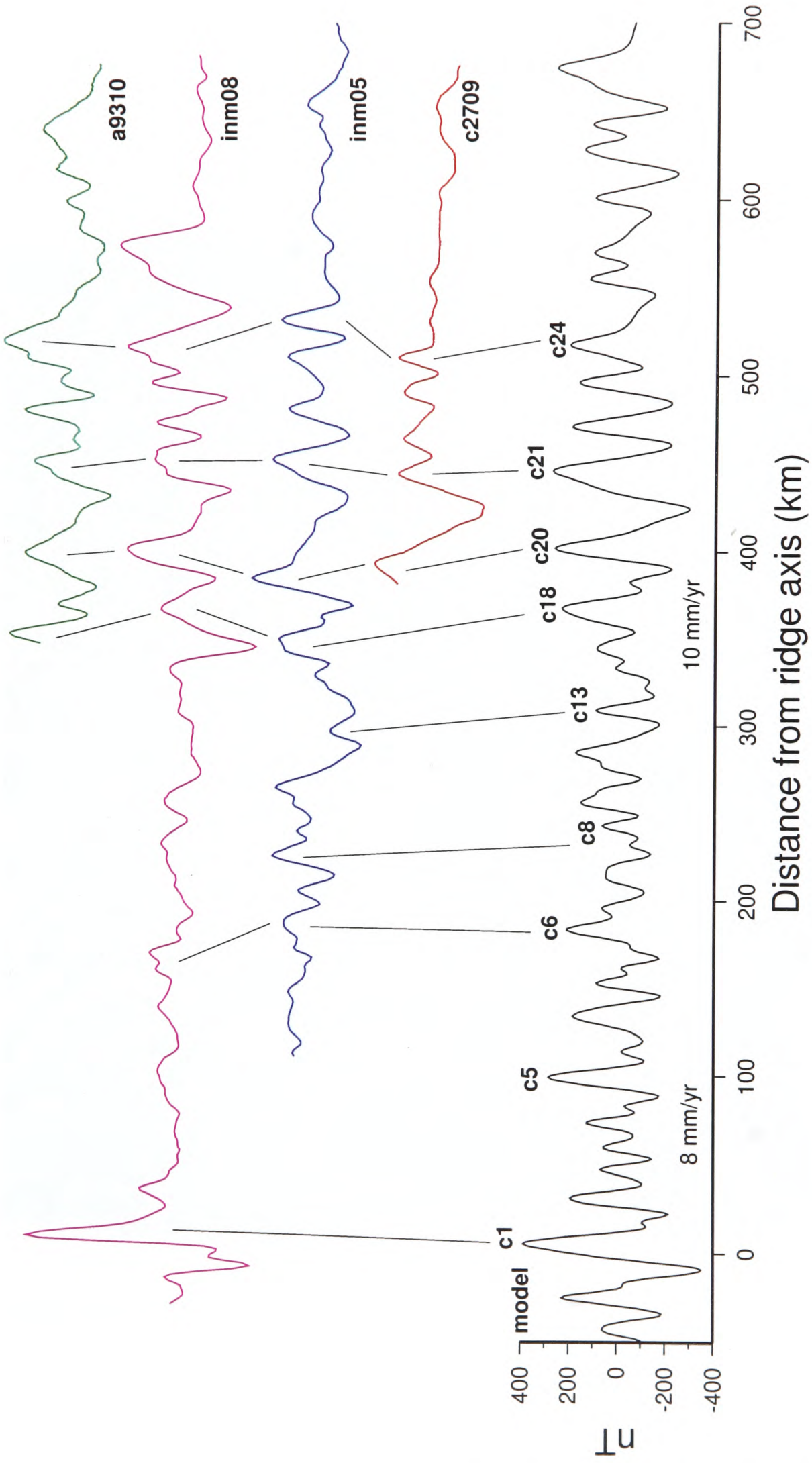

Figure 3.18: A series of along-track magnetic profiles from four ship tracks north of the Atlantis II fracture zone on the Southwest Indian Ridge, projected onto N 10°E, with a synthetic profile shown for comparison and selected anomalies identified on the profiles.

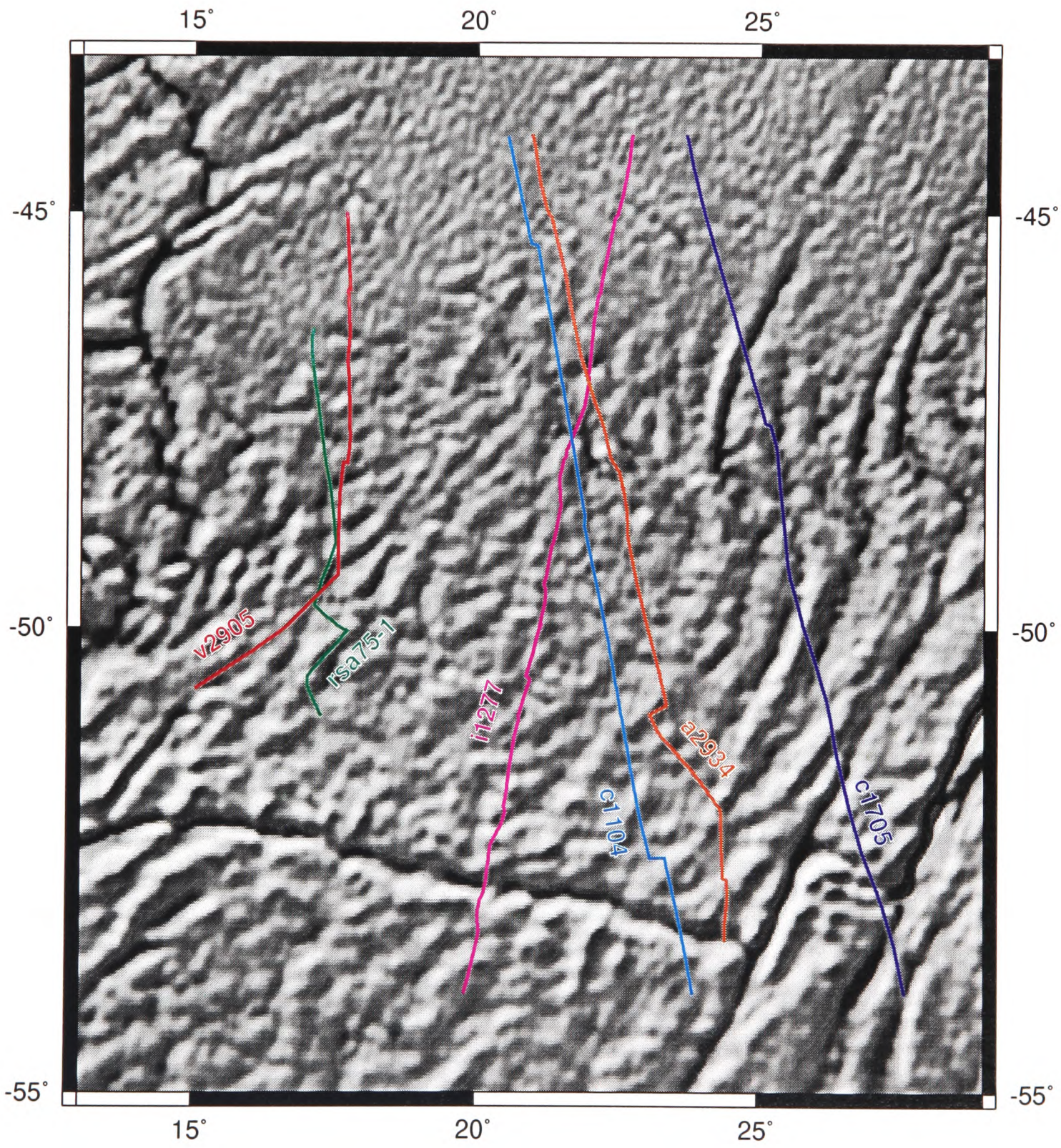

Figure 3.19: Maps showing the ship tracks from which the profiles displayed in Figure 3.20 were obtained.

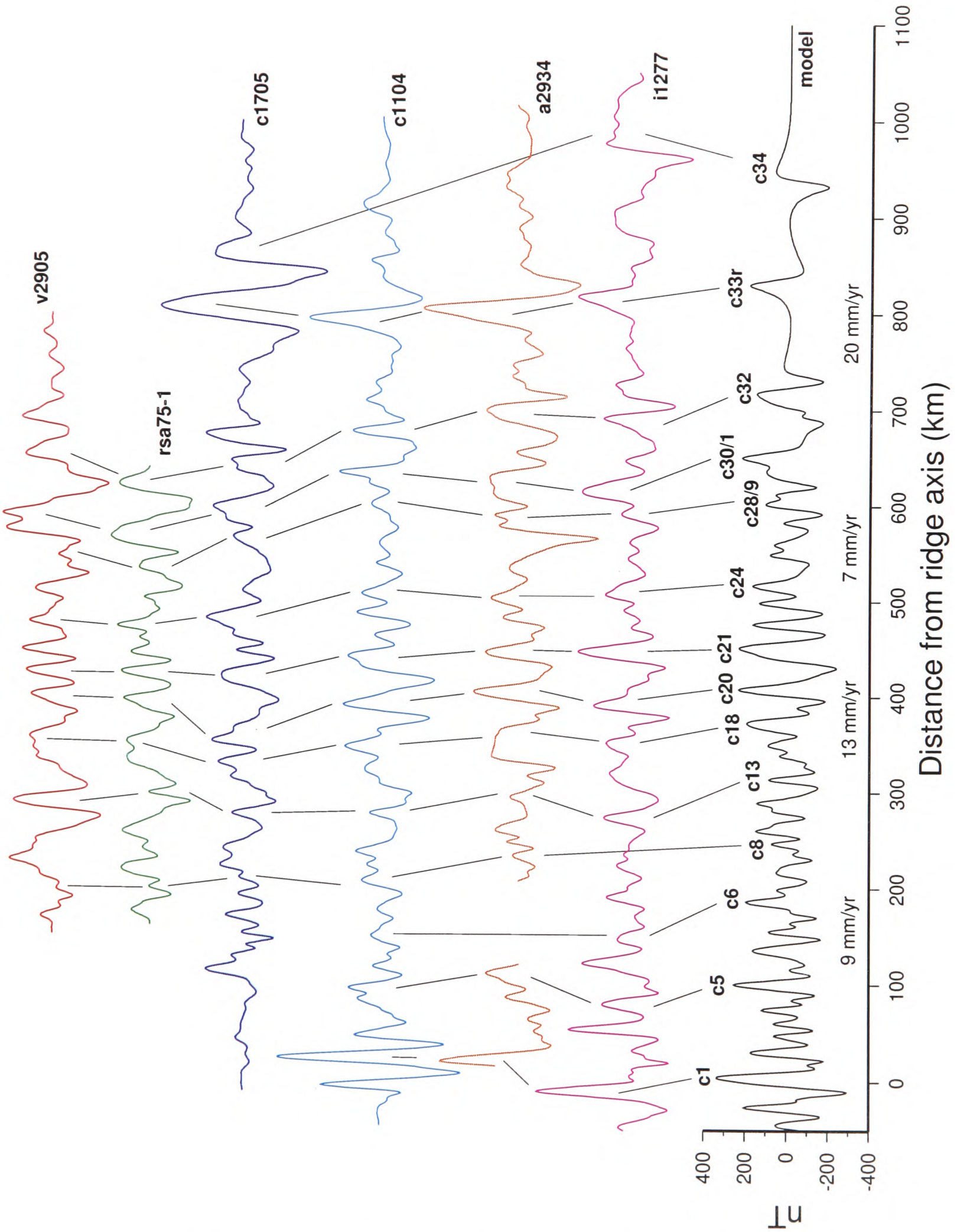

Figure 3.20: Along-track magnetic profiles from a series of cruises on the northern flank of the Southwest Indian Ridge, south of the Agulhas Basin, projected onto N 20°E, with a synthetic profile shown for comparison, and selected anomalies identified on the profiles.

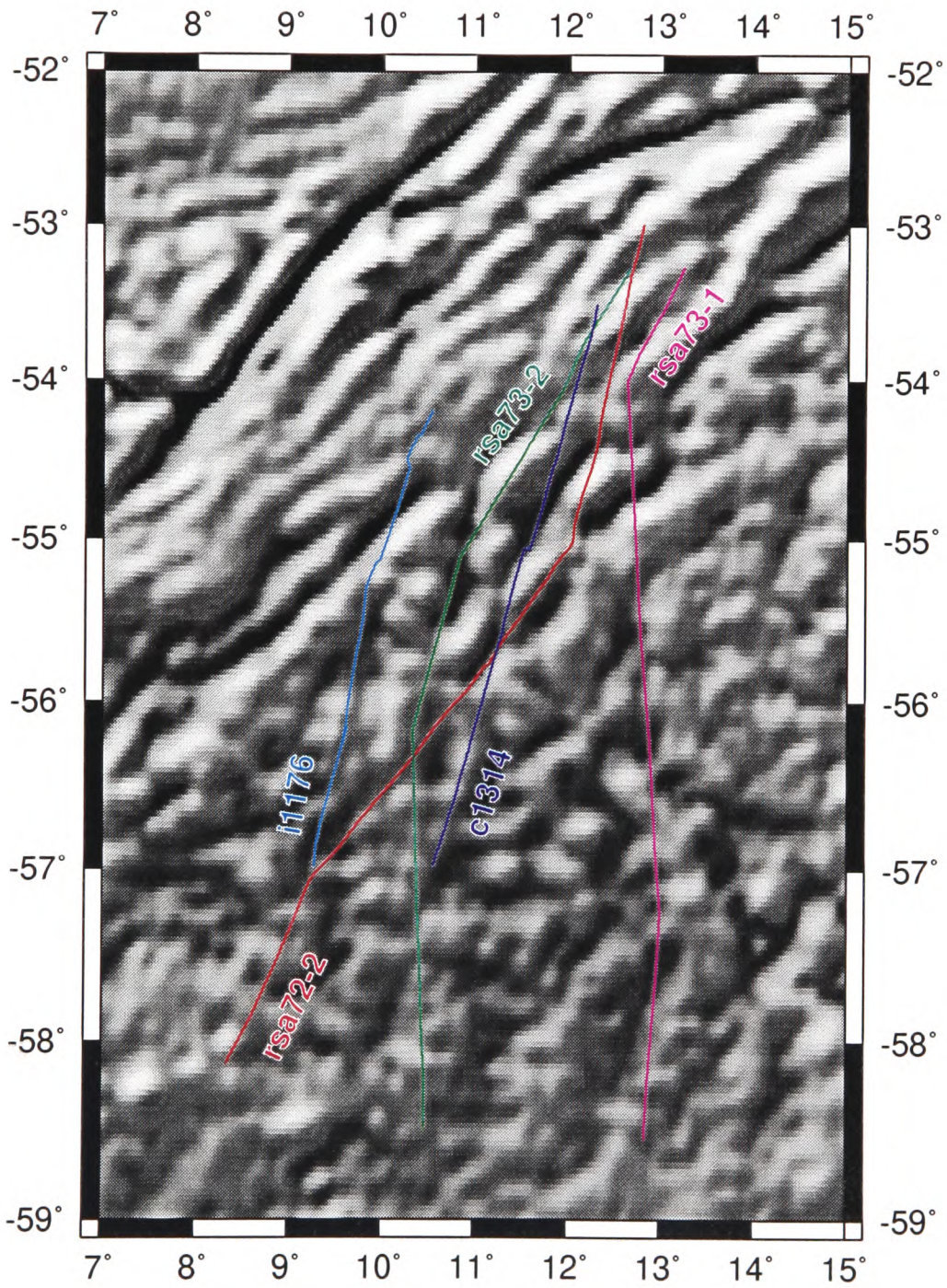

Figure 3.21: Maps showing the ship tracks from which the profiles displayed in Figure 3.22 were obtained.

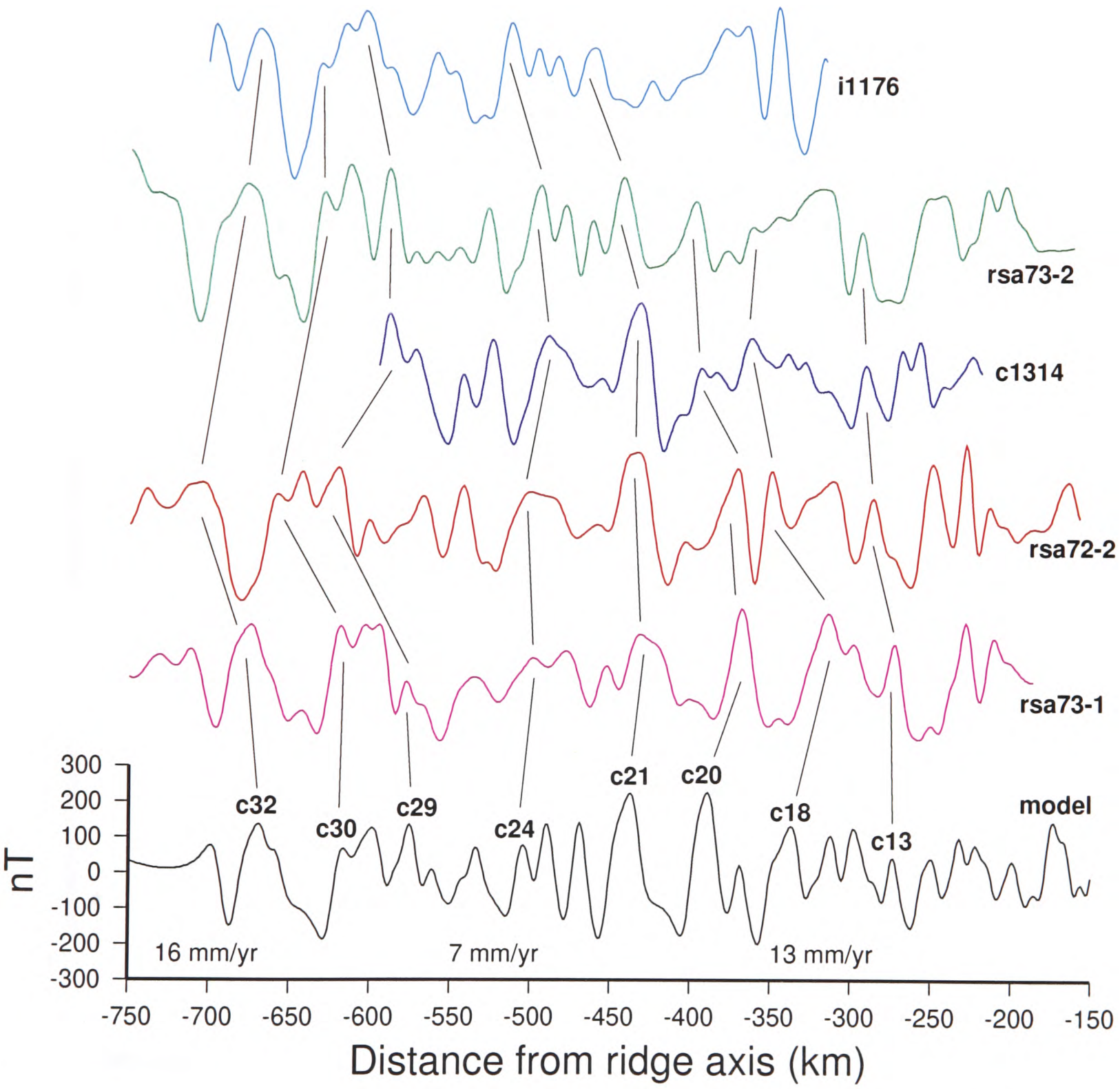

Figure 3.22: Along-track magnetic profiles from a series of cruises on the southern flank of the Southwest Indian Ridge, projected onto N 20°E, with a synthetic profile shown for comparison, and selected anomalies identified on the profiles.

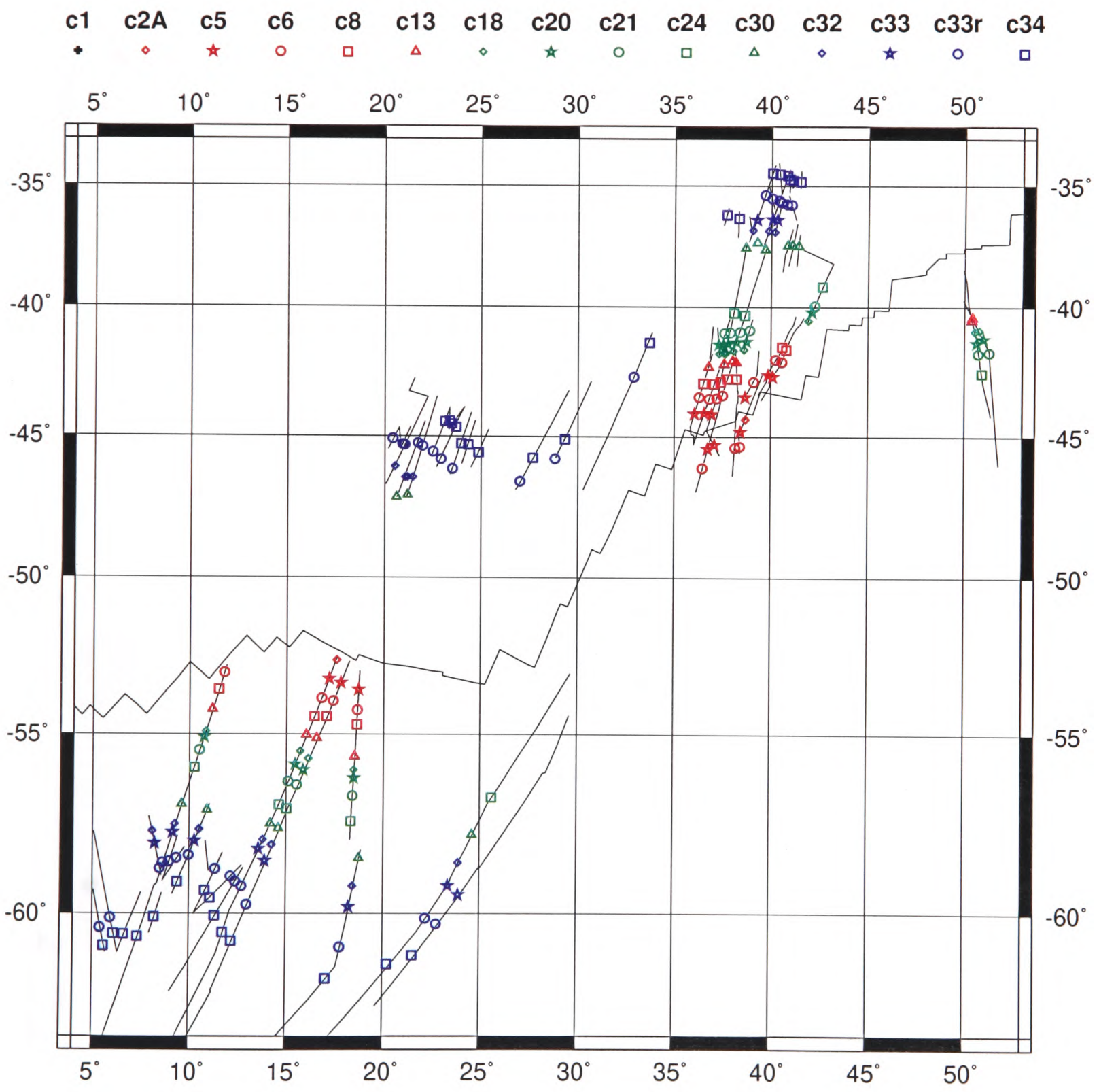

Figure 3.23: A map showing the set of picks digitised from Royer *et al.* (1988) and Fisher & Sclater (1983).

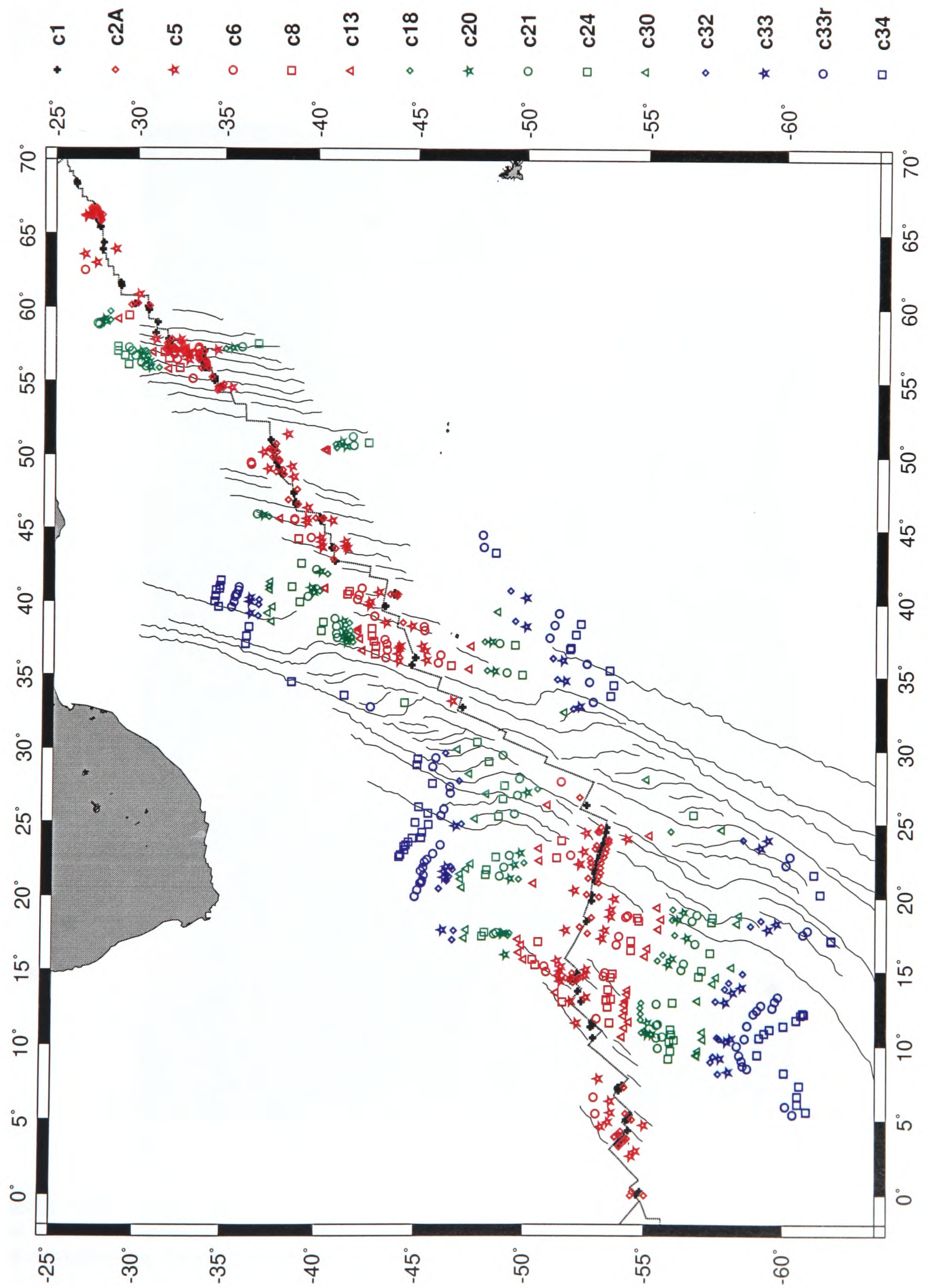

Figure 3.24: A map showing the complete set of magnetic anomaly identifications made for Antarctic - African spreading.

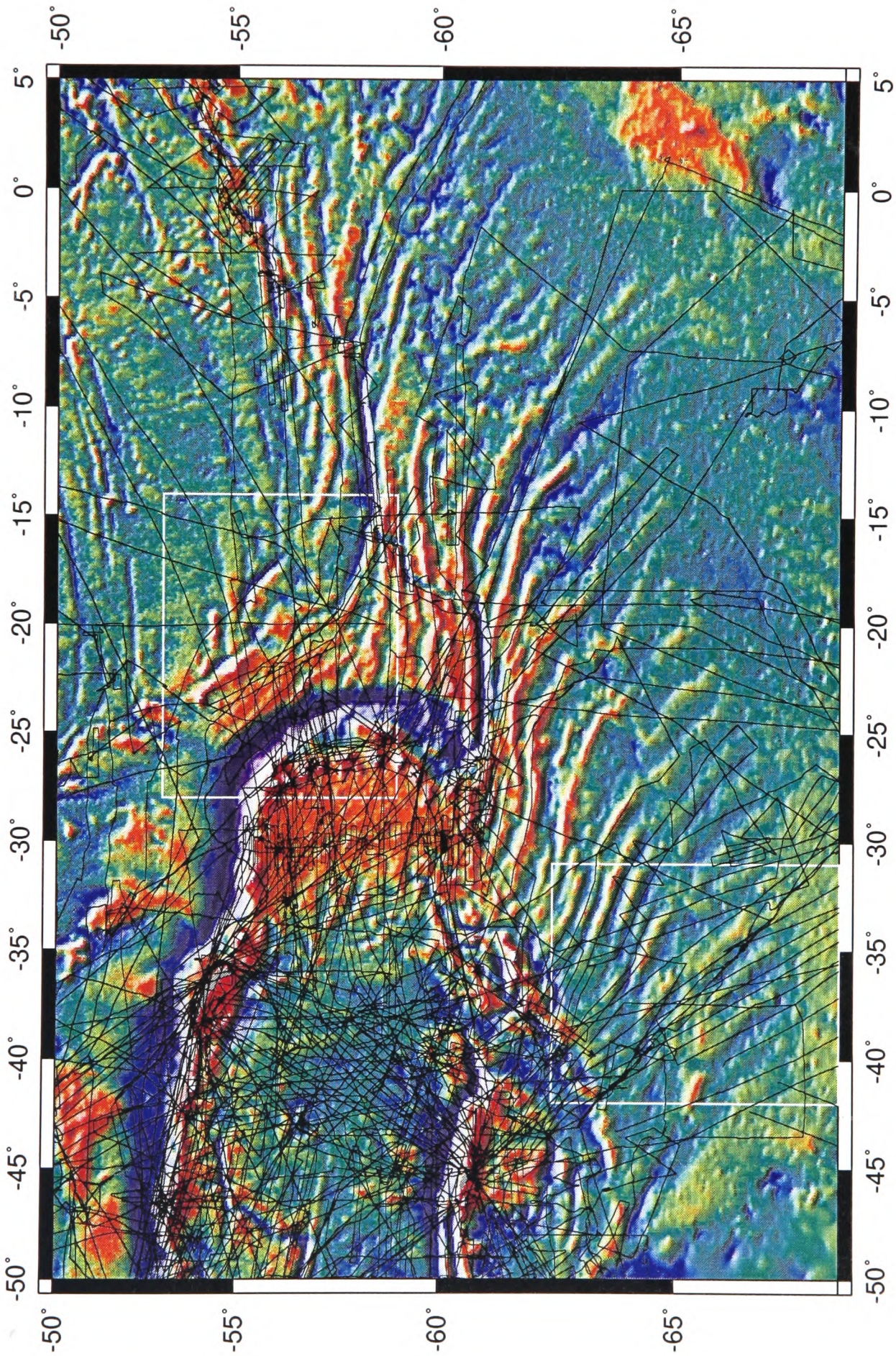

Figure 3.25: A chart showing the ship tracks from which magnetic anomalies created from South American - Antarctic spreading were identified. The boxed areas show the regions from which selected profiles and corresponding anomaly identifications, displayed in Figures 3.27 and 3.29.

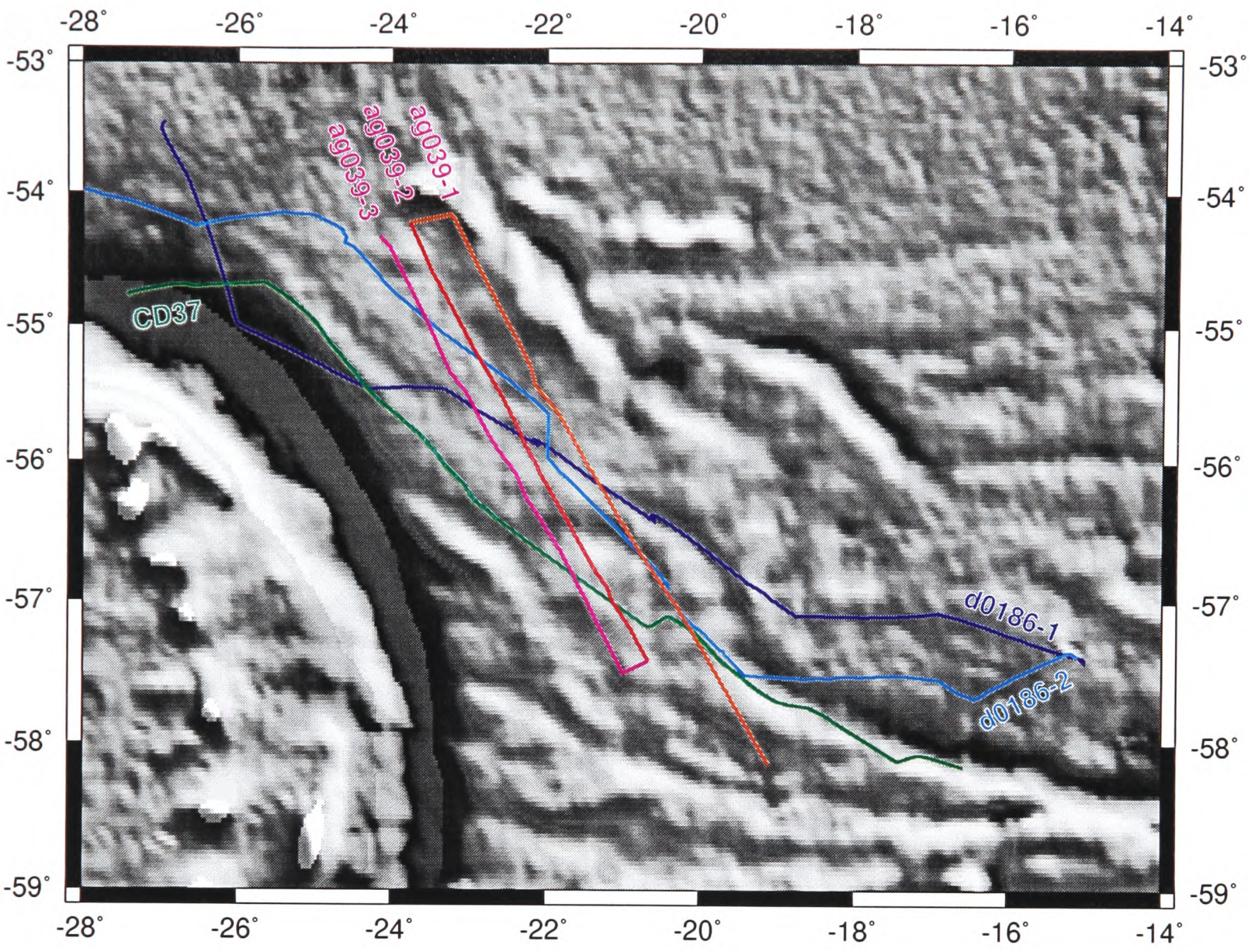

Figure 3.26: A map showing the ship tracks from which the profiles displayed in Figure 3.27 were obtained.

3.4.3 South America - Antarctica seafloor spreading

The majority of the magnetic anomaly identifications for South American - Antarctic spreading was provided by R.A. Livermore, of the British Antarctic Survey (BAS). The cruise files were obtained from the NGDC database, and from the comprehensive database of Antarctic cruises held at BAS.

Figure 3.25 shows a trackchart of all the cruises from which along-track magnetics were used to identify anomalies from South American-Antarctic spreading. Two sets of example profiles and interpretations are shown: from a region bordering the present-day South American-Antarctic Ridge (Figures 3.26 and 3.27); and from the western Weddell Sea (Figures 3.28 and 3.29). Figure 3.30 shows the collection of magnetic anomaly picks made for South American - Antarctic spreading.

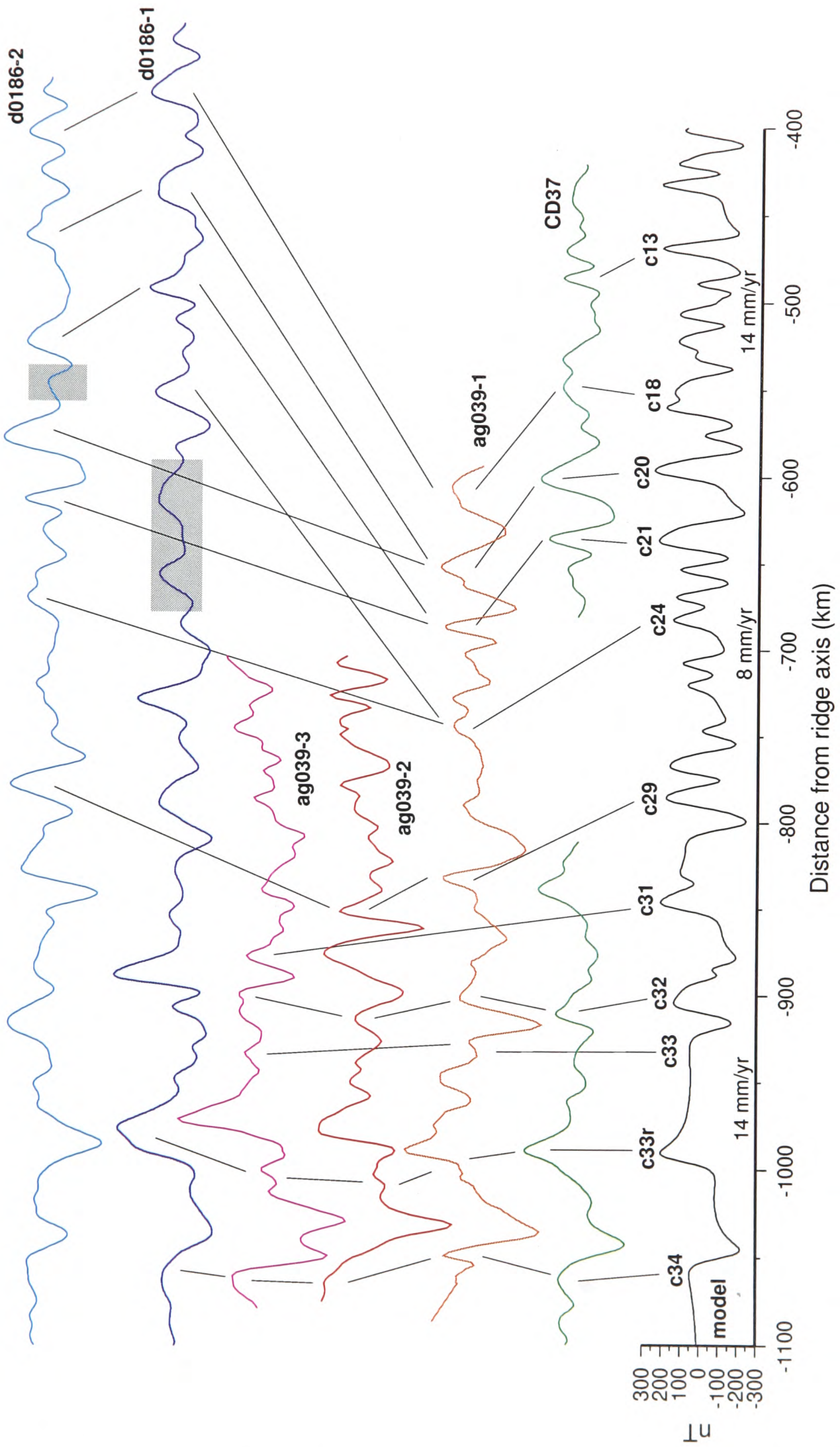

Figure 3.27: Along-track magnetic profiles from a series of cruises on the western flank of the South American-Antarctic Ridge, just to the northeast of the South Sandwich Trench, projected onto N 30°W, with a synthetic profile shown for comparison, and selected anomalies identified on the profiles. The grey areas mark fracture zone crossings.

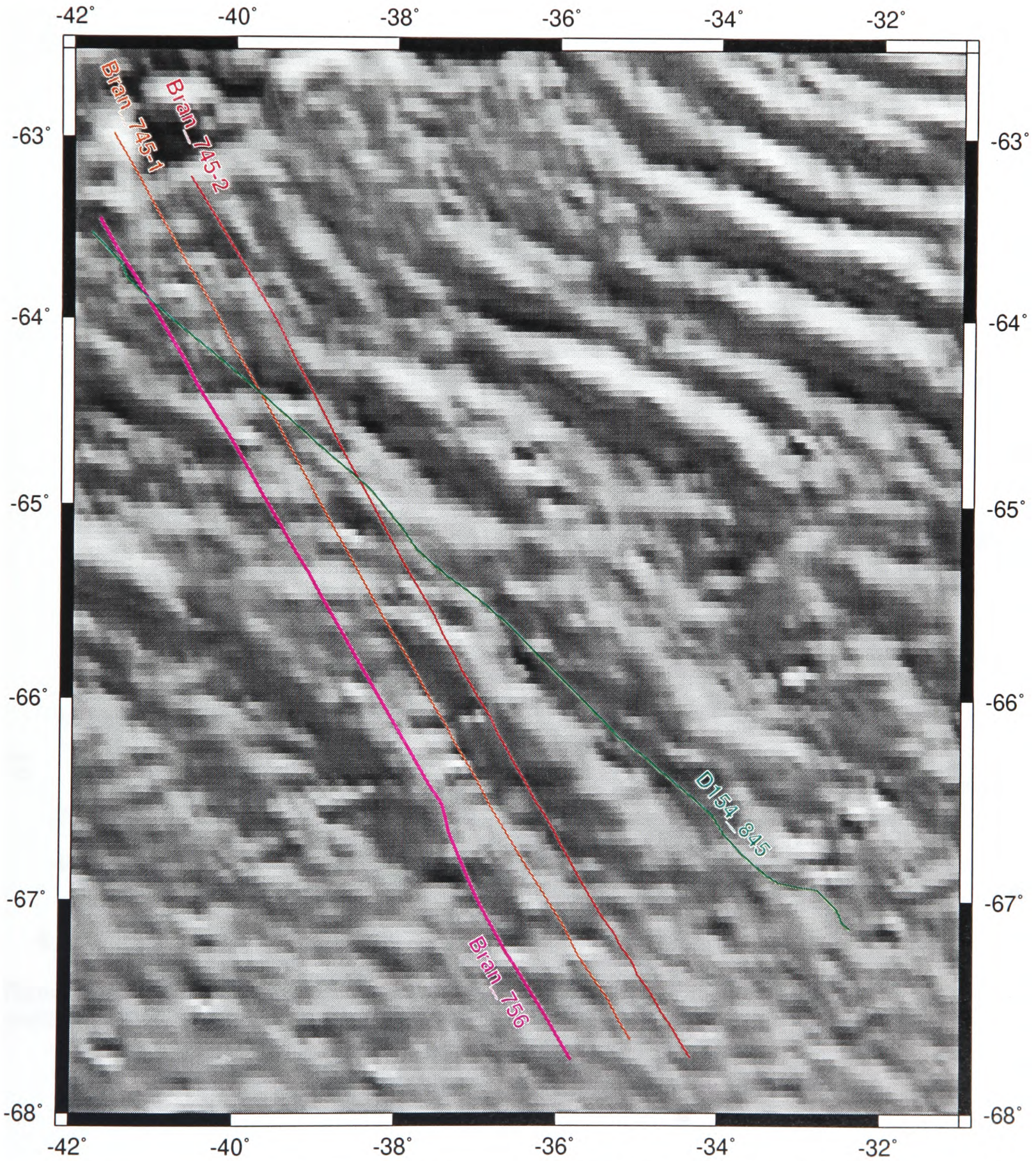

Figure 3.28: Maps showing the ship tracks from which the profiles displayed in Figure 3.29 were obtained.

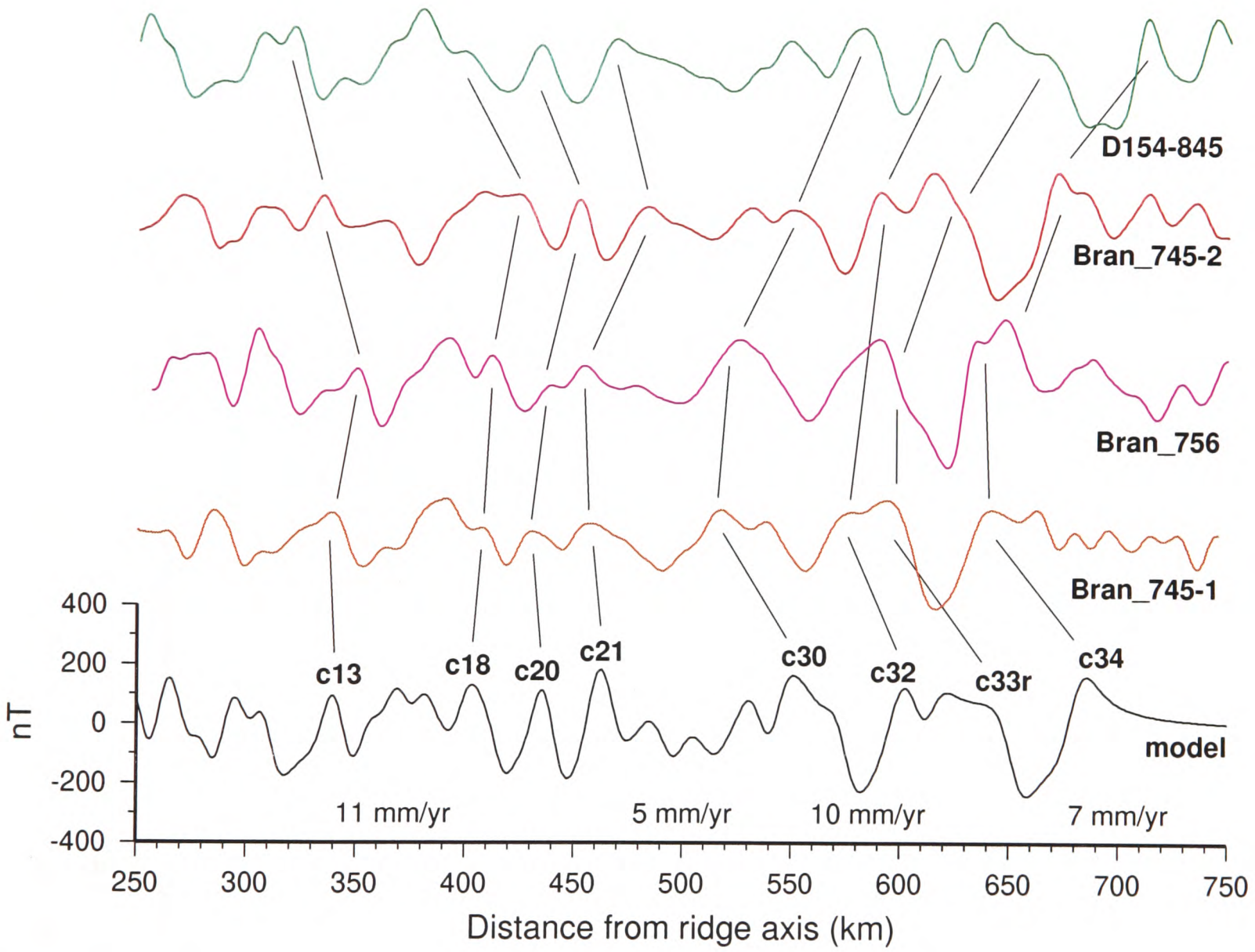

Figure 3.29: Along-track magnetic profiles from a series of cruises in the western Weddell Sea, with a synthetic profile shown for comparison, and selected anomalies identified on the profiles.

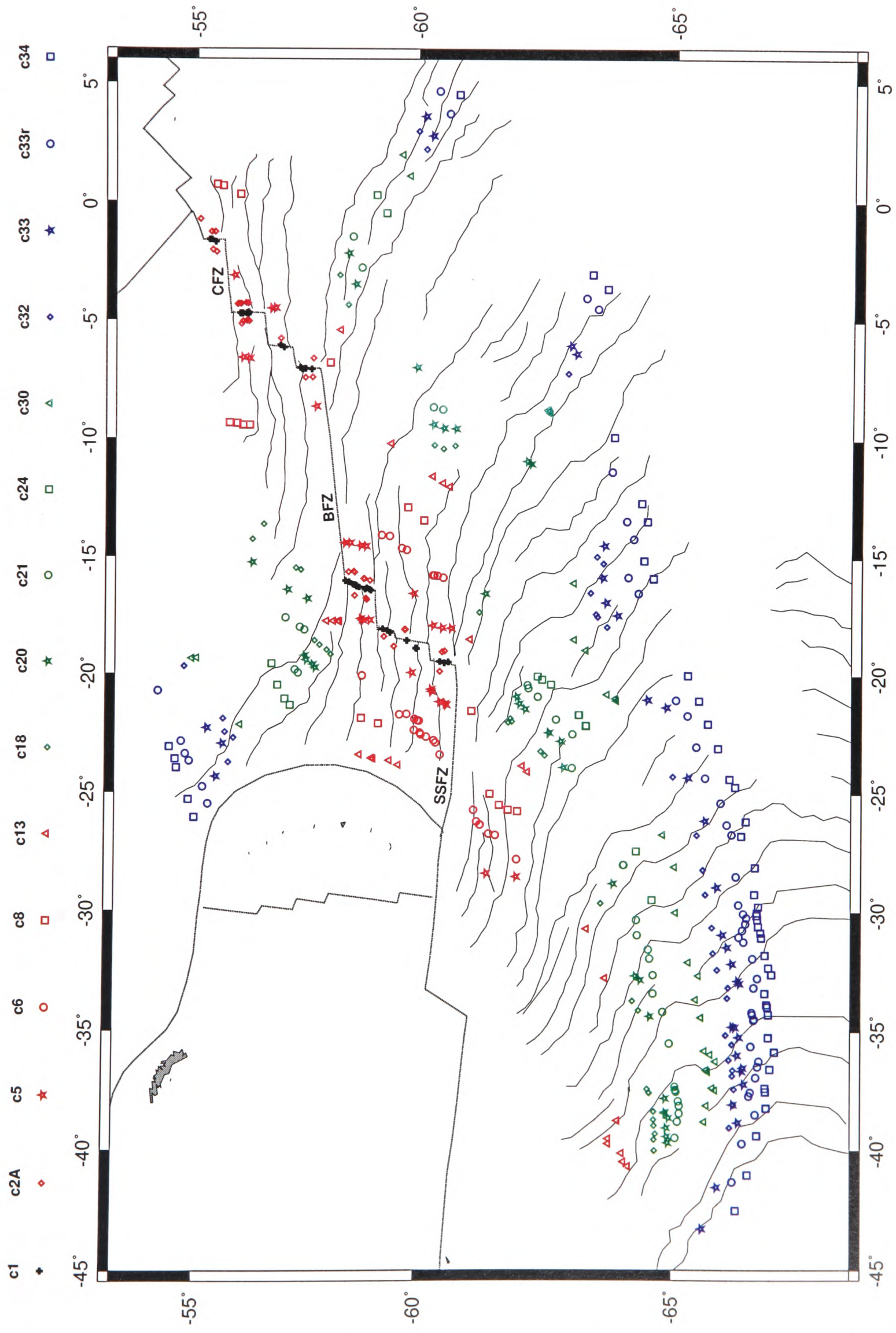

Figure 3.30: A map showing the complete set of magnetic anomaly identifications made for South American - Antarctic spreading. (Annotation abbreviations: CFZ - Conrad Fracture Zone; BFZ - Bullard Fracture Zone; SSFZ - South Sandwich Fracture Zone.)

Chapter 4

An inversion method for 2 and 3-plate reconstructions

4.1 Basics of spherical geometry and rotations on a sphere

4.1.1 Notation

Throughout, a 3-vector is denoted by a bold lower case character, or by three components enclosed by square brackets, such as

$$\mathbf{x} = \begin{bmatrix} x_1 \\ x_2 \\ x_3 \end{bmatrix} \tag{4.1}$$

A 3x3 matrix is denoted by a bold upper case character such as **A**, or by the nine elements arranged in 3 rows within square brackets, such as

$$\mathbf{A} = \begin{bmatrix} A_{11} & A_{12} & A_{13} \\ A_{21} & A_{22} & A_{23} \\ A_{31} & A_{32} & A_{33} \end{bmatrix} \tag{4.2}$$

Within some equations, particularly those involving partial derivatives, it may not be clear that a quantity is a vector or a matrix rather than a scalar, so that in such cases the quantity is enclosed in square brackets for clarity.

In operations involving vectors and matrices, it is sometimes necessary to break the matrices

and vectors down into their component elements. In such cases, summation notation is used such that when one of the indices (i, j, k) appears twice, then this indicates that the term should be summed for that index. For example, consider premultiplying the vector $\mathbf{x}$ by the matrix $\mathbf{A}$ to produce the vector $\mathbf{y}$, such that

$$\mathbf{y} = \mathbf{A}\mathbf{x} \tag{4.3}$$

This can instead be expressed in terms of elements, so that

$$\begin{aligned} y_i &= A_{ik}x_k \\ &= \sum_k A_{ik}x_k \end{aligned} \tag{4.4}$$

giving

$$y_1 = A_{11}x_1 + A_{12}x_2 + A_{13}x_3$$

$$y_2 = \ldots$$

4.1.2 Coordinate systems

The first problem to be confronted when dealing with calculations on a sphere is which coordinate system to use. To represent a point on a sphere, two systems are used, Cartesian coordinate, and geographical representations. In the first system, the point P is represented by a 3-vector, $\mathbf{p}$, where $|\mathbf{p}| = 1$, such that the sphere has unit radius. The second, geographical system is the standard latitude-longitude representation (θ, ϕ).

Conversion from one to another is relatively straightforward, with

$$\mathbf{p} = \begin{bmatrix} p_1 \\ p_2 \\ p_3 \end{bmatrix} = \begin{bmatrix} \cos(\theta)\cos(\phi) \\ \cos(\theta)\sin(\phi) \\ \sin(\theta) \end{bmatrix} \tag{4.5}$$

and

$$\theta = \sin^{-1}(p_3) \qquad \phi = \tan^{-1}(p_2/p_1) \tag{4.6}$$

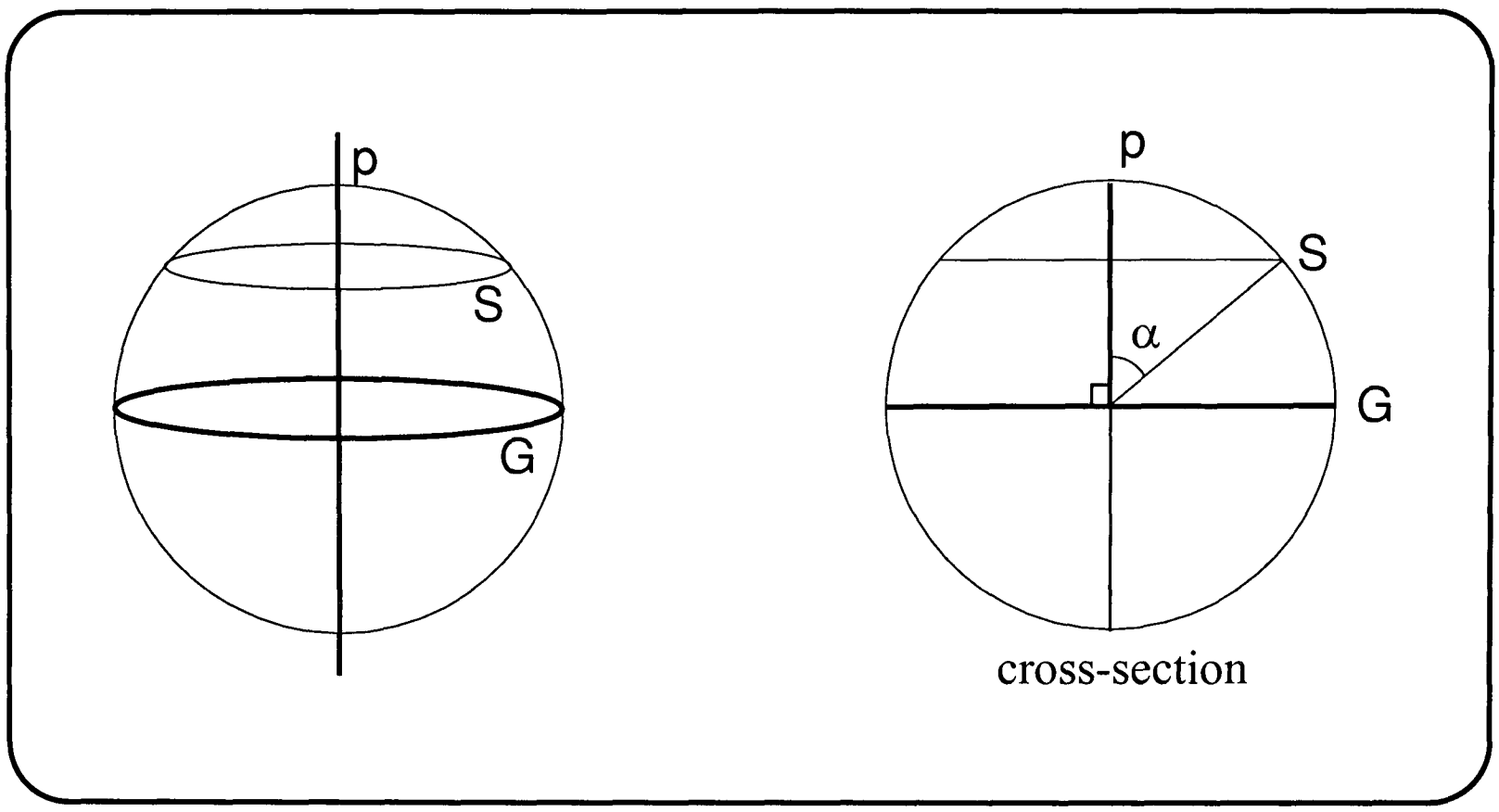

Figure 4.1: A diagram showing two small circles on a sphere, S and G, centred around the pole p, where S is defined by the angle α and G is a special case of a small circle, a great circle, where $\alpha = \pi/2$.

4.1.3 Circles on a sphere

Small circles are of great importance in the geometrics of plate tectonics. For any plane intersecting a sphere, the loci of points that represent the intersection of the plane and the surface of the sphere is a small circle. For every small circle there is an unique axis which passes through the centre of the sphere and the centre of the circle, such that a given point on the axis is equidistant from every point on the small circle. The pole of a small circle is defined as one of the points where the axis intersects the surface of the sphere. For example, lines of latitude on the globe are small circles, with the axis being the notional rotational axis of the earth, and the poles being the North and South poles. There are an infinite number of small circles for a given axis, but any can be specified uniquely by giving one of the poles of the axis, and the colatitude ($\pi/2$ - latitude) of any point on the small circle from that pole. This is displayed graphically in Figure 4.1, where S and G are small circles on the sphere and **p** the pole for both. On the cross-section, it is shown that any vector representation of a point on the small circle S makes an angle α with the pole **p**, where the centre of the sphere is taken as the origin.

The circle G is a special case of a small circle, a great circle, where the centre of the sphere is in the plane of the circle, so that the vector of any point on the circle is perpendicular to the

pole. An example of a great circle is the equator on the globe. A great circle is special in that the shortest distance between two points on a sphere is along the arc of the unique great circle joining the two points.

4.1.4 Vector products

Both the the dot (scalar) and cross (vector) product of two vectors have applications in spherical geometry.

The dot product of two vectors, **a** and **b**, is defined as

$$\begin{aligned} \mathbf{a}.\mathbf{b} &= a_i b_i \\ &= |\mathbf{a}||\mathbf{b}| \cos(\theta) \end{aligned} \tag{4.7}$$

where θ is the angle between the two vectors.

Thus, where both **a** and **b** are unit vectors, the dot product directly yields the angular separation of the two vectors, which can easily be converted into the great circle distance between the two points, which is very useful in this context. So, for two vectors **a** and **b** representing points on a unit sphere, the angular separation θ between the two points is given by

$$\theta = \cos^{-1}(\mathbf{a}.\mathbf{b}) \tag{4.8}$$

The cross product of two vectors, **a** and **b**, is defined as

$$\mathbf{c} = \mathbf{a} \wedge \mathbf{b} \tag{4.9}$$

where

$$\mathbf{c} = \begin{bmatrix} a_2 b_3 - a_3 b_2 \\ a_3 b_1 - a_1 b_3 \\ a_1 b_2 - a_2 b_1 \end{bmatrix} \tag{4.10}$$

and the magnitude of $\mathbf{c}$ is given by

$$|\mathbf{c}| = |\mathbf{a}||\mathbf{b}|\sin(\theta) \tag{4.11}$$

The vector $\mathbf{c}$ produced by the cross product of $\mathbf{a}$ and $\mathbf{b}$ is of particular interest in spherical geometry, as it is a vector which has a direction perpendicular to both $\mathbf{a}$ and $\mathbf{b}$, and is such that $\mathbf{a}$, $\mathbf{b}$ and $\mathbf{c}$ form a right handed set, akin to the x, y, z Cartesian axis system. If the vector $\mathbf{c}$ is then normalised such that $|\mathbf{c}| = 1$, representing a point on the unit sphere, then it follows that $\mathbf{c}$ is a pole for the unique great circle joining the two points $\mathbf{a}$ and $\mathbf{b}$.

4.1.5 Rotations on a sphere

There are many different ways to define a rotation on a sphere, but the convention best suited to this inversion method is the use of Euler poles. A rotation is represented by a point on the unit sphere, and an angle of rotation around an axis joining the centre of the sphere and this point. The point on the sphere can either be represented as a 3-vector, or as a geographical location. The latter is certainly easier for visualisation and has the advantage of the latitude and the longitude being independent variables, whereas only 2 of the 3 components of the 3-vector are independent. Thus the latitude-longitude method of representation is used for display and in the results, though it is more practical to use the vector representation in most of the calculations.

During calculations, the rotation is best expressed as a 3x3 matrix that operates on a 3-vector. A rotation of α degrees around a rotation axis $\mathbf{p}$, where rotations are positive in a right-handed sense and $\mathbf{p}$ is determined from θ and ϕ according to (4.5), is given by

$$\mathbf{R} = \begin{bmatrix} p_1p_1(1-\cos(\alpha)) + \cos(\alpha) & p_1p_2(1-\cos(\alpha)) - p_3\sin(\alpha) & p_1p_3(1-\cos(\alpha)) + p_2\sin(\alpha) \\ p_2p_1(1-\cos(\alpha)) + p_3\sin(\alpha) & p_2p_2(1-\cos(\alpha)) + \cos(\alpha) & p_2p_3(1-\cos(\alpha)) - p_1\sin(\alpha) \\ p_3p_1(1-\cos(\alpha)) - p_2\sin(\alpha) & p_3p_2(1-\cos(\alpha)) + p_1\sin(\alpha) & p_3p_3(1-\cos(\alpha)) + \cos(\alpha) \end{bmatrix} \tag{4.12}$$

This can be derived from the three elementary rotation matrices $\mathbf{A}$, $\mathbf{B}$ and $\mathbf{E}$, representing rotations for θ ,ϕ, and α respectively, such that $\mathbf{R} = (\mathbf{BA})^{\mathsf{T}}\mathbf{E}(\mathbf{BA})$ (Shaw, 1987). So, if we wish to rotate a point represented by the 3-vector $\mathbf{x}$ by the rotation defined by (θ, ϕ, α) or $(\mathbf{p}, \alpha)$, the

resultant point $\mathbf{y}$ is given by

$$\mathbf{y} = \mathbf{R}\mathbf{x} \tag{4.13}$$

It is important to note that during such a rotation, all points move in small circles around the rotation axis.

Using the matrix representation of a rotation, it becomes very easy to sum two rotations. If a point $\mathbf{x}$ is rotated by a rotation $\mathbf{A}$ to point $\mathbf{y}$, which is subsequently rotated by the rotation $\mathbf{B}$ to point $\mathbf{z}$, then

$$\begin{aligned} \mathbf{z} &= \mathbf{B}\mathbf{y} \\ &= \mathbf{B}(\mathbf{A}\mathbf{x}) \\ &= (\mathbf{B}\mathbf{A})\mathbf{x} \\ &= \mathbf{S}\mathbf{x} \end{aligned} \tag{4.14}$$

such that a single rotation $\mathbf{S}$ can be found that rotates $\mathbf{x}$ to $\mathbf{z}$, where the rotation matrix $\mathbf{S}$ is given by

$$\mathbf{S} = \mathbf{B}\mathbf{A} \tag{4.15}$$

Given a rotation matrix $\mathbf{R}$, then the rotation parameters (θ, ϕ, α) can be determined from the following equations

$$\theta = \sin^{-1}\left(\frac{w}{z}\right) \qquad \phi = \tan^{-1}\left(\frac{v}{u}\right) \qquad \alpha = \tan^{-1}\left(\frac{z}{s}\right) \tag{4.16}$$

and the pole in the vector form by

$$\mathbf{p} = \begin{bmatrix} \frac{u}{z} \\ \frac{v}{z} \\ \frac{w}{z} \end{bmatrix} \tag{4.17}$$

where

$$u = R_{32} - R_{23} \tag{4.18a}$$

$$v = R_{13} - R_{31} \tag{4.18b}$$

$$w = R_{21} - R_{12} \tag{4.18c}$$

$$s = R_{11} + R_{22} + R_{33} - 1 \tag{4.18d}$$

$$z = \sqrt{u^2 + v^2 + w^2} \tag{4.18e}$$

4.1.6 Exponential parametrisation

Though this method of defining rotations is not used here, it is used in several of the papers discussed, and so I have included a brief description of this form of parametrisation.

A rotation on a sphere is defined by a vector $\mathbf{t}$ representing a right-handed rotation of $\rho = |\mathbf{t}|$ radians around a pole $\mathbf{t}/|\mathbf{t}|$. A matrix $\mathbf{T}$ is defined such that

$$\mathbf{T} = \begin{bmatrix} 0 & -t_3 & t_2 \\ t_3 & 0 & -t_1 \\ -t_2 & t_1 & 0 \end{bmatrix} \tag{4.19}$$

The rotation matrix $\Phi(\mathbf{t})$ $(= \mathbf{R})$ is then given by

$$\Phi(\mathbf{t}) = -\sum_{r=0}^{\infty} \frac{\mathbf{T}^r}{r!} \tag{4.20}$$

which can be reduced to

$$\Phi(\mathbf{t}) = \mathbf{I} + \frac{\sin\rho}{\rho}\mathbf{T} + \frac{1 - \cos\rho}{\rho}\mathbf{T}^2 \tag{4.21}$$

where $\mathbf{I}$ is the 3x3 identity matrix.

4.1.7 Instantaneous, finite and stage poles

There are three different types of rotation poles that are used to describe the motions of tectonic plates. These are shown graphically in Figure 4.2 and described below.

The first type, instantaneous motion poles, detail the actual relative motion between two plates at a given point in time, usually the present ($\mathbf{I}^0$). The motion is described by giving the rotation pole and an angular rate of relative motion around that pole. Points on the mid-ocean ridge at that particular time will be moving in small circles of the instantaneous pole, away from the ridge.

Finite rotation poles do not actually explicitly describe motion, but are used to reconstruct the relative positions of two plates at a given time in the past. Thus a finite rotation such as $\mathbf{F}^{40}$, given as the latitude and longitude of the rotation pole, and an angle of rotation about that pole, will realign the anomaly isochrons created at that time in the past (40Ma), along the line of the ridge axis as it was at that time. So a finite rotation such as $\mathbf{F}^{40}$ shown in Figure 4.2 will rotate the isochron pattern at 0Ma back to give that which was present at 40Ma, removing all the seafloor created during that period. Where a plate is being rotated back using a finite rotation, the paths followed by points on that plate do not represent flowlines of plate motion during that period, except for the case where the rotation pole has remained constant. Finite rotations describe total relative motion as opposed to actual relative motion.

A stage pole is used to describe the motion of a point on a given plate during a certain period of time, and thus gives approximate flowlines for plate motion during that period. As two plates move away from each other, points on each plate move in small circles around the current pole of motion (the current instantaneous pole). If this pole remains relatively constant for a significant period, then the relative motion during this time can be successfully described by a single stage pole. If the end of the period is the present day, *i.e.* 20Ma to 0Ma, then the stage pole for each plate is the same as the finite rotation rotation pole, but with half the rotation angle (it describes only the motion for one of the plates). If it is a period in the past, between 40Ma and 20Ma say, then the two stage poles for the two plates, ${}^{40}\mathbf{S}^{20}$ and ${}^{20}\mathbf{S}^{40}$, are no longer at the same location, they are separated by the relative rotation between the two plates during this time ($\mathbf{F}^{20}$). Stage poles can determined directly, or be easily obtained from the finite rotation poles for the beginning and end of the period in question. A flowline of plate motion on a given plate

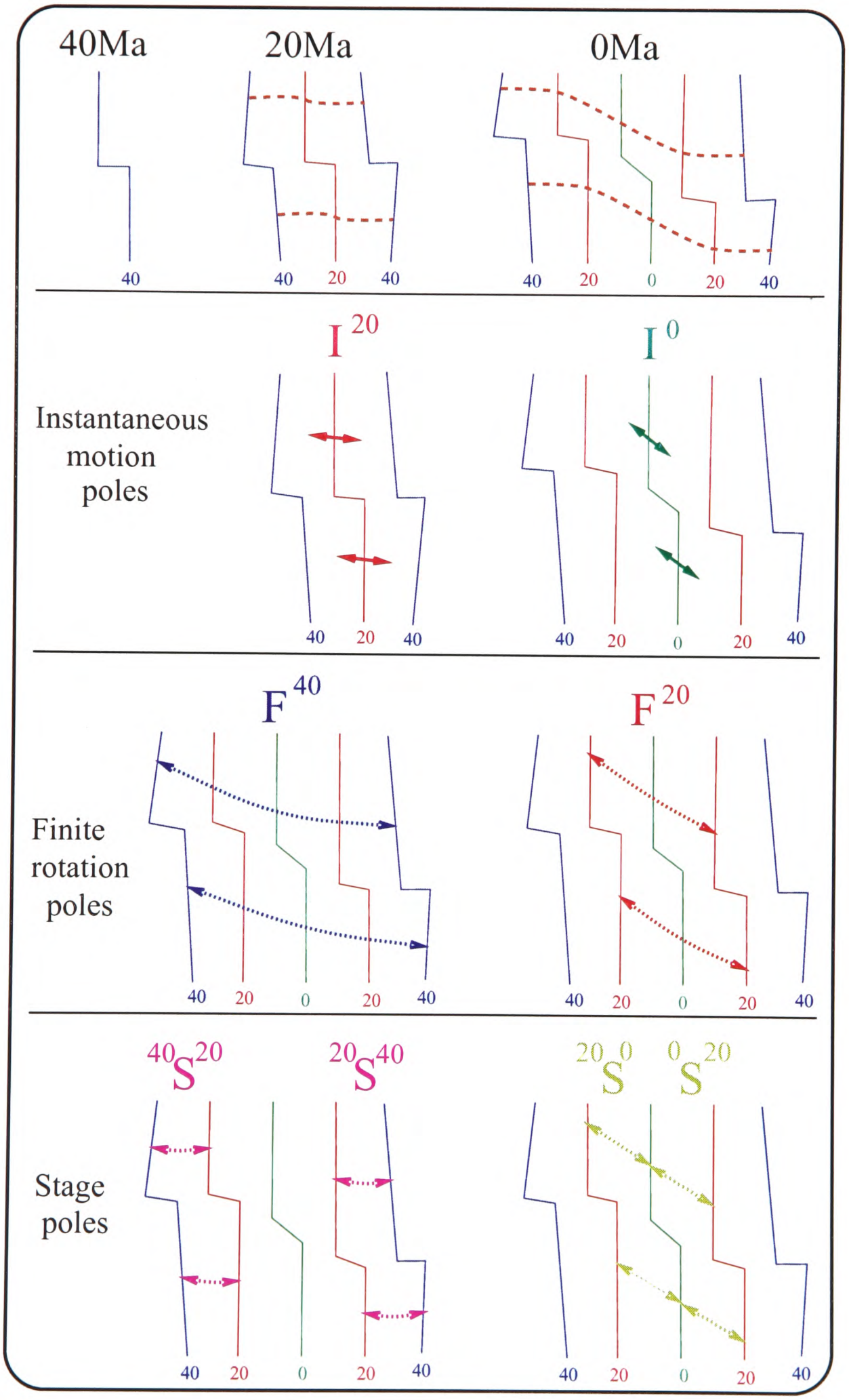

Figure 4.2: Cartoons illustrating the basic definitions and uses of instantaneous, finite and stage poles.

can thus in theory be described by a series of stage poles for several discrete periods of time, the points on the plate moving in small circles of the corresponding stage pole during each spreading 'epoch'.

4.2 Overview of inversion methods

Reconstructions to determine finite rotation poles almost invariably use one of three methods: visual fitting; minimisation grid search; or iterative inversion. A visual method involves displaying synthetic flowlines and model isochrons predicted by a set of rotations alongside the observed data. Manual adjustments are then made to the poles to improve the fit visually until a satisfactory match has been achieved. An example of such a method is that used by Nürnberg & Müller (1991) in their determination of finite rotation poles for the South Atlantic.

The grid search methods involve taking a starting set of poles and through some definition of misfit for the observed data, a test criterion is determined which inversely reflects the goodness of fit of the model, usually in the form of a sum of squared errors. The area of parameter space around the test poles is then searched for an alternative set of parameters which minimise the test criteria of the search. The search is then repeated in the region of the best-fit parameter set, typically with a reduced grid spacing each time, until a solution within the desired tolerance is obtained.

Iterative inversion techniques also define misfit criteria to determine how a set of test poles fit the data, but in addition, a set of partial derivatives is determined which defines how changes to the parameter set will affect the errors. The problem is then usually approximated to a linear least-squares inversion, the solution of which provides an adjustment to the model which has been calculated to improve the fit to the data. After a series of improvements, the model parameters should converge to a stable solution.

The defining characteristics of a reconstruction method are the type of data used, the misfit definitions for which the model is minimised, and the method of minimisation. The first major quantative reconstruction was carried out by Bullard *et al.* (1965), using a fit of the continental margins to determine a finite rotation for the opening of the Atlantic. The role of finite rotation poles was recognised as an integral part of plate tectonic theory in providing a mechanism for the quantitative description of relative motions of continents in the past.

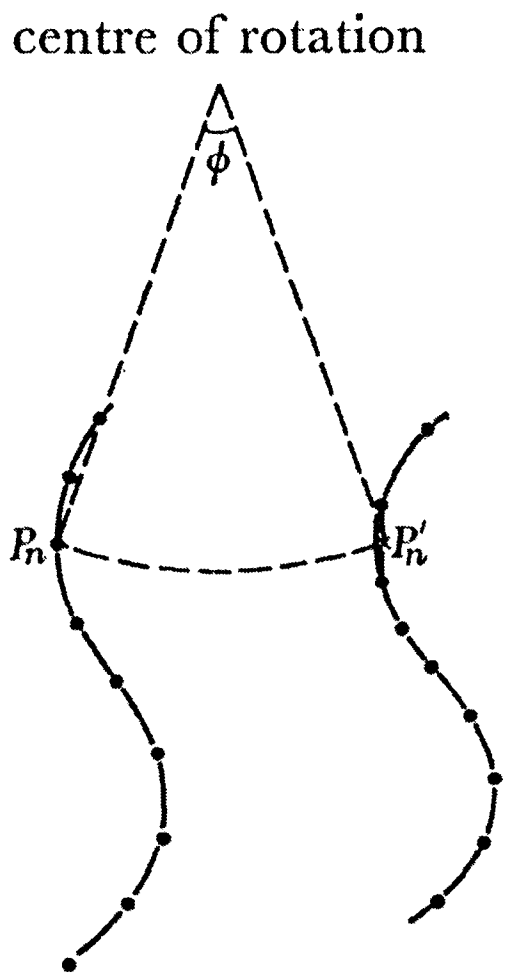

Figure 4.3: A diagram showing the fitting method of Bullard *et al.* (1965), matching the contours of the opposing continents. A point P_n on one side is fitted to a conjugate point P'_n on the same small circle (of the centre of rotation) as P_n. (From Bullard *et al.* (1965)).

Reconstruction methods were extended by various groups which realised that magnetic isochrons on opposing plates could be fitted in the same way as the continental margins in order to determine the spreading history over given intervals of time. The majority of past inversion methods have concentrated on magnetic isochrons as the main source of data, fitting conjugate sets of isochrons from opposite sides of a mid-ocean ridge to determine a finite rotation pole for that particular isochron age.

Reconstructions for finite rotations are based on the premise that although the motion of the plates is a smooth, continuous progression, it can be adequately modelled by a set of rotations determined for discrete reference times (chrons) in the past. The kinematic history is thus divided into a series of spreading periods, during each of which, the motion on a plate is governed by a single instantaneous stage pole, with the motion occurring at a fixed angular rate in small circles around that stage pole. What follows is a general review of some of the main methods for reconstructions that have been developed in the past 30 years, concentrating on the studies that have introduced new techniques or applications.

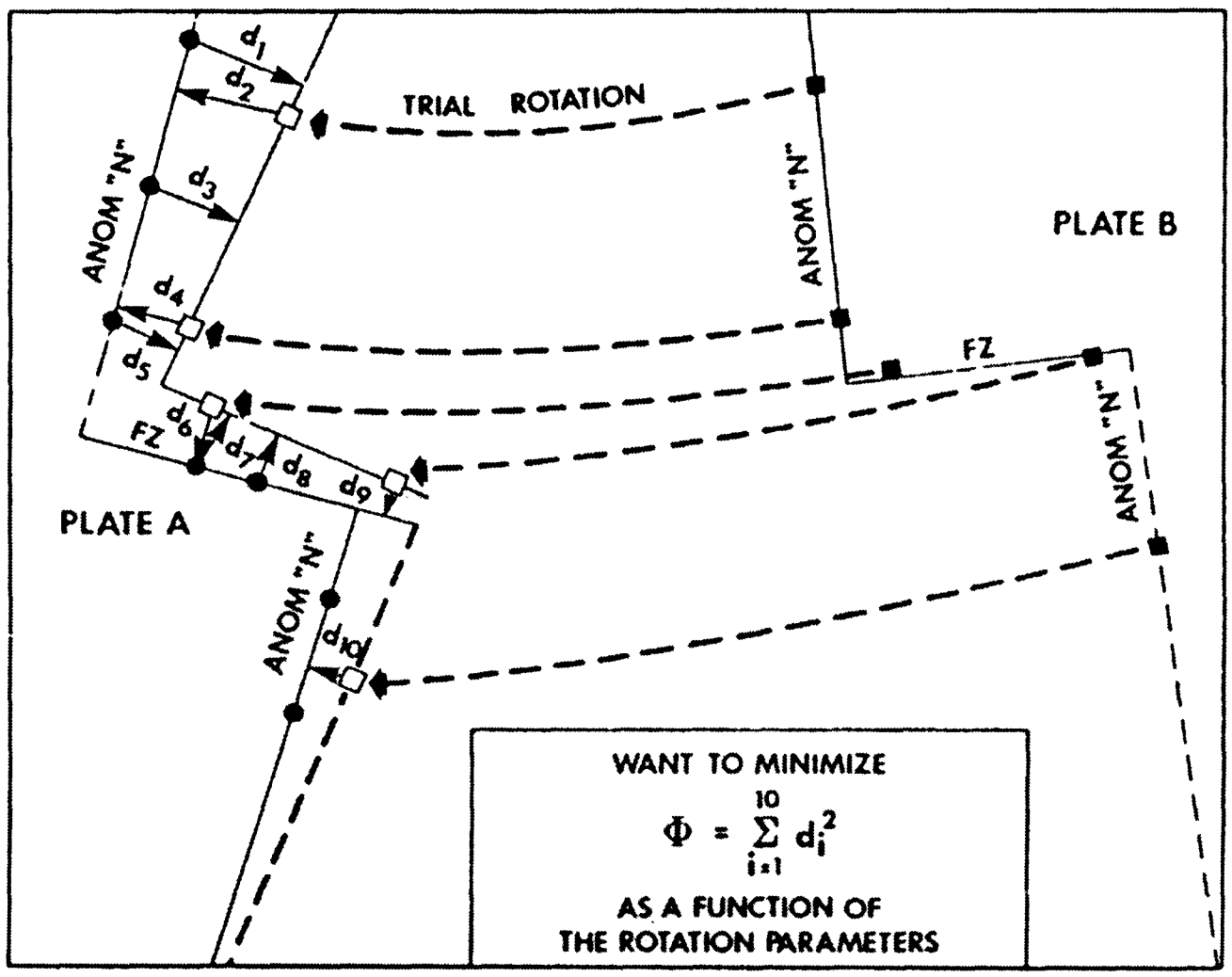

Figure 4.4: Showing the boundary fitting method introduced by Pilger (1978). Points along the continuously defined boundary of anomaly are rotated to the opposing plate and fitted to a great circle joining the two nearest points on the corresponding section of the conjugate boundary (From Pilger (1978)).

In the reconstructions of Bullard *et al.* (1965), contours of the continental shelf from opposite sides of the ocean were fitted to each other. According to Figure 4.3, for a point P_n of the contour on one side, a conjugate point P'_n was found that lay on the same small circle of the rotation ϕ (if necessary, interpolation between neighbouring points was carried out). The misfit was then defined as the distance along the small circle between the target point P_n, and the the location of the conjugate point P'_n after a rotation ϕ. This was repeated for each point on both contours, and a grid search procedure carried out to determine the rotation that minimised the mean square misfit. McKenzie & Sclater (1971) were amongst the first to fit anomaly isochrons in a similar fashion to continental boundaries. Finite rotations were used to rotate a set of picks for an anomaly isochron to the conjugate isochron on the opposing plate and the misfit area between the two sets of isochrons was minimised using a search technique in order to determine the best-fit poles.

Morgan (1968) and Le Pichon *et al.* (1973) amongst others used the strike of segments of fracture zones at several points along their length to determine poles of rotation for these intervals,

but these methods yielded only the pole locations, and not the rotation angles. Pilger (1978) was the first major study to include fracture zone locations alongside magnetic isochron data in a reconstruction method, and also to use an iterative procedure to determine finite rotations. Where a magnetic anomaly isochron on a plate was interrupted by a fracture zone, fracture zone locations on the section between the two offset isochron segments were included in this dataset as a continuation of the boundary for that anomaly. A trial rotation was then used to rotate the whole dataset for one of the plates onto the opposing plate as can be seen in Figure 4.4. The misfit for each point was defined as the distance between the rotated point and the great circle defined by the two closest points on the opposing segment. The isochron picks were fitted to the opposing isochron segment and the fracture zone data to the opposing fracture zone segment, with no interaction between the two data types, but the same misfit definition was applied to both sets. The partial derivatives of these misfits were then calculated with respect to the rotation parameters, and then a non-linear least-squares iterative method used to obtain solution poles which minimised the sum of squared misfits.

Hellinger (1981) retained the form of the dataset as a continuous boundary for each inversion chron, consisting of alternate linked sections of isochron lineations and fossil transforms, but altered the fitting criteria. After rotating one set of data to the opposite side of the ridge, a best fit great circle was then found for the combined set of rotated and unrotated points for each sub-section of the boundary. For each point, the misfit was defined as the distance of a point from its associated great circle, divided by the standard deviation of estimated error for that point. The overall fit was then defined as the sum of these squared misfits, and the best solution was found by a grid search technique. The method of deriving a single great circle fitted to the set of rotated and unrotated points, which is then used in the determination of misfits for the data, is known as two-set (two-plate) fitting (Figure 4.5). The drawback of this is that it is not suited to iterative inversions, since the fitted great circle is dependent on the rotated points and hence the rotation poles, which then makes the calculation of mathematically rigorous partial derivatives impossible, so that the problem must be solved using a grid search technique. In addition, the method fits great circles to each section of data, and whilst this is a valid assumption for anomaly isochrons, this is not true for fracture zones, though this should not have too great an effect for small offsets.

Engebretson *et al.* (1984) was the first study to consider plate boundaries where data only

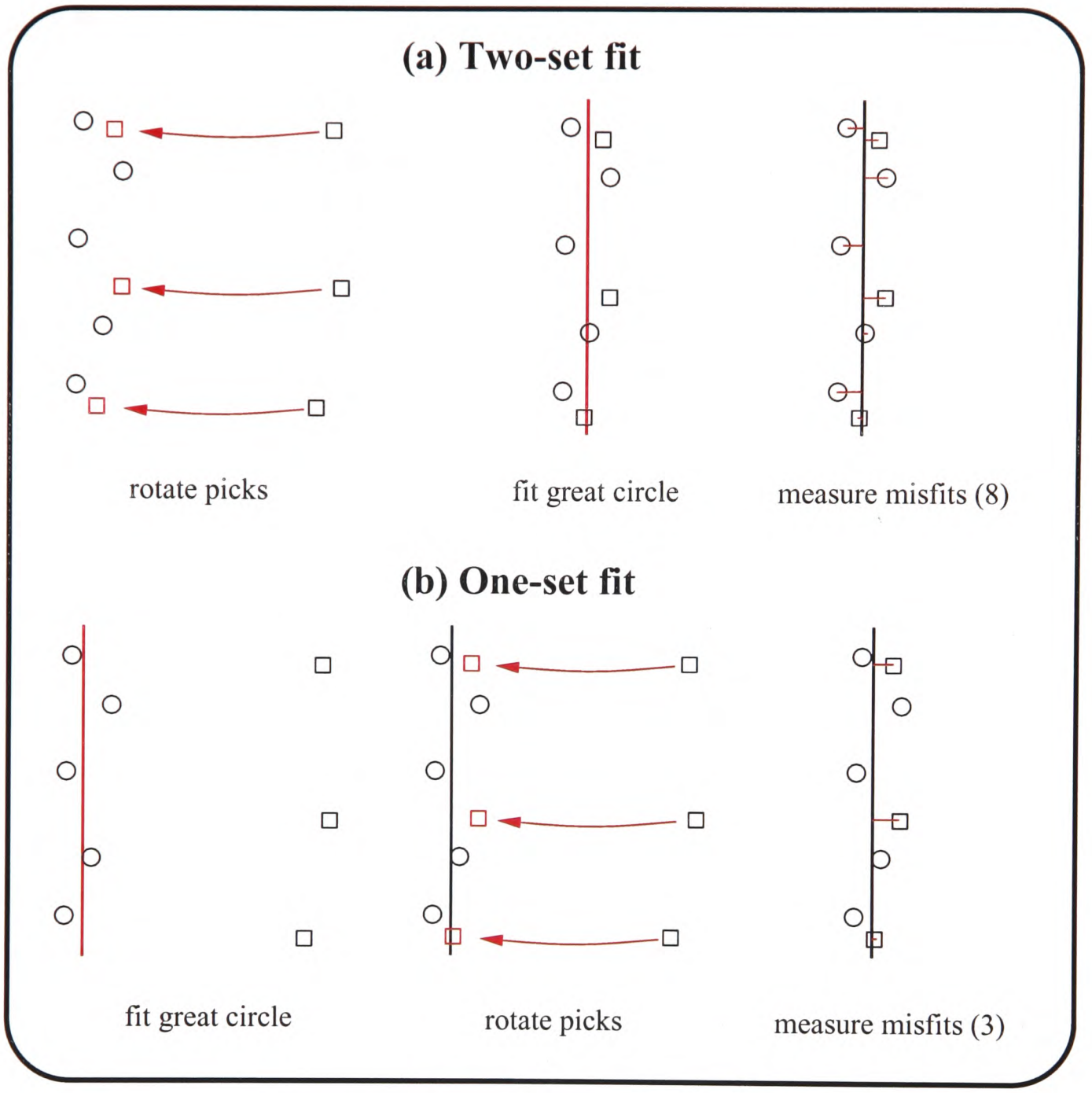

Figure 4.5: A diagram showing the difference between two-set and one-set fitting of reconstruction data (After Wilson (1993)).

---

existed for one plate of the pair, in this case for the Pacific plate and adjoining plates which have been mostly subducted at the subduction zones encircling the Pacific. In order to cope with this one-sided problem, a new inversion technique was developed. Magnetic isochron picks for a particular ridge section were projected onto the adjoining fracture zone, so that the dataset for each section was a series of locations for isochron-fracture zone intersections. Each pick was then rotated by the appropriate stage pole to every other pick along the fracture zone in turn. The misfit was then defined as the angular distance between this rotated intersection and the target intersection, as shown in Figure 4.6. Weighting was applied to ensure that the contribution from each fracture zone to the final calculation was proportional to the number of data points along that fracture zone, rather than the square of the number of intersections. The sum of the

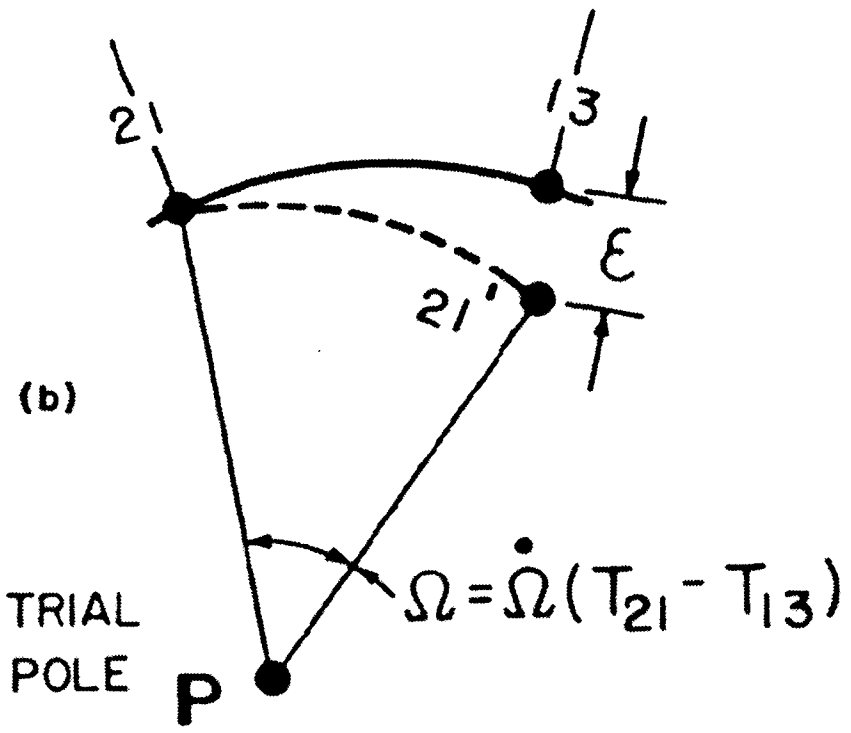

Figure 4.6: Showing the fitting method used by Engebretson *et al.* (1984) in their inversion. The intersection of the anomaly 21 isochron with the neighbouring fracture zone is rotated by a trial (anomaly 21 to anomaly 13) stage pole, and the misfit defined as the distance to the anomaly 13-fracture zone intersection. (Figure 2(b) from Engebretson *et al.* (1984)).

squares of these weighted errors was then minimised to determine the best-fit pole by way of a grid search technique. For each trial stage pole within a coarse grid, the angular rate, $\dot{\Omega}$, was first determined by minimising the fit criteria with respect to the angle, and then the pole with the overall minimum was found. The grid search was repeated with reduced grid spacing until a best-fit pole was determined within a tolerance of 0.5°. Although this method took advantage of the complementary nature of isochron and fracture zone data, and it was the first to make use of fracture zones as flowlines of plate motion, the use of fracture zone data was minimal. Fracture zone locations were truly only useful in the region of the isochron intersections, and potentially important information was likely to have been ignored.

Nishimura *et al.* (1984) used the fitting procedure of Pilger (1978), but with a slightly different misfit definition which lead to a linear least-squares problem, and carried out iterative inversions. Instead of fitting fracture zone trends, they, like Engebretson *et al.* (1984), decided to limit themselves to using the isochron-fracture zone intersections, such that the use of the fracture zone data was limited to matching pairs of points on opposing plates. However, this did allow the use of data from 'pseudofaults', traces in the seafloor where a ridge had propagated, seen as diagonal offsets in isochron patterns. Although these pseudofaults do not represent flowlines, being generated from motion which was not ridge-perpendicular, the patterns are symmetric and the pseudofault-isochron intersections can be matched to the corresponding intersection on the

opposite plate.

With the advent of satellite altimetry, a wealth of data became available for locating fracture zones. Whereas previous studies had been limited to picking fracture locations from ship tracks crossing the feature, altimeter profiles could now be used to provide a much more extensive set of fracture zone traces. Shaw (1987) was the first to use continuous fracture zone traces, picked from Seasat profiles, to determine a set of finite rotation poles for the South Atlantic. With the exception of Engebretson *et al.* (1984), all former studies had involved fitting fracture zone trends for the short sections of fracture zones offsetting isochrons. Shaw (1987) realised that due to the finite separation of the ridge-transform intersections, which are generally considered to be the zero-age point of a fracture zone, conjugate sections of a fracture zone were unlikely to match precisely. If the transform faults were short, then this effect would be minimal but nevertheless, an inherent source of error. In the method of Shaw (1987), fracture zone locations were fitted to synthetic flowlines generated from the ridge-transform intersections, with the misfit for each datum being defined as the great circle distance from the closest point on the flowline. An iterative procedure utilising partial derivatives was then used to determine a set of solution poles. By fitting fracture zone locations to a continuous flowline with the picks being fitted to a series of small circles (generated by the set of successive stage poles determined from the finite rotation poles), the method provided important constraints on the continuity of the plate motion. With the exception of the method of Engebretson *et al.* (1984), previous methods had lead to completely independent reconstructions for each isochron age. However, whilst realising the importance of the inclusion of magnetic anomaly data for reconstructions, Shaw (1987) utilised isochron information only indirectly, in the form of a set of starting poles provided by Cande *et al.* (1988) to determine an initial framework and timescale for the flowlines.

Cande *et al.* (1988) also used Seasat altimeter data to provide a comprehensive set of fracture zone locations, in addition to a substantial magnetic isochron dataset. However, in their study, they retained the method of aligning conjugate sets of anomaly isochrons and fracture zone trends, and determined finite rotation poles though visually searching for the 'best-looking' match of data.

The inversion method introduced by Shaw & Cande (1990) combined magnetic isochron picks and fracture zone locations in a single study that processed the two datasets independently, then integrated the two into a single linear inversion. Fracture locations were fitted using the methods and misfit definition of Shaw (1987). The fitting of the magnetic isochrons was carried out by

initially calculating a best-fit great circle for one of the isochron sets in each conjugate pair, and then rotating across the opposing set of picks and applying a misfit criterion similar to that defined by Hellinger (1981). This method of fitting a great circle to a single isochron set, before rotating the conjugate set across for fitting, is known as one-set (one-plate) fitting (Figure 4.5), as opposed to the two-set procedure of Hellinger (1981). By using this form of fitting, it was possible to calculate partial derivatives for the isochron pick misfits, and through combining the misfits and partial derivatives of both datasets in a single linear least-squares inversion, Shaw & Cande (1990) were able to determine a well-constrained set of finite rotation poles. The theory and misfit definitions of Shaw & Cande (1990) provided a basis for the two-plate inversion procedure used in this study.

Reconstructions for multiple plates have generally been limited to instantaneous plate motion inversions (Minster & Jordan, 1978; DeMets *et al.*, 1990), calculated for global plate circuits. When considering such reconstructions, the problem of closure within the system must be addressed. If rigid plates are assumed, then if the motion of plate B relative to plate A is known, and the motion of plate C relative to plate B also known, then the motion of plate C relative to A follows automatically from the summing the two relative motions, because of the need for closure within the 3-plate system. Thus the motions of the three plates relative to one another are not independent. Tapscott (1979) extended the fitting criteria of Hellinger (1981) to a three plate system, using variable poles for the first two independent plate pairs A$\mapsto$B and B$\mapsto$C, and using them to calculate the third, dependent, set of poles A$\mapsto$C. The set of misfits for each plate pair was calculated, and the total sum of squared misfits for all plates minimised by searching the parameter space of rotations A$\mapsto$B and B$\mapsto$C to determine a solution that simultaneously fitted the data on all three plates. As for all methods using misfit criteria based on that of Hellinger (1981), the sets of finite rotation poles determined (from the inversions carried out for each discrete chron) were entirely independent of one another.

The challenge was to produce a method for carrying out three-plate reconstructions that would fully utilise the complementary nature of fracture zone locations and magnetic anomaly isochrons to produce a continuous progression of finite rotation poles reflecting the motion and interactions of three plates over a substantial period of time.

4.3 Method for a 2-plate reconstruction

4.3.1 Inversion theory

As mentioned previously, iterative inversion methods are based on determining how well a model fits a dataset, then making a change to this model which has been calculated to improve the fit of the dataset. The process is then repeated to find out how well this improved model fits the dataset, and so on, until a satisfactory fit has been obtained. The first step is to define misfits that will give a quantitative measure of how well the model fits the dataset. In this case, different types of data are used, so a different misfit criterion is defined for each, which generates an error value (ε) for each datum, which are defined as displacements as opposed to distances, *i.e.* the error can be positive or negative. For example, the misfit for a fracture zone pick is defined as the perpendicular displacement of the pick from a synthetic flowline generated from the model parameters. If the pick lies above the flowline (Figure 4.11), then the error is positive, and negative if the pick is below the flowline. For magnetic anomaly picks, each pick is rotated towards a target great circle representing a different anomaly isochron (Figure 4.9), by a rotation determined from the model parameters which should in theory rotate the pick such that it lies exactly on the target great circle. The misfit is defined as the perpendicular displacement of this pick from the great circle; if the pick has been rotated beyond the great circle, the error is positive, and *vice versa.* The exact definitions of the misfits for each data type are given later.

In order to determine how the model can be improved, the partial derivatives of these errors with respect to the model are calculated. In other words, for each datum, the effect of altering the model parameters is calculated, for each individual model parameter in turn. A value is calculated which represents how the error for the datum in question would change if that particular pole parameter was altered $\left(\frac{\partial \varepsilon}{\partial p^{\gamma}}\right)$, *e.g.* if the rotation angle is increased for one of the rotation poles, does this result in an increase or decrease in the error? By determining a complete set of errors, and a corresponding set of partial derivatives describing how each error will increase or decrease with a change to each of the model parameters, a least-squares inversion procedure will be able to determine a combination of changes to the model parameters which will reduce the overall magnitude of the errors of the dataset from the model.

The aim of the inversion is to determine a set of l finite rotation poles, comprising of a latitude, longitude and rotation angle (θ, ϕ, α) for each pole, giving a total of $n = 3l$ pole parameters,

the set $\mathbf{p} = \{p_1, \ldots, p_j, \ldots, p_{3l}\}$. As input to the inversion, there are three sets of data: m^{fz} fracture zone location data points; m^{tf} transform fault azimuth data points; and m^{mag} magnetic isochron data points. Hypothetically there will be a perfect set of pole parameters $\mathbf{p}^*$, which will fit this combined dataset exactly. Then from the total set of $m(= m^{\text{fz}} + m^{\text{tf}} + m^{\text{mag}})$ data points, consider the ith data point, with error $\varepsilon_i(\mathbf{p})$ for the set of pole parameters $\mathbf{p}$, where for the perfect set of pole parameters

$$\varepsilon_i(\mathbf{p}^*) = 0 \tag{4.22}$$

For each data point, there exists a partial derivative relating the change in the error ε_i for a perturbation to the jth pole parameter, which is given as $\frac{\partial \varepsilon_i}{\partial p_j}$. If we assume that the set of poles parameters $\mathbf{p}$ is close to the perfect set, $\mathbf{p}^*$, then

$$\varepsilon_i(\mathbf{p}^*) - \varepsilon_i(\mathbf{p}) \approx \frac{\partial \varepsilon_i}{\partial p_j}(p_j^* - p_j) \tag{4.23}$$

then defining the difference between the pole parameters as

$$\Delta p_j = p_j^* - p_j \tag{4.24}$$

and applying equation (4.22) we obtain

$$\varepsilon_i(\mathbf{p}) \approx -\sum_j \Delta p_j \frac{\partial \varepsilon_i}{\partial p_j} \tag{4.25}$$

To combine the three datasets on an equal basis, then we need to normalise the data, which is done by dividing each datum by its corresponding uncertainty. The uncertainties of the magnetics, fracture zone and transform data are defined as σ^{mag}, σ^{fz} and σ^{tf} respectively.

A normalised matrix of partial derivatives is then constructed for each data type,

$$\hat{\mathbf{A}}_{ij}^{\text{mag}} = \frac{1}{\sigma^{\text{mag}}} \frac{\partial \varepsilon_i^{\text{mag}}}{\partial p_j} \qquad \hat{\mathbf{A}}_{ij}^{\text{fz}} = \frac{1}{\sigma^{\text{fz}}} \frac{\partial \varepsilon_i^{\text{fz}}}{\partial p_j} \qquad \hat{\mathbf{A}}_{ij}^{\text{tf}} = \frac{1}{\sigma^{\text{tf}}} \frac{\partial \varepsilon_i^{\text{tf}}}{\partial p_j} \tag{4.26}$$

Similarly vectors containing the normalised errors are constructed,

$$\hat{\mathbf{b}}_i^{\text{mag}} = -\frac{1}{\sigma^{\text{mag}}}\varepsilon_i^{\text{mag}} \qquad \hat{\mathbf{b}}_i^{\text{fz}} = -\frac{1}{\sigma^{\text{fz}}}\varepsilon_i^{\text{fz}} \qquad \hat{\mathbf{b}}_i^{\text{tf}} = -\frac{1}{\sigma^{\text{tf}}}\varepsilon_i^{\text{tf}} \tag{4.27}$$

Finally, the matrices/vectors for all three datasets are then combined into a single normalised matrix $\hat{\mathbf{A}}$ of dimensions m by n and a single vector $\hat{\mathbf{b}}$ of length m,

$$\hat{\mathbf{A}} = \begin{bmatrix} \hat{\mathbf{A}}^{\text{mag}} \\ \hat{\mathbf{A}}^{\text{fz}} \\ \hat{\mathbf{A}}^{\text{tf}} \end{bmatrix} \qquad \hat{\mathbf{b}} = \begin{bmatrix} \hat{\mathbf{b}}^{\text{mag}} \\ \hat{\mathbf{b}}^{\text{fz}} \\ \hat{\mathbf{b}}^{\text{tf}} \end{bmatrix} \tag{4.28}$$

Then from equation (4.25) we have the matrix equation

$$\hat{\mathbf{A}}\,\Delta\mathbf{p} = \hat{\mathbf{b}} \tag{4.29}$$

However, in the inversion process, additional weighting is considered necessary in order to ensure that poor quality data have a lesser influence on the inversion and so, before solving this equation, a weighting matrix is applied. Whilst processing, various weighting factors are considered, detailed in Section 4.4 and a weighting matrix $\mathbf{W}$ of dimension m by m is constructed, given by

$$\mathbf{W}_{ij} = w_i\delta_{ij} \tag{4.30}$$

where δ_{ij} is the Kronecker delta tensor, and w_i is the scalar weight for the i'th datum (summation convention not applying).

So, prior to the inversion, $\mathbf{A}$ and $\mathbf{b}$ are premultiplied by the matrix $\mathbf{W}$, such that

$$\mathbf{A} = \mathbf{W}\hat{\mathbf{A}} \qquad \mathbf{b} = \mathbf{W}\hat{\mathbf{b}} \tag{4.31}$$

To avoid using up large amounts of memory and time constructing, and premultiplying by, such a large (diagonal) matrix, the input matrices are determined more simply as

$$\mathbf{A}_{ij} = w_i\hat{\mathbf{A}}_{ij} \qquad \mathbf{b}_i = w_i\hat{\mathbf{b}}_i \tag{4.32}$$

(summation convention not being relevant), and the inversion equation becomes

$$\mathbf{A}\,\Delta\mathbf{p} = \mathbf{b} \tag{4.33}$$

This is solved using a damped least squares method (NAG, 1985) based on a Lanczos algorithm (Paige & Saunders, 1982) and from each iteration, a set of adjustments $\Delta\mathbf{p}$ to the current set of poles is produced, and after a number of inversions, a stable solution is found.

4.3.2 Magnetic anomaly isochrons

The raw magnetic anomaly data come in the form of picks, consisting of a location in terms of longitude and latitude, and an anomaly identifier, such as c13. The data are then split into groups, corresponding to anomalies created by the same continuous sections of mid-ocean ridge - *i.e.* not separated by a (significant) fracture zone or ridge offset.

This dataset is then preprocessed to provide input for the inversion, each ridge segment being considered separately. Initially, each anomaly group within the ridge segment with three or more picks has a great circle fitted to it. If there are n_c picks, $\{\mathbf{c_1}, \ldots, \mathbf{c_i}, \ldots, \mathbf{c_{n_c}}\}$ (where $\mathbf{i}$ does not represent an index of the vector $\mathbf{c}$), in the group to which we are fitting a great circle, then the correlation matrix $\mathbf{M}_c$ is constructed

$$\mathbf{M_c} = \sum_{i=1}^{n_c} \mathbf{c_i c_i}^{\mathsf{T}} \tag{4.34}$$

and the eigenvalues and eigenvectors of this matrix are determined using a singular-value decomposition method (Press *et al.*, 1986). The eigenvector corresponding to the smallest eigenvalue is a pole for the best-fit great circle to the set of points. In some cases, where data is sparse, great circles are fitted to two picks only, from the vector product of the two vector representations of the pick locations (which gives a pole for the exact, unique great circle joining the two points). Then, for each set of anomaly picks, a target great circle (representing an isochron of another anomaly chron) is chosen for the data to be fitted to.

Ideally this will be the conjugate set of anomalies; other inversion methods (McKenzie & Sclater, 1971; Pilger, 1978; Hellinger, 1981; Cande *et al.*, 1988; Shaw & Cande, 1990) have restricted themselves to fitting to only the conjugate set, but this is not possible in cases where one

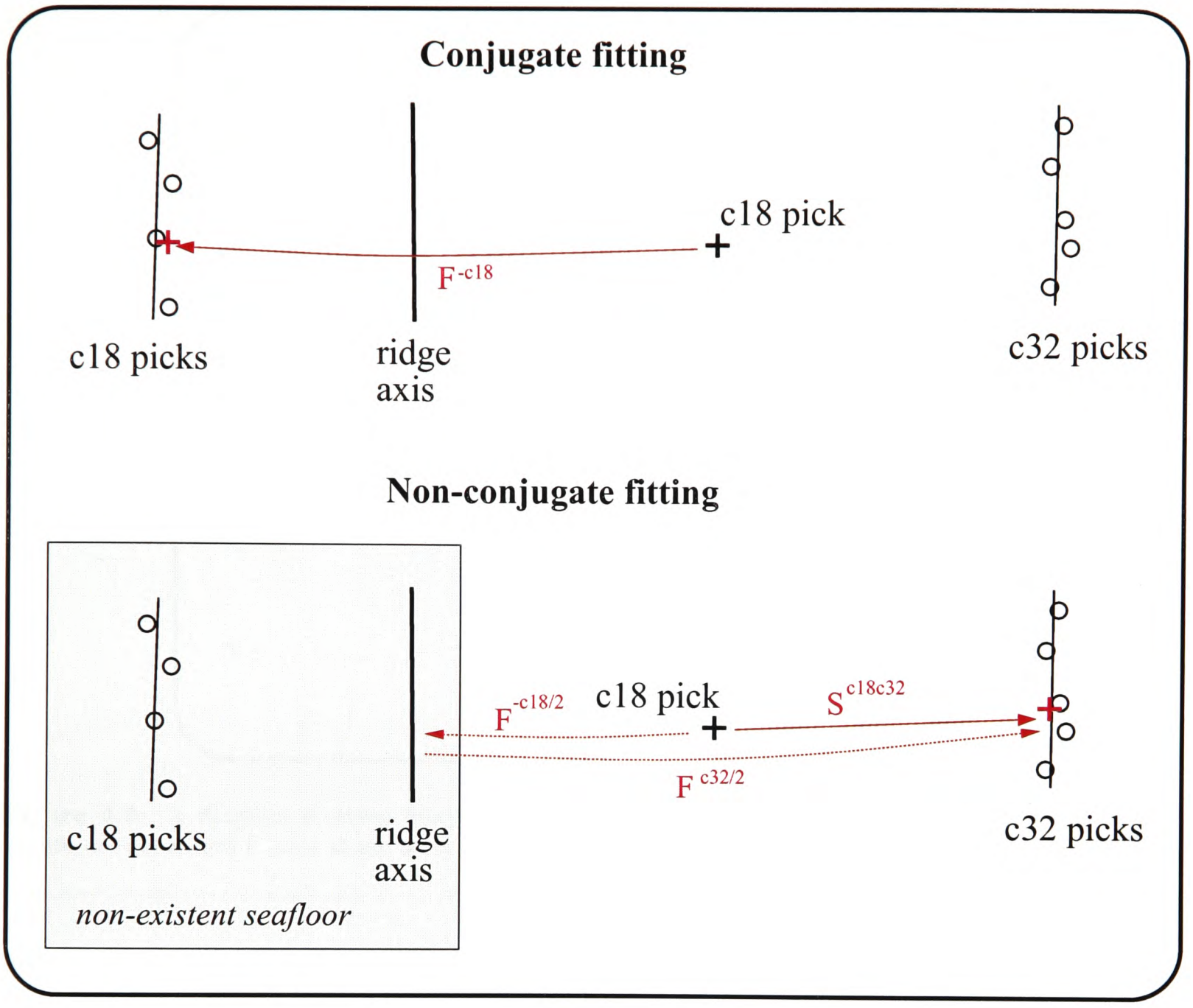

Figure 4.7: Diagram showing how in cases where seafloor has been subducted, it is not possible to rotate magnetic picks to their conjugate isochron, and must instead be fitted to picks of a different, non-conjugate, chron. **F** and **S** represent forms of finite and stage rotations respectively.

---

half of a plate pair is being, or has been, subducted and hence magnetic anomalies for many ages are only available on one side. This is particularly the case with the South American-Antarctic Ridge, where much of the South American plate which had been created at the ridge has been subducted at the South Sandwich Trench and its ancestors. Thus, picks must instead be fitted to great circles representing picks of a different chron, as shown in Figure 4.7, which adds some complexity to the calculations. In the case of conjugate fitting, the test rotation of the pick to the target great circle is derived from the finite rotation pole for that chron (either the actual finite rotation, or with a reversed rotation, depending on which side we are rotating the pick to). However, when rotating to a target great circle of a different chron, the test (stage) rotation is derived from the finite rotation poles for both chrons; it is a combination of a half rotation of the

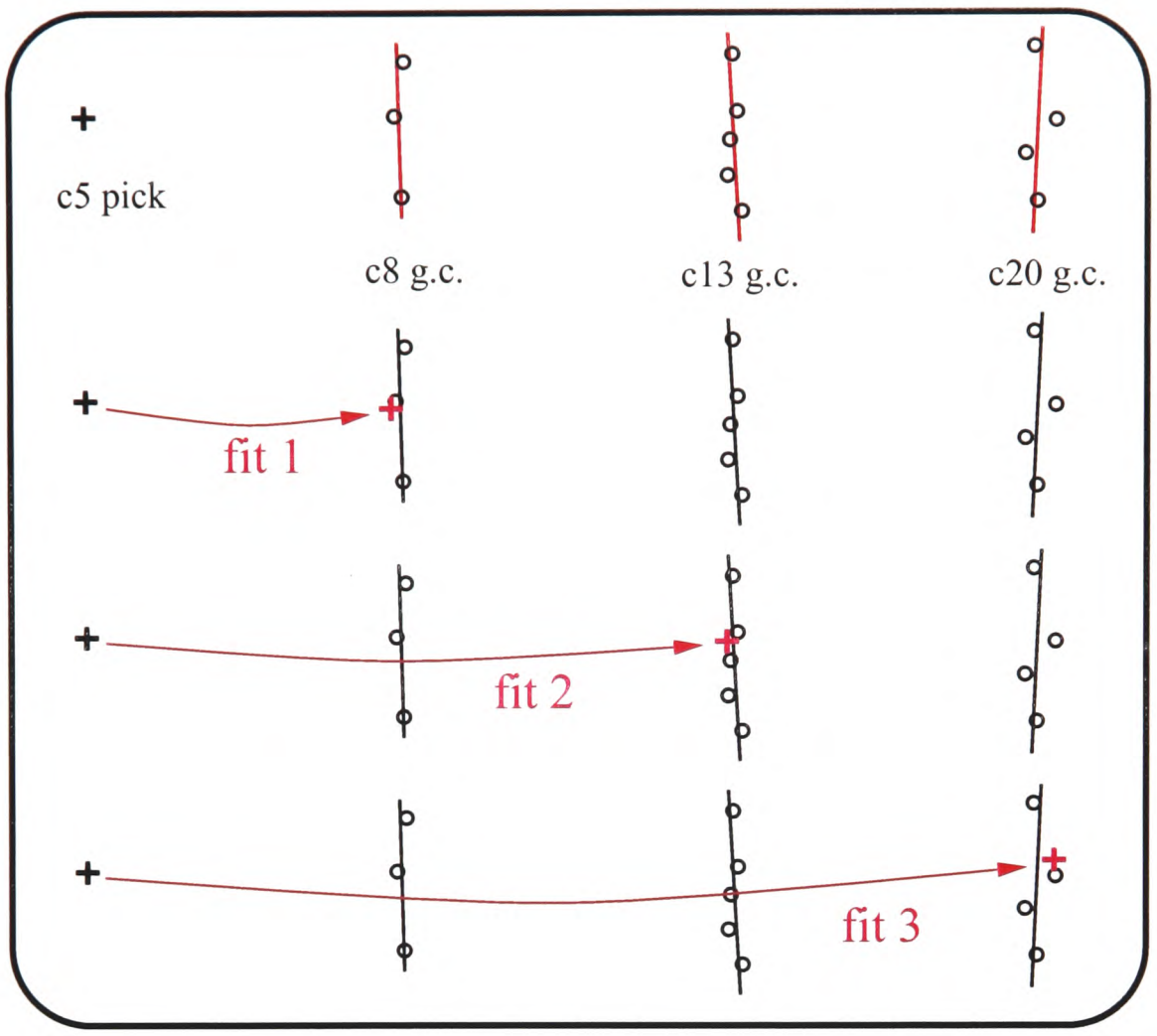

Figure 4.8: A diagram showing how when fitting anomaly picks to non-conjugate isochrons, several datum are generated from a single pick.

---

pick to the ridge axis, and then a half rotation from the ridge axis to the target great circle.

If an anomaly pick is not to be rotated to the conjugate anomaly, then a choice needs to be made as to which set of anomaly picks is to be used as the target great circle. Initially the method was tried with a set of rules, such as (i) rotating to the central anomaly, or if this doesn't exist or doesn't have enough picks to fit a great circle, then (ii) rotate to the oldest possible anomaly set on the opposite plate, or if not possible, (iii) rotate to the oldest possible anomaly on the same plate. However, this meant that certain anomaly groups were favoured for use as target isochrons, and lent undue weighting to that dataset, as the partial derivatives are dependent on both the finite rotation of the picks to be rotated, and also the finite rotation of the anomaly to which the picks are to be fitted. So, it was decided that the most sensible method was to rotate picks (without conjugate great circles) in turn to every great circle set within the same ridge section, as shown in Figure 4.8. This was a similar solution as was reached by Engebretson *et al.* (1984), who were also rotating picks to non-conjugate isochrons.

This generates several datum for each pick, *i.e.* if there are 3 great circles fitted in the ridge

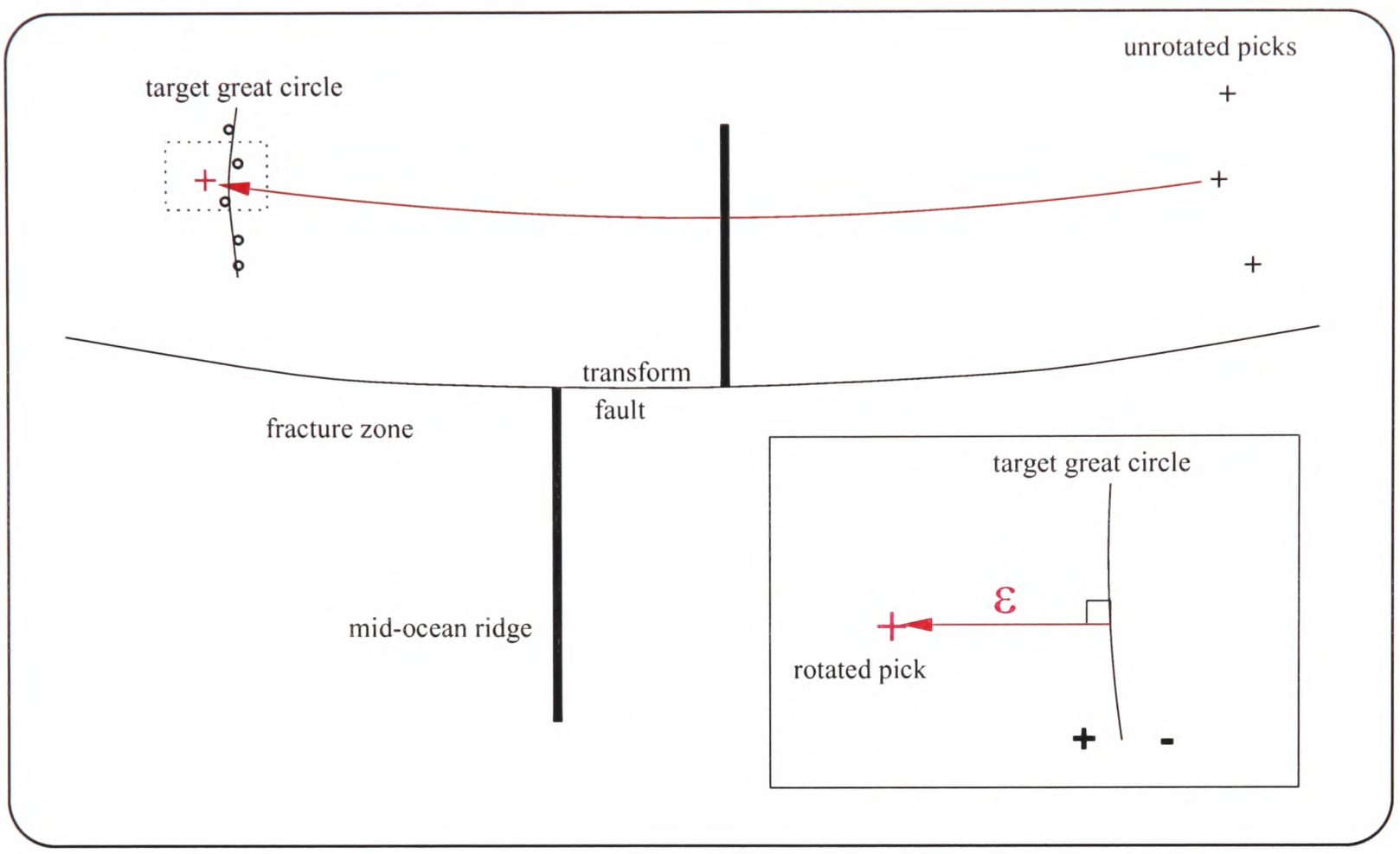

Figure 4.9: A diagram showing the misfit criteria for a magnetic pick when rotated to a target great circle

section, then an error and a set of partial derivatives are generated for each rotation and fitting in turn, leading to three sets of input data for each pick. A weight is applied to each non-conjugate generated datum, equal to the inverse of the number of great circles that the isochron pick is being rotated to. This ensures that overall contribution of a pick involved in non-conjugate fitting to the inversion is no greater than a pick involved in conjugate fitting, despite contributing a greater number of individual datum to the inversion. A feature of this method is that it allows picks for the central anomaly to be incorporated into the dataset, where the present day ridge exists. The disadvantage is that if asymmetric spreading or ridge jumps have occurred, then this will introduce inherent errors into the problem, which does not occur when fitting to conjugate isochrons.

In the inversion procedure, each individual pick is rotated by the relevant 'stage' rotation towards the target great circle. As mentioned before, this is derived from either a single finite rotation pole for conjugate fitting, or two finite rotation poles for non-conjugate fitting. For example if we are fitting an anomaly 'a' isochron pick on the second plate to the conjugate anomaly 'a' great circle on the first plate, and the set of finite rotation poles detail the motion

of the second plate relative to the first, then the stage rotation **S** is simply the reversed finite rotation for the 'a' chron, $\mathbf{F}^{-a}$ defined by (θ^a, ϕ^a, -α^a). If we are fitting an anomaly 'a' isochron pick on the second plate to an anomaly 'b' great circle also on the second plate, then the stage rotation is the sum of two rotations: a rotation of $\mathbf{F}^{-\frac{a}{2}}$, ($\theta^a$, ϕ^a, $-\frac{1}{2}\alpha^a$), followed by a rotation of $\mathbf{F}^{\frac{b}{2}}$, (θ^b, ϕ^b, $\frac{1}{2}\alpha^b$). Thus the stage rotation for this non-conjugate rotation is given by $\mathbf{S} = \mathbf{F}^{\frac{b}{2}}\mathbf{F}^{-\frac{a}{2}}$. These rotations were represented graphically in Figure 4.7, for the case where 'a' is anomaly 18, and 'b' is anomaly 32.

If the rotation is represented by the 3x3 rotation matrix **S** and the original pick by the 3-vector **d**, then the rotated pick in vector form, **r**, is given by

$$\mathbf{r} = \mathbf{S}\mathbf{d} \tag{4.35}$$

The great circle pole (chosen to be the pole on the same side of the ridge as the point **d**) is represented by the 3-vector **g**. The misfit is defined as the angular displacement of the rotated point from the closest point on the great circle, as shown in Figure 4.9. In fact, the notion of the closest point is only for figurative use, as the actual calculation of the error ε is carried out by finding the angular separation of the rotated point and the great circle pole, and subtracting 90 degrees.

$$\varepsilon = \cos^{-1}(\mathbf{r}.\mathbf{g}) - \frac{\pi}{2} \tag{4.36}$$

This eliminates the need of calculating a target point on the great circle for use in the error calculation. This is important, as when the partial derivatives are calculated, a perturbation may move the rotated pick further away from the target point, suggesting an increase in the error, but may actually be moving the pick closer to the great circle as a whole, decreasing the error. This is displayed graphically in Figure 4.10, and is an effect that previous inversion methods, such as Shaw & Cande (1990) appear to have neglected. The most obvious example of the inherent errors involved in using specific target points is if the initial error is calculated with respect to a target point on a great circle, then as a result of a perturbation to a pole parameter, the pick is rotated such that it now lies exactly on the target great circle. Thus in actuality the error is now zero, but the distance from the initial target point will be non-zero (except in the case where the pick is perturbed exactly onto the target point).

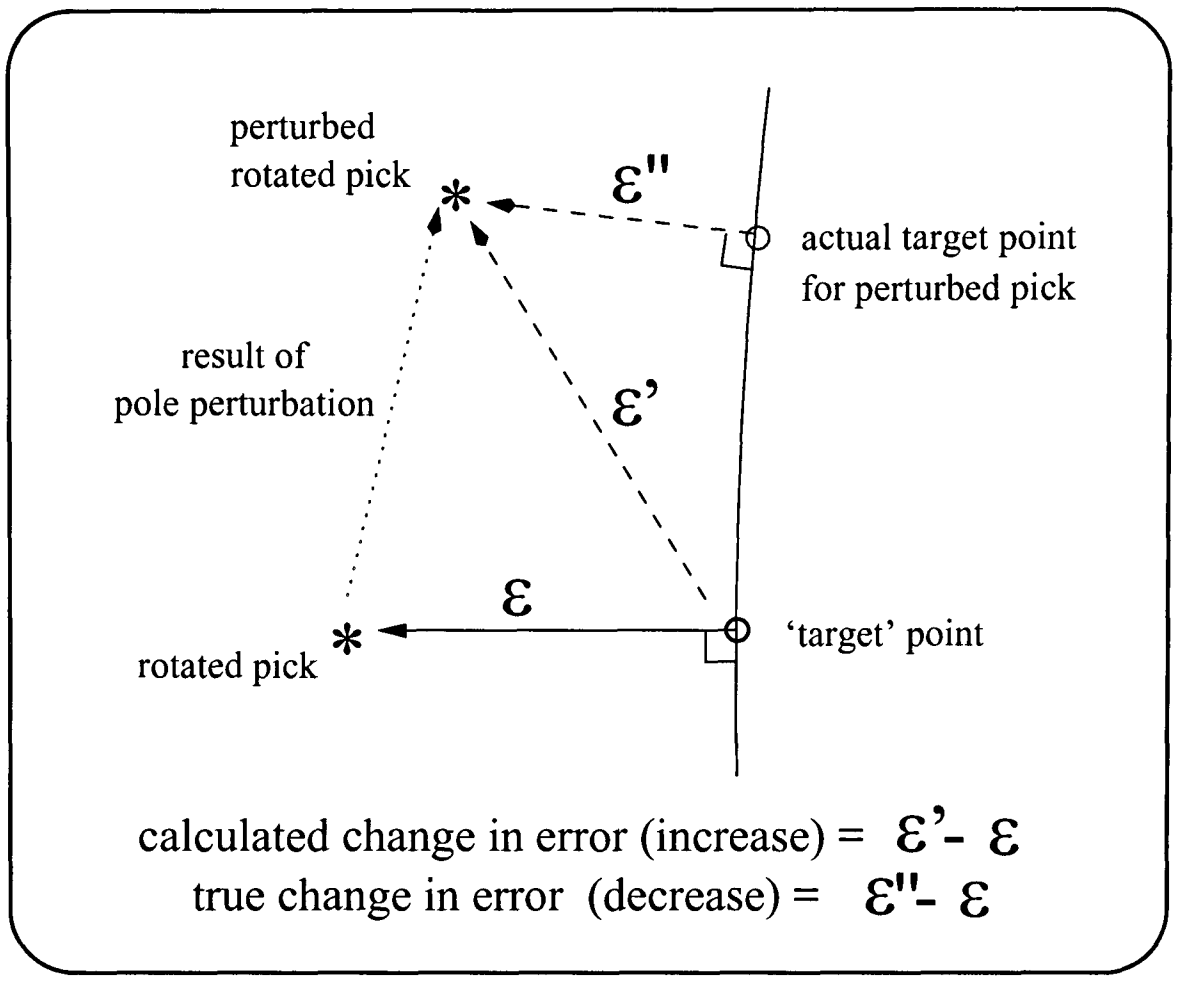

Figure 4.10: Diagram showing how partial derivatives are incorrectly determined when errors are calculated by using a target point on a great circle.

For the inversion, the partial derivatives of the error are calculated for each of the model pole parameters in turn. In the general calculation procedure for calculating partial derivatives given below, the unspecified pole parameter that has been perturbed is denoted as p^γ.

The derivative of $\cos^{-1}$ is given by

$$\frac{\partial}{\partial x}\cos^{-1}(x) = \frac{-1}{1-x^2} \tag{4.37}$$

And so by differentiating (4.36) and applying the chain rule, we obtain

$$\frac{\partial \varepsilon}{\partial p^\gamma} = \left(\frac{-1}{1-(\mathbf{r}.\mathbf{g})^2}\right)\frac{\partial(\mathbf{g}.\mathbf{r})}{\partial p^\gamma} \tag{4.38}$$

But since $\mathbf{g}$ is constant,

$$= \left(\frac{-1}{1-(\mathbf{r}.\mathbf{g})^2}\right)\mathbf{g}.\left[\frac{\partial \mathbf{r}}{\partial p^\gamma}\right] \tag{4.39}$$

and from (4.35),

$$\frac{\partial \mathbf{r}}{\partial p^\gamma} = \left[\frac{\partial \mathbf{S}}{\partial p^\gamma}\right] \mathbf{d} \tag{4.40}$$

Thus we have

$$\frac{\partial \varepsilon}{\partial p^\gamma} = \left(\frac{-1}{1-(\mathbf{r}.\mathbf{g})^2}\right) \mathbf{g}.\left[\frac{\partial \mathbf{S}}{\partial p^\gamma}\right] \mathbf{d} \tag{4.41}$$

The matrix $\frac{\partial \mathbf{S}}{\partial p^\gamma}$ must be determined, this is the partial derivative of the stage pole rotation matrix with respect to the perturbed pole parameter. The working for this is much simpler for the case where anomaly picks are matched to their conjugate set because then then 3x3 rotation matrix $\mathbf{S}$ is simply either the finite rotation matrix $\mathbf{F}$ or its inverse $\mathbf{F}^{-1}$, both solely defined by the finite rotation parameters for that anomaly. When anomaly picks are being matched to the great circle of an anomaly group of differing age, then the stage rotation $\mathbf{S}$ is a combination of two rotations, ${}_{pc}\mathbf{R}$, rotating the picks back to the present day ridge, or pseudo ridge, then a rotation ${}_{cg}\mathbf{R}$ rotating the picks to the great circle, and so $\mathbf{S}$ is dependent on a total of six finite rotation parameters. The equations to determine $\frac{\partial \mathbf{S}}{\partial p^\gamma}$ where p^γ is a parameter of the rotation(s) used to determine $\mathbf{S}$ are detailed in Section A.2.4 of Appendix A.

4.3.3 Fracture zone locations

Each fracture zone is represented by a series of latitude, longitude picks, along with a single reference seed point. The seed point is used as a basis for calculating a flowline to which the picks are fitted. The ideal seed point is the fracture zone-ridge intersection, which represents the zero-age point along the flowline, but other reference points can be used, at any point along the fracture zone, as long as the age at the reference point corresponds to one of the chrons for which the inversion is being carried out. If the reference point is off-axis, the theoretical zero-age seed is calculated using the relevant half-rotation for the seed chron, and the flowline calculated from there, a simple extension to flowline generation from the zero-age seed, a method not used by Shaw (1987) or Shaw & Cande (1990). This approach is essential in the Weddell Sea, where the mid-ocean ridge from which the fractures zones were generated is no longer in existence, and it is impossible to estimate the position of the ridge-transform intersections.

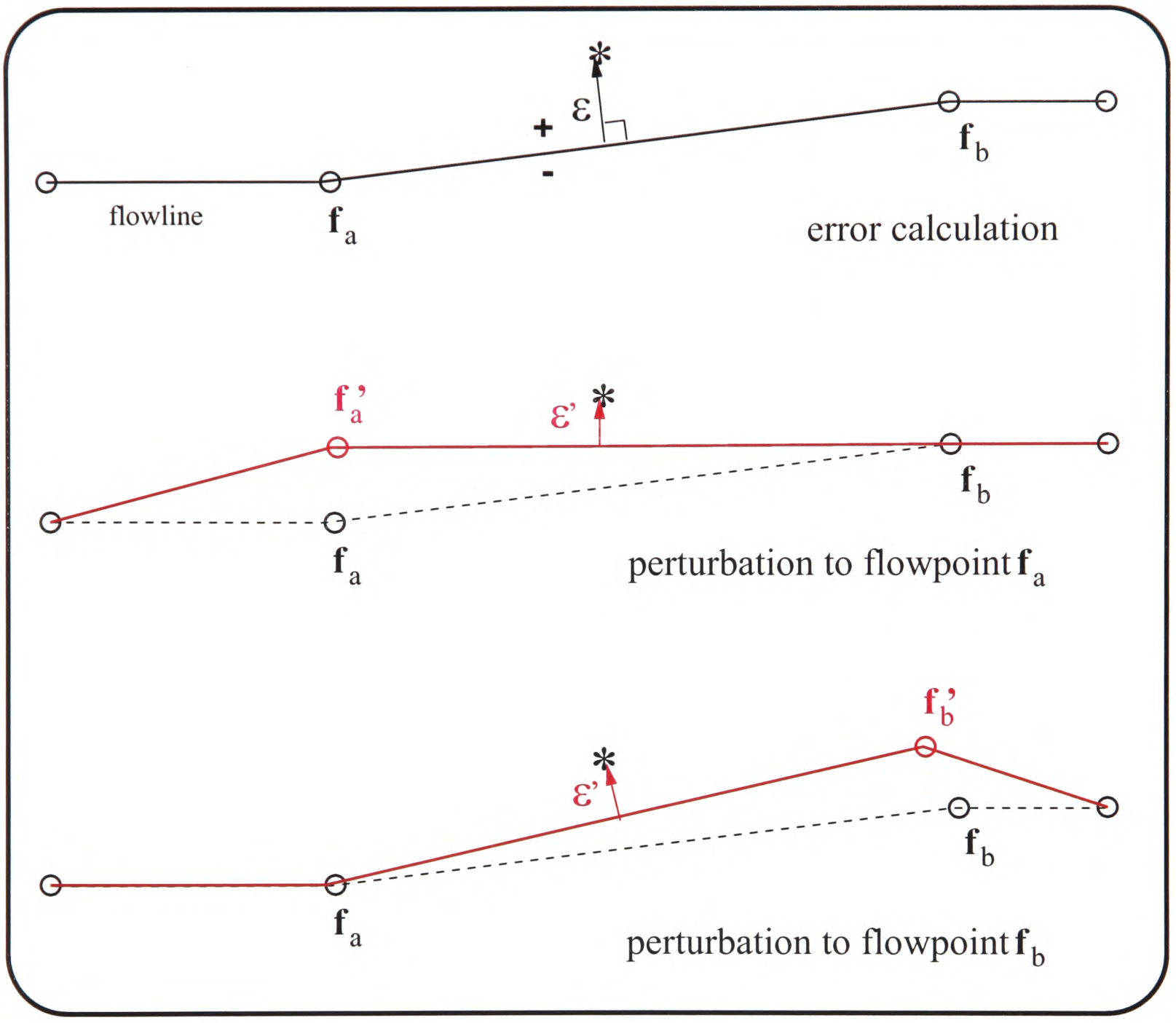

Figure 4.11: A diagram showing the misfit criteria for a fracture zone pick when fitted to a synthetic flowline, and the effect of perturbing the neighbouring flowpoints on the error.

As an additional stage, the errors in the data for the fracture zone with respect to a perturbation in the reference point are calculated. The reference point is then shifted in a direction perpendicular to the flowline for the next stage in order to minimise the errors, i.e. if the reference point is the zero-age seed, then this is perturbed in a direction perpendicular to the current direction of plate motion. This compensates for any error in the estimation of the seed point, but this perturbation is limited to $\pm$10km to avoid excessive seed shifts that might be compensating for a poor fit of the fracture zone to the synthetic flowline.

A synthetic flowline, based on the given seed point is calculated for the current rotation poles. The misfit for a fracture zone pick is given as the great circle displacement of the pick from the

closest point along the flowline, as shown in Figure 4.11. The flowline, by definition, consists of a series of small circle arcs (of the stage poles) between each pair of flowpoints determined from the finite rotation poles. The pick is represented by the 3-vector $\mathbf{d}$, the relevant stage pole by the 3-vector $\mathbf{s}$, and the two flowpoints at the ends of the relevant stage as the 3-vectors $\mathbf{f}_a$ and $\mathbf{f}_b$.

If the zero-age seed is denoted by the 3-vector $\mathbf{f}_0$, and the finite rotation (second plate relative to the first) for the chron τ , $\mathbf{F}^\tau$ has the parameters $(\theta^\tau, \phi^\tau, \alpha^\tau)$, then the flowpoint on the second plate for the chron τ is given by

$$\mathbf{f}_\tau = \mathbf{F}^{\frac{\tau}{2}}\mathbf{f}_0 \tag{4.42}$$

where $\mathbf{F}^{\frac{\tau}{2}}$ is a rotation of $(\theta^\tau, \phi^\tau, \frac{1}{2}\alpha^\tau)$. Similarly the flowpoint on the first plate for the chron τ is given by

$$\mathbf{f}_\tau = \mathbf{F}^{-\frac{\tau}{2}}\mathbf{f}_0 \tag{4.43}$$

where $\mathbf{F}^{-\frac{\tau}{2}}$ is a rotation of $(\theta^\tau, \phi^\tau, -\frac{1}{2}\alpha^\tau)$.

If the stage rotation between chrons 'a' and 'b' on the second plate is defined as $\mathbf{S}^{ab}$, then

$$\mathbf{S}^{ab} = \mathbf{F}^{\frac{b}{2}}\mathbf{F}^{-\frac{a}{2}} \tag{4.44}$$

such that

$$\mathbf{f}_b = \mathbf{F}^{\frac{b}{2}}\mathbf{f}_0 = \mathbf{F}^{\frac{b}{2}}\mathbf{F}^{-\frac{a}{2}}\mathbf{f}_a = \mathbf{S}^{ab}\mathbf{f}_a \tag{4.45}$$

The stage pole vector $\mathbf{s}$ is easily obtained from the rotation matrix $\mathbf{S}^{ab}$ (equation (4.17)). By the nature of small circles, any point $\mathbf{p}$ on the flowline between points $\mathbf{f}_a$ and $\mathbf{f}_b$ is a constant angular distance α from the stage pole $\mathbf{s}$ (see Figure 4.1) such that

$$\cos^{-1}(\mathbf{p}.\mathbf{s}) = \cos^{-1}(\mathbf{f}_a.\mathbf{s}) = \cos^{-1}(\mathbf{f}_a.\mathbf{s}) = \alpha \tag{4.46}$$

So the error for pick $\mathbf{d}$ is given by

$$\begin{aligned}\varepsilon &= \cos^{-1}(\mathbf{f}_a.\mathbf{s}) - \cos^{-1}(\mathbf{d}.\mathbf{s}) \\ &= \cos^{-1}(\mathbf{f}_b.\mathbf{s}) - \cos^{-1}(\mathbf{d}.\mathbf{s})\end{aligned} \tag{4.47}$$

The partial derivative is then calculated for a perturbation to pole parameter p^γ, using the result of equation (4.37).

$$\begin{aligned}\frac{\partial\varepsilon}{\partial p^\gamma} &= \left(\frac{-1}{1-(\mathbf{f}_a.\mathbf{s})^2}\right)\frac{\partial(\mathbf{f}_a.\mathbf{s})}{\partial p^\gamma} - \left(\frac{-1}{1-(\mathbf{d}.\mathbf{s})^2}\right)\frac{\partial(\mathbf{d}.\mathbf{s})}{\partial p^\gamma} \\ &= \left(\frac{-1}{1-(\mathbf{f}_b.\mathbf{s})^2}\right)\frac{\partial(\mathbf{f}_b.\mathbf{s})}{\partial p^\gamma} - \left(\frac{-1}{1-(\mathbf{d}.\mathbf{s})^2}\right)\frac{\partial(\mathbf{d}.\mathbf{s})}{\partial p^\gamma}\end{aligned} \tag{4.48}$$

If p^γ is a parameter of finite rotation pole $\mathbf{F}^a$, then flowpoint $\mathbf{f}_b$ is unaffected and vice versa, such that

$$\frac{\partial\varepsilon}{\partial p^\gamma} = \begin{cases}\left(\frac{-1}{1-(\mathbf{f}_a.\mathbf{s})^2}\right)\mathbf{f}_a.\left[\frac{\partial\mathbf{s}}{\partial p^\gamma}\right] - \left(\frac{-1}{1-(\mathbf{d}.\mathbf{s})^2}\right)\mathbf{d}.\left[\frac{\partial\mathbf{s}}{\partial p^\gamma}\right] & p^\gamma \in \{\theta^b, \phi^b, \alpha^b\} \\ \left(\frac{-1}{1-(\mathbf{f}_b.\mathbf{s})^2}\right)\mathbf{f}_b.\left[\frac{\partial\mathbf{s}}{\partial p^\gamma}\right] - \left(\frac{-1}{1-(\mathbf{d}.\mathbf{s})^2}\right)\mathbf{d}.\left[\frac{\partial\mathbf{s}}{\partial p^\gamma}\right] & p^\gamma \in \{\theta^a, \phi^a, \alpha^a\}\end{cases} \tag{4.49}$$

Thus all that remains is to determine the partial derivative of the relevant stage pole in vector form with respect to the perturbation of one of the poles, $\frac{\partial\mathbf{s}}{\partial p^\gamma}$. This is related to the problem in the previous section, and is tackled in a similar way in that the partial derivative of the stage rotation matrix is calculated, $\frac{\partial\mathbf{S}}{\partial p^\gamma}$, and from this, the required partial derivative found. The steps required to obtain this are given in Section A.2.4, Appendix A.

Although Shaw & Cande (1990) fitted fracture zone picks to continuous flowlines in the same way, the calculations required to calculate errors and partial derivatives were unnecessarily complicated. The method described here is far more straightforward, leading to far simpler, and more mathematically rigorous, calculations, and in addition avoids the problems of using 'target points' in the calculations.

4.3.4 Transform fault locations

In order to provide additional constraints on the first (effectively the current) rotation pole, it was decided to include transform fault data in the inversion. In inversions to determine instantaneous

spreading poles, transform fault azimuths are used as input data. The method used here is similar, though misfits are calculated for each individual transform pick, as opposed to simply determining the azimuth of the transform from the set of picks and obtaining the misfit of this azimuth from the model.

The strike of a transform fault is in theory a small circle defined by the current spreading pole. To determine the errors and partial derivatives for the transform picks, a small circle needs to be found for the transform in question, to fit the data to. It could be generated by a single seed point, as for the fracture zone data, but instead, it is determined by finding the best fit small circle (of the current pole) for the transform picks. A small circle of a pole $\mathbf{p}$ can be uniquely defined by an angle α such that for the loci of points on the small circle $\mathbf{s}$

$$\cos^{-1}(\mathbf{p}.\mathbf{s}) = \alpha \tag{4.50}$$

If we have a set of n transform picks, $\{t_0, \ldots, t_i, \ldots, t_n\}$, then the best fit small circle is defined by the angle α where

$$\alpha = \frac{1}{n}\sum_{i=1}^{n} \cos^{-1}(\mathbf{p}^1.\mathbf{t}_i) \tag{4.51}$$

where $\mathbf{p}^1$ is the vector pole for the instantaneous pole of motion (The first finite rotation pole of the series, provided this is for a sufficiently recent chron, such as anomaly 2A, $\approx$2.5Ma).

Thus the error for the i'th pick is calculated as the great circle distance from this pick to the closest point on the small circle, which is equivalent to the difference between the angle α, and the angular separation between the pick and the pole $\mathbf{p}^1$. Thus, the error is given by

$$\varepsilon_i = \alpha - \cos^{-1}(\mathbf{p}^1.\mathbf{t}_i) \tag{4.52}$$

This error can only be affected by a change in the latitude or the longitude of the current pole, θ_1 and ϕ_1 respectively; it is unaffected by a change in the rotation angle of the current pole, or parameters of any of the other, older, poles.

The partial derivatives of the error for a perturbation to the pole parameter p^γ is given by

$$\begin{aligned}\frac{\partial \varepsilon_i}{\partial p^\gamma} &= \frac{\partial \alpha}{\partial p^\gamma} - \frac{\partial}{\partial p^\gamma}\cos^{-1}(\mathbf{p}^1.\mathbf{t}_i) \\ &= \frac{1}{n}\frac{\partial}{\partial p^\gamma}\left(\sum_{i=1}^{n}\cos^{-1}(\mathbf{p}^1.\mathbf{t}_i)\right) - \left(\frac{-1}{1-(\mathbf{p}^1.\mathbf{t}_i)^2}\right)\frac{\partial(\mathbf{p}^1.\mathbf{t}_i)}{\partial p^\gamma} \\ &= \frac{1}{n}\left\{\sum_{i=0}^{n}\left(\frac{-1}{1-(\mathbf{p}^1.\mathbf{t}_i)^2}\right)\left[\frac{\partial \mathbf{p}^1}{\partial p^\gamma}\right].\mathbf{t}_i\right\} - \left(\frac{-1}{1-(\mathbf{p}^1.\mathbf{t}_i)^2}\right)\left[\frac{\partial \mathbf{p}^1}{\partial p^\gamma}\right].\mathbf{t}_i\end{aligned} \tag{4.53}$$

The partial derivative $\frac{\partial \mathbf{p}^1}{\partial p^\gamma}$ is elementary for the pole parameters θ^1 and ϕ^1, and can be determined simply from equations (A.10) and (A.11) in Appendix A.

4.4 Data weighting and selection

In addition to the normalisation of the data, some selection and basic weighting was applied to the different data sets in order to guarantee that the inversion was not unduly influenced by data outliers or a particular set of inconsistent data. An additional factor was allowed, in that each data type was allocated a biasing factor, (β^{mag}, β^{fz}, β^{tf}), so that if desired, one could be favoured over the others. However, this was found to be unnecessary, and the ratio of biases set as 1:1:1, having no influence on the inversion. The weighting schemes are now described, but it is important to note that the weighting factors given are inverse weights, which are converted into true weights by the inversion method at a later stage.

4.4.1 Magnetics data

For each magnetic anomaly group, the weighting was determined by four factors: (i) the number of great circles to which the current anomaly group is being rotated; (ii) the RMS misfit of all the picks in the isochron groups (those used to determine the great circle and those being rotated) to the great circle ; (iii) whether the target great circle was generated through fitting to 2 or 3+ picks ; (iv) the type of great circle to which the pick is being rotated (conjugate, central, non-conjugate).

First of all, the weighting factor w_{ng} for the number of great circles (n_{gcs}) that the pick is to

be rotated to, is given by

$$w_{\mathrm{ng}} = n_{\mathrm{gcs}} \tag{4.54}$$

If there are n_{r} picks in the current anomaly group being rotated to a great circle determined from n_{c} picks, and the great circle displacement of the i'th of these points from the great circle is given as d_i^{c} and d_i^{r} respectively, then the RMS error is given by

$$\xi = \sqrt{\frac{\sum_{i=1}^{n_{\mathrm{r}}} d_i^{\mathrm{r}2} + \sum_{i=1}^{n_{\mathrm{c}}} d_i^{\mathrm{c}2}}{n_{\mathrm{c}} + n_{\mathrm{r}}}} \tag{4.55}$$

Now, if the great circle was fitted to just two picks then this is an exact fit such that

$$\sum_{i=1}^{n_{\mathrm{c}}} d_i^{\mathrm{c}2} = 0 \tag{4.56}$$

so this needs to be taken into account, or the RMS error given in equation (4.55) would be artificially low. The correct weighting factor for the fit of all the points to the great circle, w_{e}, is thus

$$w_{\mathrm{e}} = \begin{cases} \sqrt{\frac{\sum_{i=1}^{n_{\mathrm{r}}} d_i^{\mathrm{r}2}}{n_{\mathrm{r}}}} & n_{\mathrm{c}} = 2 \\ \\ \sqrt{\frac{\sum_{i=1}^{n_{\mathrm{r}}} d_i^{\mathrm{r}2} + \sum_{i=1}^{n_{\mathrm{c}}} d_i^{\mathrm{c}2}}{n_{\mathrm{c}}+n_{\mathrm{r}}}} & n_{\mathrm{c}} \geqslant 3 \end{cases} \tag{4.57}$$

Finally a couple of more subjective weighting factors are included. Because the azimuth of a great circle fitted through two points is going to be very sensitive to an error in one of the points, particularly when the two are very close together, we would prefer the system to be biased towards great circles fitted to 3 or more picks, so an additional weighting factor w_{np} is defined,

$$w_{\mathrm{np}} = \begin{cases} 2 & n_{\mathrm{c}} = 2 \\ \\ 1 & n_{\mathrm{c}} \geqslant 3 \end{cases} \tag{4.58}$$

The most useful information is going to come from fitting anomalies to conjugate great circles,

since this will not be affected by asymmetrical spreading or changes in ridge geometry. After this, then picks rotated to/from the central anomaly are favourable because the rotation is dependent on only one rotation pole, and finally come picks rotated to a great circle of a different chron age. So a weighting factor w_{r} is defined as

$$w_{\mathrm{r}} = \begin{cases} 1 & \text{rotating to conjugate anomaly} \\ 1.5 & \text{rotating to ridge axis} \\ 2 & \text{rotating to independent anomaly} \end{cases} \tag{4.59}$$

The final weighting factor is a combination of these, except that all the picks with a weighting less than the standard deviation for the isochron data, σ^{mag}, are given unit weighting, and those with greater are assigned a normalised weight, such that the total weight W (including any bias, β^{mag}) is given as

$$W = \begin{cases} \beta^{\mathrm{mag}} & (w_{\mathrm{ng}} \times w_e \times w_{\mathrm{np}} \times w_r) \leqslant \sigma^{\mathrm{mag}} \\ \frac{\sigma^{\mathrm{mag}} \times \beta^{\mathrm{mag}}}{w_{\mathrm{ng}} \times w_e \times w_{\mathrm{np}} \times w_{\mathrm{r}}} & (w_{\mathrm{ng}} \times w_{\mathrm{e}} \times w_{\mathrm{np}} \times w_{\mathrm{r}}) > \sigma^{\mathrm{mag}} \end{cases} \tag{4.60}$$

This may appear complex, but it is designed to reflect the fact that the most reliable source of data is expected to be a pick rotated to a great circle fitted to the conjugate anomaly group consisting of 3 or more picks.

4.4.2 Fracture zone data

The weighting for fracture zones is much simpler, and is based purely on the premise that the best source of data comes from fracture zones which have the best overall fit to the synthetic flowlines. For a fracture zone with n_{f} picks, with the i'th pick having an error d_i, the RMS error ξ is given by

$$\xi = \sqrt{\frac{\sum_{i=1}^{n_{\mathrm{f}}} d_i^2}{n_{\mathrm{f}}}} \tag{4.61}$$

and in accordance with (4.60), with the standard deviation of the fracture zone data given by σ^{fz}, and any bias by β^{fz}, the weighting for each pick along the fracture zone is given by

$$W = \begin{cases} \beta^{\text{fz}} & \xi \leqslant \sigma^{\text{fz}} \\ \frac{\sigma^{\text{fz}} \times \beta^{\text{fz}}}{\xi} & \xi > \sigma^{\text{fz}} \end{cases} \tag{4.62}$$

4.4.3 Transform fault data

As for the fracture zone data, the weighting for the transform data is simply a case of calculating a normalised weight for a particular transform relative to the overall distribution of errors for the transform data. So for a transform fault with n_{t} picks, with the i'th pick having an error d_i, the RMS error ξ is given by

$$\xi = \sqrt{\frac{\sum_{i=1}^{n_{\text{t}}} d_i^2}{n_{\text{t}}}} \tag{4.63}$$

and the weighting for each pick along the transform is given by

$$W = \begin{cases} \beta^{\text{tf}} & \xi \leqslant \sigma^{\text{tf}} \\ \frac{\sigma^{\text{tf}} \times \beta^{\text{tf}}}{\xi} & \xi > \sigma^{\text{tf}} \end{cases} \tag{4.64}$$

where σ^{tf} is the overall standard deviation for the transform fault data, and β^{tf} the transform biasing factor.

4.4.4 Outliers and data selection

An inevitable consequence of the data collection process is the presence of outliers. This is particularly so in the case of magnetics data, where the data need to be very carefully grouped. If a group of anomalies is included in a ridge section from which it should actually be separated, due to an unmapped fracture zone or offset of the ridge axis, then the errors for this group of data, or other picks rotated to this group (if it has a great circle fitted) will be spuriously high. This is because the errors arise not from any unsatisfactory pole parameters, but from an error in the grouping of the data itself. This applies equally for cases where there has been a change in ridge geometry or a past ridge jump, or where there has been asymmetric spreading.

Despite rigorous grouping, such outliers will still exist unless we choose to reduce the size of the dataset substantially. In some cases, in order to obtain groupings of picks big enough to generate data in some regions where anomaly picks are sparse, it is accepted that a certain number of outliers will be included (*e.g.* ensuring the inclusion of an isochron set with 2+ picks, in a group with other anomaly picks, so that a great circle can be fitted and used as a target for the other anomaly picks). This is sometimes necessary in order to have sufficient data points for the inversion to be meaningful, in the sense that poor data is better than no data at all. However, in order to reduce the effect of such outliers on the inversion, prior to the final inversion, data selection is carried out, quite independent of any data weighting. A cutoff criterion Γ is decided upon such that any datum with a magnitude of misfit greater than Γ standard deviations is discarded. The value of Γ is subjective, but a suitable value can be usually be determined after viewing q-q plots of the data misfits (Section 4.5.1).

The problem of outliers is less important in the case of fracture zone and transform fault data. In particular it is very unlikely that there will be any significant outliers along a transform fault, and only a slight chance of a mis-pick caused by morphological anomalies along the transform valley, so Γ^{tf} can be set fairly high. For a fracture zone, there are two possible sources of outliers. The first is the whole fracture zone existing as an unrepresentative flowline, possibly due to plate deformation warping the trace of the fracture zone, or asymmetric spreading which would leading to a fracture zone deviating from a synthetic flowline. Additionally there is the possibility of errors made during the picking procedure. Although each pick was checked manually and adjusted when the automatic picking was adjudged to have made a mistake, as detailed in Section 2.4, it is possible that in regions where the gravity signal was low or difficult to distinguish, an incorrect pick could have been made. However, general confidence in the fracture zone picks is substantially higher than for the magnetics data, and so it is possible to set Γ^{fz} correspondingly higher if desired.

The actual values chosen for the inversions are given in Section 5.1.5, Chapter 5, along with justification for the values chosen.

4.5 Statistical analysis

4.5.1 Distribution of errors

A key factor of the inversion procedure is an accurate estimation of errors. The initial assumption is made that there is a Gaussian distribution, though it is accepted that this assumption will become invalid towards the 'tails' of the distribution, with the inevitable presence of outliers in the dataset. A reliable test of the theoretical Gaussian distribution of the errors in the data is made by carrying out q-q (quantile-quantile) analysis.

This procedure consists of plotting the quantiles of the distribution of calculated error values (misfits) against the corresponding quantiles of the theoretical distribution (usually a Gaussian distribution of mean 0 and standard deviation 1). If the two distributions are identical, then the quantiles would also be defined equally, and so a straight line would result. The first step is to sort the n values of the dataset $\{x_1, \ldots, x_i, \ldots, x_n\}$ by size into the ordered set $\{x^1 \leqslant x^2 \leqslant x^3 \ldots x^{n-1} \leqslant x^n\}$. The assumption is made that this set is a series of independent random variables with an unknown probability density function (pdf). By nature, these ordered values should then divide the probability density function into $n+1$ equal areas of size $\frac{1}{n+1}$, (regions $-\infty \leftrightarrow x^1, x^1 \leftrightarrow x^2$ and so on). Figure 4.12 shows the probability density function for a Gaussian distribution of mean 0 and standard deviation 1. It can be seen that the set of normally distributed values shown divide the region below the pdf into equal areas.

A quantile $Q(p)$ is the value at which the fraction p of the data lies below this point. Figure 4.12 shows the cumulative distribution for a Gaussian distribution of mean 0 and standard deviation 1, displaying the 10% quantiles. Since we have a discrete dataset, we can only determine quantiles where we have a measurement. So, determining the fraction of the data below the measurement x_i to be $\frac{i-1+\frac{1}{2}}{n} = \frac{i-\frac{1}{2}}{n}$ (*i.e.* specifying the i'th observation to be half in the upper section and half in the lower section), we have values for the set of quantiles $Q(p_i)$ where $p_i = \frac{i-\frac{1}{2}}{n}$ for $i = 1, n$. Obviously the quantiles for our observed dataset are simply the observed values themselves, such that $Q^O(p_i) = x^i$, but to complete the analysis, we need to obtain the values of $Q(p_i)$ for the test distribution. The cumulative distribution function for the Gaussian distribution is given by

$$G(t) = \frac{1}{\sqrt{2\pi}} \int_{-\infty}^{t} e^{-s^2/2} ds \tag{4.65}$$

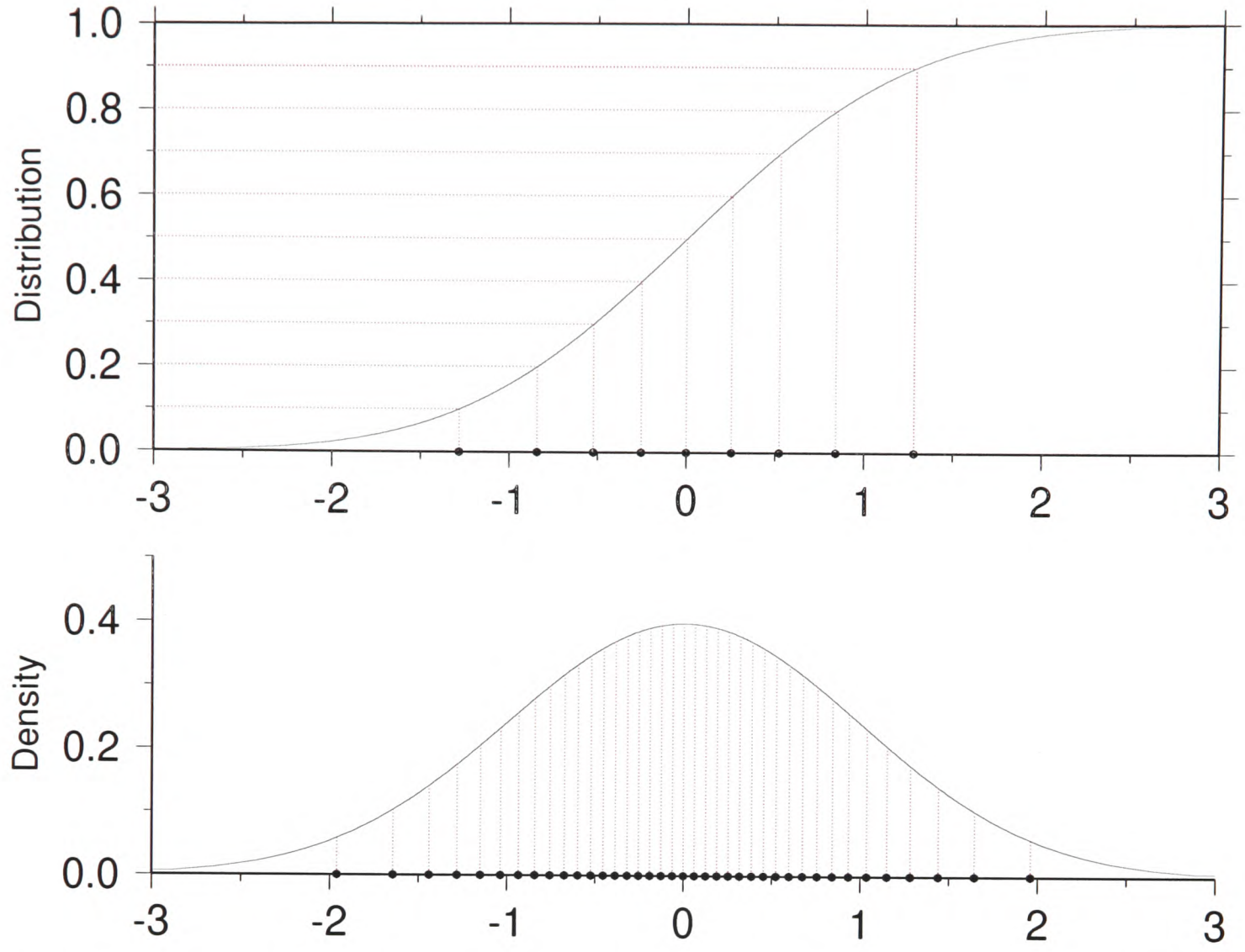

Figure 4.12: The probability density function (pdf) and the cumulative density function for a Gaussian distribution with mean 0 and standard deviation 1.

---

and so the p_i'th quantile is given by $Q^G(p_i) = G^{-1}\left(\frac{i-\frac{1}{2}}{n}\right)$. These values were determined inversely by finding the value of $Q^G(p_i)$ that satisfied $G(Q^G(p_i)) = \frac{i-\frac{1}{2}}{n}$.

A q-q plot can then be made of $x^i (= Q^O(p_i))$ against $Q^G(p_i)$. If the distribution is Gaussian, then the plot will be linear. Testing against a (0,1) Gaussian distribution has the advantage of the zero intercept yielding an estimate of the mean of the sample dataset, and the gradient an estimate of the standard deviation. Because of the nature of the datasets, the q-q plots are expected to be linear close to the origin, but deviating from the straight line when outliers become apparent. In practice the standard deviation was determined from the plot within the boundaries of ± 1 standard deviation, in order that this was determined from the best-fitting region of data.

The q-q plots are a very good visual test for the Gaussian nature of the distribution of errors, with reliable estimates of the sample statistics able to be determined. In addition to this method, the best-fit Gaussian distribution was determined for each set of data residuals, and the best-fit mean and standard deviation compared with those obtained from the q-q plots, and those

calculated from the dataset. However, the most reliable estimates are those from the q-q plots, as the presence of outliers has no significant effect on the determination of the statistics.

4.5.2 Confidence intervals

Chang (1987, 1988) determined a rigorous mathematical method for determining covariance matrices and confidence regions for plate inversions, based on the great circle fitting method of Hellinger (1981). While this could be applied to the fitting of the magnetics data in this inversion, the fitting method for the fracture zone and transform fault data is incompatible with Chang's method. Most of the work done on confidence regions (Hellinger (1981); Stock & Molnar (1983); Jurdy & Stefanick (1987); Chang (1987, 1988); Hanna & Chang (1990); Royer & Chang (1991)) has been based on the boundary fitting method, where the fracture zone is only considered as a segment linking offset lineations of a magnetic isochron and fitted to the corresponding segment on the opposing side, in the same way as magnetic anomalies are fitted to conjugate anomaly sets. The method of fitting whole fracture zones to a single continuous flowline as used here does not lend itself to the same analysis.

Stock & Molnar (1983) developed a qualitative method for determining uncertainty regions for the boundary fitting method, by determining a set of poles away from the solution that would cause different degradations of the solution (skewed or mismatched data) within a certain limit (10 km, as the considered uncertainty for individual data points). Jurdy & Stefanick (1987) developed this further and determined covariance matrices from the pole uncertainties suggested by the method of Stock & Molnar (1983), and from these obtained confidence regions. It was this approach that Chang (1987, 1988) extended by taking a much more mathematically and statistically rigorous approach. Given a best-fit rotation $\tilde{A}$, obtained as an estimate of the rotation A that would align the datasets for a given pole, a set of small rotations $\Phi(\mathbf{h})$ was defined that would degrade the fit within the limits of the uncertainties in the data such that $\tilde{A} = A\Phi(\mathbf{h})$. The rotation set $\mathbf{h}$ was explicitly defined in a relatively complex equation involving factors derived from the best-fit rotation, locations of the datapoints and a criterion set by the assumed distribution of the data, such the critical point of a χ^2 distribution with 3 degrees of freedom. The set $\mathbf{h}$ thus describes a confidence region around the best fit solution, with a confidence specified by the critical point used for the chosen distribution. Methods of graphically representing this confidence region were detailed in Hanna & Chang (1990).

Chang *et al.* (1990) took a slightly broader view of uncertainties in rotations, and considered the differences between the various possible parametrisations of a rotation, favouring the exponential parametrisation described in Section 4.1.6, and determining that in fact the standard (latitude, longitude, angle) form was in fact the least practical. In addition, they studied the effect of combining rotations and determined the covariance matrix for such a combined rotation in terms of the two rotations and corresponding covariance matrices. Wilson (1993) considered several different techniques of determining confidence regions:from a covariance matrix determined from a linear inversion (Shaw & Cande, 1990); from grid-test searches for poles satisfying an F-test statistic (Engebretson *et al.*, 1984); and a bootstrap resampling method. The latter involved carrying out a large number of inversions using random subsets of data, and a confidence region (*e.g.* 95%) is determined from the volume of parameter space that contains the most clustered 95% of the solutions for the resampled sets.

The confidence intervals used in this study are those obtained from the covariance matrix which is intrinsically defined by the inversion (Shaw & Cande, 1990; Wilson, 1993).

The governing equation for the inversion, given by (4.29), is

$$\hat{\mathbf{A}}\,\Delta\mathbf{p} = \hat{\mathbf{b}} \tag{4.66}$$

where $\hat{\mathbf{A}}_{ij} = \frac{\partial \hat{\varepsilon}_i}{\partial p_j}$ is the partial derivative matrix showing how changes in the pole parameters affect the normalised errors $\hat{\varepsilon}$. From this, the matrix

$$\left[\hat{\mathbf{A}}^{\mathsf{T}}\hat{\mathbf{A}}\right]_{ij} = \frac{\partial \hat{\varepsilon}_k}{\partial p_i}\frac{\partial \hat{\varepsilon}_k}{\partial p_j} \tag{4.67}$$

is the correlation matrix for changes in the errors of the data with respect to the poles, and then the inverse,

$$\mathbf{C} = \left[\hat{\mathbf{A}}^{\mathsf{T}}\hat{\mathbf{A}}\right]^{-1} \tag{4.68}$$

is the auto-covariance matrix for the solution, relating uncertainties in the solution poles to the uncertainties in the data.

This is easily seen by considering that if the solution has a high uncertainty, then another parameter set close to the determined solution set $\tilde{\mathbf{p}}$ would not alter the errors significantly, hence

the values of $\hat{\mathbf{A}}^{\mathsf{T}}\hat{\mathbf{A}}$ would be low, leading to large values for $\mathbf{C}$. The validity of this as a method of determination of the covariance matrix relies strongly on the assumption that the problem is linear in the region of the solution. It is important to note that the error vector $\mathbf{b}$ does not appear, this covariance matrix is generated by the relative stabilities of the errors, as opposed to the absolute errors themselves.

The normalised matrix $\hat{\mathbf{A}}$ is used, before applying the pick weights, as this is the purest equation of the inversion and gives a true measure of how changes in the pole parameters will affect the errors, ahead of any bias that we might wish to give the inversion, as created by the weighting process. If we consider the effects of including the weights and data biases, from equations (4.32) and (4.68), we see that by weighting down a large amount of data, the values of the covariances would increase, or similarly by having no weighting, but biasing the values in favour of one data type the covariances would decrease. However, this does also show the importance of determining the correct distribution of errors for each data type, since an error in the standard deviations used to normalise the data would lead to a corresponding error in the covariance matrices, and hence the confidence ellipses.

From the matrix $\mathbf{C}$, the 3x3 submatrices for the individual poles can be extracted, such that the symmetric covariance matrix $\mathbf{C}^i$ for the i'th pole $(\theta^i, \phi^i, \alpha^i)$ is obtained,

$$\mathbf{C}^i = \begin{bmatrix} \sigma^2_{\theta^i} & \sigma_{\theta^i\phi^i} & \sigma_{\theta^i\alpha^i} \\ \sigma_{\theta^i\phi^i} & \sigma^2_{\phi^i} & \sigma_{\phi^i\alpha^i} \\ \sigma_{\theta^i\alpha^i} & \sigma_{\phi^i\alpha^i} & \sigma^2_{\alpha^i} \end{bmatrix} \tag{4.69}$$

where σ_{θ^i}, σ_{ϕ^i} and σ_{α^i} are the variances for ϕ, θ and α components of the pole, and $\sigma_{\theta^i\phi^i}$, $\sigma_{\theta^i\alpha^i}$ and $\sigma_{\phi^i\alpha^i}$ are the covariances between each pair of components ($\sigma_{xy} = \rho_{xy}\sigma_x\sigma_y$, where ρ_{xy} is the correlation coefficient between x and y).

The next step is to determine the eigenvectors of this matrix, which will represent the semi-major axes of the confidence ellipse in 3-D parameter space, and the corresponding eigenvalues which yield the squared variances along these axes. It is now that problems occur with the co-ordinate system we are using, since although θ and α are equivalent spatially, both representing variables of great circle distance, ϕ represents distance along a small circle. In order to compute meaningful confidence ellipses, a conversion factor needs to be included for the terms involving ϕ, which converts degrees of longitude (at a given latitude) into great circle distances according

to

$$^{*}\phi = \cos(\theta)\ \phi \tag{4.70}$$

so the adjusted covariance matrix $^{*}\mathbf{C}^{i}$ for a linear 3-dimensional parameter space is determined as

$$^{*}\mathbf{C}^{i} = \begin{bmatrix} \sigma^2_{\theta^i} & \cos(\theta^i)\ \sigma_{\theta^i\phi^i} & \sigma_{\theta^i\alpha^i} \\ \cos(\theta^i)\ \sigma_{\phi^i\theta^i} & \cos^2(\theta^i)\ \sigma^2_{\phi^i} & \cos(\theta^i)\ \sigma_{\phi^i\alpha^i} \\ \sigma_{\alpha^i\theta^i} & \cos(\theta^i)\ \sigma_{\alpha^i\phi^i} & \sigma^2_{\alpha^i} \end{bmatrix} \tag{4.71}$$

The 3 eigenvectors, $(\mathbf{e}_1, \mathbf{e}_2, \mathbf{e}_3)$ and eigenvalues $(\sigma_1^2, \sigma_2^2, \sigma_3^2)$ are then determined from this matrix. The confidence ellipsoid is defined by these three axes, and the magnitude is determined by referring to χ^2 tables, such that the axes are multiplied by a factor of 2.79 to represent 95% confidence in three dimensions. Sometimes it is easier to represent the confidence intervals as an ellipse rather than a surface, (Shaw & Cande, 1990), and so the eigenvectors and eigenvalues are determined for the reduced covariance matrix

$$^{*}\mathbf{C}^{i'} = \begin{bmatrix} \sigma^2_{\theta^i} & \cos(\theta^i)\ \sigma_{\theta^i\phi^i} \\ \cos(\theta^i)\ \sigma_{\phi^i\theta^i} & \cos^2(\theta^i)\ \sigma^2_{\phi^i} \end{bmatrix} \tag{4.72}$$

The angle is considered fixed, and so the 95% confidence region for 2 degrees of freedom is represented by an ellipse of 2.45σ.

4.5.3 Data importances

Whilst running inversions, a useful property to know is the data importance of each pick. First used as an inversion statistic by Minster *et al.* (1974), this is a measure of how important each datum is to the final inversion. The value of importance for the k'th datum in a dataset is defined as $\mathcal{I}_k$, the k'th element on the diagonal of the symmetric matrix $\mathbf{P}$ where $\mathbf{P}$ is defined as

$$\mathbf{P} = \mathbf{A}(\mathbf{A}^{\mathsf{T}}\mathbf{A})^{-1}\mathbf{A}^{\mathsf{T}} \tag{4.73}$$

where $\mathbf{A}$ is the partial derivative matrix for the dataset. This can either be the matrix for the whole dataset, or a subset such as the partial derivative matrix for the fracture zone picks alone.

Since only the elements along the diagonal of $\mathbf{P}$ are required, the calculation can be simplified by avoiding building the large matrix $\mathbf{P}$ by defining

$$\mathcal{I}_k = \mathbf{A}_k(\mathbf{A}^\mathsf{T}\mathbf{A})^{-1}\mathbf{A}_k^\mathsf{T} \tag{4.74}$$

where $\mathbf{A}_k$ is the k'th row of the matrix $\mathbf{A}$. Each value of importance is a positive number, and it is a property of $\mathbf{P}$ that the trace of this matrix, the sum of the elements along the leading diagonal, is equal to the rank of the matrix, also the rank of $\mathbf{A}$, which is the number of model parameters n (if the problem is determinate).

Qualitatively, the matrix $(\mathbf{A}^\mathsf{T}\mathbf{A})^{-1}$ is the covariance matrix, so leading on from this, $\mathcal{I}_k$ is a measure of how the changes in the i'th datum correlate with the stability of the model. If $\mathcal{I}_k$ is large, then this suggests that the uncertainties in the i'th datum are linked to those in the model, and so this datum has a significant effect on the inversion. Similarly the converse applies, if a datum has a low importance then it will have less effect on the result, and is relatively redundant. In other words, the importance is a measure of the contribution of the i'th datum to the model relative to the dataset in general, and thus is a measure of this point's independence from this dataset. As with the covariance matrix, the actual errors ($\mathbf{b}$) do not appear in the determination of the importances, which are generated by the nature and distribution of the dataset, and the distribution of information within the dataset.

Large values of $\mathcal{I}_k$ are bad for the inversion, since if there are any inherent errors in the data with large importances, then this will be carried through significantly into the inversion. Ideally all the importances would be equal, suggesting a representative distribution of data with no single datum having a significant effect on the result. Furthermore, considering the importance as the measure of the redundancy of that datum, a large value would tend to suggest that similar data, of that type, or in that region, would be desirable.

The importance values are additive, and so the importance of a subset of data can be obtained by summing the importances of the subset. This is particularly relevant for the magnetics dataset, as one pick may yield several data (Figure 4.8), and so the overall importance of that pick is simply found by adding the importances of each datum generated from that pick. As a rule, the data

importances were determined for the different types of data separately, this showed clearly where there were areas with sparse data coverage. The data importances were always determined from **A**, the final normalised and weighted matrix, as this represented the true effect of each data point on the result of the inversion.

4.6 Extension to a 3-plate problem

4.6.1 General consequences

When the problem is extended to three plates (1, 2 and 3), there is a set of l finite rotation poles (and hence $n = 3l$ pole parameters) for each plate pair, leading to a total of $3n(9l)$ pole parameters. However, because of the nature of the plate circuit, if we know the poles for two of the plate pairs, then we already have all the information we need to determine the third set of poles, so, we only in fact have $2n$ independent pole parameters. We take the first two sets of poles, $1 \mapsto 2$ and $2 \mapsto 3$, and use the parameters for these two sets of poles as the parameter set for the three plate inversion.

For the first plate pair, the calculations are carried out as before, the misfits determined, and the partial derivatives calculated relative to pole parameters $\{p_1, ..., p_n\}$. For the second plate pair, again the calculations are carried out as for a two plate problem, but with the partial derivatives being calculated and stored relative to pole parameters $\{p_{n+1}, ..., p_{2n}\}$. For the third set of data, $1 \mapsto 3$, a third set of finite rotation poles is calculated in order to determine the misfits to the current set of pole parameters. This is simply done by summing the relevant rotations for each pole, for example, the k'th rotation pole for the plate pair $1 \mapsto 3$ is determined by combining the two rotation matrices for the relevant poles for plate pairs $1 \mapsto 2$ and $2 \mapsto 3$, such that

$$ {}^{13}\mathbf{F}^k = \left[{}^{23}\mathbf{F}^k\right] \left[{}^{12}\mathbf{F}^k\right] \tag{4.75} $$

and the misfits determined from this set of poles, as for a 2-plate inversion. However, when calculating partial derivatives, the effect of this third set of poles is ignored and instead the derivatives are determined with respect to the two sets of poles which were used to obtain the third set, *i.e.* for parameters $\{p_1, \ldots, p_{2n}\}$ (this is covered in more detail in the next section).

The final partial derivative matrix is constructed from the three partial derivative matrices

from each plate pair, but all entries in the **A** matrix will be zero for parameters $\{p_{n+1}, \ldots, p_{2n}\}$ for data from the 1↦2 dataset or for $\{p_1, \ldots, p_n\}$ from the 2↦3 dataset. Thus, the matrix **A** is given by

$$\mathbf{A} = \begin{bmatrix} {}^{12}\mathbf{A}_{1,1} & \ldots & {}^{12}\mathbf{A}_{i,n} & 0 & \ldots & 0 \\ \ldots & & & & & \\ {}^{12}\mathbf{A}_{12_{m,1}} & \ldots & {}^{12}\mathbf{A}_{12_{m,n}} & 0 & \ldots & 0 \\ 0 & \ldots & 0 & {}^{23}\mathbf{A}_{1,n+1} & \ldots & {}^{23}\mathbf{A}_{1,2n} \\ \ldots & & & & & \\ 0 & \ldots & 0 & {}^{23}\mathbf{A}_{23_{m,n+1}} & \ldots & {}^{23}\mathbf{A}_{23_{m,2n}} \\ {}^{13}\mathbf{A}_{1,1} & \ldots & & & & {}^{13}\mathbf{A}_{1,2n} \\ \ldots & & & & & \\ {}^{13}\mathbf{A}_{13_{m,1}} & \ldots & & & & {}^{13}\mathbf{A}_{13_{m,2n}} \end{bmatrix} \tag{4.76}$$

where a prefix such as ^{12} denotes a quantity or parameter for the plate pair 1↦2.

The basic theory behind the inversion remains unchanged, there is just a larger amount of data, and double the number of pole parameters. The inversion will now be solving for a parameter set consisting of the two subsets of pole parameters $^{12}\mathbf{p}$ and $^{23}\mathbf{p}$, whilst in the process effectively also solving for the third set, in order to satisfy equally the datasets on all three plates. The output of the inversion will be adjustments to the first two sets of pole parameters, and when these new poles have been calculated, the new set of poles for the third plate can be determined. It makes no difference in which order the plate circuit is used or which set of poles is considered to be the redundant set, the same solution should be reached, within the limits of operational error (this is checked during the inversion process).

4.6.2 Partial derivatives

Where in a 2-plate inversion for the plate pair 1↦3 we would determine partial derivatives with respect to the parameters of the k'th rotation pole $^{13}\mathbf{F}^k$, $\left({}^{13}\theta^k, {}^{13}\phi^k, {}^{13}\alpha^k\right)$, in a 3-plate inversion, partial derivatives are instead determined for the pole parameters of the two independent poles used to determine $^{13}\mathbf{F}^k$, which are $\left({}^{12}\theta^k, {}^{12}\phi^k, {}^{12}\alpha^k, {}^{23}\theta^k, {}^{23}\phi^k, {}^{23}\alpha^k\right)$.

In the simplest case, this is similar to the problem tackled previously when wishing to deter-

mine partial derivatives for a stage pole with respect to the parameters of the two finite poles used to generate it. However, most of the operations in the inversion involve the calculation of stage poles for the third set of parameters, and whereas for the two plate case, a stage pole was dependent on 6 parameters, the equivalent stage pole for the third plate is now dependent on 12 parameters.

The basic equations to obtain the partial derivatives are the same, *i.e.* for magnetics data, equation (4.41) still applies. However, the key element of the equation is the partial derivative matrix $\frac{\partial \mathbf{S}}{\partial p^\gamma}$, where $\mathbf{S}$ is the stage pole matrix rotating the pick to the target great circle. $\mathbf{S}$ is now dependent on 6 parameters if rotating to the conjugate great circle or ridge axis, or 12 if rotating to an anomaly group of a different chron.

Similarly, when considering the fracture zone data, equation (4.49) still applies, where the key element is $\frac{\partial \mathbf{s}}{\partial p^\gamma}$, where $\mathbf{s}$ is the 3-vector location of the stage pole for the relevant flowline stage. Except in the case where the pick is within the range of the first finite rotation pole, when it is dependent on 6, the vector $\mathbf{s}$ is dependent on 12 parameters, and each flowpoint dependent on 6 parameters, such that (4.49) becomes

$$\frac{\partial \varepsilon}{\partial p^\gamma} = \begin{cases} \left(\frac{-1}{1-(\mathbf{f}_a.\mathbf{s})^2}\right) \mathbf{f}_a . \left[\frac{\partial \mathbf{s}}{\partial p^\gamma}\right] - \left(\frac{-1}{1-(\mathbf{d}.\mathbf{s})^2}\right) \mathbf{d}. \left[\frac{\partial \mathbf{s}}{\partial p^\gamma}\right] & p^\gamma \in \{{}^{12}\theta^b, {}^{12}\phi^b, {}^{12}\alpha^b, {}^{23}\theta^b, {}^{23}\phi^b, {}^{23}\alpha^b\} \\ \left(\frac{-1}{1-(\mathbf{f}_b.\mathbf{s})^2}\right) \mathbf{f}_b . \left[\frac{\partial \mathbf{s}}{\partial p^\gamma}\right] - \left(\frac{-1}{1-(\mathbf{d}.\mathbf{s})^2}\right) \mathbf{d}. \left[\frac{\partial \mathbf{s}}{\partial p^\gamma}\right] & p^\gamma \in \{{}^{12}\theta^a, {}^{12}\phi^a, {}^{12}\alpha^a, {}^{23}\theta^a, {}^{23}\phi^a, {}^{23}\alpha^a\} \end{cases} \tag{4.77}$$

The steps taken to determine the partial derivatives for the stage pole and its rotation matrix for the three plate problem are detailed in Section A.3.3, Appendix A.

Calculating partial derivatives for the transform data is a relatively straightforward task, as the misfits are dependent on only the first pole of motion, and from equation (4.53), $\frac{\partial \mathbf{p}^1}{\partial p^\gamma}$ is dependent on $\left({}^{12}\theta^1, {}^{12}\phi^1, {}^{12}\alpha^1, {}^{23}\theta^1, {}^{23}\phi^1, {}^{23}\alpha^1\right)$ only and equations defining the partial derivatives are detailed in Section A.3.2 of Appendix A.

4.6.3 Statistical analysis

With the extension of the method to 3 plates, there is no change in the overall inversion theory as detailed before, just an increase in the number of parameters. The distributions of the data

are still considered to be Gaussian and can be tested using q-q plots. The data importances are calculated just as before, from equation (4.74), with no further steps needing to be taken.

However, in order to determine the confidence intervals for the poles, a little more care needs to be taken. Equation (4.68) will determine the autocovariance matrix for the inversion, as with the 2-plate method. From this can be obtained the 3x3 submatrices that describe the covariances of each set of 3 pole parameters that are determined by the inversion. This is only possible for the first two sets of poles however, as the inversion was only solving for these parameters. Intuitively, there must be confidence intervals that exist for the third set of poles - if the other poles were known exactly, then of course, the third set would be defined exactly, but while there are uncertainties in the location of the first two sets, there will be corresponding uncertainties in the locations of the third set.

The problem for deriving a covariance matrix for a rotation pole obtained through the summation of a plate circuit was considered by both Jurdy & Stefanick (1987) and Chang (1988), for the exponential parametrisation of a rotation (Section 4.1.6) and a comparatively straightforward result obtained. For the (θ, ϕ, α) parametrisation used here, the corresponding formula was much more complex, and determined by Chang *et al.* (1990); Chang (1993) to be

$$\mathbf{D}\left[{}^{13}\mathbf{C}\right]\mathbf{D}^{\mathsf{T}} = \mathbf{G}\left[{}^{12}\mathbf{C}\right]\mathbf{G}^{\mathsf{T}} + \mathbf{F}\left[{}^{23}\mathbf{C}\right]\mathbf{F}^{\mathsf{T}} \tag{4.78}$$

where ${}^{13}\mathbf{C}$ is the covariance matrix for the rotation described by the pole parameters $({}^{13}\theta, {}^{13}\phi, {}^{13}\alpha)$, similarly for ${}^{12}\mathbf{C}$ and ${}^{23}\mathbf{C}$, and $\mathbf{D}$, $\mathbf{F}$ and $\mathbf{G}$ are 3x3 matrices determined from the parameters of the three rotations, and extremely complex.

However, this assumes only data from boundaries $1 \mapsto 2$ and $2 \mapsto 3$ are used in the determination of the poles, and through the combination of covariances given above, estimates of the covariances for ${}^{13}\mathbf{F}$ will be comparatively larger than those for the calculated poles ${}^{12}\mathbf{F}$ and ${}^{23}\mathbf{F}$, through the propagation of errors. It does not consider the effect of including data from the third plate boundary, as the problem they were considering was that of necessarily summing two rotations to obtain the relative rotation of the third relative to the first since no boundary existed between those two plates.

So, considering that it should make no difference to the result which direction the plate circuit is taken, or which two sets of parameters are used, it follows that the confidence ellipses for each

set of poles will be unchanged by the choice of plate pairs. If initially inverting for $1\mapsto 2$ and $2\mapsto 3$, the covariance matrix ${}^{23}\mathbf{C}$ should be identical (again, within operational error) to that obtained from inverting for $2\mapsto 3$ and $3\mapsto 1$. And so the covariance matrix ${}^{31}\mathbf{C}$ obtained from this second inversion should also be valid. The procedure was then to determine a solution $\tilde{\mathbf{p}} = \{{}^{12}\tilde{\mathbf{p}}, {}^{23}\tilde{\mathbf{p}}\}$ for the circuit $1\mapsto 2\mapsto 3$, and from the partial derivative matrix $\mathbf{A}(\tilde{\mathbf{p}})$, the covariance matrices ${}^{12}\mathbf{C}$ and ${}^{23}\mathbf{C}$ are obtained. The best-fit parameter set for $1\mapsto 3$, ${}^{13}\tilde{\mathbf{p}}$, is then determined from ${}^{12}\tilde{\mathbf{p}}$ and ${}^{23}\tilde{\mathbf{p}}$, and the circuit is then changed to $1\mapsto 3\mapsto 2$. The partial derivative matrix $\mathbf{A}(\tilde{\mathbf{p}}) = \mathbf{A}({}^{13}\tilde{\mathbf{p}}, {}^{32}\tilde{\mathbf{p}})$ is then calculated and from this, the covariance matrix ${}^{13}\mathbf{C}$ determined. (The parameter set ${}^{32}\tilde{\mathbf{p}}$ is the same as ${}^{23}\tilde{\mathbf{p}}$, except that the signs of the rotation angles are reversed). To check on this, the confidence regions obtained from calculations for each different plate circuit ($1\mapsto 2\mapsto 3$, $1\mapsto 3\mapsto 2$ and $3\mapsto 1\mapsto 2$) can be compared.

Chapter 5

A new set of finite rotation poles for the SAM-AFR-ANT 3-plate system

5.1 Inversion procedure

Once a complete set of data for a plate pair had been obtained, the next step was to prepare the data for use in the reconstruction routines.

5.1.1 Preparation of fracture zone data

For each fracture zone, a seed point needed to be obtained, from which to generate the synthetic flowline to which the fracture zone picks would be fitted. The best possible seed point was naturally the ridge-transform intersection for that fracture zone, corresponding to the zero-age point of the fracture zone and flowline. Sometimes this was not possible where a fracture zone was created by a ridge section no longer in existence. An example of this are the fracture zones in the Weddell Sea, which were created by parts of the South American-Antarctic Ridge which have since been subducted into the South Sandwich Trench. In other cases, the transform faults which gave rise to some fracture zones no longer exist, as a result of re-organisation and changes in segmentation on the ridge itself. Consequently, the locations of the corresponding ridge-transform intersections were not easily estimated, and these sections of fracture zone often began far from the ridge, so it would be highly speculative to attempt to determine a point along the ridge from where the fracture zone trace might have been generated. In these cases, a seed point needed to be located along the fracture zone, which would have to be at an age corresponding to one of the anomaly chrons used in the reconstruction. In this way, a non-zero-age seed point could be used just as easily to generate a flowline for the current poles.

Seed point locations for the ridge-transforms were best identified from the satellite gravity maps, where the ridge-transform locations were often clearly visible. Alternatively, if the fracture zone began in an area where there were several magnetic anomaly identifications for the central Brunhes anomaly, these could be used to determine the zero-age point. For fracture zones where it was not possible to pick a zero-age seed point, a little more work had to be done. In the best case scenario, an isochron pick on or close to the fracture zone was used to determine a seed point on the fracture zone. If the nearest isochron picks were not very close to the fracture zone, then the local direction of spreading needed to be considered and a theoretical isochron interpolated from picks to determine the intersection with the fracture zone. For these methods, it was important to ensure that anomalies on the younger flank of the fracture zone were used.

In other cases, if the fracture zone had a distinctive feature, such as a kink at a change of spreading direction, which was mirrored in a neighbouring fracture zone which had sufficient isochron picks in the proximity to be able to confidently determine an age for that feature, then this dating could be used to provide a seed point for the undated fracture zone at that feature. Some of these methods do appear to be somewhat subjective in the choice of seed and often the choice was made to exclude a fracture zone from the dataset if a satisfactory seed point could not easily be determined.

Any mistakes in setting a seed point soon become apparent as an inversion proceeds, and are easily rectified. In cases where there was a significant change in spreading direction, fracture zones which were badly dated gave rise to flowlines which clearly had a kink, or altered direction, in an obviously incorrect place, giving rise to substantial mismatches between the fracture zone and the synthetic flowline. This was often indicated by a large shift in the seed point, when the fracture zone processing routine was attempting to find a best-fit flowline for the fracture zone, and failing to reach a satisfactory solution within the allowed limits. If this occurred, then an attempt was usually made to find a more consistent seed for the fracture zone, but if this was not possible and the choice of the seed became too subjective, then that fracture zone was eliminated from the fracture zone data set.

Not all of the fracture zone picks made were used in the inversions: if a fracture zone section was particularly short in comparison to the rest in the dataset, then it was excluded; if there were a large number of fracture zones in a given region where the importance of the data was determined to be minimal, some of the least well-defined fracture zones were removed from the

dataset; and as stated above, if a satisfactory seed could not be determined for a fracture zone, it was excluded.

5.1.2 Preparation of magnetic data

After ensuring in the initial processing stages that an internally consistent set of anomaly picks had been obtained (*i.e.* no immediately obvious outliers), the important step was to split the data set up into groups that were created at the same ridge segment. This could be done by studying the fracture zones and splitting up any anomaly groups that were clearly separated by a large offset fracture zone. In many cases, in a region where there was a large set of anomalies of a particular age, any offset in the groups was clearly visible and so the division was clear. Because of the nature of the reconstruction routines, it was possible to make an anomaly grouping which only contained picks on one side of the ridge and yet not preclude the use of these picks in the inversion. However, it is preferable for a group to contain picks on both sides of the ridge in order to be able to carry out as much conjugate fitting as possible, and so one-sided groups were only constructed when this was unavoidable, usually where only one side of the ridge was in existence, such as in the Weddell Sea.

5.1.3 xsortdata

Once the basic picks had been made for both sets of data, *i.e.* sets of picks for a number of fracture zones and a large number of anomaly picks, then it was desirable to view the two sets of data together to enable the final preparation stages, detailed above, to be carried out. This would enable fracture zones to be 'dated' by viewing any isochron picks in the vicinity, and to group anomalies by studying whether any given group was separated by a mapped fracture zone.

To make these tasks easier a further program was written for X-Windows, **xsortdata**. All the magnetic picks are stored and loaded as a single file, and the fracture zone data loaded by initially reading in a single file listing the names and locations of all the individual fracture zone data files, and then loading each of these in turn. Both these sets of data are then displayed simultaneously on screen, set onto a flat-earth basemap. The magnetic picks are displayed as crosses, 'x' or '+', depending on which side of the ridge they are located, and the fracture zones displayed as lines linking the picks made for that fracture zone. The current ridge axis can also

be loaded, and is displayed as a thick dashed line.

Both sets of data can be edited and saved independently. When editing the magnetics dataset, using only the mouse and associated buttons, the picks can be split up into multiple ridge sections, containing as few or as many picks as required. At any time, all the picks in the current ridge section being edited are highlighted. Any other pick or group of picks can be added to the active group by dragging or clicking with the mouse, the choice of mouse button specifying on which plate the picks are considered to be. When all the desired editing of the magnetic picks has been carried out, the data can then be outputted as a single file, in which the data are split up into the ridge sections as chosen interactively, and is suitable for entry in the preprocessing stages of the inversion procedure. In addition to grouping the picks, this routine could be used to remove any spurious picks from the dataset. After studying the results of an inversion, the magnetics dataset can be directly re-entered into this routine to rearrange the groupings, sub-divide ridge sections further, or remove any obvious outliers.

When editing the fracture zone data, only one fracture zone is 'active' at any stage. When active, a new seed can be chosen for that fracture zone - this can be done by choosing the fracture-zone/ridge intersection from studying the intercept of the fracture zone with a digitised ridge which has been loaded into the program and displayed on screen. Alternatively, because all the magnetics data are displayed on screen simultaneously, the cursor can be used to query the chron (age) of any of the magnetics picks. Thus as discussed previously, the location of a magnetic anomaly isochron pick (or group) can be used to provide a non-zero-age seed for the fracture zone. In addition, any individual pick within the fracture zone could be removed from the dataset if it appeared that it was a bad pick, but replaced again if desired. If a fracture zone contained too few points to be useful, was too irregular to represent a likely flowline, or simply was too far from the ridge or any other magnetic picks to be a given a sufficiently reliable seed, then the fracture zone could be de-selected and removed from the dataset entirely.

When all the required sorting is completed, a new file is written, or the old file over-written, for each fracture zone for which details have been changed, and then a single file written listing the filenames for all the chosen fracture zones. Both are in the exact format required for the inversion routines, and can be used without any further alteration. As such, these files can be continually re-entered into the program to adjust any obviously incorrect seed points, or to remove individual picks within a fracture zone that are giving rise to large errors, or to remove

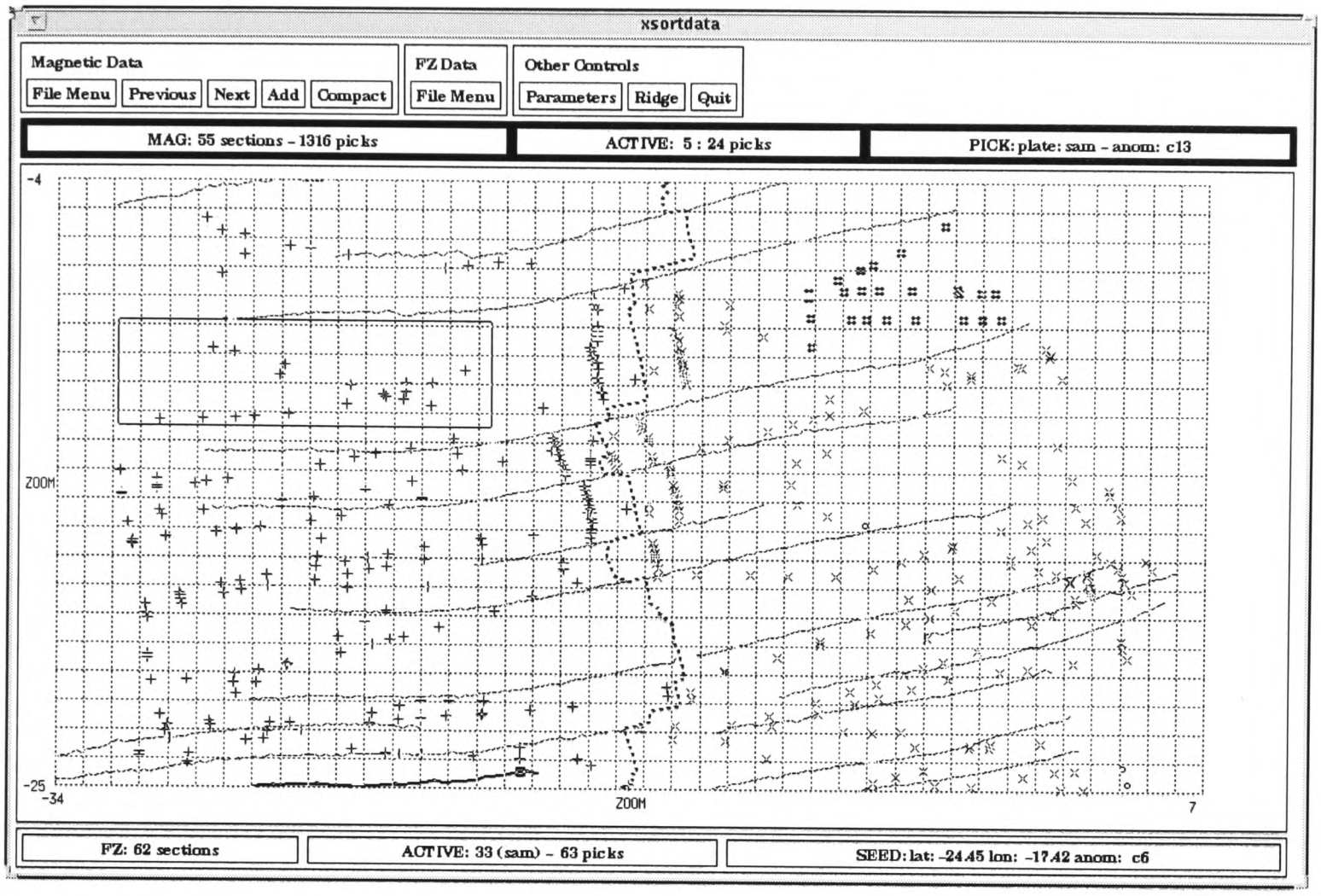

(a) Selecting a group of isochron picks.

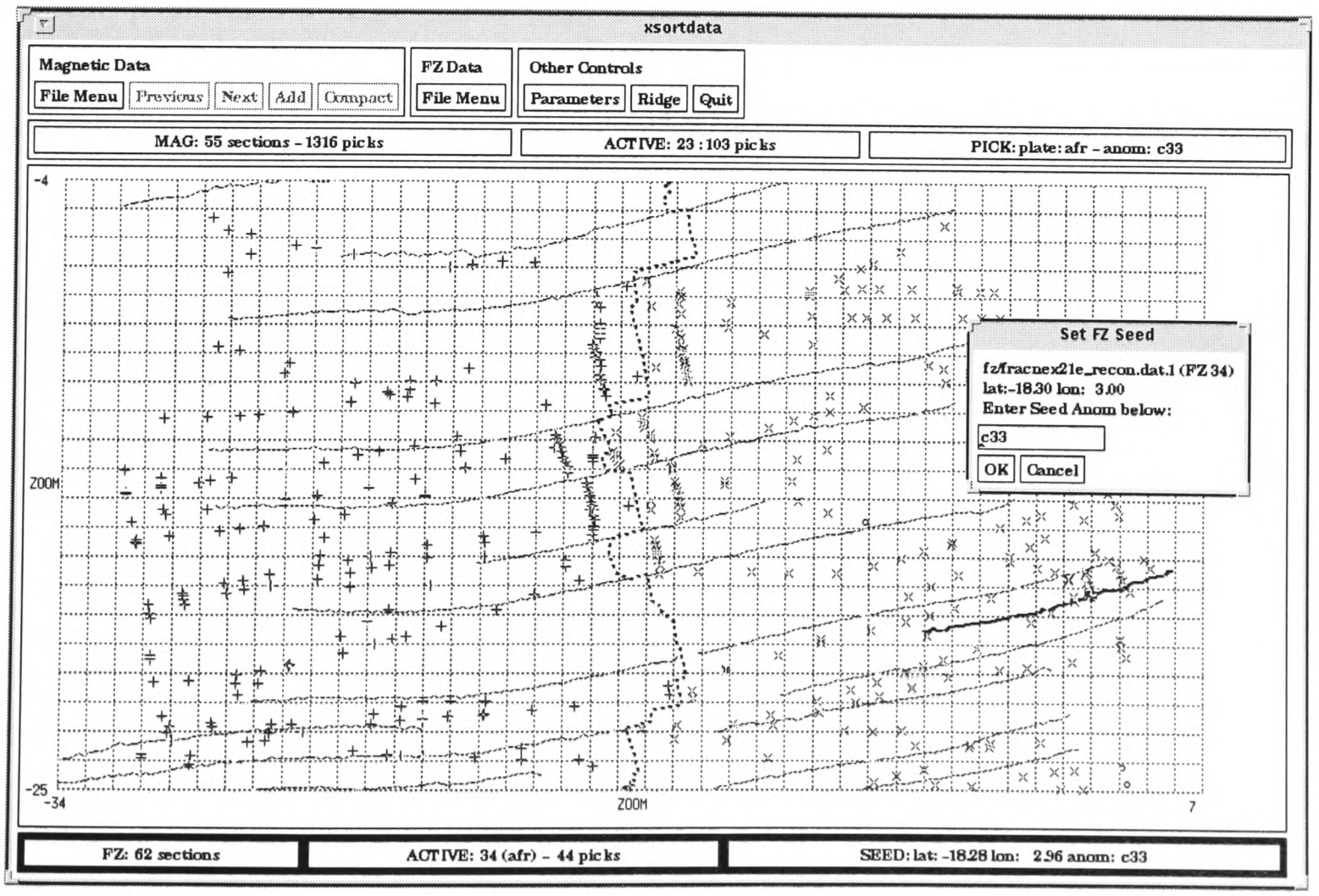

(b) Setting the reference 'seed' point for a fracture zone.

Figure 5.1: The interactive plate reconstruction data processing program **xsortdata** in use.

whole fracture zones from the inversion procedure.

5.1.4 Preprocessing of magnetic data

Once the magnetic data had been split up into sections, the next step was to preprocess the dataset so that it was in a format ready for entry into the iterative inversion routines. The most important function of this stage was to fit great circles to sets of anomaly picks, and to pair sets of picks with great circles to which they would be rotated during the inversion procedure. This was carried out by the FORTRAN routine **magprepro**, which did most of the required work automatically, taking a file consisting of anomaly sets grouped together within ridge sections, and fitting great circles wherever possible to each set of picks. The next stage was to allocate target great circles to each set of picks within a ridge section. If the choice was made to rotate only to conjugate isochrons, then this pairing was carried out automatically: if a isochron set had a conjugate set on the opposing flank, with 3 or more picks within the group such that a best-fit great circle could be fitted, then this was chosen as the target great circle, otherwise the set of picks was not used in the inversion.

In the case where there was no isochron set within the ridge section group containing more than two picks, then a single pair of picks within the ridge section was chosen to be used as a target great circle for all the isochron sets, for reasons described in Chapter 4. Thus for this case, some interactive input was required. A list of the sets of isochrons containing two picks was displayed, and one of these was then chosen as the pair most likely to provide a representative great circle (after studying the location of the picks with **xsortdata**), or if wished, the whole ridge section could be skipped and excluded from use in the inversion.

The output of the preprocessing was a single file containing lists of isochron picks and target great circles, ready for direct use in the inversion routines.

5.1.5 Iterative inversions

Once the datasets were in a suitable format for entry into the main inversion procedure, the files were transferred into a single working directory, and a series of iterative inversions carried out, until the solution had converged to within a certain tolerance. The iterative process is summarised by the flowchart shown in Figure 5.2, giving the names of the main programs used,

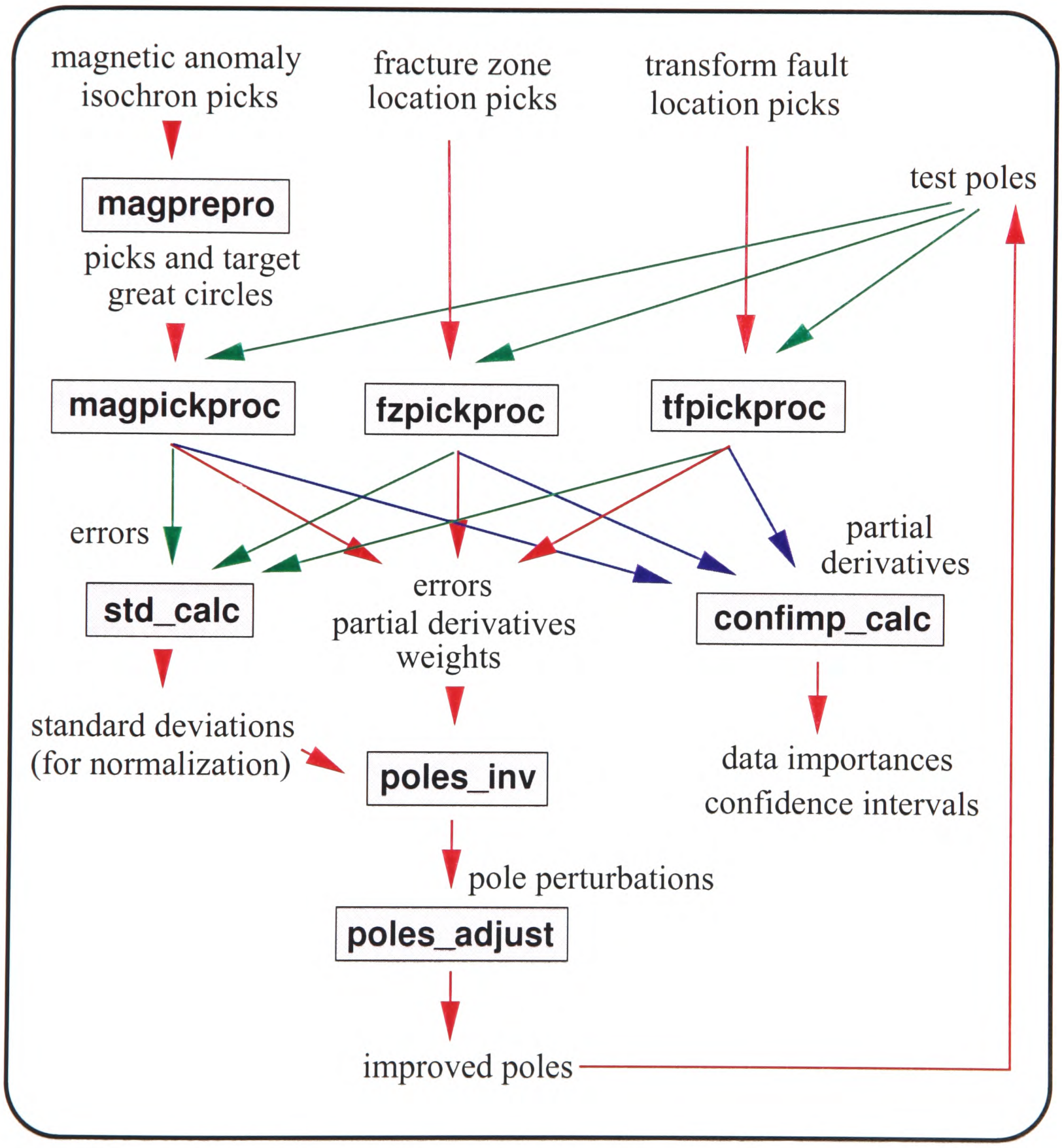

Figure 5.2: A flowchart showing the computational stages involved in the iterative inversion method.

and the main input/output of each routine. Further summaries of the programs can be found in Appendix B.

The reconstruction methods had been designed to allow biasing of the inversion towards a particular type of data, but in the event, this was not actually used because the only effect it appeared to have was to make the inversion converge quicker with respect to the favoured set of data, without necessarily improving the overall fit. The relative biases for each type of data, (β^{mag}, β^{fz} and β^{tf}) were all set equal to 1, and in addition, the cutoff criterion for each data type (Γ^{mag}, Γ^{fz} and Γ^{tf}) were also kept at the same value. For the first five or ten iterations, the data cutoff criteria was set to $\pm 5\sigma$, such that virtually all of the input data were used, and the weighting systems described in Section 4.4 'turned off' so that each datum was treated equally. This made sure that the choice of starting poles would have minimal effect so that the first few iterations would lead the inversion towards the solution which satisfied the majority of the data. The cutoff criterion was then reduced to $\pm 3\sigma$ and the weighting schemes reinstated. Although this excludes only the most extreme outliers, and means including a significant amount of data points that the q-q plots subsequently suggest were data outliers, their effect will be minimised by the weighting schemes. The reason for their continued inclusion was that for many areas, the distribution of the data was sufficiently sparse that it was felt that poor quality data was better than no data at all. For the determination of the confidence intervals of the final solution poles, the cutoff Γ was set to $\pm 1\sigma$, so that only the data representing a clear Gaussian distribution were used, though in fact it was found that this made little difference to the confidence intervals obtained. The parameters governing the behaviour of the damped least-squares inversion were kept the same for each individual reconstruction.

5.2 South America - Africa 2-plate reconstruction

For the SAM-AFR inversions, it was decided to rotate anomalies to their conjugate isochrons only, as this would increase the accuracy of the results obtained. This precludes the use of some of the data in the inversion, but the size of the magnetics dataset was still sufficiently large after removing redundant points that could not be fitted to conjugate great circles.

The set of solution poles obtained is displayed graphically in Figure 5.3. The entire sequence of poles is close to that of Shaw & Cande (1990), which is to be expected as similar datasets

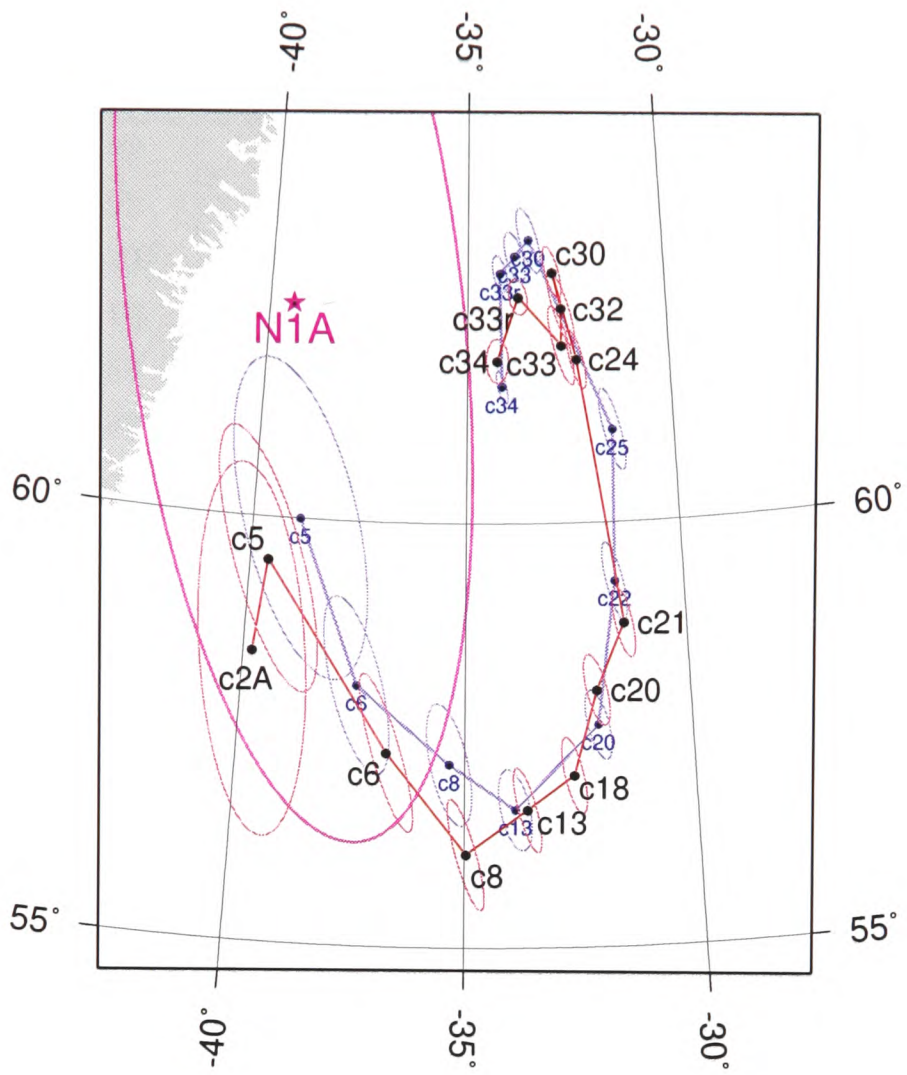

Figure 5.3: The set of solution poles obtained for SAM-AFR spreading shown in red, with corresponding 95% confidence ellipses. The poles and confidence ellipses obtained by Shaw & Cande (1990) are shown in light blue, and the NUVEL-1A instantaneous pole (N1A) in purple, for comparison.

---

were used, and in particular, a virtually identical set of magnetic anomaly isochrons was used. The grouping of the isochrons was different in some cases though, and the set of fracture zone locations was obtained through a different method. However, the general trend of the poles is very similar, though some of the chrons used in their inversion differ, Shaw & Cande (1990) inverting for c22, c25, whilst this inversion used c21, c24 and also included chrons c18 and c32.

For the majority of chrons in common, the poles lie very close to each other, with substantial overlap between the confidence intervals. The exception to this is for c33/c33r, though this is most likely due to the inclusion of c32 in my dataset, which will alter the nature of the flowlines, and hence solution poles in this section (c30-c32-c33). The other major difference is that the pole for c24 obtained here lies further to the north in the progression in poles than that obtained by Shaw & Cande (1990) for c25, which is not what would be expected. Both sets of poles predict a relatively significant shift in the poles of motion at this time (c30 to c21/22) but those of Shaw & Cande (1990) suggest the change occurred at around c30, whilst the poles determined here

Chron	Age (Ma)	Latitude	Longitude	Angle	95% confidence ellipsoid			
					Axis 1	Axis 2	Axis 3	Azimuth
c2A	2.58	58.42	-39.80	0.77	0.90	0.25	0.01	97.73
c5	9.74	59.50	-39.58	3.13	0.66	0.16	0.01	109.52
c6	19.05	57.29	-36.72	7.06	0.40	0.07	0.01	107.85
c8	25.82	56.10	-34.97	10.04	0.28	0.05	0.04	106.00
c13	33.06	56.63	-33.65	13.42	0.21	0.04	0.01	104.30
c18	38.43	57.03	-32.63	15.79	0.19	0.04	0.02	102.09
c20	42.54	58.03	-32.08	17.49	0.17	0.05	0.01	102.66
c21	46.26	58.81	-31.42	19.07	0.17	0.04	0.01	100.74
c24	52.36	61.91	-32.31	21.18	0.15	0.03	0.02	103.31
c30	65.58	62.92	-32.87	24.74	0.13	0.03	0.01	104.06
c32	71.07	62.50	-32.66	26.54	0.19	0.04	0.01	106.02
c33	73.62	62.07	-32.67	28.06	0.20	0.04	0.03	104.29
c33r	79.08	62.64	-33.74	30.99	0.09	0.04	0.01	100.76
c34	83.00	61.90	-34.26	33.49	0.10	0.05	0.01	90.43

Table 5.1: The solution poles obtained for the motion of Africa relative to South America. The 2 semi-major axes, 1&2, of the confidence ellipsoid lie almost entirely within the surface of the globe, representing the variation in pole location, with an orientation given by the azimuth (of Axis 1) in the table. The third axis effectively gives the variation in rotation angle.

suggest the major change occurred later at around c24. From studying the data importances for the fracture zone data (Figure 5.6), the fracture zones north of the equator have most effect on the poles, and the difference in the poles probably comes from the inclusion of different fracture zones in this region. As such, it is impossible to say that one set is more or less correct than the other. An inversion was attempted in which the fracture zones north of the equator were excluded, but this was found to degrade the overall quality of the solution.

The NUVEL-1A model is calculated for the instantaneous plate motion, out to the centre of c2A (DeMets *et al.*, 1990, 1994), and so it would be expected to lie close to the c2A pole obtained here. Both the c2A and c5 poles are within 5° of the NUVEL-1A instantaneous pole of motion (62.5°N, 39.4°W, 0.31°/Ma), and contained within the 95% confidence interval of this pole (though the reverse is not true). The NUVEL-1A pole has the additional constraints of earthquake fault plane solutions, which will often give a better indication of the true current direction of plate motion, however, the confidence interval is significantly larger. Because the series of poles appear to trace out a circular path, the c2A pole would be expected to continue in this pattern and lie to the NW of the c5 pole, but instead, it breaks from the pattern and lies to the SW. There is no obvious reason for this, and it must also be noted that the maximum

uncertainty for this pole is in the N-S direction, and there is considerable overlap between the 95% confidence interval and the approximate location for the c2A pole that would be predicted from the progression of poles. The location of the c2A pole is constrained by the transform data, which not used in the determination of the other poles, and so it could possibly be due to the delay between changes in spreading direction being manifested in the strike of transform faults, and the younger sections of fracture zones.

The set of solution poles obtained for South American - African spreading are given in Table 5.1. Although the confidence intervals displayed in Figure 5.3 are for a fixed rotation angle, for ease of display, details of the 95% ellipsoid (representing the variation in all 3 parameters) are given in the table.

The set of fracture zone data used in the inversion, along with a set of flowlines produced by the set of solution poles are shown in Figure 5.4. The synthetic flowlines are very smooth, with no abrupt changes in spreading direction visible, though to the north, closer to the poles of rotation, the change in spreading direction at around c24 can be seen. Inclusion of these northerly fracture zones in no way disrupted the fit to the southernmost fracture zones, and with the additional constraints they were found to provide on the solution poles, there was no evidence to suggest that these fracture zones did not represent South American - African spreading.

The final set of magnetic anomaly isochron picks used in the inversion, the great circles to which they were fitted, and the rotated picks are shown in Figure 5.5. The dataset is substantially reduced from the original dataset through the necessity to group the isochron picks within ridge sections, and the requirement of a minimum of three picks in an isochron group in order to fit a great circle. However, a large number remain, and as can be seen from the proximity of the rotated picks to the target great circles along the whole length of the ridge, the set of solution poles fits the dataset well.

The data importances for each set of data are shown in Figure 5.6. As mentioned previously, the fracture zone importances are greatest to the north, since these are closest to the poles of motion and hence reflect any changes in the poles more significantly than flowlines further away. Fracture zone picks in the older flowline sections (out to c34) also have larger data importances as not all of the fracture zones extend that far. For the magnetic anomaly picks, as expected, the importances are greatest for picks where few other picks for that chron exist, and naturally these data become very 'important' to the inversion. Importances are only calculated and displayed

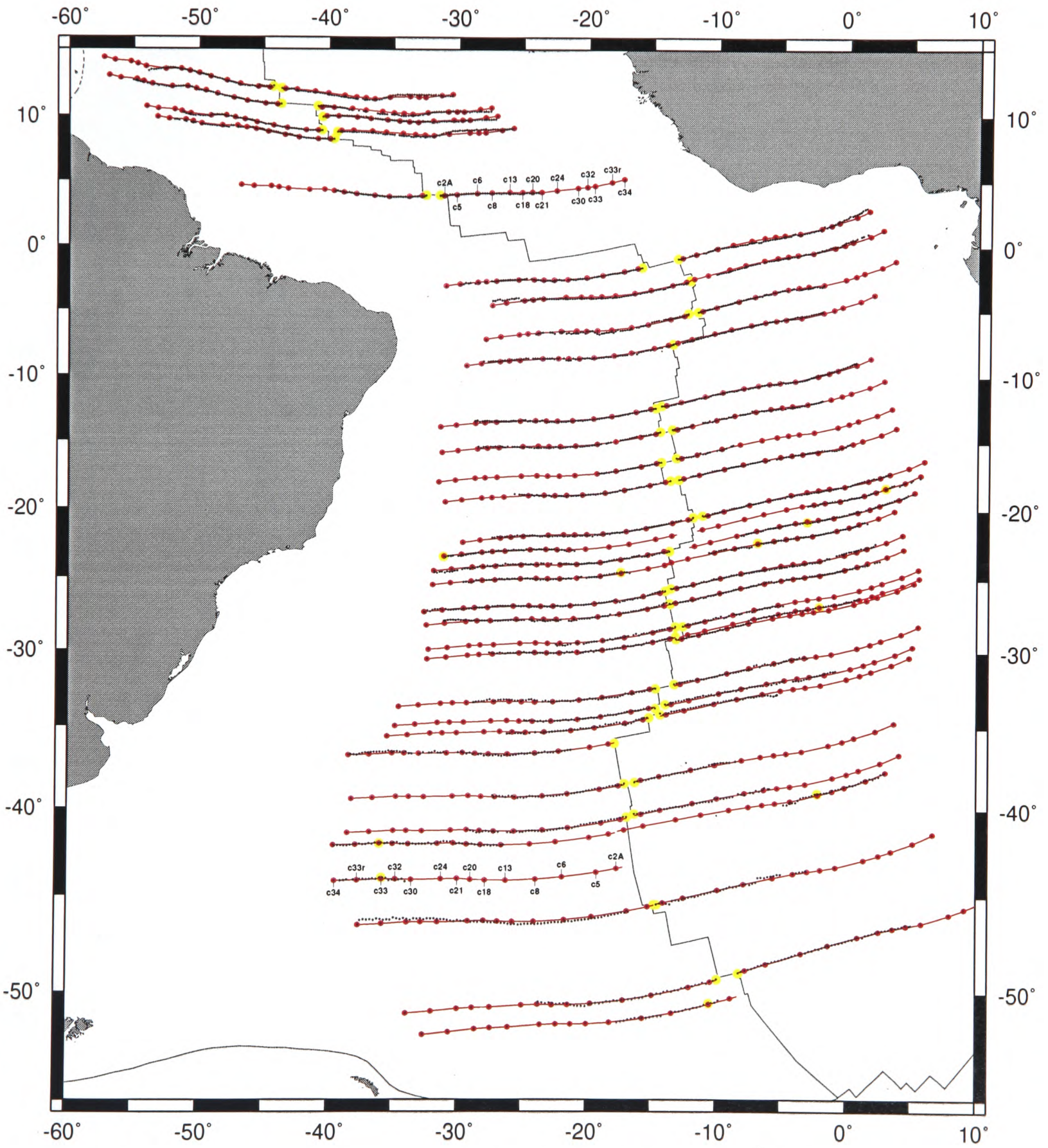

Figure 5.4: The selected set of fracture zone picks used in the inversion for SAM-AFR spreading, and the flowlines generated by the final solution poles. The fracture zone picks are marked by black stars, and the flowlines depicted by the red lines, with circles marking the end of each flowline stage. For two of the flowlines, the corresponding chrons for each flowpoint are labelled. The seed points from which each flowline is generated are marked by yellow circles.

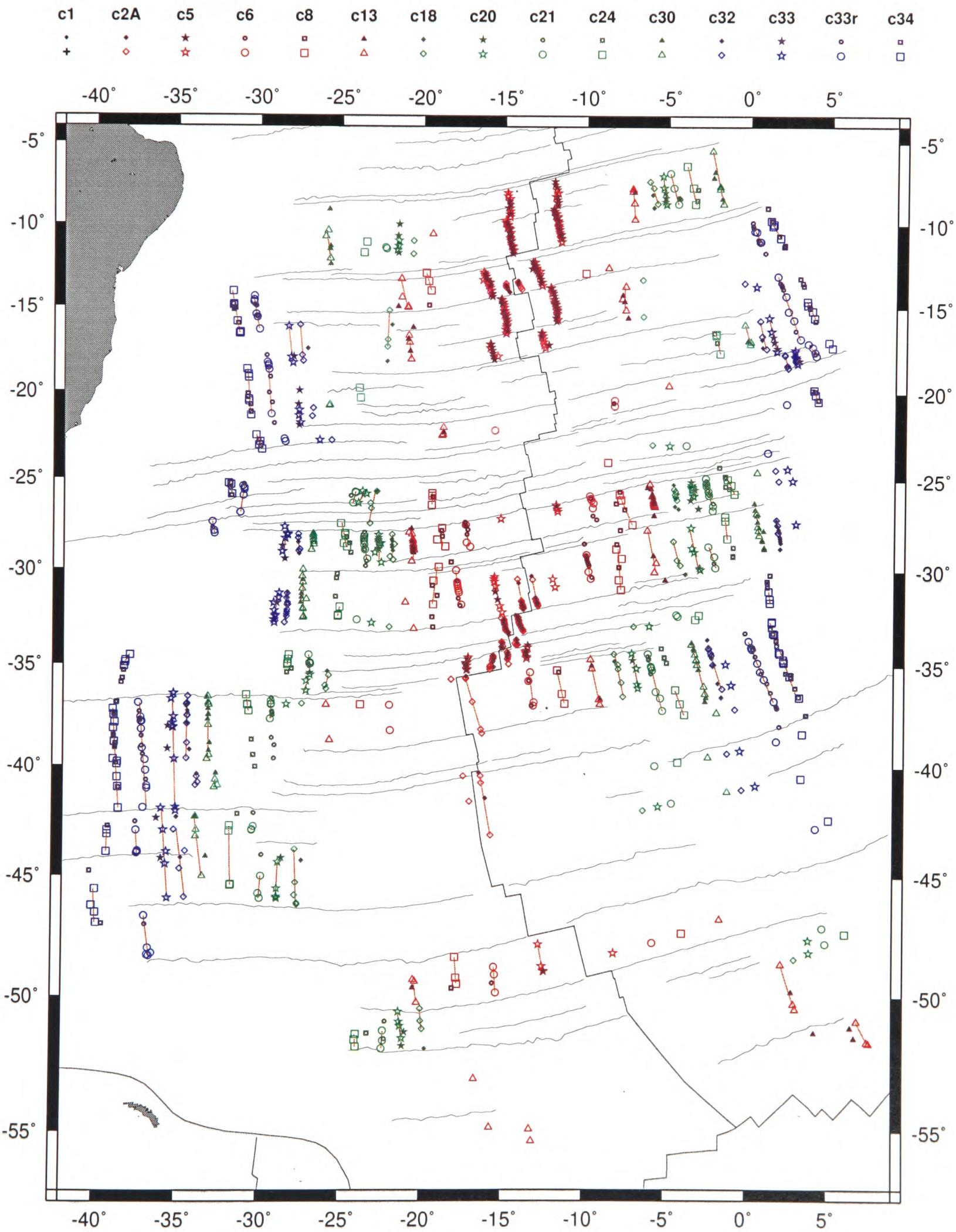

Figure 5.5: The anomaly picks used in the inversion for SAM-AFR spreading, with the fitted great circles shown in orange, the positions of the unrotated picks and picks used to fit great circles represented by the same symbol scheme as used previously, and the rotated picks shown as smaller, darker symbols.

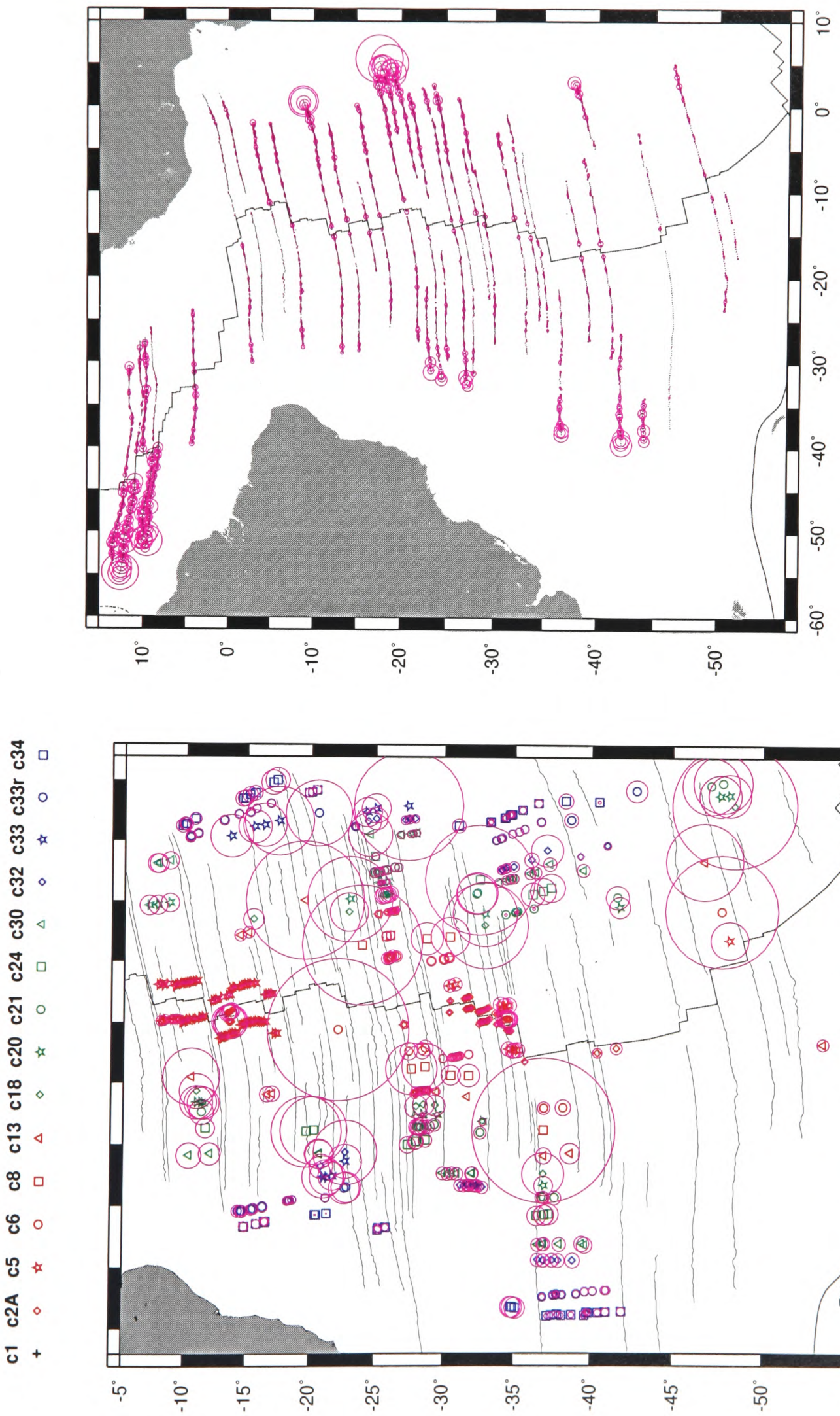

Figure 5.6: The data importances of the magnetic anomaly picks and fracture zone locations used in the inversion for SAM-AFR spreading. The fracture zone picks are marked by small crosses, and magnetic anomaly picks by the corresponding symbol, with the importance of each pick represented by a circle centred at the location of the pick with a radius proportional to the corresponding data importance.

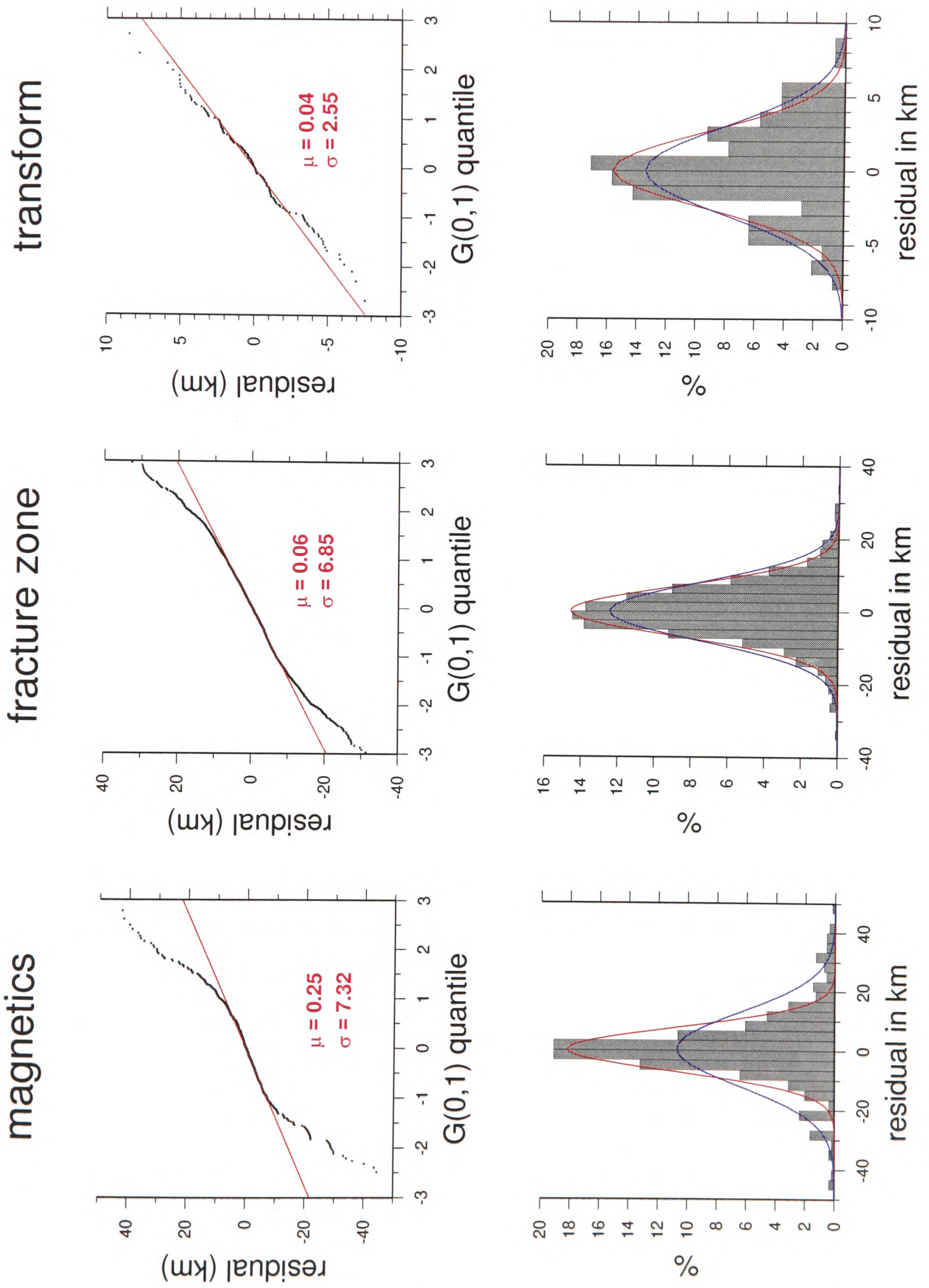

Figure 5.7: Quantile-quantile (q-q) plots and histograms for the residuals for each type of data used in the inversion for SAM-AFR spreading. In the q-q plots, the red line represents the best fit line, through linear regression, for the central $\pm 1\sigma$ of the test distribution (Gaussian(0,1)). In the histograms, the red line represents the Gaussian distribution defined by the statistics obtained from the q-q plots, and the blue line represents the Gaussian distribution with statistics defined by the the sample mean and standard deviation of the dataset.

for the picks that are being rotated, and not the target great circles, though in effect, the value actually represents both the importance of the pick and the great circle to which it is fitted.

The distributions of the residuals for each set of data are shown in Figure 5.7. For each dataset, a quantile-quantile plot is displayed, showing the best-fit straight line for the data within a standard deviation of the mean of the test distribution. Below, a histogram of the residuals is plotted, with a line drawn showing the distribution that would be expected from the estimates of the standard deviation (σ) and mean (μ) obtained from the quantile-quantile plots. The Gaussian distribution with mean and standard deviation equal to that of the sample mean and standard deviation is also displayed, but in each case it gives a broader distribution which doesn't appear to fit the sample distribution as well as the q-q Gaussian model. The fracture zone residuals have the closest to a Gaussian distribution, with far fewer outliers, when compared to the distribution of magnetic anomaly residuals, as would be expected.

5.3 Antarctica - Africa 2-plate reconstruction

Although both flanks are present in this region, there are not really sufficient data to fit only to conjugate isochrons, as this would result in only 5 or so data in the whole dataset for some of the chrons for which the inversion was being run. So, in order to use as much of the available data as possible in this area, non-conjugate fitting was used for the magnetics dataset. Whilst incorporating a greater amount of data, this would still, through the weighting system, favour the data which represented conjugate fitting.

The sequence of solution poles obtained is displayed graphically in Figure 5.8. The NUVEL-1A pole and the pole for c2A obtained here lie very close together, in fact surprisingly so, considering the size of the confidence intervals for both poles. Royer *et al.* (1988) inverted only for poles for c20 and older, holding that the pole of motion since then has been fairly constant. That belief is substantiated through the poles derived here, with all of the poles from c6 to c21 clustered very close together, at around 10° N, 40° W, with considerable overlap between the confidence intervals. The poles for c2A and c5 (and the NUVEL 1A pole) are slightly away from this group, suggesting there may have been a slight change in spreading direction in recent times, but the confidence ellipses are also significantly larger and so this may not in fact be a 'real' feature. The sequence of poles shows that poles of motion slowly migrated from c34 to c33, after which

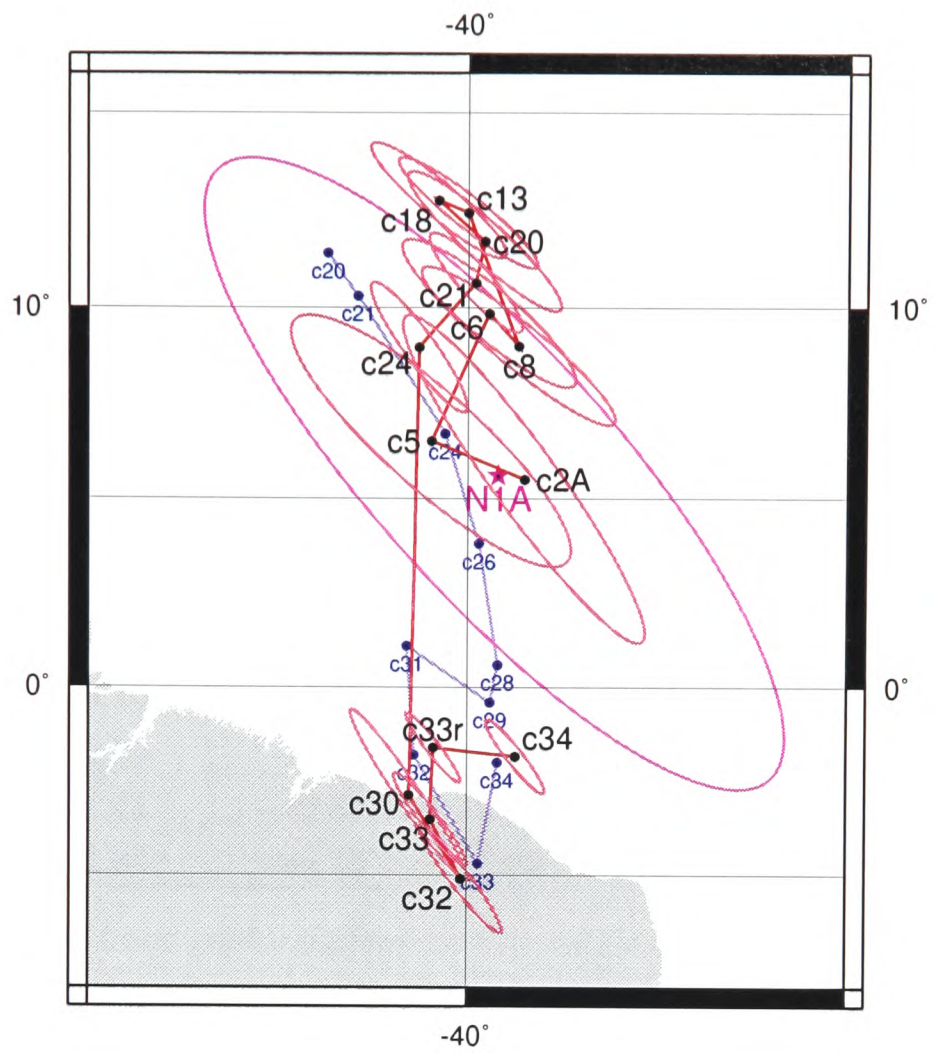

Figure 5.8: The set of solution poles obtained for ANT-AFR spreading shown in red, with corresponding 95% confidence ellipses. The poles and confidence ellipses obtained by Royer *et al.* (1988) are shown in light blue, and the NUVEL-1A instantaneous pole (N1A) in purple, for comparison.

---

the pole of motion remained virtually constant until c30 (taking the confidence intervals into consideration). There was a large change from c30 to c24, reflected in the large curve in the flowlines in the region, but by c21, the pole of motion had stabilised again, and as mentioned above, has not significantly changed since then.

Royer *et al.* (1988) did not present formal confidence intervals for their poles and so direct comparison is not entirely possible. However, the poles do show the same pattern of migration from south to north through time, though they inverted for a larger number of chrons from c29 to c21, and for this period, the progression is shown much smoother. It is important to note that although Royer *et al.* (1988) had a larger magnetics dataset available, and only used a form of conjugate fitting, no fracture zone data were used in the inversion, and so the poles presented here have the additional constraints provided by the flowlines.

The set of solution poles obtained for Antarctica - Africa spreading are given in Table 5.2. As before, values for the 95% confidence ellipsoid are given in the table, whereas the confidence

Chron	Age (Ma)	Latitude	Longitude	Angle	95% confidence ellipsoid			
					Axis 1	Axis 2	Axis 3	Azimuth
c2A	2.58	5.50	-38.50	0.39	2.16	0.35	0.01	126.02
c5	9.74	6.51	-40.95	1.47	1.95	0.51	0.01	138.52
c6	19.05	9.85	-39.45	3.23	1.18	0.26	0.02	140.07
c8	25.82	9.00	-38.66	3.88	1.31	0.24	0.03	141.14
c13	33.06	12.44	-40.00	5.62	0.92	0.16	0.02	142.03
c18	38.43	12.76	-40.78	6.88	0.91	0.18	0.02	139.99
c20	42.54	11.71	-39.57	7.60	1.07	0.20	0.02	137.96
c21	46.26	10.64	-39.81	8.48	0.70	0.16	0.02	132.87
c24	52.36	8.96	-41.29	9.78	0.85	0.16	0.02	126.02
c30	65.58	-2.87	-41.53	11.88	1.12	0.12	0.03	124.12
c32	71.07	-5.10	-40.16	13.35	0.73	0.11	0.02	127.00
c33	73.62	-3.52	-40.97	13.82	0.64	0.10	0.03	127.57
c33r	79.08	-1.61	-40.89	15.82	0.48	0.07	0.02	127.65
c34	83.00	-1.84	-38.73	17.92	0.51	0.09	0.02	128.12

Table 5.2: The solution poles obtained for the motion of Africa relative to Antarctica.

intervals (ellipses) displayed in Figure 5.8 are for a fixed rotation angle.

The set of fracture zone data used in the inversion, along with flowlines produced by the solution poles are shown in Figure 5.9. The flowlines remain relatively smooth throughout, even though they incorporate quite significant changes in spreading direction. As the sequence of poles suggests, the direction of motion appears quite steady up until around c32-c30, when the motion begins to change from NNE-SSW around to the NW-SE motion seen from c30-c24, after which it begins to return to the original spreading direction, and from c21 until the present, the spreading has remained in the prevailing NNE-SSW direction. Some of the flowlines do not begin exactly at the ridge, but mostly this is due to changes in ridge orientation and the 'dying-out' of fracture zones, and in some cases arises from the difficulty in identifying active ridge segments, particularly in the region of the A.Bain and Prince Edward fracture zones.

West of around 15°E, the fracture zones along the Southwest Indian Ridge are very short in length, having been created comparitively recently by the (relative) westwards propagation of the Bouvet Triple Junction. Similarly, towards the eastern end of the ridge, east of around 42°E, the fracture zones do not seem to extend beyond the anomaly 24 node on the synthetic flowlines, and the implications of this are discussed later.

The final set of magnetic anomaly isochron picks used in the inversion and the great circles

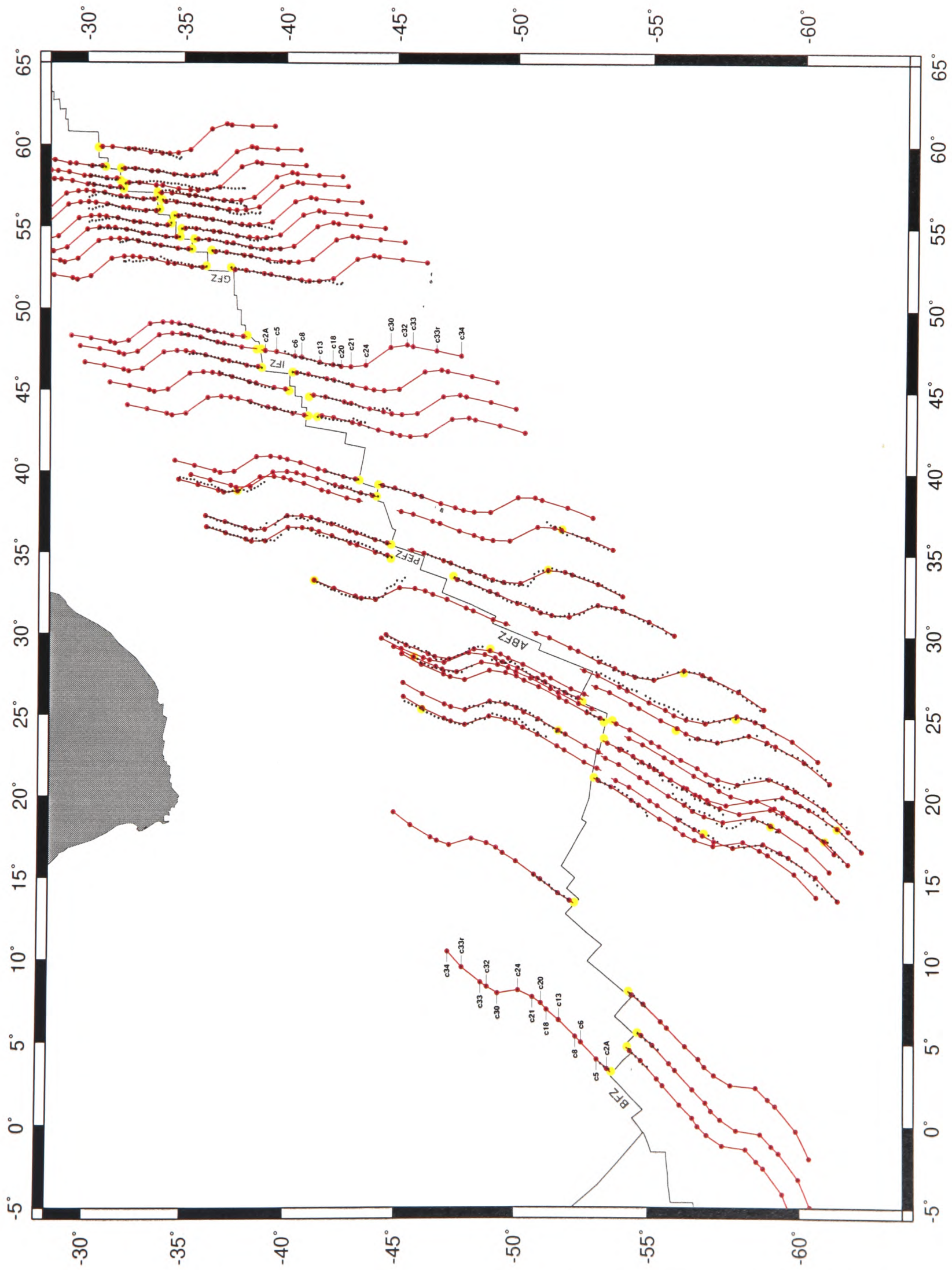

Figure 5.9: The fracture zone picks used in the inversion for ANT-AFR spreading, and the flowlines generated by the final solution poles. The fracture zone picks are marked by black stars, and the flowlines depicted by the red lines, with circles marking the end of each flowline stage. The seed points from which each flowline is generated are marked by yellow circles. (Annotation abbreviations: BFZ-Bouvet Fracture Zone; ABFZ-A.Bain Fracture Zone; PEFZ-Prince Edward Fracture Zone; DFZ-Discovery Fracture Zone; GFZ-Gallieni Fracture Zone.)

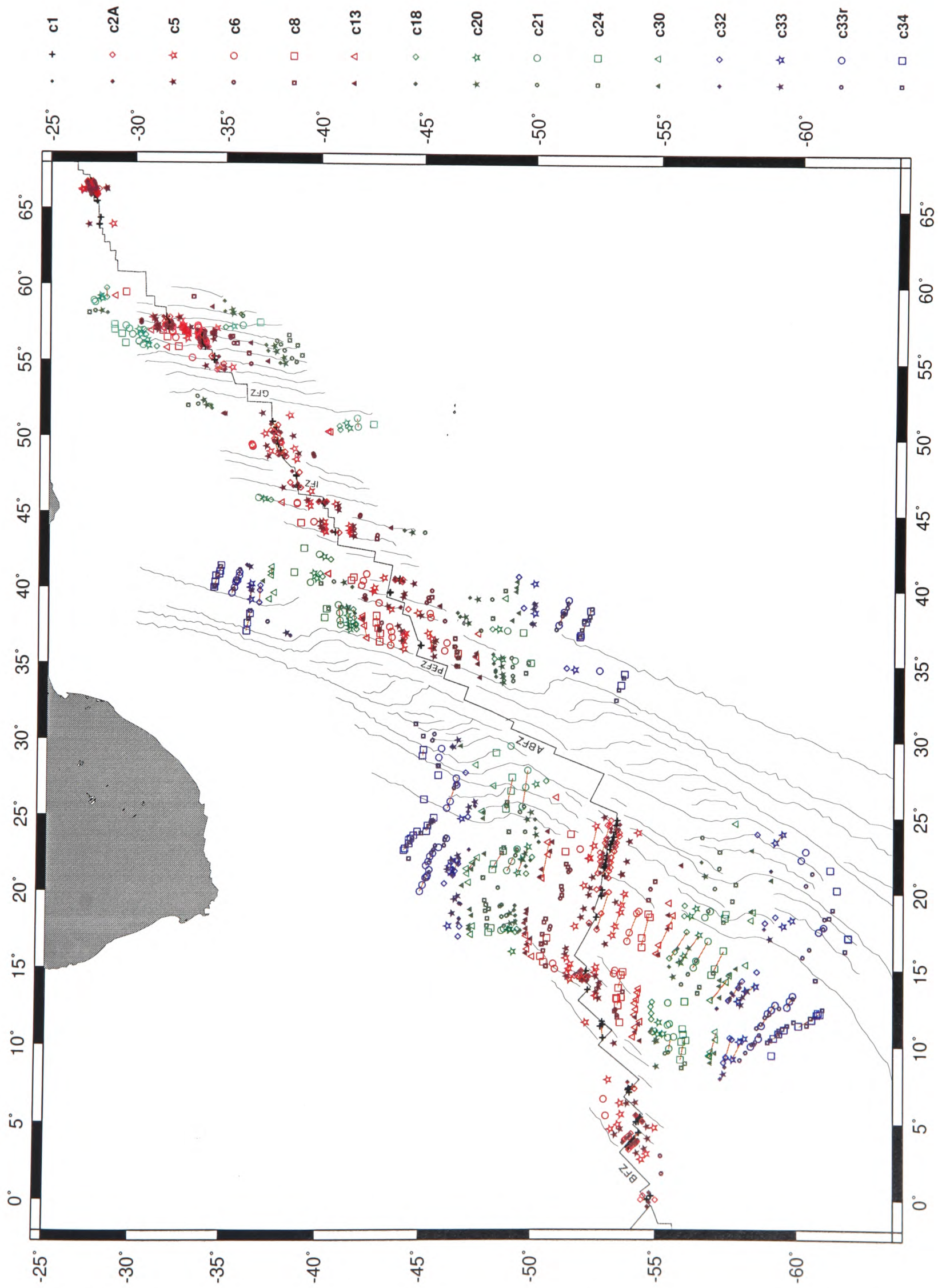

Figure 5.10: The anomaly picks used in the inversion for ANT-AFR spreading, with the fitted great circles shown in purple, the positions of the unrotated picks and picks used to fit great circles shown as solid symbols, and rotated picks shown as fainter dotted symbols. (Annotation abbreviations: BFZ-Bouvet Fracture Zone; ABFZ-A.Bain Fracture Zone; PEFZ-Prince Edward Fracture Zone; DFZ-Discovery Fracture Zone; GFZ-Gallieni Fracture Zone.)

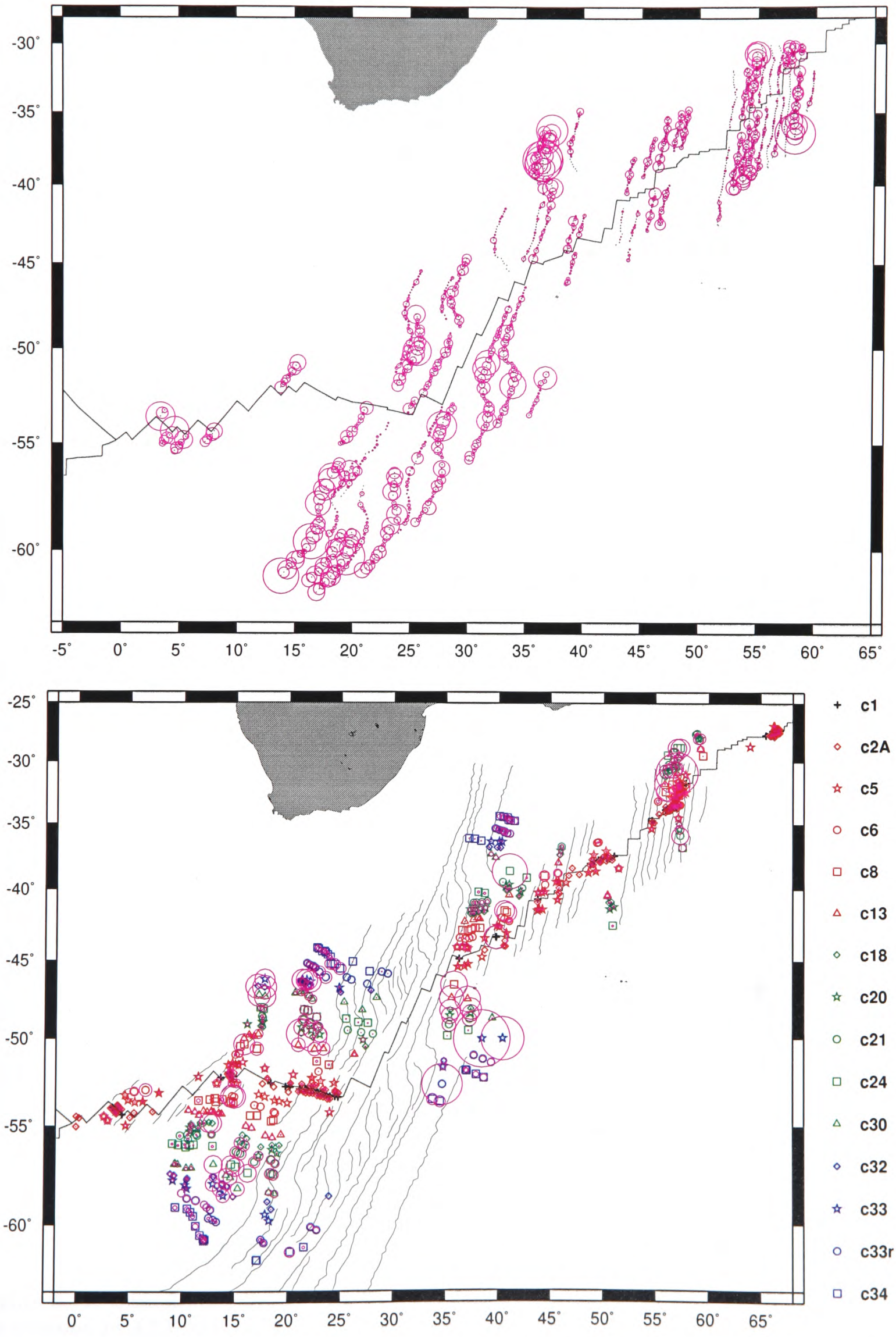

Figure 5.11: The data importances of the magnetic anomaly picks and fracture zone locations used in the inversion for ANT-AFR spreading. The fracture zone picks are marked by small crosses, and magnetic anomaly picks by the corresponding symbol, with the importance of each pick represented by a circle centred at the location of the pick with a radius proportional to the corresponding data importance.

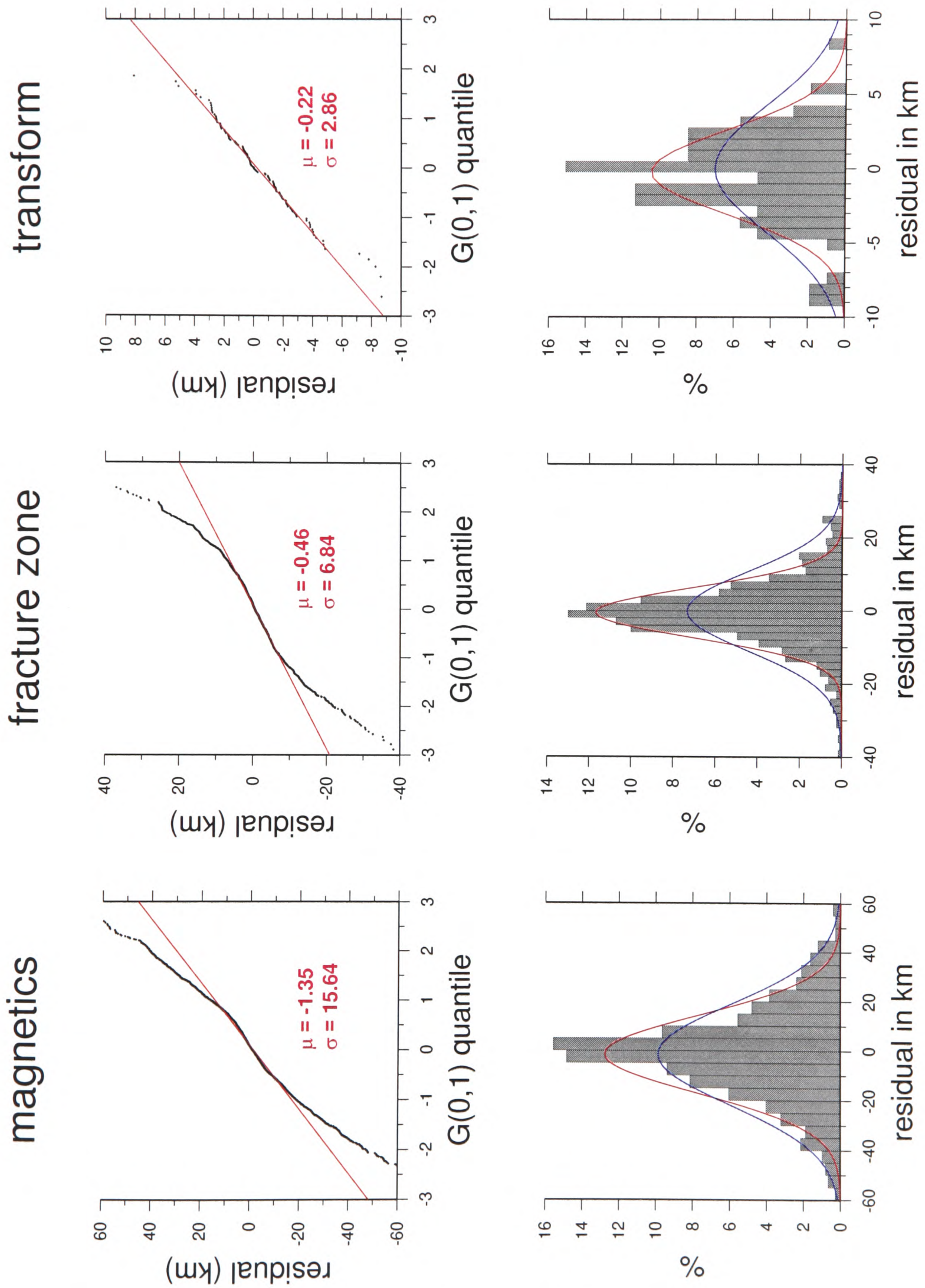

Figure 5.12: Quantile-quantile (q-q) plots and histograms for the residuals for each type of data used in the inversion for ANT-AFR spreading. In the q-q plots, the red line represents the best fit line, through linear regression, for the central $\pm 1\sigma$ of the test distribution (Gaussian(0,1)). In the histograms, the red line represents the Gaussian distribution defined by the statistics obtained from the q-q plots, and the blue line represents the Gaussian distribution with statistics defined by the the sample mean and standard deviation of the dataset.

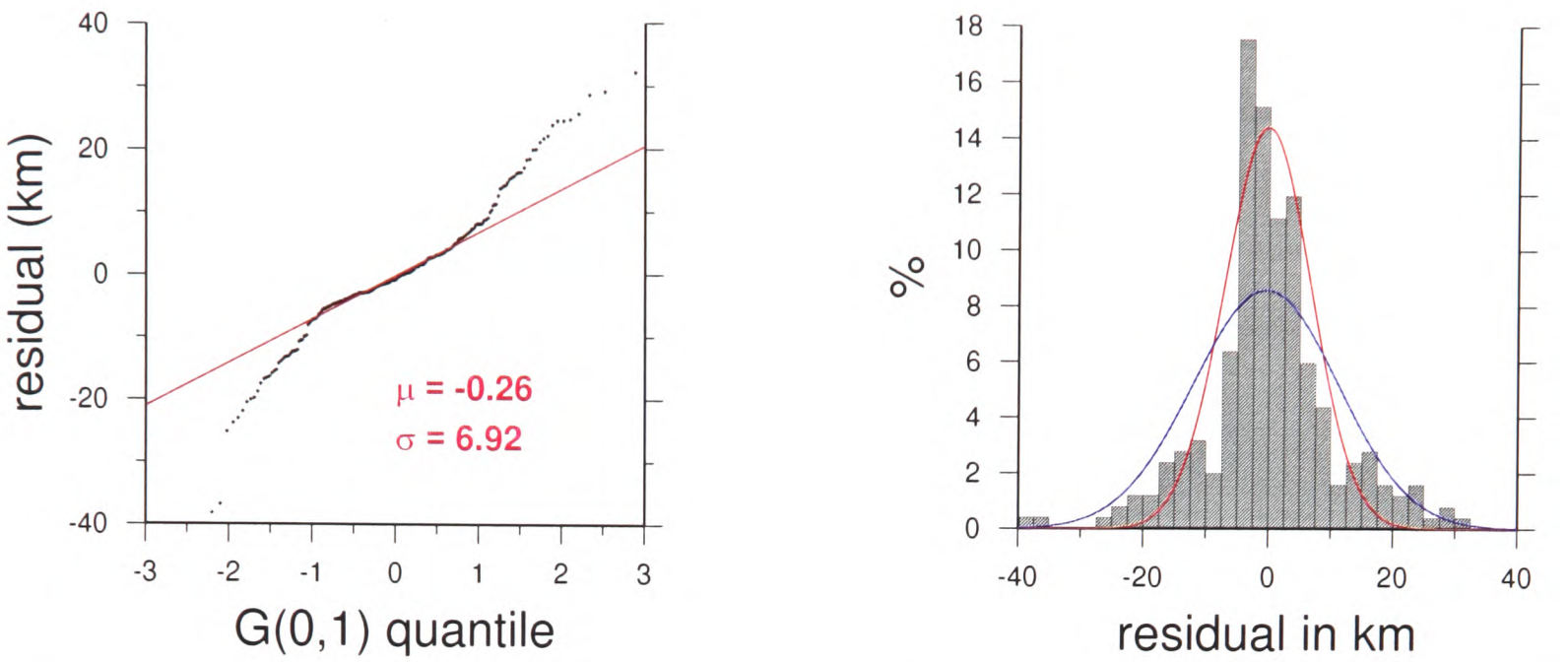

Figure 5.13: The quantile-quantile plot and histogram for the residuals of the magnetic isochron data along the Southwest Indian Ridge, using the poles obtained from the full ANT-AFR inversion, but fitting isochron picks only to their conjugate anomalies.

---

to which they were fitted are shown in Figure 5.10. As the isochron picks were mostly rotated to non-conjugate great circles, displaying the complete set of rotated picks used for fitting would be confusing. Instead, each isochron is rotated onto the opposing flank in Figure 5.10, as if it were being rotated to a conjugate isochron, which should give a clearer indication of the fit of the data to the model. As such, the picture is not so clear as it was for the SAM-AFR dataset, but the general match between the anomalies can be seen. Very little information is reaped from the vicinity of the A Bain Fracture Zone (25° E to 35 ° E) since the region has such a complicated seafloor morphology, it is hard both to identify anomaly sequences and to group them together as being created at the same ridge segment.

The data importances for each dataset are displayed in Figure 5.11. The variation of importances is much more evenly distributed for the fracture zone dataset than it was for the SAM-AFR dataset, with large importances appearing at both ends of the ridge and both to the north and south. The magnetic anomaly importances follow the same pattern as before, and as would be expected, the largest importances appear where an anomaly for a given chron is relatively isolated.

The distributions of the residuals for each set of data are shown in Figure 5.12. The fracture zone residuals again have the closest to the Gaussian distribution predicted by the sample statistics from the q-q plot, with a standard deviation almost identical to that of the SAM-AFR fracture zone residuals, though the fit to the Gaussian model is not quite as good. The standard

deviation of the magnetics dataset is much greater than that for the SAM-AFR magnetic anomaly residuals. This is due to the fact that the magnetics picks were being rotated to non-conjugate isochrons, and as such, non-random sources of errors could be introduced in the form of oblique and asymmetric spreading. Both these effects, if observed, would increase the distribution of errors around the best-fit solution. In addition, significant changes in spreading direction also lead to a general increase in the errors when fitting to non-conjugate isochrons.

To show that the greater standard deviation of the magnetics dataset was more due to the consequences of non-conjugate fitting as opposed to a significantly poorer set of data, another final run was carried out for ANT-AFR spreading, but only rotating the magnetics picks to conjugate isochrons where they existed, giving the distribution of errors shown in Figure 5.13. The fit of the data is much improved, with a standard deviation which is almost half of that determined for the main inversion, and comparable to that of the SAM-AFR residuals.

5.4 South America - Antarctica 2-plate reconstruction

As with the ANT-AFR inversion, non-conjugate magnetics fitting was used for the SAM-ANT inversion. The was necessary because of the total lack of any data on the South American flank west of the South Sandwich Trench, which was primarily the reason for the development of the one-sided fitting method. Due to the lack of a suitable number of c24 picks in the region, in particular in the Weddell Sea, where it proved impossible to identify any clear c24 anomalies, this chron was not included in the inversion, as the constraints on this pole would be minimal and could possibly disturb the accuracy of the other poles obtained.

The set of solution poles and confidence intervals is shown graphically in Figure 5.14, along with the poles of Barker & Lawver (1988), and also the instantaneous pole for SAM-ANT motion from the NUVEL-1A model. In common with the other 2-plate systems, the poles of motion from c34 to c30 appear to have been quite stable, followed by the major change in pole location from c30 to c21, which corresponds to the kink in the flowlines seen in the northern Weddell Sea. The sequence of poles from c21 to c8 represent a smooth migration westward, suggesting another substantial period of time during which the variation in spreading direction remained relatively constant. The young poles determined in this model, certainly those prior to c8, are poorly constrained, due to the short length of active mid-ocean ridge, as reflected in the large

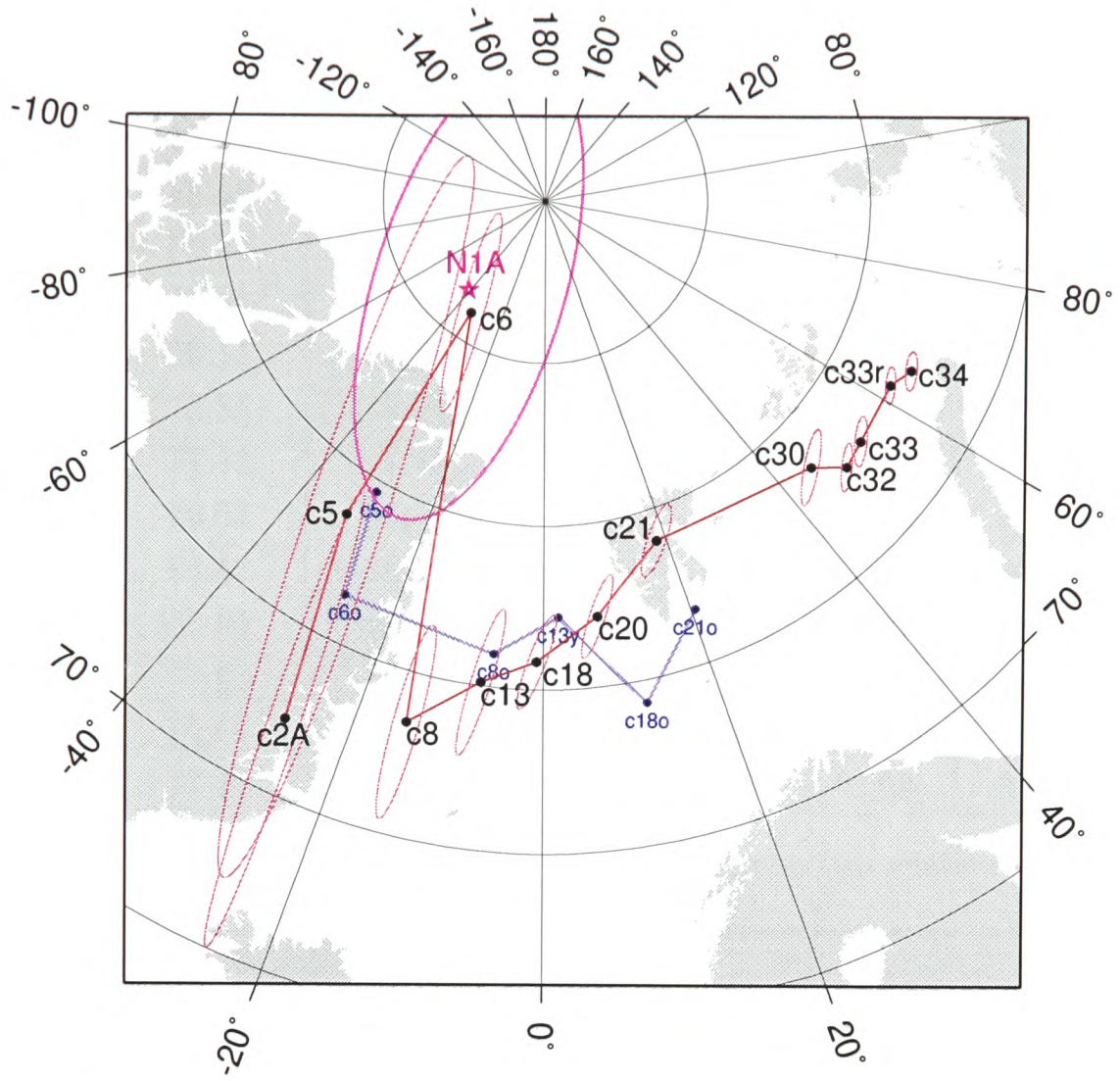

Figure 5.14: The set of solution poles obtained for SAM-ANT spreading shown in red, with corresponding 95% confidence ellipses. The poles and confidence ellipses obtained by Barker & Lawver (1988) are shown in light blue, and the NUVEL-1A instantaneous pole (N1A) in purple, for comparison.

---

ellipses of the 95% confidence intervals. The ellipses are elongated in a direction perpendicular to the flowlines for this reason, a large variation in latitude for any of the young poles would have little noticeable effect on the azimuths of the flowlines over such a short ridge section. The c6 pole does appear to be significantly away from the progression of the poles, and as there does not appear to be a change in the flowlines along the South American-Antarctic Ridge at that time, it could be that this is in error, although it does lie close to the NUVEL-1A pole. The confidence interval for this pole is relatively small, but this is because the confidence intervals are derived from the errors in the data, and when there is only a small amount of data for any particular chron, it may be simple to obtain a reasonable fit, but due to the limited distribution of the data, the pole and confidence intervals may not be completely realistic.

Although the youngest (c2A, c5) poles are not particularly close to the NUVEL-1A pole, they are displaced in a direction parallel to the large uncertainty in the poles, and the c5 confidence interval overlaps quite considerably with the confidence interval of the instantaneous pole. The

Chron	Age (Ma)	Latitude	Longitude	Angle	95% confidence ellipsoid			
					Axis 1	Axis 2	Axis 3	Azimuth
c2A	2.58	72.25	-26.48	0.60	2.97	0.19	0.02	97.69
c5	9.74	78.60	-32.21	2.47	4.75	0.48	0.02	103.65
c6	19.05	85.88	-33.56	6.79	1.31	0.16	0.04	107.86
c8	25.82	73.48	-14.73	7.35	1.25	0.16	0.05	89.16
c13	33.06	75.11	-7.39	10.26	0.97	0.12	0.04	80.13
c18	38.43	75.85	-0.79	12.46	0.64	0.11	0.05	70.10
c20	42.54	77.15	7.47	14.02	0.57	0.10	0.05	64.53
c21	46.26	79.02	18.47	16.42	0.51	0.11	0.05	53.02
c30	65.58	78.43	45.32	19.31	0.55	0.09	0.06	34.29
c32	71.07	77.64	48.92	22.31	0.36	0.07	0.06	35.72
c33	73.62	77.80	53.07	23.76	0.39	0.08	0.07	32.21
c33r	79.08	77.97	62.23	27.29	0.30	0.06	0.05	23.91
c34	83.00	77.59	65.42	29.16	0.34	0.08	0.06	20.15

Table 5.3: The solution poles obtained for the motion of Antarctica relative to South America.

poles determined by Barker & Lawver (1988) only go as far back as anomaly 21, and no confidence intervals were determined for these poles, so little comparison can be made. However, the series of poles are certainly close, and differences may arise from the fact that the poles of Barker & Lawver (1988) were obtained as part of a rudimentary 3-plate inversion, where the majority of the dataset was from other ridges in the SAM-AFR-ANT plate circuit, whereas this inversion is using only data from the South American-Antarctic Ridge. The actual solution poles obtained for South America - Antarctica spreading are given in Table 5.3.

The set of fracture zone data used in the inversion, along with a set of flowlines produced by the set of solution poles are shown in Figure 5.15. The final set of magnetic anomaly isochron picks used in the inversion and the great circles to which they were fitted are also shown, since for the majority of the region, no conjugate flank exists, and showing the location of magnetics picks rotated to their conjugate flanks would be of little use in showing the fit of the data. The flowlines show fairly steady east-west spreading since anomaly 6, before which spreading was more SE-NW. However this may not be such an abrupt change because the anomaly 6 pole does seem a little out of line, compared with the rest of the poles and so the change in spreading direction may well be much smoother.

South of the present-day ridge, in the northern Weddell Sea, the youngest section of the synthetic flowlines (back as far as c6/8) do not align at all well with the observed fracture zone trends

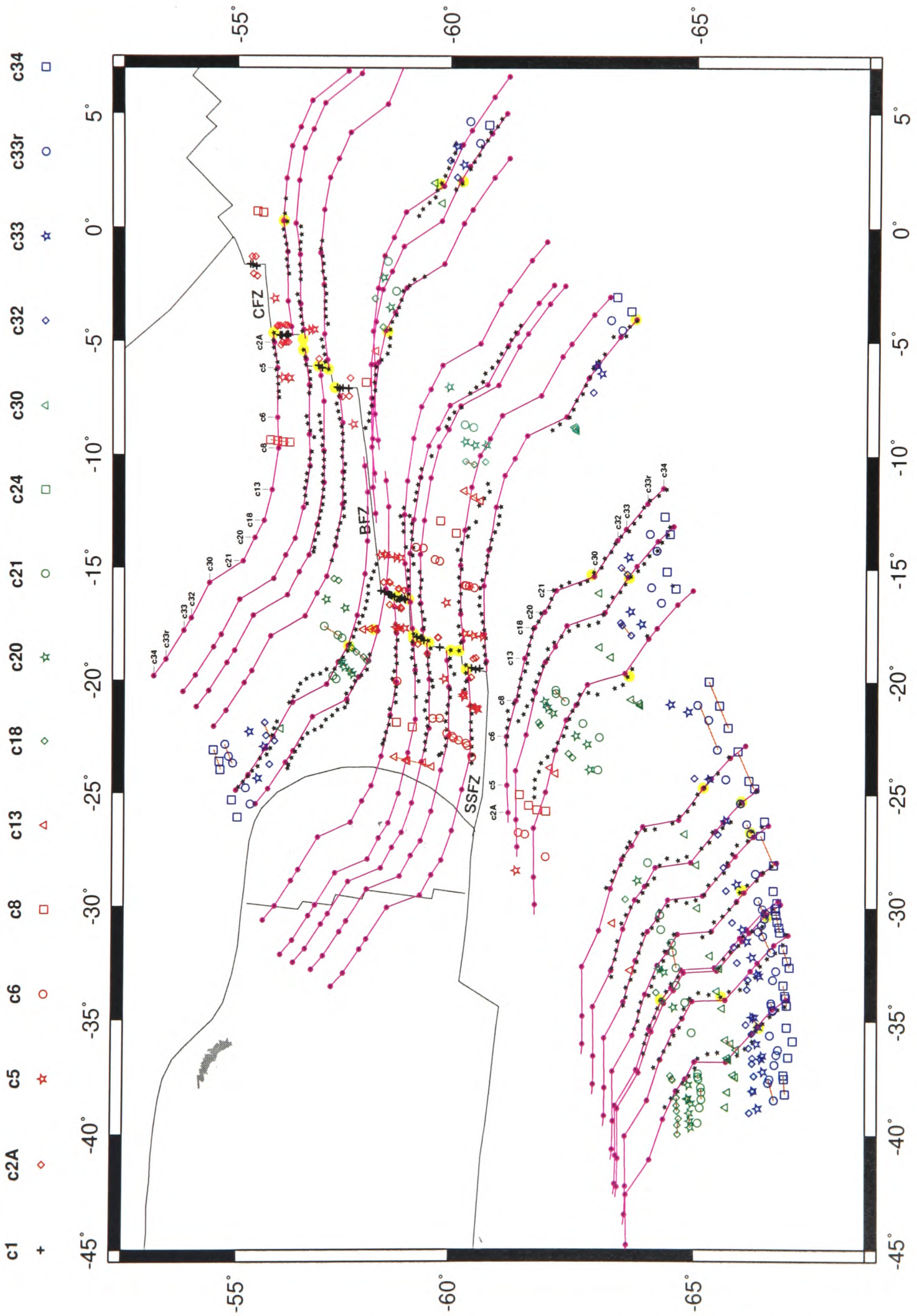

Figure 5.15: The magnetic anomaly and fracture zone picks used in the inversion for SAM-ANT spreading, along with the flowlines generated by the final solution poles. The fracture zone picks are marked by black stars and the flowlines depicted by the purple lines, with solid circles marking the end of each flowline stage. The seed points from which each flowline is generated are marked by yellow circles. The magnetic anomalies are represented by the appropriate symbols, as shown in the symbol table, and the fitted great circles shown in orange. (Abbreviations: CFZ - Conrad Fracture Zone; BFZ - Bullard Fracture Zone; SSFZ - South Sandwich Fracture Zone.)

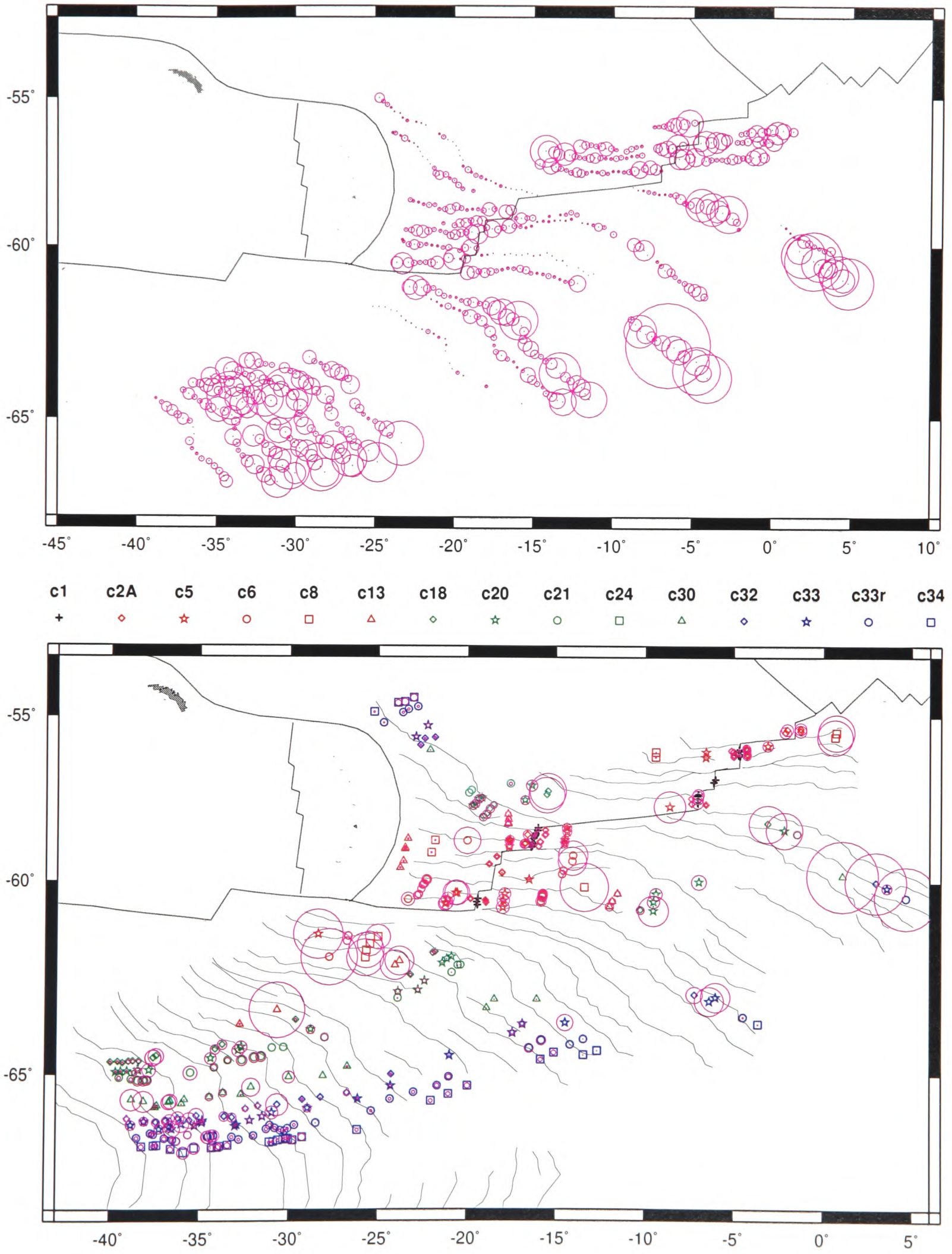

Figure 5.16: The data importances of the magnetic anomaly picks and fracture zone locations used in the inversion for SAM-ANT spreading. The fracture zone picks are marked by small crosses, and magnetic anomaly picks by the corresponding symbol, with the importance of each pick represented by a circle centred at the location of the pick with a radius proportional to the corresponding data importance.

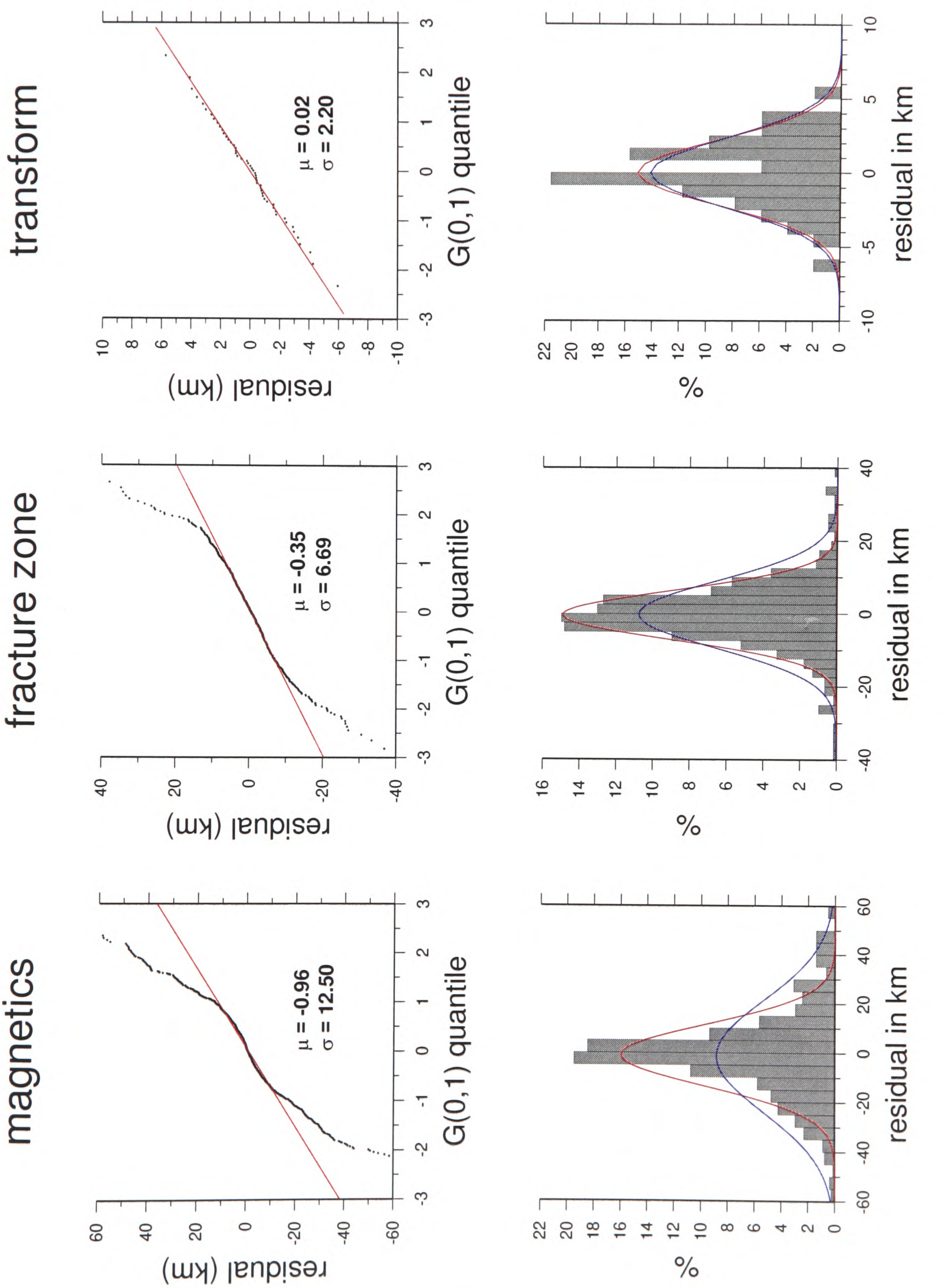

Figure 5.17: Quantile-quantile (q-q) plots and histograms for the residuals for each type of data used in the SAM-ANT inversion. In the q-q plots, the red line represents the best fit line, through linear regression, for the central $\pm 1\sigma$ of the test distribution (Gaussian(0,1)). In the histograms, the red line represents the Gaussian distribution defined by the statistics obtained from the q-q plots, and the blue line represents the Gaussian distribution with statistics defined by the the sample mean and standard deviation of the dataset.

seen in Figure 2.32, despite the satisfactory fit for recent spreading along the South American-Antarctic Ridge. These sections of fracture zones in the Weddell Sea were excluded from the inversion dataset because of their proximity to the Antarctic Plate/Scotia Plate boundary, and suspicion that interaction with the South Sandwich Trench in the past had led to some form of rotational deformation in the region. This is reflected in the incompatibility of the fracture zone azimuths with those of a corresponding age along the present-day South American-Antarctic Ridge, and the synthetic flowlines produced by the inversion.

The 'kinks' in the Weddell Sea appear to be modelled well, in particular for the one fracture zone which it was not felt possible to consider as a single feature across the disruption to the flowlines seen in the Weddell Sea: the two flowline models match perfectly across the division. To the north, in the region around the Bullard Fracture Zone, some of the synthetic flowlines appear to extend beyond and beneath the transform fault. This is due to the fact that, as Barker & Lawver (1988) noted, this transform would not have existed in its present geometry for the whole of its history. In response to changes in spreading direction at the ridge, some ridge re-organisation was likely to have occurred, and some earlier fracture zones became extinct.

Though not as simple as checking the fit of the anomalies by rotating the picks to the conjugate flanks, looking at the location of magnetic anomalies with respect to the corresponding points on the flowlines does give some idea of the fit of the data. In general, the match is good throughout, though offset in some regions due probably to changes in ridge geometry and slightly oblique spreading. However, it is interesting to note how to both sides of the Bullard transform, the gap between the sets of young (pre c21) and older (post c30) anomalies in the region is greater than predicted by the flowlines, though this problem does not occur in the Weddell Sea. The reasons for, and implications of, this effect are discussed in more detail later on.

The data importances for both datasets are shown in Figure 5.16. The large fracture zone data importances are not really confined to any particular area, though of course the importances on the Antarctic flank are quite large in general, since any 'conjugate' fracture zones have been wholly or partially subducted, and the inversion is relying on these Antarctic flowlines for information in these regions. The Weddell Sea flowlines will also have slightly larger data importances in general because they are closer to the poles of rotation. The largest data importances for the magnetics data are seen to the east of the Bullard Fracture Zone, for the few magnetic picks that are actually able to be fitted to conjugate isochrons. In addition, the few young isochron

picks (c5-c13) in the Weddell Sea also have quite large data importances, whilst the majority of picks in the Weddell Sea have quite small importances due to the relatively high density, and hence redundancy, of data. It is possible that the large variation in pole location from c8-c6-c5 is related to these large data importances for the young anomalies in the Weddell Sea.

The distributions of the residuals for each set of data are shown in Figure 5.17. Again, the fracture zone residuals have the closest to a Gaussian distribution, with far fewer outliers, when compared to the distribution of magnetic anomaly residuals. The misfits derived from conjugate fitting would again be expected to be modelled by a distribution with a smaller standard deviation that that seen for the total set. The overall distribution of the magnetics misfits could in fact be considered as two separate distributions, of conjugate and non-conjugate misfits, with small and large relative standard deviations respectively, but this distinction is not made in the inversion method.

5.5 A SAM-AFR-ANT 3-plate reconstruction

Due to the lack of anomaly c24 picks in the SAM-ANT dataset, it was not included in the set of chrons for the 3-plate inversion. The magnetic datasets for SAM-AFR and ANT-AFR spreading were kept unchanged, but had to be preprocessed again to exclude fitting to c24 great circles. Aside from that, the datasets for each plate pair were left unchanged from those used in the 2-plate inversions.

As an additional weighting option, relative weights for each plate pair could be set, so that data from a given plate pair would be favoured relative to another. However, this was not actually used because the existing weighting schemes already carried out such biasing intrinsically. For the SAM-AFR dataset, the magnetics isochrons were much better defined than those observed for the other plate pairs, with a standard deviation significantly less than that of the overall magnetics dataset. Thus the weights calculated through the schemes outlined in Section 4.4 would automatically favour this set of data over the less well defined datasets from the other plate pairs.

The data importances for the fracture zone and magnetic datasets are shown in Figure 5.18. The importances show little change from those determined for the individual 2-plate inversions, showing how the inversion uses information from all the three plates on a reasonably equal basis

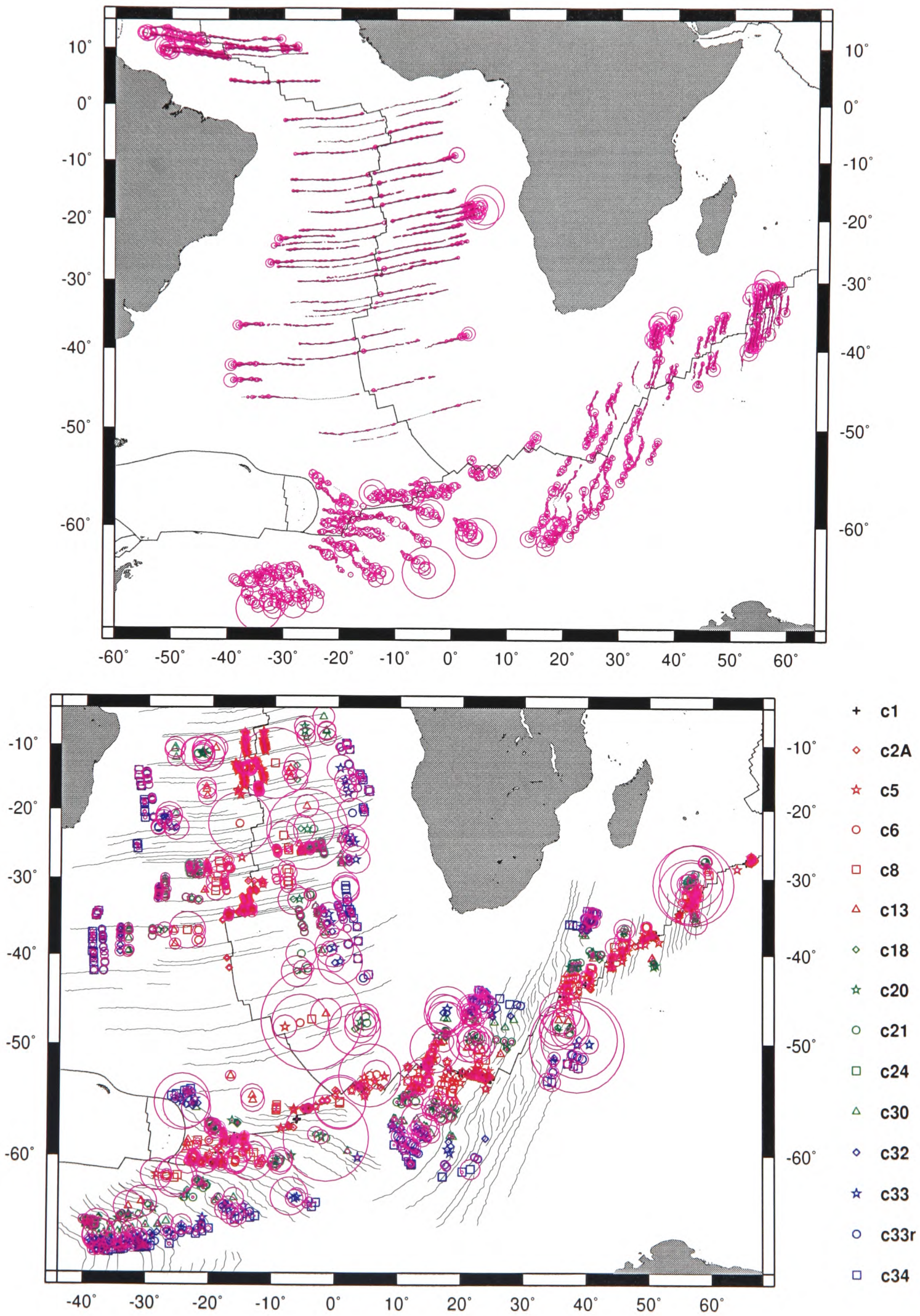

Figure 5.18: The data importances of the magnetic anomaly isochron and fracture zone location picks used in the 3-plate inversion for SAM-AFR-ANT spreading. The fracture zone picks are marked by small crosses, and magnetic anomaly picks by the corresponding symbol, with the importance of each pick represented by a circle centred at the location of the pick with a radius proportional to the corresponding data importance.

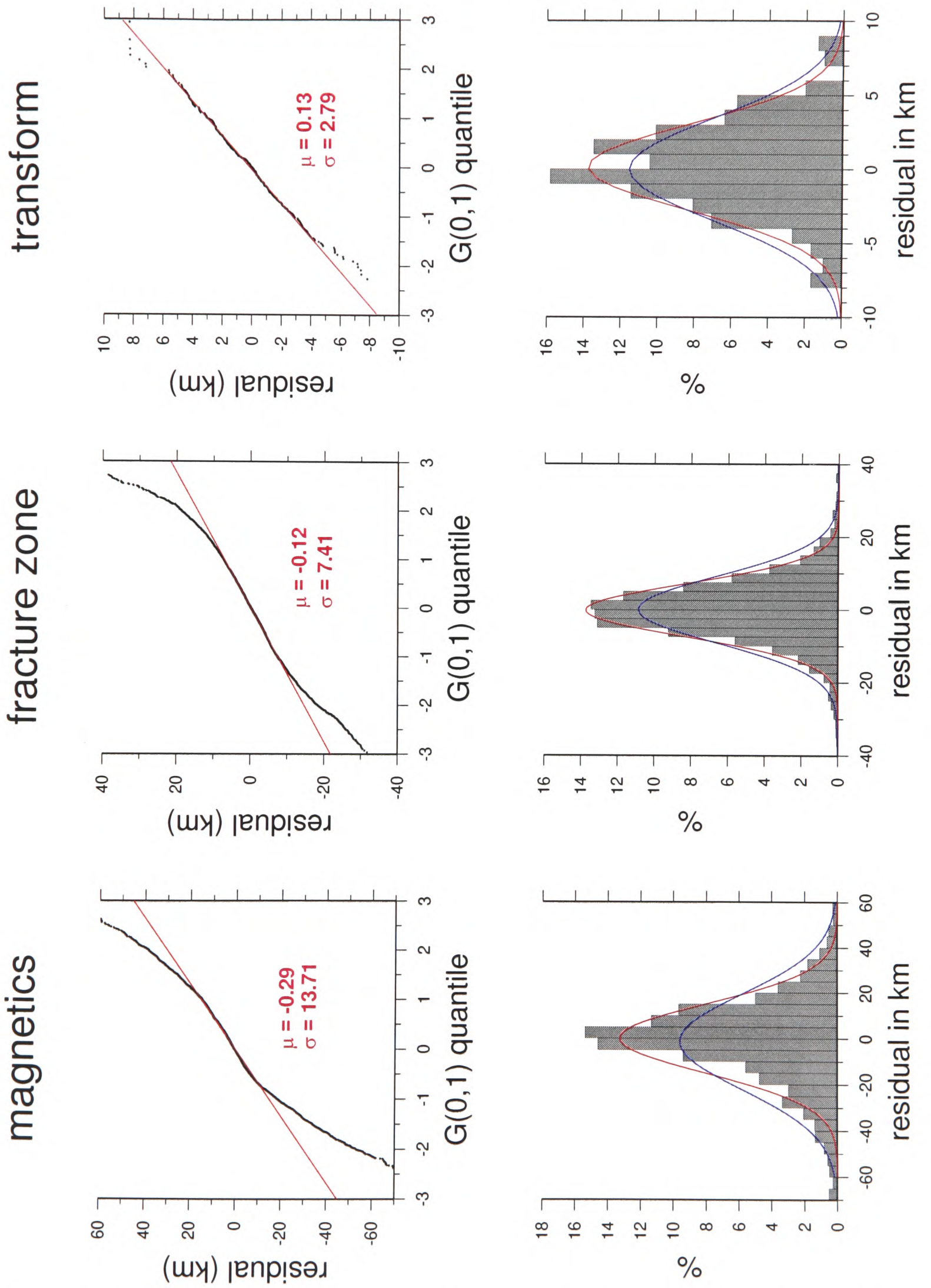

Figure 5.19: Quantile-quantile (q-q) plots and histograms for the residuals for each type of data used in the SAM-AFR-ANT inversion. In the q-q plots, the red line represents the best fit line, through linear regression, for the central $\pm 1\sigma$ of the test distribution (Gaussian(0,1)). In the histograms, the red line represents the Gaussian distribution defined by the statistics obtained from the q-q plots, and the blue line represents the Gaussian distribution with statistics defined by the the sample mean and standard deviation of the dataset.

to determine the solution poles. The residuals from the 3-plate inversion are shown in Figure 5.19. The fracture zone residuals again have the closest to a Gaussian distribution, with a standard deviation slightly greater than for the individual 2-plate inversions. The magnetic data residuals show a smoother distribution than for the 2-plate inversions, with a standard deviation of around 15km, which is due to the fact that the dataset is now dominated by non-conjugate fitting, which generates a larger number of data values, with greater uncertainties, than conjugate fitting.

Table 5.4: The solution poles obtained from the 3-plate inversion.

Chron	Age (Ma)	Latitude	Longitude	Angle	95% confidence ellipsoid			
					Axis 1	Axis 2	Axis 3	Azimuth
South America - Africa								
c2A	2.58	55.78	-37.95	0.80	0.87	0.25	0.01	99.71
c5	9.74	57.46	-37.28	3.16	0.59	0.17	0.01	107.69
c6	19.05	56.19	-35.69	7.08	0.35	0.07	0.02	106.77
c8	25.82	55.56	-34.40	9.96	0.26	0.05	0.04	105.11
c13	33.06	55.86	-33.09	13.45	0.19	0.04	0.02	103.66
c18	38.43	56.62	-32.24	15.86	0.19	0.05	0.03	100.96
c20	42.54	57.77	-31.77	17.49	0.18	0.05	0.02	102.21
c21	46.26	58.63	-31.02	19.11	0.14	0.03	0.02	101.06
c30	65.58	63.42	-32.82	24.74	0.11	0.03	0.02	103.83
c32	71.07	62.12	-32.18	26.52	0.16	0.04	0.02	105.80
c33	73.62	62.24	-32.48	27.98	0.15	0.04	0.03	104.53
c33r	79.08	62.48	-33.30	30.98	0.10	0.04	0.02	101.49
c34	83.00	61.75	-33.79	33.50	0.12	0.05	0.02	98.25
Antarctica - Africa								
c2A	2.58	6.20	-38.73	0.36	1.37	0.28	0.01	122.87
c5	9.74	5.24	-41.46	1.36	1.53	0.60	0.01	129.08
c6	19.05	8.42	-39.43	3.00	0.71	0.27	0.02	132.02
c8	25.82	11.02	-41.59	3.98	0.70	0.23	0.02	135.57
c13	33.06	13.32	-41.96	5.56	0.50	0.17	0.02	135.26
c18	38.43	11.88	-40.48	6.73	0.43	0.17	0.02	128.53
c20	42.54	10.13	-40.70	7.55	0.54	0.21	0.02	119.61
c21	46.26	12.31	-38.89	8.20	0.53	0.17	0.02	123.49
c30	65.58	-1.78	-42.09	11.92	0.58	0.11	0.02	120.23
c32	71.07	-1.74	-43.14	12.98	0.45	0.11	0.02	121.59
c33	73.62	-1.65	-42.68	13.81	0.42	0.10	0.03	122.49
c33r	79.08	-1.07	-41.46	15.81	0.33	0.07	0.02	122.95
c34	83.00	-0.41	-40.09	17.78	0.35	0.08	0.02	121.53

continued on next page

continued from previous page

Chron	Age (Ma)	Latitude	Longitude	Angle	95% confidence ellipsoid			
					Axis 1	Axis 2	Axis 3	Azimuth
South America - Antarctica								
c2A	2.58	81.80	-33.55	0.63	1.19	0.24	0.01	104.35
c5	9.74	81.63	-17.17	2.57	0.78	0.43	0.02	104.74
c6	19.05	79.15	-17.17	5.53	0.46	0.20	0.03	101.03
c8	25.82	75.38	-12.33	7.67	0.45	0.14	0.04	98.87
c13	33.06	74.98	-4.31	10.13	0.29	0.12	0.03	91.05
c18	38.43	76.47	1.81	12.09	0.26	0.11	0.04	76.21
c20	42.54	77.55	10.52	13.66	0.26	0.12	0.04	70.51
c21	46.26	78.14	11.80	14.74	0.27	0.10	0.04	81.14
c30	65.58	79.30	59.56	22.54	0.24	0.05	0.04	33.66
c32	71.07	77.78	53.96	23.92	0.20	0.06	0.04	36.24
c33	73.62	77.73	55.63	25.22	0.18	0.07	0.04	34.97
c33r	79.08	77.61	61.48	27.81	0.15	0.06	0.03	28.95
c34	83.00	77.36	64.44	29.64	0.16	0.06	0.04	20.49

The set of solution poles obtained from the 3-plate inversion for South American - African - Antarctic spreading are given in Table 5.4. As detailed in Section 4.6.3, the initial inversion was carried out for the circuit SAM-AFR-ANT, which led to the determination of confidence intervals for the SAM-AFR and AFR-ANT poles. The circuit was then rearranged to SAM-ANT-AFR, and a single iteration carried out using the same set of solution poles (with a reversed sign of rotation angle where necessary) so that confidence intervals were obtained for the sets of SAM-ANT and ANT-AFR solution poles. Because the ANT-AFR and AFR-ANT solution poles are identical except for a reversed sign of rotation angle, the confidence intervals should be identical, within the limits of computational accuracy. This was the case, with an RMS difference between the axes of the two sets of confidence intervals of less than 0.2%.

The poles for South American - African spreading obtained from the inversion are shown in Figure 5.20. As the SAM-AFR datasets are the better defined out of the three, and hence most 'dominant' within the 3-plate inversion, the poles are relatively unchanged. The whole sequence has shifted slightly in order to satisfy the plate circuit, but the progression through the chrons is almost identical. The set of flowlines generated from the poles are shown in Figure 5.21 along with the fracture zone picks, and the magnetic isochron picks and great circles used in the inversion. Though the rotated magnetic picks are not shown, in order to keep the figure relatively clear,

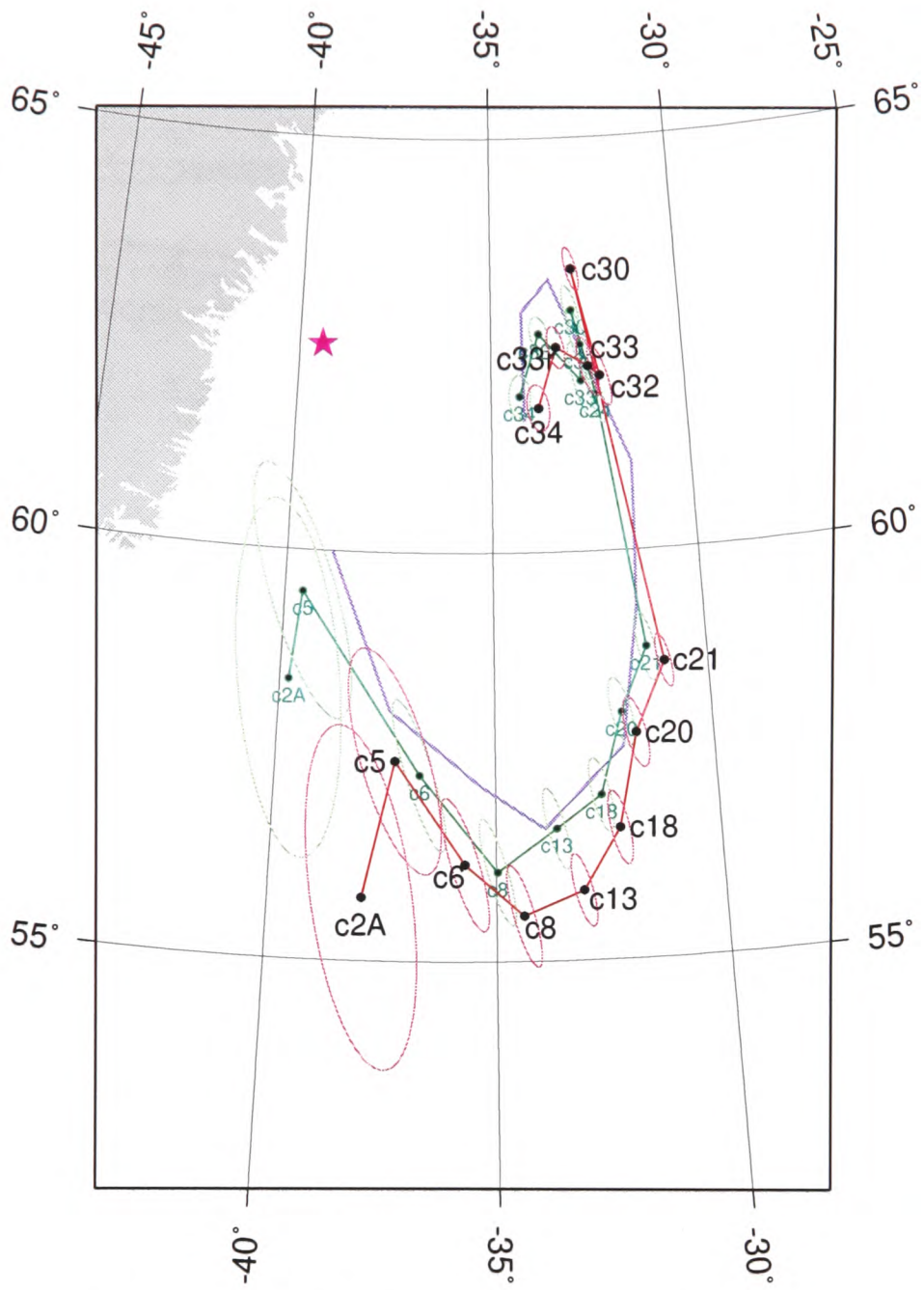

Figure 5.20: The set of solution poles for SAM-AFR spreading obtained from the 3-plate inversion shown in red, with corresponding 95% confidence ellipses. The poles and confidence ellipses determined from the 2-plate SAM-AFR inversion are shown in green, and the trace of the poles obtained by Shaw & Cande (1990) in light blue. The NUVEL-1A instantaneous pole is marked by a purple star.

---

the fit of the magnetic data can be seen by comparing the spacing between anomalies to the corresponding sections of neighbouring flowlines. As would be expected from the great similarity between the sets of poles, the fit of the data to the model is as good as was obtained from the 2-plate inversion.

The poles for Antarctic - African spreading obtained from the 3-plate inversion are shown in Figure 5.22. The location of the oldest finite rotation poles have not really changed significantly, although the c32 and c33 poles have moved NW slightly, this is in the direction of least constraint on the poles, as indicated by the longer axes of the confidence ellipses in that direction, and in any case is closer to the location of the other poles of the neighbouring chrons, suggesting that

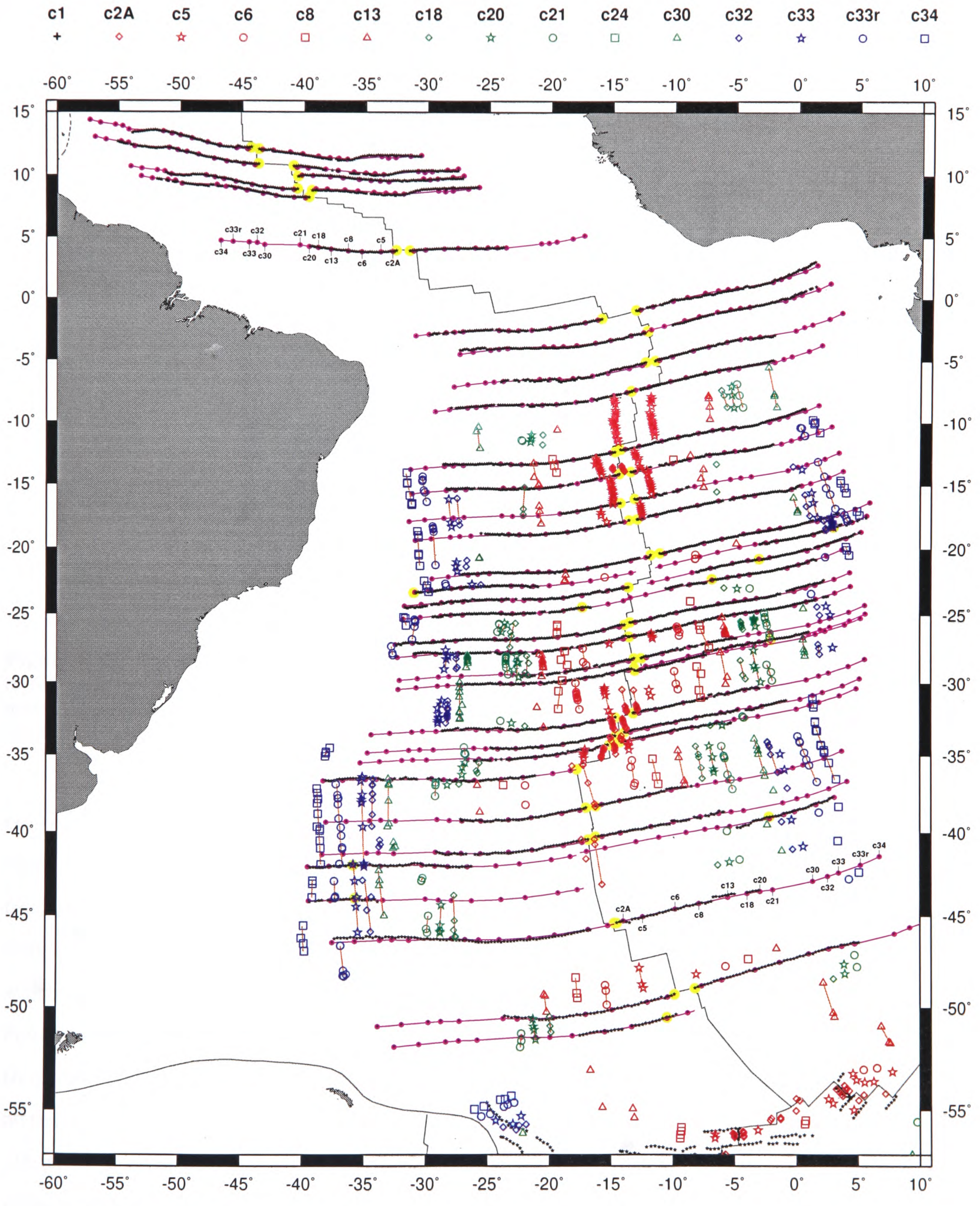

Figure 5.21: The magnetic anomaly and fracture zone picks for SAM-AFR spreading used in the 3-plate inversion, along with the flowlines generated by the final solution poles. The fracture zone picks are marked by black stars and the flowlines depicted by the purple lines with solid circles marking the end of each flowline stage. The fracture zone seed points are marked by yellow circles. The magnetic anomalies are represented by the appropriate symbols, as shown in the symbol table, and the fitted great circles shown in orange.

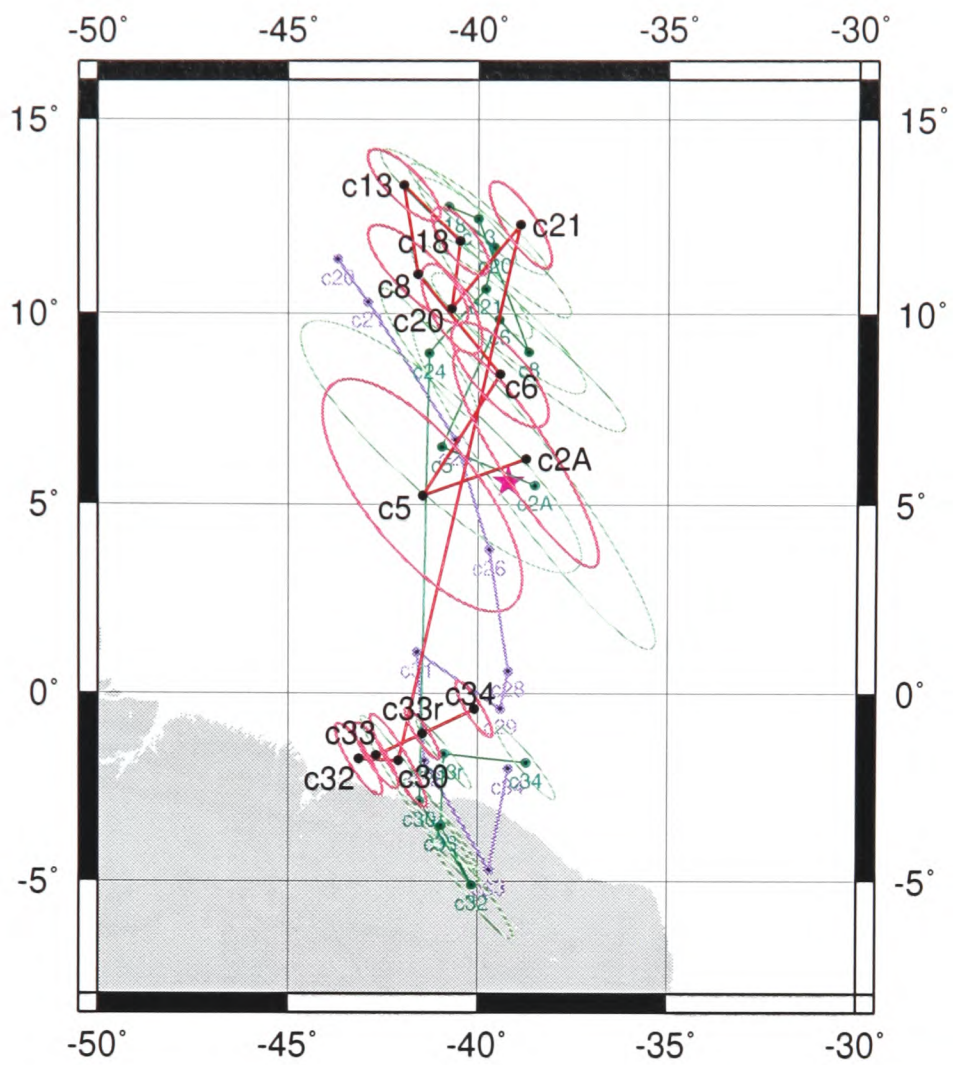

Figure 5.22: The set of solution poles for ANT-AFR spreading obtained from the 3-plate inversion shown in red, with corresponding 95% confidence ellipses. The poles determined by the two plate ANT-AFR inversion are shown in green, and the poles obtained by Royer *et al.* (1988) in light blue. The NUVEL-1A instantaneous pole is marked by a purple star.

---

the poles of motion were very stable from anomaly c34 to c30 (83 to 66Ma). There is then a large jump north from the c30 to the c21 pole (made more substantial by the exclusion of the c24 pole from the inversion). The progression of poles has altered slightly from the 2-plate inversion in that whereas the 2-plate inversion showed a northwards progression of the poles until c18, after which the poles generally moved southwards again, there is a large jump north to c21, then a drop South again to c20, then a progression N to c13. This is somewhat surprising as it was expected that the 3-plate would have more of a smoothing effect on the progression of poles. The majority of the younger poles have not altered by very much, in fact for each pole after and including c18, there is considerable overlap between the 95% confidence ellipses, and the progression of the poles is very similar to that from the 2-plate inversion, with the poles migrating south after c13.

The corresponding flowlines from these new poles, along with the fracture zone picks, magnetic picks and isochron great circles, are shown in Figure 5.23. Taking into consideration the absence of the c24 flowpoint from the flowlines, they are again very similar to those from the 2-plate

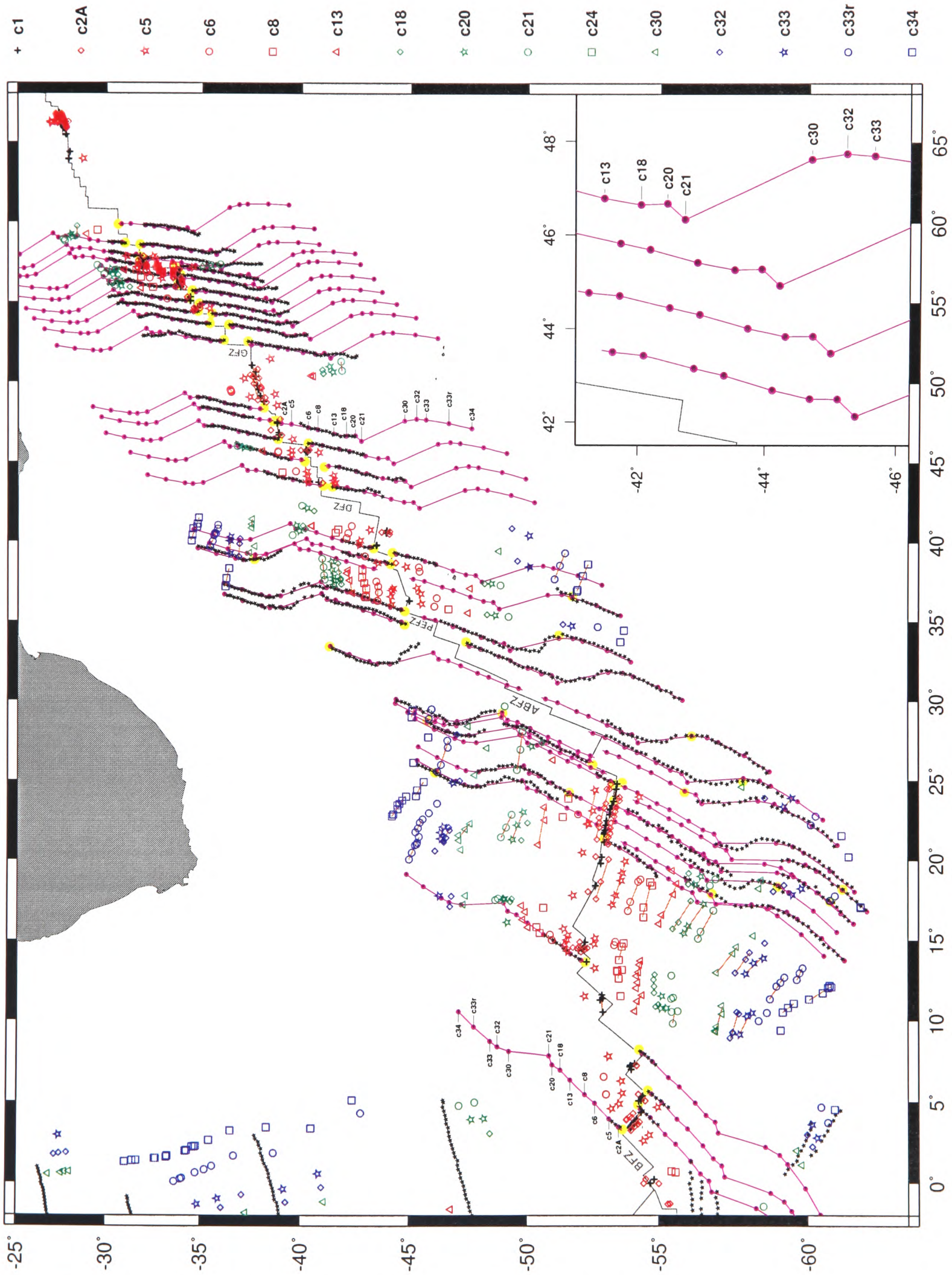

Figure 5.23: The magnetic anomaly and fracture zone picks for ANT-AFR spreading used in the 3-plate inversion, along with the flowlines generated by the final solution poles. The fracture zone picks are marked by black stars and the flowlines depicted by the purple lines, with solid circles marking the end of each flowline stage. The fracture zone seed points are marked by yellow circles. The magnetic anomalies are represented by the appropriate symbols, as shown in the symbol table, and the fitted great circles shown in orange. (Annotation abbreviations: BFZ-Bouvet Fracture Zone; ABFZ-A.Bain Fracture Zone; PEFZ-Prince Edward Fracture Zone; DFZ-Discovery Fracture Zone; GFZ-Gallieni Fracture Zone.)

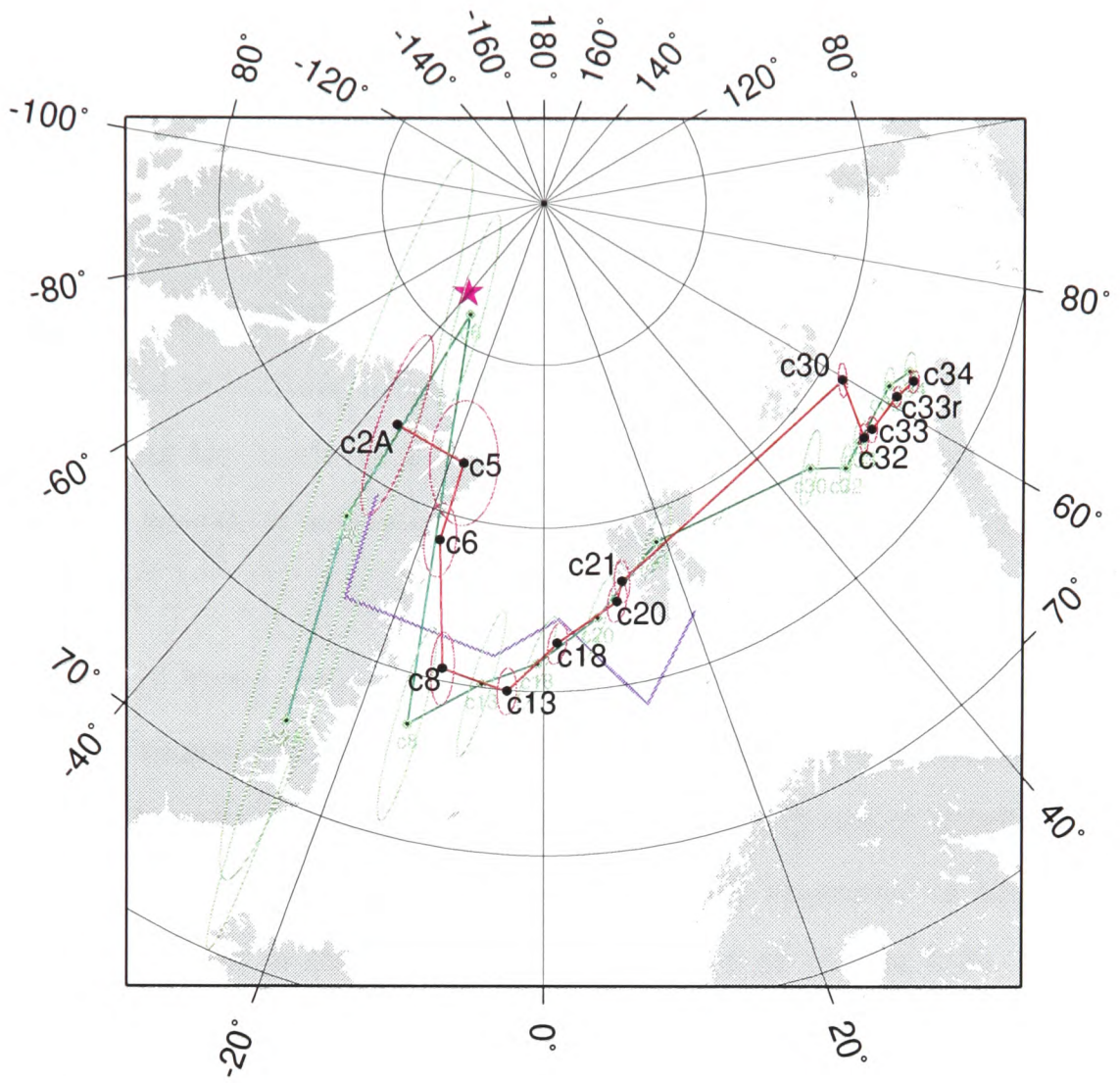

Figure 5.24: The set of solution poles for SAM-ANT spreading obtained from the 3-plate inversion shown in red, with corresponding 95% confidence ellipses. The poles and confidence ellipses determined from the 2-plate SAM-ANT inversion are shown in green, and the poles obtained by Barker & Lawver (1988) in light blue. The NUVEL-1A instantaneous pole is marked by a purple star.

---

inversion, with the exception of the section c18-c20-c21, as highlighted in the inset, where a kink has appeared in the flowlines which did not appear previously, and does not appear to fit the majority of the fracture zone data. Thus this has appeared as a result of the 3-plate inversion, and corresponds to the altered sequence of poles, c21-c20-c18, seen in Figure 5.22. Other than this, the flowlines are smoother and fit the data just as well as the 2-plate flowlines, which makes the appearance of this kink more surprising. The origins of this are more clear once the third set of solution poles are studied.

The set of solution poles for South American - Antarctic spreading determined from the 3-plate inversion are shown in Figure 5.24. From c34 to c32, the poles are virtually unchanged, the only shift in the poles occurring in the direction of the larger axes of the confidence intervals, and the poles are now in fact grouped even closer than before. This concurs with the results seen for the other plate boundaries, that the poles of motion were quite stable at this time. The c30

pole however, has moved quite significantly eastward, against the general drift of the younger poles towards the west, and then there is a large jump westward to c21, which in contrast to the other poles, is located to the west of the corresponding 2-plate inversion pole. After c18 however, the poles are closer to the 2-plate poles, but the large north-south shift in the poles c8-c6-c5 has been smoothed out by the 3-plate inversion, and a more realistic progression of poles has been produced. A substantial reduction in the size of the confidence intervals of the c2A and c5 poles can be seen, illustrating the usefulness of the 3-plate inversion in constraining the SAM-ANT poles, where the short length of active spreading ridge has limited the accurate determination of finite rotation poles.

The quality of fit of these poles to the actual data can be seen in Figure 5.25, where the synthetic flowlines are shown alongside the fracture zone and magnetic isochron datasets. At first, the result appears to be very satisfactory, with quite a smooth set of flowlines being produced. However, the kink in the c18-c20-c21 flowline section that appeared in the 3-plate ANT-AFR flowlines appears again, and is shown clearly in the inset of Figure 5.25. The kink is not so severe as in the ANT-AFR flowlines, but with the rest of the flowlines varying relatively smoothly throughout, it is quite apparant. The fact that this kink occurs in both the ANT-AFR and SAM-ANT flowlines, and yet does not appear to improve the fit to the fracture zone data in either case seems to suggest that it is not developed by the inversion to satisfy the 3-plate fracture zone dataset. Instead, it seems it has in fact been caused by the inversion catering for the magnetic isochron dataset, which is surprising because the magnetic isochron dataset generally has more effect on the length of flowline sections than on the direction.

The major problem with the set of solution poles becomes apparent on inspecting the fit of the data to the model in the western Weddell Sea. The abrupt change in spreading direction that was observed from the 2-plate flowlines is no longer observed. This also has the effect that whereas previously the two flowline sections for the discontinuous fracture zone in the Weddell Sea, had matched up perfectly, now the flowlines are no longer aligned, suggesting that the two sections are in fact parts of independent fracture zones. The poor fit is most apparent on observing the distance between the c21 and c30 anomalies in the Weddell Sea, and that predicted by the corresponding flowline section. The flowlines, and hence the 3-plate model, suggest there should be much greater extension during this period than is seen in the Weddell Sea. All of the 'continuous' fracture zones in this region were dated in the older section, and so all the older

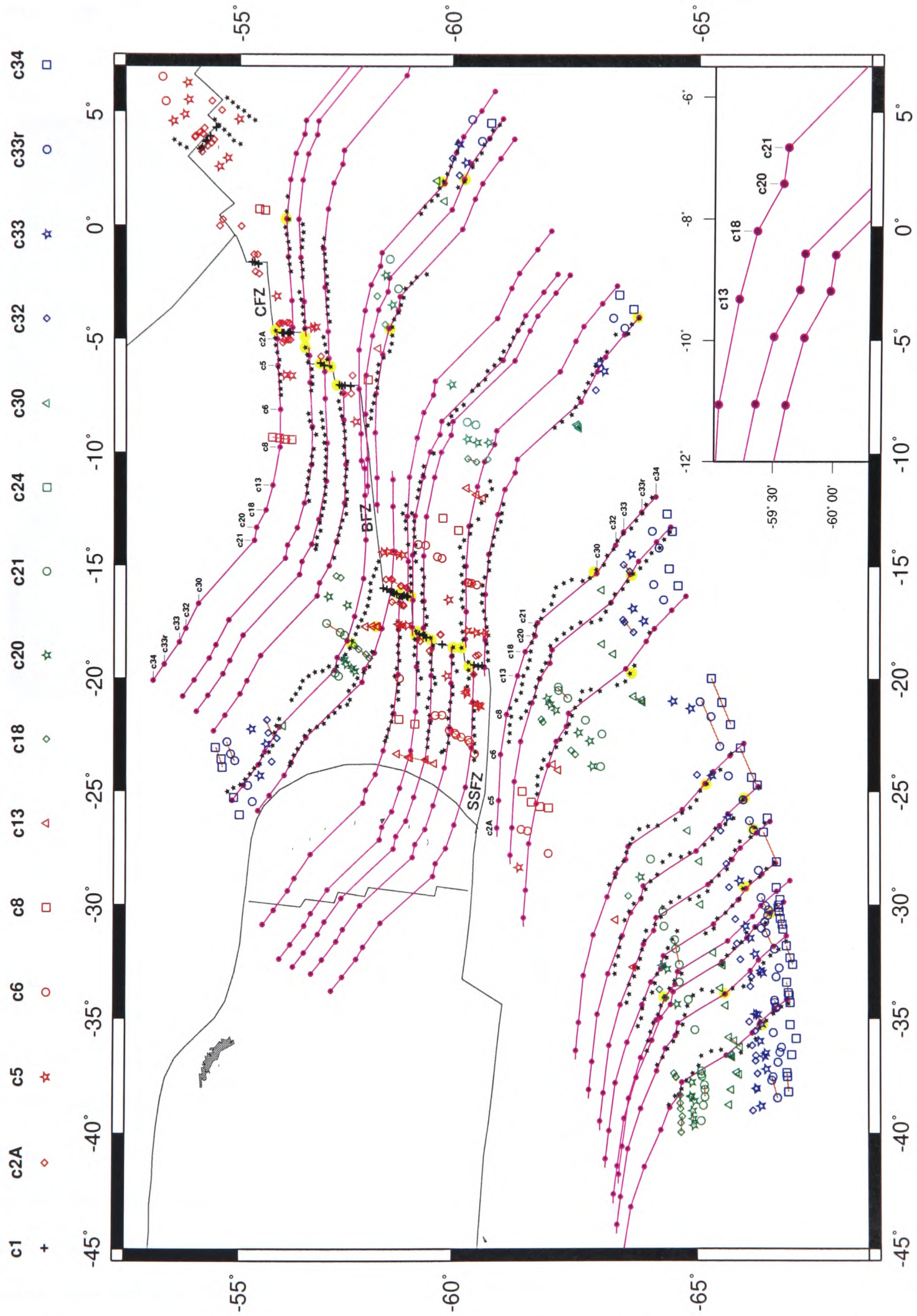

Figure 5.25: The magnetic anomaly and fracture zone picks for SAM-ANT spreading used in the 3-plate inversion, along with the flowlines generated by the final solution poles. The fracture zone picks are marked by black stars and the flowlines depicted by the purple lines, with solid circles marking the end of each flowline stage. The seed points from which each flowline is generated are marked by yellow circles. The magnetic anomalies are represented by the appropriate symbols, as shown in the symbol table, and the fitted great circles shown in orange. (Annotation abbreviations: CFZ - Conrad Fracture Zone; BFZ - Bullard Fracture Zone; SSFZ - South Sandwich Fracture Zone.)

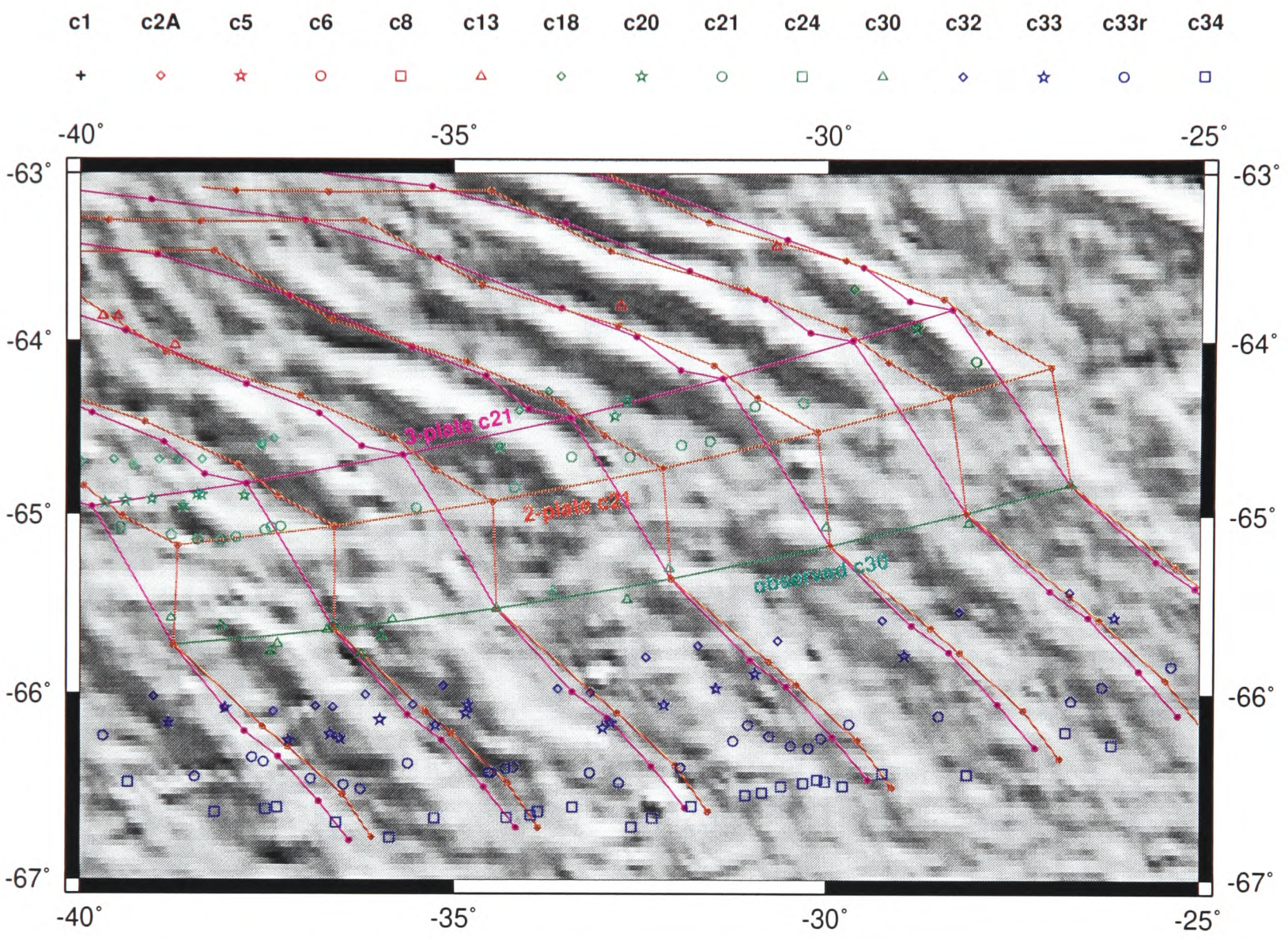

Figure 5.26: Theoretical c21 isochrons, relative to the observed c30 isochron, predicted by the 2 and 3-plate models for South American - Antarctic spreading in the Weddell Sea. The green line marks a best-fit great circle to the c30 anomaly locations, from which the synthetic flowlines are generated. The synthetic isochron and flowlines for the 2-plate model are marked in orangee, and for the 3-plate model in purple. The observed magnetics are marked by the usual symbols.

---

anomalies can be seen to align with the flowpoints, whereas after c30, there is a significant offset between the anomaly picks and the corresponding flowpoints in the Weddell Sea. However, the relative spacing c21-c20-c18 and younger anomalies is still accurate, despite the offset in the flowlines, suggesting that it is the c21-c30 stage pole that is in error.

This is shown more clearly in Figure 5.26, where the synthetic flowlines and c21 isochrons are shown for the 2 and 3-plate reconstructions, relative to a best-fit great circle to the observed c30 anomaly picks. The difference in predicted spreading direction during the period c30-21 is considerable, and the amount of seafloor extension predicted by the 3-plate model is approximately twice that predicted by the 2-plate model.

To the north, on the seafloor flanking the present-day South American-Antarctic Ridge, the anomalies are generally in very good agreement with the flowlines throughout, but the most

important information comes from the flowlines to the east and west of the long-offset Bullard Fracture Zone. Contrary to what was seen in the results of the 2-plate inversion, the gap between the young (pre c21) and old (post c30) anomalies is now in agreement with the synthetic flowlines. Thus, a significant difference between the 2-plate and 3-plate models has appeared for SAM-ANT spreading. Whereas previously the discrepancy in the c21-c30 anomalies to the North was attributed to ridge reorganisation in the neighbourhood of the Bullard Fracture Zone, it now appears that this is not necessarily the case, and that between chrons c30 and c21, there have been changes in plate motion in the Weddell Sea that do not agree with the overall SAM-AFR-ANT motion at that time, as determined by the 3-plate inversion. These contradictions in the data around the c21-c30 period are also likely to have caused the c18-c20-c21 kink seen in the SAM-ANT flowlines and ANT-AFR flowlines (through the integration of the different datasets around the 3-plate circuit), and so the reliability of the whole 3-plate inversion is brought into question. However, away from the Weddell Sea, the fit of the data on all three plate boundaries is sufficiently good to suggest that this is in fact a localised problem, and that if this could be solved, then a much improved set of solution poles for the 3-plate system could be obtained.

Explanations for the discrepancies observed, and a new set of poles from a revised 3-plate inversion are presented in the following chapter.

Chapter 6

Implications for seafloor spreading in the Southern Ocean

6.1 Evidence for a discontinuity in seafloor spreading in the Weddell Sea

On inspecting the results of the 3-plate inversion, it became clear that the solution poles did not satisfactorily describe the past motion of the 3-plate system, as described by the fracture zone and magnetic anomaly datasets. The greater part of the spreading history appeared to have been well resolved, with the exception of the small kink observed in the ANT-AFR and SAM-ANT flowlines at c18-c20-c21 and, most importantly, the discrepancy between the predicted and observed amount of extension between anomalies c21 and c30 in the Weddell Sea.

Figure 6.1 shows the spreading rates predicted by the 2 and 3-plate inversions for seafloor spreading in the Weddell Sea. Prior to c30 and after c20, the two models are in close agreement, with no particularly substantial differences between the predicted spreading rates. Between anomalies c32 and c20 however, the rates for South American-Antarctic spreading predicted by the 2 and 3-plate inversions differ greatly. In particular, between anomalies c30 ($\approx$66Ma) and c21 ($\approx$46Ma), the 2-plate model suggests spreading rates of below 4mm/yr in the western Weddell Sea, whilst the 3-plate model predicts spreading rates almost double this, at around 7mm/yr. The 2-plate model also predicts large fluctuations in the spreading rate during this period, from around 15mm/yr (c32-c30) right down to 4mm/yr (c30-c21) and then back up to approximately 13mm/yr (c21-c20). Such huge variations in spreading rate do appear unlikely, with the 3-plate model predicting a far smoother variation in spreading rates.

Comparing the flowline plots for the 2 and 3-plate inversions in the Weddell Sea, Figures 5.15

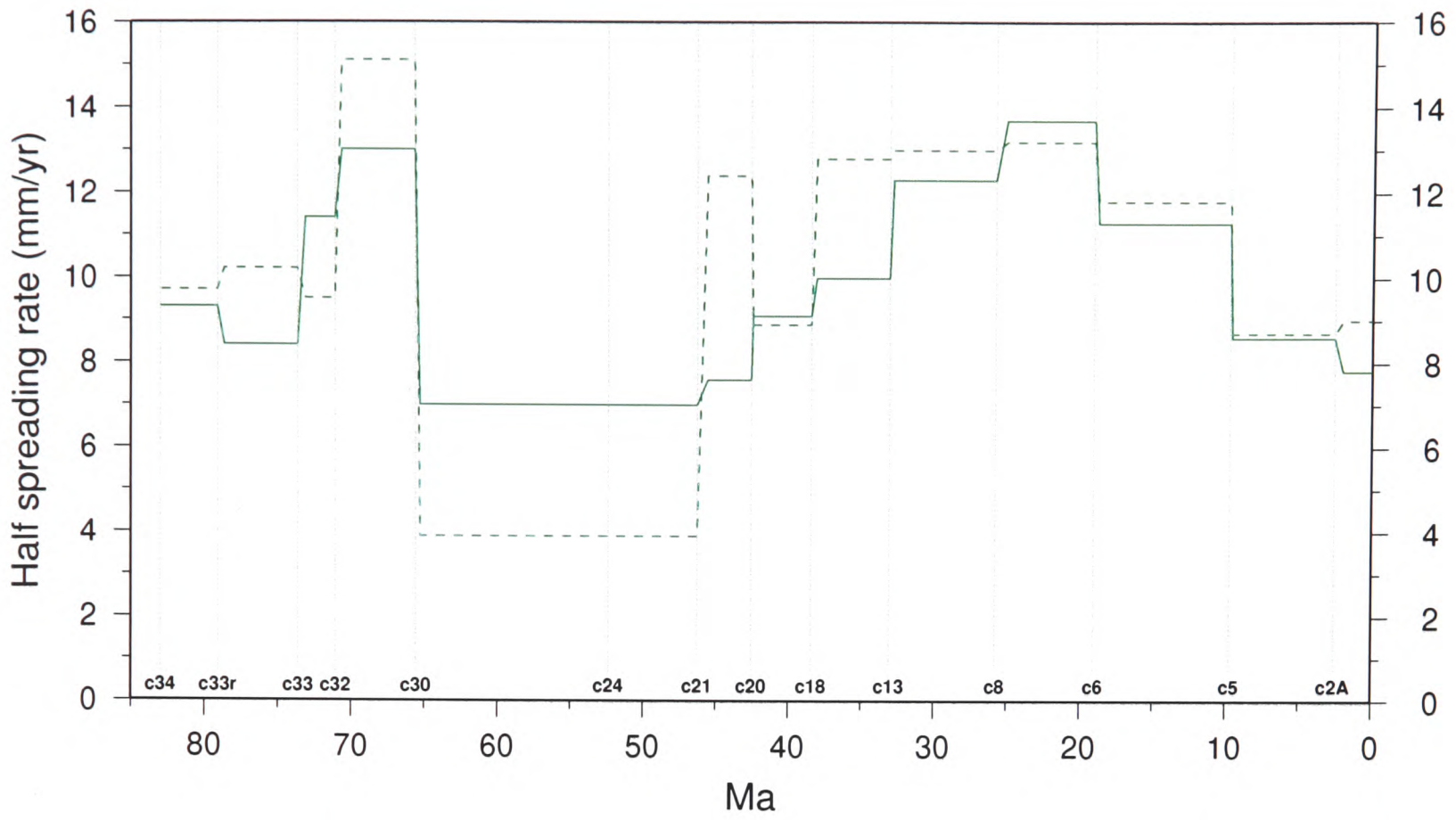

Figure 6.1: Spreading rates (half rates) for South American-Antarctic spreading in the Weddell Sea, along a flowline originating at 40°W, 63°S. The solid line gives the rates predicted by the 3-plate inversion, with the dotted line representing those predicted by the 2-plate inversion.

---

and 5.25 in Chapter 5, the latter clearly shows a far greater amount of extension from c21-c30 than is reflected in the spacing of the identified anomalies in the region, or that predicted by the 2-plate model. However, to the north, in the few long series of identified anomalies generated from the present day South American-Antarctic Ridge, the distance between the c21 and c30 anomalies is much closer to that predicted by the 3-plate flowlines, and so this lack of extension appears to be confined to the Weddell Sea. The flowline plots for ANT-AFR and SAM-ANT spreading generated from the 3-plate inversion, Figures 5.23 and 5.25 in Chapter 5, both show a small kink in the flowline at c18-c20-c21, just before the major kink seen on both sets of flowlines from the 2-plate inversions. It appears that the inversion is trying to compensate for the lack of extension expected in the Weddell Sea by compressing the flowlines in a concertina effect.

The mismatches between the 3-plate model and the data appear only in the period from around c32 to c20: both before and after this time the flowlines and the spreading rates are similar for both the 2 and 3-plate models, for all three plate pairs. The discrepancies are most prominent in the Weddell Sea, and it is equally likely that where the 3-plate reconstruction gives a poor fit on the other plate boundaries, this originates from the spreading rate and flowline anomalies seen in the Weddell Sea. It thus becomes apparent that there is less extension in the

Weddell Sea than would be expected, which could be due to the occurrence of ridge jumps in this region, asymmetric spreading, or interaction with another (micro)plate.

These discrepancies can not be accounted for by any interaction with the proposed Malvinas plate (LaBrecque & Hayes, 1979; Shipboard Scientific Party, 1988), postulated to have been in existence from around c34 to c31. This plate was believed to have been located to the west of the spreading centre in the Agulhas Basin, possibly extending into the Weddell Sea, as shown in Figure 1.10. The westward extent of this proposed plate is not really known, and so any evidence for its existence would be more likely to be found in the northern region of the SAM-ANT plate boundary, closest to the Agulhas Basin. Thus, particularly as it is not known whether this plate would have extended as far west as the Weddell Sea, it is extremely unlikely that a Malvinas Plate would have given rise to features observed in the Weddell Sea which cannot be seen further east in the seafloor flanking the northern South American-Antarctic Ridge.

The spreading rates in the Weddell Sea that would be predicted by the Malvinas stage pole of LaBrecque & Hayes (1979) are much greater than those observed (Livermore & Woollett, 1993). As stated previously, prior to c30/32, the spreading rates and directions observed in the southern Weddell Sea are in agreement with those predicted by the SAM-AFR-ANT 3-plate inversion, during a period when the Malvinas Plate is thought to have been in existence, and so this discontinuity in seafloor spreading appears to be unrelated to interaction with the Malvinas Plate.

As noted earlier, the gravity maps show a discontinuity in the flowlines at this time, suggesting some form of ridge reorganisation during this period, which is given further credence by these results. Figure 6.2 shows a perspective view of a gravity map of the region, where the discontinuity in the flowlines can clearly be seen running through the middle. However, due to the subduction of the South American plate, it is not possible to examine the corresponding region on the opposing flank for any further evidence that could help determine the exact nature of the discontinuity in spreading. There are no obvious sites of a fossil ridge visible on gravity maps in the Weddell Sea, and so if there was a (temporary) ridge jump in the region, it must have been located to the north, on the South American plate.

The main problem of attributing the discrepancy in spreading to major ridge jumps is that it requires the whole of the spreading centre in the Weddell Sea to have jumped northwards to another location on the South American plate, where spreading would have continued for around

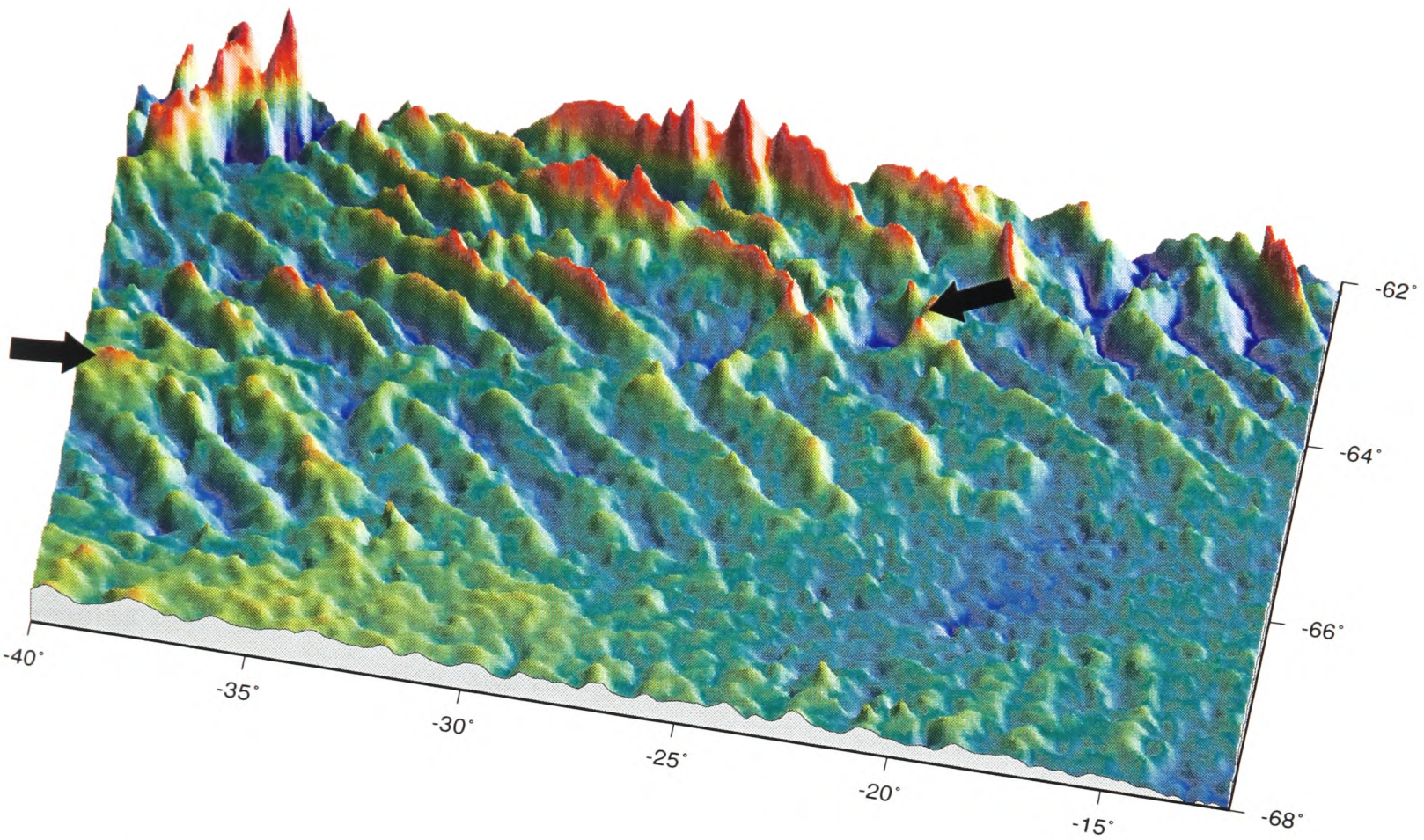

Figure 6.2: A perspective gravity map of a region in the Weddell Sea, showing the discontinuity in the flowlines running through the centre.

10Ma, followed by a further ridge jump back to close to the original location. If spreading hadn't restarted close to the original site, then a reversed sequence of anomalies should be seen on seafloor originally on the South American Plate, but captured by the Antarctic Plate through the ridge jumps, but this is not observed. This ridge jump hypothesis does appear unlikely as the number of fracture zone traces and the magnetic anomaly patterns in the Weddell Sea suggest that the ridge was highly segmented, consisting of a whole series of short spreading centres and transform faults, and it requires the whole system to have jumped to one flank and then returned again.

As the discontinuity has occurred during a time of change in plate motions in the SAM-AFR-ANT system (as reflected in the change in ANT-AFR flowlines from c30-c24), it is feasible for a ridge jump to have occurred in response to a change in spreading direction. The approximate timing coincides with the ridge jumps seen along the Mid-Atlantic Ridge, south of the Falklands-Agulhas Fracture Zone (Barker, 1979; LaBrecque & Hayes, 1979), which occurred from around anomaly 31 (68Ma) until anomaly 24 (53Ma), when the offset along the fracture zone was considerably shortened, possibly in response to a change in spreading direction (LaBrecque & Hayes, 1979). Although the fracture zones in the Weddell Sea all appear to have relatively small offsets,

they are close to the stage poles of motion, and so the effect of changes in the direction of plate motion in that region are magnified. However, the scenario of the ridge jumping back to the site of the former spreading centre is extremely unlikely, and the evidence does not point toward substantial ridge jumps having occurred.

Initially it was thought that no distinct anomalies between c21 and c30 could be identified in the westernmost Weddell Sea due to the extremely slow spreading rates, of below 5mm/yr. However, it could be possible that in fact the sequence of anomalies has been broken by the a ridge jump. Figure 3.29 in Chapter 3 showed a series of magnetic profiles in the western Weddell Sea, compared to a model for a slow spreading rate of 5mm/yr from around c21 to c30. At this spreading rate, there are no identifiable anomalies between c21 and c30 in the model, with the signal predominantly negative, and most of the ship profiles showing just a low in the recorded magnetic anomaly between the identified c21 and c30 anomalies, though a c28/9 peak possibly appears in the D154-845 and the Bran_745-2 profiles. This meant that the profiles fitted well to the model, but in truth could not be matched with any real confidence from c21 to c28/9 due to the lack of correlating anomalies, which also meant that no evidence for a ridge jump could to be found in the form of a missing anomaly sequence.

Figure 6.3 shows more profiles, but from further east in the Weddell Sea, in comparison to synthetic models for both slow and fast spreading rates. If there had been a ridge jump, then the profiles would be expected to match the faster spreading models, but with a visible break in the sequence of anomalies. In the recorded profiles, a c28/9 peak can be identified, but because of the indistinct nature of the observed anomalies between this and the c21 anomaly, it is virtually impossible to determine the timing of any hypothetical ridge jump. There is no obvious interruption to the series of anomalies, in comparison to the faster spreading synthetic profile and if anything, the observed magnetic profiles are closer to the slower rate synthetic profile.

Another possible cause of the proposed lack of extension seen on the Antarctic flank is asymmetric spreading, which would give rise to the observation of slower spreading rates than would be predicted, as is seen in the Weddell Sea. Comparing the length of flowline sections between anomalies 21 and 30, and the difference in predicted spreading rates, the amount of extension observed is approximately half that predicted by the synthetic flowlines from the 3-plate inversion. For this to be accounted for by asymmetric spreading, the ratio of South American to Antarctic plate accretion would have to be in the region of 3:1, which is highly asymmetric, and unlikely to

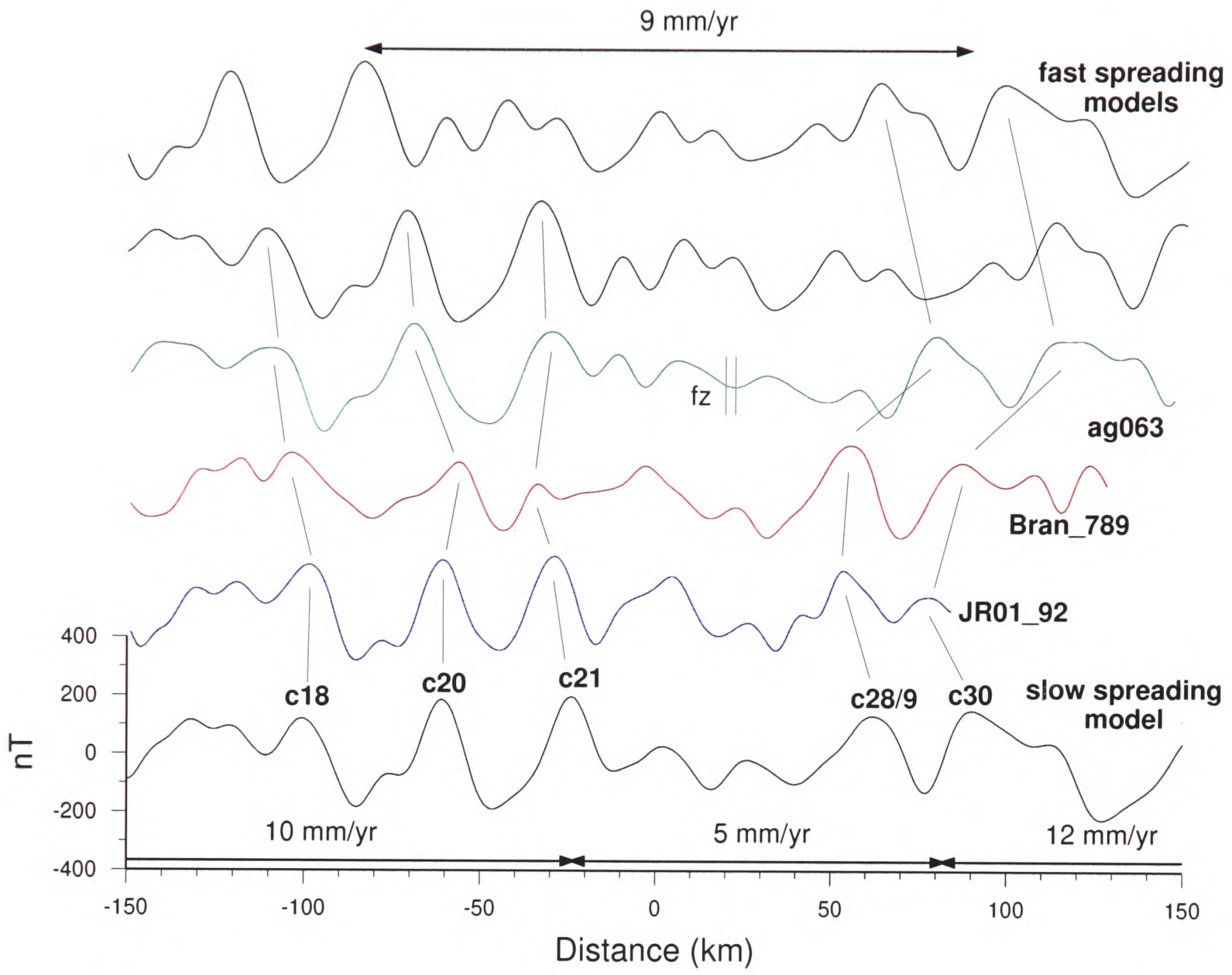

Figure 6.3: A series of magnetic profiles from the eastern Weddell Sea, displayed in comparison to synthetic magnetic profiles for both slow and fast spreading rates from c21 to c30.

---

have occurred over such a substantial period of time (≈20Ma). Asymmetric spreading has been determined to exist in two differing forms. True asymmetric spreading is where the discrepancy in apparent spreading rates is the result of greater accretion on one of the plates. The exact causes for this are not exactly known, though it has been suggested that the the ridge is being affected by a slightly off-centre heat source (Rea, 1978), or that the different rates of accretion are related to differing velocities of the plates relative to the underlying mantle (Stein *et al.*, 1977). Asymmetry of this form is more likely to lead to more long-term asymmetry, whereas the pattern of spreading in the Weddell Sea could only be explained through such true asymmetric spreading occurring only from around c30 to c21, beginning and ending reasonably abruptly. In addition, accretionary asymmetry of this form rarely gives rise to asymmetry greater than the order of 50% (Rea, 1978), far less than that predicted in the Weddell Sea (closer to 300%). If pure asymmetric spreading was occurring in the Weddell Sea, and was the only reason for the the

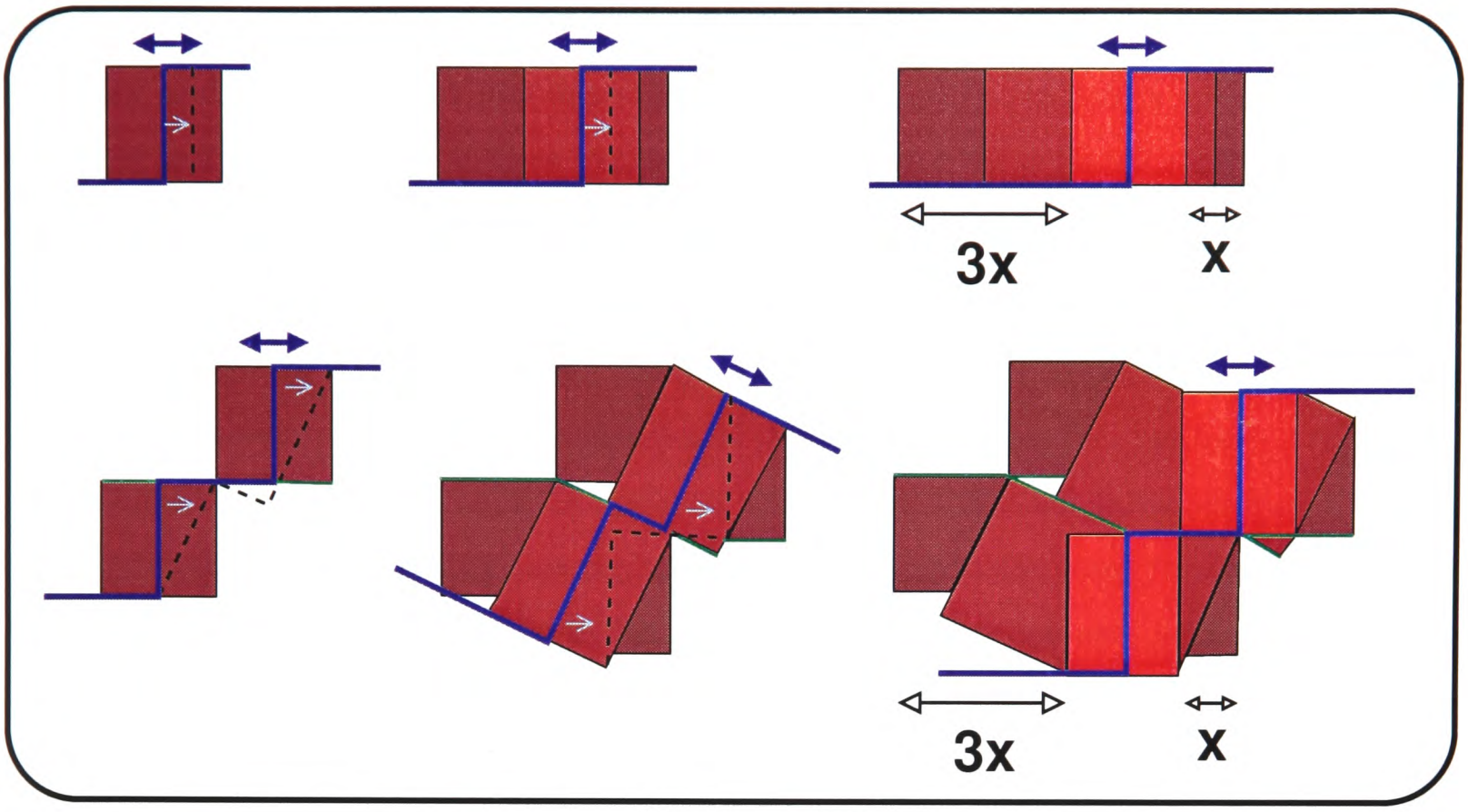

Figure 6.4: Two series of schematic diagrams showing how repeated ridge jumps can lead to apparent asymmetry in the seafloor created at a mid-ocean ridge. The first series shows straightforward ridge jumps onto one flank of a ridge, the second shows how ridge re-orientation in response to changes in spreading direction can lead to asymmetry. The green lines mark the traces of the transforms on the ridge flanks.

lack of extension, then there would not necessarily be the disturbance to the flowlines that is seen (Figure 6.2). It would be expected that the spreading would still occur at the same spreading centres and no ridge re-organisation would usually occur as a result of the difference in accretion rates, and so the fracture zones would remain undisturbed.

Pseudo-asymmetric spreading occurs when there are a series of discrete ridge jumps along a mid-ocean ridge, which are sufficiently small that magnetic anomaly patterns and seafloor topography are not overly disrupted (Rea, 1978; Marks & Stock, 1995). The asymmetry results not from greater accretion on one plate, but through seafloor initially created on one flank being 'captured' by the opposing flank as the result of a ridge jump.

Figure 6.4 shows how asymmetry can occur from ridge jumps occurring along a spreading centre. The first set of diagrams shows how a couple of spontaneous ridge jumps towards one flank leads to this pseudo-asymmetry. If the coloured bands are considered as magnetic anomaly reversal epochs, then it can be seen how it could be hard to differentiate between this and true asymmetric spreading, since the only difference between the two sides is in the width of the anomaly 'stripes'. The second series shows how ridge jumps in response to changes in spreading

direction could lead to asymmetry. It is important to note how the repeated changes in transform geometry lead to the fracture zone trace becoming indistinct, in particular on the flank which shows the less extension. So, if there was a succession of small ridge jumps in this way, it would account for both the seafloor deficit and also for the indistinct fracture zone traces.

A requirement for such an effect accounting for the amount of asymmetry believed to have occurred is that the ridge jumps were always towards the Antarctic plate, but this is not an unreasonable assumption. Cormier & Macdonald (1994) describe how the propagation of discrete ridge jumps onto one flank results in apparent asymmetry and ridge reorganisation along the East Pacific Rise. The timing for this postulated ridge reorganisation along the South American-Antarctic Ridge does coincide with the changes in spreading direction seen in the fracture zones flanking the Southwest Indian Ridge, and known ridge jumps at the southern Mid-Atlantic Ridge (Barker, 1979; LaBrecque & Hayes, 1979). Though any suggestions for the pattern of ridge jumps would be purely hypothetical, a 2-stage model, such as that shown in Figure 6.4, with the first change in spreading direction and ridge re-orientation occurring shortly after c30, and a return to the original spreading direction and ridge geometry sometime after c24, seems likely.

Thus, it has been argued that true asymmetric spreading is unlikely to have produced such a shortfall in accretion, and would not have caused the discontinuities observed in the flowlines. A large scale ridge jump to another location on the South American Plate, returning later to the former position, would be hard to justify from the evidence available. The existence of a Malvinas Plate in the Weddell Sea could not account for the observed features, which are not seen in the seafloor to the north created at the present-day South American-Antarctic Ridge closest to the postulated location of a Malvinas Plate, and which occur at a time outside the period during which the Malvinas Plate is believed to have existed. Thus the most likely scenario for the discrepancy of seafloor spreading seen in the Weddell Sea is that there has been small-scale ridge re-orientation in response to changes in spreading direction. This would account for both the disrupted flowlines seen in the Weddell Sea between anomalies c21 and c30, and for the lack of extension during this period relative to that predicted from the 3-plate circuit.

6.2 A revised 3-plate reconstruction for the SAM-AFR-ANT system

After considering the implications of the discontinuity in the Weddell Sea, it was decided that this was likely to have had a disruptive effect on the 3-plate inversion which had been carried out assuming continuous spreading in the Weddell Sea. A further 3-plate inversion was then carried out, in which the fracture zones in the Weddell Sea were split into 2 sections across the discontinuity, and the magnetic anomaly groupings were also divided across this region, arranged into groups of c21 and younger, and c30 and older. The drawback of the division of the fracture zone dataset in this way was that this meant there would be very few, if any, fracture zone picks in the c21-c30 sections of the flowlines, and so the fracture zones in the Weddell Sea would contribute little to the determination of these poles. The remainder of the SAM-ANT dataset was kept unchanged, as were the datasets from the other plate boundaries. The inversion was carried out for all anomalies, including c24, with the c24 anomalies observed in the flanking the present-day South American-Antarctic Ridge included in the SAM-ANT dataset. It was hoped that since the discontinuity in the Weddell Sea at around this time had been discovered, and its effect on the inversion nullified, the information from the SAM-AFR and ANT-AFR plate boundaries, and the lesser contribution from the SAM-ANT dataset, would be sufficient to resolve the c24 finite rotation poles for the 3 plate system.

Table 6.1: The set of finite rotation poles obtained for the SAM-AFR-ANT system from the revised 3-plate inversion.

Chron	Age (Ma)	Latitude	Longitude	Angle	95% confidence ellipsoid			
					Axis 1	Axis 2	Axis 3	Azimuth
South America - Africa								
c2A	2.58	55.85	-38.10	0.80	0.87	0.25	0.01	99.93
c5	9.74	57.54	-37.66	3.16	0.58	0.16	0.01	107.97
c6	19.05	56.47	-35.99	7.08	0.34	0.07	0.02	107.19
c8	25.82	55.76	-34.61	9.97	0.26	0.05	0.04	105.42
c13	33.06	55.96	-33.22	13.46	0.19	0.04	0.02	103.81
c18	38.43	56.88	-32.45	15.85	0.18	0.04	0.03	101.24
c20	42.54	57.80	-31.85	17.50	0.17	0.05	0.02	101.95
c21	46.26	58.63	-31.27	19.08	0.17	0.04	0.02	100.47
c24	52.36	61.31	-31.90	21.32	0.15	0.03	0.03	103.32
c30	65.58	63.15	-32.87	24.74	0.12	0.03	0.02	104.66

continued on next page

Chron	Age (Ma)	Latitude	Longitude	Angle	95% confidence ellipsoid			
					Axis 1	Axis 2	Axis 3	Azimuth
continued from previous page								
c32	71.07	62.13	-32.28	26.53	0.16	0.04	0.02	106.11
c33	73.62	62.36	-32.58	27.97	0.14	0.04	0.03	104.70
c33r	79.08	62.27	-33.41	30.98	0.10	0.04	0.02	102.48
c34	83.00	61.65	-33.81	33.50	0.12	0.05	0.02	99.41
Antarctica - Africa								
c2A	2.58	6.45	-38.76	0.36	1.39	0.29	0.01	122.40
c5	9.74	6.39	-41.38	1.34	1.52	0.59	0.01	128.92
c6	19.05	9.82	-40.02	2.90	0.72	0.27	0.02	131.91
c8	25.82	11.84	-41.70	3.96	0.64	0.23	0.02	134.39
c13	33.06	13.66	-41.58	5.54	0.51	0.16	0.02	134.39
c18	38.43	12.52	-40.70	6.79	0.46	0.17	0.02	130.60
c20	42.54	12.25	-40.65	7.50	0.49	0.18	0.02	125.22
c21	46.26	11.47	-40.31	8.40	0.48	0.16	0.02	126.01
c24	52.36	7.13	-39.06	9.57	0.72	0.17	0.02	121.77
c30	65.58	-0.42	-43.44	11.71	0.59	0.11	0.02	118.64
c32	71.07	-2.11	-42.68	12.98	0.45	0.11	0.02	121.59
c33	73.62	-1.65	-42.58	13.73	0.41	0.10	0.03	122.72
c33r	79.08	-1.22	-41.30	15.80	0.32	0.07	0.02	123.44
c34	83.00	-0.45	-40.01	17.77	0.34	0.08	0.02	123.05
South America - Antarctica								
c2A	2.58	81.95	-34.13	0.63	1.19	0.24	0.01	104.91
c5	9.74	81.26	-20.34	2.55	0.78	0.42	0.02	106.54
c6	19.05	78.27	-18.83	5.51	0.44	0.19	0.03	101.38
c8	25.82	75.31	-13.04	7.65	0.41	0.13	0.04	96.82
c13	33.06	75.10	-5.50	10.12	0.29	0.12	0.03	92.37
c18	38.43	76.81	2.98	12.02	0.28	0.12	0.04	80.04
c20	42.54	77.22	8.33	13.42	0.25	0.12	0.04	74.00
c21	46.26	78.03	17.00	14.78	0.25	0.11	0.03	71.08
c24	52.36	80.78	35.35	17.55	0.33	0.09	0.05	59.58
c30	65.58	78.76	54.29	22.22	0.23	0.06	0.04	37.28
c32	71.07	78.09	54.27	24.00	0.19	0.05	0.04	35.43
c33	73.62	77.91	55.44	25.23	0.17	0.07	0.04	34.98
c33r	79.08	77.77	60.68	27.79	0.14	0.05	0.03	30.34
c34	83.00	77.43	64.08	29.62	0.16	0.07	0.04	21.38

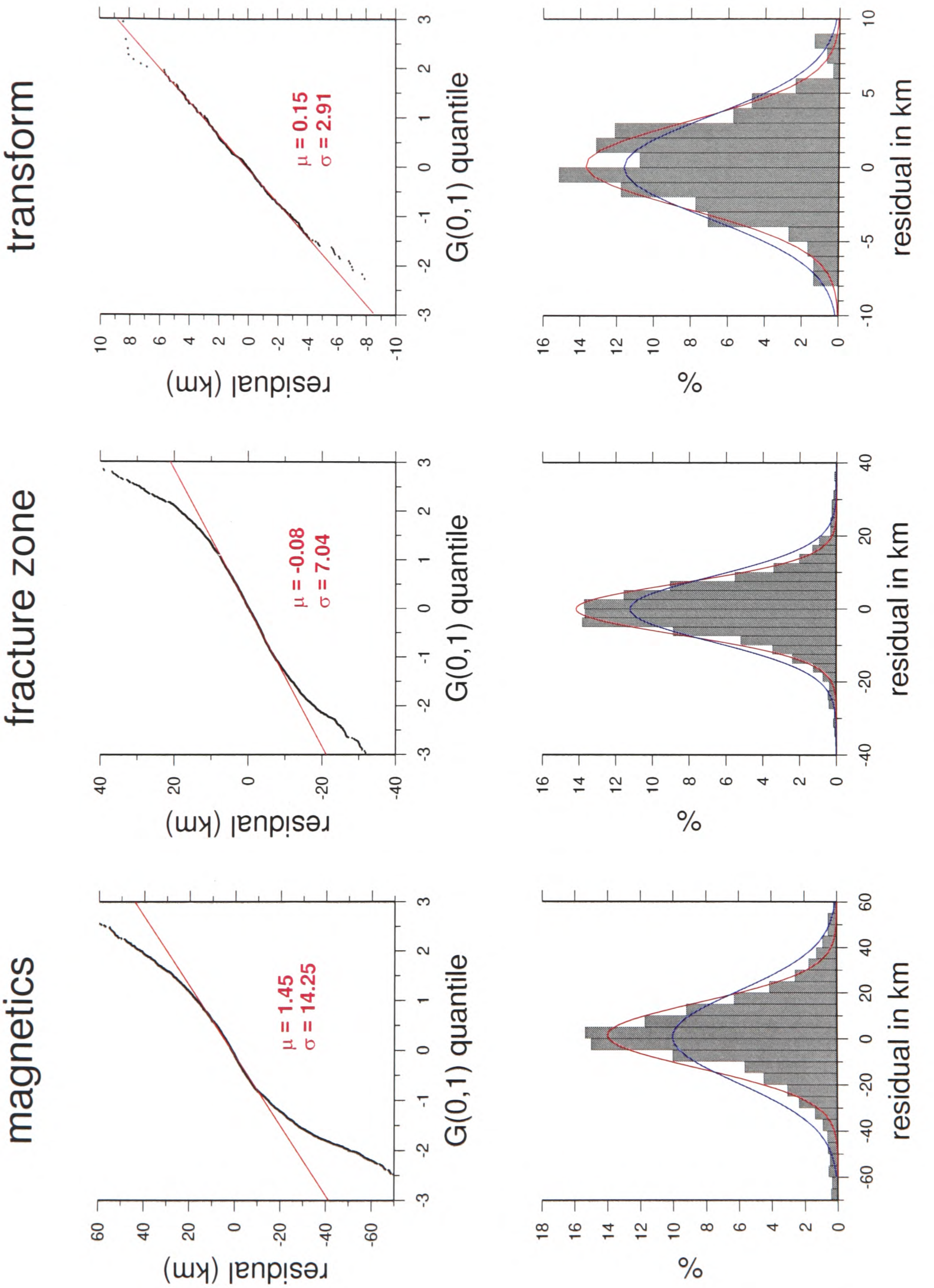

Figure 6.5: Quantile-quantile (q-q) plots and histograms for the residuals for each type of data used in the revised SAM-AFR-ANT 3-plate inversion. In the q-q plots, the red line represents the best fit line, through linear regression, for the central $\pm 1\sigma$ of the test distribution (Gaussian(0,1)). In the histograms, the red line represents the Gaussian distribution defined by the statistics obtained from the q-q plots, and the blue line represents the Gaussian distribution with statistics defined by the the sample mean and standard deviation of the dataset.

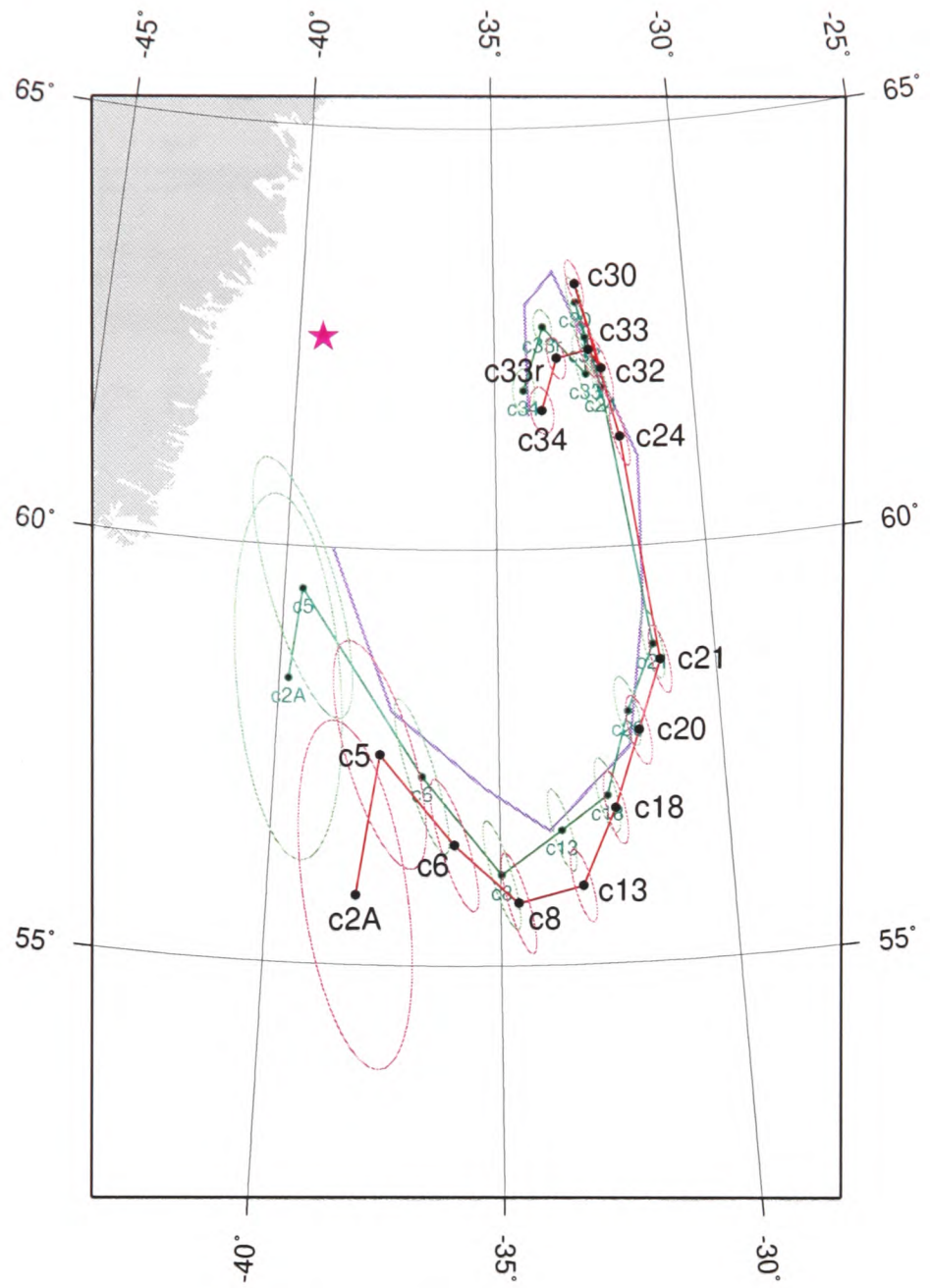

Figure 6.6: The set of solution poles for SAM-AFR spreading obtained from the revised 3-plate inversion shown in red, with corresponding 95% confidence ellipses. The poles and confidence ellipses determined from the 2-plate SAM-AFR inversion are shown in green, and those obtained by Shaw & Cande (1990) in light blue. The NUVEL-1A instantaneous pole is marked by a purple star.

The set of solution poles obtained from the revised 3-plate inversion for South American - African - Antarctic spreading are given in Table 6.1. The residuals from the 3-plate inversion are shown in Figure 6.5. Though the distributions for the transform and fracture zone residuals have changed very little, the distribution of the magnetic residuals has improved, with the standard deviation derived from the q-q plot decreasing from around 15 to 14 km, and the histogram appearing more symmetric than that for the previous 3-plate inversion. The data importances are virtually unchanged from those shown in Figure 5.18 in Chapter 5, and so are not displayed here.

The improvement in the 3-plate inversion is seen more clearly when viewing the solution

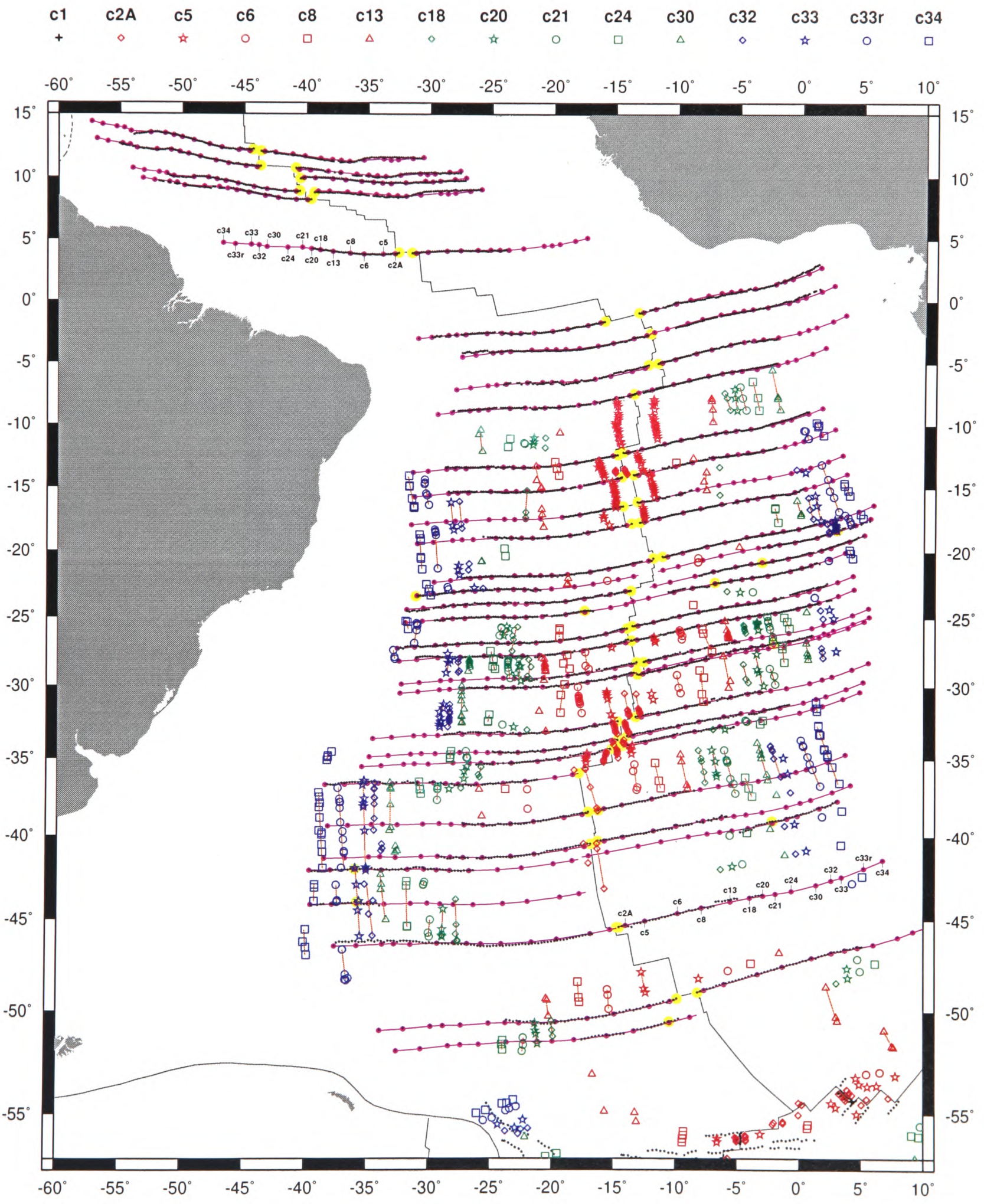

Figure 6.7: The magnetic anomaly and fracture zone picks for SAM-AFR spreading used in the revised 3-plate inversion, along with the flowlines generated by the final solution poles. The fracture zone picks are marked by black stars and the flowlines depicted by the purple lines, with solid circles marking the end of each flowline stage. The magnetic anomalies are represented by the appropriate symbols, as shown in the symbol table, and the fitted great circles shown in orange.

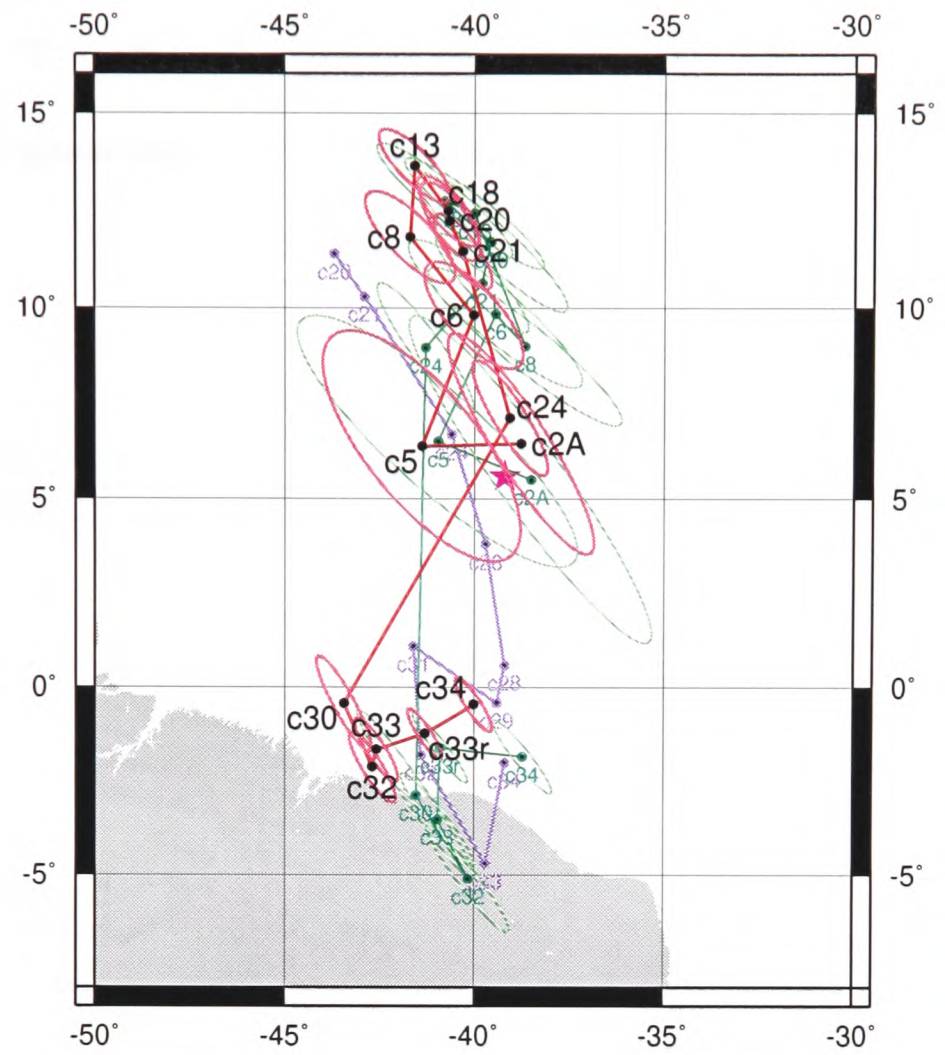

Figure 6.8: The set of solution poles for ANT-AFR spreading obtained from the revised 3-plate inversion shown in red, with corresponding 95% confidence ellipses. The poles determined by the two plate ANT-AFR inversion are shown in green, and those obtained by Royer *et al.* (1988) in light blue. The NUVEL-1A instantaneous pole is marked by a purple star.

---

poles and synthetic flowlines. Figure 6.6 shows the poles for South American - African spreading obtained from the revised 3-plate inversion. Because of the dominance of the South-American data within the overall datasets, the poles are little different from the previous 3-plate poles. The major difference from the results of the previous 3-plate inversion is the inclusion of the c24 pole in the inversion. This appears to the south of the c24 pole obtained from the 2-plate reconstruction, which was originally thought to be further north than expected. This new c24 pole is now close to the c25 pole of Shaw & Cande (1990) and at a more likely location in the general progression of poles.

The set of flowlines generated from the poles is shown in Figure 6.7 along with the fracture zone picks, magnetic isochron picks and isochron great circles used in the inversion. This shows very little difference from that produced by the previous 3-plate inversion (Figure 5.21, Chapter 5), with the exception of the additional c24 'node' appearing in the flowlines.

The poles for Antarctic - African spreading obtained from the 3-plate inversion are shown

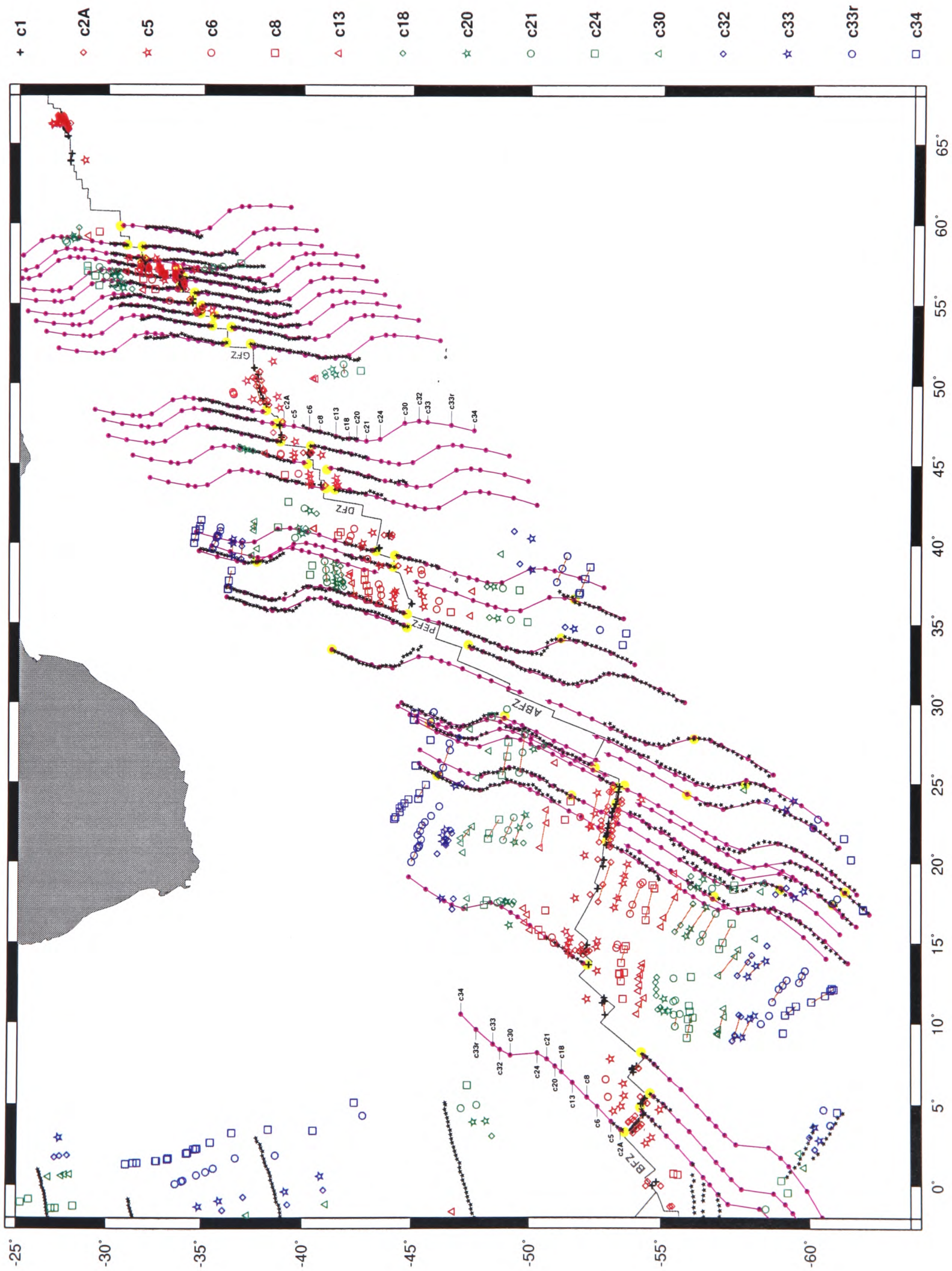

Figure 6.9: The magnetic anomaly and fracture zone picks for ANT-AFR spreading used in the revised 3-plate inversion, along with the flowlines generated by the final solution poles. The fracture zone picks are marked by black stars and the flowlines depicted by the purple lines, with solid circles marking the end of each flowline stage. The magnetic anomalies are represented by the appropriate symbols, as shown in the symbol table, and the fitted great circles shown in orange. (Annotation abbreviations: BFZ-Bouvet Fracture Zone; ABFZ-A.Bain Fracture Zone; PEFZ-Prince Edward Fracture Zone; DFZ-Discovery Fracture Zone; GFZ-Gallieni Fracture Zone.)

in Figure 6.8. An improvement from the initial 3-plate inversion can be seen here, with the c21 pole no longer showing a digression from the general migration of solution poles. The poles are relatively stable from c34 to c30, with a slight drift westward, then there is a migration north to the c24 pole, which incidentally lies quite close to that of Royer *et al.* (1988). From c21 to c8, the poles appear very stable, with each of the poles located within a couple of degrees of the others, with considerable overlap between the confidence ellipses, and in particular, the c18,20 and c21 poles are very close indeed. From c13 to the most recent pole, c2A, there is a further steady drift to the south, virtually unchanged from the initial 2-plate inversion.

The overall stability of the poles from c34-c30 and c21 to present is reflected in flowlines corresponding to these new poles, which are shown in Figure 6.9, along with the fracture zone picks, magnetic picks and isochron great circles. The c18-c20-c21 kink that appeared in the previous 3-plate inversion ANT-AFR flowlines has disappeared, showing that this was purely an artifact of the Weddell Sea discontinuity. The flowlines now show steady spreading up until c32, after which the spreading direction begins to rotate anti-clockwise so that from c30-c24 the spreading direction has changed by around 45 degrees. After c24, it has virtually returned back to the previous direction, and certainly from c21 until the present day the direction of spreading has remained virtually constant, in an almost identical direction to that seen prior to c30.

As before, the fracture zones and magnetic anomalies at the eastern end of the Southwest Indian Ridge are all younger than c24, suggesting that seafloor spreading at this ridge has only been occurring since anomaly 24 (≈50Ma). However, in this region, from 42°E to 60°E, there is not a gradual decrease in length of fracture zone trace and maximum anomaly age towards the Indian Ocean Triple Junction (70°E, 25°S). Instead, along this whole length of ridge, around 1500km, spreading appears to have begun almost simultaneously, indicating a sudden break, as opposed to a gradual propagation of the Indian Ocean Triple Junction eastward.

The set of finite rotation poles for South American - Antarctic spreading obtained from the revised 3-plate reconstruction are displayed graphically in Figure 6.10. As with the revised ANT-AFR solution poles, they are very similar to the set of poles from the initial 3-plate inversion, with the exception of the c21 and c30 poles, and the addition of the c24 pole. The progression of poles from c34 to c30 is very similar to that seen in the previous 2-plate inversion, with c30 conforming with the westward migration of the poles, as opposed to the apparently anomalous position of the c30 pole from the initial 3-plate inversion. As seen with both the other plate pairs,

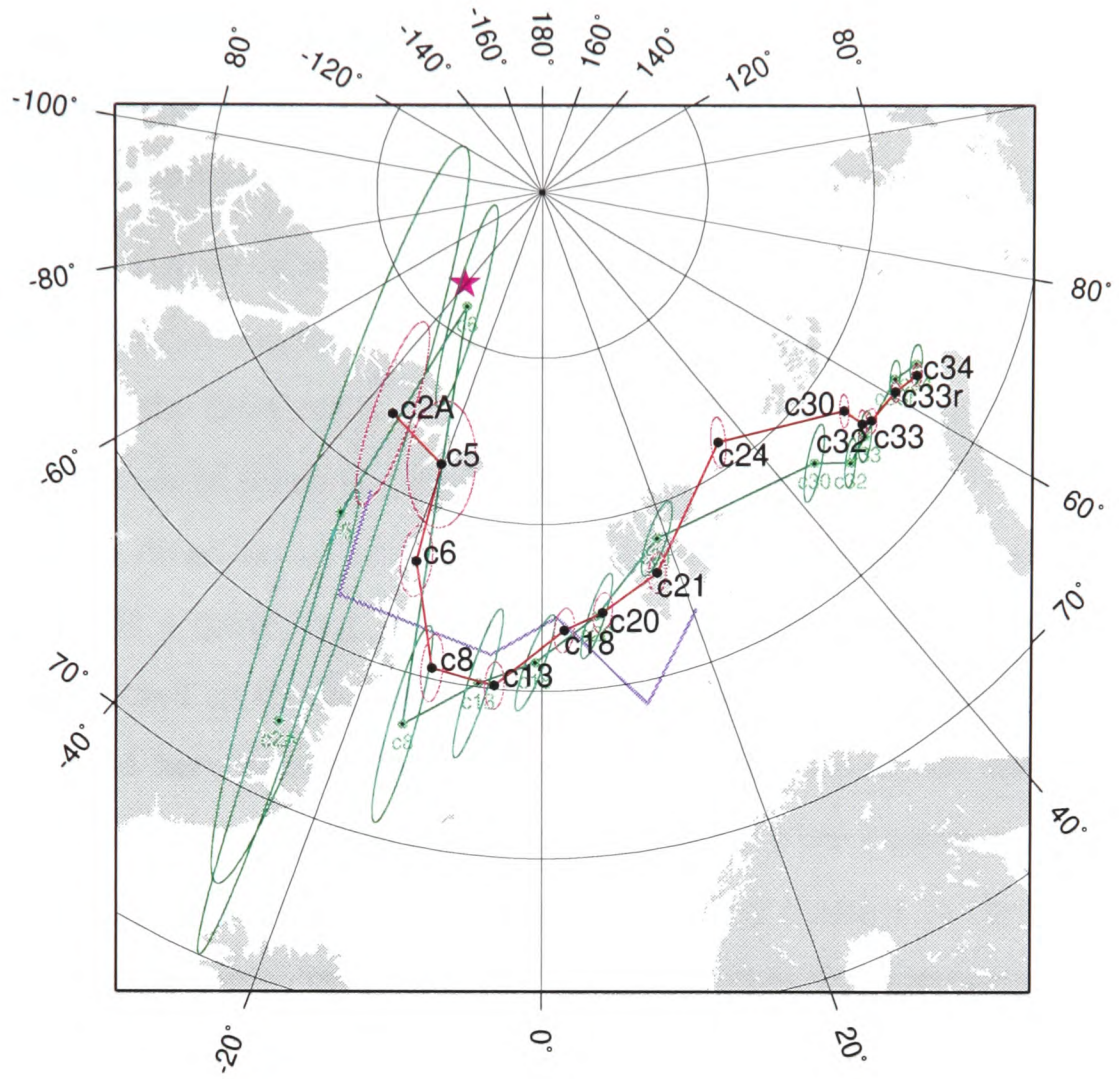

Figure 6.10: The set of solution poles for SAM-ANT spreading obtained from the revised 3-plate inversion shown in red, with corresponding 95% confidence ellipses. The poles and confidence ellipses determined from the 2-plate SAM-ANT inversion are shown in green, and those obtained by Barker & Lawver (1988) in light blue. The NUVEL-1A instantaneous pole is marked by a purple star.

---

these poles are grouped closely together, representing relatively stable plate motion, during this period. The c24 pole is the first derived for this plate pair, and despite the lack of c24 data in the SAM-ANT dataset, the pole appears in a perfectly reasonable location. Though the size of the confidence interval for the c24 pole is quite small, this is mainly related to the minimal amount of data that exist in the Weddell Sea contributing to the determination of this pole, and given more SAM-ANT data for this chron, the location of this pole might well change.

There is quite a significant jump westward from c30 to c24, as would be expected from the predicted change in spreading direction at that time, and the pole fits in reasonably well with the overall eastward migration of poles. The c21 pole is close to the location of the 2-plate pole, and as with the c30 pole, this similarity in locations suggesting that the c21 pole from the previous 3-plate inversion was in error. From c20 to c8, the poles are very close to those obtained from both the 2-plate and the initial 3-plate inversion, with a steady migration to the south-west. The sequence of the c13-c8-c6 poles is now much smoother than that seen in the two-plate inversion,

with the migration of poles switching at the c8 pole from a south-westerly direction to northwards. The c6 and more recent poles are virtually unchanged from those obtained by the initial 3-plate inversion, and are a definite improvement on those obtained from the 2-plate inversion.

Figure 6.11 shows the set of synthetic flowlines generated from this new set of solution poles for SAM-ANT spreading, along with the fracture zone and magnetic anomaly datasets. The first thing to notice is that the flowlines are much smoother than those obtained previously. As could be predicted from the set of solution poles obtained, and in line with the other plate boundaries, from c34 to c30, the direction of seafloor spreading remains virtually constant. The flowline section from c30 to c24 is quite long, but there is no longer such a significant change in spreading direction as was predicted by the 2-plate model. In fact the change in spreading direction may be greater than predicted here because the major source of information on the spreading direction is provided by the fracture zones in the Weddell Sea, as they are closest to the poles of motion. As stated previously, this means that they would reflect any changes in the stage poles, through changes in spreading direction, much greater than any other fracture zones in the SAM-ANT dataset.

In splitting the fracture zones across the Weddell Sea discontinuity, we have at a stroke removed the most reliable guide to changes in spreading direction from c30 to c24/c21, but this unfortunately cannot be avoided, and so the majority of data contributing information on the spreading direction during this period comes from the northern South American-Antarctic Ridge which does not reflect changes in pole location so clearly. As such, it is likely that the change in spreading direction during this period is more extreme than is seen in the flowlines, particularly as it is thought to have been the driving force behind substantial ridge reorganisation in the western Weddell Sea during this period, but this is speculation and cannot really be justified. It can be seen that the synthetic flowlines corresponding to the two halves of the fracture zones split across the Weddell Sea discontinuity no longer match up, though this effect generally becomes less apparent towards the east and it is possible that the discontinuity is only significant in the western Weddell Sea.

Despite reservations on the wisdom of including c24 in the inversion, the c24 node fits well into the flowlines throughout, though it does give rise to a small kink in the western Weddell Sea. As with the ANT-AFR flowlines, the kink that appeared from c21-c20-c18 has disappeared. From c24 until around c8/c6, the flowlines show a steady anti-clockwise rotation in spreading

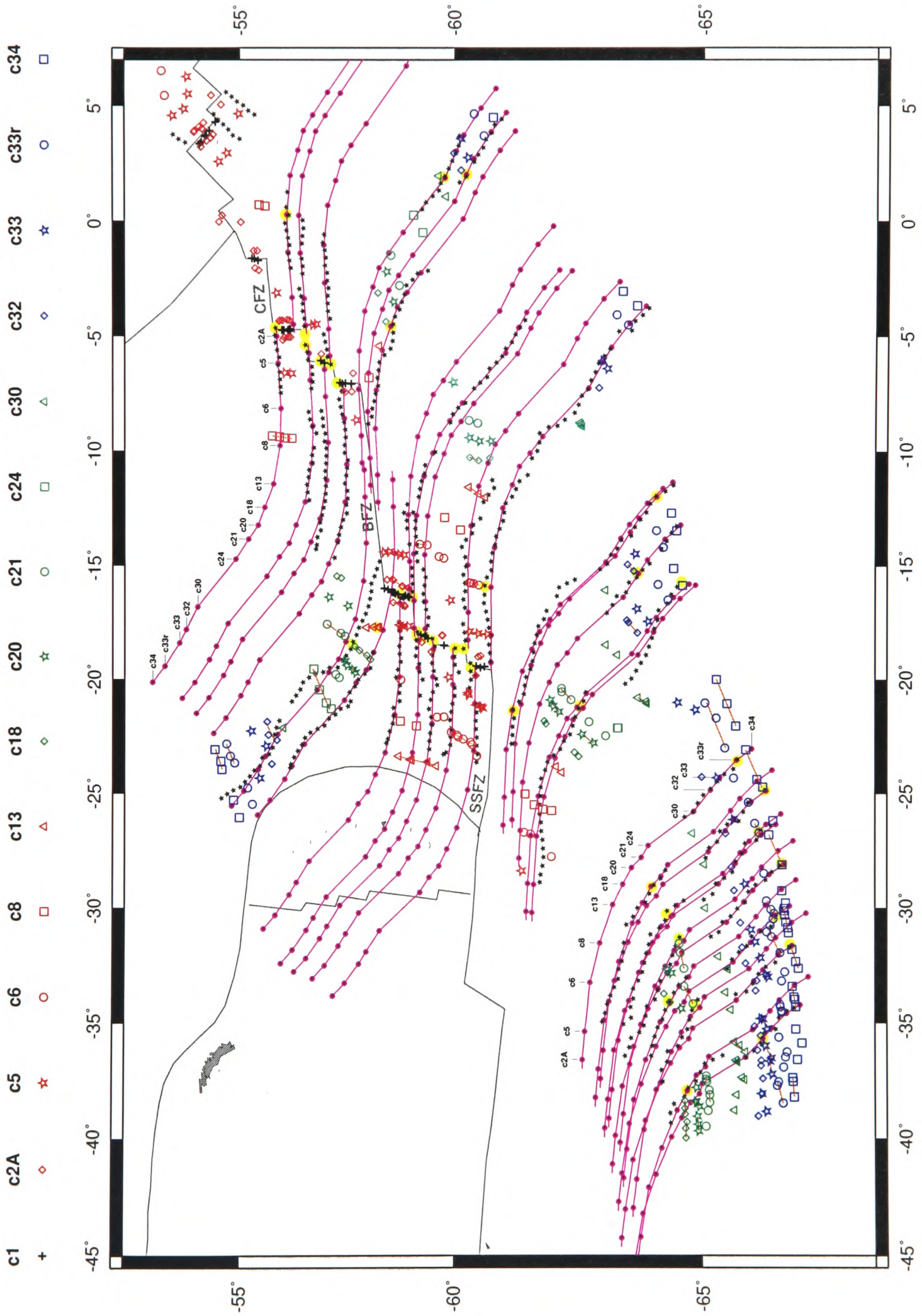

Figure 6.11: The magnetic anomaly and fracture zone picks for SAM-ANT spreading used in the revised 3-plate inversion, along with the flowlines generated by the final solution poles. The fracture zone picks are marked by black stars and the flowlines depicted by the purple lines, with solid circles marking the end of each flowline stage. The seed points from which each flowline is generated are marked by yellow stars. The magnetic anomalies are represented by the appropriate symbols, as shown in the symbol table, and the fitted great circles shown in orange.

direction, corresponding to the south-western migration of the finite rotation poles. From around c8, the direction of motion remains fairly constant, with pretty much east-west spreading along the length of the South American-Antarctic Ridge. This recent spreading direction is very close to that seen in the flowlines generated from the previous 2 and 3-plate inversions, and in the actual fracture zone traces flanking the South American-Antarctic Ridge. This is further evidence for the youngest parts of the fracture zone traces in the northern Weddell Sea being unrepresentative of the actual spreading direction at the time they were formed. It is suggested that there has been some small-scale rotation of small fragments of the Antarctic plate in this region during the period when the opposing (South American) flank was being subducted beneath the eastward moving South Sandwich Trench, which has led to the 'warping' of the fracture zones from the expected azimuths. This form of deformation has been seen elsewhere in the fragmentation of the Farallon Plate through pivoting subduction seen off the California coast by Menard (1978).

The match of the anomalies to the flowlines is now much more consistent throughout the region, with the Weddell Sea discontinuity taken into account. In particular, in the regions flanking the present-day South American-Antarctic Ridge, where a full range of anomalies lie alongside a continuous fracture zone, the anomaly isochrons and the flowline nodes correspond very well, with the exception of the two c24 anomalies to the east of the Bullard Fracture Zone.

6.3 Implications for South America - Antarctica seafloor spreading

There was clearly a significant improvement in the quality of the results obtained from the 3-plate inversion, once a discontinuity had been assumed in the Weddell Sea. The new fit for South-American spreading not only provided a very satisfactory fit to the data both in the Weddell Sea and in the vicinity of the South American-Antarctic Ridge, but was also in agreement with plate motion within the 3-plate SAM-AFR-ANT circuit. So, it can now be stated with some confidence that the disruption seen in the flowlines in Figure 6.2 is likely to have been caused by a discontinuity in South American - Antarctic spreading at the section of mid-ocean ridge, no longer in existence, that gave rise to the seafloor in the Weddell Sea.

Figure 6.12 shows the position of the magnetic anomaly picks rotated by a half-finite rotation back to theoretical location of the ridge segment at which each anomaly pick was created, overlaid

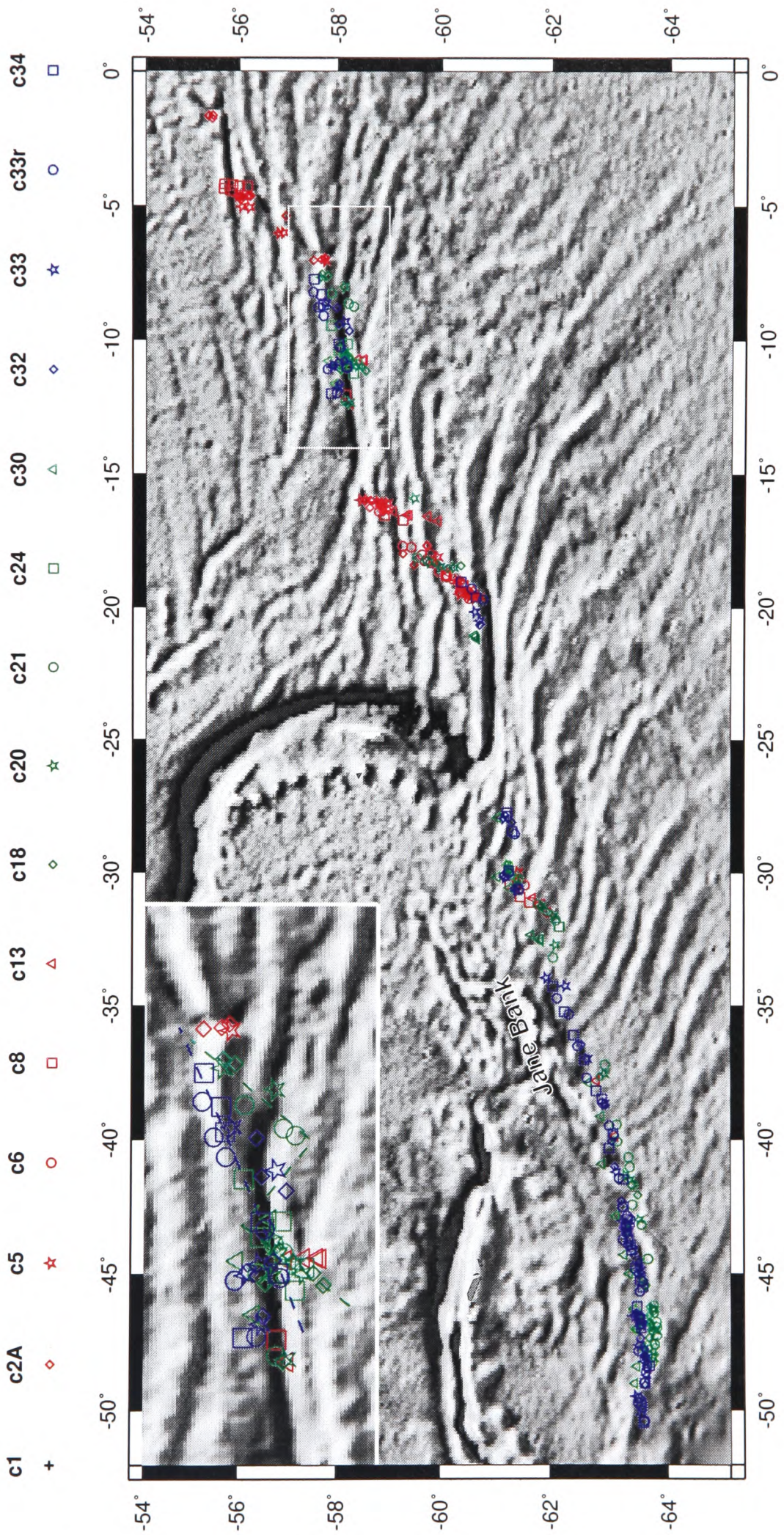

Figure 6.12: The complete set of anomaly picks for SAM-ANT spreading, rotated by a half finite rotation back to the theoretical position of the ridge at which they were created. The unrotated picks are shown as the normal symbols, and the rotated picks shown as smaller, darker symbols.

on top of a gravity basemap. If the ridge had remained in the same geometric orientation throughout the period covered by the inversion, then all of these picks should in theory rotate exactly back to the ridge segment at which they were created, which would be the same as the present-day spreading centres. If the ridge has changed its geometry during this period, then some of the picks should appear to form a band which is not coincident with the present-day mid-ocean ridge, but which is offset if a ridge jump has occurred, or is slightly rotated if the ridge has changed orientation. In the Weddell Sea, it can be seen the rotated picks form a relatively continuous belt, representing a series of ridge segments, slightly offset in places, that gave rise to the closely space series of short offset fracture zones visible in the Weddell Sea. Towards the western end, the rotated picks are split into two belts, which results from the ridge reorganisation across the discontinuity. At the eastern end of the Weddell Sea, a significant offset can be seen however, indicating the existence of quite a large transform at the ridge crest.

It is important to note the position of the band of rotated picks with respect to the gravity field, to the west of this offset in the Weddell Sea. The band coincides almost exactly with the apparent boundary of the Antarctic Plate with the South Scotia Ridge. Initially, this appears to confirm the views of Barker *et al.* (1984) that no Antarctic plate has been subducted by the South Sandwich Trench (and its ancestor), with subduction probably ceasing on collision with the active mid-ocean ridge with the trench. However, the study of Barker *et al.* (1984) estimated the ridge-crest collision at Jane Bank, $\approx$36°W, to have occurred at around 20/21Ma, but the band of rotated picks in that region lie very close to where this collision was estimated to have taken place. If spreading had in fact ceased at around this time, then the pseudo-ridge, as represented by the rotated picks would be expected to lie beyond this point, and beyond the end of the flowlines, but this is not seen. This pattern is seen from about 34°W across to around 42°W, but beyond this, the strike of the rotated picks and the line of apparent termination of Antarctic seafloor are both parallel to the flowlines from around c8 to present, and so any offset would not be apparent.

The obvious conclusion would appear to be that either the ridge collision occurred relatively recently, or that seafloor spreading has continued on the Antarctic flank after collision. However, it is clear from the mismatch between the fracture zone traces and predicted flowlines in the vicinity that there has been significant plate deformation in the region, and it would be unwise to draw such conclusions based on these results alone.

Along the present-day South American-Antarctic Ridge, the rotated picks are, in the most part, close to the location of the active ridge crest. Between the long-offset South Sandwich and Bullard fracture zones, at approximately 60°S, it can be seen that there are two main spreading centres, with minor offsets along each, but with a significant offset between the two at around 59°S. From the location of the rotated picks, it appears that a section of spreading centre that is currently aligned with the southern section of ridge crest was previously located to the west, in line with the more northern section. From the grouping of anomalies in the region, it appears that this jump occurred sometime between anomalies c13 and c8, at around 30Ma.

It was recognised by Barker & Lawver (1988) that the strike of the Bullard transform was incompatible with the spreading direction prior to anomaly 6, and this is reflected by the position of the rotated picks in the region. A large cluster of rotated picks occur along the current transform, but unfortunately the grouping is quite diffuse and no clear fossil ridge locations can be identified. In the inset in Figure 6.12, two dashed lines are drawn, showing two possible previous ridge geometries. The green line provides a reasonable fit to the rotated picks from anomaly c13 up to c21/24, suggesting a ridge jump between anomalies c13 and c8, which is in agreement with the timing of both the known changes in spreading direction along the ridge, and the minor ridge jump seen just to the south. The blue line approximately fits the rotated picks from c24/30 to c34, with no great confidence, but certainly providing a better fit to these picks than the green line representing the suggested ridge geometry after anomaly 24. No other ridge segments are suggested by rotated picks at the western end of the Bullard transform, but this is more likely due to the lack of anomaly picks flanking this region, rather than suggesting that there was already a large transform in existence in the region prior to anomaly c6/8.

6.4 Seafloor spreading history of the SAM-AFR-ANT 3-plate system

The first conclusion that can be drawn from the results of the revised 3-plate inversion is that by fitting the data satisfactorily on each of the plates, with a fit no worse than that obtained from the individual 2-plate inversions, it has been proved that we are dealing with a 3-plate system. There is no evidence of interaction with any other plates, and in particular, during the proposed period of existence of the Malvinas Plate, from c34 (83Ma) until around c30 (66Ma),

there is perfect agreement between the three sets of poles, with no anomalous spreading rates or directions being predicted. Thus from the data presented here, and the results of the 3-plate inversion, there is no evidence for the existence of a Malvinas Plate.

The stage poles obtained from the 3-plate inversion are displayed in Figure 6.13, for one of the plates in each plate pair. The South America - Africa stage poles for the African plate show a steady migration of the poles around a looping path, with the exception of the c32-c30 stage pole, which shows a significant divergence from the path being traced out by the stage poles. This is not due to any large changes in plate motion at the time, but instead is purely an artifact of the short time interval between these poles. As can be seen from Figure 6.7, the gap between the c30 and c32 flowpoints in the Mid-Atlantic flowlines north of the equator is very small, in a region where the data are most important to the inversion. As such, any slight errors in the finite rotation poles will be magnified in the calculation of the stage pole because of the short length of that stage. This point aside, the greatest changes in the stage poles occur in the period from c30 to c24, but as suggested by the very long, straight flowlines seen at the Mid-Atlantic Ridge, the changes in plate motion are not particularly dramatic. The greatest change in plate motion seems to be at c24-21, which is hinted at by a slight bend in the northernmost flowlines, but does not appear very significant.

The Antarctica - Africa stage poles shown in Figure 6.13 show a very different story. The stage poles for all plate motion from c34 to c32, and after c21 are all very closely grouped together, showing that the motion of Africa away from Antarctica has been very stable, except for the intervening period. There is a large jump in the stage poles from c33-32 to c32-30, as the change in plate motion begins, then again to the c30-24 stage pole, which represents the period when ANT-AFR spreading was at almost 45° to the steady-state spreading direction, reflected in the large bend in the ANT-AFR flowlines (Figure 6.9). By c24-21, plate motion is beginning to return to normal, and by c21, the Antarctic - African stage poles have returned to their extremely stable location, centred around 40°W, 10°N.

The South America - Antarctica stage poles show a different story again, with the poles initially showing a steady migration westward from c34, but after c30, there is a jump east against the trend to the c30-24 stage pole. There is then another jump east to the c24-21 stage pole. This pole has a degree of uncertainty attached to it however, because as with the c32-30 SAM-AFR stage pole, there was very little flowline information for this stage, in particular in the

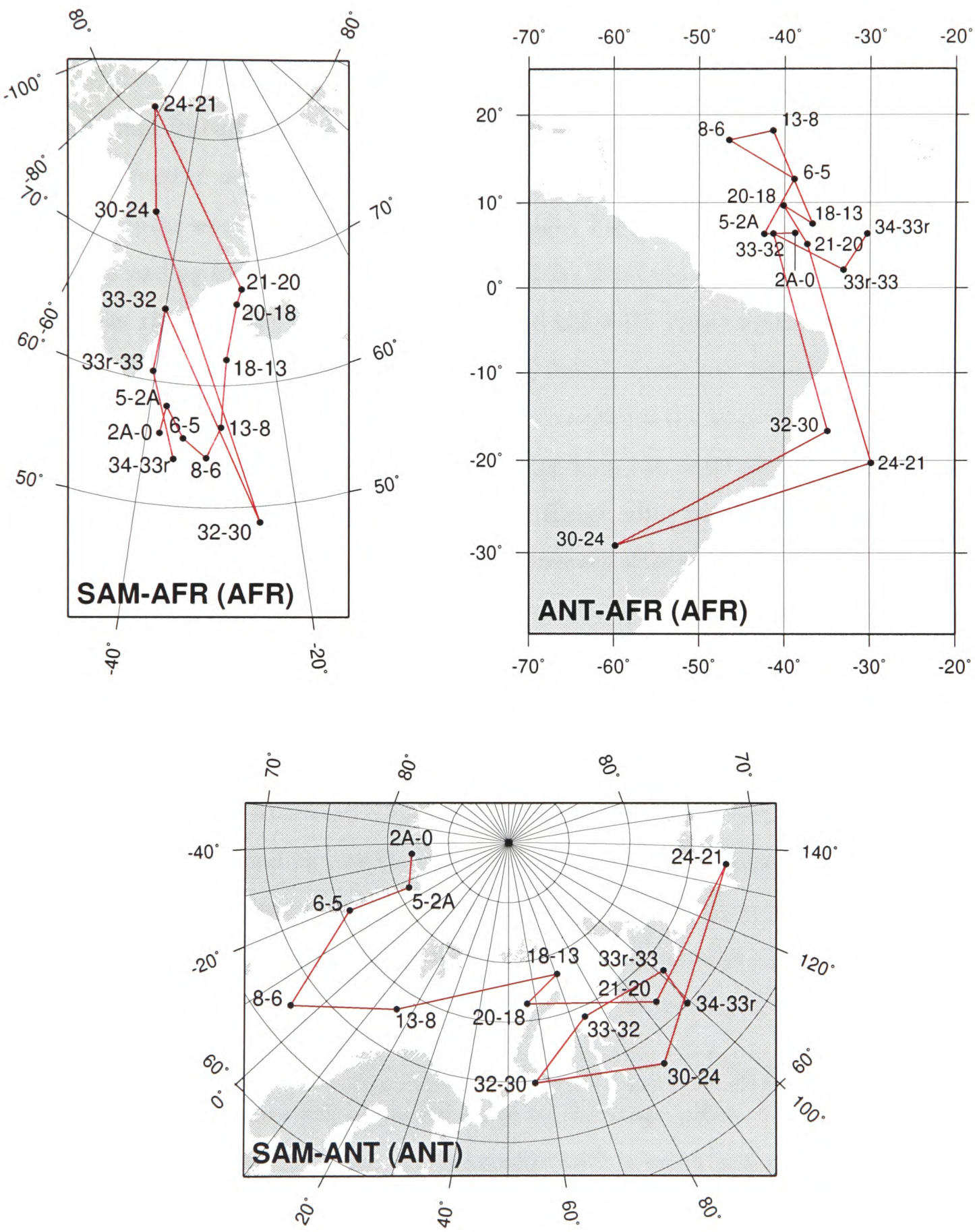

Figure 6.13: Sets of stage poles for each plate pair for the SAM-ANT-AFR 3-plate system, as determined by the revised 3-plate inversion. The flank for which the stage poles are calculated is given in brackets.

Weddell Sea, where it was known the fracture zone data had the greatest importances. Beyond c21, the stage poles resume their steady drift westward until anomaly 6, after which the stage poles begin to move north. This gradual migration of the stage poles is reflected in the gentle curving of the flowlines seen in Figure 6.11.

The common features in these three sets of stage poles are the changes at around c30-c24. To determine further any possible links and coordination between these changes, the spreading rates and azimuths were examined for each plate pair. Figure 6.14 shows the rates and azimuths of seafloor spreading for each of the plate pairs, along flowlines beginning at the central section of each of the ridges (with the exception of the SAM-ANT data, which were generated along a flowline in the eastern Weddell Sea, originating from a point not actually at the present-day South American-Antarctic Ridge). The first thing to notice is the huge drop in spreading rates at the Mid-Atlantic Ridge and Southwest Indian Ridge from c34 until c30 (≈65Ma) The spreading rate remains low until c24 along the Mid-Atlantic Ridge, after which it begins to increase again up to a half-rate of around 26mm/yr, but then decreases after anomaly 8 (25Ma) to the present day rate of rate of approximately 17mm/yr. The rate at the Southwest Indian Ridge never really recovers again, hovering at around 11 mm/yr half-rate until anomaly 8, after which it decreases slightly to the present day half-rate of around 8mm/yr.

The large variations in spreading rate seen at the two other ridges in the 3-plate system are simply not seen in South American - Antarctic spreading. Although the 2-plate SAM-ANT model does show significant spreading rate changes, both increases and decreases, from c32 to c20, these do not appear in the 3-plate rates. The rate appears quite steady, at approximately 10mm/yr, from c34 until c24 (≈53Ma), when it briefly drops to around 6mm/yr. The rate then increases to a half-rate of around 13mm/yr from 25 to 20Ma, before decreasing to the present-day half-rate of around 8mm/yr.

The spreading directions tell a similar story to the stage poles. The azimuth of spreading at the Mid-Atlantic Ridge changes very gradually, with a small but steady clockwise rotation until around 45Ma (anomaly 21/20), after which it rotates slightly anti-clockwise, but remains virtually constant. Changes in Antarctic - African spreading azimuths at the Southwest Indian Ridge are dominated by the significantly different spreading direction from anomaly 30 until anomaly 24 (52Ma). As with the ANT-AFR stage poles, the change begins at c32 (71Ma) and by c21 (45Ma), the spreading direction has returned to the predominant azimuth of around N25°E.

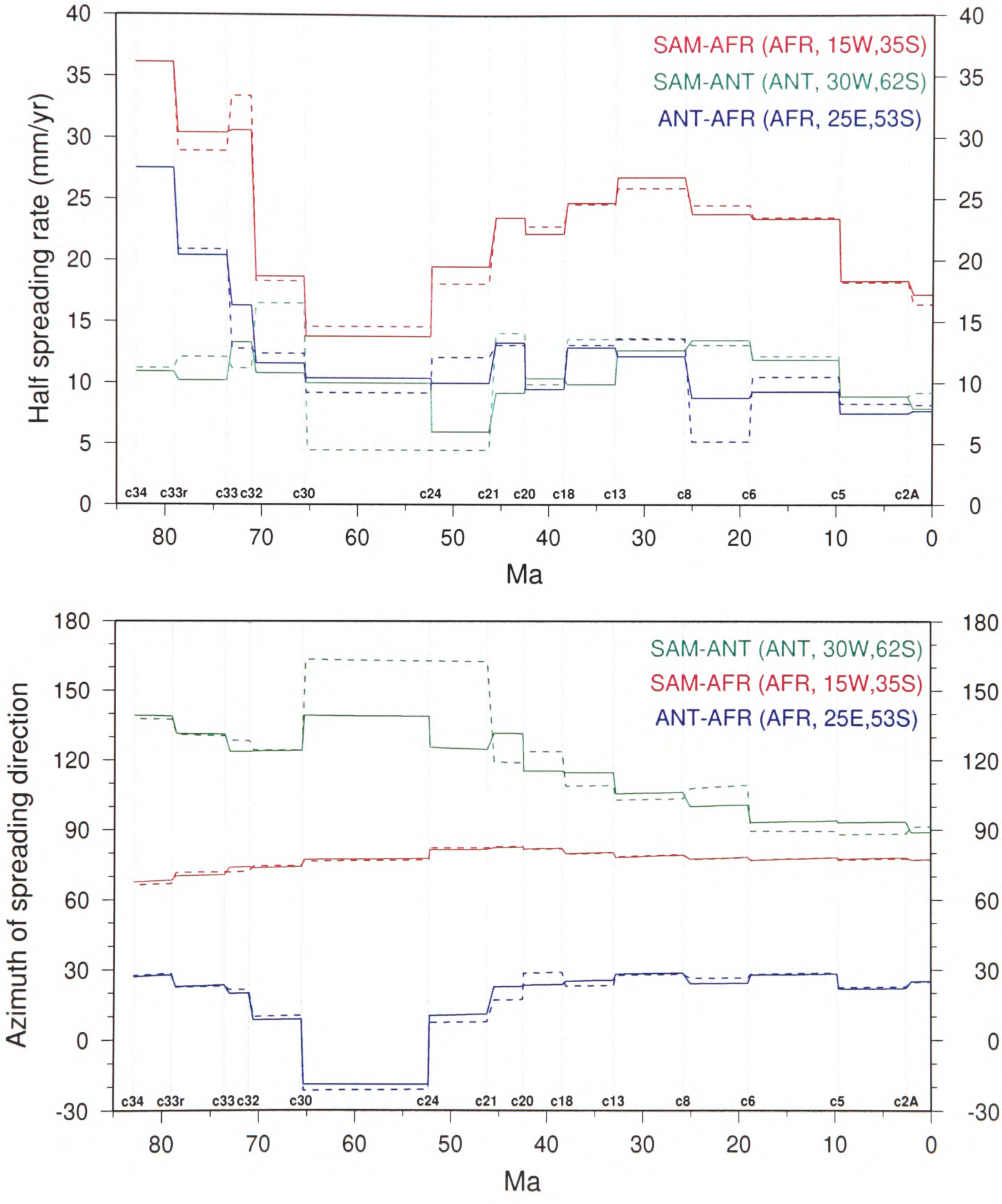

Figure 6.14: Typical spreading rates (half rates) and directions determined from the inversions for SAM-AFR spreading along the Mid-Atlantic Ridge (shown in red), ANT-AFR spreading along the Southwest Indian Ridge (blue), and SAM-ANT spreading at the South American-Antarctic Ridge (green). The solid lines show the rates and azimuths predicted by the 3-plate inversion, and the dotted lines represent those from the 2-plate inversions.

The South American - Antarctic spreading direction (on the Antarctic plate) shows a reasonably steady anti-clockwise rotation with time, with the main exception of the period from c30 (75Ma) to c24 (52Ma). During this time, the spreading direction rotates clockwise, against the general trend (even more so in the since-discredited 2-plate SAM-ANT azimuths).

What becomes clear from these various studies is that an event seems to have occurred that had a significant effect on the plate motions within the 3-plate circuit, resulting in the considerable slow-down in rates of Antarctic - African and South American - African seafloor spreading. This disturbance appears to have come to a head at around anomaly 32 (72Ma). Shortly after this time, the spreading rates reached their minimum at the Mid-Atlantic Ridge and Southwest Indian Ridge and there was a large change in the direction of Antarctic-African plate motion. There were also large ridge jumps at the southernmost Mid-Atlantic Ridge (Barker, 1979; LaBrecque & Hayes, 1979) and there was significant disruption to South American - Antarctic spreading in the region of the Weddell Sea. The source of these changes appears unlikely to originate within the 3-plate system, and one must look elsewhere for some instigating mechanism.

Figure 6.15 shows the rotations of the South American and African continents away from Antarctica which is held fixed, a reasonable assumption as its position is thought to have changed little since around 80Ma (Lawver *et al.*, 1992). An outline is drawn for each successive inversion chron, with the continental positions at c34 (80Ma) drawn in red, changing through to black at the present-day locations, so that the migration of the continents with time can clearly be seen. The largest gap between the outlines occurs at c30-c24, and this is useful as a marker. The motion of South America can be clearly be seen to be a kind of pivoting motion around a pole somewhere around the Antarctic Peninsula. The motion appears very steady, but if you look at the notch in the NW coastline marked by a green arrow, then the apparent westward movement changes more to more south-westerly from c24-c21, and then resumes its westerly motion once more, with the spreading rate slowly picking up again (Figure 6.14). The whole motion of Africa appears to be more of a straightforward translation away from Antarctica. Africa moves smoothly northwards until anomaly 30, though of course it was slowing down considerably during this period. From anomaly 30 until anomaly 24 the whole of Africa appears to have been shifted sideways, an effect which is most apparent in the motion of North Africa, and also the path followed by Madagascar. After this north-westward movement, the general northward movement continued, but at a considerably reduced rate.

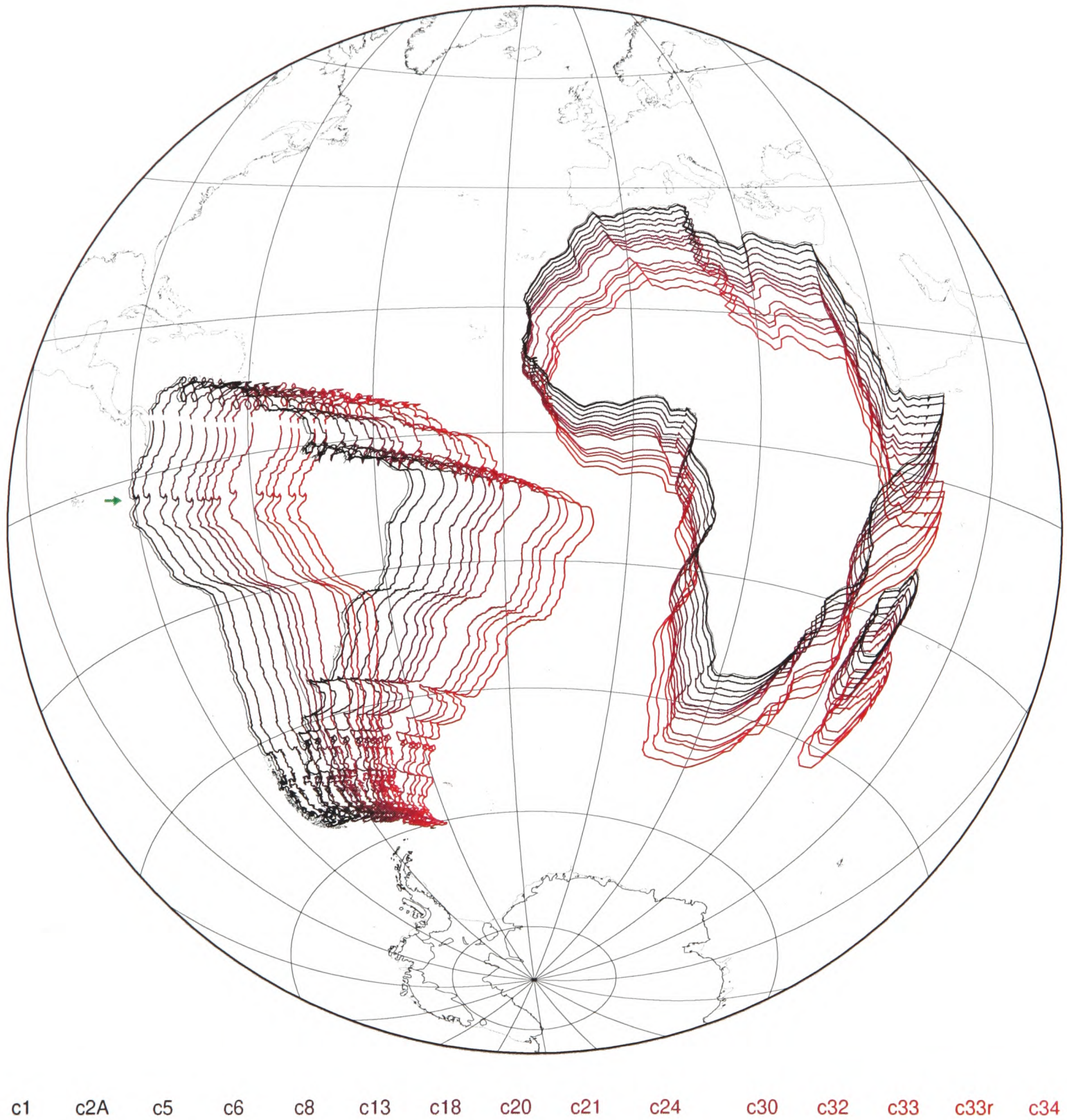

Figure 6.15: The motions of the South American and African plates away from the Antarctic continent. An outline is drawn for each chron in the final 3-plate inversion, with the the anomaly 34 (83Ma) outline in red, and subsequent outlines fading through to black for the present day positions of the continents. The noticeably bigger gap occurs between the c30 and c24 outlines, as reflected in the legend.

The main link in all these changes appears to be the African continent. The most significant changes in plate motion appear related to the motion of Africa, and the substantial drops in spreading rate leading up to the change in plate motion at anomaly 30 occur at the boundaries of Africa with its neighbouring plates. The plate boundary at which there appears to be the least changes in spreading rate is the South American-Antarctic Ridge, which is the furthest away from the African continent. If the motion of Africa is seen as intrinsically responsible for the disturbances to the SAM-AFR-ANT system, then one must then consider what external mechanisms could have led to changes in the motion of Africa that would account for the effects seen.

One possible cause is to relate it to the driving forces behind plate motion: had there been a change in one of the forces affecting the motion of the African tectonic plate? The northward motion of Africa is associated with the closure of the Mediterranean Sea and with the creation of the Alpine orogenic belt. If the northward motion of Africa was being driven by subduction forces, such as slab-pull, thought to be one of the stronger plate driving forces (Forsyth & Uyeda, 1975), then possibly disruption to a subduction process at Africa's northern margin could have resulted in the gradual decrease in plate motion, then a re-adjustment in direction before normal service was resumed, so to speak. However, this is pure speculation and could not be substantiated by the work in this thesis.

Another possible cause for the observed effect, which could be related to the former suggestion, is that Africa began to collide with another tectonic unit as a result of its northward motion. Africa then slowed as it began to collide with this hypothetical block, and finally began to slide past to the side (west) once its northward motion was hindered to a sufficient extent, suggesting that the hindrance was to the north-east of Africa. Then once the problem had been overcome, or circumnavigated, then Africa resumed its previous motion to the north. This hypothesis does have some evidence to support it, with studies on Africa-Eurasian kinematics revealing some significant changes in the motion of Africa relative to Europe. Work carried out by Livermore & Smith (1985) and Dewey *et al.* (1989) showed a dramatic drop in relative African-European motion between anomaly 31 (65Ma) and anomaly 21 (51Ma), which resulted in the previous pattern of convergence ceasing entirely during this period, then continuing again after anomaly 21. This is shown in Figure 6.16. Dewey *et al.* (1989) accepted that this could be attributed to data uncertainties and simple computational error, but considered this very unlikely, since the

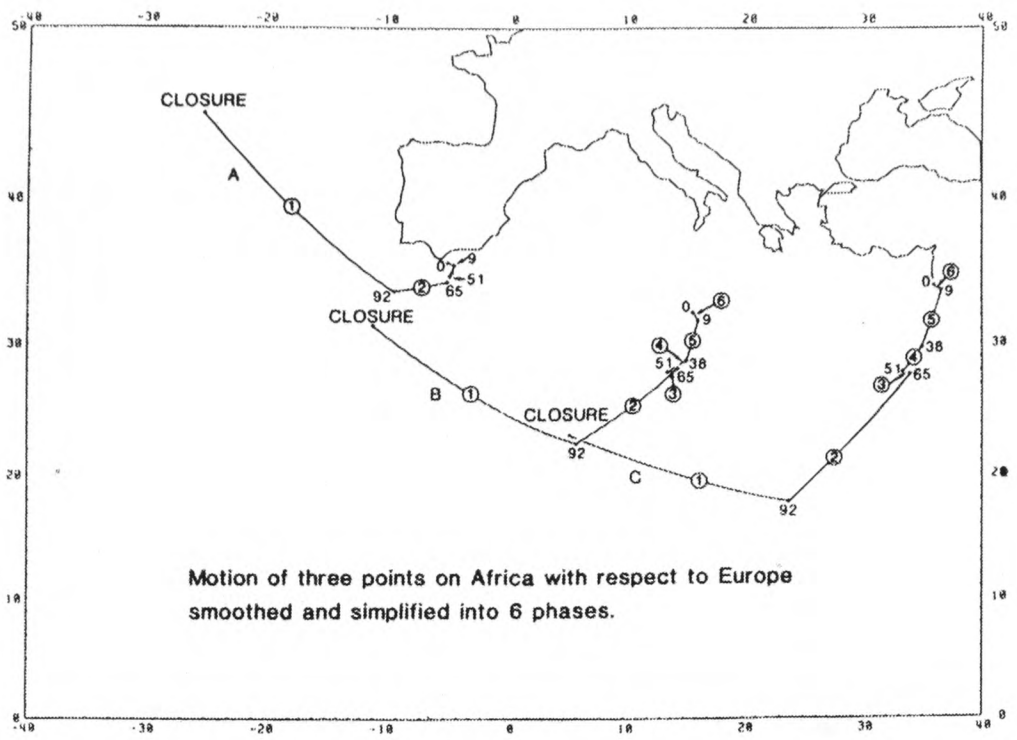

Figure 6.16: The relative motions of Africa and Europe, from closure to the present day, showing the cessation in relative motion between 65Ma and 51Ma. After Dewey *et al.* (1989)

same results had been obtained elsewhere, by Livermore & Smith (1985) and others.

The tectonics of the Mediterranean region are extremely complex, but it is known that African-Eurasian motion is likely to have involved a pattern of collision and subduction (Smith, 1971; Dewey *et al.*, 1973; Livermore & Smith, 1985; Savostin *et al.*, 1986) since the late Cretaceous. The scenario described above, though highly speculative, would appear to find some corroboration from the cessation of African-European motion, at precisely the time when changes in African plate motion appear to have to disturbed the entire 3-plate South American-African-Antarctic system. To find further evidence to either substantiate or disprove this notion, work would have to be done on the absolute motions of all of the plates involved, and on the geological history of the Mediterranean, but the prospects of coming up with any solid proof would appear to be very slim.

6.5 Gravity field reconstructions

To further investigate some of the implications of the reconstruction poles obtained, gravity fields were reconstructed for two times in the past, c24 (52Ma) and c34 (84Ma). The procedure, using c24 as an example, was as follows:

- A theoretical isochron was determined for c24 on each plate, using synthetic flowlines and

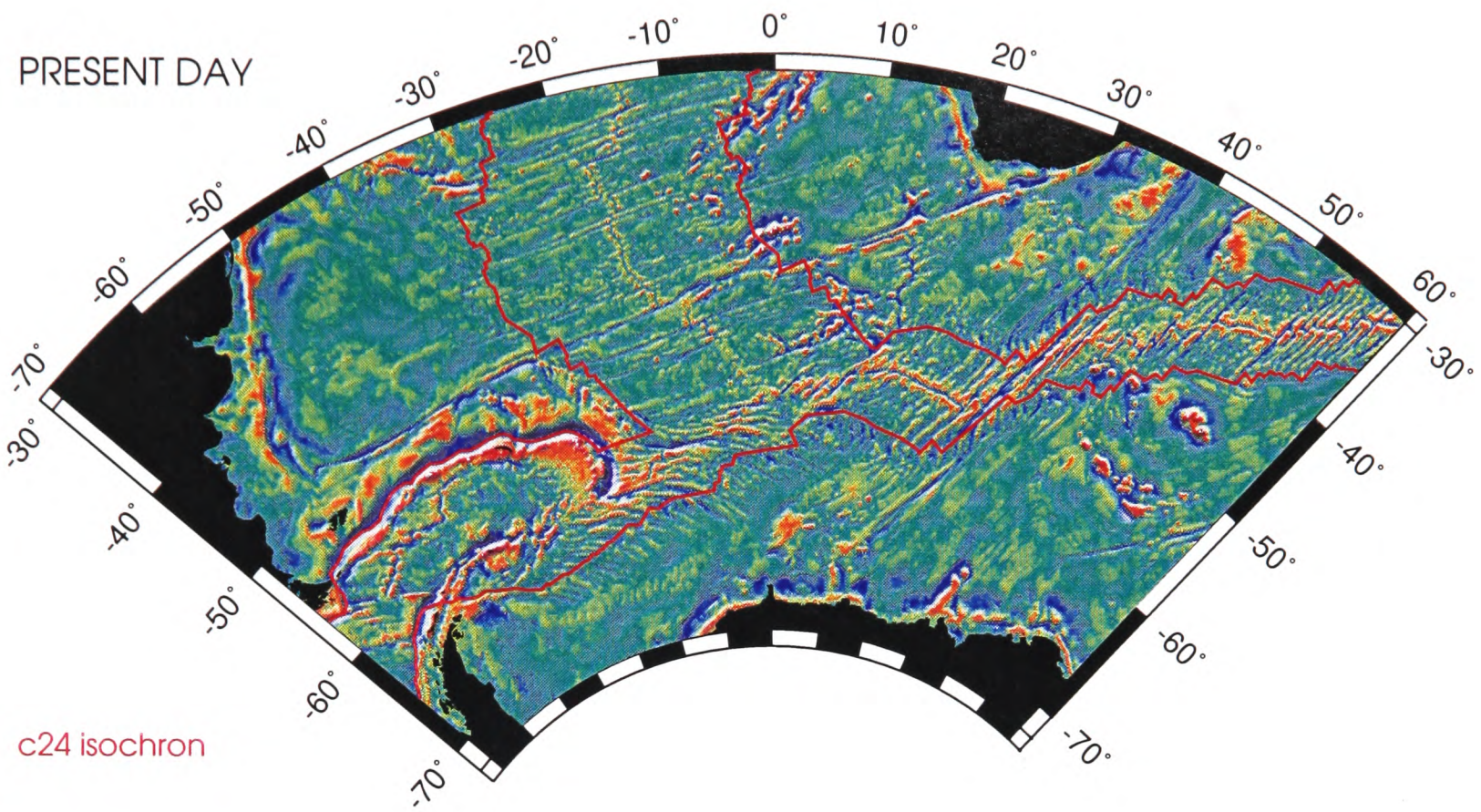

Figure 6.17: The theoretical c24 isochron (marked in red) determined for the Antarctic, South American and African plates. The seafloor between these boundaries is determined to have been created since c24 (52Ma), or not necessarily created by SAM-AFR, SAM-ANT or ANT-AFR spreading (Scotia Sea).

rotated ridge locations;

- All of the gravity field designated as seafloor created since c24 was discarded;
- The gravity field for each continent (regions older than c24) was rotated back to its position at that time relative to Antarctica (held fixed);
- The rotated gravity field was then re-gridded to create the reconstructed gravity map for c24.

The initial gravity field was based on the gravity image of Smith & Sandwell (1995), high-pass filtered to remove long-wavelength ($> \approx$1000km) features, so that the joins in the re-gridded maps for each age would be relatively 'seamless'. For all of the tectonic features mentioned in the following analysis, reference should be made to Figure 1.7 in the introductory chapter.

6.5.1 c24 (52 Ma) reconstruction

Determining the isochron for c24 on each plate was a relatively simple task, as there were no significant ridge jumps in the region from c24 to present. Because of this, rotating the present

ridge axis by a half-finite rotation either side created a simple synthetic isochron which is very close to the true isochron. Ideally the isochron could be determined by drawing a line through all of the c24 anomaly picks on each plate, but where the data distribution is sparse, this is not possible. Care needed to be taken in the region where two spreading regimes adjoined, *i.e.* close to the triple junction trace, where the synthetic isochrons for two ridges intersected. The isochrons had to be carefully matched, so that when they were rotated back, the gravity fields for the three plates joined together like jigsaw pieces, with no gaps or overlaps.

Figure 6.17 shows the c24 isochrons determined for each plate, overlain on top of the gravity field to be rotated. The main features to note are that at the southernmost end of the Mid-Atlantic Ridge, the c24 isochron lies very close to the eastern edge of the Falkland Plateau, indicating that seafloor spreading had only begun shortly before c24, after the ridge had jumped to that location from the fossil spreading centre in the Agulhas Basin to the east. At the eastern end of the Southwest Indian Ridge, east of 42°E, the c24 isochron demarcates the boundary of African-Antarctic spreading at that section of ridge, suggesting, as previously mentioned, that this length of ridge was not in existence prior to c24. The reconstructed gravity field for c24 (52Ma) is shown in Figure 6.18.

Along the length of the Mid-Atlantic Ridge, reasonable alignment on conjugate fracture zone traces can be seen, with the exception of the southernmost section, east of the Falkland Plateau. Seafloor spreading there would only have begun relatively recently after a ridge jump of several hundred kilometres, and a regular pattern of orthogonal spreading centres and transform had apparently not yet been established. Previous studies using reversal sequences (Barker, 1979; LaBrecque & Hayes, 1979) have determined that spreading commenced in this region at sometime between c31 and c25. It seems likely, from studying the gravity reconstructions and synthetic isochrons, that this was in fact at around c30, which would account for the remaining tectonic fabric flanking the inferred ridge axis at c24, including the traces of the Islas Orcadas and Meteor Rises which are believed to have been formed at the time the Mid-Atlantic Ridge jumped to this location.

Further north, at around 40°S, the hotspot traces of the Rio Grande Rise and Walvis Ridge can be seen to approximately intersect close to the theoretical ridge location. The two traces are somewhat different in nature, the Walvis Ridge showing several apparently discrete seamount patterns whilst there are distinct lineations (marked by gravity lows) within the overall grav-

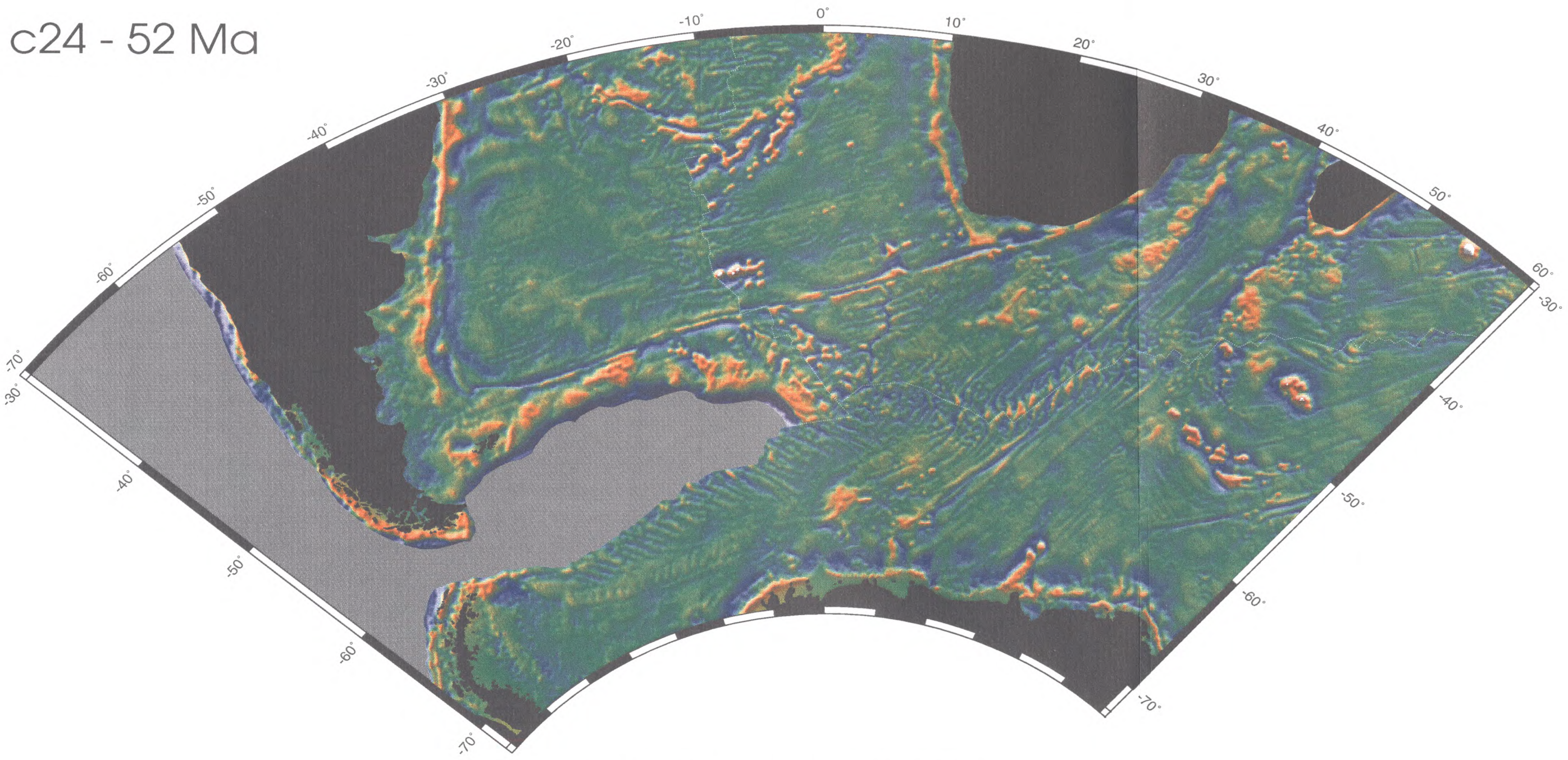

Figure 6.18: The reconstructed gravity field for c24 (52Ma).

ity/topographic highs of the Rio Grande Rise. However, the V-like trace of the two features does reflect the pattern that would be expected from a hotspot moving south relative to the two plates, aligned approximately with the ridge axis.

Along the South American-Antarctic Ridge, there is only a very small length of ridge remaining, with the seafloor where the ridge would have been expected to have been found long since subducted by the eastward moving trench system. Similarly, only a small fragment of South American seafloor created by SAM-ANT spreading remains, at the south-eastern tip of the Falkland Plateau. In the Weddell Sea, where of course no corresponding South American seafloor exists because of subduction, the traces remaining on the Antarctic flank show that the change in plate motion that led to the sharp discontinuity/kink in the SAM-ANT flowlines had occurred shortly before c24.

Close to the predicted location of the triple junction at that time, there is quite a disrupted pattern of spreading around the western end of the Southwest Indian Ridge, with no clear spreading centres, transforms or fracture zone traces. This is likely to be related to the ridge jump that occurred at the neighbouring section of the Mid-Atlantic Ridge at around c30 (65Ma), and the large changes in spreading direction along the Southwest Indian Ridge from c30 to c24, causing ridge reorganisation and possible minor ridge jumps.

Along the central section of the Southwest Indian Ridge, at the corresponding location of the present-day A. Bain transform, it can be clearly seen that spreading had most recently been at an angle of around 45° to the strike of the current transform, in a series of *en echelon* transforms. The match of these conjugate features is not exact, but is nevertheless quite impressive.

East of 40°E, it can be seen that the pattern of N-S African - Antarctic spreading flanking the ridge has been totally eliminated, and the seafloor surrounding the theoretical location of the ridge no longer has any tectonic fabric clearly generated from ANT-AFR motion. Below around 55°S, some faint SSW-NNE traces, aligned with those further west, are visible and are clearly generated from early Antarctica - Africa opening. However, between 55°S and Madagascar to the north, no locations for a fossil ridge or spreading fabric can be seen, but considerable seafloor spreading must have occurred in this region, corresponding to the motion of Madagascar away from Antarctica.

Certainly there is quite complicated gravity/topography in the region, particularly the features of the Madagascar Rise and Crozet Plateau at around 45°E. If one considers that plate motion in

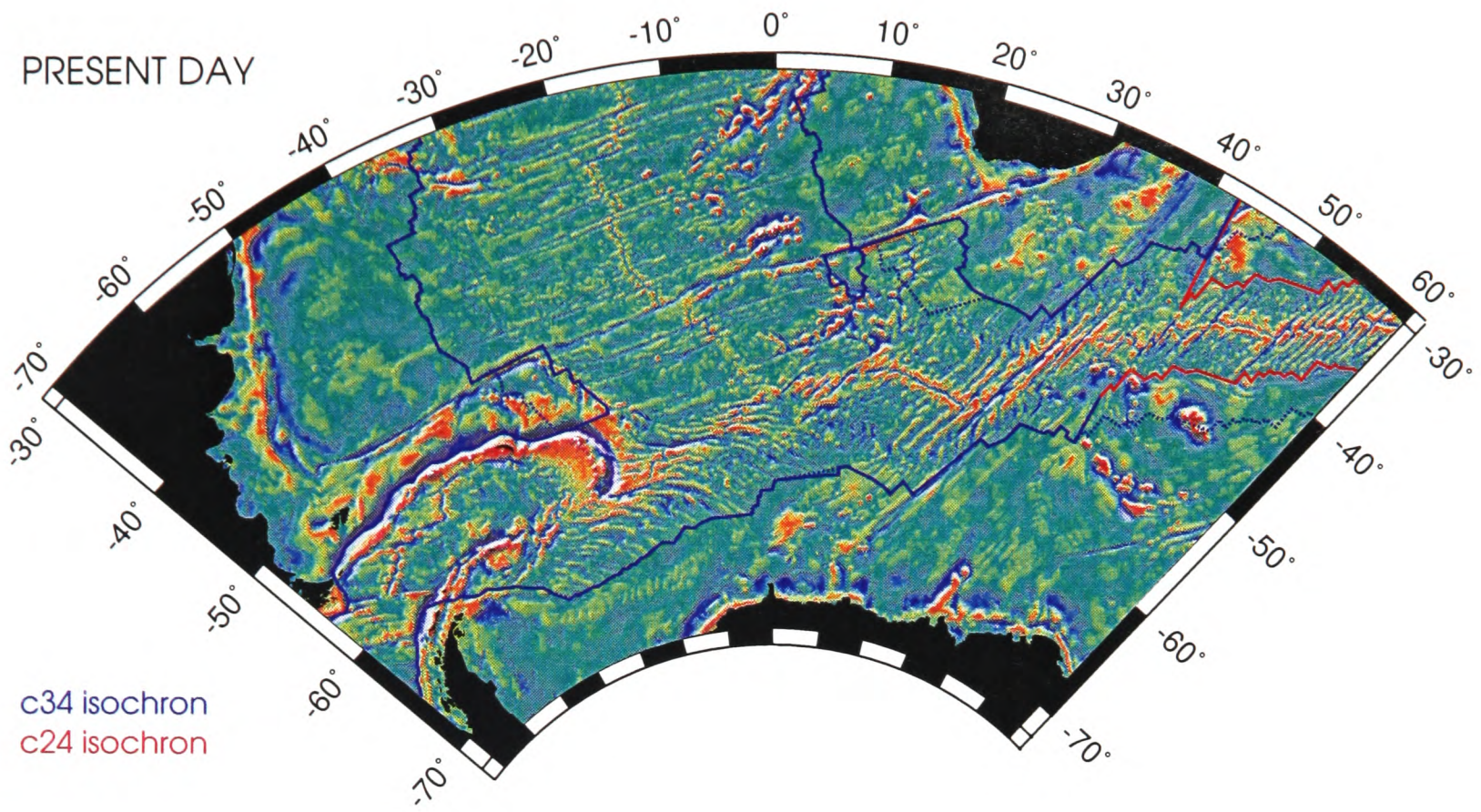

Figure 6.19: The theoretical c34 isochron (marked in blue) determined for the Antarctic, South American and African plates. The seafloor between these boundaries is determined to have been created since c34 (84Ma), or not necessarily created by SAM-AFR, SAM-ANT or ANT-AFR spreading (Scotia Sea). The dotted blue lines indicate the location of this c34 isochron generated from the present-day ridge axes before adjustment to take ridge jumps into account. The red lines mark the region where the c24 isochrons were to be reconstructed instead of c34, due to the unknown nature and location of ANT-AFR spreading from c34-c24.

---

the region would have been most recently NW-SE, then it can be seen that reversing this motion would join together the gravity highs at the south of the Madagascar Rise and the west of the Crozet Plateau. Surprisingly, just to the north of the Crozet Plateau, there is some E-W trending fabric, both sides of the line of the theoretical ridge axis, the origin of which is not clear, since it is aligned almost perpendicular to the spreading direction (ANT-AFR) at the time at which it was likely to have been formed. East of 50°E, the seafloor fabric is dominated by SW-NE trending lineations, generated from Antarctic - Indian/Australian motion.

6.5.2 c34 (84 Ma) reconstruction

For reconstructing the gravity field at c34 (84Ma), the process of determining the synthetic c34 isochron shown in Figure 6.19 was much more complicated. The first problem was that at around c30 (65Ma), South American - African spreading jumped from the ridge located in the Agulhas Basin to the present day Southern Mid-Atlantic Ridge. The original synthetic c34

isochron generated from the present-day Mid-Atlantic Ridge in this region (shown as a dotted line) can be seen to include a significant region of the Falkland Plateau, generally considered to be continental crust, and also encroaches on the Agulhas spreading regime to the east. To account for this, spreading is taken to have occurred from c30 until the present day at the southernmost section of the Mid-Atlantic Ridge, but prior to that, from c34 to c30, SAM-ANT spreading took place in the Agulhas Basin. By generating synthetic isochrons for this period of spreading at the Agulhas fossil ridge, it can be seen that a section of seafloor exists, older than c34, that was on the South American flank during spreading at the Agulhas ridge, but after the ridge jumped to the west, to its present-day location, this fragment went to being part of the African plate. Thus for this gravity field reconstruction, this fragment is rotated by the c30 AFR-SAM finite rotation back to the South American Plate, and then rotated by the c34 SAM-ANT rotation to join up with the Antarctic Plate.

At the eastern end of the Southwest Indian Ridge, the region of seafloor created by AFR-ANT spreading at the current ridge axis was almost completely eliminated by the c24 gravity field reconstruction. It can be seen that the synthetic c34 isochrons (shown as dotted blue lines in this region) enclose seafloor that is not necessarily created through Antarctic - African spreading, and certainly some that was generated from Antarctic - Indian/Australian spreading. No fossil ANT-AFR ridge has been identified and hence the nature and location of Antarctic - African spreading in this region prior to c24 is uncertain, and so no further reconstruction (beyond c24) has been carried out to the east of 40°E.

The gravity field reconstruction for c34 (84Ma) is shown in Figure 6.20. A mesh as been drawn over the gravity field east of 40°E because this region does not truly represent a c34 reconstruction.

Along the Mid-Atlantic Ridge, it can be seen that the Rio Grande/Walvis hotspot traces still meet in a form of V-shape at the predicted ridge axis, but this V is not as symmetrical as was seen in the c24 reconstruction. A quite significant ridge jump must have occurred in this region at around c34 because, looking at the spatial location of the ridge axis north of the large offset at around 40°S, the ridge is far closer to the African continental margin than to the South American continental margin. Unless significant asymmetric spreading had taken place over a substantial period of time, the ridge axis would be expected to lie equidistant between the margins, representing the original break between the continents. This is seen in the location

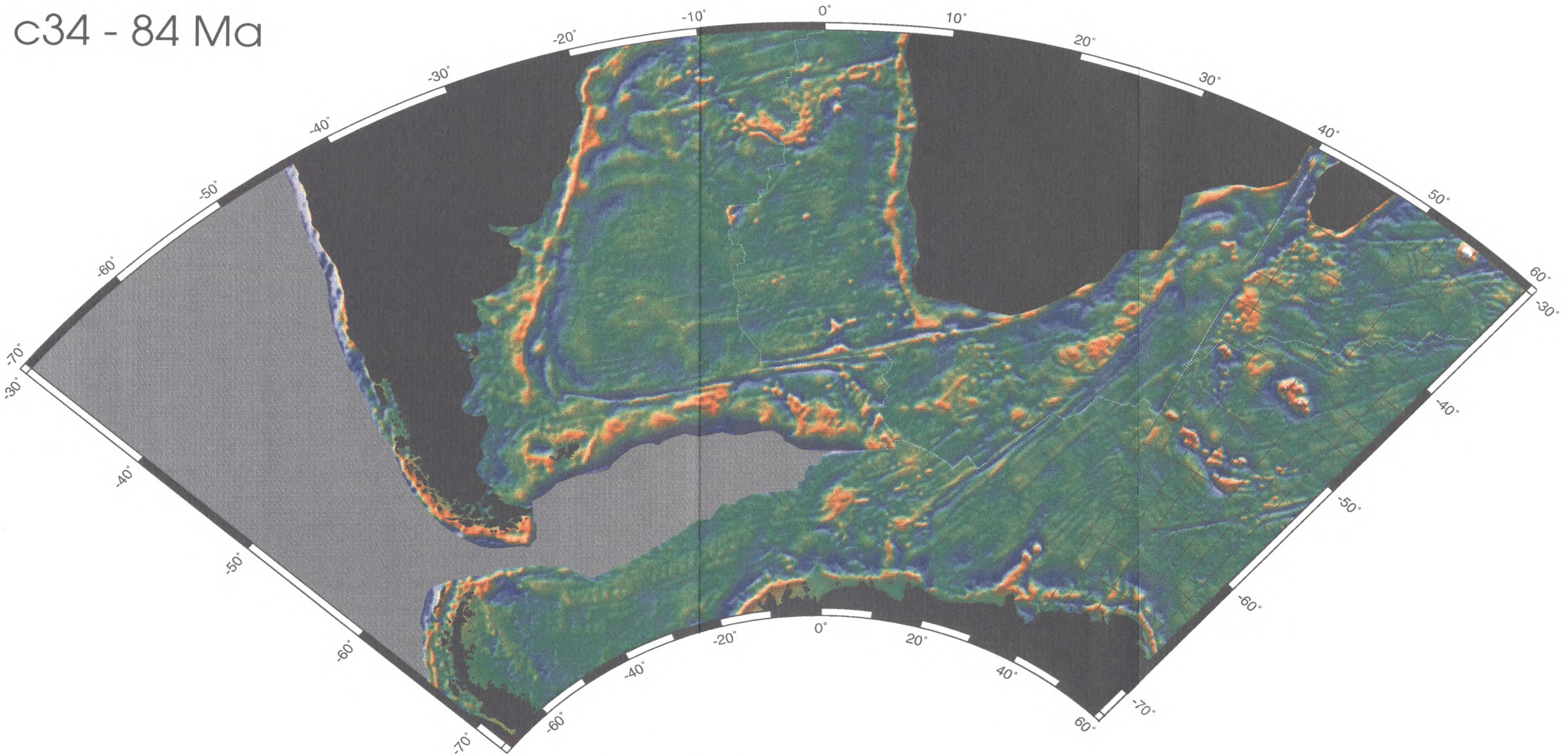

Figure 6.20: The reconstructed gravity field for c34 (84Ma).

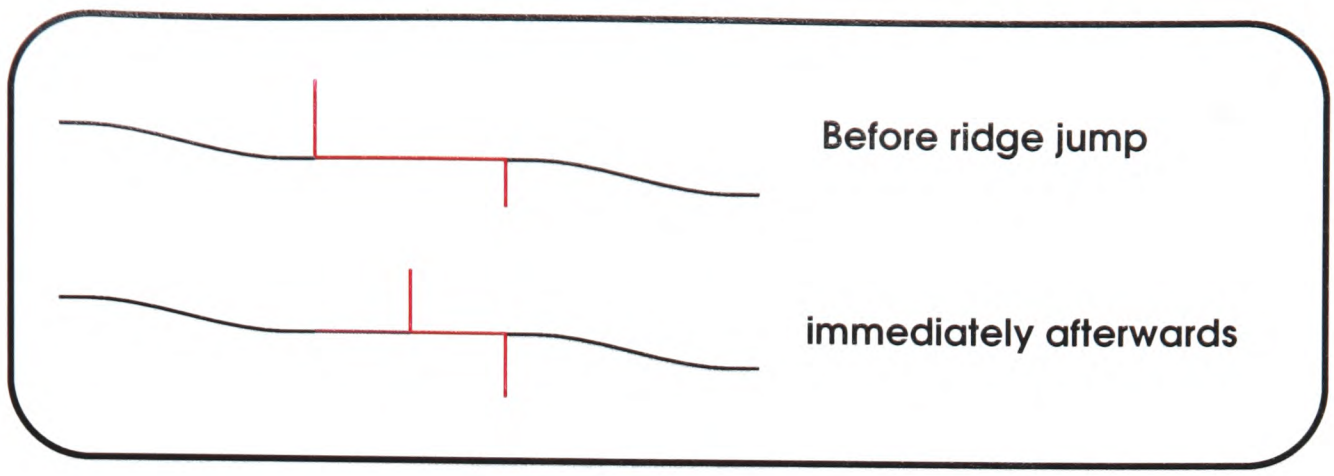

Figure 6.21: Diagram showing the effect of a significant ridge jump on the symmetry of the fracture zone traces of a long-offset transform fault.

of the southern Mid-Atlantic Ridge (north of the Falkland Plateau), which seems to divide the seafloor between the continents almost exactly in two. Further evidence for a large shift in the location of the ridge axis is that to the north of the hotspot traces, the inferred ridge axis no longer bisects the fracture zone traces that are visible.

To the south, there is considerable disruption around the location of the Falkland-Agulhas Fracture Zone, where there are several overlapping lineations. This complicated feature suggests that there has been significant deformation occurring in the vicinity of this fracture zone, justifying its exclusion from the fracture zone datasets as a poor indicator of plate motion, because of the large stresses that are likely to build up along a long-offset transform. The situation is further complicated by the fact that below this fracture zone, the ridge has jumped by several hundred kilometres at one stage, which would have led to a significant length of transform becoming inactive when the ridge jumped to the west. This section of inactive transform would not represent a section of true fracture zone because its strike would represent the direction of relative plate motion along the transform at the time the ridge jump occurred, as opposed to recording the varying direction of plate motion over a long period of time as the fracture zone section developed and moved away from the mid-ocean ridge. This is demonstrated in Figure 6.21, which shows how such a ridge jump leads to asymmetry of fracture zone traces across a transform. This asymmetry, combined with a degree of deformation along a long-offset transform, would lead to the overlapping fracture zone traces seen on Figure 6.20.

The location of the Mid-Atlantic Ridge east of the Falkland Plateau is not clear prior to spreading at the Agulhas fossil ridge, where spreading had probably been taking place for at least a short period of time before c34. However, SAM-AFR spreading is expected to account

for all of the seafloor lying between the Falkland Plateau and the eastern end of the Natal Basin, and so the spreading centre would be expected to lie far more centrally within this region. The Agulhas Plateau has been suggested as a location for a former spreading centre (Scrutton, 1973; Barker, 1979; LaBrecque & Hayes, 1979), but as this period of spreading was during the Cretaceous magnetic quiet zone, no evidence can be found from studying reversal sequences. The Agulhas Plateau lies well to the east of the Agulhas fossil ridge but is not equidistant between the continental margins as seen at c34, and so it appears likely that spreading must also have occurred elsewhere to account for all of the intervening seafloor.

Barker (1979) suggested that a jump westward from the initial spreading centre to the Agulhas Plateau occurred at around 98 Ma, which would be in agreement with the inferences above. The initial spreading in this region following opening would intuitively have to have occurred at a ridge axis separated from the Mid-Atlantic Ridge to the north by a transform offset the length of the Falkland Plateau. This roughly corresponds to the location of the gravity low seen in the Natal Basin, which may or may not be significant.

The tectonic fabric in the whole region surrounding the predicted location of the triple junction at c34, particularly to the east and south, suggests that the nature and geometry of the three plate boundaries were probably quite complex prior to then. There is clear ANT-AFR spreading fabric visible between 10°E and 20°E in this region, west of the site of the proposed SAM-AFR spreading centre on the Agulhas Plateau. This puts potential constraints of the timing of any jump from a ridge axis in the Agulhas Plateau to the (fossil) ridge in the Agulhas Basin. If SAM-AFR spreading had taken place in the neighbourhood of the Agulhas Plateau until only a short time before c34, another large offset transform (with the opposite sense to the Falkland-Agulhas transform) would have to had existed to the south, in order to link SAM-AFR spreading at the Agulhas Plateau with ANT-AFR spreading south of the the Falkland Plateau. A more likely pattern is for both SAM-AFR and ANT-AFR spreading to have occurred some time after opening at the Agulhas Plateau (and hence the triple junction would also be located in the region). Then, a significant period of time before c34 judging by the length of Southwest Indian Ridge flowlines visible in the region, SAM-AFR spreading jumped to the ridge system in the Agulhas Basin, and ANT-AFR spreading to just to the SW of the Falkland Plateau, causing a simultaneous shortening of the Falkland-Agulhas transform and lengthening of the what is now the A. Bain transform.

Along the whole length of the Southwest Indian Ridge (up to 40°E where the nature of spreading is uncertain) there exists a series of very linear traces perpendicular to the inferred ridge, which suggest that prior to c34, the motion of Africa away from Antarctica was very stable in a SSW-NNE orientation. It can be seen that the conjugate traces of these fracture zones match extremely well all along this region, so that they run straight across the join, with little or no offset. They are aligned almost perfectly with the strike of the present day A. Bain transform, indicating that this is and has been the dominant spreading direction between the two plates since opening began. The location of the ridge is quite hypothetical now, and unlikely to have been exactly the pattern of ridges and transforms shown, but the spatial location is correct because it always lies close to midway between the continental outlines. Certainly the large offset represented by the ancestor of the A. Bain transform would exist, as this accurately reflects the shape of the African continental shelf north of 35°S.

Beyond 40°E, no further conclusions can be drawn, because no reconstruction was made beyond c24 because of the uncertain nature an location of Antarctic - African spreading in this region. As a result, Madagascar lies closer to the coast of Africa than it would have been at that time, Africa and Madagascar having been considered as moving as a single unit since around 80Ma.

There is now virtually no evidence remaining of an ancestor of the South American-Antarctic Ridge, with only a minute fragment of South American plate created by SAM-ANT spreading remaining, just to the NW of the theoretical triple junction location. The inferred location of the ridge is no longer valid, as the direction of spreading was then at around 45° to the present-day strike of the South American-Antarctic Ridge. In the Weddell Sea, the closely spaced series of fracture zone traces indicate that at c34, the spreading direction was approximately ESE-WNW. However, in the traces visible, there is a very large change of direction, showing that shortly before c34, the spreading direction was orientated at around SSW-NNE, meaning that the spreading direction had changed by approximately 135°, a huge change. This is particularly significant because the flowlines older than c34 seen at the other 2 plate boundaries show very steady linear traces for a long period of time, with no indication of any changes in spreading direction, almost back to opening itself.

Thus it seems to suggest that the flowlines in the Weddell Sea prior to this large kink are not in fact reflecting South American - Antarctic opening. However, if the spreading rates

at the Mid-Atlantic Ridge and Southwest Indian Ridge were very similar, with the poles of motion lying reasonably close together, then it would be possible for small changes in these poles to significantly affect the direction of motion at the apparently much slower spreading South American-Antarctic Ridge. As with many questions about South American - Antarctic spreading, no real conclusions can be drawn because there is no opportunity to interpret information from the missing (subducted) South American flank.

Seafloor spreading between South America and Antarctica between c34 (84Ma) and the present day has clearly not been sufficient to account for the seafloor that would have existed in the space currently occupied by the Scotia Sea. The seafloor making up the Weddell Sea, if created by South American - Antarctic spreading, would easily account for the void in the Scotia Sea area. However the origin of the Weddell Sea is unclear and although the seafloor in the northern Weddell Sea was created by SAM-ANT spreading, the same cannot be said with any certainty for that south of 70°S, and the western Weddell Sea bordering the Antarctic Peninsula.

The age of development of the Scotia Sea cannot be determined from these gravity field reconstructions, but the c34 reconstruction does show that at 84Ma, the Drake Passage, the gap between the Antarctic Peninsula and the tip of South America, is very narrow. The two bodies do not overlap physically, but they do in the respect that the tip of South America lies further south than the northern Antarctic Peninsula, and so the Antarctic circumpolar current would be significantly restricted. The choice of the northern limit of the Antarctic Peninsula was made relatively arbitrarily, and the continental crust may have extended further north, such that the Drake Passage did not exist at this time. What is certain though, is that turning the clock back any further would soon lead to overlap between the southernmost part of South America and the western Weddell Sea, east of 45°W, which does not appear to have been created from SAM-ANT spreading. This is accounted for by the rotation of West Antarctica (incorporating the Antarctic Peninsula) independently from East Antarctica, to enable the completion of the Gondwanaland jigsaw.

6.6 Conclusions

Having determined that a tectonic process occurring between Africa and Europe was the likely cause of the disruptions seen to the plate motions of South America, Africa and Antarctica

between around anomaly c30 (65 Ma) and c24 (52Ma), reconstructing the gravity fields yielded further information about the timing of these events. It was seen that although the spreading rates between Africa and Antarctica, and Africa and South America both decreased dramatically shortly after c34 (84 Ma), major disruption to spreading processes did not occur until around c32/30.

The major changes are seen along the Southwest Indian Ridge, where this event triggers a major change in spreading direction, around 45° from the long-term, steady-state spreading direction between Africa and Antarctica. The disturbance to African-Antarctic spreading appears to be temporary, as the direction of plate motion returns to almost exactly the same direction as before the disruption, albeit at a reduced rate. Coinciding with the return to the long term spreading direction and ridge geometry along the central Southwest Indian Ridge, the pattern of spreading to the east, between Madagascar/Africa and Antarctica, changes significantly. For the period before c24 the spreading regime in this region is unclear, but towards the end of the period of disturbance, spreading is initiated at a new section of mid-ocean ridge, over 1000km in length.

Disruption to South American - African spreading along the Mid-Atlantic Ridge at this time is less apparent. The major change was the instigation of a large westward ridge jump to the east of the Falkland Plateau. This was presumably caused by the build up of intra-plate stresses in the region due to the incompatibility of the long-offset Falkland-Agulhas transform with the changes in spreading direction at that time. The flowlines along the majority of the Mid-Atlantic Ridge show reveal little alteration in relative plate motion at this time, but changes can be seen in the fracture zone traces north of the equator, and in the SAM-AFR stage poles. These changes in spreading direction would not need to be too big before their effect, amplified by the large extent of the transform (nearly 1000km in length at that time), was felt along the Falkland-Agulhas transform. The actual ridge jump appears to have occurred at the beginning of this period of disruption, at around c30, and regular seafloor spreading seems to have already been well established at the location of the new (present-day) ridge system by c24, the time when the spreading direction at the Southwest Indian Ridge was only just returning to normal. Along the rest of the Mid-Atlantic Ridge, the transforms appear to have adjusted smoothly to the changes in spreading at this time. However, it is interesting to note how the number of fracture zone traces appears to significantly increase after around c24 (Figure 6.17), though this may well be

related to the changes in spreading rate along the Mid-Atlantic Ridge.

Along the South American-Antarctic Ridge, there has not been a predominant spreading direction since opening, as is seen on the other two ridges, and relative South American - Antarctic motion has been continually changing. As such, any changes related to the disturbances in SAM-AFR-ANT motion are less obvious in the flowlines. However, there appears to have been significant disruption to seafloor spreading in the Weddell Sea between c30 and c24, most likely towards the end of this period. It is in this region, closest to the poles of relative Antarctic - South American motion, that any changes would have the greatest effect, and this seems to have been the case, though the exact nature of the disruption to the spreading processes is not clear.

One question to be raised is why the disruption to the African - Antarctic spreading direction is so more significant than the disruption to African - South American spreading. Changes to patterns of seafloor spreading are seen along the whole length of the Southwest Indian Ridge, but along the South American-Antarctic Ridge and Mid-Atlantic Ridge, changes in ridge geometry and more minor changes in spreading direction have only occurred in regions where there are other factors to be taken into consideration (long-offset transforms, proximity to poles of motion). It seems likely that since these changes appear to be related to the temporary cessation of relative African - European motion, orientated SSW-NNE (Figure 6.16), the effect is greater on seafloor spreading between adjoining plate pairs with a similar direction of relative plate motion.

Chapter 7

Evolution of the Bouvet Triple Junction

Once a set of internally consistent poles for South American - African - Antarctic spreading have been obtained, it is possible to apply these to determine the instantaneous velocity triangles for motion between the three plates at various times in the past. This enables a study to be made of the past configuration and motion of the triple junction between the three plates, the Bouvet Triple Junction.

7.1 Stability and motion of a triple junction

There are two possible configurations in which the Bouvet Triple Junction would be a stable feature: ridge-ridge-ridge (RRR); and ridge-fault-fault (RFF). Of these, the RFF configuration is less stable than the RRR mode. Figure 7.1 shows these 2 configurations, along with the corresponding velocity triangles around the triple junction. The requirements for stability of the triple junction and its velocity with respect to each plate when in a stable configuration are also given. In the RRR configuration, the triple junction is always stable, provided that the spreading at each of the ridges is symmetric and non-oblique. The velocity of the triple junction is always non-zero, relative to each of the three plates. When in the RFF configuration, the triple junction is theoretically only stable when the plate velocities form an isoceles triangle, again assuming normal spreading at the mid-ocean ridge branch. In the RFF configuration, the triple junction remains at the same location relative to the third (C=Antarctic) plate, and hence in the frame of the other two (A=South American, B=African) plates, the triple junction moves at the relative velocity of the third plate.

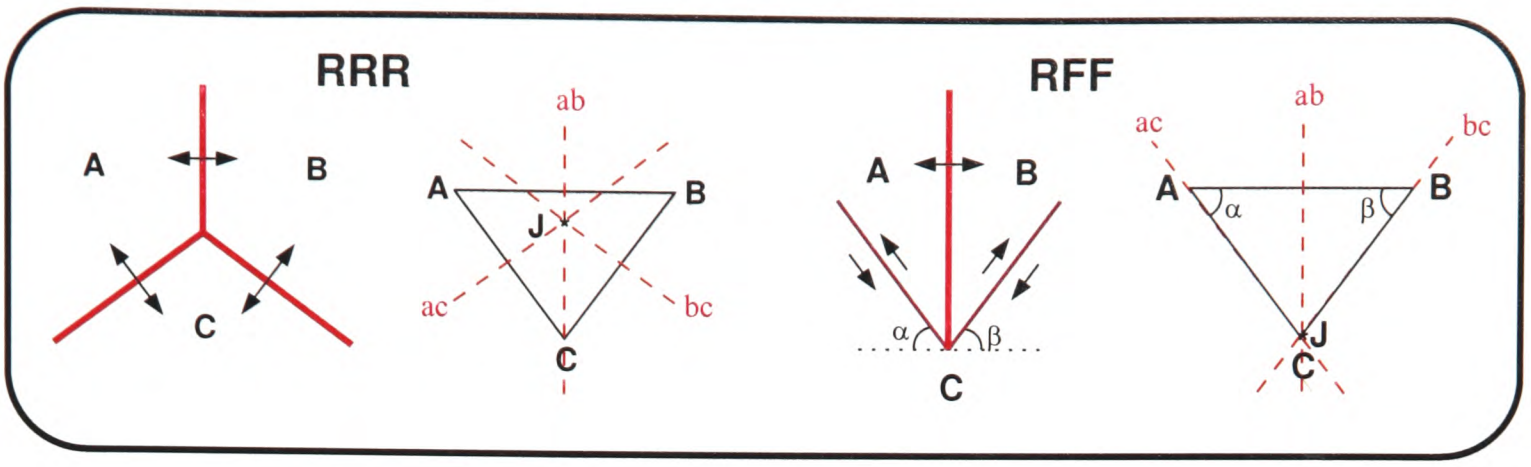

Figure 7.1: Geometry and stability of a triple junction in RRR and RFF configurations. The dashed lines ab, ac and bc mark the invariant velocity lines which would keep the geometry of the plate boundaries (A↔B, A↔C and B↔C respectively) unchanged. The intersection of these lines, the point J, marks the location of the stable triple junction in velocity space. If the lines do not intersect, then the triple junction is unstable.

In theory, when the RFF configuration becomes unstable, the triple junction is most likely to evolve into to the more stable RRR mode, but the conditions for the junction to change to RFF from a RRR configuration are not clear. However, for the Bouvet Triple Junction, it is clear that the RFF configuration has been present for much of the recent history of the triple junction (Sclater *et al.*, 1976; Apotria & Gray, 1985, 1988). It could be considered that the triple junction would convert to RFF as soon as the relative plate velocities form an isoceles triangle. This was the conclusion of Apotria & Gray (1985, 1988), who considered that as soon as the triple junction ceased to have an isoceles vector triangle, the configuration would change to RRR until the subsequent motion of the triple junction caused the velocity triangle became isoceles again, when the triple junction would again revert to RFF.

The evolution and configuration of a triple junction is not dependent only on the relative plate velocities around it. Consideration must also be given to the morphology in the vicinity of the triple junction. Ligi *et al.* (1997) have suggested that changes in the magma supply to the region of the triple junction have led to a bifurcation in the triple junction leading to changes in the configuration, and a jump in the location of the triple junction. Mechanical constraints, such as the existence of long-offset transforms on the branches of the triple junction, will also affect the nature of the triple junction.

However, to model the theoretical evolution of the triple junction over a substantial period of time, these effects cannot really be included. If the velocity triangle for the triple junction is known, then the configuration can be predicted, and the motion of the triple junction relative to each of the three plates can be determined. In this way, the evolving configuration and motion

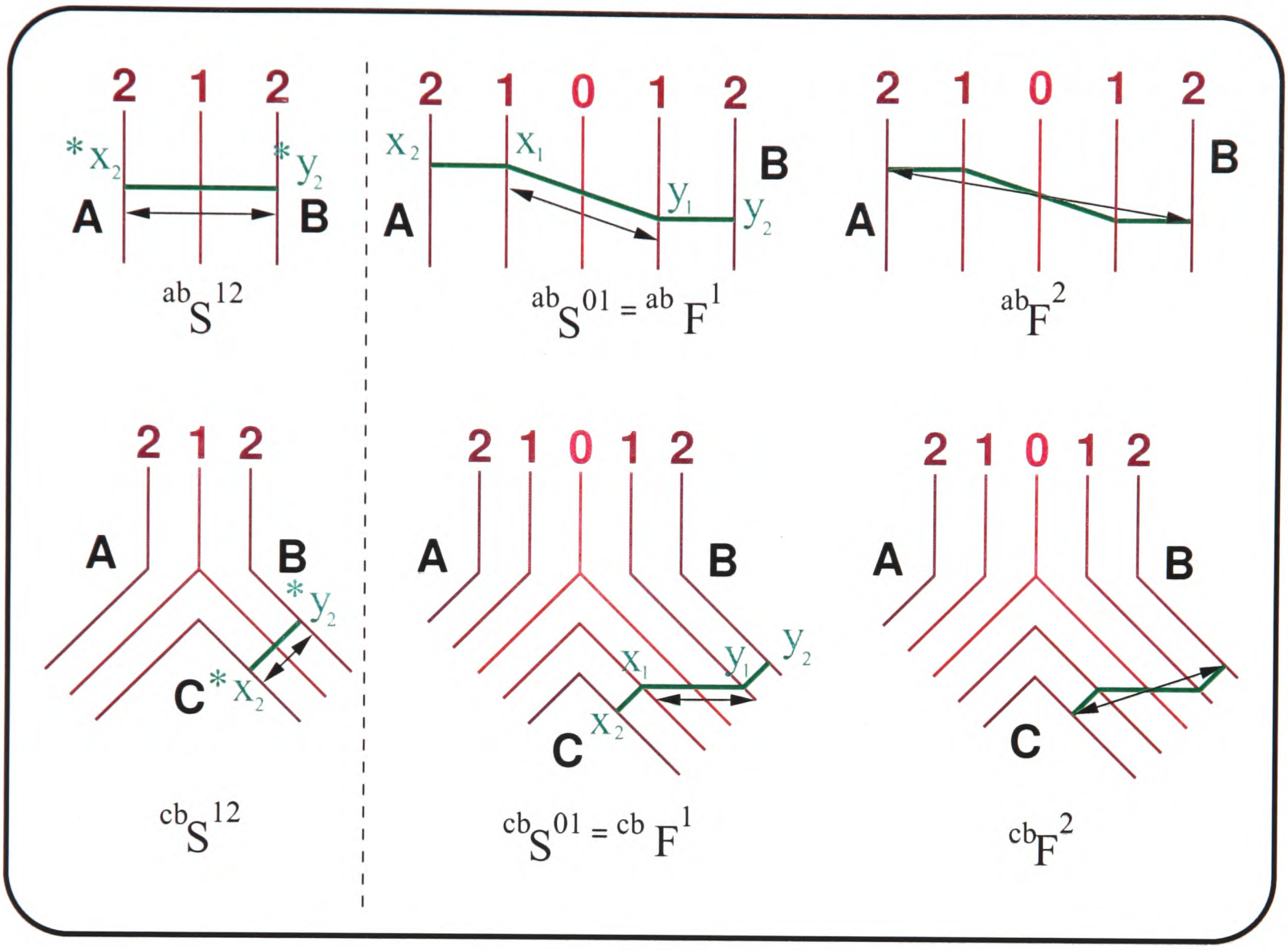

Figure 7.2: A series of cartoons illustrating the definition of instantaneous stage poles (such as ${}^{cb}S^{12}$) and finite rotation poles (such as ${}^{cb}F^{2}$) for 2 and 3-plate systems, for use in determining the past history of a triple junction. For the purpose of clear distinction between the two periods of plate motion, oblique spreading is shown for A↔C (For this diagram to be strictly geometrically correct, oblique spreading A↔B is also required.)

---

of the triple junction can be modelled, provided that the plate motions are known.

7.2 Modelling the configuration and motion of the Bouvet Triple Junction

Obtaining the current velocity triangle for the plate motion around the triple junction is trivial, but determining the velocity triangles in the past is more complicated. The first problem is that the instantaneous stage poles of motion need to be determined, which are not the same as the stage poles used to calculate flowlines on one flank. The standard stage poles between two anomalies, say c8 and c13, are different on the opposing flanks of the ridge, since they are

separated by the c8 finite rotation. Figure 7.2 shows how the means by which the instantaneous stage poles are calculated for a 3-plate system. A fixed reference frame needs to be chosen in which to determine the instantaneous stage poles from the set of finite rotation poles, which is usually one of the 3 plates. If plate A is held fixed, then determining the stage poles for plate pairs AB and AC is trivial. If we require the instantaneous stage pole between anomalies '2' and '1' between plates A and B, ${}^{ab}\mathbf{S}^{12}$, then we can obtain this from the finite rotation poles for these anomalies, ${}^{ab}\mathbf{F}^{2}$ and ${}^{ab}\mathbf{F}^{1}$ respectively.

Initially, at time '1' we have

$$ {}^{*}y_2 = [{}^{ab}\mathbf{S}^{12}]\ {}^{*}x_2 \tag{7.1}$$

then at time '0',

$$ y_2 = [{}^{ab}\mathbf{F}^{2}]\ x_2 \tag{7.2}$$

but since plate A is fixed, then we also have

$$ x_2 = {}^{*}x_2 \qquad\qquad y_2 = [{}^{ab}\mathbf{F}^{1}]\ {}^{*}y_2 \tag{7.3}$$

such that,

$$ {}^{*}y_2 = [{}^{ab}\mathbf{F}^{1}]^{-1}\ y_2 \tag{7.4}$$

$$ = [{}^{ab}\mathbf{F}^{1}]^{-1}[{}^{ab}\mathbf{F}^{2}]\ x_2 \tag{7.5}$$

$$ = [{}^{ab}\mathbf{F}^{1}]^{-1}[{}^{ab}\mathbf{F}^{2}]\ {}^{*}x_2 \tag{7.6}$$

which gives

$$ {}^{ab}\mathbf{S}^{12} = [{}^{ab}\mathbf{F}^{1}]^{-1}[{}^{ab}\mathbf{F}^{2}] \tag{7.7}$$

Similarly,

$$ {}^{ac}\mathbf{S}^{12} = [{}^{ac}\mathbf{F}^{1}]^{-1}[{}^{ac}\mathbf{F}^{2}] \tag{7.8}$$

For the third plate pair, C↦B, the calculation is more tricky, because neither plate is fixed in this reference frame (A fixed). At time '1',

$$ {}^{*}y_2 = [{}^{cb}\mathbf{S}^{12}]\ {}^{*}x_2 \tag{7.9} $$

then at time '0',

$$ y_2 = [{}^{cb}\mathbf{F}^{2}]\ x_2 \tag{7.10} $$

with plate A fixed, both ${}^{*}x_2$ and ${}^{*}x_2$ have moved with respect to the reference frame, such that

$$ x_2 = [{}^{ac}\mathbf{F}^{1}]\ {}^{*}x_2 \qquad\qquad y_2 = [{}^{ab}\mathbf{F}^{1}]\ {}^{*}y_2 \tag{7.11} $$

This gives

$$ {}^{*}y_2 = [{}^{ab}\mathbf{F}^{1}]^{-1}\ y_2 \tag{7.12} $$

$$ = [{}^{ab}\mathbf{F}^{1}]^{-1}[{}^{cb}\mathbf{F}^{2}]\ x_2 \tag{7.13} $$

$$ = [{}^{ab}\mathbf{F}^{1}]^{-1}[{}^{cb}\mathbf{F}^{2}][{}^{ac}\mathbf{F}^{1}]\ {}^{*}x_2 \tag{7.14} $$

which gives

$$ {}^{cb}\mathbf{S}^{12} = [{}^{ab}\mathbf{F}^{1}]^{-1}[{}^{cb}\mathbf{F}^{2}][{}^{ac}\mathbf{F}^{1}] \tag{7.15} $$

In order to determine the rates and azimuths around the triple junction from the instantaneous stage poles, the location of the triple junction in the chosen reference frame is required. If the triple junction location itself had been chosen as the reference frame, then obviously it would be constant, but this would have complicated the calculation of the stage poles. Since one of the plates will been chosen as the reference frame, then the location of the triple junction with respect to this plate is required, which normally changes with time. The migration of the triple junction generates a trace on the plate, which represents a boundary between the seafloor created from spreading between the two different neighbouring plates.

Determining the location of the triple junction on a plate at any given time is a relatively simple task if there is a large amount of magnetic anomaly data in the vicinity of the triple

junction trace on one of the plates. However, this is not really the case for the Bouvet Triple Junction, and although a triple junction trace can be approximately identified on each of the plates in the region, there are certainly not sufficient anomaly picks to be able to satisfactorily date the motion of the triple junction.

Thus an estimate of the trace needs to be found, which is done by in effect using a circular argument. If the velocity triangle at a given reference time (the present) is known, then the stable configurations of the triple junction can be determined. If the configuration of the triple junction is known, then the velocity of the triple junction relative to any given plate can be calculated from the relative plate velocity triangle. Thus the location at the beginning of that 'stage' of motion can be determined. So from the current velocity triangle (from the c2A-present stage poles), the location of the triple junction at c2A can be estimated. This enables the instantaneous velocities at c2A to be calculated from the c5-2A instantaneous stage poles, and from the corresponding velocity triangle, the estimated triple junction location at the beginning of the stage, anomaly c5, is calculated. This is repeated, back as far as anomaly 21, shortly before which it is known that the Mid-Atlantic Ridge north of the Bouvet Triple Junction jumped by several hundred kilometres (Barker, 1979; LaBrecque & Hayes, 1979), and so the Bouvet Triple Junction did not exist before this time.

As stated previously, the Bouvet Triple Junction has two possible stable geometries, RRR and RFF. The RRR configuration is always stable, whilst the RFF is in theory only stable when the relative velocities form an isoceles triangle, and so the RRR can be considered the more stable, and hence the most likely, long-term configuration for the Bouvet Triple Junction. However, it soon becomes apparent that this is not the case, and the RFF configuration has proved to be more prevalent than expected, and an attempt was made to model this quantatively. To determine the past configuration and motion of the triple junction, a set of criteria needs to be followed in order to estimate what configuration the triple junction will be in, given knowledge of its velocity triangle. In theory, the RRR configuration is the more stable of the two, and it could be specified that the triple junction has always been in this geometry. This is easily disproved, and so the next step is to to specify that if the velocity triangle is isoceles, then the triple junction is in a RFF configuration. However, the triple junction is unlikely to remain in an exact isoceles triangle for long, and so a degree of tolerance is introduced into the modelling process.

If two internal acute angles of the velocity triangle, α and β were found to be within ζdegrees

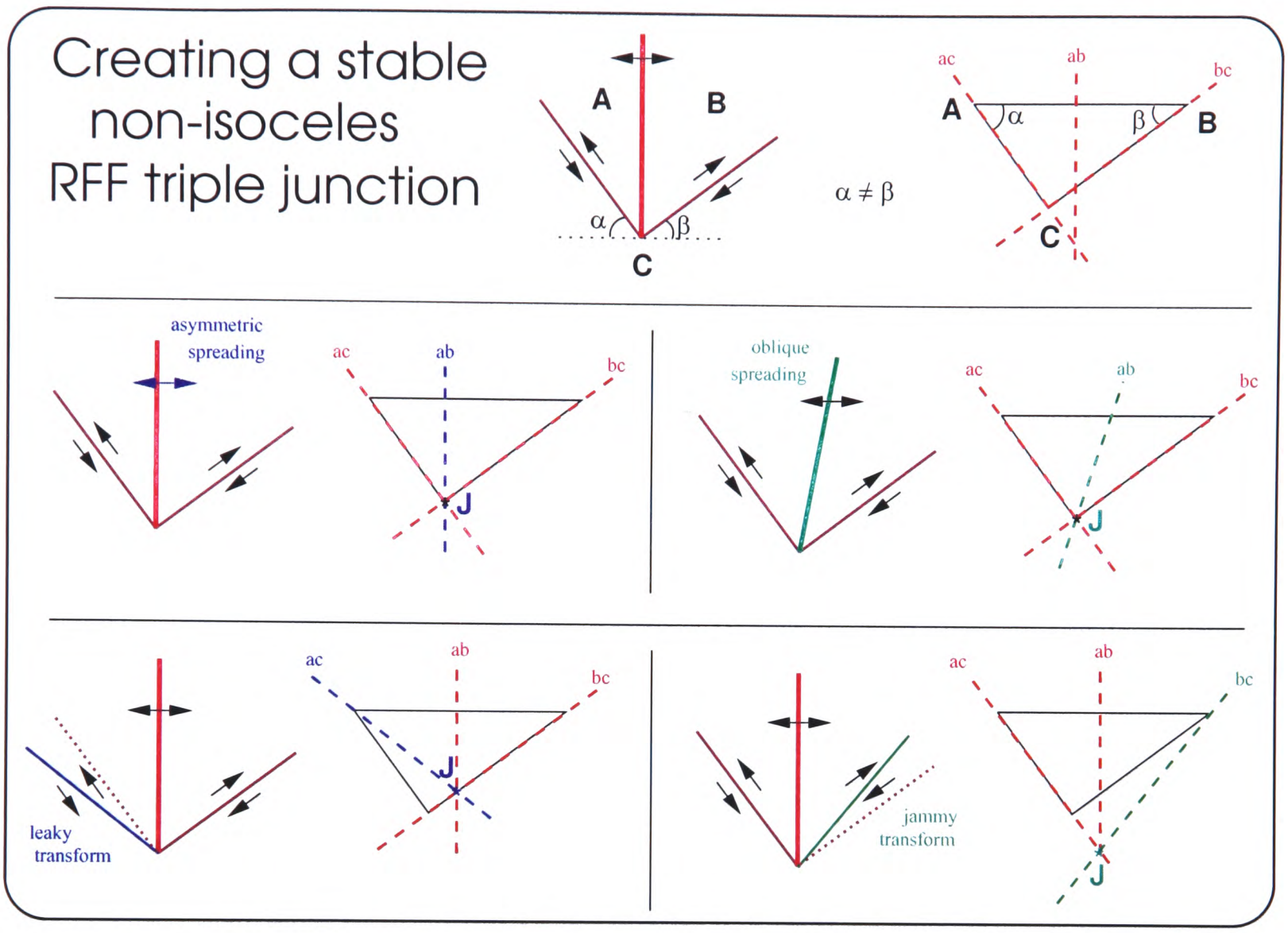

Figure 7.3: Geometry and stability of a triple junction in a non-isoceles RFF configuration. The dashed lines ab, ac and bc mark the invariant velocity lines which would keep the geometry of the plate boundaries (A↦B, A↦C and B↦C respectively) unchanged. The point J marks the location of the triple junction in velocity space.

---

of each other, *i.e.* $|\alpha - \beta| \leqslant \zeta$, then the configuration of the triple junction was taken to be RFF, and the velocity of the triple junction calculated accordingly. If the velocity triangle is non-isoceles ($\alpha \neq \beta$), then the 3 invariant lines ab, ac and bc will no longer meet up at a point, and hence the triple junction is unstable, as shown in Figure 7.3. However, if the spreading at the ridge boundary is made slightly oblique, or slightly asymmetric, then the triple junction remains stable in the RFF configuration. An alternative to this is that spreading continues at the mid-ocean ridge branch of the triple junction as normal, but that the transforms either side are considered to be 'leaky', such that the relative plate motion is no longer parallel at the transforms and some plate accretion occurs along the transforms. The drawback to this model is that by varying the degree of leakiness for both of the transforms, the invariant lines, ab, ac, and bc, can be made to intersect at any point, and hence the triple junction velocity is totally subjective, through the choice of degree of oblique spreading along the transforms. In the previous method,

only the line ab is variable (through the degree of asymmetry and/or obliqueness), which means the the lines can only intersect at one point (at C), which is predetermined.

Although the instantaneous stage poles only changed at each of the inversion chrons, the plate velocities continually change with the motion of the triple junction, and so the evolution was modelled at 1Ma intervals. Thus from using only the 3-plate finite rotation poles and specifying the parameter ζ, the velocity triangles around the triple junction, and hence the motion and configuration of the triple junction, can be determined at any given time in the past from the model.

7.3 Models for the evolution of the Bouvet Triple Junction

It is important to note that the model is purely a theoretical one, based entirely on the velocity triangles, as determined from the stage poles obtained from the 3-plate finite rotation poles. It does not take into account the present or past geometry of the ridge, as far as could be obtained from magnetic, topographic and magnetic anomaly information, which was the basis of the past studies of the triple junction evolution (Sclater *et al.*, 1976; Apotria & Gray, 1985, 1988). It does not, and cannot, take into account any possible jumps of the triple junction, or overlapping spreading segments in the region of the triple junction (such as proposed by Ligi *et al.* (1997)).

In the modelling, the South American Plate was held fixed, and the trace of the triple junction predicted on this plate. Figure 7.4 shows the theoretical traces of the Bouvet Triple Junction on the South American Plate, back to anomaly 21 (46.3 Ma), for various values of ζ. An estimate of the triple junction trace from the features on the gravity map is drawn, and a series of theoretical isochrons (for each inversion chron) displayed for South American - African spreading. The estimated trace was interpreted from the gravity map through consideration of tectonic fabric, as could be inferred from the gravity anomalies, and from obvious features such as long transforms and termination of fracture zones. This may appear somewhat subjective, but the true trace is unlikely to lie far from the estimated trace shown. The first thing to notice is that the trace predicted by the fixed RRR configuration model (ζ=0°) is far from the true triple junction trace, and in fact not even on the South American Plate. Theoretical traces are shown for ζ=6°, 6.66°, 8° and 15°. The stability model with the value of ζ=6.66° provided the best fit to the estimated trace up until anomaly 6, with the triple junction having been most recently in RFF mode, preceded

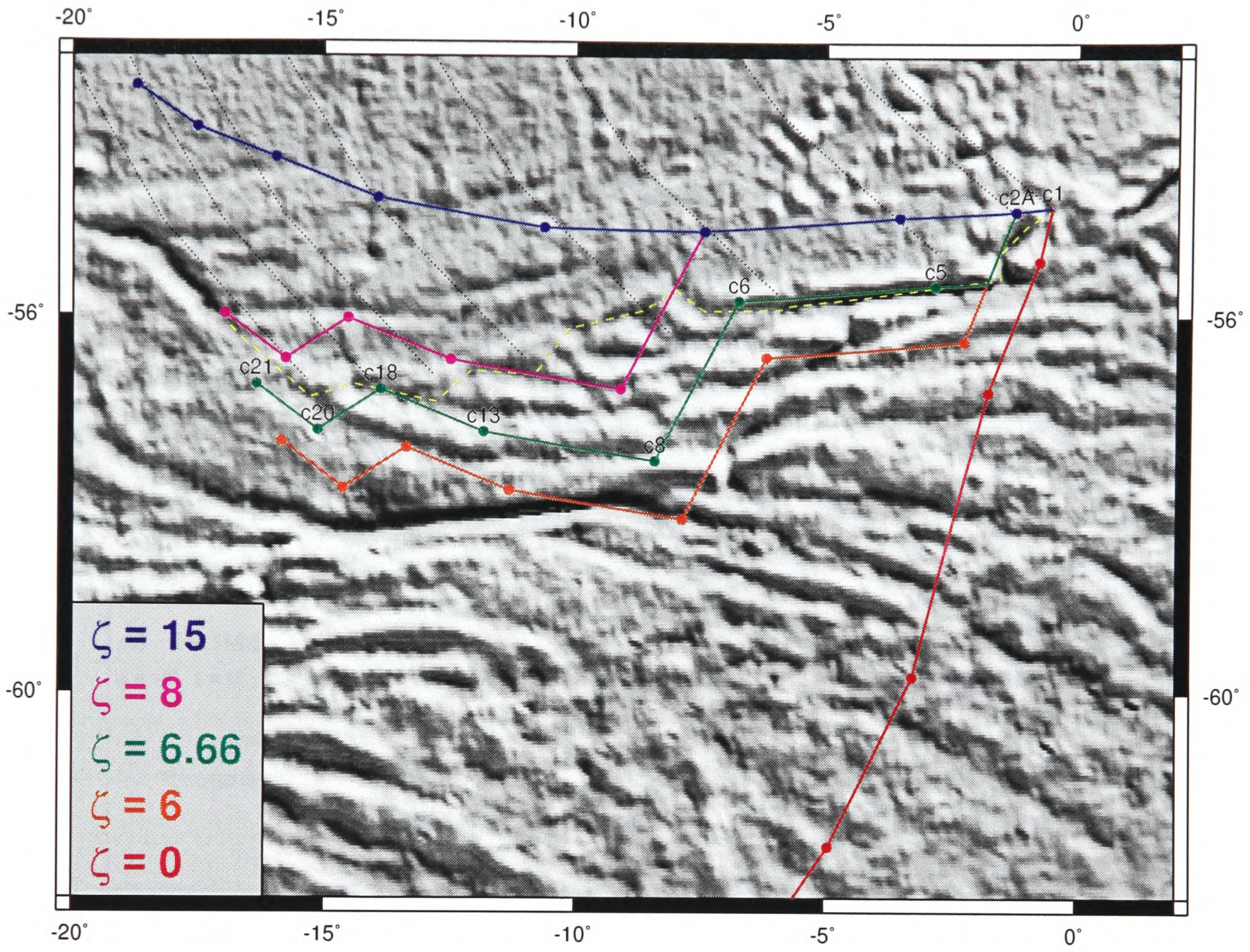

Figure 7.4: The traces of the SAM-AFR-ANT triple junction on the South American Plate predicted by stability models of the Bouvet Triple Junction with $\zeta = 0$, 6, 6.66, 8, and 15°. The $\zeta = 0$ model represents the trace for a fixed RRR-configuration and the $\zeta = 15$ model effectively represents the trace for a fixed RFF-configuration. The solid circles mark the location of the triple junction at each of the inversion chrons up until c21 (c2A,5,6,8,13,18,20,21). An estimate of the actual triple junction trace, as interpreted from the underlying gravity map, is marked by a dotted yellow line. The faint black lines represent synthetic isochrons determined for SAM-AFR spreading from the 3-plate inversions, for the above set of chrons.

---

by a short period in RRR configuration, and before then spending around 15Ma in RFF mode, giving rise to the medium-offset Conrad Fracture Zone, as predicted by the mechanical models of Sclater *et al.* (1976); Apotria & Gray (1985, 1988).

From the models shown, it is apparent that the RFF configuration has been dominant for most of this period, with the triple junction often existing in a RFF configuration where the velocity triangle is up to around 6-8 degrees away from isoceles. Thus the RFF configuration is far more stable than might be expected, in conditions where the velocity triangle is significantly non-isoceles. The velocity triangles at each discrete chron are shown in Figure 7.5 for the ζ=6.66°

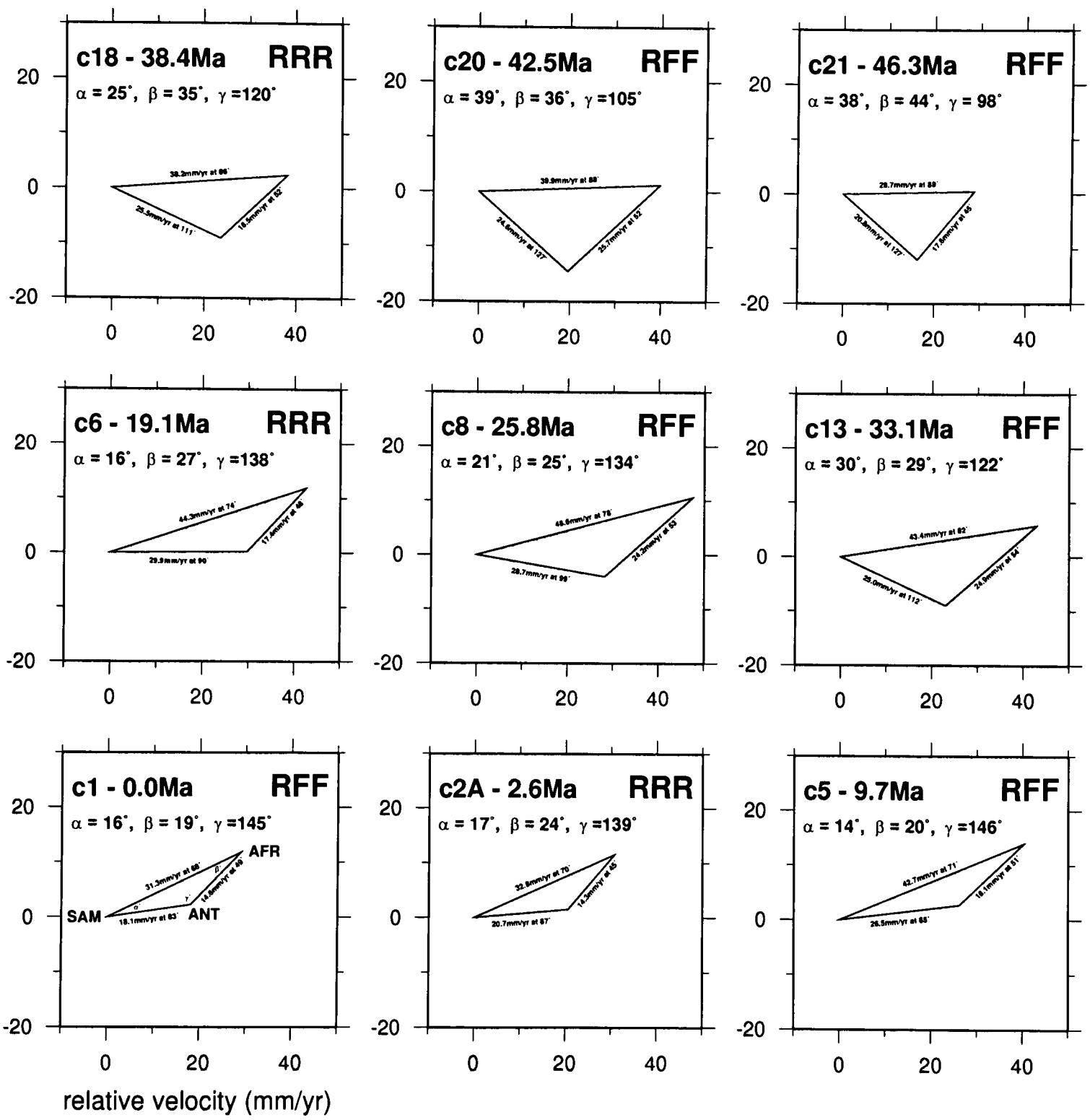

Figure 7.5: Velocity triangles at the SAM-ANT-AFR triple junction shown for several discrete times in the past (the chrons used in the inversion), for the ζ=6.66° stability model. The spreading rates and azimuths for each plate pair are displayed, along with the internal angles for each velocity triangle, and the predicted configuration.

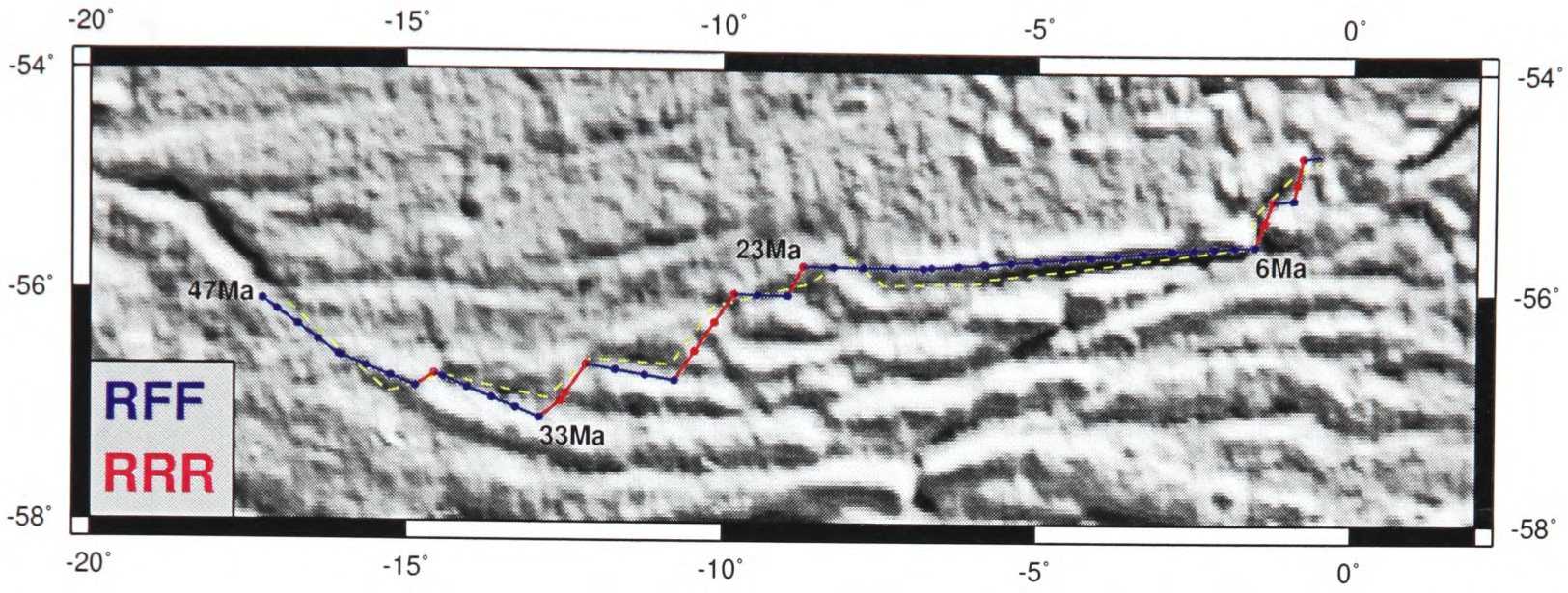

Figure 7.6: The modelled trace of the SAM-AFR-ANT triple junction on the South American Plate showing the best fit to the estimated trace from the gravity map. The configuration of the triple junction is specified at 1Ma intervals in order to keep the predicted trace as close as possible to that of the observed trace, but the motion of the triple junction is strictly defined by the plate velocities calculated as before.

model. Incidentally, there were no problems with closure of the velocity triangles, due to the requirement for closure in the plate circuit during the 3-plate reconstruction. The sequence shows the clear prediction of the configuration alternating between RRR and RFF. It is interesting to note the rotation of the velocity triangle after anomaly 6, and how it gradually becomes more equilateral, predominantly due to the significant drop in South American-African spreading rates after anomaly 13.

A further model was constructed in which the configuration of the triple junction was specified explicitly at every 1Ma stage of the model, in order to follow the observed trace as close as possible. The results of this model are shown in Figure 7.6. The periods when the triple junction is thought to have been in RRR mode are marked by a red trace, and the RFF configuration by a blue trace. The fit to the observed trace is very good, particularly as there is a degree of uncertainty in the interpretation of the actual trace from the gravity map. The fit could be improved even further if the modelling interval was reduced to less than 1Ma. The azimuths in the model and observed trace are very close throughout and certainly interpolation of the triple junction motion from c21 to c20 would appear to correspond well with the approximate location of the triple junction after it jumped west shortly after c24 (52Ma). This model enables an accurate estimate for the time of the triple junction in each mode to be calculated. It predicts that the Bouvet Triple Junction has been in a RFF configuration for close to 36 of the last 46Ma, approximately 78% of the time.

Previous models for the evolution of the Bouvet Triple Junction were based on the visible plate

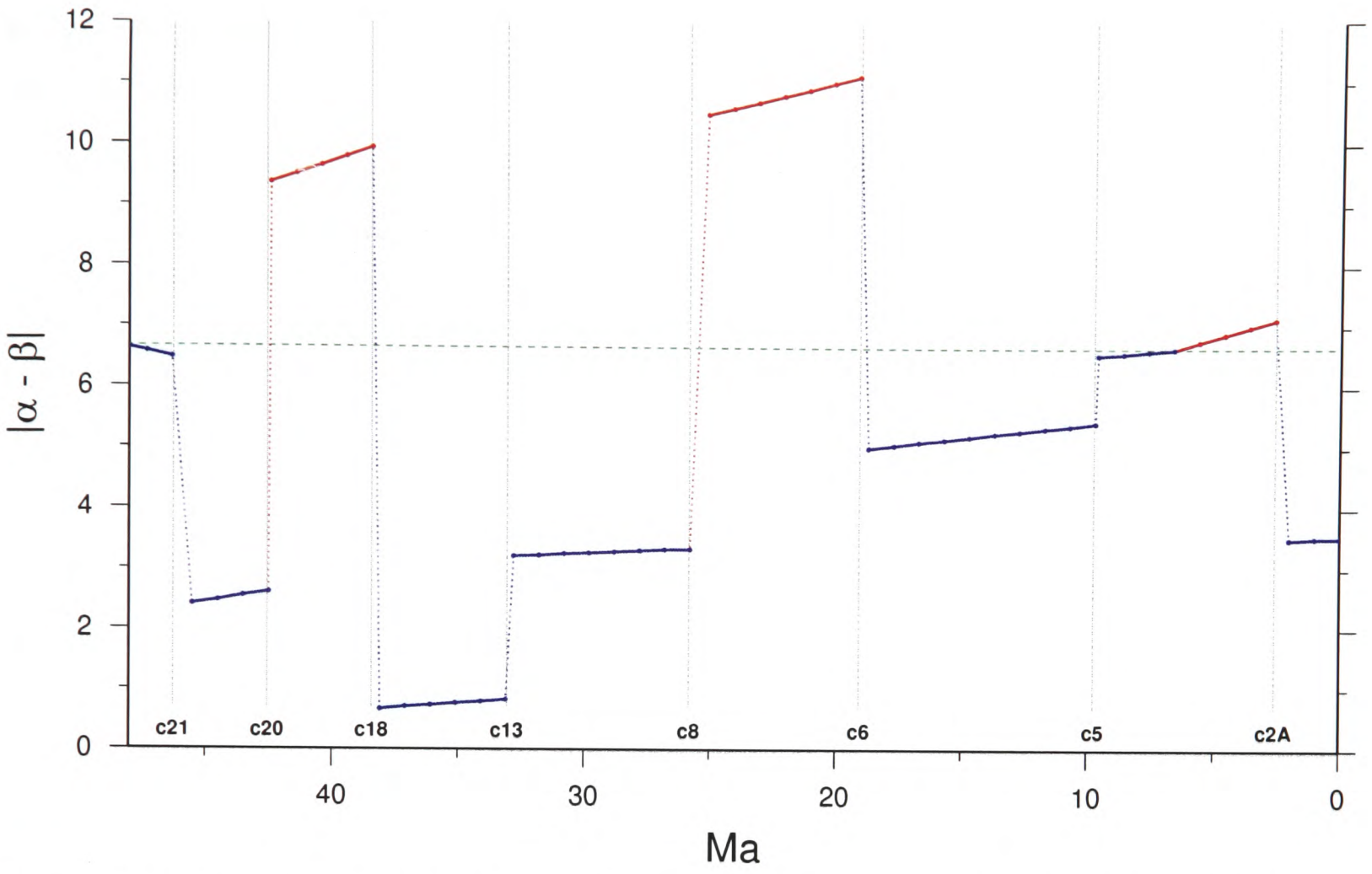

Figure 7.7: The degree of non-isocelesness of the Bouvet Triple Junction, as predicted by the ζ=6.66° model. Periods of RRR configuration are marked in red, and RFF configuration by blue. The ζ=6.66° threshold is marked by a dashed green line.

---

mechanics of the region (Sclater *et al.*, 1976; Apotria & Gray, 1985, 1988), with the existence of the relatively long Conrad and Bouvet transforms (on the South American-Antarctic Ridge and Southwest Indian Ridge respectively) suggesting a prolonged period in the RFF configuration (from approximately 31Ma to 18Ma (Apotria & Gray, 1985, 1988)). When considering the stability and configuration, these studies used the current instantaneous poles of motion, and assumed constant motion for the periods of time covered by the models (up to 31Ma in Apotria & Gray (1985, 1988), which is not realistic). However, the basic conclusions are the same, that the RFF configuration is far more stable than would be predicted, and that the triple junction alternates between short periods as RRR and much longer periods in the RFF configuration.

Comparing the results of the modelling carried out here with the observed spreading rates and directions for the 3-plate system shown in Figure 6.14, it can be seen that the period when the triple junction appears to be frequently altering between a RFF and RRR configurations ($\approx$23-33Ma) coincides with the approximate period of maximum spreading rates on all three plates (up to anomaly 21). This is not surprising because the RFF configuration is increasingly less stable

at faster spreading rates, because it increases the degree of compression/extension occurring at the transforms.

It was suggested by Apotria & Gray (1985, 1988), that the motion of the triple junction whilst in RRR mode served to return the velocity triangle to isoceles, whilst in the RFF mode, it led to the velocity triangle becoming less isoceles. Figure 7.7 shows the values of $|\alpha - \beta|$ for the ζ=6.66° model, which shows that the stimulus for the changes in configuration was, in all but one case, purely changes in the stage poles altering the velocity triangle at the chron boundaries, rather than the motion of the triple junction altering the geometry of the velocity triangle. When in RFF mode, there was in general little change in the isoceles relationship, with, if anything, a slight drift away from isoceles, but not particularly significantly. When in RRR mode however, in every case, the motion of the triple junction appears to be making the velocity triangle less isoceles, which is exactly the opposite to the model of Apotria & Gray (1985, 1988). The difference could come from the fact that they placed the Bouvet Triple Junction at 61.8°S, 0°E, which is around 700km from its true position, which would cause a considerable difference in the velocity triangles calculated from the instantaneous poles.

If the set of finite rotation poles could be determined for the 3-plate system for more chrons than obtained here, this would reduce the time interval between the instantaneous poles. This would then hopefully result in a smoother variation in the velocity triangles, without the large jumps shown in Figure 7.7 at the inversion chrons. This would probably lead to an overall improvement in the models of the triple junction, and enable a more precise study to be made of the stability of the triple junction, as far as could be carried out without including any mechanical constraints.

Chapter 8

Evaluation of inversion methods and future work

8.1 Success of the 2 and 3-plate inversion methods

The inversion method of 2-plate reconstructions in general worked very well. By being able to rotate to both conjugate and non-conjugate isochrons, and to define non-zero-age seed points for the fracture zones, the method proved to be very flexible. The benefits of the method are most apparent when working with a relatively sparse dataset, where a method fitting only conjugate isochrons would have few valid data points, such as the dataset for ANT-AFR spreading used here. The 2-plate method makes full use of the available data, and constrains the poles far better than a method fitting a few poorly distributed conjugate isochrons could manage. The problems of using data from only one flank of a plate pair in determining finite rotation poles were seen in the SAM-ANT 2-plate reconstruction. Use of data from seafloor created during a period of oblique or asymmetric spreading will not be 'cancelled out' by the inclusion of data on the conjugate flank, and so any divergence from normal symmetric spreading goes unnoticed. However, this is not really a failure of the method, since in order to reconstruct 2-plate motion in the form of finite rotation poles from just one flank, the assumption of symmetric spreading must always be made.

One way to allow for asymmetric spreading would be to use the set of stage poles on both sides of the ridge as the parameter set, such that if we are inverting for n chrons, for plates A and B, and the stage pole between anomalies i and j on plate B is given by ${}^{AB}\mathbf{S}^{i,j}$, then the parameter set would comprise of the latitude, longitude and rotation angle for each of the stage poles $\{{}^{BA}\mathbf{S}^{1,2}, \ldots, {}^{BA}\mathbf{S}^{n-1,n}, {}^{AB}\mathbf{S}^{12}, \ldots, {}^{AB}\mathbf{S}^{n-1,n}\}$. This would double the numbers of

parameters, but more importantly, it would substantially complicate the calculations throughout the inversion. For example, to rotate a pick on isochron 'n' on one plate to the conjugate isochron 'n' would require the determination of the finite rotation ${}^{AB}\mathbf{F}^{n}$, which is the sum of all the stage rotations, and so the misfit would be affected by every single parameter. Thus the partial derivative matrix would go from being relatively sparse to extremely packed, which would lead to much slower inversions, quite apart from the multiple stages that would be required in the calculations of errors and partial derivatives. This method would still not be able to cope with localised discontinuities however, such as that seen in the Weddell Sea, and so the present method appears to be best.

The 2-plate reconstruction of Antarctic-African spreading is the first for the region to combine both fracture zone and magnetic anomaly data, and to obtain poles from as far back as anomaly 34 (83Ma) up to the present day. Similarly, the 2-plate reconstruction for South American-Antarctic spreading is the first to use only data from this plate pair, and to include data from the Weddell Sea in the determination of SAM-ANT finite rotation poles.

The initial results of the 3-plate inversion seemed to be fairly poor, not providing as good a fit as was hoped, but it was proved to be the input data at fault, and not the inversion method. In fact, the 3-plate reconstruction could be considered a success as it revealed a feature that had not been apparent before, and in truth, a 3-plate reconstruction that reveals no more information than the individual 2-plate reconstructions is relatively pointless and redundant. In this way, the 3-plate method is most useful where there is poor data coverage for one plate pair, and so new information and results are produced through use of the three plate circuit. Once the discontinuity in the Weddell Sea had been accounted for, the 3-plate inversion worked very well, determining smooth progressions of poles for each plate pair, straightening out any extraneous kinks in the flowlines, and satisfying each dataset as well as, if not better than, the original 2-plate reconstructions.

The determination of the spreading discontinuity in the Weddell Sea was an unexpected result of the implementation of the 3-plate reconstruction. Although the disruption to the flowlines had always been apparent in the gravity map, it had not been considered as overly significant. There had been no previous inversions for South American-Antarctic spreading incorporating data from both the Weddell Sea and the present-day South American-Antarctic Ridge, and so it was not surprising it had not been revealed previously.

The internal consistency of the 3-plate inversion proved that Antarctica, South America, and Africa have operated as a closed 3-plate system since anomaly 34. No data for South American/Malvinas-African spreading was included from the Agulhas Basin, and so the existence of a Malvinas Plate could not be disproved entirely. However, the excellent fit of the anomalies and flowlines from c34 to c31 on all 3 plate boundaries suggests that if a Malvinas Plate did exist, then it was confined entirely within the Agulhas Basin, and certainly didn't extend as far west as the Weddell Sea.

8.2 Future applications of the inversion method

While carrying out the work, it became apparent that although the magnetic anomaly datasets for SAM-AFR and SAM-ANT spreading were quite complete and as comprehensive as possible, the dataset along the South-West Indian Ridge was not so. This was not necessarily due to lack of data coverage, since many studies have been carried out over the area, but rather from lack of access to the data. The large amount of ship track data shown to be included in the studies of Sclater *et al.* (1996), would have been of invaluable use to the inversions for ANT-AFR spreading, and would no doubt put much greater constraints on the reconstruction poles obtained. If more data was made available, then it would be useful to include this into the dataset, and hence obtain an improved set of rotation poles for Antarctic - African spreading. However, the set of poles that were obtained are the first set of finite rotation poles for the South-West Indian Ridge dating from the present back as far as anomaly 34 obtained from such a reconstruction method.

Though much time was spent processing and compiling the datasets for the South American, African and Antarctic plates, the main focus of work for this study was in developing the inversion methods. As a method for a two plate inversions, where there is full coverage of data on both flanks, the method represents an improvement over that of Shaw & Cande (1990) in that the definition and calculations of the misfits and partial derivatives are much improved, but the basic inversion theory remains the same. The method could be applied to such plate pairs elsewhere on the globe to good effect, but the major advance in the reconstruction method is the application to plate pairs where one has since been partially or totally subducted beneath an adjacent plate. An area where this situation occurs is the Pacific, where there is subduction around the whole of the perimeter, and so there is a possibility of determining finite rotations between several pairs

of plates in the region, where previously the past motion has only been determined through the summation of rotations through plate circuits.

As a 3-plate system, the South American-African-Antarctic set of plates did not have the most ideal datasets to show off the full capabilities of the 3-plate reconstruction method. Although a high-quality dataset was obtained for South-American spreading, the spreading rates on the South-West Indian Ridge are very slow at times, uniquely so, and also the anomalies are highly skewed, making interpretation much more difficult, hampered further by the often complex topography in the region. The dataset of South American-Antarctic spreading was limited by the short length of the current ridge axis and the lack of data on both flanks in the Weddell Sea. However, in the end, it was ironically this lack of data for the third plate pair which made the application of the three plate method most desirable, as it provided a way to constrain the plate motions more accurately than previously possible, and revealed the spreading discontinuity that had not been previously detected or suggested by other means.

The 3-plate reconstruction method could be put to good use for many three plate systems around the globe - the most obvious application would be to work around the Indian Ocean Triple Junction, and it could then be compared to the previous, more basic, 3-plate inversion method of Tapscott (1979). For three plate systems with good data coverage, the basic rotation poles would probably not be too different from those determined previously, but information about closure and coordination of any changes within the system would be most useful. Given sufficient data coverage, then it would be hoped that the 3-plate reconstruction would be able to identify smaller scale plate deformation through comparison with the individual 2-plate reconstructions.

8.3 Extensions to the inversion method

The extension to a 3-plate reconstruction method from a 2-plate method was reasonably straightforward in concept, though the calculations were necessarily made more complex. However, by the very nature of extending the method to 3 plates through use of a plate circuit, it would be a relatively easy step to extend the method further to any number of plates within a circuit. Thus, if we consider a plate circuit $\mathcal{P}(1) \mapsto \mathcal{P}(2) \ldots \mathcal{P}(i) \ldots \mathcal{P}(N)$, then a two plate inversion method could be used to derive the errors and partial derivatives for the plate pairs $\mathcal{P}(1) \mapsto \mathcal{P}(2)$ to $\mathcal{P}(N-2) \mapsto \mathcal{P}(N-1)$. The final plate pair $\mathcal{P}(1) \mapsto \mathcal{P}(N)$, would be treated in a similar way

to the third plate pair in the three plate reconstruction.

The finite rotation poles can be determined from summing through the circuit, such that the finite rotation for plate $\mathcal{P}(N)$ with respect to $\mathcal{P}(1)$ is given by

$$^{1,N}\mathbf{F} = {}^{N-1,N}\mathbf{F} \ldots {}^{2,3}\mathbf{F}\,{}^{1,2}\mathbf{F} \tag{8.1}$$

The errors for this plate are then calculated from the set of finite rotation poles determined as above. The partial derivatives of the datum for the summed plate pair are defined in terms of the partial derivatives of the finite rotation matrix, $\frac{\partial^{1,N}\mathbf{F}}{\partial p^\gamma}$. The partial derivative of a rotation matrix obtained through repeated matrix multiplication, with respect to a parameter of the ith plate pair of the circuit is simply given by the multiplication of the matrices, in a similar fashion to (8.1), but where one of the matrices is a partial derivative matrix.

$$\frac{\partial^{1,N}\mathbf{F}}{\partial p^\gamma} = {}^{N-1,N}\mathbf{F} \ldots \frac{\partial^{i,i+1}\mathbf{F}}{\partial p^\gamma} \ldots {}^{1,2}\mathbf{F} \tag{8.2}$$

The determination of $\frac{\partial^{i,i+1}\mathbf{F}}{\partial p^\gamma}$ was previously defined for the 2-plate inversion, and so the only new step is summing N-1 rotations as opposed to summing 2 rotations, and is not mathematically more complex. A similar technique could be used to incorporate information from any other plate pair not included in the main circuit (*i.e.*. $\mathcal{P}(2) \mapsto \mathcal{P}(4)$). Thus this method could be used to determine a global plate circuit of plate motions (for extensional boundaries).

8.4 Development of an interactive reconstruction program.

A substantial amount of time was spent writing computer programs for the processing and manipulation of data for the inversions, in particular the interactive graphics programs for X-Windows. There was no interaction between the picking programs, **xfzpick** and **xmagpick**, the data sorting program **xsortdata**, and the reconstruction routines. However, it was envisaged that with some effort, these could be incorporated into a single package. The user would be able to pick the coarse sample points and a reference seed point for a fracture zone from a gravity map displayed on screen. The generation of profiles, and making of fracture zone picks, could then be carried out using a pop-up profile picking window in the form of **xfzpick**. The magnetics would be able to be picked from cruise data using a separate window, similar to **xmagpick**. The main display would

be as for **xsortdata**, displaying the two types of data simultaneously. If an outlier was spotted in the magnetics data, then the **xmagpick** window would appear with the relevant cruise data, and the actual pick could be checked, similarly for the fracture zone data with **xfzpick**. Once the data had been sorted as required, the reconstructions could be run from the main windows program, and could be used to show the synthetic flowlines generated, and the fitted great circles, and rotated magnetics picks, all on the same screen display alongside the datasets.

A complex piece of programming possibly, but once created, it would provide a very quick and simple graphical interface for compiling the required datasets and carrying out plate reconstructions, with the ease of use that windows programs enjoy.

Appendix A

Partial Derivatives for Rotations

A.1 Partial derivatives of matrix and vector products

Consider a constant vector $\mathbf{v}$, and a variable vector $\mathbf{x}(t)$. Then the dot product of $\mathbf{v}$ and $\mathbf{x}$ is given by

$$\mathbf{v}.\mathbf{x} = v_i x_i \tag{A.1}$$

and the derivative with respect to t is given by

$$\frac{\partial(\mathbf{v}.\mathbf{x})}{\partial t} = \frac{\partial(v_i x_i)}{\partial t} = v_i \frac{\partial x_i}{\partial t} \tag{A.2}$$

and so we obtain

$$\frac{\partial(\mathbf{v}.\mathbf{x})}{\partial t} = \mathbf{v}.\left[\frac{\partial \mathbf{x}}{\partial t}\right] \tag{A.3}$$

Similarly, the derivative of the vector product of a constant vector $\mathbf{v}$ and a variable vector $\mathbf{x}(t)$ can be shown to be

$$\frac{\partial(\mathbf{v}\wedge\mathbf{x})}{\partial t} = \mathbf{v}\wedge\left[\frac{\partial \mathbf{x}}{\partial t}\right] \tag{A.4}$$

Next, we consider the effect of a matrix operation on a 3-vector. If we premultiply the variable vector $\mathbf{x}(t)$ by the constant matrix $\mathbf{M}$, then

$$[\mathbf{M}\mathbf{x}]_i = \mathbf{M}_{ik} x_k \tag{A.5}$$

and the derivative of this with respect to t is given by

$$\begin{aligned}\frac{\partial [\mathbf{Mx}]_i}{\partial t} &= \frac{\partial (\mathbf{M}_{ik} x_k)}{\partial t} \\ &= \mathbf{M}_{ik} \frac{\partial x_k}{\partial t}\end{aligned} \tag{A.6}$$

and so we obtain

$$\frac{\partial (\mathbf{Mx})}{\partial t} = \mathbf{M} \left[\frac{\partial \mathbf{x}}{\partial t} \right] \tag{A.7}$$

If we then consider the situation where we are premultiplying the constant vector $\mathbf{v}$ by the variable matrix $\mathbf{A}(t)$, by the same method as above, it can be shown that

$$\frac{\partial (\mathbf{Av})}{\partial t} = \left[\frac{\partial \mathbf{A}}{\partial t} \right] \mathbf{v} \tag{A.8}$$

A.2 Partial derivatives for a 2-plate inversion

A.2.1 Derivatives of a pole as a vector

A rotation pole, as detailed previously, can either be given as a geographical position and a rotation, or a unit vector and a rotation and during the inversion calculations it is sometimes necessary to switch between the two. As such, the partial derivatives of the pole vector with respect to the pole latitude and longitude need to be determined. The pole vector $\mathbf{p}$ is given in terms of θ and ϕ as

$$\mathbf{p} = \begin{bmatrix} \cos(\theta)\cos(\phi) \\ \cos(\theta)\sin(\phi) \\ \sin(\theta) \end{bmatrix} \tag{A.9}$$

and from this it is straightforward to obtain

$$\frac{\partial \mathbf{p}}{\partial \theta}(\theta, \phi) = \begin{bmatrix} -\sin(\theta)\cos(\phi) \\ -\sin(\theta)\sin(\phi) \\ \cos(\theta) \end{bmatrix} \tag{A.10}$$

and

$$\frac{\partial \mathbf{p}}{\partial \phi}(\theta, \phi) = \begin{bmatrix} -\cos(\theta)\sin(\phi) \\ \cos(\theta)\cos(\phi) \\ 0 \end{bmatrix} \tag{A.11}$$

These results are required to determine the partial derivatives for transform fault datum as defined in equation (4.53), and also to determine the partial derivatives for fracture zone picks within the first spreading section (within the bounds of the first finite rotation).

A.2.2 Derivatives of a rotation matrix

Given a finite rotation pole described by the latitude θ, the longitude ϕ and the rotation angle α, the rotation can be described by a 3x3 matrix R such that a point on a sphere represented by a 3-vector **a** is premultiplied by the matrix to give the rotated point as the 3-vector **b**

$$\mathbf{b} = \mathbf{R}\mathbf{a} \tag{A.12}$$

It is easiest to calculate the matrix having converted the pole location into the 3-vector $\mathbf{p}(\theta, \phi)$. The rotation matrix $\mathbf{R}$ is then given as

$$\mathbf{R}(\theta, \phi, \alpha) = \begin{bmatrix} p_1p_1(1-\cos(\alpha))+\cos(\alpha) & p_1p_2(1-\cos(\alpha))-p_3\sin(\alpha) & p_1p_3(1-\cos(\alpha))+p_2\sin(\alpha) \\ p_2p_1(1-\cos(\alpha))+p_3\sin(\alpha) & p_2p_2(1-\cos(\alpha))+\cos(\alpha) & p_2p_3(1-\cos(\alpha))-p_1\sin(\alpha) \\ p_3p_1(1-\cos(\alpha))-p_2\sin(\alpha) & p_3p_2(1-\cos(\alpha))+p_1\sin(\alpha) & p_3p_3(1-\cos(\alpha))+\cos(\alpha) \end{bmatrix} \tag{A.13}$$

So, if one of the pole parameters $p^\gamma \in (\theta, \phi, \alpha)$ is altered, then $\mathbf{R}$ will have changed. The matter is slightly complicated by the fact that $\mathbf{R}$ is defined in terms of the pole vector $\mathbf{p}$ rather than the latitude and longitude and so in order to determine the derivatives or $\mathbf{R}$ with respect to θ and ϕ, we must first determine the derivatives of $\mathbf{R}$ with respect to $\mathbf{p}$. From (A.13) we get

$$\frac{\partial \mathbf{R}}{\partial p_1} = \begin{bmatrix} 2p_1(1-\cos(\alpha)) & p_2(1-\cos(\alpha)) & p_3(1-\cos(\alpha)) \\ p_2(1-\cos(\alpha)) & 0 & -\sin(\alpha) \\ p_3(1-\cos(\alpha)) & \sin(\alpha) & 0 \end{bmatrix} \tag{A.14}$$

$$\frac{\partial \mathbf{R}}{\partial p_2} = \begin{bmatrix} 0 & p_1(1-\cos(\alpha)) & \sin(\alpha) \\ p_1(1-\cos(\alpha)) & 2p_2(1-\cos(\alpha)) & p_3(1-\cos(\alpha)) \\ -\sin(\alpha) & p_3(1-\cos(\alpha)) & 0 \end{bmatrix} \tag{A.15}$$

$$\frac{\partial \mathbf{R}}{\partial p_3} = \begin{bmatrix} 0 & -\sin(\alpha) & p_1(1-\cos(\alpha)) \\ \sin(\alpha) & 0 & p_2(1-\cos(\alpha)) \\ p_1(1-\cos(\alpha)) & p_2(1-\cos(\alpha)) & 2p_3((1-\cos(\alpha)) \end{bmatrix} \tag{A.16}$$

The derivatives of $\mathbf{p}$ with respect to θ and ϕ were given in equations (A.10) and (A.11) respectively and so the chain rule is applied to give

$$\frac{\partial \mathbf{R}}{\partial \theta}(\theta, \phi, \alpha) = \frac{\partial \mathbf{R}}{\partial p_i}\frac{\partial p_i}{\partial \theta} \tag{A.17}$$

$$\frac{\partial \mathbf{R}}{\partial \phi}(\theta, \phi, \alpha) = \frac{\partial \mathbf{R}}{\partial p_i}\frac{\partial p_i}{\partial \phi} \tag{A.18}$$

The partial derivative with respect to α are straightforward and can be obtained directly from (A.13).

$$\frac{\partial \mathbf{R}}{\partial \alpha}(\theta, \phi, \alpha) = \begin{bmatrix} (p_1p_1-1)\sin(\alpha) & p_1p_2\sin(\alpha)-p_3\cos(\alpha) & p_1p_3\sin(\alpha)+p_2\cos(\alpha) \\ p_2p_1\sin(\alpha)+p_3\cos(\alpha) & (p_2p_2-1)\sin(\alpha) & p_2p_3\sin(\alpha)-p_1\cos(\alpha) \\ p_3p_1\sin(\alpha)-p_2\cos(\alpha) & p_3p_2\sin(\alpha)+p_1\cos(\alpha) & (p_3p_3-1)\sin(\alpha) \end{bmatrix} \tag{A.19}$$

And thus we have obtained the derivatives of the rotation matrix with respect to a change in one of its defining parameters,

$$\frac{\partial \mathbf{R}}{\partial p^\gamma}(\theta, \phi, \alpha) \quad p^\gamma \in (\theta, \phi, \alpha)$$

A.2.3 Partial derivatives of a rotation pole from its matrix

When calculating errors and partial derivatives for fracture zone data, the partial derivatives of the stage pole vector are required, where the stage pole vector is obtained from directly from the stage rotation matrix. Thus it is necessary to determine the partial derivatives of the pole parameters of a rotation with respect to the pole parameters of another rotation which is used to determine the former. The simplest way is to determine the required partial derivatives in terms of the partial derivatives of the defining stage rotation matrix. The first step to obtaining this is to determine an inverse set of equations from which we can obtain the pole 3-vector ($\mathbf{p}$) in terms of the elements of the corresponding rotation matrix $\mathbf{R}$. This is given below,

$$\mathbf{p}(\mathbf{R}) = \begin{bmatrix} \frac{u}{z} \\ \frac{v}{z} \\ \frac{w}{z} \end{bmatrix} \tag{A.20}$$

where

$$u = R_{32} - R_{23} \tag{A.21a}$$

$$v = R_{13} - R_{31} \tag{A.21b}$$

$$w = R_{21} - R_{12} \tag{A.21c}$$

$$z = \sqrt{u^2 + v^2 + w^2} \tag{A.21d}$$

So if the elements of a rotation matrix are affected by a change in an unspecified parameter p^γ then the derivative of the pole vector $\mathbf{p}$ with respect to its source rotation matrix $\mathbf{R}$ and its derivative $\frac{\partial \mathbf{R}}{\partial p^\gamma}$ is given by

$$\frac{\partial \mathbf{p}}{\partial p^\gamma}\left(\mathbf{R}, \frac{\partial \mathbf{R}}{\partial p^\gamma}\right) = \begin{bmatrix} \frac{z\frac{\partial u}{\partial p^\gamma} - u\frac{\partial z}{\partial p^\gamma}}{z^2} \\ \frac{z\frac{\partial v}{\partial p^\gamma} - v\frac{\partial z}{\partial p^\gamma}}{z^2} \\ \frac{z\frac{\partial w}{\partial p^\gamma} - w\frac{\partial z}{\partial p^\gamma}}{z^2} \end{bmatrix} \tag{A.22}$$

where

$$\frac{\partial u}{\partial p^\gamma} = \frac{\partial R_{32}}{\partial p^\gamma} - \frac{\partial R_{23}}{\partial p^\gamma} \tag{A.23a}$$

$$\frac{\partial v}{\partial p^\gamma} = \frac{\partial R_{13}}{\partial p^\gamma} - \frac{\partial R_{31}}{\partial p^\gamma} \tag{A.23b}$$

$$\frac{\partial w}{\partial p^\gamma} = \frac{\partial R_{21}}{\partial p^\gamma} - \frac{\partial R_{12}}{\partial p^\gamma} \tag{A.23c}$$

$$\frac{\partial z}{\partial p^\gamma} = \frac{1}{z}\left(u\frac{\partial u}{\partial p^\gamma} + v\frac{\partial v}{\partial p^\gamma} + w\frac{\partial w}{\partial p^\gamma}\right) \tag{A.23d}$$

A.2.4 Partial derivatives of a stage pole

A stage pole is dependent on the pole parameters of the two finite rotation poles which are used to determine the stage pole. Defining the finite rotation pole for time τ as having parameters θ^τ, ϕ^τ, α^τ and rotation matrix $\mathbf{F}^\tau$, the stage poles between times τ_a and τ_b $(= \tau_a + \Delta\tau)$ are defined as $\mathbf{S}^{ab}$ and $\mathbf{S}^{ba}$ where

$\mathbf{S}^{ab}$ is a rotation of θ^a, ϕ^a, $-\frac{\alpha^a}{2}$ followed by a rotation of θ^b, ϕ^b, $\frac{\alpha^b}{2}$.

$\mathbf{S}^{ba}$ is a rotation of θ^a, ϕ^a, $\frac{\alpha^a}{2}$ followed by a rotation of θ^b, ϕ^b, $-\frac{\alpha^b}{2}$.

To make the steps simpler, define further $\mathbf{F}^{\frac{a}{2}}$ as a rotation of θ^a, ϕ^a, $\frac{\alpha^a}{2}$ and $\mathbf{F}^{-\frac{a}{2}}$ as a rotation of θ^a, ϕ^a, $-\frac{\alpha^a}{2}$.

Two rotations, $\mathbf{A}$ followed by $\mathbf{B}$, are summed to give a third rotation $\mathbf{S}$ as follows

$$\mathbf{S} = \mathbf{BA} \tag{A.24}$$

and applying the product rule, we obtain the derivative

$$\frac{\partial \mathbf{S}}{\partial p^\gamma} = \mathbf{B}\left[\frac{\partial \mathbf{A}}{\partial p^\gamma}\right] + \left[\frac{\partial \mathbf{B}}{\partial p^\gamma}\right]\mathbf{A} \tag{A.25}$$

So, what we require is the partial derivative of $\mathbf{S}^{ab}(= \mathbf{F}^{\frac{b}{2}}\mathbf{F}^{-\frac{a}{2}})$ with respect to p^γ where

$p^\gamma \in \{\theta^a, \phi^a, \alpha^a, \theta^b, \phi^b, \alpha^b\}$. From (A.25) we obtain

$$\frac{\partial(\mathbf{S}^{ab})}{\partial p^\gamma} = \begin{cases} \mathbf{F}^{\frac{b}{2}} \left[\frac{\partial \mathbf{F}^{-\frac{a}{2}}}{\partial p^\gamma}\right] & p^\gamma \in \{\theta^a, \phi^a, \alpha^a\} \\ \left[\frac{\partial \mathbf{F}^{\frac{b}{2}}}{\partial p^\gamma}\right] \mathbf{F}^{-\frac{a}{2}} & p^\gamma \in \{\theta^b, \phi^b, \alpha^b\} \end{cases} \tag{A.26}$$

Although we know $\mathbf{F}^a$ in terms of θ^a, ϕ^a and α^a, in order to obtain the derivatives we require, such as $\frac{\partial \mathbf{F}^{-\frac{a}{2}}}{\partial p^\gamma}$ we must implement the chain rule.

Using $\mathbf{F}^{-\frac{a}{2}}$ as an example, we have

$$\theta^{-\frac{a}{2}} = \theta^a \qquad \phi^{-\frac{a}{2}} = \phi^a \qquad \alpha^{-\frac{a}{2}} = -\frac{\alpha^a}{2} \tag{A.27}$$

with

$$\frac{\partial(\theta^{-\frac{a}{2}})}{\partial \theta^a} = 1 \qquad \frac{\partial(\phi^{-\frac{a}{2}})}{\partial \phi^a} = 1 \qquad \frac{\partial(\alpha^{-\frac{a}{2}})}{\partial \alpha^a} = -\frac{1}{2} \tag{A.28}$$

which leads to

$$\begin{aligned} \frac{\partial(\mathbf{F}^{-\frac{a}{2}})}{\partial \theta^a} &= \frac{\partial(\mathbf{F}^{-\frac{a}{2}})}{\partial \theta^{-\frac{a}{2}}} \frac{\partial \theta^{-\frac{a}{2}}}{\partial \theta^a} \\ &= \frac{\partial(\mathbf{F}^{-\frac{a}{2}})}{\partial \theta^{-\frac{a}{2}}} \\ &= \frac{\partial \mathbf{R}}{\partial \theta}(\theta^a, \phi^a, -\tfrac{1}{2}\alpha^a) \end{aligned} \tag{A.29}$$

$$\begin{aligned} \frac{\partial(\mathbf{F}^{-\frac{a}{2}})}{\partial \phi^a} &= \frac{\partial(\mathbf{F}^{-\frac{a}{2}})}{\partial \phi^{-\frac{a}{2}}} \frac{\partial \phi^{-\frac{a}{2}}}{\partial \phi^a} \\ &= \frac{\partial(\mathbf{F}^{-\frac{a}{2}})}{\partial \phi^{-\frac{a}{2}}} \\ &= \frac{\partial \mathbf{R}}{\partial \phi}(\theta^a, \phi^a, -\tfrac{1}{2}\alpha^a) \end{aligned} \tag{A.30}$$

$$\begin{aligned}\frac{\partial(\mathbf{F}^{-\frac{a}{2}})}{\partial\alpha^a} &= \frac{\partial(\mathbf{F}^{-\frac{a}{2}})}{\partial\alpha^{-\frac{a}{2}}}\frac{\partial\alpha^{-\frac{a}{2}}}{\partial\alpha^a} \\ &= -\frac{1}{2}\frac{\partial(\mathbf{F}^{-\frac{a}{2}})}{\partial\alpha^{-\frac{a}{2}}} \\ &= -\frac{1}{2}\frac{\partial\mathbf{R}}{\partial\alpha}(\theta^a,\phi^a,-\tfrac{1}{2}\alpha^a)\end{aligned} \tag{A.31}$$

where $\frac{\partial\mathbf{R}}{\partial\theta}$, $\frac{\partial\mathbf{R}}{\partial\phi}$ and $\frac{\partial\mathbf{R}}{\partial\alpha}$ are given in (A.17), (A.18) and (A.19) respectively.

So, from (A.26), we have

$$\frac{\partial\mathbf{S}^{ab}}{\partial p^\gamma} = \begin{cases} \mathbf{F}^{\frac{b}{2}}\left[\frac{\partial\mathbf{R}}{\partial p^\gamma}(\theta^a,\phi^a,-\frac{1}{2}\alpha^a)\right] & p^\gamma\in\{\theta^a,\phi^a\} \\ -\frac{1}{2}\mathbf{F}^{\frac{b}{2}}\left[\frac{\partial\mathbf{R}}{\partial p^\gamma}(\theta^a,\phi^a,-\frac{1}{2}\alpha^a)\right] & p^\gamma\in\{\alpha^a\} \\ \left[\frac{\partial\mathbf{R}}{\partial p^\gamma}(\theta^b,\phi^b,\frac{1}{2}\alpha^b)\right]\mathbf{F}^{-\frac{a}{2}} & p^\gamma\in\{\theta^b,\phi^b\} \\ \frac{1}{2}\left[\frac{\partial\mathbf{R}}{\partial p^\gamma}(\theta^b,\phi^b,\frac{1}{2}\alpha^b)\right]\mathbf{F}^{-\frac{a}{2}} & p^\gamma\in\{\alpha^b\} \end{cases} \tag{A.32}$$

This form of partial derivative, $\frac{\partial\mathbf{S}}{\partial p^\gamma}$, is the result required for determining the partial derivatives of the error for a magnetic anomaly pick, as defined in (4.41) on page 140. Now that we have $\mathbf{S}^{ab}$ and $\frac{\partial\mathbf{S}^{ab}}{\partial p^\gamma}$, then it is straightforward to obtain the derivative of the stage pole 3-vector s^{ab}, according to (A.22),

$$\begin{aligned}\frac{\partial\mathrm{s}^{ab}}{\partial p^\gamma} &= \frac{\partial\mathbf{p}}{\partial p^\gamma}\left(\mathbf{S}^{ab},\ \frac{\partial\mathbf{S}^{ab}}{\partial p^\gamma}\right) \\ &= \begin{cases} \frac{\partial\mathbf{p}}{\partial p^\gamma}\left(\mathbf{S}^{ab},\mathbf{F}^{\frac{b}{2}}\left[\frac{\partial\mathbf{R}}{\partial p^\gamma}(\theta^a,\phi^a,-\frac{1}{2}\alpha^a)\right]\right) & p^\gamma\in\{\theta^a,\phi^a\} \\ \frac{\partial\mathbf{p}}{\partial p^\gamma}\left(\mathbf{S}^{ab},-\frac{1}{2}\mathbf{F}^{\frac{b}{2}}\left[\frac{\partial\mathbf{R}}{\partial p^\gamma}(\theta^a,\phi^a,-\frac{1}{2}\alpha^a)\right]\right) & p^\gamma\in\{\alpha^a\} \\ \frac{\partial\mathbf{p}}{\partial p^\gamma}\left(\mathbf{S}^{ab},\left[\frac{\partial\mathbf{R}}{\partial p^\gamma}(\theta^b,\phi^b,\frac{1}{2}\alpha^b)\right]\mathbf{F}^{-\frac{a}{2}}\right) & p^\gamma\in\{\theta^b,\phi^b\} \\ \frac{\partial\mathbf{p}}{\partial p^\gamma}\left(\mathbf{S}^{ab},\frac{1}{2}\left[\frac{\partial\mathbf{R}}{\partial p^\gamma}(\theta^b,\phi^b,\frac{1}{2}\alpha^b)\right]\mathbf{F}^{-\frac{a}{2}}\right) & p^\gamma\in\{\alpha^b\} \end{cases}\end{aligned} \tag{A.33}$$

which is the form of partial derivative ($\frac{\partial\mathrm{s}}{\partial p^\gamma}$) required to calculate the partial derivatives for fracture zone datum, as defined in (4.49).

The partial derivatives for $\mathbf{S}^{ba}$ and $\frac{\partial\mathbf{S}^{ba}}{\partial p^\gamma}$ are obtained in identical fashion, but with the signs reversed for the rotation angles.

A.3 Partial derivatives for a 3-plate inversion

A.3.1 Partial derivatives of a rotation matrix

For the 3-plate problem, the third set of rotation poles is obtained by summing the two other, independent, poles. So, given rotations ${}^{12}\mathbf{F}$ and ${}^{23}\mathbf{F}$, the third rotation pole ${}^{13}\mathbf{F}$ is obtained by summation of the rotation matrices such that

$$ {}^{13}\mathbf{F} = {}^{23}\mathbf{F}\,{}^{12}\mathbf{F} \tag{A.34} $$

We wish to find the partial derivative of ${}^{13}\mathbf{F}$ with respect to the pole parameters of ${}^{12}\mathbf{F}$ and ${}^{23}\mathbf{F}$, and it is a simple step from (A.25) to obtain

$$ \begin{aligned} \frac{\partial({}^{13}\mathbf{F})}{\partial p^\gamma} &= \begin{cases} {}^{23}\mathbf{F}\left[\frac{\partial({}^{12}\mathbf{F})}{\partial p^\gamma}\right] & p^\gamma \in \{{}^{12}\theta, {}^{12}\phi, {}^{12}\alpha\} \\ \left[\frac{\partial({}^{23}\mathbf{F})}{\partial p^\gamma}\right] {}^{12}\mathbf{F} & p^\gamma \in \{{}^{23}\theta, {}^{23}\phi, {}^{23}\alpha\} \end{cases} \\ &= \begin{cases} {}^{23}\mathbf{F}\left[\frac{\partial \mathbf{R}}{\partial p^\gamma}({}^{12}\theta, {}^{12}\phi, {}^{12}\alpha)\right] & p^\gamma \in \{{}^{12}\theta, {}^{12}\phi, {}^{12}\alpha\} \\ \left[\frac{\partial \mathbf{R}}{\partial p^\gamma}({}^{23}\theta, {}^{23}\phi, {}^{23}\alpha)\right] {}^{12}\mathbf{F} & p^\gamma \in \{{}^{23}\theta, {}^{23}\phi, {}^{23}\alpha\} \end{cases} \end{aligned} \tag{A.35} $$

And so the partial derivative of ${}^{13}\mathbf{F}$ is given in terms of the partial derivatives of the two initial poles, the details of which are given in section A.2.2 and so this is quite straightforward.

A.3.2 Partial derivatives of a rotation pole from its matrix

When calculating the partial derivatives of the transform data for the third plate, the partial derivatives of the instantaneous pole, $\frac{\partial({}^{13}\mathbf{p}^1)}{\partial p^\gamma}$, need to be determined. In Section A.2.3 it was shown how to obtain the derivatives of a pole vector in terms of its rotation matrix, such that

$$ \frac{\partial({}^{13}\mathbf{p}^1)}{\partial p^\gamma} = \frac{\partial \mathbf{p}}{\partial p^\gamma}\left({}^{13}\mathbf{F}, \frac{\partial({}^{13}\mathbf{F})}{\partial p^\gamma}\right) \tag{A.36} $$

and, with the derivative $\frac{\partial({}^{13}\mathbf{F})}{\partial p^\gamma}$ defined above, this is straightforward. This result is also required when determining the partial derivatives for fracture zone data within the first spreading section (within the bounds of the first finite rotation).

When determining the derivatives of stage poles in the 3-plate problem, the partial derivatives of pole parameters in terms of the derivatives of their rotation matrix need to be found, in the same way as the partial derivatives of the pole vector were defined in Section A.2.3.

To do this, we begin from the set of equations which give the rotation parameters in terms of the rotation matrix elements. For the parameters θ, ϕ and α of a rotation $\mathbf{R}$, we have

$$\theta = \arccos\left(\frac{w}{z}\right) \qquad \phi = \arctan\left(\frac{v}{u}\right) \qquad \alpha = \arctan\left(\frac{z}{s}\right) \tag{A.37}$$

with $u, v, w,$ and z defined as before in (A.21) and s defined as

$$s = R_{11} + R_{22} + R_{33} - 1 \tag{A.38}$$

such that

$$\frac{\partial s}{\partial p^\gamma} = \frac{\partial R_{11}}{\partial p^\gamma} + \frac{\partial R_{22}}{\partial p^\gamma} + \frac{\partial R_{33}}{\partial p^\gamma} \tag{A.39}$$

The derivatives of these with respect to an unspecified parameter p^γ are then given as

$$\frac{\partial \theta}{\partial p^\gamma}\left(\mathbf{R}, \tfrac{\partial \mathbf{R}}{\partial p^\gamma}\right) = \frac{1}{\sqrt{1-\left(\frac{w}{z}\right)^2}}\left(\frac{z\frac{\partial w}{\partial p^\gamma} - w\frac{\partial z}{\partial p^\gamma}}{z^2}\right) \tag{A.40a}$$

$$\frac{\partial \phi}{\partial p^\gamma}\left(\mathbf{R}, \tfrac{\partial \mathbf{R}}{\partial p^\gamma}\right) = \frac{1}{1+\left(\frac{v}{u}\right)^2}\left(\frac{u\frac{\partial v}{\partial p^\gamma} - v\frac{\partial u}{\partial p^\gamma}}{u^2}\right) \tag{A.40b}$$

$$\frac{\partial \alpha}{\partial p^\gamma}\left(\mathbf{R}, \tfrac{\partial \mathbf{R}}{\partial p^\gamma}\right) = \frac{1}{1+\left(\frac{z}{s}\right)^2}\left(\frac{s\frac{\partial z}{\partial p^\gamma} - z\frac{\partial s}{\partial p^\gamma}}{s^2}\right) \tag{A.40c}$$

A.3.3 Partial derivatives of a stage pole

This becomes increasingly more complex, since the stage pole for the third plate is calculated from four independent poles and so has 12 independent parameters. To keep the working simple, I shall show only the steps for the derivation of one case.

Consider the stage pole ${}^{13}\mathbf{S}^{ab}$, which is a rotation of ${}^{13}\theta^a$, ${}^{13}\phi^a$, $-\frac{1}{2}{}^{13}\alpha^a$ followed by a rotation of ${}^{13}\theta^b$, ${}^{13}\phi^b$, $\frac{1}{2}{}^{13}\alpha^b$.

As a starting point, we consider the derivative of the stage pole rotation matrix, as given in (A.32)

$$\frac{\partial({}^{13}\mathbf{S}^{ab})}{\partial p^\gamma} = \begin{cases} \left[\frac{\partial({}^{13}\mathbf{F}^{\frac{b}{2}})}{\partial p^\gamma}\right] {}^{13}\mathbf{F}^{-\frac{a}{2}} & p^\gamma \in \{{}^{12}\theta^a, {}^{12}\phi^a, {}^{12}\alpha^a, {}^{23}\theta^a, {}^{23}\phi^a, {}^{23}\alpha^a\} \\ {}^{13}\mathbf{F}^{\frac{b}{2}} \left[\frac{\partial({}^{13}\mathbf{F}^{-\frac{a}{2}})}{\partial p^\gamma}\right] & p^\gamma \in \{{}^{12}\theta^b, {}^{12}\phi^b, {}^{12}\alpha^b, {}^{23}\theta^b, {}^{23}\phi^b, {}^{23}\alpha^b\} \end{cases} \tag{A.41}$$

Finding a derivative such as $\frac{\partial({}^{13}\mathbf{F}^{-\frac{a}{2}})}{\partial p^\gamma}$ is not so easy, since we cannot link this directly to the parameters of ${}^{12}\mathbf{F}^a$ and ${}^{23}\mathbf{F}^a$ and must instead work through the matrix ${}^{13}\mathbf{F}^a$. Since the matrix ${}^{13}\mathbf{F}^a$ is a function of its parameters $({}^{13}\theta^{-\frac{a}{2}}, {}^{13}\phi^{-\frac{a}{2}}, {}^{13}\alpha^{-\frac{a}{2}}) = ({}^{13}\theta^a, {}^{13}\phi^a, -\frac{1}{2}{}^{13}\alpha^a)$, the chain rule is used to obtain

$$\begin{aligned} \frac{\partial({}^{13}\mathbf{F}_{ij}^{-\frac{a}{2}})}{\partial p^\gamma} &= \frac{\partial({}^{13}\mathbf{F}_{ij}^{-\frac{a}{2}})}{\partial({}^{13}\theta^a)}\frac{\partial({}^{13}\theta^a)}{\partial p^\gamma} + \frac{\partial({}^{13}\mathbf{F}_{ij}^{-\frac{a}{2}})}{\partial({}^{13}\phi^a)}\frac{\partial({}^{13}\phi^a)}{\partial p^\gamma} + \frac{\partial({}^{13}\mathbf{F}_{ij}^{-\frac{a}{2}})}{\partial({}^{13}\alpha^{-\frac{a}{2}})}\frac{\partial({}^{13}\alpha^{-\frac{a}{2}})}{\partial p^\gamma} \\ &= \frac{\partial({}^{13}\theta^a)}{\partial p^\gamma}\left[\frac{\partial({}^{13}\mathbf{F}_{ij}^{-\frac{a}{2}})}{\partial({}^{13}\theta^{-\frac{a}{2}})}\right] + \frac{\partial({}^{13}\phi^a)}{\partial p^\gamma}\left[\frac{\partial({}^{13}\mathbf{F}_{ij}^{-\frac{a}{2}})}{\partial({}^{13}\phi^{-\frac{a}{2}})}\right] - \frac{1}{2}\frac{\partial({}^{13}\alpha^a)}{\partial p^\gamma}\left[\frac{\partial({}^{13}\mathbf{F}_{ij}^{-\frac{a}{2}})}{\partial({}^{13}\alpha^{-\frac{a}{2}})}\right] \\ &= \frac{\partial\theta}{\partial p^\gamma}\left({}^{13}\mathbf{F}^a, \frac{\partial({}^{13}\mathbf{F}^a)}{\partial p^\gamma}\right)\left[\frac{\partial\mathbf{R}}{\partial\theta}\left({}^{13}\theta^a, {}^{13}\phi^a, -\tfrac{1}{2}{}^{13}\alpha^a\right)\right] \\ &\quad + \frac{\partial\phi}{\partial p^\gamma}\left({}^{13}\mathbf{F}^a, \frac{\partial({}^{13}\mathbf{F}^a)}{\partial p^\gamma}\right)\left[\frac{\partial\mathbf{R}}{\partial\phi}\left({}^{13}\theta^a, {}^{13}\phi^a, -\tfrac{1}{2}{}^{13}\alpha^a\right)\right] \\ &\quad - \frac{1}{2}\frac{\partial\alpha}{\partial p^\gamma}\left({}^{13}\mathbf{F}^a, \frac{\partial({}^{13}\mathbf{F}^a)}{\partial p^\gamma}\right)\left[\frac{\partial\mathbf{R}}{\partial\alpha}\left({}^{13}\theta^a, {}^{13}\phi^a, -\tfrac{1}{2}{}^{13}\alpha^a\right)\right] \end{aligned} \tag{A.42}$$

The first terms of each pair are given by (A.17), (A.18) and (A.19) and the second terms by (A.40). The matrices ${}^{13}\mathbf{F}^a$ and $\frac{\partial({}^{13}\mathbf{F}^a)}{\partial p^\gamma}$ are as defined previously in equations (A.34) and (A.35) and are simply determined from the parameter set, as are the pole parameters $({}^{13}\theta^a, {}^{13}\phi^a, {}^{13}\alpha^a)$. The same method is then used to obtain $\frac{\partial({}^{13}\mathbf{F}^{\frac{b}{2}})}{\partial p^\gamma}$ such that

$$\begin{aligned} \frac{\partial({}^{13}\mathbf{F}_{ij}^{\frac{b}{2}})}{\partial p^\gamma} &= \frac{\partial\theta}{\partial p^\gamma}\left({}^{13}\mathbf{F}^b, \frac{\partial({}^{13}\mathbf{F}^b)}{\partial p^\gamma}\right)\left[\frac{\partial\mathbf{R}}{\partial\theta}\left({}^{13}\theta^b, {}^{13}\phi^b, \tfrac{1}{2}{}^{13}\alpha^b\right)\right] \\ &\quad + \frac{\partial\phi}{\partial p^\gamma}\left({}^{13}\mathbf{F}^b, \frac{\partial({}^{13}\mathbf{F}^b)}{\partial p^\gamma}\right)\left[\frac{\partial\mathbf{R}}{\partial\phi}\left({}^{13}\theta^b, {}^{13}\phi^b, \tfrac{1}{2}{}^{13}\alpha^b\right)\right] \\ &\quad + \frac{1}{2}\frac{\partial\alpha}{\partial p^\gamma}\left({}^{13}\mathbf{F}^b, \frac{\partial({}^{13}\mathbf{F}^b)}{\partial p^\gamma}\right)\left[\frac{\partial\mathbf{R}}{\partial\alpha}\left({}^{13}\theta^b, {}^{13}\phi^b, \tfrac{1}{2}{}^{13}\alpha^b\right)\right] \end{aligned} \tag{A.43}$$

and then both are used into equation (A.41) to obtain $\frac{\partial({}^{13}\mathbf{S}^{ab})}{\partial p^\gamma}$. This the form required to

determine the partial derivatives for a magnetic isochron datum as defined in (4.41) and from this, is is only a simple step to obtain the derivatives of the stage pole vector ${}^{13}\mathbf{s}^{ab}$ with respect to the solution parameter set, as required to determine the partial derivatives for a fracture zone datum (Equation (4.49)). From (A.22)

$$\frac{\partial({}^{13}\mathbf{s}^{ab})}{\partial p^{\gamma}} = \frac{\partial \mathbf{p}}{\partial p^{\gamma}} \left({}^{13}\mathbf{S}^{ab}, \frac{\partial({}^{13}\mathbf{S}^{ab})}{\partial p^{\gamma}} \right) \tag{A.44}$$

where the matrix $\frac{\partial({}^{13}\mathbf{S}^{ab})}{\partial p^{\gamma}}$ is determined from (A.41).

Appendix B

Summaries of computer programs for data processing and analysis

B.1 Reconstruction programs

magprepro.f : Inputs a set of magnetic anomaly isochron picks and according to the users choice, fits great circles to anomaly groups, and for each pick within a ridge section, decides which great circle(s) the pick will be rotated to during th reconstruction procedure. Outputs a processed isochron data file, ready for use with **magpickproc**.

magpickproc.f : Inputs a set of preprocessed magnetic anomaly isochron picks and great circles, and a set of reconstruction poles. The misfits of the data for the given poles, and the partial derivatives with respect to the poles are calculated and outputted as data files.

fzpickproc.f : Inputs a set of picks of fracture zone locations, and a set of reconstruction poles. The misfits of the data for the given poles, and the partial derivatives with respect to the poles are calculated and outputted as data files.

tfpickproc.f : Inputs a set of picks of transform fault locations, and a set of reconstruction poles. The misfits of the data for the given poles, and the partial derivatives with respect to the poles are calculated and outputted as data files.

std_calc.f : Calculates the mean and standard deviation for each of the reconstruction dataset error files, and outputs to a file *std.dat* used in later stages of the inversion, and a file *stdconv.dat* which stores a list of the means and standard deviations for each iteration, along with a chi-square statistic, giving an indication of the convergence of the inversion.

gstd_calc.f : Similar to **std_calc**, but on the assumption that the errors have normal distributions, determines the best-fit gaussian statistics for each set of errors. Outputs the same files as **std_calc**.

poles_inv.f : Takes the error and partial derivative files for each dataset and, after normalisation and weighting, runs a damped least-squres inversion, outputting a set of peturbations to the current set of poles.

confimp_calc.f : From the files of partial derivatives of each dataset, determines the confidence ellipses for the currrent set of poles and outputs these into a file. Also calculates the data importances for each dataset.

confimp_calc3d.f : Similar to **confimp_calc.f**, but calculates 3-d confidence ellipsoids for the current set of poles.

poles_adjust.f : Takes a set of pole peturbations produced by **poles_inv** and adjusts the current set of poles accordingly.

sort_magerr.f : Takes the file containing the full set of errors for the magnetics dataset, and collates the errors for the picks which have been used to create several datum. A file is outputted which has only a single RMS error for each isochron pick used.

magdat_count.f : Given a data file of isochron picks for a reconstruction, determines the number of picks fror each isochron.

magcheck.f : Given a set of rotation poles and a reconstruction dataset, rotates each magnetic anomaly pick back to the notional ridge axis at which it was formed.

calcrate.f : Given the location of a point on a ridge axis and a current rotation pole, calculates the local spreading rate and azimuth.

calcrates.f : Given the location of a point on a ridge axis and a set of rotation poles, calculates a series of spreading rates and azimuths for the spreading history covered by the given rotation poles.

3p_magpickproc.f : The 3-plate version of **magpickproc**, taking a set of reconstuction poles for a 3-plate system, and calculating the misfits and partial derivatives of the magnetic anomaly isochrons for each plate pair.

3p_fzpickproc.f : The 3-plate version of **fzpickproc**, taking a set of reconstuction poles for a 3-plate system, and calculating the misfits and partial derivatives of the fracture zone locations for each plate pair.

3p_tfpickproc.f : The 3-plate version of **tfpickproc**, taking a set of reconstuction poles for a 3-plate system, and calculating the misfits and partial derivatives of the transform fault locations for each plate pair.

3poles_inv.f : The 3-plate version of **poles_inv**.

3pconfimp_calc2.f : The 3-plate version of **confimp_calc3d**.

3poles_adjust.f : The 3-plate version of poles_adjust.

B.2 Reconstruction subroutines

B.2.1 Main subroutines

sub_openfile.f : Reads a filename from keyboard entry and opens the file as a logical unit, according to the requirements (read/write/new/old *etc.*).

sub_readpolesfile.f : Reads a file containing a set of finite rotation poles for a plate pair, and stores them in an array.

sub_read3polesfile.f : Reads a file containing the finite rotation poles for a 3-plate set. Stores first two sets of poles in arrays, but ignores third, dependent set.

sub_calc3rdpoles.f : From 2 sets of reconstruction poles for A↦B and B↦C, calculates the third, dependent set of reconstruction poles A↦C.

sub_magpickproc.f : The basis of programs **magpickproc** and **3p_magpickproc**, determines the errors and partial derivatives for a complete set of magnetic anomaly isochrons for one plate pair.

sub_gcfit.f : Determines the best-fit great circle passing through a set of locations on a sphere.

sub_dcmake.f : Builds a correlation matrix for a series of points which is used to determine the best-fit great circle.

sub_sortpnts.f : Given a series of locations on a sphere, sorts them into a progressive sequence along an axis joining the two-furthest separated points. Used for arranging in order the closest points on a great circle for the set of points used to generate the best-fit great circle.

sub_magpickcalc.f : Given a group of picks for a certain isochron, and the conjugate great circle to which to rotate them, calculates the error and partial derivatives for each datum. Uses epdcalc.

sub_magpickcalc_2pol.f : Given a group of picks for a certain isochron, and a non-conjugate target great circle to which to rotate them, calculates the error and partial derivatives for each datum. Uses epdcalc.

sub_magpickcalc3p.f : The 3-plate version of sub_magpickcalc used when processing data for the third plate boundary A↦C. The partial derivatives are calculated with respect to the 2 independent sets of poles, A↦B, and B↦C.

sub_magpickcalc3p_2pol.f : The 3-plate version of sub_magpickcalc_2pol used when processing data for the third plate boundary A↦C. The partial derivatives are calculated with respect to the 2 independent sets of poles, A↦B, and B↦C.

sub_epdcalc.f : Given a single rotated isochron location and a target great circle, calculates the misfit, and the partial derivative of the error with respect to the position of the rotated point.

sub_fzpickproc.f : The basis of programs **fzpickproc** and **3p_fzpickproc**, determines the errors and partial derivatives for a complete set of fracture zone locations for one plate pair.

sub_readpickfile.f : Reads in a file containing a set of picks for a fracture zone, along with the relevant seed information.

sub_fpoles2stage.f : From a set of finite reconstruction poles, calculates the 2 sets of stage poles, for each flank of the plate pair.

sub_flowline.f : From a set of reconstruction poles, determines a flowline from a given point.

sub_seedinv.f : Given a set of fracture zone locations and estimated seed point, adjusts the seed point (within limits) to provide a best-fit flowline for the set of picks.

sub_fzpickcalc_seed.f : Calculates the misfits of fracture zone locations from a test flowline, and the partial derivatives with respect to the seed point of the flowline. Used in the

determination of the seed point which gives the best-fit flowline for a particular fracture zone.

sub_dqr.f : Determines the solution to an over-determined least-squares problem $\mathbf{Ax} = \mathbf{b}$. Used in the adjustment of seed points for flowlines in**sub_seedinv**.

sub_pdflowseedx.f : Determines the changes in a flowline with respect to changes in the zero-age seed.

sub_fzpickcalc.f : For a set of picks along a fracture zone, determines the misfits from a given flowline, and the partial derivatives with respect to the finite rotation poles used to generate the flowlines.

sub_fzpickcalc3p.f : The 3-plate version of **sub_fzpickcalc** used when processing data for the third plate boundary A↦C. The partial derivatives are calculated with respect to the 2 independent sets of poles, A↦B, and B↦C.

sub_tfpickproc.f : The basis of programs **tfpickproc** and **3p_tfpickproc**, determines the errors and partial derivatives for a complete set of transform fault locations for one plate pair.

sub_std.f : For a series of data values, calculates the mean and standard deviation.

sub_gauss.f : Calculates the best-fit Gaussian distribution for a set of data.

sub_writepolesfile.f : Writes a set of finite rotation poles for a plate pair to file.

sub_write3polesfile.f : Writes the finite rotation poles for a 3-plate set to file.

sub_dfgcalc.f : From the covariance matrices for the reconstruction poles A↦B and B↦C, determines the matrices D, F and G required to calculate the covariance matrix for the resultant A↦C reconstruction poles (given no data input from A↦C plate boundary).

sub_mtxmul.f : Carries out the basic matrix multiplication $\mathbf{C} = \mathbf{BA}$.

sub_mtxvtr.f : Carries out the basic matrix operation $\mathbf{y} = \mathbf{Ax}$.

sub_writematrix.f : Writes a 2-dimensional array to file.

sub_writevector.f : Writes a 1-dimensional array to file.

sub_int2char.f : Simple routine converting an integer between zero and ninety nine into character*2 format (used in creating the incremental filenames for successive iterative inversions).

sub_intch.f : Simple routine converting an integer between zero and ninety nine into a character variable of the same length.

sub_strcat.f : Concatenates two character arrays, skipping any blank spaces. Used of creating filenames when supplied with a directory name and file name separately.

B.2.2 Geometric operations and partial derivative subroutines

sub_pnt2vec.f : Converts a point location in longitude and latitude to a 3-vector on a unit sphere.

sub_normvec.f : Normalises a vector to represent a vector on a unit sphere.

sub_vec2pnt.f : Converts a 3-vector on a unit sphere to a point location in longitude and latitude.

fun_vecdprod.f : Calculates the dot product of two vectors.

sub_vecxprod.f : Calculates the vector (cross) product of two vectors.

fun_pangsep.f : Calculates the angular seperation of two points on a sphere.

fun_vangsep.f : Calculates the angular seperation of two vectors.

fun_angpdcalc.f : Calculates the change in angular seperation of two vectors when a peturbation is applied to one of the vectors.

sub_pol2mat.f : Converts a rotation pole in the form of latitude, longitude and angle into a 3x3 rotation matrix.

sub_mat2pol.f : Determines the pole parameters, latitude, longitude and angle from the corresponding 3x3 rotation matrix.

sub_sumrots.f : Combines two rotation matrices $\mathbf{A}$ and $\mathbf{B}$ to obtain a third, $\mathbf{C} = \mathbf{BA}$.

sub_addmats.f : Adds two matrices $\mathbf{A}$ and $\mathbf{B}$ to obtain a third, $\mathbf{C} = \mathbf{A} + \mathbf{B}$.

sub_add3mats.f : Adds three matrices $\mathbf{A}$, $\mathbf{B}$, and $\mathbf{C}$, to obtain a fourth, $\mathbf{D} = \mathbf{A}+\mathbf{B}+\mathbf{C}$.

sub_matscal.f : Scales a matrix $\mathbf{A}$ by a constant c, such that $\mathbf{A}' = c\mathbf{A}$.

sub_matxvec.f : Carries out the basic matrix operation $\mathbf{y} = \mathbf{Ax}$ for the 3x3 matrix $\mathbf{A}$ and 3-vectors $\mathbf{x}$ and $\mathbf{y}$.

sub_rotatepnt.f : Given a rotation matrix $\mathbf{R}$ and a vector $\mathbf{p}$, calculates the rotated vector (on a unit sphere) $\mathbf{p}'$.

sub_rotatevec.f : Given a rotation matrix $\mathbf{R}$ and a point location on a sphere (ϕ, θ), calculates the rotated point on the sphere, (ϕ', θ').

sub_diamg.f : Given a point location on a sphere, calculates the antipode of this point on the sphere.

sub_pnt2pdvecs.f : Given a point location on a sphere, calculates the partial derivatives of the 3-vector representation of the point with respect to latitude and longitude.

sub_pol2pdmats.f : Given the pole parameters of a rotation, (latitude, longitude, angle), determines the partial derivatives of the rotation matrix with respect to each of these parameters.

sub_mats2polpds.f : Given a rotation matrix, and the partial derivative of this matrix with respect to an unknown peturbation, calculates the partial derivatives of the correpsonding pole parameters with respect to the unknown peturbation.

sub_mats2vecpds.f : Given a rotation matrix, and the partial derivative of this matrix with respect to an unknown peturbation, calculates the partial derivatives of the 3-vector repsentation of the coresonding rotation pole with respect to the unknown peturbation.

sub_poles2stpds.f : From a set of finite rotation poles, calculates the partial derivatives of each stage pole (in vector form) on both flanks, with respect to the finite rotation pole parameters.

sub_x2poles2stpds.f : The 3-plate version of sub_poles2stpds, where the stage poles for the third plate pair are dependant on the finite rotation poles of the two previous plate pairs.

sub_stpdarraybld.f : Used in **sub_poles2stpds** and **sub_x2poles2stpds** to build the arrays of partial derivatives for the stage poles. Calculates the partial derivative for one stage pole and stores it in the specified location within an array.

sub_rotnpd2scpd.f : A complex routine which calculates the partial derivative of a rotation matrix $\mathbf{C}$ with respect to an unknown pole parameter, where $\mathbf{C}$ represents a rotation around the same pole as for the rotation matrix $\mathbf{S}$ (which is the sum of the two rotation matrices, $\mathbf{A}$ and $\mathbf{B}$) but with a scaled rotation angle. The effect of the peturbation is supplied as a peturbation to one of the rotation matrices $\mathbf{A}$ or $\mathbf{B}$.

B.3 Programs for data manipulation and display

addrot.c : A simple test program which reads two rotation poles from the keyboard, and displays the resultant on screen.

stagepoles.c : Reads a set of finite rotation poles from file and then calculates the set of stage poles for each flank of the plate pair. The stage poles are displayed on screen and outputted to a file in a format suitable for the **gmt** routines **psxy** and **psvelomeca**.

tripcalc.c : Given a set of finite rotation poles for a 3-plate system, the current location of the triple junction between the three plates, and a tolerance value for the RFF configuration, calculates a series of velocity triangles for several times in the past. The likely configuration and motion of the triple junction over this time period is calculated.

controt.c : Given a set of finite rotation poles for a 3-plate system, and a continental outline/coastline file, this program rotates the relevant continents to their positions at each poles chron, whilst keeping one of the plates fixed.

calcell.c : Reads in a file containing information about the confidence ellipses for a set of rotation poles, and calculates a loci of points on the surface of the earth, representing the limits of a specified confidence interval.

calcellsurf.c : Similar to **calcell**, but reads in information about the 3d confidence ellipsoids for a set of rotation poles and calculates the upper surface of the ellipsoids intersection with the surface of the earth, representing the limits of a specified confidence interval.

create_data.c : Generates 1-d profiles for (a) Geoid steps across a fracture zone or (b) simple topography models - either Gaussian or straight lines.

multi_fzgeoid.c : Generates a 1-d geoid profile across a series of up to 4 fracture zones with specified ages and offsets.

data2grav.c : Converts 1-d topographic or geoid profiles into gravity anomalies.

create_gauss.c : Given the parameters of a Gaussian distribution, generates a series of points which can be used to plot the distribution.

flowlines.c : Reads in a set of finite rotation poles form a file and displays on screen the corresponding sets of stage poles for each flank.

makeprofs.c : Reads a set of approximate locations along a fracture zone from a database file, and uses these to generate a series of perpendicular profiles across the fracture zone. Gravity values along the profiles are then sampled from a specified gravity grid, and if required, the minimum picking routine **pick_min** is run. This can be more generally used for generating perpendicular profiles across any feature, and sample from any kind of grid (gravity, topography, magnetics *etc.*).

pick_min.c : Given a series of perpendicular profiles across a fracture zone, this routine attempts to find a minimum for each profile, representing the centre of the fracture zone valley. The output is in the form of a file suitable for use in the program **xfzpick** and a log file recording information for each profile.

mgd77toxyz.c : Reads in a data file in mgd77 format, and outputs the required type of data (magnetics, gravity or topography) in ASCII x,y,value format, within specified limits or regions if desired. If the mgd77 file contains data from more than one cruise, then the data can be written out as a single file, separate files for each cruise, and/or only from specific cruises.

manu_data.c : Given a set of finite rotation poles and a series of ridge-transform intersections, generates a set of synthetic fracture zone locations and magnetic anomaly isochrons, with intrinsic random errors if required. Outputted in file formats suitable for use in reconstruction routines, in order to be used for testing reconstruction methods.

ridgeflow.c : Given a set of finite rotation poles and a series of points representing the location of the present ridge axis, generates a series of rotated locations of the ridge axis for each rotation chron.

mpicks2recin.c : Takes a set of magnetic anomaly isochron picks made from the program **xmagpick** and converts them into the format required for the reconstruction routines.

mpicks2screen.c : Takes set(s) of magnetic anomaly isochron picks made from the program **xmagpick** and generates a command file to display them as a postscript file. The different anomalies are represented according a specified file containing a symbol table. Options are included to limit the display to a certain region, to plot the current ridge axis and/or fracture zones, and also to plot the ship tracks from which the picks were made.

rpicksort.c : Given a set of magnetic anomaly files in reconstruction format and a geographical region, outputs a list if picks which are contained within the area. Used for sorting the picks before an inversion, but since superseded by **xsortdata**.

rpix2screen.c : Reads 1 or more files containing magnetic anomaly isochron picks in reconstruction format and generates a command file to display them as a postscript file. The different anomalies are represented according a specified file containing a symbol table. Options are included to limit the display to a certain region and to plot the current ridge axis and/or fracture zones.

split_fzpicks.c : Take an output file from **xfzpick** and writes the fracture zone picks either into a single file, or different types into separate files, splitting each into multiple segments if a specified inter-pick distance is exceeded. The format of the output file is either in (x,y) for use with **psxy**, or in a format for use in the reconstruction routines.

split_magpicks.c : Take an output file from **xmagpick** and writes the magnetic anomaly isochron picks into separate files for each different isochron.

rdata_replace.c : Reads in a magnetics reconstruction dataset, and a magnetics file from a single cruise. If any picks within the cruise file have been changed, added, or removed, then this program updates the reconstruction dataset. This avoids having to rebuild the reconstruction file from scratch, from the cruise files, if any picks are adjusted, so leaving grouping and organisation of the picks within ridge sections unchanged.

ipix2screen.c : Reads the magnetic isochron data output file from the inversion methods, and generates a command file to display the original picks, target great circles, and rotated picks as a postscript file. The original and/or rotated anomaly picks are represented according to different specified files containing symbol tables. Various selection and display options are included, such as drawing the data errors and/or importances on the same plot.

quantile.c : This program reads in a series of (random) data sample values and calculates points for a quantile-quantile plot of the dataset, using a Gaussian test function with a mean of 0 and standard deviation 1.

xycrop.c : Reads a series of $x, y(, z \ldots)$ data points from a data file, or **stdin** and only outputs the points which lie within the desired range.

xysplit.c : Reads a series of $x, y(, z \ldots)$ data points from a data file, or **stdin**, and splits it into continuous ascending/descending sequences with respect to x, (with a specified tolerance to account for possible random errors), splitting the sequences further if a specified data gap is exceeded, and only outputting data above a specified minimum segment length.

xyfilter.c : Reads in a continuous ascending/descending sequence of (x, y) data points, and filters the data in the time domain. The data can be resampled onto a regular spacing if required, and either a mean offset or a trend is removed before the profile is tapered and filtered. The filter can be hi-pass, lo-pass, or both.

add_data.c : Takes two (x, y) profiles and adds the data points for any common values, and outputting these data points.

rms_data.c : Reads in two profiles of (x, y, z) data points and calculates the RMS difference between the profiles.

samplecalc.c : Calculates the minimum, maximum, mean and standard deviation for a series of sample values.

xyfit.c : Reads a series of x, y data points from a data file, or **stdin** and uses linear regression to determine a best fit line, and outputs points for plotting said line.

B.4 UNIX/AWK scripts

getpicks : Given a file containing a list of fracture zone files, as used in the reconstructions, reads in these files and outputs the full set of data in a single x-y file suitable for plotting.

getseeds : Given a file containing a list of fracture zone files, as used in the reconstructions, reads in these files and outputs the reference seed point for each fracture zone into a single x-y file suitable for plotting.

diffpoles/diff3poles : Given two files containing sets of finite rotation poles, determines the differences between the two.

rmsdiffpoles/rmsdiff3poles : Given two files containing sets of finite rotation poles, determines the RMS differences for latitude, longitude and rotation angle between the two.

rmsdiff_allpoles/rmsdiff_all3poles : Calculates the RMS difference between each successive pair of finite rotation poles for an iterative 2/3 plate inversion.

tripvel2plot : From an output file from **tripcalc** creates a script to plot the series of velocity triangles in a single postscript file.

Bibliography

Abrams, L.J., Detrick, R.S., & Fox, P.J. 1988. Morphology and crustal structure of the Kane fracture zone transverse ridge. *J. Geophys. Res.*, **93**, 3,195–3,210.

Apotria, T.G., & Gray, N.H. 1985. Absolute motion and evolution of the Bouvet triple junction. *Nature*, **316**, 623–625.

Apotria, T.G., & Gray, N.H. 1988. The evoution of the Bouvet triple junction: implications of its absolute motion. *Tectonophysics*, **148**, 177–193.

Barazangi, M., & Dorman, J. 1969. World seismicity maps compiled from ESSA, Coast & Geodetic Survey, epicenter data, 1961-1967. *Bull. Seism. Soc. Am.*, **59**, 369–380.

Barker, P.F. 1979. The history of ridge-crest offset at the Falklands - Agulhas Fracture Zone from a small-circle geophysical profile. *Geophys. J. R. Astron. Soc.*, **59**, 131–145.

Barker, P.F., & Burrell, J. 1977. The opening of Drake Passage. *Marine Geology*, **25**, 15–34.

Barker, P.F., & Griffiths, D.H. 1971. The evolution of the Scotia Ridge and Scotia Sea. *Phil. Trans. R. Soc. Lond.*, **271**, 151–183.

Barker, P.F., & Hill, I.A. 1981. Back-arc extension in the Scotia Sea. *Phil. Trans. R. Soc. Lond.*, **300**, 249–262.

Barker, P.F., & Jahn, R.A. 1980. A marine geophysical reconnaissance of the Weddell Sea. *Geophys. J. R. Astron. Soc.*, **63**, 271–283.

Barker, P.F., & Lawver, L.A. 1988. South American - Antarctic plate motion over the past 50 Myr, and the evolution of the South American - Antarctic ridge. *Geophys. J. R. Astron. Soc.*, **94**, 377–386.

Barker, P.F., Barber, P.L., & King, E.C. 1984. An early miocene ridge crest-trench collision on the south scotia ridge near 36°W. *Tectonophysics*, **102**, 315–332.

Bergh, H.W. 1977. Mesozoic sea floor off Dronning-Maud land. *J. Geophys. Res.*, **269**, 686–687.

Bergh, H.W., & Norton, I.O. 1976. Prince Edward fracture zone and the evolution of the Mozambique Basin. *J. Geophys. Res.*, **81**, 5221–5239.

Binks, R.M., & Fairhead, J.D. 1992. A plate tectonic setting for Mesozoic rifts of West and Central Africa. *Tectonophysics*, **213**, 141–151.

Bullard, E., Everett, J.E., & Smith, G.A. 1965. The fit of continents around the atlantic. *Pages 41–51 of: A symposium on continental drift.* Philosophical Transactions of the Royal Society of London, Series A: Mathematical and Physical Sciences, vol. 258. Royal Society of London, UK.

Cande, S.C., & Kent, D.V. 1976. Constraints imposed by the shape of marine magnetic anomalies on the magnetic source. *J. Geophys. Res.*, **81**, 4157–4162.

Cande, S.C., & Kent, D.V. 1995. Revised calibration of the geomagnetic polarity time scale for the late Cretaceous and Cenozoic. *J. Geophys. Res.*, **100**, 6093–6095.

Cande, S.C., LaBrecque, J.L., & Haxby, W.F. 1988. Plate kinematics of the South Atlantic: Chron 34 to present. *J. Geophys. Res.*, **93**, 13,479–13,492.

Carrigan, C.R., & Gubbins, D. 1979. The source of the Earth's magnetic field. *Scientific American*, **240**, 92–101.

Chang, T. 1987. On the statistical properties of estimated rotations. *J. Geophys. Res.*, **92**, 6319–6329.

Chang, T. 1988. Estimating the Relative Rotation of Two Tectonic Plates From Boundary Crossings. *J. am. statist. ass.*, **83**, 1178–1183.

Chang, T. 1993. Spherical Regression and the Statistics of Tectonic Plate Reconstructions. *International statistical review*, **61**, 299–316.

Chang, T., Stock, J.M., & Molnar, P. 1990. The rotation group in plate tectonics and the representation of uncertainties of plate reconstructions. *Geophys. J. Int.*, **101**, 649–661.

Cheney, R.E., Douglas, B.C., Agreen, R.W., Miller, L., Porter, D.L., & Doyle, N.S. 1987. *Geosat altimeter geophysical data record user handbook: NOAA Technical Memorandum NOS NGS-46.* US Department of Commerce, Rockville, Maryland, USA.

Cheney, R.E., Doyle, N.S., Douglas, B.C., Agreen, R.W., Miller, L., Timmerman, E.L., & McAdoo, D.C. 1991. *The complete Geosat altimeter GDR handbook: NOAA Manual NOS NGS-7.* US Department of Commerce, Rockville, Maryland, USA.

Collette, B.J. 1974. Thermal contraction joints in a spreading seafloor as origin of fracture zones. *Nature*, **251**, 299–300.

Cormier, M.H., & Macdonald, K.C. 1994. East Pacific Rise 18°- 19°S: asymmetric spreading and ridge reorientation by ultrafast migration axial discontinuities. *J. Geophys. Res.*, **67**, 543–564.

Cox, A., & Doell, R.R. 1962. Magnetic properties of the basalt in Hole EM7, Mohole Project. *J. Geophys. Res.*, **67**, 3997–4004.

Cox, A., Doell, R.R., & Dalrymple, G.B. 1963. Geomagnetic polarity epochs and Pleistocene geochronometry. *Nature*, **198**, 1049–1051.

Cox, A., Doell, R.R., & Dalrymple, G.B. 1964. Reversals of the Earth's Magnetic Field. *Science*, **144**, 1537–1543.

DeMets, C., Gordon, R.G., Argus, D.F., & Stein, S. 1990. Current plate motions. *Geophys. J. Int.*, **101**, 425–478.

DeMets, C., Gordon, R.G., Argus, D.F., & Stein, S. 1994. Effect of recent revisions to the geomagnetic reversal time scale on estimates of current plate motions. *Geophys. Res. Let.*, **21**, 2191–2194.

Detrick, R.S., & Purdy, G.M. 1980. The crustal structure of the Kane fracture zone from seismic refraction studies. *J. Geophys. Res.*, **85**, 3759–3778.

Detrick, R.S., Cormier, M.H., Prince, R.A., Forsyth, D.W., & Ambos, E.L. 1982. The crustal structure of the Kane fracture zone from seismic refraction studies. *J. Geophys. Res.*, **87**, 10,599–10,612.

Dewey, J.F., Pitman, W.C., III, Ryan, W.B.F., & Bonnin, J. 1973. Plate tectonics and the evolution of the Alpine systems. *Geol. Soc. Am. Bull.*, **84**, 3137–3180.

Dewey, J.F., Helman, M.L., Turco, E., Hutton, D.H.W., Hutton, S.D., & Knott, S.D. 1989. Kinematics of the western Mediterranean. *Pages 3137–3180 of:* Coward, M.P., Dietrich, D., & Park, R.G. (eds), *Alpine Tectonics.* Geol. Soc. Spec. Pub., no. 45. The Geological Society.

Dickson, G.O., Pitman, W.C., III, & Heirtzler, J.R. 1968. Magnetic anomalies in the South Atlantic and ocean floor spreading. *J. Geophys. Res.*, **73**, 289–307.

Dietz, R.S. 1961. Continent and ocean floor evolution by spreading of the seafloor. *Nature*, **190**, 854–857.

Driscoll, M.L. 1987. *Application of Seasat altimetry to tectonic studies of fracture zones in the Southern Oceans.* Ph.D. thesis, Woods Hole Oceanographic Institution / MIT.

Driscoll, M.L., & Parsons, B. 1988. Cooling of the oceanic lithosphere - evidence from geoid anomalies across the Udintsev and Eltanin fracture zones. *Earth Plan. Sci. Let.*, **88**, 289–307.

du Plessis, A. 1977. Seafloor spreading south of the Agulhas Fracture Zone. *Nature*, **270**, 719–721.

Du Toit, A.L. 1937. *Our wandering continents: A hypothesis of continental drifting.* Oliver and Boyd.

Elsasser, W.M. 1956a. Background of the geomagnetic dynamo theory. *J. Geophys. Res.*, **61**, 340–347.

Elsasser, W.M. 1956b. Hydromagnetic dynamo theory. *Reviews of Modern Physics*, **28**, 135–163.

Engebretson, D.C., Cox, A., & Gordon, R.G. 1984. Relative motions between oceanic plates of the Pacific basin. *J. Geophys. Res.*, **89**, 10,291–10,310.

Fairhead, J.D. 1988. Mesozoic plate tectonic reconstructions of the central South Atlantic Ocean: the role of the West and Central African rift system. *Tectonophysics*, **155**, 181–191.

Fairhead, J.D., & Binks, R.M. 1991. Differential opening of the Central and South Atlantic Oceans and the opening of the West African rift system. *Tectonophysics*, **187**, 191–203.

Fisher, R.L., & Sclater, J.G. 1983. Tectonic evolution of the Southwest Indian Ocean since the Mid-Cretaceous: plate motions and stability of the pole of Antarctica/Africa for at least 80 Myr. *Geophys. J. R. Astron. Soc.*, **73**, 553–576.

Forsyth, D.W. 1975. Fault plane solutions and tectonics of the South Atlantic and Scotia Sea. *J. Geophys. Res.*, **80**, 1429–1443.

Forsyth, D.W., & Uyeda, S. 1975. On the relative importance of the driving forces of plate motion. *Geophys. J. R. Astron. Soc.*, **43**, 163–200.

Fox, P.J., & Gallo, D.G. 1984. A tectonic model for ridge-transform-ridge plate boundaries: implications for the structure of oceanic lithosphere. *Tectonophysics*, **104**, 205–242.

Fox, P.J., & Opdyke, N.D. 1973. Geology of the Ocean Crust: Magnetic properties of oceanic rocks. *J. Geophys. Res.*, **78**, 5139–5154.

Fox, P.J., Schreiber, E., Rowlett, H., & McCamy, K. 1976. The geology of the Oceanographer Fracture Zone: A model for fracture zones. *J. Geophys. Res.*, **81**, 4117–4128.

Francheteau, J., & Le Pichon, X. 1972. Marginal fracture zones as structural framework of continental margins in South Atlantic Ocean. *Bull. Am. Ass. Pet. Geol.*, **56**, 991–1007.

Francheteau, J., Choukroune, P., Hekinian, R., Le Pichon, X., & Needham, H.D. 1976. Oceanic fracture zones do not provide deep sections in the crust. *Can. J. Earth Sci..*, **13**, 1223–1235.

Freedman, A.P., & Parsons, B. 1990. Geoid anomalies over two South Atlantic fracture zones. *Earth Plan. Sci. Let.*, **100**, 18–41.

Gibert, D., Courtillot, V., & Olivet, J-L. 1989. Seasat altimetry and the South Atlantic geoid: 2. Short-wavelength undulations. *J. Geophys. Res.*, **94**, 5545–5559.

Goodwillie, A.M. 1993. *Tectonics of the south central Pacific.* Ph.D. thesis, University of Oxford.

Hanna, M.S., & Chang, T. 1990. On graphically representing the confidence region for an unknown rotation in three dimensions. *Computers and Geosciences*, **16**, 163–194.

Heirtzler, J.R., Pickson, G.O., Herron, E.M., Pitman, W.C., III, & Le Pichon, X. 1968. Marine magnetic anomalies, geomagnetic field reversals and motions of the ocean floor and continents. *J. Geophys. Res.*, **73**, 2119–2136.

Hellinger, S.J. 1981. The Uncertainties of Finite Rotations in Plate Tectonics. *J. Geophys. Res.*, **86**, 9312–9318.

Hess, H.H. 1962. History of ocean basins. *Pages 599–620 of:* Engel, A.E.J., James, H.L., & Leonard, B.F. (eds), *Petrological studies: a volume in honour of A.F.Buddington.* Geol. Soc. Am.

Hill, I.A., & Barker, P.F. 1980. Evidence for Miocene back-arc spreading in the central Scotia Sea. *Geophys. J. R. Astron. Soc.*, **63**, 427–440.

Holmes, A. 1926. Contributions to the theory of magmatic cycles. *Geol. Mag.*, **LXIII**, 306–329.

Holmes, A. 1944. *The machinery of continental drift: the search for a mechanism.* Thomas Nelson and Sons, Ltd. Pages 505–509.

Isacks, B., Oliver, J., & Sykes, L.R. 1968. Seismology and the new global tectonics. *J. Geophys. Res.*, **73**, 5855–5899.

Jurdy, D.M., & Stefanick, M. 1987. Errors in plate rotations as described by covariance matrices and their combination in reconstructions. *J. Geophys. Res.*, **92**, 6310–6318.

Kleinrock, M.C., & Morgan, J. Phipps. 1988. Triple junction reorganization. *J. Geophys. Res.*, **93**, 2981–2996.

LaBrecque, J.L., & Barker, P. 1981. The age of the Weddell Basin. *Nature*, **290**, 489–492.

LaBrecque, J.L., & Hayes, D.E. 1979. Seafloor spreading history of the Agulhas Basin. *Earth Plan. Sci. Let.*, **45**, 411–428.

LaBrecque, J.L., Kristofferson, Y., Haxby, W.F., Raymond, C., & Brozena, J.M. 1979. The Malvinas Plate: microplate or megaplate? *EOS Trans. AGU.*, **69**, 1431.

Ladd, J.W. 1974. *South-atlantic sea-floor spreading and caribbean tectonics.* Ph.D. thesis, Columbia Univ., N.Y.

Larson, R.L., & Ladd, J.W. 1973. Evidence for the opening of the South Atlantic in the Early Cretaceous. *Nature*, **246**, 209–212.

Lawver, L.A., & Dick, H.J.B. 1983. The American - Antarctic Ridge. *J. Geophys. Res.*, **88**, 8193–8202.

Lawver, L.A., Gahagan, L.M., & Coffin, M.F. 1992. The development of paleoseaways around Antarctica. *Antarctic Research Series*, **56**, 7–30.

Le Pichon, X. 1968. Sea-floor spreading and continental drift. *J. Geophys. Res.*, **73**, 3661–3705.

Le Pichon, X., & Hayes, D.E. 1971. Marginal offsets, fracture zones and the early opening of the South Atlantic. *J. Geophys. Res.*, **76**, 6283–6293.

Le Pichon, X., Francheteau, J., & Bonnin, J. 1973. *Plate tectonics.* Developments in Geotectonics, vol. 8. Elsevier.

Ligi, M., Bonatti, E., Bortoluzzi, G., Carrara, G., Fabretti, P., Penitenti, D., Gilod, D., Peyve, A.A., Skolotnev, S., & N.Turko. 1997. Death and transfiguration of a triple junction in the South Atlantic. *Science*, **276**, 243–245.

Livermore, R.A., & Hunter, R.J. 1996. Mesozoic seafloor spreading in the southern Weddell Sea. *Pages 227–241 of:* Storey, B.C., King, E.C., & Livermore, R.A. (eds), *Weddell Sea Tectonics and Gondwana Breakup.* Geol. Soc. Spec. Pub., no. 108. The Geological Society.

Livermore, R.A., & Smith, A.G. 1985. Some boundary conditions for the evolution of the Mediterranean region. *Pages 83–98 of:* Stanley, D.J., & Wezel, F.C. (eds), *Geological evolution of the Mediterranean Basin.* Springer-Verlag.

Livermore, R.A., & Woollett, R.W. 1993. Seafloor spreading in the Weddell Sea and southwest Atlantic since the Late Cretaceous. *Earth Plan. Sci. Let.*, **117**, 475–495.

Livermore, R.A., McAdoo, D., & Marks, K. 1994. Scotia Sea tectonics from high-resolution satellite gravity. *Earth Plan. Sci. Let.*, **123**, 255–268.

Marks, K.M., & Stock, J.M. 1995. Asymmetric seafloor spreading and short ridge jumps in the Australian-Antarctic discordance. *Marine Geophys. Res.*, **17**, 361–373.

Marsh, J.G. et al. 1988. A new gravitational model for the Earth from satellite tracking data: GEM-T1. *J. Geophys. Res.*, **93**, 6169–6215.

Martin, A.K., Goodlad, S.W., Hartnady, C.J.H., & du Plessis, A. 1982. Cretaceous palaeopositions of the Falkland Plateau relative to Southern Africa using Mesozoic seafloor spreading anomalies. *Geophys. J. R. Astron. Soc.*, **71**, 567–579.

Matuyama, M. 1929. On the direction of magnetisation of basalt in Japan, Tyôsen and Manchuria. *Japan Academy Proceedings*, **5**, 203–205.

McDougall, I.M., & Tarling, D.H. 1963. Dating of Polarity Zones in the Hawaiian Islands. *Nature*, **200**, 54–56.

McKenzie, D.P., & Morgan, W.J. 1969. Evolution of triple junctions. *Nature*, **224**, 125–133.

McKenzie, D.P., & Parker, R.L. 1967. The North Pacific: an example of tectonics on a sphere. *Nature*, **216**, 1276–1280.

McKenzie, D.P., & Sclater, J.G. 1971. The evolution of the Indian Ocean since the Late Cretaceous. *Geophys. J. R. Astron. Soc.*, **24**, 437–528.

Menard, H.W. 1955. Deformation of the Northeastern Pacific Basin and the West Coast of North America. *Geol. Soc. Am. Bull.*, **66**, 1149–1198.

Menard, H.W. 1978. Fragmentation of the Farallon Plate by pivoting subduction. *Journal of Geology*, **86**, 99–110.

Minster, J.B., & Jordan, T.H. 1978. Present day plate motions. *J. Geophys. Res.*, **83**, 5331–5354.

Minster, J.B., Jordan, T.H., Molnar, P., & Haines, E. 1974. Numerical modelling of instantaneous plate tectonics. *Geophys. J. R. Astron. Soc.*, **36**, 541–576.

Morgan, W.J. 1968. Rises, trenches, great faults and crustal blocks. *J. Geophys. Res.*, **73**, 1959–1982.

Morley, L.W. 1986. Early Work Leading to the Explaination of the Banded Geomagnetic Imprinting of the Ocean Floor. *EOS Trans. AGU.*, **67**, 665–666.

Mutter, J.C., Hegarty, K.A., Cande, S.C., & Weissel, J.F. 1985. Breakup between Australia and Antarctica: a brief review in the light of new data. *Tectonophysics*, **114**, 255–279.

NAG. 1985. *F04QAF - NAG Fortran library routine document.* Numerical Algorithms Group.

Nishimura, C., Wilson, D. S., & Hey, R. H. 1984. Pole of rotation analysis of present-day Juan de Fuca plate motion. *J. Geophys. Res.*, **89**, 10,283–10,290.

Norton, I.O., & Sclater, J.G. 1979. A model for the evolution of the Indian Ocean and the breakup of Gondwanaland. *J. Geophys. Res.*, **84**, 6803–6830.

Nürnberg, D, & Müller, R.D. 1991. The tectonic evolution of the South Atlantic from Late Jurassic to present. *Tectonophysics*, **191**, 27–53.

O'Connor, J.M., & Duncan, R.A. 1990. Evolution of the Walvis Ridge-Rio Grande Rise hot spot system: implications for African and South American plate motions over plumes. *J. Geophys. Res.*, **95**, 17,475–17,502.

Paige, C.C., & Saunders, M.A. 1982. LSQR: An algorithm for sparse linear equations and sparse least-squares. *Pages 43–71 of: ACM Trans. Math. Software*, vol. 8. ACM.

Parsons, B., & Sclater, J.G. 1977. An analysis of the variation of ocean floor bathymetry and heat flow with age. *J. Geophys. Res.*, **82**, 803–827.

Patriat, P., Segoufin, J., Goslin, J., & Beuzart, P. 1985. Relative positions of Africa and Antarctica in the Upper Cretaceous: evidence for non-stationary behaviour of fracture zones. *Earth Plan. Sci. Let.*, **75**, 204–214.

Peddie, N.W. 1982. International geomagnetic reference field 1980; a report by IAGA Division I Working Group I. *Geophys. J. R. Astron. Soc.*, **68**, 265–268.

Pilger, R.H., Jr. 1978. A method for finite plate reconstructions, with applications to Pacific-Nazca plate evolution. *Geophys. Res. Let.*, **5**, 469–472.

Press, W.H., Flannery, B.P., Teukolsky, S.A., & Vetterling, W.T. 1986. *Numerical Recipes: The Art of Scientific Computing.* Cambridge University Press.

Rabinowitz, P.D. 1976. Geophysical study of the continental margin of southern Africa. *Geol. Soc. Am. Bull.*, **87**, 1643–1653.

Rabinowitz, P.D., & LaBrecque, J. 1979. The Mesozoic South Atlantic Ocean and evolution of its continental margin. *J. Geophys. Res.*, **84**, 5973–6002.

Raff, A.D., & Mason, R.G. 1961. Magnetic survey off the west coast of North America, 40 degrees N latitude to 52 degrees N latitude. *Geol. Soc. Am. Bull.*, **72**, 1267–1270.

Rea, D.K. 1978. Asymmetric sea-floor spreading and a nontransform axis offset: The East Pacific Rise 20°S survey area. *Geol. Soc. Am. Bull.*, **89**, 836–834.

Royer, J-Y, & Chang, T. 1991. Evidence for Relative Motions Between the Indian and Australian Plates During the Last 20 m.y. From Plate Tectonic Reconstructions: Implications for the Deforemation of the Indo-Australian Plate. *J. Geophys. Res.*, **96**, 11,779–11,802.

Royer, J-Y, Patriat, P., Bergh, H.W., & Scotese, C.R. 1988. Evolution of the Southwest Indian Ridge from the Late Cretaceous (anomaly 34) to the Middle Eocene (anomaly 20). *Tectonophysics*, **155**, 235–260.

Runcorn, S.K. 1959. Rock magnetism. *Science*, **129**, 1002–1011.

Sandwell, D.T. 1981. *Thermal isostasy: spreading ridges, fracture zones and thermal swells.* Ph.D. thesis, UCLA.

Sandwell, D.T. 1984. Thermomechanical evolution of oceanic fracture zones. *J. Geophys. Res.*, **89**, 11401–11413.

Sandwell, D.T. 1992. Antarctic marine gravity field from high-density satellite altimetry. *Geophys. J. Int.*, **109**, 437–448.

Sandwell, D.T., & Schubert, G. 1982. Lithospheric flexure at fracture zones. *J. Geophys. Res.*, **87**, 4657–4667.

Savostin, L.A., Sibuet, J.-C., Zonenshain, L.P., Le Pichon, X., & Roulet, M.-J. 1986. Kinematic evolution of the Tethys belt from the Atlantic Ocean to the Pamirs since the Triassic. *Tectonophysics*, **123**, 1–35.

Schouten, H., & White, R.S. 1980. Zero-offset fracture zones. *Geology*, **8**, 175–179.

Schouten, J.A. 1971. A fundamental analysis of magnetic anomalies over oceanic ridges. *Marine Geophys. Res.*, **1**, 111–144.

Sclater, J.G., & McKenzie, D.P. 1973. Palaeobathymetry of the South Atlantic. *Geol. Soc. Am. Bull.*, **84**, 3203–3216.

Sclater, J.G., Brown, C., Hey, R., Hoskins, H., Pierce, J., Phillips, J., & Tapscott, C. 1976. The Bouvet Triple Junction. *J. Geophys. Res.*, **81**, 1857–1869.

Sclater, J.G., Fisher, R.L., Patriat, P., Tapscott, C., & Parsons, B. 1981. Eocene to recent development of the South-west Indian Ridge, a consequence of the evolution of the Indian Ocean Triple Junction. *Geophys. J. R. Astron. Soc.*, **64**, 587–604.

Sclater, J.G., Munschy, M., Fischer, R.L., Weatherall, P.A., Cande, S.C., Patriat, P., Bergh, H.W., & Schlich, R. 1996. *Geophysical Synthesis of the Indian/Southern Oceans: Part 1, the Southwest Indian Ocean.* Tech. rept. Indian Ocean Data Compilation Project.

Scrutton, R.A. 1973. Structure and evolution of the seafloor south of South Africa. *Earth Plan. Sci. Let.*, **19**, 250–256.

Searle, R. 1981. The active part of Charlie-Gibbs fracture zone: a study using sonar and other geophysical techniques. *J. Geophys. Res.*, **86**, 243–262.

Shaw, P.R. 1987. Investigations of relative plate motions in the South Atlantic using Seasat altimeter data. *J. Geophys. Res.*, **92**, 9363–9375.

Shaw, P.R., & Cande, S.C. 1990. High resolution inversion for South Atlantic plate kinematics using joint altimeter and magnetic anomaly data. *J. Geophys. Res.*, **95**, 2625–2644.

Shipboard Scientific Party. 1988. Site 698. *In:* Ciesielski, P.F., *et al.* (eds), *Proc. ODP, Init. Repts.* 114: College Station, TX (Ocean Drilling Program).

Sibuet, J-C., & Mascle, J. 1978. Plate kinematic implications of Atlantic equatorial fracture zone trends. *J. Geophys. Res.*, **83**, 3401–3421.

Simpson, E.S.W., Sclater, J.G., Parsons, B., Norton, I., & Meinke, L. 1979. Mesozoic magnetic lineations in the Mozambique Basin. *Earth Plan. Sci. Let.*, **43**, 260–264.

Smith, A.G. 1971. Alpine deformation and the oceanic area of the Tethys, Mediterranean, and Atlantic. *Geol. Soc. Am. Bull.*, **82**, 2039–2070.

Smith, A.G., & Hallam, A. 1970. The fit of the southern continents. *Nature*, **225**, 139–144.

Smith, W.H.F., & Sandwell, D.T. 1995. Marine gravity field from declassified geosat and ERS-1 altimetry. *EOS Trans. AGU, fall 1995 supplement*, **76**, F151.

Stein, S., Melosh, H.J., & Minster, J.B. 1977. Ridge migration and asymmetric sea-floor spreading. *Earth Plan. Sci. Let.*, **36**, 51–62.

Stock, J.M., & Molnar, P. 1983. Some geometrical aspects of uncertainties in combined plate reconstructions. *Geology*, **11**, 697–701.

Sykes, L.R. 1967. Mechanism of earthquakes and nature of faulting on the mid-ocean ridges. *J. Geophys. Res.*, **72**, 2131–2153.

Tamsett, D, & Searle, R. 1990. Structure of the Alula-Fartak fracture zone, Gulf of Aden. *J. Geophys. Res.*, **95**, 1239–1254.

Tapscott, C.R. 1979. *The evolution of the Indian Ocean Triple Junction and the finite rotation problem.* Ph.D. thesis, Woods Hole Oceanographic Institution / MIT.

Tapscott, C.R., Patriat, P., Fisher, R.L., Sclater, J.G., Hoskins, H., & Parsons, B. 1980. The Indian Ocean Triple Junction. *J. Geophys. Res.*, **85**, 4273–4739.

Turcotte, D.L. 1974. Are transform faults thermal contraction cracks. *J. Geophys. Res.*, **79**, 2573–2577.

Vine, F.J. 1966. Spreading of the ocean floor: New evidence. *Science*, **154**, 1405–1415.

Vine, F.J., & Matthews, D.H. 1963. Magnetic anomalies over oceanic ridges. *Nature*, **199**, 947–949.

Wegener, A. 1924. *The origins of continents and oceans.* New York: E.P.Dutton & Co.

Weiland, C., Wilson, D.S., & Macdonald, K. 1995. High-resolution plate reconstruction of the southern Mid-Atlantic Ridge. *Marine Geophys. Res.*, **17**, 143–166.

Wessel, P., & Haxby, W.F. 1989. Geoid anomalies at fracture zones and thermal models for the oceanic lithosphere. *Geophys. Res. Let.*, **16**, 827–830.

Wessel, P., & Haxby, W.F. 1990. Thermal stresses, differential subsidence, and flexure at oceanic fracture zones. *J. Geophys. Res.*, **95**, 375–391.

White, R.S., Detrick, R.S., Sinha, M.C., & Cormier, M.H. 1984. Anomalous seismic structure of oceanic fracture zones. *Geophys. J. R. Astron. Soc.*, **79**, 779–798.

Wilson, D.S. 1993. Confidence Intervals for Motion and Deformation of the Juan de Fuca Plate. *J. Geophys. Res.*, **98**, 16,053–16,071.

Wilson, J.T. 1965. A new class of faults and their bearing on continental drift. *Nature*, **207**, 343–347.